Density Functional Theory Studies on Transition Metal Fulleride Complexes and CO$_2$ Capture by Anions, Fullerides, and N-rich Molecular Systems

By

Anila Sebastian

10CC17A39007

A thesis submitted to the
Academy of Scientific and Innovative Research
for the award of the degree of
DOCTOR OF PHILOSOPHY
in
SCIENCE

Under the supervision of
Dr. C. H. Suresh

**CSIR-National Institute for Interdisciplinary
Science and Technology (CSIR-NIIST),
Thiruvananthapuram – 695 019**

Academy of Scientific and Innovative Research
AcSIR Headquarters, CSIR-HRDC campus
Sector 19, Kamla Nehru Nagar,
Ghaziabad, U.P. – 201 002, India

August 2022

Council of Scientific & Industrial Research
National Institute for Interdisciplinary Science and Technology
Thiruvananthapuram-695019, Kerala, India

Dr. C. H. Suresh
Chief Scientist
Chemical Sciences & Technology Division
Tel: +91- 4712515472
E-mail: sureshch@gmail.com
 sureshch@niist.res.in

5th August 2022

CERTIFICATE

This is to certify that the work incorporated in this Ph. D. thesis entitled "**Density Functional Theory Studies on Transition Metal Fulleride Complexes and CO$_2$ Capture by Anions, Fullerides, and N-rich Molecular Systems**" submitted by Ms. Anila Sebastian to the Academy of Scientific and Innovative Research (AcSIR) in fulfillment of the requirements for the award of the Degree of Doctor of Philosophy in Science, embodies original research work done carried out by the student. We further certify that this work has not been submitted to any other University or Institution in part or full for the award of any degree or diploma. Research materials obtained from other sources have been duly acknowledged in the thesis. Images, illustrations, figures, tables, etc., used in the thesis from other sources, have been duly cited and acknowledged.

05/08/2022

Anila Sebastian

5/8/2022

Dr. C. H. Suresh

(Thesis Supervisor)

i

STATEMENTS OF ACADEMIC INTEGRITY

I, Anila Sebastian, a Ph.D. student of the Academy of Scientific and Innovative Research (AcSIR) with Registration No. 10CC17A39007 hereby undertake that, the thesis entitled **"Density Functional Theory Studies on Transition Metal Fulleride Complexes and CO_2 Capture by Anions, Fullerides, and N-rich Molecular Systems"** has been prepared by me and that the document reports original work carried out by me and is free of any plagiarism in compliance with the UGC Regulations on *"Promotion of Academic Integrity and Prevention of Plagiarism in Higher Educational Institutions (2018)"* and the CSIR Guidelines for *"Ethics in Research and in Governance (2020)"*.

Name: Anila Sebastian

Date: 05/08/2022

Place: Thiruvananthapuram

It is hereby certified that the work done by the student, under my supervision, is plagiarism–free in accordance with the UGC Regulations on *"Promotion of Academic Integrity and Prevention of Plagiarism in Higher Educational Institutions (2018)"* and the CSIR Guidelines for *"Ethics in Research and in Governance (2020)"*.

Name: Dr. C. H. Suresh

Date: 05/08/2022

Place: Thiruvananthapuram

DECLARATION

I Anila Sebastian, bearing AcSIR Registration No. 10CC17A39007, declare that my Ph. D. thesis entitled "**Density Functional Theory Studies on Transition Metal Fulleride Complexes and CO_2 Capture by Anions, Fullerides, and N-rich Molecular Systems**" is plagiarism free in accordance with the UGC Regulations on *"Promotion of Academic Integrity and Prevention of Plagiarism in Higher Educational Institutions (2018)"* and the CSIR Guidelines for *"Ethics in Research and in Governance (2020)".*

I would be solely held responsible if any plagiarised content in my thesis is detected, which is violative of the UGC regulations 2018.

Anila Sebastian

Date: 05/08/2022

Place: Thiruvananthapuram

Acknowledgments

CONTENTS

Chapter 1

Part A: Carbon Dioxide Capture and Fullerene Chemistry

Part B: Computational Chemistry Methods

Chapter 2

Formation of Large Clusters of CO_2 Around Anions: DFT Study Reveals Cooperative CO_2 Adsorption

Chapter 3

Part A: Guanidine as a Strong CO_2 Adsorbent: A DFT Study on Cooperative CO_2 Adsorption

Part B: Demarcating Noncovalent and Covalent Bond Territories: Imine-CO_2 Complexes and Cooperative CO_2 Capture

Chapter 4

Part A: Imidazolium-fulleride Ionic Liquids – A DFT Prediction

Part B: Polyanionic Cyano-fullerides for CO₂ Capture

Chapter 5

Part A: Endo- and Exohedral Chloro-fullerides as η^5 ligands: A DFT study on the first-row transition   metal complexes

Part B: Fulleride-metal η^5 sandwich and multi-decker sandwich complexes

List of Figures

List of Schemes

List of Tables

energy per Fe(II) ($\Delta E_{/Fe(II)}$) and the free energy change (ΔG_{total}). Value in kcal/mol at M06L/6-311++G**//M06L/6-31G** level DFT.

List of Abbreviations

AO	: Atomic Orbitals
$[BMIm]^+$	: 1-butyl-3-methylimidazolium cation
BO	: Born-Oppenheimer
BSSE	: Basis Set Superposition Error
CBS	: Complete Basis Set
CC	: Coupled Cluster
CCS	: Carbon Capture And Storage/Sequestration
CG	: Contracted Gaussian
CGTO	: Contracted Gaussian-Type Orbitals
CI	: Configuration Interaction
CP	: Critical Point
DAC	: Direct Air Capture
$[dc]^-$	: dicyanamide
DFT	: Density Functional Theory
$[dtrz]^-$	: 3,5-dinitro 1,2,4-triazolate
DZ	: Double-Zeta
E_b	: Binding Energy
ECP	: Effective Core Potential
$[EMIm]^+$	: 1-ethyl-3-methylimidazolium cation
FMO	: Frontier Molecular Orbital
G	: Guanidine
GGA	: Generalized Gradient Approximation
GTOs	: Gaussian Type Orbitals
HF	: Hartree-Fock
KE	: Kinetic Energy
LDA	: Local Density Approximation
LSDA	: Local Spin Density Approximation
MD	: Molecular Dynamics
MESP	: Molecular Electrostatic Potential

MM   : Molecular Mechanics

MP   : Moller-Plesset Perturbation

NBO   : Natural Bond Orbital

NETs   : Negative Emissions Technologies

$[NH_2tz]^-$: 5-amino tetrazolate

NMR   : Nuclear Magnetic Resonance

PCC   : Post-Combustion Capture

PCM   : Polarizable Continuum Model

PES   : Potential Energy Surface

PGTO   : Primitive Gaussian-type Orbital

QM   : Quantum Mechanics

QTAIM   : Quantum Theory of Atoms In Molecule

QZ   : Quadruple-Zeta

RHF   : Restricted Hartree-Fock

SCF   : Self Consistent Field

STOs   : Slater-Type Orbitals

SCRF   : Self Consistent Reaction Field

SMD   : Solvation Model Density

$[trz]^-$: 1,2,4-triazolate

TZ   : Triple-Zeta

ZPE   : Zero-Point Energy

PREFACE

Carbon dioxide capture and storage (CCS) has been a hot topic of discussion for past few decades, in both theoretical, and experimental studies which aims to isolate, extract, and store carbon dioxide emissions from various sources. CO_2 capture and storage depends on the CO_2 interaction with the storage materials. A covalent interaction can lead to chemisorption while a non-covalent interaction can lead to physisorption. Though CO_2 is electrically neutral, strong electrostatic interactions can develop with charged species due to their polarizability. The theoretical and experimental studies on the interactions between CO_2 and halide ions (anions) and various functional molecules have been a field of interest for a long time. Recent studies have shown that the nitrogen (N)-rich and carbonaceous molecular systems play an essential role in the CO_2 capture. In this regard, the thesis focuses on the interaction of CO_2 with different anionic and N-rich molecular systems using density functional theory (DFT). In this DFT study starting from the simple molecular anions, neutral N-rich molecules like guanidine and its derivatives and cyano-fulleride based ion-pairs are studied for their CO_2 capture capability. Considering the various studies on the application of fullerene in organometallic chemistry, we also analyzed the coordinating ability of the anionic fullerides as η^5 ligand towards transition metal centers. Apart from the structure and energetics molecular electrostatic potential (MESP) based approach has been used to interpret the reactivity of various molecular systems towards CO_2 adsorption. Further, the nature of interaction of the molecular systems with CO_2 has been analyzed using quantum theory of atoms in molecules (QTAIM). The thesis is divided into five chapters.

The first part of **Chapter 1** provides a brief account of various CO_2 capture and storage techniques and important theoretical and experimental works on the capability of fullerene based systems to act as an organometallic η^5 ligand. In **part B**, an overview of computational chemistry and methodologies employed in the thesis are included.

Chapter 2 demonstrates the substantial affinity of the anions such as F^-, Cl^-, Br^-, OH^-, NH_2^-, NO_2^-, CN^-, and ClO^- to bind with a large number of CO_2 molecules. Our findings are based on structure and energetics studies of CO_2 complexes of these anions

at M06L/6-311++G(d,p) level of DFT. The QTAIM electron density analysis, proved the key role of secondary O...C interactions in stabilizing the anionic complexes. Based on QTAIM analysis the total binding energy has been partitioned into primary and secondary contributions. The remarkable ability of the anions to interact with a large number of CO_2 molecules is due to the cooperativity resulting from the secondary O...C interactions which compensate for the weakening of the primary anion...C interactions as the cluster size increases. This property of the anion-CO_2 interactions can be employed for developing anionic or anion-incorporated materials for CO_2 storage.

Chapter 3 is divided into two parts. **Part A** discuss about the substantial affinity of guanidine (G) to bind with a large number of CO_2 molecules. Also the transformation of noncovalent G...CO_2 complex to a strongly interacting G-CO_2 covalent complex under the influence of multiple G and CO_2 is revealed. In comparison to the noncovalent G...CO_2 interaction the $(G-CO_2)_8$ cluster showed a fivefold increase in the binding energy for every G-CO_2 interaction. The N-CO_2 bonding gives $(G^+)-(CO_2^-)$ zwitterion character for G-CO_2 unit and such zwitterion units preferred a cyclic arrangement in $(G-CO_2)_n$ clusters due to the support of three strong intermolecular O...HN hydrogen bonds. The QTAIM analysis confirmed the nature and strength of the covalent/noncovalent interactions in $(G-CO_2)_n$ clusters. MESP analysis also showed that the cyclic cluster is stabilized due to the delocalization of charges accumulated on the $(G^+)-(CO_2^-)$ zwitterion *via* multiple O...HN interactions.

Part B shows the transformation of noncovalent to covalent bonding scenarios between cyclic/acyclic imine based functional molecules (XN) and CO_2. Formation of only noncovalent (**nc**) XN...CO_2 complexes is observed for a group of imines while more saturated imines (XN') produced both **nc** and covalent (**c**) complex $XN'^+-(CO_2)^-$. Also noncovalent and covalent bonding territories are clearly demarcated with the identification of a transition state (**ts**) as the crossover point. Invoking the concept of bond stretch isomerism by Hoffmann, the covalent complex $XN'^+-(CO_2)^-$ stretches from the N-C chemical bond territory through the **ts** to the noncovalent territory to yield XN'...CO_2. Further, conversion of the imine complex **1**...CO_2 to the covalent zwitterionic

complex $CH_3CN...\mathbf{1}^+–(CO_2)^-$ explains a hitherto unknown phenomenon in chemical bonding scenario, the formation of a covalent bond under the influence of a noncovalent bond. When 'n' units of $XN...CO_2$ are assembled, it becomes a covalent cluster of general formula $(XN^+–(CO_2)^-)_n$. The cluster showed multiple $NH...OC$ hydrogen bond interactions between $XN'^+–(CO_2)^-$ units and large positive cooperativity strengthens the N-C coordinate covalent bonding. Exergonic formation of $(XN^+–(CO_2)^-)_n$ cluster suggests potential use of many such imines for CO_2 capture.

Chapter 4 is divided into two parts. **Part A** demonstrates that the exohedral addition of anionic X^- moieties to C_{60} (X = H, F, OH, CN, NH_2, and NO_2) is thermodynamically a viable process to create large X-fulleride anions $(C_{60}X)^-$. The addition of X^- to C_{60} is modelled by locating the transition state for the reaction between C_{60} and 1,3-dimethyl-2X-Imidazole (IMX) at M06L/6-311++G(d,p)//M06L/6-31G(d,p) level. The reaction is slightly endergonic for X = H, F, OH, and NH_2 while X = CN show a significant exergonic character. The X-fulleride formation is not observed when X = Cl and Br. QTAIM analysis showed that C-X bonding in $(C_{60}X)^-$ is covalent while that in $(IM^+...X^-)...C_{60}$ (for X = Cl and Br) is noncovalent. Further, MESP analysis showed that the X-fulleride could behave as a large spherical anion due to the delocalization of the excess electron in the system over the entire carbon framework. The large anionic character of the X-fulleride is also revealed by the identification of several close lying local energy minima for the $IM^+...(C_{60}X)^-$ ion-pair. The low $E_{ion-pair}$ value, significant contribution of dispersion to $E_{ion-pair}$ and spherical nature of the anion predict low melting and highly viscous IL formation from X-fullerides and imidazolium cation.

In **Part B** the formation of imidazolium-based ionic complexes of polyanionic fullerides, $(IM^+)_n...(C_{60}(CN)_n)^{n-}$ from the reaction of C_{60} fullerene with 'n' molecules of 1,3-dimethyl-2,3-dihydro-2-cyano-imidazole (IMCN) is demonstrated. The reaction is exothermic for n = 1 to 6 and can be considered as a thermodynamically viable process to create large polyanionic cyano-fullerides. The MESP analysis has revealed that the extra 'n' electrons in the ion-pair system as well as in the bare $(C_{60}(CN)_n)^{n-}$ are delocalized mainly on the unsaturated carbon centers of the fullerene unit while the CN groups

remain as a neutral unit on the sp^3 carbon. The $(IM^+)_n...(C_{60}(CN)_n)^{n-}$ ion-pair systems showed strong interactions with CO_2 molecules. As the 'n' value increases, the interaction of CO_2 with the carbon cage becomes stronger from -2.3 kcal/mol for n = 1 to -18.6 kcal/mol for n = 6. From the trianionic fulleride onwards, the $C...CO_2$ noncovalent (***nc***) interaction changes to $C—CO_2$ covalent (***c***) interaction with carboxylate character on the adsorbed CO_2. All these results prove that cyano-fullerides are promising candidates for CO_2 capture and conversion.

Chapter 5 is divided into two parts. **Part A** shows the coordinating ability of endohedral and exohedral chloro-fullerides to acts as η^5-ligands. A comparison of the coordinating ability of $Cl^-@C_{60}$ and Cl^-C_{60} with that of Cp^- ligand is done for early to late transition metals of the first row using M06L/6-31G(d,p) level of density functional theory. For each $(Cl^-@C_{60})(ML_n)^+$ and $(Cl^-C_{60})(ML_n)^+$ complex, the energetics for the transformation to C_{60} and ML_nCl is evaluated which showed exothermic character for all endohedral and exohedral Co(I) and Ni(II) complexes. The rest of exohedral complexes, *viz.* the Sc(I), Ti(II), Ti(IV), V(I), Cr(II), Mn(I), Fe(II) and Cu(I), systems showed endothermic value in the range 2 - 35 kcal/mol. The anionic modification makes the C_{60} unit a strong η^5 ligand similar to Cp^- for cationic transition metal fragments. The bulky anionic nature and strong coordination ability of chloro-fulleride ligands suggest new design strategies for organometallic catalysts.

Part B illustrates that similar to Cp^-, the bulky anion, $(C_{60}CN)^-$, acts as a strong η^5 ligand to form sandwich complexes with Fe(II), Ru(II), Cr(II), Mo(II), and Ni(II). The structural parameters of these complexes and the corresponding Cp^- complexes showed very close resemblance. The $(C_{60}CN)^-$ ligand behaved as one of the bulkiest ligands in the chemistry of sandwich complexes. Further, the coordinating ability of the dianion, $(C_{60}(CN)_2)^{2-}$ is evaluated which showed strong coordination ability simultaneously with two metal centers leading to the formation of multi-decker sandwich and pearl-necklace type polymeric structures.

Chapter 1

Part A

Carbon Dioxide Capture and Fullerene Chemistry

Part B

Computational Chemistry Methods
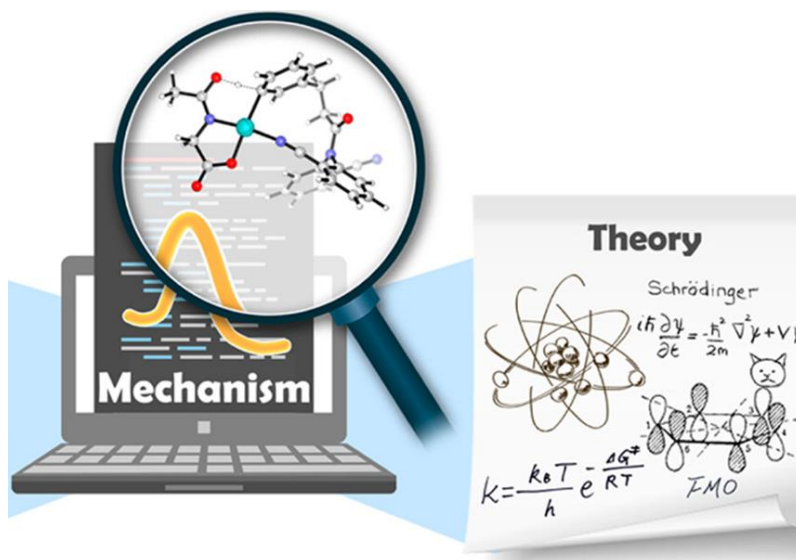
Part A: Carbon Dioxide Capture and Fullerene Chemistry

1.1 Carbon capture and sequestration - The background

Carbon dioxide (CO_2) is a heat trapping gas, which is produced into the atmosphere *via* biological as well as anthropogenic interventions.[1, 2] Though there are other green house gases like CO, CH_4, SO_x, nitrous oxide, water vapor, ozone, and perfluorocarbons/chlorofluorocarbons, the influence of CO_2 on the climate changes is drastic due to its very large percentage of contribution, of almost 75% of greenhouse gases.[3] One detrimental effect of CO_2 is its relatively long residence times, i.e., it remains in the atmosphere for long periods of time. CO_2 along with other greenhouse gases in the atmosphere can trap the heat and thereby lead to drastic climatic changes like global warming. The growing dependancy of mankind on the fossil fuels, for power generation, accounts for the major CO_2 pollutant in the atmosphere, which will not be effectively reduced by the natural carbon cycle process. This alarming situation urgently calls for technologies of CO_2 capture and sequestration (CCS), for the isolation, extraction, and storage of CO_2 emitted from various sources to alleviate the emission of CO_2 into the atmosphere.

There have been several initiatives in national as well as international levels across the globe attempting to control the CO_2 emission and thereby to protect the environment.[4] Kyoto protocol was constituted in 1997 which urged the European Union and 37 industrialized countries to reduce the greenhouse gas emission on an average to 5.7% from 1990 during the period of 2008 to 2012.[5] In 2015 December, a new global agreement to combat climate change under the United Nations framework convention on climate change (UNFCCC) was signed by countries that had an intention to reduce the climatic changes.[6] A recent report in 2021 on the country-wise CO_2 emissions from fossil fuels across the world is shown in Figure 1.1.[7] The top six countries that are responsible for about 60% global CO_2 emission are China, USA, India, Russia, Japan, and Germany.
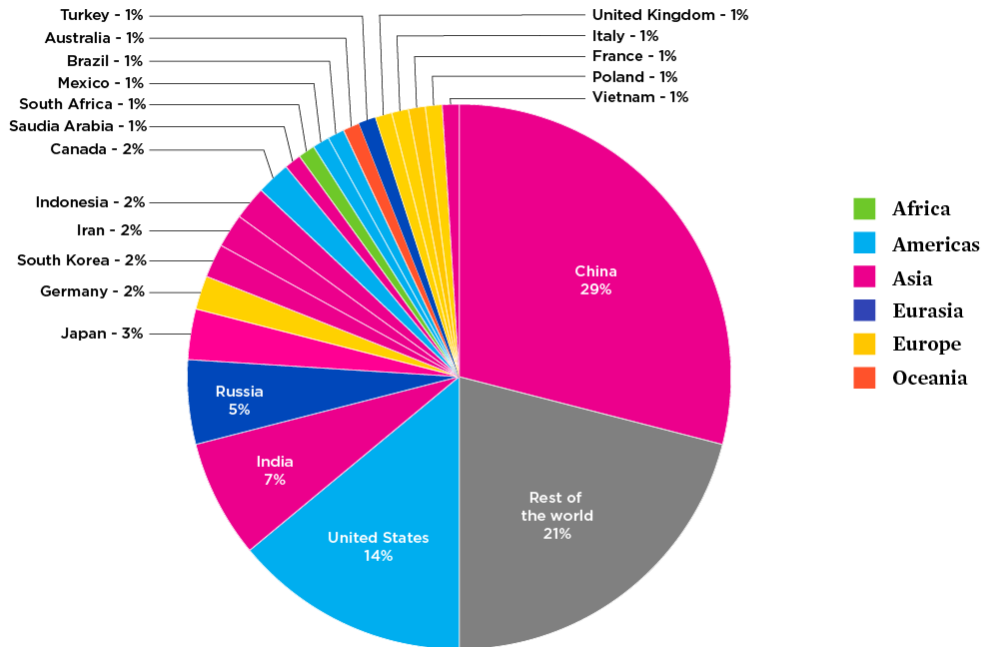
Figure 1.1 Worldwide CO_2 emission by various countries.[8]

CO$_2$ emissions to the atmosphere continue to steadily increase every year over the past century out of human activity leading to a rise in the atmospheric concentration of CO$_2$ from the preindustrial value of 280 ppm to 412 ppm in 2021.[9-11] Global energy-related CO$_2$ emissions rose by 6% in 2021 to 36.3 billion tonnes, their highest ever level, as the world economy rebounded strongly from the Covid-19 crisis and relied heavily on coal to power that growth.[12] The Intergovernmental Panel on Climate Change (IPCC) has reported in their Fifth Report (2013 and 2014 projects data) that the global surface temperature will likely increase anywhere from 0.3 to 4.8°C relative to 1986–2005 data.[13, 14] Based on the first installment of the IPCC's sixth assessment report, the climate impacts are already more widespread and severe than expected.[15] We are locked into even worse impacts from climate change in the near-term and the risks will escalate quickly with higher temperatures, often causing irreversible impacts of climate change. The next few years offer a narrow window to realize a sustainable, livable future for all. To reduce atmospheric CO$_2$ concentration and thereby to manage the long-run risks of persistent climate changes it has become highly important to remove CO$_2$ from the air faster than nature does.[16, 17] Changing course will require immediate, ambitious and

concerted efforts to slash emissions, build resilience, conserve ecosystems, and dramatically increase finance for adaptation and addressing loss and damage. CO_2 capture was proposed by the IPCC as a technology necessary to restrain the growing atmospheric CO_2 concentration, is getting more prominence in the past decade.[18]
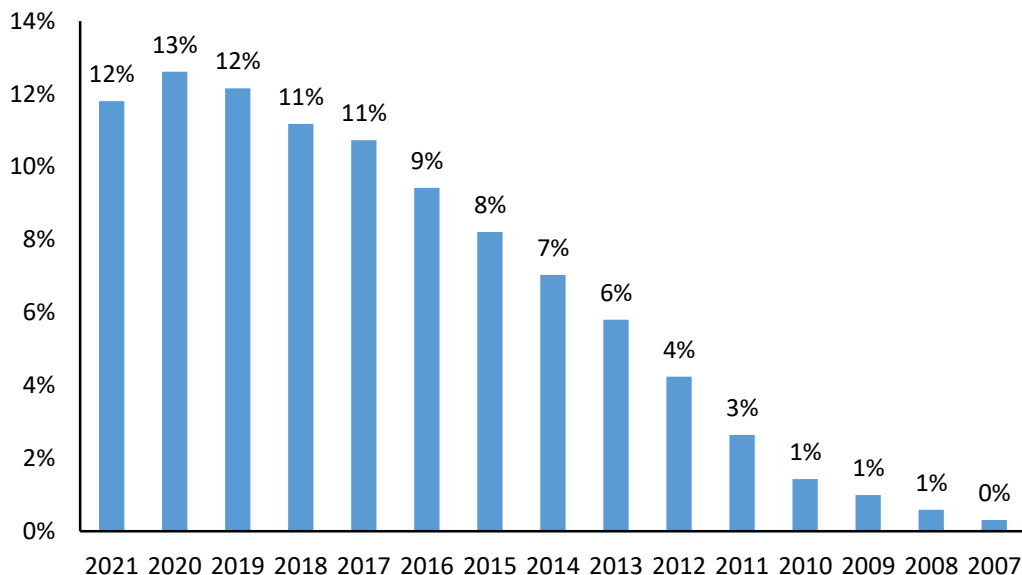
Figure 1.2 Year-wise classification of publications on CO_2 capture and/or adsorption from the year 2007 to 2021.
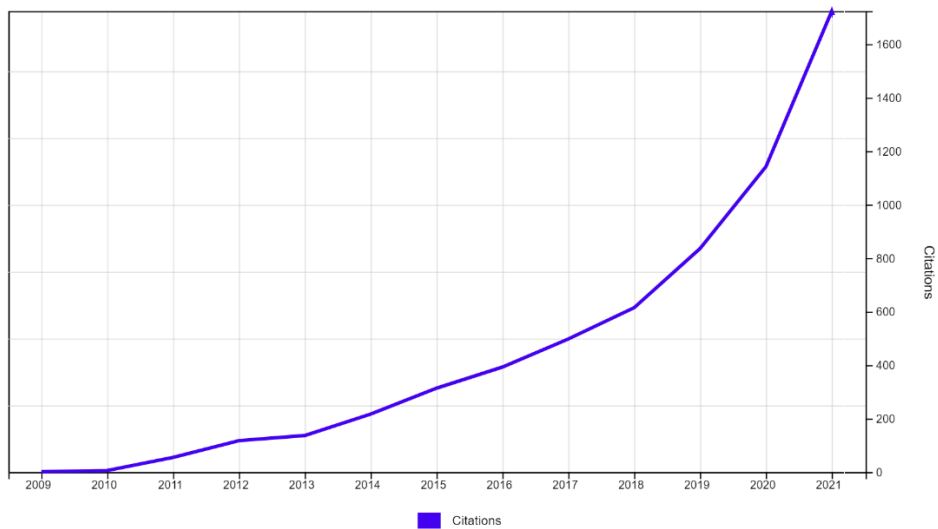
Figure 1.3 Citation report of DFT study in CO_2 capture and/or adsorption for past 12 years.

Many researches are proceeding globally in the field of CO_2 capture technologies to come up with better solution to the growing concern of tremendously increasing atmospheric CO_2 levels.[19] Large number of reviews/articles and a number of patents filed under this topic shows the depth of the research getting shape in this area.[20-22] Figure 1.2 gives year-wise distribution of publications on CO_2 capture and/or adsorption based on the year of their publication. The demand for better technologies is keeping this field of research proactive. A number of patents are also getting filed across the globe. Derwent innovations index shows a total of 13 patents in the research of nitrogen-rich materials for CO_2 capture. In addition to the experimental studies several theoretical studies also support the research in CO_2 capture. The increasing citation index of the DFT studies on CO_2 cpature and /or adsorption in the past 12 years (Figure 1.3) again shows the increasing passion in this particular field of research.

The conventional methods of CO_2 capture were to solve the CO_2 emissions from large stationary sources, like fossil-fuel based power stations, cement plants, oil refineries, and iron or steel industry installations.[19] Though we are running out of the conventional energy sources, the increasing energy demands in various fields of life never end. This calls for the urgent shift from the conventional non-renewable energy sources to renewable energy sources. However, complete decarbonization still appears to be highly challenging as we still depend on various non-renewable energy sources resulting in the release of tens of billions of tons every year. In this phase, the development of efficient CO_2 capture systems engaged with the continuous production of power from fossil fuels is attractive since it can drive the sustainable development of fossil-fired energy technologies with near-zero emissions.

Carbon capture and storage/sequestration (CCS) refers to the set of technologies to capture the CO_2 gas in the atmosphere released by all sources including industries, power sectors, anthropogenic, etc., followed by handling the gas, transporting it, and storing it in a place which will not release the gas to the atmosphere once again, for example, injection and storage in deep geological formations.[23, 24] Without limiting access to fossil energy resources the level of CO_2 in the atmosphere could be controlled only if CO_2 is collected and disposed of away from the atmosphere at concentrated sources itself,

without ever letting it enter the atmosphere. Due to the fundamental infrastructural obstacles and the prohibitively expensive side, this method of CO_2 capture right at the sources itself seems to be impossible.[25] CO_2 disposal technologies are usually classified as pre-combustion (reduces the carbon capacity of fuels before combustion occurs), post-combustion (flue gases generated after combustion are cleaned), and oxy-fuel combustion (makes use of pure O_2 as oxidizer) (Figure 1.4).[26]
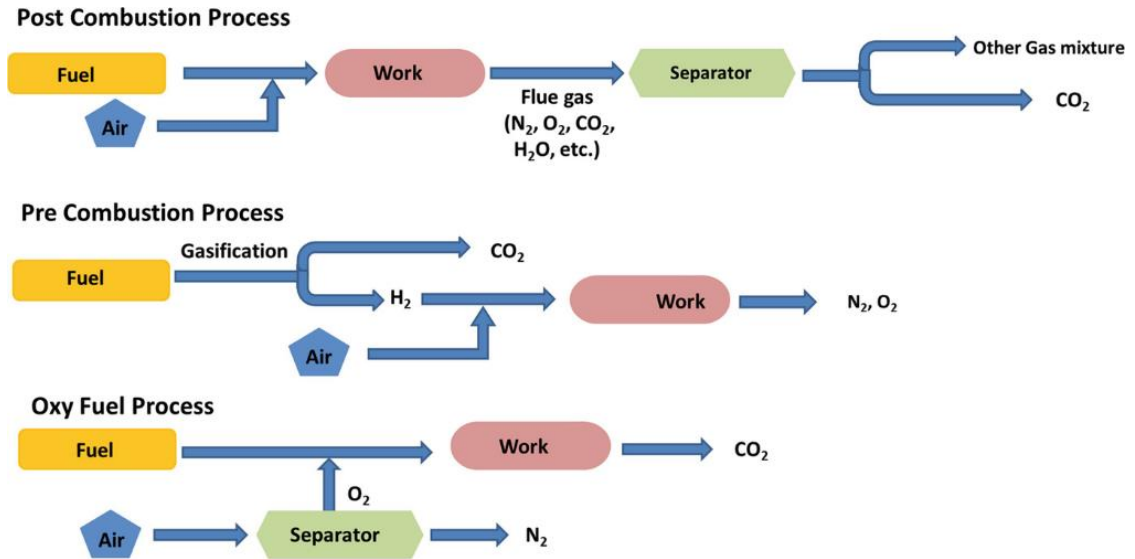
Figure 1.4 Pictorial representation of the three CCS processes.[26]

Among the currently available technologies for capturing CO_2, post-combustion capture (PCC) is the most easily applied technology for existing sources of emissions (Figure 1.5). PCC uses both wet and dry adsorbents for gas separation and separates and collects CO_2 by adsorption/desorption. In general, PCC technologies include dry adsorption, wet absorption, membrane-based technologies, and cryogenics. Wet absorption is good for treating large emission volumes from combustion and is very useful for changing the density of CO_2; however, it requires high energy for absorbent regeneration. Amine scrubbing is a robust technology, which has been used to separate CO_2 from natural gas and hydrogen since the 1930s in both dry and wet forms.[27] For industrial applications, aqueous solutions of amines are extensively used as chemical absorbents or solvents. However, amine reaction with CO_2 results in stable carbamate formation, which in turn leads to high energy usage for regeneration and promotes

additional corrosion problems. Also, the amine solutions decompose over time and their CO_2 capturing ability decreases significantly.[28] Current research focuses on dry adsorption systems using dry adsorbents.
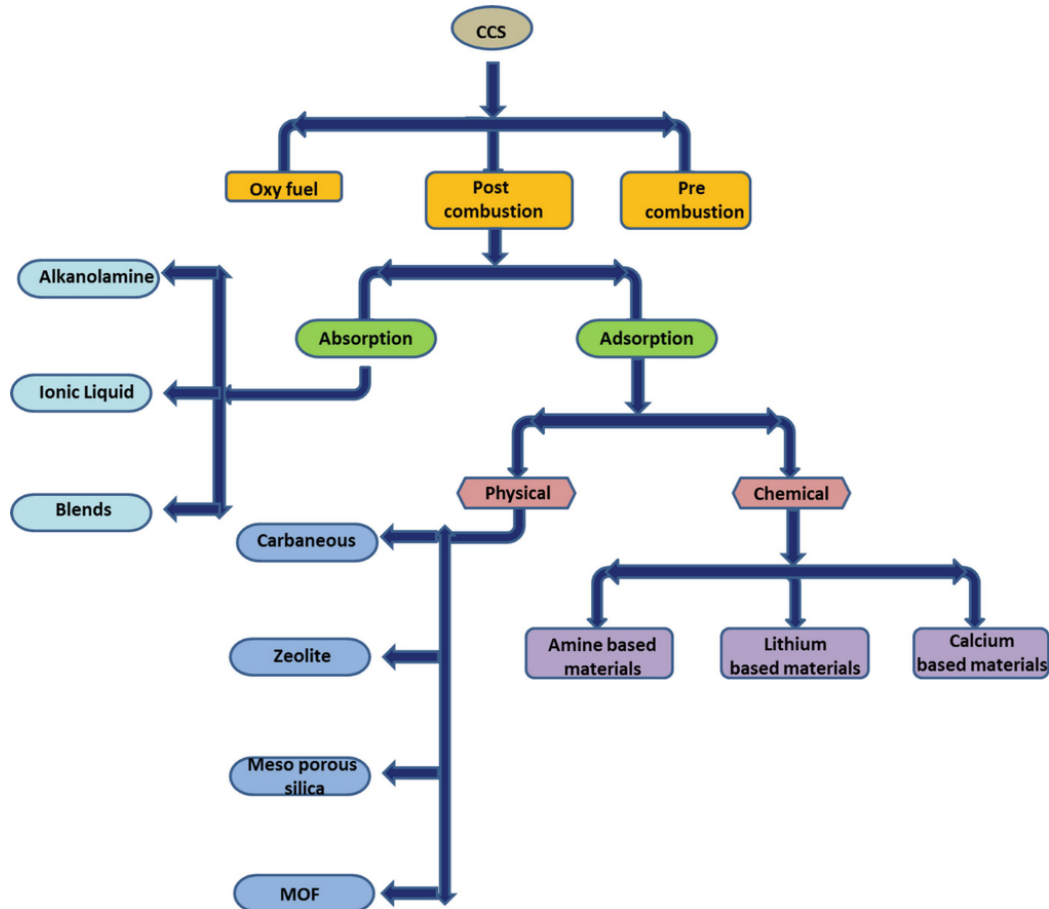
Figure 1.5 Overview of different techniques under CCS process.[26]

While CCS technologies have traditionally been implemented at point sources of CO_2 emissions, recent integrated assessment models have increasingly emphasized the need for negative emissions technologies (NETs) to limit global warming below 2 °C by 2100.[29, 30] NETs can capture the CO_2 from discrete emitters involved in transportation, which currently account for about 50% of the annual greenhouse gas emissions. NETs when coupled with efficient methods to convert the CO_2 removed from air into fuels using renewable energy sources have the potential to close the carbon cycle and generate carbon-neutral fuels.[31-33] One promising approach among various NETs, like afforestation/reforestation, or bioenergy with carbon capture and storage (BECCS),

which aim at reducing the atmospheric CO_2 concentration is direct air capture (DAC), a process that removes CO_2 from the air by engineered chemical reactions.[34, 35]

Compared to other NETs, which are constrained by land availability and present threats to biodiversity and food security, DAC has the potential for high capacity, the flexibility of placement, and the generation of high-purity CO_2 streams. However, the most significant challenge with DAC is the very low atmospheric concentration of CO_2 (about 0.04%), thereby requiring sorbents that can bind CO_2 quickly, strongly, and selectively against other components in the air, which will, in turn, result in the requirement of large energy inputs and high temperatures for release of the CO_2 and to regenerate the sorbent.[36] Many sorbents have been studied for CO_2 capture for the past few decades for the physisorption as well as for the chemisorption of CO_2 from the atmosphere. The interaction between the sorbate and sorbent is said to be chemisorption when a chemical bond is formed between them, whereas physisorption relies on typically weaker physical interactions such as van der Waals or ion–quadrupole interactions. Each of the methods of sorption technique has its own virtues and drawbacks. The sorbent regeneration is energetically much easier for materials operating through physisorption than from chemisorbed materials because of the weaker bonds. However, at atmospheric CO_2 levels, lower selectivity and uptake capacity is observed for physisorption due to the reduced thermodynamic drivers for CO_2 capture. Although most of the air capture processes use solid sorbents, the sorbents can be liquids[37-39] or solids[40]. In this thesis, we will be focusing more on the nitrogen(N)-rich sorbents used in CO_2 captures like amines, amino acids and their derivatives, N-rich compounds like guanidine and its derivatives, and nitrogen doped materials.

1.1.1 Amines as CO_2 sorbents

The application of aqueous amine solutions is one among the primitive CO_2 capture techniques used for the separation of CO_2 from CO_2-rich natural gas stream, like those used in submarines to purify breathing air.[27] Two different sorption mechanisms are observed: in dry conditions and in moist conditions. In dry conditions, primary and secondary amines react with CO_2 to form carbamate or carbamic acid.[41-43] Pinto *et al.*

studied CO_2 sorption by amine-modified materials under dry conditions *via* solid-state NMR spectroscopy. [42] They found that a fraction of carbamic acid could remain unreacted when a large amount of CO_2 is incorporated and only a small amount of R-NH_2 is still available. In this case, carbamic acid is produced during CO_2 sorption. In moist conditions, amines react with CO_2 to produce bicarbonate.[44, 45] Though this process is comparatively mature, its high heat capacities and their heat losses from evaporation make the process of regeneration energy intensive and costly which stops its use in the long run.

Amine/Ammonia + CO_2+ H_2O $\longrightarrow$ Ammonium Carbonate/Ammonium Bicarbonate

(Eq. 1.1)
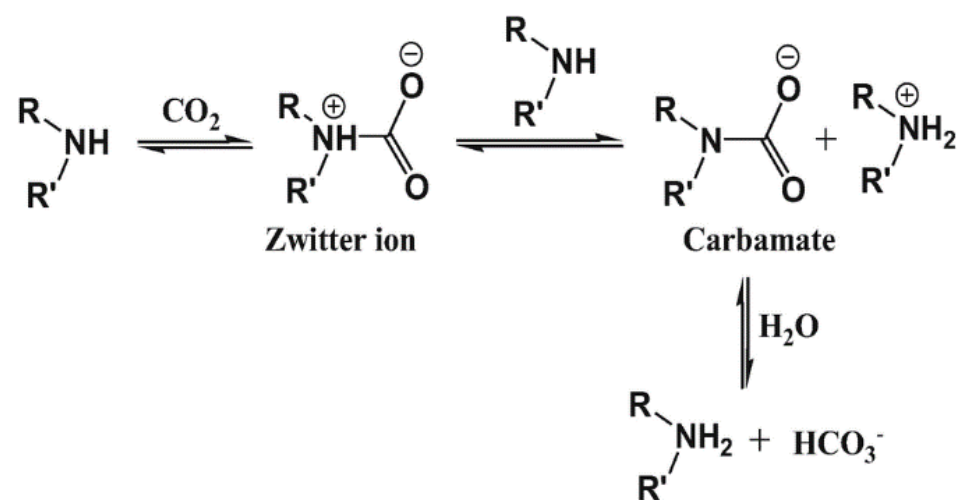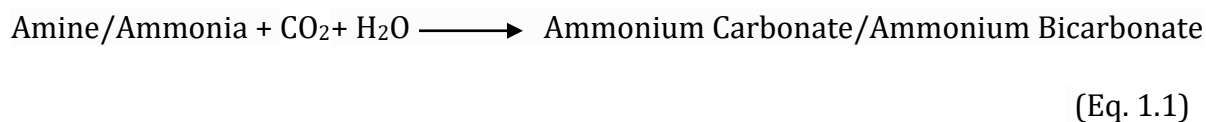
Scheme 1.1 Schematic representation of primary and secondary amine reacting with CO_2 in presence of water and formation of bicarbonates.[4]

Amines and polyamines on solid supports have been proposed to lower energy costs.[46] The studies reported so far on sorbents for DAC of CO_2 have focused on the use of solid-supported amine materials.[47, 48] The interaction between the sorbate (CO_2) and the sorbent (supported amine materials) is the chemisorption and it involves a chemical reaction between CO_2 and the amines, creating strong bonds and allowing significant uptakes even at low CO_2 partial pressures (Scheme 1.1). The associated heat of sorption and the selectivity toward CO_2 are higher for physical sorbents and this makes organic–inorganic hybrid materials based on amines highly suitable for direct air

capture.[35] The mechanism of CO_2–amine reaction under anhydrous conditions was explained by Caplow and Danckwerts and this mechanism requires one CO_2 molecule and two primary (Eq. 1.2) or secondary amine moieties (Eq. 1.3) to give an ammonium carbamate.

$$CO_2 + 2RNH_2 \longleftrightarrow RNH_3^+ + RNHCOO^- \qquad \text{(Eq. 1.2)}$$

$$CO_2 + 2R_1R_2NH \longleftrightarrow R_1R_2NH_2^+ + R_1R_2NCOO^- \qquad \text{(Eq. 1.3)}$$
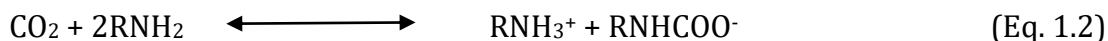
The amine-containing sorbents can be divided into three classes: (i) class 1 sorbents, prepared by impregnating amines into the pores of support, (ii) class 2 sorbents, consisting of amines covalently bonded to the walls of porous materials, and (iii) class 3 sorbents, where amine monomers have been polymerized in situ, resulting in polyamine structures bound to the walls. [49, 50] Jafari *et al.* reported a series of highly hydrophobic porous organic polymers of poly divinylbenzene (PDVB) with amine modification vinyl imidazole (VI) and vinyl triazole (VT) resulting in PDVB-VI and PDVB-VT adsorbents.[51] They observed maximum CO_2 adsorption of 2.65 mmoleg^{-1} at 273 K/1 bar, for triazole-based adsorbent (PDVB-VT) with 0.7 g of VT. Theoretical modeling confirmed the active site is nitrogen on the imidazole/triazole ring and that incorporation of VT into the polymeric networks enhanced the adsorptive properties better than vinyl imidazole (VI) due to more active sites. Alahmed *et al.* combined two approaches—electrostatic and covalent attachment—to maximize amine loading in 4,4′-bis(chloromethyl)-1,1′-biphenyl (BCMBP)-derived hypercrosslinked polymers (HCPs) in an attempt to increase CO_2/N_2 selectivity.[52] Their study showed that decoration of the parent polymer with CO_2-philic imidazole followed by electrostatic ammonium salt incorporation blocked some of the micropores reducing the selectivity which re-emphasizes the role and importance of pore width for CO_2/N_2 selectivity. The area of research on amines as CO_2 sorbent is so wide that a large number of reviews are available in this particular area.[53-56] Two potentially attractive fields of application were identified for the CO_2 capture on supported amine sorbents: (1) production of CO_2 enriched air using low regeneration temperatures and (2) the production of pure CO_2 at elevated

pressure.[57] The latter option may be considered for geoengineering (*via* CCS) or for synthetic fuels from renewable energy and atmospheric CO_2.

1.1.2 Nitrogen doped materials for CO_2 capture

Various carbon capture materials have been developed in the past few decades as a promising solution for reducing CO_2 emissions. However, adsorbent materials that are tolerant to the humid condition of real flue gases are rare.[58-60] Wang *et al.* obtained N-rich porous material which showed excellent CO_2 capture capacity (18.2 wt%) and CO_2/N_2 selectivity (45 at 273 K and 42 at 298 K).[61] This showed higher activities for the conversion of pure CO_2 or a mixture of gases (CO_2:N_2 = 15:85) into various cyclic carbonates than homogeneous catalysts under mild conditions, which demonstrated a synergistic effect of selective CO_2 capture and conversion between a porous azo polymer and its supported metal catalyst.

Kou *et al.* reported the application of nitrogen-doped porous carbons (NPCs) for CO_2 capture.[62] They used nitrogen-rich polymer NUT-1 (NUT represents Nanjing Tech University) as the precursor, for the first time, which on carbonization at temperatures ranging from 500 to 800^0C yielded a series of NPCs possessing various porosity and nitrogen contents. The adsorption performance of NPCs is dependent on their pore structure and nitrogen doped "CO_2-philic" sites. The optimum material NPC-1-600 exhibits much higher adsorption capacity (7.5 mmolg−1 at 273 K and 1 bar,) than benchmark materials including 13X zeolite and activated carbon as well as most if not all reported carbon-based adsorbents. No visible loss of adsorption capacity was observed in the adsorption of CO_2 even after seven cycles of adsorption.

Aminal-linked inorganic-organic hybrid nanoporous materials (HNMs) with cyclophosphazene moieties in the frameworks were synthesized through a Schiff base condensation by Raeesh *et al.*, which could capture 18.9 wt% CO_2 at 273 and 77 K.[63] Structure-thermodynamic-property relationships of cyanovinyl-based microporous polymer networks were explored by Yassin *et al.* for the future design of advanced carbon capture materials.[64] Their study has shown that isosteric heats of CO_2 adsorption are directly proportional to the amount of their functional group. This was also supported by

the theoretical calculations which showed the increase of binding sites with the increase of Ph-C-C(CN)-Ph functionality in a network. The influence of nitrogen moieties on CO_2 capture by polyaminal-based porous carbon was investigated by several groups. [65-70] Nitrogen-rich porous polymers (NRPPs) derived from 4-bis-(2,4-diamino-1,3,5-triazine)-benzene building block was prepared and tested for use in CO_2 capture by Abdelmoaty *et al.* and they found that combination of high nitrogen content, π-electron conjugated structure, and microporosity makes NRPPs very effective in CO_2 uptake and capture.[71] Walczak *et al.* illuminated the origin of the strong interaction between CO_2 and N-rich carbon materials prepared by molecular design and they also have shown the general possibility of CO_2 molecular sieving with metal-free materials.[72] Superiority of the N-doped carbon derived from polypyrrole in the development of CO_2 capture from humid flue gases was confirmed by Wang *et al.*[73] Selectivity in CO_2 adsorption was fabricated by Song *et al.*[74] from cross-linkable linear polyimides whereas the same was demonstrated by Principe *et al.*[75] *via* melamine-resorcinol-formaldehyde xerogels.

1.1.2.1 Nitrogen doped MOFs for CO_2 capture

Dooris *et al.* synthesized a series of metal-organic framework (MOF) materials using a range of metal centers (Co, Ni, and Zn) with the 1,4-bis(pyridin-4-yl)-1,2,4,5-tetrazine (pytz) organic linker, in the presence of ammonium hexafluorosilicate.[76] Three new MOF materials *viz.* Zn-pytz(hydro) 1D chains, and Ni-pytz and Co-pytz isostructural 1D Ladders, with embedded Lewis base functionalities, imparted by the nitrogen-rich ligand, has displayed an affinity for CO_2. Co-pytz shows an uptake of 47.53 mg CO_2/g of sorbent, which equates to 15 wt% based on available nitrogen sites within the structure, demonstrating the potential for carbon capture applications.

In 2016 Wang *et al.* came up with a series of N-rich porous carbons derived from polyamine-incorporated metal-organic framework materials which displayed a high CO_2-selective capture performance.[77] Simulation studies by Forrest *et al.* have shown CO_2 sorption in an rht-metal-organic framework with 1,2,3-triazole groups.[78] A combined experimental and computational investigation for remarkable gas/vapor sorption, selectivity, and affinity by a porous nitrogen-rich covalent organic framework (COF) was carried out by Das *et al.* through a triazine-based benzbis(imidazole)-bridged COF

(TBICOF) has been synthesized under polycondensation conditions.[79] CO_2 sorption is highly selective over N_2 and CH_4 because of very strong interactions between CO_2 and triazine and benz-bis(imidazole)-functionalized pore walls of TBICOF as clearly evident from the isosteric heat of adsorption and ideal adsorbed solution theory calculation, which is higher than other reported functionalized MOFs or COFs. Computational studies based on density functional theory and grand canonical Monte Carlo molecular simulations further support the selectivity of CO_2 (over N_2 and CH_4). MOFs and COFs-based CO_2 capture is one of the most developing areas of materials research in past few decades.[80]

1.1.3 Amino acids for CO_2 capture

Amino acids behave as base, neutral, or zwitterion depending on the pH values.[81] Due to the similar functional group between amino acids and alkanolamines, the reaction mechanism of the amino acids can be considered as those of alkanolamines. Based on the reactions of amino acids with CO_2, the base form of amino acids is the active form. Therefore, amino acids need to be deprotonated to react with CO_2 at neutral pH.[82, 83] Some of the bases considered to neutralize amino acids are MEA, KOH, and NaOH. The deprotonation step is necessary in order to make the amine group reactive toward CO_2.[84, 85] Amino acids are potential candidates for CO_2 capture. Current studies mainly focus on the thermodynamic properties and kinetic reaction of amino acids with CO_2. Along with the determination of the properties of the amino acids, the performance of several amino acids for CO_2 capture in small-scale technologies has been studied. Amino acids' performance is similar to or in some cases better than the conventional solvents. CO_2 capture with a high concentration of amino acids and high CO_2 loadings leads to precipitation of the amino acid or (bi) carbonates or a mixture of both.[86] Following scheme 1.2 gives the CO_2 by absorption with aqueous amino acids and carbonate crystallization as studied by Seipp *et al.* with bis-iminoguanidine ligands (BIGs).[87]
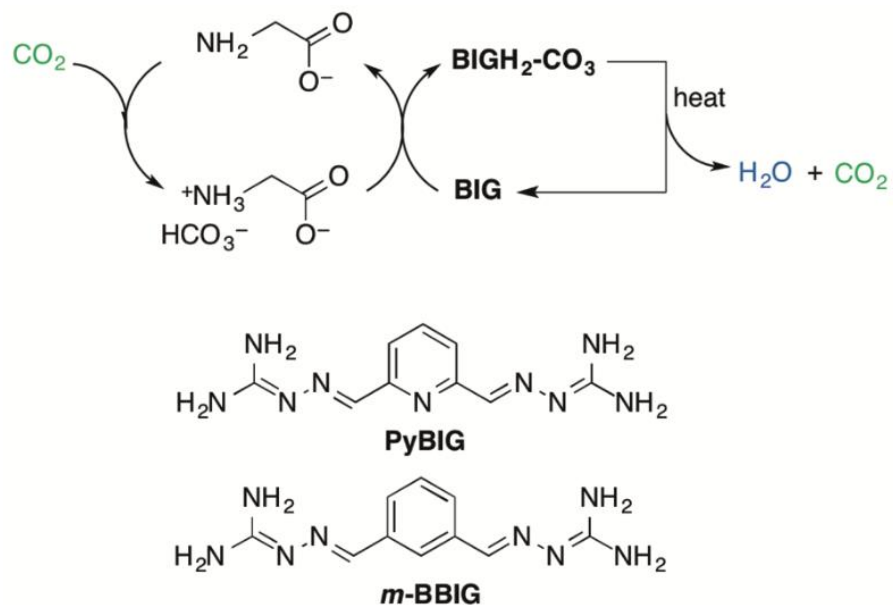
Scheme 1.2 DAC of CO_2 by absorption with aqueous amino acids and carbonate crystallization with BIGs.[87]

1.1.4 Amino acid/ Guanidine related compounds as CO_2 sorbents

A bench-scale study on the direct air capture (DAC) process was carried out by Custelcean *et al.* comprising CO_2 absorption with aqueous amino acid salts (i.e., potassium glycinate, potassium sarcosinate).[88] The amino acids were regenerated by reaction with solid meta-benzene-bis(iminoguanidine) (mBBIG), resulting in crystallization of the hydrated m-BBIG carbonate salt, which on mild heating released CO_2. Though first reported in 1898 by the German chemist Johannes Thiele,[89] iminoguanidines are grabbing more attention in the last two decades due to the studies by Custelcean *et al.* showing its high recognition abilities towards hydrophilic oxyanions through strong and complementary hydrogen bonding from the guanidinium groups.

The same group has came up with the observation of using guanidine, an amino acid-related compound as a potential CO_2 sorbent.[90, 91] An aqueous solution of 2,6-pyridine-bis(iminoguanidine) (PyBIG) that was left open to ambient air for a few days led to the formation of large prism-shaped single crystals with an elemental composition consistent with the tetrahydrated carbonate salt of PyBIG (PyBIGH$_2$(CO$_3$)(H$_2$O)$_4$). Single-

crystal X-ray diffraction analysis confirmed this composition. Custelcean *et al.* also patented guanidine compounds for carbon dioxide capture (US10583387B2).[92] The guanidine like aminoacid related compounds are now being investigated for the CO_2 adsorption in CCS.

In the area of CO_2 capture and conversion with guanidine and related compounds, 1,5,7-triazabicyclo[4.4.0]dec-5-ene (TBD) compound is widely studied for CO_2 interactions. In 2003, Barbarini *et al.* reported a comparative study of the catalytic efficiency of homogeneous guanidine 7-methyl-1,5,7-triazabicyclo[4.4.0]dec-5-ene (MTBD) and heterogeneous MCM-41- TBD in the cycloaddition of CO_2 with epoxides. They concluded that reactions performed with heterogeneous catalyst are slower than that with homogeneous MTBD but show the great advantage that the catalyst can easily be recovered and reused for at least three further cycles.[93] The reaction of TBD with CO_2 has been studied in different aspects by various groups. In the synthesis of cyclic carbonates by employing polyethylene glycol (PEG)-functionalized basic ionic liquids as an efficient and recyclable catalyst, Yang *et al*. proposed a mechanism where the secondary nitrogen of the TBD core reversibly coordinates with CO_2 to afford the carbamic acid.[94] This activated form of CO_2 then interacts with the epoxide through hydrogen bonding, resulting in epoxide activation. In 2013, Wei-Li *et al.* reported a series of functional guanidinium-based ionic liquids (FGBILs) that contain both Lewis acid and basic sites. They used these compounds as catalysts for the synthesis of cyclic carbonates through the cycloaddition of CO_2 to epoxides in the absence of any co-catalyst or solvent.[95] In 2013, Wang *et al.* reported TBD -mediated carboxylation of acetylene and alkynes using CO_2.[96] They proposed a reaction mechanism in which acetylene carboxylation was initiated by the formation of the TBD–CO_2 adduct, which subsequently undergoes nucleophilic addition of acetylene to afford the propiolate TBD salt. The authors concluded that although TBD-mediated CO_2 additions to alcohols and amines have been reported previously, the TBD-mediated carboxylation of acetylene was reported for the first time under conditions that are free of transition metals, inorganic salts, and organometallic reagents. Depending on the alkyne substituent, the reactions also proceed without the use of any solvent. Nicholls *et al.* reported that while cyclic

guanidines TBD and MTBD form stable and detectable complexes with CO_2, guanidine TMG and tertiary amines (TEA and DABCO) do not.[97] Villiers *et al.* have synthesized and characterized the isolated nitrogen-base–CO_2 adduct, TDB-CO_2 including its X-ray crystal structure, and suggested that this species could enable the activation of CO_2 for catalytic conversion into high-value chemicals.[98] The X-ray diffraction analysis and theoretical calculations showed the zwitterionic nature of TBD-CO_2, with a N–C(CO_2) distance of 1.48 A°. The TBD-CO_2 adduct was readily transformed into the bicarbonate salt [TBDH$^+$][HCO$_3^-$] in the presence of water, either in the solid state in the air or in solution in wet solvents. Concurrently Ma *et al.* described a theoretical study on the mechanism of the reaction of propylene glycol with CO_2 catalyzed by TBD by using DFT at the B3LYP/6-311++G(d,p) level. Through analyzing the optimized structures and energy profiles along the reaction pathways, the propylene glycol-activated route was identified as most likely.[99]

Pérez *et al.* suggested that CO_2 is nucleophilically activated by 1,8-diazabicyclo[5.4.0]undec-7-ene (DBU) forming a DBU-CO_2 zwitterionic carbamate complex.[100, 101] Simultaneously, Jessop *et al.* reported that the reaction between DBU and CO_2 only forms the DBU bicarbonate salt [DBUH$^+$] [HCO$_3^-$] in the presence of water, and there is no reaction in the absence of water.[102] González *et al.* suggested that carbamate formation is favored in dry DBN but in the presence of water, decomposition occurs into the bicarbonate.[103] They also reported a study of CO_2 fixation – activation by the guanidines, TBD and tetramethylguanidine (TMG) which discussed the nature of the guanidine-CO_2 complexes and the CO_2 fixation and release by these guanidines.[104] These guanidines formed bicarbonates presumably *via* the preceding formation of water-solvated carbamic intermediates. CO_2 fixation with both TBD and TMG was a kinetically reversible process. The corresponding fixation products were shown to be useful as transcarboxylating agents, and this behavior mimics a transcarboxylase activity. TBD-CO_2 products display interesting thermal stability with CO_2 release occurring at moderated temperatures. This could be useful for the selective separation of CO_2 from complex gas mixtures by TBD or TBD-related compounds. In 2010, Prasetyanto *et al.* synthesized melamine tri-silsesquioxane (TBTS) bridged periodic mesoporous organosilica and investigated this hybrid organic-inorganic material as a catalyst for the

CO_2 activation in the coupling of propylene oxide with CO_2.[105] Rether *et al.* showed the formation of stable dimers of guanidinium based zwitterion in both solid as well as in solution.[106] They also explained the importance of the planar arrangement of the zwitterion fragments in the dimerization, as head-to-tail dimers assisted *via* a network of six hydrogen bonds, which was confirmed by X-ray crystallography.

Very recently Lukas *et al.* reported the first photoswitchable nitrogen superbases based on guanidines equipped with a photochromic dithienylethene unit.[107] Through multiple cycles they have shown that these N-heterocyclic imines (NHIs) undergo reversible, near quantitative electrocyclic isomerization upon successive exposure to UV and visible irradiation. This photoswitching between the ring-opened and ring-closed states is associated with a substantial pK_a shift of the NHIs by up to 8.7 units and only the ring-closed isomers are sufficiently basic to activate CO_2 *via* the formation of zwitterionic Lewis base adducts. Thus the cycling between the two isomeric states enables the light-controlled capture and release of CO_2.

1.1.5 Carbonaceous materials for CO_2 capture

Besides the amine scrubbing,[27, 28] contemporary research on CO_2 capture focuses on dry adsorption systems using dry adsorbents. Adsorption is a separation technology with the potential to reduce the cost of PCC.[108] The process of capturing CO_2 using a dry adsorbent involves selective separation of CO_2 based on gas–solid interactions. In general, universal dry adsorbents such as activated carbons and molecular sieves are used in packed columns.[109] Though metal-organic frameworks (MOFs) have emerged as solid CO_2 adsorbent materials due to their tunable chemical and physical properties, still there is a growing interest in metal-free carbon-based materials for gas adsorption.[110-113] Carbon-based nanomaterials such as fullerene, carbon nanotubes, graphene, and hetero-fullerenes[114] offer excellent thermal and chemical stability as CO_2 adsorbents.[69, 115, 116] Fullerenes, the class of hollow-spherical molecules comprising only C atoms varying in number,[117] exhibit low reduction potentials, and strong electron acceptor properties.[118, 119] Zhang *et al.* have shown that the inner cavities of many fullerenes and carbon nanotubes are regions of positive electrostatic potential, and are electron-

withdrawing in character.[120] Many theoretical[121, 122] and experimental[123-125] studies have been carried out on endohedral[126-128] as well as exohedral[117, 129] modifications on the fullerene cage. In the case of endohedral fullerenes, the encapsulated species influence the reactivity. Apart from these endohedral modifications on fullerenes the exohedral changes also have an influence on the chemical reactivity and properties of the C_{60} cage.[130, 131] Their electronic properties such as the complexation energy, ionization potentials, and the stability concerning internal electron transfer can be determined by the electrostatic potential at the cage center.[132]

Fullerene-based systems have been used as adsorbents for various gases. B. Gao $et\ al.$[133] studied CO_2 adsorption on calcium decorated C_{60} fullerene and F. Gao $et\ al.$[134] studied O_2 adsorption on nitrogen-doped fullerene. Sun $et\ al.$[115] predicted enhanced CO_2 adsorption on $1e^-$- and $2e^-$-charged boron nitride sheets and nanotubes, which show very little chemical affinity towards CO_2 in their neutral state. They also showed that chemical interactions between boron–carbon nanotubes (B_2CNT) and CO_2 can be enhanced by introducing extra electrons to the system.[135] They explained that the enhanced interactions are due to the Lewis acidity of CO_2, which prefers to accept electrons. Further, Jiao $et\ al.$ proved the enhanced interaction of CO_2 with adsorbent materials by electron injection.[136] de Silva $et\ al.$ investigated the CO_2 adsorption on BC_{59} fullerene in both the neutral and the $1e^-$-charged states.[137] They showed that the negatively charged BC_{59} fullerene exhibits a stronger interaction with CO_2 than the neutral BC_{59} fullerene. For neutral BC_{59} fullerene, the interaction with the CO_2 molecule was physical which changed to a substantial chemical interaction with CO_2 in the case of charged BC_{59}. In 2016 Ralser $et\ al.$ have shown, both experimentally and theoretically, that the adsorption of CO_2 is sensitive to charge on a capturing carbonaceous surface model.[138] Very recently Wang $et\ al.$ proposed a design of the graphene/ionic liquid (GIL) composite materials for gas separation by opening up the interlayer space between graphene sheets by intercalated ions of different sizes.[139] Their density functional theory (DFT) and Monte Carlo simulations suggested a new strategy to achieve tunable pore sizes via the graphene/IL composites for highly selective CO_2/N_2 and CO_2/CH_4 adsorption.

1.2 Fullerene chemistry

A significant transfiguration to the chemistry of carbon has taken place in 1958 with the discovery of fullerenes by Curl, Kroto, and Smalley.[140, 141] The class of hollow-spherical molecules comprising only C atoms varying in number as 24, 28, 32, 36, 50, 60, 70, 72, 76, 84, etc. are known as fullerenes.[117] The most common one among these is C_{60}, which has the truncated-icosahedral shape with the 60 sp^2 hybridized carbon atoms arranged in 12 pentagons and 20 hexagons. The all-carbon molecule C_{60} has the same configuration as that of a soccer ball is known as buckminsterfullerene, or just fullerene, due to its resemblance to the geodesic dome designed by visionary architect Buckminster Fuller. This molecular form of the element carbon can be manipulated and functionalized by a wide range of techniques to generate various derivatives of fullerenes. The synthesis, characterization, and study of reactivity of fullerenes and their derivatives have been discussed for the past three decades. The fascinating physical and chemical properties exhibited by fullerenes and their derivatives provide great potential in both experimental as well as theoretical fields.

Fullerenes are valuable spherical molecules that exhibit low reduction potentials and strong electron acceptor properties.[118, 119] Zhang *et al.* have shown that it is the electron-withdrawing cavity not the curvature of the fullerene or carbon nanotube that plays a dominant role in the formation of the large electrophilic regions on the molecular surface. The inner cavities of many fullerenes and carbon nanotubes are the regions of positive electrostatic potential and are electron-withdrawing in character. They successfully used the important role of the large electrophilic regions of fullerenes to explain some experimental observations in crystal engineering.[120] Shortly after the discovery of fullerenes, many chemical modifications of fullerenes were developed. Some of the important fullerene species are exohedral-, endohedral- and hetero-fullerenes.[117, 129, 142] Both theoretical and experimental studies on endohedral as well as exohedral modifications on the fullerene cage have been done to generate the new materials of interest.[121-125, 143, 144]

1.2.1 Endohedral fullerenes

Endohedral fullerene (EF) is one of the most studied fields of fullerenes, which are formed by encapsulating atoms, ions, and small molecules into the cavity inside the spherical molecules. These are stable under ambient conditions, show electronic structures basically different from those of the parent empty cages, and are able to encapsulate metals with magnetic or radioactive properties thus they find many applications in the fields of materials science and biomedical applications. [126-128, 143] The computational studies by Cioslowski and colleagues on EFs using the Hartree-Fock method employing the 4-31G basis set for the cage molecule and double zeta polarised (DZP) basis set for the guest species have created significant interest among the theoretical community to unravel the chemistry of EFs, which showed that upon encapsulation of atoms, ions, and molecules, there are no changes in the structure of C_{60}.[145] Ravinder and Subramanian studied the endohedral complexes of different anions such as F^-, Cl^-, and Br^- with C_{30}, C_{32}, C_{34}, C_{36}, C_{60}, and C_{70} molecules using B3LYP/6-311+G* method and also the structure and stability of OH and CN inside the C_{60} and C_{70}.[146] The effect of spatial confinement on water clusters by encapsulating them in a fullerene cage have been investigated by Ramachandran and Sathyamurthy using MP2/6-31G calculation and found that water clusters adopt structures significantly different from those in the gas phase. Due to the pressure effect introduced by the C_{60} cage, the hydrogen bonds are not intact in the endohedral complex.[147] Sathyamurthy and co-workers have studied the spatial effect on the vibrational spectra for the HF, H_2O, NH_3, and CH_4 encapsulated fullerenes and found that the vibrational modes of these small molecules exhibit a blue shift in X–H stretching frequency due to structural and electronic confinement.[148]

A detailed investigation of the electronic and structural properties of $M@C_{60}$ (where M = H_2O, Li^+, Na^+, K^+, Be^{2+}, Mg^{2+}, and Ca^{2+}) using quantum chemical calculations at the DFT/B3LYP/6-31G** level was carried out by Oliveira and Gonçalves. The energy gap calculated for the EFs based on the HOMO and LUMO energy difference is less than that of pure C_{60}.[149] A large number of studies have been done on the influence of the reactivity of EFs, by the ions encapsulated by them. The tuning of exohedral reactivity of

fullerenes by the encapsulation of ions inside the cage is highly important in the preparation of new species having different electronic/optical properties. Diels Alder (DA) reactions between 1,3- cyclohexadiene and ion-encapsulated fullerenes of the type $M@C_{60}$ ($M = Li^+$, Na^+, K^+, Cl^-) were studied by García-Rodeja *et al.* and found that the reaction proceeds concertedly *via* highly synchronous transition states, and thus resemble the corresponding process involving the parent C_{60} fullerene. A clear enhancement towards the DA reactions is found for those systems having an endohedral cation, whereas the behavior of those with anionic compounds is the opposite.[150] EFs with nitrogen[151] or phosphorus[152] atoms encaged in C_{60} or C_{70} cage was first accomplished by Weidinger *et al.* by bombarding C_{60} with nitrogen ions from a conventional plasma discharge ion source which was carried out in a vacuum of 10^{-5} mbar. Similarly, $N@C_{70}$, $N_2@C_{70}$, and $P@C_{60}$ were also synthesized using the ion implantation method. [153,154]

1.2.2 Exohedral modifications on fullerenes

Apart from these endohedral modifications on fullerenes the exohedral changes also have an influence on the chemical reactivity and properties of the C_{60} cage (Figure 1.6). The most important and most versatile of all species of fullerenes is exohedral fullerenes, which are molecules formed by a chemical reaction between fullerenes and other chemical groups. Anion–π interactions on fullerenes[22, 130] for the use of fullerenes in catalysis have been explored by Ló´pez-Andarias *et al.* wherein the interaction with enolate was studied.[155, 156] Exohedral modifications on the fullerene unit has found to have an influence on the stabilization of anionic transition states and the enantioselectivity as well. Matile *et al.* have shown that the molecular electrostatic potential (MESP) surface of C_{60} is overall positive with highly localized areas of positive potential, a bit like the dimples on a golf ball.[157] These π holes suggested that anion–π catalysis on fullerenes could occur with unique selectivities.[158] Nakamura *et al.* have shown that the pentamethyl[60]fullerene halides are useful for the synthesis of a variety of η^5-fullerene metal complexes.[159, 160] Such fullerene modifications are known as pseudofullerenes.
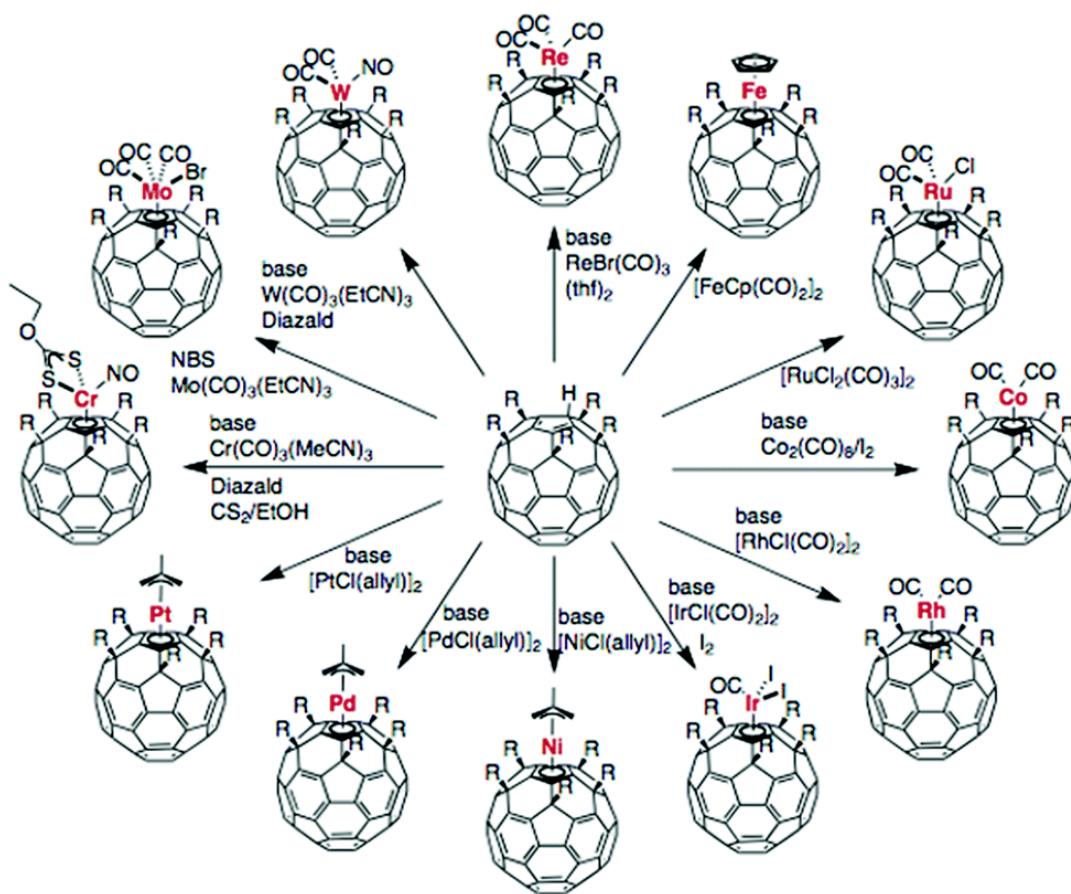
Figure 1.6 Overview of synthesis paths for exohedral metal fullerene complexes.[161]

1.2.3 Fullerenes in organometallic chemistry

The ability of the double bond in C_{60} to act as an isolated moiety was first demonstrated by Hawkins *et al.* with the one-to-one C_{60}-osmium tetroxide adduct $C_{60}(OsO_4)$(4-tert-butylpyridine)$_2$.[162] Afterwards complexes of Pt(0)[163, 164], Ir(1)[165, 166], Pd(1)[167-169] with C_{60} as a ligand connected in η^2 format to the metal centre. Formation of Fe fullerides from the reaction of $Fe(CO)_5$ and C_{60} was reported by Rao *et al.* in 1992.[170] Later Baird *et al.* showed that reactions of the carbonylate salts $A[Mn(CO)_5]$, $A[Co(CO)_4]$, and $A[Re(CO)_5]$ (A = Na, bis(triphenylphosphoranylidene)ammonium (PPN)) with C_{60} in THF results in electron transfer to give $[C_{60}]^-$ and the metal-centered radicals $Mn(CO)_5$, $Co(CO)_4$, and $Re(CO)_5$, respectively. Coupling of the latter with $[C_{60}]^-$ then gives the anionic complexes $A[Mn(CO)_4(\eta^2\text{-}C_{60})]$, which are unusually stable because of enhanced back-bonding.[171, 172] Alvarez *et al.* studied the co-ordination of buckminsterfullerene as

well as that of corannulene bucky bowls to the metal fragments. Though C_{60} and corannulene have very similar structural features, their preferences for metal complex coordination are completely different. The buckminsterfullerene C_{60} coordinates to a variety of mononuclear metal complexes through two carbon atoms (η^2), while corannulenes prefer η^6 coordination.[173] Being a polyolefin, fullerene moiety (neutral ligand) can interact in η^2, $\eta3$, η^4, η^5, or η^6 fashion with the metallic fragment. In the η^5/η^6 coordination, it acts as a 6-electron donor, similar to cyclopentadienyl anion (anionic ligand)/ phenyl ligand (neutral ligand) with the transition metal fragment to form organometallic complexes. The C_{60} fullerene has been reported as a η^2–type ligand for several transition metal complexes whereas other possible coordination modes such as η^3, η^4, η^5, and η^6 have been rarely observed. Although the literature shows evidence for the formation of η^5/η^6- fullerene – organometallic complexes, a synthetically viable strategy for promoting such a coordination behavior is available only for pseudo fullerenes. Chemists have achieved disruption in the 60-π electron conjugation by saturating five α positions around a 5-membered ring of C_{60}. The area of fullerene is still flourishing ever since the Nobel prize-winning discovery by Kroto *et al.* on this magnificent molecule.[140, 141]

Part B: Computational Chemistry Methods

1.3 An overview of computational chemistry

Chemistry deals with the science of construction, transformation and properties of molecules. Theoretical chemistry is an important area in chemistry where mathematical methods are combined with fundamental laws of physics to study processes of chemical relevance.[174-176] Computational chemistry, also called molecular modeling is rapidly emerging as a subfield of theoretical chemistry, has its roots in the late 19th century and in the first part of the 20th century. This incorporates a set of techniques for investigating chemical problems on a computer. It does not replace experiment, which remains the final arbiter of truth. However, computation has become so reliable in some respects that, more and more, scientists in general are employing it before embarking on an experimental project. Ever since its advent, computational chemistry has grown to the state it is today and became popular being immensely benefited from the tremendous improvements in computer hardware and software during the last several decades.[177] Computational chemistry appears to be the pinnacle of the view that chemistry is best understood as the manifestation of the behaviour of atoms and molecules, and that these are real entities rather than merely convenient intellectual models.[178] It is about simulating the behaviour of real physical entities with the aid of intellectual models using mathematical calculations based on the fundamental laws. Quantum mechanics based on Schrödinger equation and classical mechanics based on Newton's equation of motion are the two basic theories in computational chemistry. With high computing power using parallel or grid computing facilities and with faster and efficient numerical algorithms, computational chemistry can be very effectively used to solve complex chemical and biological problems.

The major computational investigations are:

- Molecular geometry optimization from an empirical input: the shapes of molecules – bond lengths, angles and dihedrals

- Bond energies, reaction energies, reaction pathway and all thermodynamic properties
- Energies of molecules and transition states: this tells us which isomer is favoured at equilibrium, and how fast a reaction should go.
- The interaction of a substrate with an enzyme: seeing how a molecule fits into the active site of an enzyme is one approach to designing better drugs.
- Molecular orbitals
- Atomic charges and electrostatic potential
- Vibrational frequencies- Infrared (IR) and Raman
- Ultraviolet–visible (UV), nuclear magnetic resonance (NMR) and circular dichroism (CD) spectra can be calculated, even if the molecule is unknown and someone trying to make it knows what to look for
- Magnetic properties
- Polarizabilities and hyper polarizabilities
- Properties *viz.* the ionization potential, electron affinity, proton affinity, etc.
- Modelling the excited states
- The physical properties of substances: these depend on the properties of individual molecules and on how the molecules interact in the bulk material and so on

In studying these questions computational chemists have a set of tools/methods ranging from highly accurate ones feasible only for small systems to very approximate methods for larger systems available belong to five broad classes: *ab initio* quantum chemical methods, semi empirical methods, density functional theory, molecular mechanics, and molecular dynamics. The selection of the method depends on the nature of system and the required accuracy. As the name indicates *ab initio* (Latin term for "from the beginning") methods solve the Schrödinger equation through computations derived directly from theoretical principles and using universal constants *viz.* the speed of light, the masses and charges of electrons and nuclei, Planck's constant and so on with no inclusion of empirical data. Density functional theory derives the electron distribution (electron density function) directly and uses electron density as a functional to find the total energy of a system.

Semiempirical methods are similar to *ab initio* but more approximations are made in solving it and experimental values are used to find approximate solutions (parameterization) of the Schrödinger equation. It is based on quantum mechanics, by neglecting all integrals involving more than two nuclei in the construction of the Fock matrix.[179, 180] These calculations are basically derived from the HF model but use many approximations based on empirical data and were useful in the earlier days, when execution of HF calculations without any further approximations was hard to perform with the minimal computational facilities. The cost of performing an HF calculation arises from the number of two-electron integrals necessary for constructing the Fock matrix.[181] Semiempirical methods reduced the computational cost (the N^4 complexity in HF calculation typically reduced to N^2) by reducing the number of these integrals. Generally, the entire core (the nucleus and core electrons) of atoms is replaced by a parameterized function and to compensate for the errors caused by these approximations, empirical parameters are introduced into the remaining integrals and calibrated against reliable experimental or theoretical reference data.

Molecular mechanics (MM) methods also known as Force field methods are based on a rather simple mathematical model where molecules are described by a "ball and spring" model in force field methods, with atoms having different sizes and "softness" and bonds having different lengths and "stiffness".[182-185] MM uses the classical laws of physics to predict the structure and energy of a molecule ignoring the electronic motion, where atoms are considered as individual particles but not the electrons. Hence the potential energy of a molecule is expressed in terms of bond stretching, angle bending, dihedral angles and non-bonded interactions, as

$$E_{MM} = E_{str} + E_{bend} + E_{tors} + E_{vdw} + E_{el} + E_{cross} \qquad \text{(Eq.1.4)}$$

E_{str} is the energy function for stretching a bond between two atoms, E_{bend} represents the energy required for bending an angle, E_{tors} is the torsional energy for rotation around a bond, E_{vdw} and E_{el} describe the non-bonded atom–atom interactions, and finally E_{cross} describes coupling between the first three terms.

Molecular dynamics (MD) applies Newton's laws of motion to the molecules.[186] MD techniques can be used to predict thermodynamic, structural and dynamic properties of the molecule such as diffusion coefficients, correlation functions, vibrational motions, and radial distribution etc. The energy of a system at a fixed time is obtained by incorporating the molecular mechanics force field. In addition to these hybrid quantum mechanics/molecular mechanics (QM/MM) method is also developed based on different theories and approximations in the classical and quantum mechanical domains.

1.3.1 *Ab initio* quantum chemistry methods

Similar to any other quantum chemical method, the essence of *ab initio* calculations also rests on solving the Schrödinger equation.[187] This is an approximate quantum mechanical calculation where all the computations are derived directly from theoretical principles without any inclusion of experimental data. Here all the approximations are usually mathematical approximations, such as using a simpler functional form for a function or finding an approximate solution to a differential equation.

The quantum mechanical description of molecules is in terms of the electrons, nuclei and their interactions and molecular geometry is in terms of their minimum energy arrangement. The non-relativistic time-independent Schrödinger equation[188] for such a system in its simplest form is:

$$H\Psi \ = \ E\Psi \tag{Eq. 1.5}$$

where H is the Hamiltonian operator, Ψ is the many-electron wave function and E is the energy eigenvalue of the system. The Hamiltonian operator for a many-body system of N electrons and M nuclei can be written as:

$$H = -\sum_{i=1}^{N}\frac{1}{2}\nabla_i^2 - \sum_{A=1}^{M}\frac{1}{2M_A}\nabla_A^2 - \sum_{i=1}^{N}\sum_{A=1}^{M}\frac{Z_A}{\mathbf{r}_{iA}} + \sum_{i=1}^{N}\sum_{j>i}^{N}\frac{1}{\mathbf{r}_{ij}} + \sum_{A=1}^{M}\sum_{B>1}^{M}\frac{Z_A Z_B}{\mathbf{R}_{AB}} \tag{Eq. 1.6}$$

The first and second term accounts for electronic and nuclear kinetic energy (KE) operators. The third term is the potential energy operator representing the coulombic

attraction between electrons and nuclei. The fourth and fifth terms are the potential energy operators corresponding to electron-electron, and nuclear-nuclear repulsions respectively. $\mathbf{R}_A$ and $\mathbf{r}_i$ are the position vector of nuclei and electrons, $\mathbf{r}_{iA}$ is the distance between i^{th} electron and A^{th} nucleus, $\mathbf{r}_{ij}$ is the distance between i^{th} and j^{th} electrons and $\mathbf{R}_{AB}$ is the distance between A^{th} and B^{th} nucleus. M_A is the ratio of mass of the nucleus to the mass of the electron and Z_A is the atomic number.

The major computational effort of *ab initio* calculations is in solving the electronic Schrödinger equation for a given set of nuclear coordinates. The exact solution for Schrödinger equation is only possible for hydrogen atom and for all other systems, approximations are necessary to get qualitatively correct solutions to the many-body Schrödinger equation. The most essential part of solving the Schrödinger equation is the Born-Oppenheimer (BO)[189] approximation where the coupling between the nuclei and electronic motion is neglected. According to BO approximation the nuclei being much heavier and move much slower than the electrons the nuclear motion could be neglected. Thus electronic part is solved with the nuclear positions as parameters to obtain potential energy surface (PES). With this approximation that the electrons in a molecule are moving in the field of static nuclei, the second term (KE of nuclei) in (Eq. 1.6) becomes zero, and the last term (repulsion between the nuclei) becomes a constant. The remaining electronic Hamiltonian describing the motion of N electrons in the field of M point charges is given by,

$$H_{\text{elec}} = -\sum_{i=1}^{N} \frac{1}{2}\nabla_i^2 - \sum_{i=1}^{N}\sum_{A=1}^{M} \frac{Z_A}{\mathbf{r}_{iA}} + \sum_{i=1}^{N}\sum_{j>i}^{N} \frac{1}{\mathbf{r}_{ij}} \qquad \text{(Eq. 1.7)}$$

The Schrödinger equation corresponding to the electronic Hamiltonian can be written as:

$$H_{\text{elec}}\Phi_{\text{elec}}(\{\mathbf{r}_i\};\{\mathbf{R}_A\}) = E_{\text{elec}}\Phi_{\text{elec}}(\{\mathbf{r}_i\};\{\mathbf{R}_A\}) \qquad \text{(Eq. 1.8)}$$

where, $\mathbf{r}_i$ and $\mathbf{R}_A$ accounts for the position of electrons and nuclei respectively. The solution to Eq. 1.8 gives the electronic wave function which describes the motion of electrons and depends explicitly on the electronic coordinates and parametrically on the

nuclear coordinates. BO approximation could effectively separate electronic and nuclear Hamiltonians and their corresponding wave functions. Thus the molecular wavefunction can be represented as the product of electronic and nuclear counterparts:

$$\Psi(\{\mathbf{r}_i\}\,;\{\mathbf{R}_A\}) = \Phi_{\text{elec}}(\{\mathbf{r}_i\}\,;\{\mathbf{R}_A\})\Phi_{\text{nucl}}(\{\mathbf{R}_A\})$$

(Eq. 1.9)

Once the wave function Ψ is known from the Schrödinger equation, any experimental observable can be computed with appropriate operator. The main applications of *ab initio* method are calculating molecular geometries, energies, vibrational frequencies, spectra, ionization potentials and electron affinities, and properties like dipole moments which are connected with electron distribution. Being a complete mathematical approximation, *ab initio* calculations can be performed for any kind of molecular system rather than only system for which empirical parameters are available. But the main disadvantage of *ab initio* method is its high computational cost. These are relatively slow calculations in comparison with other methods such as molecular mechanics, semiempirical calculations and density functional calculations. Also they require relatively more memory and disk space to be done effectively.

1.3.1.1 Hartree-Fock approximation

The simplest and common type of *ab initio* calculation is called a Hartree-Fock calculation (HF), in which the primary approximation is the central field or mean filed approximation.[190, 191] This is an approximation for the determination of the wavefunction and the energy of a quantum many-body system in a stationary state. Here the coulombic electron-electron repulsion is taken into account by integrating the repulsion term. This gives the average effect of the repulsion, but not the explicit repulsion interaction. One of the most important desirability of this method is that many-electron Schrodinger equation is fragmented into many simpler one-electron equations. Each one electron equation is solved to yield a single-electron wave function, called an orbital, and the energy, called an orbital energy. The orbital describes the behaviour of an electron in the net field of all the other electrons (central field or mean field). Thus the total Hamiltonian

(H) of a many-electron system can be represented as the sum of single electron Hamiltonian (h),

$$H = \sum_{i=1}^{N} h(i) \qquad \text{(Eq. 1.10)}$$

Here, $h(i)$ corresponds to the operator describing the kinetic and potential energies of electron i. A set of eigenfunctions, represented as spin orbitals, χ_j can be proposed for $h(i)$.

$$h(i)\chi_j(\mathbf{x}_i) = \varepsilon_j \, \chi_j(\mathbf{x}_i) \qquad \text{(Eq. 1.11)}$$

Then the corresponding many-electron wave function can be written as the product of individual spin orbital wave functions and is called the *Hartree Product* (HP), given by,

$$\Psi^{HP}\left(\mathbf{x}_1, \mathbf{x}_2, \ldots, \mathbf{x}_N\right) = \chi_i(\mathbf{x}_1)\chi_j(\mathbf{x}_2)\ldots\chi_N(\mathbf{x}_N) \qquad \text{(Eq. 1.12)}$$

Electrons being the indistinguishable fermions (particles with a spin of 1/2) their overall wave function must be antisymmetric. This can be achieved conveniently by arranging these orbitals in the form of Slater determinant.[189] Slater determinant for an N-electron wave function can be written as:

$$\Psi(\boldsymbol{x}_1, \boldsymbol{x}_2, \ldots, \boldsymbol{x}_N) = \frac{1}{\sqrt{N!}} \begin{vmatrix} \chi_i(\boldsymbol{x}_1) & \chi_j(\boldsymbol{x}_1) & \cdots & \chi_N(\boldsymbol{x}_1) \\ \chi_i(\boldsymbol{x}_2) & \chi_j(\boldsymbol{x}_2) & \cdots & \chi_N(\boldsymbol{x}_2) \\ \cdot & \cdot & & \cdot \\ \cdot & \cdot & & \cdot \\ \cdot & \cdot & & \cdot \\ \chi_i(\boldsymbol{x}_N) & \chi_j(\boldsymbol{x}_N) & \cdots & \chi_N(\boldsymbol{x}_N) \end{vmatrix} \qquad \text{(Eq. 1.13)}$$

The best set of orbitals is determined by the variational principle, i.e. the HF orbitals give the lowest energy within the restriction of the wave function being a single Slater determinant and this calculated approximate energy is equal to or greater than the exact energy. The shape of a given molecular orbital describes the probability of finding an electron, where the attraction to all the nuclei and the average repulsion to all the

other electrons are included. Since the other electrons are described by their respective orbitals, the HF equations depend on their own solutions, and must therefore be solved iteratively. When the molecular orbitals are expanded in a basis set, the resulting equations can be written as a matrix eigenvalue problem.

$$\mathbf{FC} = \mathbf{SC}\varepsilon \qquad\qquad \text{(Eq. 1.14)}$$

where $\mathbf{F}$ is the Fock matrix, $\mathbf{C}$ is a square matrix of expansion coefficients, $\mathbf{S}$ is the overlap matrix of the basis functions and ε is the diagonal matrix of orbital energies, ε_i. Fock matrix, $\mathbf{F}$ is the matrix representation of the one-electron operator, called the Fock operator, $f(i)$, defined as:

$$f(i) = -\frac{1}{2}\nabla_i^2 - \sum_{A=1}^{M}\frac{Z_A}{\mathbf{r}_{iA}} + V^{\text{HF}}(i) \qquad\qquad \text{(Eq. 1.15)}$$

The term $V^{\text{HF}}(i)$ is the average potential experienced by the ith electron due to the remaining electrons known as Hartree–Fock potential. It can be written as:

$$V^{\text{HF}}(i) = \sum_{i=1}^{N}\sum_{i,j=1}^{N}(J_{ij} - K_{ij}) \qquad\qquad \text{(Eq. 1.16)}$$

$$J_{ij} = \iint \psi_i(\mathbf{x}_1)\psi_i^*(\mathbf{x}_1)\frac{1}{\mathbf{r}_{12}}\psi_j^*(\mathbf{x}_2)\psi_j(\mathbf{x}_2)d\mathbf{x}_1 d\mathbf{x}_2 \qquad\qquad \text{(Eq. 1.17)}$$

$$K_{ij} = \iint \psi_i(\mathbf{x}_1)\psi_j^*(\mathbf{x}_1)\frac{1}{\mathbf{r}_{12}}\psi_i(\mathbf{x}_2)\psi_j^*(\mathbf{x}_2)d\mathbf{x}_1 d\mathbf{x}_2 \qquad\qquad \text{(Eq. 1.18)}$$

where the Coulomb operator J_{ij} represents the Coulombic repulsion between the electrons, and the exchange operator K_{ij} denotes the quantum correlation due to Pauli exclusion principle.

Since the electron repulsion is treated in an average way in HF approximation, the complicated many-electron problem is simplified as a one-electron problem. The Hartree-Fock potential $V^{\text{HF}}(i)$, or the field experienced by the ith electron depends on the

spin orbitals of the remaining electrons. *i.e.*, the Fock operator depends on its eigenfunctions. Thus the Hartree-Fock equation is nonlinear and must be solved iteratively. The iterative procedure for solving the non-linear HF equation by repeated diagonalizations of a Fock matrix is called self-consistent-field (SCF) method (Figure 1.7). For that, an initial guess at the spin orbitals is made to get the average fields to solve the eigenvalue equation for a new set of spin orbitals. The new spin orbitals will give new fields and the procedure is repeated until the spin orbitals of one cycle are essentially the same as those of the next cycle. These self-consistent spin orbitals are used to construct the HF wavefunction (in the form of Slater determinant).
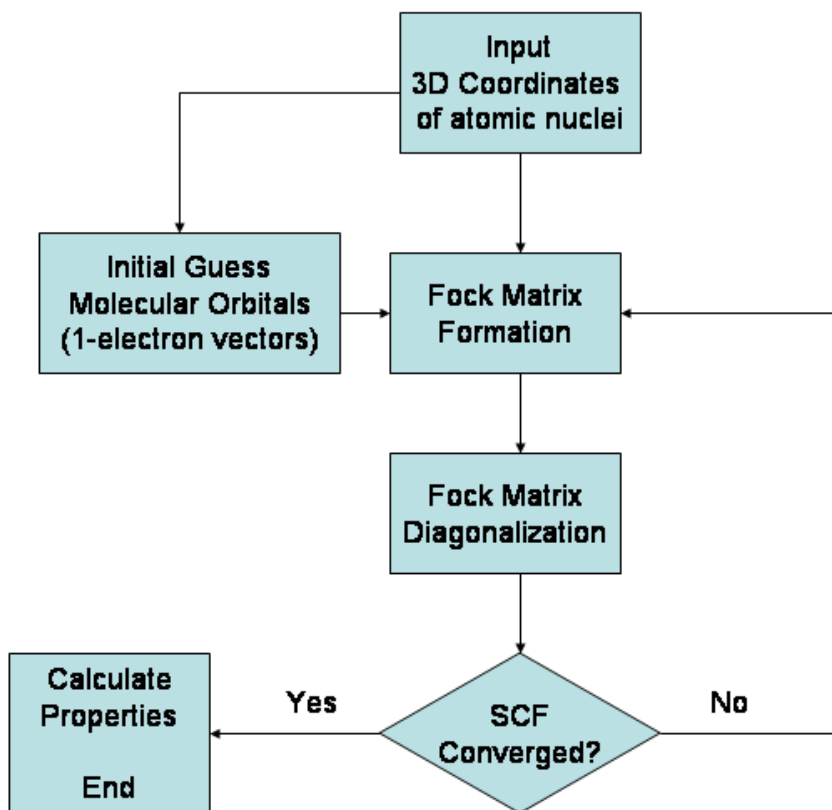
Figure 1.7 The SCF procedure for more accurate treatments.

If the molecule has a singlet spin, then the same orbital spatial function can be used for both the alpha and beta spin electrons in each pair. This is called restricted Hartree-Fock (RHF) method. To construct an HF wave function for a molecule with

unpaired electron (cases where the number of alpha and beta spin electrons are different). One technique is to use two completely separate sets of orbitals for the alpha and beta electrons. This method is called unrestricted Hartree-Fock (UHF) method. Here paired electrons will not have the same spatial distribution. This introduces an error into the calculation, called spin contamination. However, we use it since the error may be insignificant in many chemical systems. Another method is restricted open shell Hartree-Fock (ROHF) method. Here the paired electrons share the same spatial orbital, there is no spin contamination. The restriction of identical spatial orbital is retained. But it needs relatively more CPU time to execute. ROHF is primarily used for cases where spin contamination is large if UHF is used.

In this HF method effects arising from the deviations of mean/central field approximation, known as electron correlation, are completely neglected for the electrons of opposite spin, but are taken into account for electrons of parallel spin. Because of the mean/central field approximation, the energies from HF calculations are always greater than the exact energy and tend to a limiting value called the Hartree-Fock limit as the basis set is improved.

1.3.1.2 Post Hartree-Fock methods

HF method does not consider electron correlation instead average effect of electron repulsion (not the explicit electron-electron interaction) is taken into account which limits the accuracy of the method.[192] Post Hartree-Fock methods are a set of electron correlation methods which go beyond SCF to add electron correlation more precisely. The correlation energy is defined as the difference between the energy in the Hartree-Fock limit (E_{HF}) and the exact nonrelativistic energy of a system (ε_0).

$$E_{corr} = \varepsilon_0 - E_{HF} \qquad\qquad \text{(Eq. 1.19)}$$

The methods *viz.* configuration interaction (CI),[193] multi-configurational self-consistent field (MCSCF), Møller-Plesset perturbation theory (MPn, where n is the order of correlation), coupled cluster theory (CC),[194] are examples of post HF methods. The post HF methods try to calculate the correlation energy as the difference between the exact *ab initio* energy and exact (complete basis) HF energy.

1.3.2 Density functional theory

The foundations of density functional theory (DFT) lies in the fact that the energy of an electronic system can be defined using its electron density, $\rho(\mathbf{r})$ rather than wave function which is used in Hartree-Fock theory.[195-197] The wave function has 3N level dependence with the number of electron (N) and as the number of electron increases, the wave function becomes too complicated to work with. In DFT electron density, $\rho(\mathbf{r})$ is a function of its many body wave function and the dependence is reduced to 3 spatial coordinates (or four, if the spin is included) regardless the value of N facilitates the application of DFT on systems with hundreds or even thousands of atoms. Also, electron density, when integrated over all space, gives the total number of electrons, N.

$$N = \int \rho(\mathbf{r})d\mathbf{r} \qquad\qquad \text{(Eq. 1.20)}$$

The works by Thomas and Fermi in 1927, soon after the fundamental report of Schrödinger in 1926 has initiated the concept of DFT approach.[198] However, it was after the work of Hohenberg, Kohn, and Sham in the 1960s that the widespread application of DFT became a reality.[199, 200] DFT maintains a good balance between accuracy and computational cost and applies to larger systems with hundreds or even thousands of atoms. The 1998 Nobel Prize in Chemistry was shared by Walter Kohn, the founding father of DFT, and John Pople, who was instrumental in implementing DFT in computational chemistry. This has revealed significance of DFT in understanding the science of molecules and grabbed attention from various spheres of science. These days, a majority of electronic-structure calculations in physics and chemistry utilizes DFT, which includes the analysis of electrical, magnetic, and structural properties of materials.[201, 202].

1.3.2.1 Thomas-Fermi model

The Thomas–Fermi (TF) model,[203, 204] named after L. H. Thomas and E. Fermi, is a quantum mechanical theory for the electronic structure of many-body systems developed semi classically, shortly after the introduction of the Schrödinger equation, can be considered as a precursor to modern density functional theory. [53, 54] In 1927,

starting ftom the uniform electron gas concept, Thomas and Fermi, used fermion statistical mechanics to derive the kinetic energy of a system where the energy is expressed as a function of the total electron density.

$$T_{\text{TF}}[\rho(\mathbf{r})] = \frac{3}{10}(3\pi^2)^{2/3}\int d\mathbf{r}\,\rho^{5/3}(\mathbf{r})$$ (Eq. 1.21)

It is approximated that the KE of the electrons depends exclusively on the electron density. Thus, a total energy in terms of electron density can be obtained by adding the interaction between electron-nucleus and electron-electron as below:

$$E[\rho(\mathbf{r})] = \frac{3}{10}(3\pi^2)^{\frac{2}{3}}\int d\mathbf{r}\,\rho^{\frac{5}{3}}(r) - Z\int \frac{\rho(\mathbf{r})}{\mathbf{r}}d\mathbf{r} + \frac{1}{2}\iint \frac{\rho(\mathbf{r}_1)\rho(\mathbf{r}_2)}{|\mathbf{r}_1 - \mathbf{r}_2|}d\mathbf{r}_1 d\mathbf{r}_2$$ (Eq. 1.22)

The second term corresponds to electron-nucleus interaction and the third term denotes the electron-electron interactions.

The Thomas–Fermi equations, together with an assumed variational principle, represented the first effort to define a density functional theory (DFT); the energy is computed with no reference to a wave function. However, while these equations are of significant historical interest with an elegant mathematical derivation, it is not accurate enough for the practical application that they find no use in modern chemistry.

1.3.2.2 Hohenberg-Kohn theorems

In 1964 Hohenberg and Kohn proved two theorems critical to establishing DFT as a legitimate quantum chemical methodology.[199] In the language of DFT, electrons interact with one another and with an 'external potential'. The first theoerm known as the Hohenberg–Kohn existence theorem, has shown that the ground-state density determines the external potential (V_{ext}) and thus the Hamiltonian, and thus the wave function. Also the Hamiltonian determines not just the ground-state wave function, but all excited-state wave functions as well, so there is a tremendous amount of information coded in the density. The first theorem of Hohenberg and Kohn is an existence theorem and in a second theorem Hohenberg and Kohn showed that, also just as with MO theory, the density obeys a variational principle. Consequently, the ground state energy E is

uniquely determined variationally from the ground-state charge density: the density that minimizes the total energy is the exact ground state density. The ground state energy functional can be written as the sum of two terms:

$$E[\rho(\mathbf{r})] = \int V_{\text{ext}}(\mathbf{r})\rho(\mathbf{r})d\mathbf{r} + F[\rho(\mathbf{r})] \qquad \text{(Eq. 1.23)}$$

The first term represents the interaction of the electrons with an external potential $V_{\text{ext}}(\mathbf{r})$ and $F[\rho(\mathbf{r})]$ is the sum of the kinetic energy of the electrons and the contribution from the interelectronic interactions. The DFT equivalent of Schrödinger equation can be written as:

$$\left(\frac{\delta E[\rho(\mathbf{r})]}{\delta\rho(\mathbf{r})}\right)_{V_{\text{ext}}} = \mu \qquad \text{(Eq. 1.24)}$$

where μ is a Lagrangian multiplier which can be identified with the chemical potential for the electron for its nuclei.

1.3.2.3 The Kohn-Sham equations

Although the Hohenberg-Kohn theorems are extremely powerful, the final step is still solution of the Schrödinger equation, which is prohibitively difficult in most instances and thus do not offer a way of computing the ground-state density of a system in practice. The difficulty derives from the electron–electron interaction term in the correct Hamiltonian. Later in 1965, Kohn and Sham devised a simple method for carrying out DFT calculations, that retains the exact nature of DFT.[200] Kohn and Sham realized that calculations would be considerably simpler if only the Hamiltonian operator were one for a non-interacting system of electrons. Starting with a fictitious system of non-interacting electrons that have same overall ground-state density and then divide the energy functional into specific components to facilitate further analysis.

$$F[\rho(\mathbf{r})] = E_{\text{KE}}[\rho(\mathbf{r})] + E_{\text{H}}[\rho(\mathbf{r})] + E_{\text{XC}}[\rho(\mathbf{r})] \qquad \text{(Eq. 1.25)}$$

The first term, $E_{KE}[\rho(\mathbf{r})]$, is defined as the kinetic energy of a system of non-interacting electrons with the same density $\rho(\mathbf{r})$ as the real system and is defined as

$$E_{KE}[\rho(\mathbf{r})] = \sum_{i=1}^{N} \int \Psi_i(\mathbf{r}) \left(-\frac{\nabla^2}{2}\right) \Psi_i(\mathbf{r}) d\mathbf{r} \tag{Eq. 1.26}$$

$E_H[\rho(\mathbf{r})]$, is the Hartree electrostatic energy or electron-electron coulombic energy and is given by,

$$E_H[\rho(\mathbf{r})] = \frac{1}{2} \iint \frac{\rho(\mathbf{r}_1)\rho(\mathbf{r}_2)}{|\mathbf{r}_1 - \mathbf{r}_2|} d\mathbf{r}_1 d\mathbf{r}_2 \tag{Eq. 1.27}$$

The third term, $E_{XC}[\rho(\mathbf{r})]$ corresponds to the energy contributions from exchange and correlation.

Combining Eq. 1.26 and Eq. 1.27 and adding electron-nuclear interaction leads to the full expression for the energy of an N-electron system within the Kohn-Sham scheme:

$$E[\rho(\mathbf{r})] = \sum_{i=1}^{N} \int \Psi_i(\mathbf{r}) \left(-\frac{\nabla^2}{2}\right) \Psi_i(\mathbf{r}) d\mathbf{r} + \frac{1}{2} \iint \frac{\rho(\mathbf{r}_1)\rho(\mathbf{r}_2)}{|\mathbf{r}_1 - \mathbf{r}_2|} d\mathbf{r}_1 d\mathbf{r}_2$$

$$+ E_{XC}[\rho(\mathbf{r})] - \sum_{A=1}^{M} \int \frac{Z_A}{\mathbf{r} - \mathbf{R}_A} \rho(\mathbf{r}) d\mathbf{r} \tag{Eq. 1.28}$$

Here the exchange-correlation energy functional not only comprises of the contributions due to exchange and correlation but also a contribution due to the difference between the exact and non-interacting kinetic energy of the system. Kohn and Sham proposed that the electron density of the system can be written as the sum of the square moduli of a set of N one-electron orbitals:

$$\rho(\mathbf{r}) = \sum_{i=1}^{N} |\psi_i(\mathbf{r})|^2 \tag{Eq. 1.29}$$

Introducing Eq. 1.29 for electron density and applying the appropriate variational condition leads to the one-electron Kohn-Sham equation:

$$\left\{ -\frac{\nabla_1^2}{2} - \left(\sum_{A=1}^{M} \frac{Z_A}{\mathbf{r}_{1A}} \right) + \int \frac{\rho(\mathbf{r}_2)}{\mathbf{r}_{12}} d\mathbf{r}_2 + V_{XC}[\mathbf{r}_1] \right\} \psi_i(\mathbf{r}_1) = \varepsilon_i \psi_i(\mathbf{r}_1) \qquad \text{(Eq. 1.30)}$$

where ε_i represent the orbital energies and V_{XC} corresponds to the exchange-correlation potential which is related to the exchange-correlation energy by:

$$V_{XC}[\mathbf{r}] = \frac{\delta E_{XC}[\rho(\mathbf{r})]}{\delta\rho(\mathbf{r})} \qquad \text{(Eq. 1.31)}$$

A self-consistent approach is incorporated to solve the Kohn-Sham equations. An initial guess of the density in Eq. 1.30 will derive a set of orbitals, leading to an improved value of density, which is then employed in the second iteration and so on to attain the convergence.

1.3.2.4 Exchange-correlation functionals

In principle E_{xc} not only accounts for the difference between the classical and quantum mechanical electron–electron repulsion, but it also includes the difference in kinetic energy between the fictitious non-interacting system and the real system. The exchange-correlation energy, E_{XC} comprises an exchange term E_X (associated with the interaction of electrons of the same spin) and a correlation term E_C (associated with the interaction of electrons of opposite spin). The corresponding functionals are exchange functional and correlation functional:

$$E_{XC}[\rho(\mathbf{r})] = E_X[\rho(\mathbf{r})] + E_C[\rho(\mathbf{r})] \qquad \text{(Eq. 1.32)}$$

The functional dependence of E_{xc} on the electron density is expressed as an interaction between the electron density and an 'energy density' ε_{xc} that is *dependent* on the electron density, *viz.*

$$E_{XC}[\rho(\mathbf{r})] = \int \rho(\mathbf{r})\, \varepsilon_{xc}[\rho(\mathbf{r})]d\mathbf{r} \qquad \text{(Eq. 1.33)}$$

ε_{xc} is the sum of individual exchange and correlation contributions. The electron density is a per unit volume density whereas the energy density is a per particle density, within this formalism the Slater exchange energy density is:

$$\varepsilon_x[\rho(\mathbf{r})] = -\frac{9\alpha}{8}\left(\frac{3}{\pi}\right)^{\frac{1}{3}}\rho^{\frac{1}{3}}(\mathbf{r})$$
(Eq. 1.34)

Kohn-Sham DFT is formally accurate and describes the ground state properties. But it does not lead to the exact form of exchange-correlation functional V_{XC}. Several approximations such as (i) Local density approximation (LDA) (ii) Generalized gradient approximation (GGA) (iii) meta-GGA and, (iv) Hybrid functionals have been designed by modifying the exchange-correlation potential for the practical applications of DFT.

1.3.2.4.1 Local density approximation (LDA)

Local density approximation (LDA), based on the uniform electron gas, is the simplest approximation for the exchange-correlation functional and is the basis for all approximate exchange-correlation functional. The term LDA was originally used to indicate any density functional theory where the value of E_{xc} at some position $\mathbf{r}$ could be computed exclusively from the value of ρ at that position, i.e., the 'local' value of ρ. In principle, then, the only requirement on ρ is that it be single-valued at every position, and it can otherwise be wildly ill-behaved.[205] In LDA the number of electrons N as well as the volume V of the gas are considered to approach infinity, while the electron density attains a constant value everywhere and the the exchange function is can be represented as:

$$E_X^{LDA}[\rho(\mathbf{r})] = -\frac{3}{4}\left(\frac{3}{\pi}\right)^{\frac{1}{3}}\int\rho^{\frac{4}{3}}(\mathbf{r})d\mathbf{r}$$
(Eq. 1.35)

Systems including spin polarization (e.g., open-shell systems) must use the spin-polarized formalism. The local spin density approximation (LSDA) proposed by J.C. Slater, represents a more general application of LDA, which introduces spin densities into the functionals.[206] The exchange functional in LSDA approach is given by:

$$E_X^{LDA}[\rho(\mathbf{r})] = -2^{1/3}\left(-\frac{3}{4}\left(\frac{3}{\pi}\right)^{\frac{1}{3}}\right)\int\left(\rho_\alpha^{\frac{4}{3}}(\mathbf{r}) + \int \rho_\beta^{\frac{4}{3}}(\mathbf{r})\right)d\mathbf{r} \qquad \text{(Eq. 1.36)}$$

where α and β represent spin up and down, respectively.

In LSDA approximation applied to a molecule, invoking uniform electron gas theory doesn't intend that the electron density of the molecule is a constant throughout space. Instead, it is an assumption that the exchange-correlation energy density at every position in space for the molecule is the same as it would be for the uniform electron gas having the same density as is found at that position.

1.3.2.4.2 Generalized gradient approximation (GGA)

One best way to improve the correlation functional is to make it depend not only on the local value of the density, but on the extent to which the density is locally changing, i.e., the gradient of the density, $\nabla\rho(\mathbf{r})$. The first derivative of a function at a single position is a local property, so the more common term in modern nomenclature for functionals that depend on both the density and the gradient of the density is 'gradient corrected'. Including a gradient correction defines the 'generalized gradient approximation' (GGA).

$$E_{XC}\left[\rho_\alpha(\mathbf{r}), \rho_\beta(\mathbf{r})\right] = \int \varepsilon_{xc}(\rho_\alpha(\mathbf{r}), \rho_\beta(\mathbf{r}), \nabla\rho_\alpha(\mathbf{r})\rho_\beta(\mathbf{r}))d^3\mathbf{r} \qquad \text{(Eq. 1.37)}$$

Generally, the GGA functionals are constructed by adding a correction term to the LDA functionals. The development of GGA methods is based on two main lines; one based on numerical fitting procedures proposed by Becke[207] and a more rational-based one advocated by Perdew.[208]

1.3.2.4.3 meta-GGA

Higher order gradient or meta- GGA methods allow the exchange and correlation functionals to depend on higher order derivatives of the electron density, with the Laplacian $\nabla^2\rho(\mathbf{r})$ being the second-order term. Meta-GGA functionals depend explicitly on higher order density gradients which involve derivatives of the occupied Kohn-Sham orbitals. These functionals show considerable improvement over GGA methods. In general, meta-GGAs tend to outperform GGAs for atomization energies and barrier

heights, and a few can even incorporate some 'medium-range' dispersion. Minnesota functional, developed by Truhlar and coworkers at Minnesota University are based on the meta-GGA approximation.[209-213] These functionals used in traditional quantum chemistry and solid-state physics calculations are all based on complicated functional forms parameterized on high quality benchmark databases.

In addition to these functionals, there are hybrid density functional methods: hybrid GGA (H-GGA) methods and Hybrid-meta GGA (HM-GGA) methods. These are a combination of exchange-correlation of a conventional GGA/m-GGA method with a percentage of HF exchange. The percentage of HF exchange is precisely built-in semiempirically from experimental atomization energies, ionization potentials, proton affinities, total atomic energies, *etc.* for a representative set of small molecules. HM-GGA methods depend on HF exchange, electron density, the gradient of electron density and the kinetic energy density. B3LYP, B3P86, B3PW91, B97-1, MPWB1K, and X3LYP are examples of H-GGA methods and B1B95, BB1K, MPW1B95, M11, M06-2X, and TPSS1KCIS are examples for HM-GGA methods.

The Minnesota functional family includes one meta-GGA (M06-L), two meta-NGAs (M11-L and MN12-L), seven global-hybrid meta-GGAs (M05, M05-2X, M06-2X, M08-HX, and M08-SO), one range-separated hybrid meta-GGA (M11) and one screened exchange hybrid meta-NGA (MN12-SX). Among all these, the M06 family is one of the frequently used and most popular methods. It is composed of four functionals that have similar functional forms for the DFT part, with each having parameters optimized with a different percentage of HF exchange. M06-L is intended to be fast and is applicable for inorganic and organometallic systems. M06 is the most versatile of the 06 functionals because of its large applicability. M06-2X, is used for top-level across-the-board performances in all areas of chemistry including thermochemistry and reaction kinetics, but excluding multi-reference systems such as those containing transition metals and M06-HF is suitable for calculation of spectroscopic properties of charge-transfer transitions, where elimination of self-interaction error is of prime importance.

1.3.2.5 Perdew's Jacob's ladder of density functionals

The hierarchy of exchange–correlation functionals of DFT approximations is often represented by the concept of Jacob's ladder (the famous allusion from the book of Genesis), put forward by Perdew and Schmidt in 2001.[214]

Heaven	**Chemical Accuracy**
Rung 5	*+ dependence on virtual orbitals* **double hybrids**: ωB97X-2, XYG3
Rung 4	*+dependence on occupied orbitals* **hybrid GGA**: B3LYP, ωB97X-V / **hybrid meta-GGA**: M06-2X, M11
Rung 3	*+dependence on the kinetic energy density* **meta-GGA**: TPSS, M06-L
Rung 2	*+dependence on the gradient of the density* **GGA**: PBE, BLYP
Rung 1	*dependence on the density* **LDA**: GVWN, GPW92
Earth	Hartree World

Figure 1.8 Perdew's metaphorical Jacob's Ladder, composed of five rungs corresponding to increasingly sophisticated models for the unknown exchange-correlation functional of DFT.[215]

The ladder (Figure 1.8) with its foundations in the 'Hartree World', introduces additional ingredients into the functional form while moving up the ladder terminating in the 'Heaven' of chemical accuracy. In the 'Hartree World', the exchange-correlation energy is zero and the electron– electron interaction is provided solely by classical

electrostatics. Perdew's symbolic Jacob's Ladder is composed of five rungs corresponding to increasingly superior (and also the complexity) models for the unknown exchange-correlation functional of DFT.[216] Each rung contains new physical content that is missing in lower rungs. Hence an improved accuracy of the functional (the exchange-correlation part) is accomplished at each higher level.[217]

1.3.2.6 Dispersion corrections

Since the 'motions' of electrons are correlated (or the electronic wave functions being correlated), the two atoms simultaneously develop electrical moments that are oriented so as to be mutually attractive. The force associated with this interaction is referred to variously as 'dispersion', the 'London' force, or the 'attractive van der Waals' force. Dispersion is a purely quantum mechanical effect associated with the interactions between instantaneous local moments favourably arranged owing to correlation in electronic motions. Incorporation of dispersive interactions may enhance the accuracy of theoretical calculations. The Minnesota functionals can be considered as such an attempt for calculating the noncovalent interactions within its framework. Such long-range van der Waals type interactions in molecules are added to the KS-DFT functionals and the total energy of the system can be represented as:

$$E_{DFT-D} = E_{KS-DFT} + E_{disp} \qquad \text{(Eq. 1.38)}$$

where $E_{KS\text{-}DFT}$ accounts for the self-consistent Kohn-Sham energy functional and $E_{KS\text{-}DFT}$ is the dispersion energy. The dispersion energy can be written as:

$$E_{disp} = -S_6 \sum_{i=1}^{N_{at}-1} \sum_{j=i+1}^{N_{at}} \frac{C_6^{ij}}{R_{ij}^6} f_{dmp}(\mathbf{R}_{ij}) \qquad \text{(Eq. 1.39)}$$

where N_{at} is the number of atoms in the system, S_6 is a global scaling factor which depends on the dispersion function, C_6^{ij} is the dispersion coefficient for atom pair ij, $\mathbf{R}_{ij}$ is the interatomic distance, and f_{dmp} is the damping function which must be used to avoid near-singularities for small interatomic distance.

1.3.3 Basis sets

Basis functions are mathematical functions for single electrons in an atom. The basis functions are also termed as atomic orbitals. Linear combination of these basis functions provides basis set used in computational chemistry calculations. Thus basis set refers to the linear combinations of a pre-defined set of non-orthogonal one-electron wave functions used to build molecular orbitals, with the weights or coefficients to be determined. In electronic structure calculations generally we use two types of basis functions *viz.* Slater Type Orbitals (STO) and Gaussian Type Orbitals (GTO). The basis function represents all the possible ways that electrons behave in a molecule. We have to include enough functions to model the orbitals properly. Molecular orbitals and entire wave functions are created by taking linear combinations of basis functions and angular functions. The list of all basis functions used in a calculation to describe the shapes of the orbitals in an atom is termed as a basis set. The time required for a calculation scales as the fourth power of the number of basis functions.
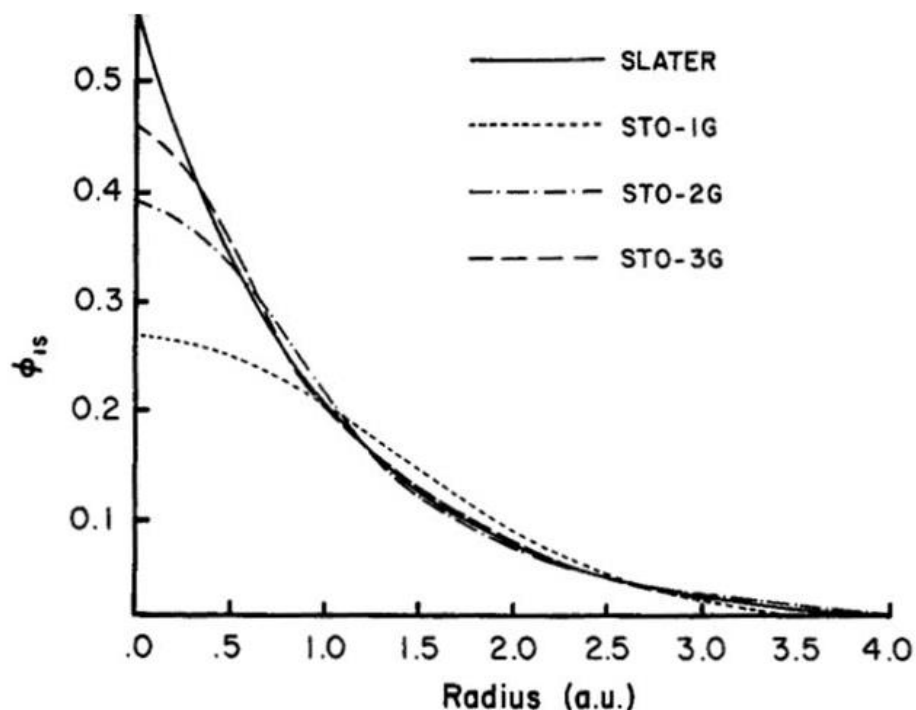
Figure 1.9 Comparison of the quality of the least squares fit of a 1s Slater function (ζ = 1.0) obtained at the STO-1G, STO-2G, and STO-3G levels.[189]

J. C. Slater developed a set of basis functions which decay exponentially with the distance from the nuclei (Figure 1.9) .[218, 219] Initially molecular calculations used STOs as basis sets. STOs have the exponential dependence: $e^{-\zeta r}$ and are given by the mathematical expression:

$$\Phi_{abc}^{STO}(x, y, z) = Nx^a y^b z^c e^{-\zeta r} \tag{Eq. 1.40}$$

where N is the Normalization constant, a, b, c are components of angular momentum (L = a + b + c), and ζ is the orbital exponent which determine the expansion of the orbital, x, y, z are the cartesian coordinates and r is the radius in Å. But the difficulty in calculating some of these integrals was solved by the introduction of Gaussian-type orbitals (GTOs) by S. F. Boys in 1950s from Cambridge University in the UK which contains the exponential $e^{-\zeta r^2}$. GTOs are mathematically expressed as:

$$\Phi_{abc}^{GTO}(x, y, z) = Nx^a y^b z^c e^{-\zeta r^2} \tag{Eq. 1.41}$$

This function is usually known as primitive Gaussian-type orbital (PGTO). Such functions are very easy to evaluate. According to Gaussian product theorem, the product of two primitive Gaussians gives rise to another Gaussian function centered at the weighted midpoint of the two functions. This makes the GTOs more advantageous over STOs.[220, 221] But the limitation of using GTOs is that these functions are less accurate compared to STOs. Linear combinations of primitive gaussians known as contracted Gaussian-type orbitals (CGTOs) can be used to overcome this difficulty (Figure 1.11). The CGTO functions can mimic STOs and are expressed as:

$$\Phi_{abc}^{CGTO}(x, y, z) = N \sum_{i}^{n} c_i \, x^a y^b z^c e^{-\zeta_i r^2} \tag{Eq. 1.42}$$

where n gives the number of Gaussians to mimic the STO and c_i corresponds to their coefficients.[222-224] The simplest type of contracted gaussians (CGs) is the STO-nG basis sets which attempt to approximate Slater-type orbitals (STOs) by n primitive Gaussians.[225, 226]

The STO-nG basis sets are rather inadequate as they include only one CG per atomic orbital. For improving the calculations, two or more functions can be used to describe each type of orbital. Double-zeta (DZ), triple-zeta (TZ) and quadruple-zeta(QZ) basis sets are examples of such kind which use more than one basis functions.[227] Pople and coworkers introduced split valence basis sets of type 'k-nlmG', where the valence orbitals are represented by multiple zeta and the core orbitals by a single basis function. Here 'k' indicates how many primitive Gaussians are used for representing the core orbitals and 'nlm' indicates both how many functions the valence orbitals are split into and how many primitive Gaussians are used for their representation.[228] The basis sets such as 3-21G, 4-21G, 6-31G, 6-311G, etc. are examples of split-valence basis sets. In 6-31G basis set, the core electrons are represented as the sum of six gaussian functions and the valence orbitals are represented by two basis functions of which one is a sum of three primitive gaussians and the second is one gaussian function. Moreover, the addition of polarization or diffuse functions improves the basis sets. The polarization functions are represented as * or ** [(d) or (d, p)] following G in the notation of the basis sets. The (d, p) polarization function employs an extra set of d-orbitals on heavy atoms and p-orbitals on hydrogens. Diffuse basis sets are useful for describing anions, molecules with lone pairs, excited states, and transition states and are denoted by + or ++ signs. For example, 6-31+G basis set adds s and p diffuse functions to non-hydrogen atoms and 6-311++G adds diffuse functions to both non-hydrogen and hydrogen atoms.[229] For heavier atoms such as transition metals with large inner core, number of basis functions needed to describe the system is high. Since only the valence electrons are involved in the bonding, the core electrons can be replaced by a potential which fit to all-electron calculations called effective core potentials (ECPs).[230-232] For a large core ECP, all orbitals except (n+1)s, and nd orbitals are treated as core electrons and these core electrons are replaced with an approximate pseudopotenial. Such a treatment usually gives a good geometry for the molecule but the energetics are often found to be approximate. This can be rectified by using a small core ECP where the ns, np, nd and (n+1)s forms the valence orbitals. Such a treatment often increases the computational cost. The popular pseudopotentials commonly used include those of Hay and Wadt developed by Los Alamos National Laboratory (LANL), [233] those of Stevens *et al*. [234] and the Stuttgart–

Dresden pseudopotentials developed by Dolg and co-workers. [235] Later, Check *et al.* incorporated polarization and diffuse functions in conjunction with the LANL double zeta basis set. [236]

The basis sets employed for the calculations in the thesis are (a) Pople's split-valence basis sets 6-31G(d,p) and 6-311++G(d,p) with d polarization functions for non-hydrogen atoms and p polarization function for hydrogen atom and diffuse functions for non-hydrogen and hydrogen atoms[237, 238] (b) Hay and Wadt double zeta basis set with the overall combination of ECP and valence basis set, LANL2DZ for defining transition metal Ru and Mo.

1.3.4 Basis set superposition error

The use of complete basis set (CBS) results in high computational effort by increasing the basis functions to hundreds or a few thousand at best and thus limits the practical application. Any finite basis set may not have the same quality at all geometries, since the electron density around one nucleus may be described by functions centred at another nucleus. This is leads to several errors in calculating small effects, such as energies of van der Waals complexes and hydrogen bonds. For example, consider any noncovalent dimer, AB where basis functions from one molecule, A compensate for the basis set incompleteness on the other molecule, B and vice versa. Thus the dimer will be artificially lowered in energy and the strength of the hydrogen bond over estimated. This effect of artificial shortening of intermolecular distances and concomitant strengthening of intermolecular interactions in weakly bound clusters while using smaller basis sets is known as the basis set superposition error (BSSE). In the limit of a complete basis set, the BSSE will be zero, and adding more basis functions will not give any improvement but the calculations using finite basis sets are susceptible to BSSE error. The Counterpoise (CP) correction method introduced by Boys and Bernardi is an approximate way of assessing BSSE.[239] BSSE is estimated as the difference between monomer energies with the regular basis and the energies calculated with the full set of basis functions for the whole complex. For the dimer AB, the complexation energy is calculated as the dimer energy minus the monomer energies. with A and B, each having

regular nuclear-centred basis sets denoted with subscripts a and b, and the complex AB having the combined basis set ab;

$$\Delta E_{complexation} = E(AB)_{ab} - [E(A)_a + E(B)_b] \qquad (Eq.\ 1.43)$$

where $E(AB)_{ab}$, $E(A)_a$ and $E(B)_b$ are the energies of AB, monomer A, and monomer B, respectively. To estimate how much of this complexation energy is due to BSSE, four additional energy calculations are needed *viz.* using the 'a' basis set for A, and the 'b' basis set for B, the energies of each of the two fragments are calculated with the geometry they have in the complex. Two additional energy calculations of the fragments at the complex geometry are then carried out with the full ab basis set. This means that the energy of A is calculated in the presence of both the normal a basis functions and with the b basis functions of fragment B located at the corresponding nuclear positions, but without the B nuclei present, and vice versa. Such basis functions located at fixed points in space are often referred to as ghost orbitals and these ghost functions make the basis more complete and thereby lower the fragment energy for A. The Counterpoise (CP) correction is defined as

$$\Delta E_{CP} = E(A)^*_{ab} + E(B)^*_{ab} - E(A)^*_a - E(B)^*_b \qquad (Eq.\ 1.44)$$

where $E(A)^*_{ab}$ and $E(B)^*_{ab}$ are the energies of monomer A and B respectively, in the structure they adopt in the dimer (AB) with the full basis set of the dimer available. $(A)^*_a$ and $E(B)^*_b$ are the energies of A and B, respectively, in the structure they adopt in the dimer with only their basis functions.

The counterpoise-corrected complexation energy is then given as $\Delta E_{complexation} - \Delta E_{CP}$. For non-bonded intermolecular interactions, the CP correction is well defined, although it may not be as accurate as desired. For intramolecular cases, however, it is difficult to define a unique procedure for estimating the BSSE, and it is almost always ignored.

1.3.5 Potential energy surface (PES)

On solving the Newton or Schrödinger dynamical equations for the particles in the system in computational chemistry, the Born–Oppenheimer[240] separation of the

electronic and nuclear motions appears as a cornerstone. This is also important in computational chemistry not simply because it simplifies the application of the Schrödinger equation to molecules by allowing us to focus on the electronic energy and add in the nuclear repulsion energy later but also makes the concept of molecular shape (geometry) meaningful, and makes possible the concept of the potential energy surface (PES).
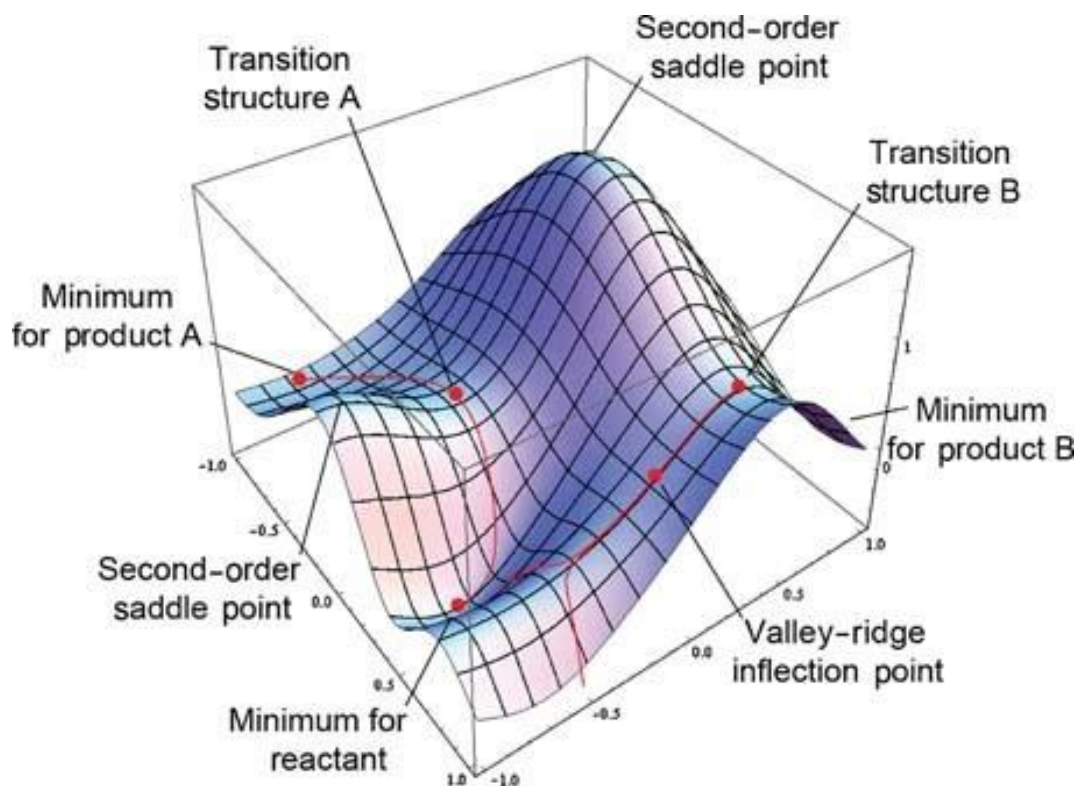
Figure 1.10 A model representation of potential energy surface.[241]

PES is obtained on solving the dynamical equations for a large number of nuclear geometries of a given molecule, because in the process of mimicing the actual experiment it is very important to consider all the possible structures not only one structure of a given molecule.[174, 242] A PES is the mathematical or graphical representation of the relationship between the energy of a molecule and its geometry. [178] The motion of the nuclei on the PES can then be solved either classically (Newton) or by quantum (Schrödinger) methods and the methods aimed at solving the electronic Schrödinger equation are also broadly referred to as "electronic structure calculations".[232] PESs aid

us in visualizing and understanding the relationship between potential energy and molecular geometry, and also in understanding how computational chemistry programs locate and characterize structures.[243] It gives a complete description of all the conformers and isomers possible for a system. In the case of a diatomic molecule, PES can be represented by a two-dimensional plot with the inter-nuclear separation on the *x*-axis and the energy at that bond distance on the *y*-axis; in this case, the potential energy surface is a curve. For larger systems, the dimensions also incresses owing to the higher degrees of freedom within the molecule. The PES illustration reflects only two of the degrees of freedom within the molecule, and plots the energy above the plane defined by them, creating a surface. Each point represents a particular molecular geometry and the height of the surface at that point denotes the energy of that structure.

The PES in Figure 1.10 contains three minima: a minimum is a point at the bottom of a valley, from which motion in any direction leads to a higher energy. Two of them are local minima, corresponding to the lowest point in some limited region of the potential surface, and one of them is the global minimum, the lowest energy point anywhere on the potential surface.[241] Different minima correspond to different conformations or structural isomers of the molecule under investigation. Figure 1.10 also shows saddle points and transition state structures. At both minima and saddle points, the first derivative of the energy, known as the gradient, is zero. Since the gradient is the negative of the forces, the forces are also zero at such points. A point on the PES where the forces are zero is called a stationary point.

Geometry optimizations usually locate the stationary point closest to the geometry from which they started. The minimum points on PES correspond to the stable states and any distortion from the minimum will result in a configuration with higher energy. Considering a PES of a chemical reaction, the transition state is marked as a first-order saddle point on the PES whereas the reactants and products are designated as minima.[244-247] A first-order saddle point should be a maximum in one direction and minimum in all other direction.

1.3.6 Solvation models

Majority of the chemical reactions and biologically relevant processes occur in solution, aqueous systems with rather specific pH and ionic conditions and the reactions are both qualitatively and quantitatively different under gas and solution phase conditions. Molecular properties are also sensitive to the environment such as a solvent.[248] The solvation effects can be partitioned into two main groups; specific (short-range) solvation and non-specific (long-range) solvation. Non-specific effects are primarily solvent polarization and orientation of the solvent dipoles. Specific effects include hydrogen bonds, van der Waals interactions, solvent shell structure, solvent–solute dynamics, charge transfer effects and hydrophobic effects (entropy effects).

(a)   (b)
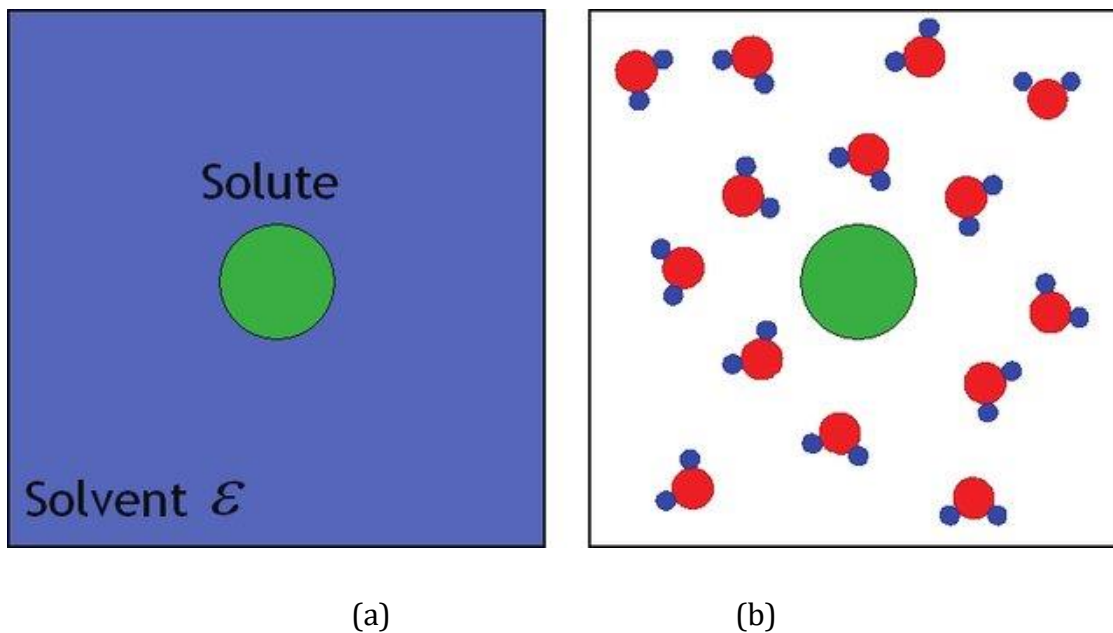
Figure 1.11 A schematic representation for (a) implicit and (b) explicit solvation models.[249]

To evaluate the solvent effect two types approximations (Figure 1.11) could be followed: those that treat the solvent as a continuous medium (implicit or continuum solvation) and those describing the individual solvent molecules (explicit solvation).[250, 251] Microsolvation, explicit solvation, places solvent molecules around the solute molecule. Explicit solvation calculations on large biomolecules in a bath of a large number of

explicit water molecules done with molecular dynamics, using molecular mechanics force fields have been reported.[252, 253] When the calculations are quantum mechanical approaches involved model will have a few solvent molecules, i.e. literally microsolvation. Inclusion of even a few solvent molecules in the quantum mechanical treatment significantly improves the theoretical description of some condensed-phase characteristics. In the explicit solvation, the solvent molecules will be inserted explicitly and then run molecular dynamics or Monte Carlo calculations to give the desirable property, which makes it the most accurate model. [254] Though it is the most rigorously correct way of modelling chemistry in solution, the primary disadvantage with the explicit solvent model is the expensive computer resources.

Continuum solvation, implicit solvation, is the easiest and most popular way of treating solvent effects. In this approximation a continuous medium, a continuum, is used to "imply" the presence of individual solvent molecules, in a best way of averaging out the effect of a large number of solvent molecules.[255] Here the solute is placed in a cavity in a solvent medium, which simulates the sea of solvent molecules and the interaction between the solute and the cavity is calculated.[251, 256] Implicit models "do not know" about hydrogen bonds, they are not likely to provide a wholly satisfactory account where specific interactions are of major importance. The charge distribution and polarizability of the solute defines the solute - solvent electrostatic interaction. SCRF (Self-Consistent Reaction Field) is a method of accounting for the effect of a polarizable solvent on the quantum system through solutions to the Poisson or Poisson-Boltzmann equation.[250] The concept for treating solute polarization in solution is the reaction field and iterating that reaction field to self-consistency is called the self-consistent reaction field (SCRF) method. This is important to include condensed-phase effects into quantum mechanical calculations and SCRF methods vary with how they define the cavity and the reaction field. SCRF calculations have been implemented in *ab initio*, semiempirical and DFT calculations.

Polarizable continuum model (PCM) introduced by Tomasi and coworkers, where the cavity is defined as the union of a series of interlocking atomic spheres is one of the most frequently used continuum solvation methods the.[251, 257, 258] PCM uses a numerical

integration over the solute charge density and generally gives good results by casting the quantum mechanical SCRF equations into a boundary element problem with apparent surface charges (ASCs) on the solute cavity surface. In PCM model the molecular free energy in solution is calculated as:

$$\Delta G_{sol} = \Delta G_{elec} + \Delta G_{disp} + \Delta G_{cav} \qquad \text{(Eq. 1.45)}$$

Here ΔG_{elec} and ΔG_{disp} accounts for the solute-solvent electrostatic interaction and solute-solvent dispersion and repulsion respectively. ΔG_{cav} is the cavitation energy, which is required to form the molecular cavity inside the continuum. All three terms are calculated using a cavity defined through interlocking van der Waals-spheres centered at atomic positions. The reaction field is represented through point charges located on the surface of the molecular cavity (ASC model). There exists various PCM formulations including the original method the dielectric PCM (D-PCM), where the surrounding medium is modeled as a dielectric, an alternative model called C-PCM, where the surrounding medium is modeled as a conductor and the third one is integral-equation-formalism protocol (IEF-PCM), where the PCM equations are allocated in integral equation formalism.

A method that is very similar to PCM is the solvation model based on density (SMD) coined by Tomasi *et al.*, in which interaction between the solute and solvent is calculated from the charge density of the former and the electric polarization field of the latter.[259] SMD is universal solvation model, since it can be applied to any charged or uncharged solute in any solvent and it uses specifically parametrized radii to construct the cavity. Here solvation free energy is obtained in terms of electrostatic term and cavity-dispersion solvent-structure term. The first term comes from the SCRF treatment involving the Poisson equation for electrostatics in IEF-PCM, whereas the second term stands for the contribution of short-range interactions between the solute and solvent in the first solvation shell.

In addition to these models combinations of these are also possible, for example by explicitly considering the first solvation shell describing the individual solvent molecules and treating the rest by a continuum model that treat the solvent as a

continuous medium. In hybrid models, the solute molecule is associated usually a few or sometime even single solvent molecule, and solute with its bound (usually hydrogen-bonded) solvent molecule(s) is subjected to a continuum calculation. Such hybrid calculations have been used in attempts to improve values of solvation free energies in connection with pKa,[260, 261] hydration of the environmentally important hydroxyl radical,[262] hydration of ubiquitous alkali metal and halide ions,[263] and also in biomolecular applications.[264] There are several solvation models available and also the models are getting constant improvisations over the years.

1.3.7 Quantum theory of atoms in molecule

Quantum theory of atoms in molecule (QTAIM) started as a theory by Richard Bader to partition a quantum mechanical system such as a molecule into mononuclear parts interacting with each other, which are defined by the topology of the electron density as subspaces with a well-defined kinetic energy of their own.[265, 266] Shortly after this was established, a second topological object was observed called a bond path. Bader *et al.* proposed that the topology of electron density $\rho(\mathbf{r})$ yields an accurate mapping of the molecular structure, and describes molecular features such as bonds, atoms, and structure. [267-269] According to this theory, the topological distribution of electronic charge in the field of nuclei and its flow in the presence of external field derived from $\rho(\mathbf{r})$, a scalar quantity provides physical information about the molecule. The electron density reaches a maximum at the nuclear positions, and each atom is portrayed by its boundaries dependent on the balance of forces of the system under consideration. Bader's QTAIM method in quantum mechanics based on the electron density is useful to define the structure of molecules and has been widely applied to unravel atom-atom covalent and non-covalent interactions in molecules, molecular clusters, small molecular crystals, proteins, DNA base pairing and stacking. Each topological feature can be described by a set of critical points (CPs), which is a point in the electron density surface where the gradient of electron density vanishes and is articulated as;

$$\nabla \rho(\mathbf{r}) = i\,\frac{d\rho}{dx} + j\,\frac{d\rho}{dy} + k\,\frac{d\rho}{dz} \quad \longrightarrow \quad \begin{cases} = \vec{0}\ \text{(at critical points (r_c) and at } \infty) \\ \neq \vec{0}\ \text{(at all other points)} \end{cases}$$

(Eq. 1.46)

The gradient of electron density, $\nabla\rho(\mathbf{r})$ is a vector quantity and points in the direction in which $\nabla\rho(\mathbf{r})$ is undergoes the maximum rate of increase, and its magnitude is equal to the rate of increase in that direction. A critical point corresponds to the maxima, minima or a saddle point of $\rho(\mathbf{r})$ and it could be distinguished on the basis of the Laplacian, $\nabla^2\rho(\mathbf{r})$. The nine possible second derivatives of electron density form Hessian matrix and the Laplacian is expressed as the sum of the eigenvalues of the Hessian matrix.

$$\nabla^2\rho(\mathbf{r}) = \nabla.\nabla\rho(\mathbf{r}) = \frac{\partial^2\rho(\mathbf{r})}{\partial x^2} + \frac{\partial^2\rho(\mathbf{r})}{\partial y^2} + \frac{\partial^2\rho(\mathbf{r})}{\partial z^2} \qquad \text{(Eq. 1.47)}$$

A critical point (CP) is labelled as an ordered pair (ω, σ), where ω is the rank and σ the signature. The rank is the number of non-zero eigenvalues of the electron density at the CP and signature is the algebraic sum of the signs of eigenvalues. If any of the eigenvalues associated with CPs is zero ($\omega < 3$) then those configurations are called degenerate and are unstable. CPs associated with the energetically stable configuration of nuclei show three non-zero eigenvalues ($\omega = 3$) and are said to be non-degenerate. For such configuration ($\omega = 3$), there are four types of CPs

i. Nuclear critical point (NCP), the (3,-3) critical point, with three negative curvatures, where $\rho(\mathbf{r})$ is a local maximum.

ii. Bond critical point (BCP), the (3,-1) critical point, with two negative curvatures where $\rho(\mathbf{r})$ is a maximum in the plane defined by these two eigenvectors and minimum along the third axis, perpendicular to this plane

iii. Ring critical point (RCP), the (3,+1) critical point ,with two positive curvatures where $\rho(\mathbf{r})$ is a minimum along the plane defined by the corresponding eigenvectors and maximum along the third axis perpendicular to this plane.

iv. Cage critical point (CCP), the (3,+3) critical point, with three positive curvatures where $\rho(\mathbf{r})$ is a local minimum.

Figure 1.12 shows different types od CPs observed for the C_{60} molecule.The interatomic bonding interaction, bond orders, the extent of charge accumulation in interatomic surface, *etc.* can be characterized by analysing the electron density at a BCP, ρ_b. The ρ_b values also give a measure of the strength of intermolecular interactions such as hydrogen bonds. The Laplacian of electron density ($\nabla^2(\rho)$) offers an understanding of the local charge concentration or depletion in the molecule and the sign of $\nabla^2\rho$ is used to differentiate the nature of the bond. Negative $\nabla^2\rho$ values are observed for shared interactions such as covalent and polarized bonds due as electron density is concentrated in the atom-atom region and positive $\nabla^2\rho$ values for interactions like van der Waals, ionic and hydrogen bonds where there is depletion of electron charge in the atom-atom region. In this thesis, AIMAll program developed by Keith *et al.*[270] has been used for the topological analysis of electron density of the complexes.
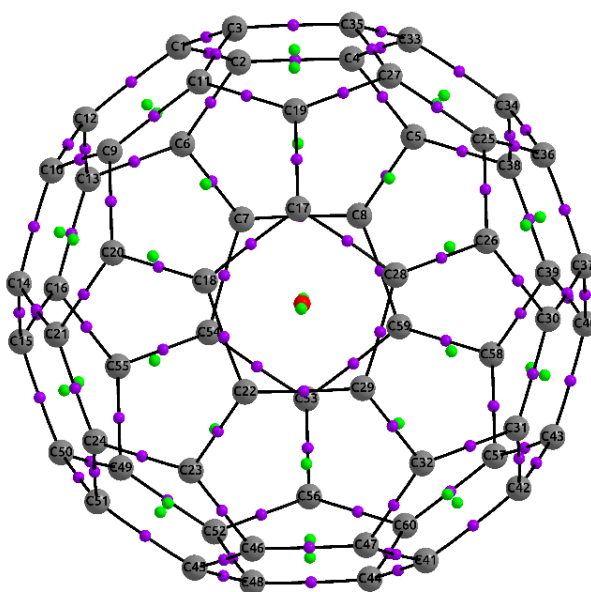
Figure 1.12 Molecular graph of C_{60} showing different critical points represented as small colored spheres (purple for (3, -1) or BCP, green for (3, +1) or RCP, and red for (3, +3) or CCP).

1.3.8 Molecular electrostatic potential

To understand condensed description of molecules like structure, bonding, and reactivity patterns buried in 3N-dimensional molecular wave function have been explored by theoretical as well as experimental chemists. Among the 3D scalar fields, bare nuclear potential (BNP), molecular electron density (MED) in position and momentum spaces and the molecular electrostatic potential (MESP), are experimentally amenable, thereby providing a vital bridge between experiment and theory. Followed by the investigations on the topology of molecular electron density by Bader *et al.* in terms of QTAIM analysis, the topology analysis of its sister field *viz.* MESP has gained wide acceptance for exploring molecular bonding and reactivity patterns. Since the pioneering works of Scrocco, Tomasi, Pullman and co-workers, MESP analysis has emerged as a sensitive electronic parameter in the study of molecular reactivity and related phenomena.
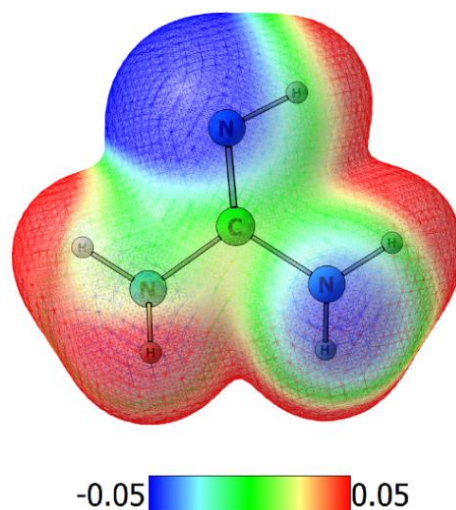
Figure 1.13 MESP plot of guanidine textured on to a 0.005 au electron density surface.

MESP generated by a chemical species (Figure 1.13) is widely used as a tool for exploring its properties and locating potential sites for interaction with other moieties. Similar to the bond critical points (BCPs), the MESP topology features are mapped in terms of the number and nature of critical points (CPs), where the first-order partial

derivatives of 3D scalar field vanish. The CP is further characterized by the evaluation of the eigenvalues of the corresponding Hessian matrix H_{ij} at the CP,

$$H_{ij} = \left[\frac{\partial^2 f}{\partial x_i \partial x_j} \right]_{CP} \qquad \text{(Eq. 1.48)}$$

The critical points are designated as an ordered pair (r,ω), where 'r' designates the rank and 'ω'is the signature. The rank stands or the number of nonzero eigenvalues of the function at the CP and signature is the algebraic sum of the signs of the eigenvalues of the Hessian matrix. A CP with any one of the eigenvalues of the Hessian matrix is zero is termed a degenerate CP. Thus, the four types of non-degenerate CPs for a 3D scalar field, are (3, +3), (3, -3), (3, +1), and (3, -1). The (3, -3) CP corresponds to a local maximum where all of the eigenvalues of the Hessian matrix become negative. The saddle points are denoted as (3, +1) and (3, -1). The (3, +3)-type is a local minimum. An important feature of MESP is that it is a real physical property and can be determined experimentally by X-ray diffraction techniques. Any distribution of electric charge, such as nuclei or electrons creates an electrical potential $V(\mathbf{r})$ in the surrounding space. MESP can be regarded as the potential of a molecule to interact with an electric charge located at a point **r** and it is defined as the work done in bringing a unit test non-interacting positive charge from infinity to a reference point with the molecule as given by the equation:

$$V(\mathbf{r}) = \sum_{A}^{N} \frac{Z_A}{|\mathbf{r} - \mathbf{R}_A|} - \int \frac{\rho(\mathbf{r'})d^3\mathbf{r'}}{|\mathbf{r} - \mathbf{r'}|} \qquad \text{(Eq. 1.49)}$$

Z_A is the charge on the nucleus located at a distance $\mathbf{R}_A$, $\rho(\mathbf{r'})$ is the electron density and $\mathbf{r'}$ is a dummy integration variable. The two terms refer to the bare nuclear potential and the electronic contributions, respectively. The MESP can attain positive, zero or negative values, in contrast to the behavior of electron densities in position, which can attain only non-negative values. A negative MESP value indicates an attractive interaction with this test charge, while positive MESP value designates repulsion. The most negative valued MESP point of a molecule, designated as V_{min}, symbolizes the sites of electron localization

in a molecule. Thus the value of $V(\mathbf{r})$ in any particular region depends on whether the effect of nuclei or electrons is dominant there and MESP is positive in the region close to nuclei and negative in the electron-rich region.

The MESP at the nucleus of an atom (V_n) in a molecule shows subtle variations with respect to changes in molecular electron density distribution. The MESP at the nucleus "A" of a molecule (V_n) can be obtained by dropping out the nuclear contribution due to Z_A from the definition of MESP, and can be written as:

$$V_n = \sum_{B \neq A} \frac{Z_B}{|\mathbf{R}_B - \mathbf{R}_A|} - \int \frac{\rho(\mathbf{r}')}{|\mathbf{R}_B - \mathbf{r}'|} d^3\mathbf{r}' \qquad \text{(Eq. 1.50)}$$

where Z_A is the charge on nucleus A with radius vector $\mathbf{R}_A$, Z_B and $\mathbf{R}_B$ represent the charge and position of nucleus B, $\rho(\mathbf{r}')$ is the electronic density function of the respective molecule, and $\mathbf{r}'$ is a dummy integration variable. The nuclei centered quantity, V_n is a local molecular property associated with the particular atom center and it measures the electrostatic potential at the position of the atom A due to all the electrons and rest of the nuclei. Similar to the change in V_{min}, change in V_n at the interacting atoms also reflects the charge transfer from donor to acceptor associated with a noncovalent bond formation.

MESP brings out electron rich regions like lone-pairs of electrons and π-bonds in the form of a negative valued (3, +3) CP. The most negative value of the MESP (V_{min}) corresponds to a point at which electrostatic potential due to the electron density term dominates maximally over the bare nuclear term. V_{min} symbolizes the sites of electron localization in a molecule i.e; the location of electron-dense region of a molecule. The concept of electrostatic potential was introduced by Scrocco and Tomasi in 1970s[271, 272] which has later emerged as a sensitive electronic parameter in the study of molecular reactivity and related phenomena.[273, 274-281] Besides the pioneering MESP based electron distribution studies by Pullman,[282] Politzer[273, 283-287] and Gadre,[179, 229, 288-296] the works of Wheeler and Houk[297-301] and Galabov[302-304] have also contributed significantly to the growth of this area. Recently a number of studies by Suresh *et al.* disclosed the efficiency of MESP based analysis to interpret and quantify resonance effect,[305] inductive effect,[306] substituent effects,[307, 308] trans influence,[309] cation-π interactions,[310-312] lone pair-π

interactions,[313] non-covalent interactions including a large variety of hydrogen bonds,[314] aromatic character of benzenoid hydrocarbons,[315, 316] stereo-electronic features of ligands in organometallic/inorganic chemistry[317-322] etc. In this thesis MESP is used as a predictive tool for analysing and quantifying intermolecular noncovalent interactions as well as predicting the reactive behaviour of molecules.

1.4 Conclusions

The part A of Chapter 1 portrayed various aspects of CO_2 adsorption and few important facets of fullerene chemistry. A brief account of some of the important adsorbents used in CO_2 capture is provided. The literature comprising the theoretical and experimental investigations on the recent advances in the field of CO_2 capture and conversion using nitrogen-rich adsorbents, including amine-functionalized, nitrogen-rich porous carbons, nitrogen-rich MOFs, and amino acid related compounds for selective CO_2 capture are also briefly accounted. The requirement of strong CO_2 binding affinity of the sorbent, associated sorbent degradation and reduced performance still remains as the need for the development of new and improved DAC methods and sorbents with optimal thermodynamics and kinetics of CO_2 binding and release, high cyclic capacities, improved chemical stabilities, and lower costs in R&D priority. The role of theoretical studies in the designing of adsorbents with improved efficiency and various types of modifications on the fullerene molecule to make it as a strong η^5 ligand are explained in detail by emphasizing the application of DFT in quantifying the covalent and noncovalent interactions.

Computational chemistry methods are inevitable in understanding the fundamental aspects of chemistry which uses the basic principles and equations that govern the subatomic world to calculate and predict the molecular structure and properties. The second part of Chapter 1 gives a brief account of basic theories underlying the computational chemistry methods such as *ab initio* methods, semi empirical methods, density functional theory, molecular mechanics, and molecular dynamics. A detailed account of the DFT methods used in the calculations discussed in the thesis is presented in this section. The principles and applications of atoms in molecules and molecular

electrostatic potential analysis employed for the quantification and characterization of weak interactions are also outlined along with the basics of basis sets, potential energy surface, and solvation models.

1.5 References

1.   D. W. Keith, G. Holmes, D. S. Angelo and K. Heidel, *Joule*, 2018, **2**, 1573-1594.
2.   G. Realmonte, L. Drouet, A. Gambhir, J. Glynn, A. Hawkes, A. C. Köberle and M. Tavoni, *Nat. Commun.*, 2019, **10**, 1-12.
3.   T. Van Gerven and A. Stankiewicz, *Ind. Eng. Chem. Res.*, 2009, **48**, 2465-2474.
4.   D. C. Kuppan and C. Yadav, in *Handbook of Ecomaterials*, eds. L. M. T. Martínez, O. V. Kharissova and B. I. Kharisov, Springer International Publishing, Cham. 2017, pp. 1-50.
5.   G. P. Peters, R. M. Andrew, T. Boden, J. G. Canadell, P. Ciais, C. Le Quéré, G. Marland, M. R. Raupach and C. Wilson, *Nat. Clim. Change.*, 2013, **3**, 4-6.
6.   P. Agreement, Paris agreement, 2015.
7.   *Each country's share of CO_2 emissions*, Union of Concerned Scientists, 2020.
8.   C. Cappiello, P. Melia, B. Pernici, P. Plebani and M. Vitali, Sustainable choices for cloud applications: a focus on CO_2 emissions, 2014.
9.   D. J. Wuebbles, D. W. Fahey and K. A. Hibbard, *Climate science special report: fourth national climate assessment, volume I*, 2017.
10.   P. Tans and R. Keeling, *NOAA ESRL Global Monitoring Division*, 2014.
11.   T. Boden, G. Marland, R. Andres and R. Global, *CDIACenter, Oak Ridge*, 2013.
12.   *IEA (2022), Global Energy Review: CO_2 Emissions in 2021, IEA,* , Paris 2022.
13.   T. F. Stocker, D. Qin, G.-K. Plattner, M. M. Tignor, S. K. Allen, J. Boschung, A. Nauels, Y. Xia, V. Bex and P. M. Midgley, Cambridge University Press2014.
14.   R. K. Pachauri, M. R. Allen, V. R. Barros, J. Broome, W. Cramer, R. Christ, J. A. Church, L. Clarke, Q. Dahe and P. Dasgupta, *Climate change 2014: synthesis report. Contribution of Working Groups I, II and III to the fifth assessment report of the Intergovernmental Panel on Climate Change*, Ipcc, 2014.
15.   J. Fuglestvedt, V. Masson-Delmotte, P. Zhai and A. Pirani, *Towards the sixth assessment report of the intergovernmental panel on climate change (IPCC)*, 2016.
16.   D. W. Keith, *Science*, 2009, **325**, 1654-1655.
17.   J. C. Stephens and D. W. Keith, *Climatic Change*, 2008, **90**, 217.
18.   B. Metz, O. Davidson and H. De Coninck, *Carbon dioxide capture and storage: special report of the intergovernmental panel on climate change*, Cambridge University Press, 2005.
19.   Y. Yuan, H. You and L. Ricardez-Sandoval, *Chin. J. Chem. Eng.*, 2019, **27**, 1554-1565.
20.   E. S. Rubin, H. Mantripragada, A. Marks, P. Versteeg and J. Kitchin, *Prog. Energy Combust. Sci.* , 2012, **38**, 630-671.
21.   Y. Zhu, C. Romain and C. K. Williams, *Nature*, 2016, **540**, 354-362.
22.   B. Li, Y. Duan, D. Luebke and B. Morreale, *Appl. Energy*, 2013, **102**, 1439-1447.

23. R. E. Hester and R. M. Harrison, *Carbon capture: sequestration and storage*, Royal Society of Chemistry, 2010.
24. G. B. Damas, A. B. Dias and L. T. Costa, *J. Phys. Chem. B*, 2014, **118**, 9046-9064.
25. K. Lackner, H.-J. Ziock and P. Grimes, *Carbon dioxide extraction from air: Is it an option?*, Los Alamos National Lab., NM (US)1999.
26. M. Songolzadeh, M. Soleimani, M. Takht Ravanchi and R. Songolzadeh, *Sci. World J.*, **2014**.
27. G. T. Rochelle, *Science*, 2009, **325**, 1652-1654.
28. K. Gottschling, L. Stegbauer, G. Sayasci, N. A. Prisco, Z. J. Berkson, C. Ochsenfeld, B. F. Chmelka and B. V. Lotsch, *Chem. Mat.*, 2019, **31**, 1946-1955.
29. E. National Academies of Sciences and Medicine, *Negative emissions technologies and reliable sequestration: a research agenda*, National Academies Press, 2018.
30. F. Creutzig, C. Breyer, J. Hilaire, J. Minx, G. P. Peters and R. Socolow, *Energy Environ. Sci.*, 2019, **12**, 1805-1817.
31. E. National Academies of Sciences and Medicine, *Gaseous carbon waste streams utilization: Status and research needs*, National Academies Press, 2019.
32. N. J. Williams, C. A. Seipp, F. M. Brethomé, Y.-Z. Ma, A. S. Ivanov, V. S. Bryantsev, M. K. Kidder, H. J. Martin, E. Holguin and K. A. Garrabrant, *Chem*, 2019, **5**, 719-730.
33. M. Fasihi, O. Efimova and C. Breyer, *J. Clean. Prod.* , 2019, **224**, 957-980.
34. K. S. Lackner, S. Brennan, J. M. Matter, A.-H. A. Park, A. Wright and B. Van Der Zwaan, The urgency of the development of CO_2 capture from ambient air, 2012.
35. E. S. Sanz-Perez, C. R. Murdock, S. A. Didas and C. W. Jones, *Chem. Rev.*, 2016, **116**, 11840-11876.
36. H. Azarabadi and K. S. Lackner, *Appl. Energy*, 2019, **250**, 959-975.
37. J. M. Hanusch, I. P. Kerschgens, F. Huber, M. Neuburger and K. Gademann, *Chem. Commun.*, 2019, **55**, 949-952.
38. Y.-H. Luo, C. Chen, D.-L. Hong, X.-T. He, J.-W. Wang, T. Ding, B.-J. Wang and B.-W. Sun, *ACS Appl. Mater. Interfaces*, 2018, **10**, 9495-9502.
39. S. Zeng, X. Zhang, L. Bai, X. Zhang, H. Wang, J. Wang, D. Bao, M. Li, X. Liu and S. Zhang, *Chem. Rev.*, 2017, **117**, 9625-9673.
40. K. S. Lackner, *Eur. Phys. J. Spec. Top.*, 2009, **176**, 93-106.
41. J. Yu and S. S. Chuang, *Ind. Eng. Chem. Res.*, 2017, **56**, 6337-6347.
42. M. L. Pinto, L. Mafra, J. M. Guil, J. Pires and J. Rocha, *Chem. Mater.*, 2011, **23**, 1387-1395.
43. Y. Zhai and S. S. Chuang, *Energy Technol.*, 2017, **5**, 510-519.
44. J. J. Lee, C.-H. Chen, D. Shimon, S. E. Hayes, C. Sievers and C. W. Jones, *J. Phys. Chem. C*, 2017, **121**, 23480-23487.
45. Z.-Z. Yang, L.-N. He, Y.-N. Zhao, B. Li and B. Yu, *Energy Environ. Sci.*, 2011, **4**, 3971-3975.
46. E. E. Ünveren, B. Ö. Monkul, Ş. Sarıoğlan, N. Karademir and E. Alper, *Petroleum*, 2017, **3**, 37-50.
47. M. Caplow, *J. Am. Chem. Soc.*, 1968, **90**, 6795-6803.
48. P. Danckwerts, *Chem. Eng. Sci.*, 1979, **34**, 443-446.
49. S. Grimme, J. Antony, S. Ehrlich and H. Krieg, *J. Chem. Phys.*, 2010, **132**, 154104.

50.   P. Bollini, S. A. Didas and C. W. Jones, *J. Mater.Chem.*, 2011, **21**, 15100-15120.

51.   T. Jafari, E. Moharreri, P. Toloueinia, A. S. Amin, S. Sahoo, N. Khakpash, I. Noshadi, S. P. Alpay and S. L. Suib, *J. CO₂ Util.*, 2017, **19**, 79-90.

52.   A. H. Alahmed, M. E. Briggs, A. I. Cooper and D. J. Adams, *J. Polym. Sci. A Polym. Chem.*, 2018, **56**, 2513-2521.

53.   F. Vega, A. Sanna, B. Navarrete, M. M. Maroto-Valer and V. J. Cortés, *Greenh. Gases: Sci. Technol.*, 2014, **4**, 707-733.

54.   X. Yang, R. J. Rees, W. Conway, G. Puxty, Q. Yang and D. A. Winkler, *Chem. Rev.*, 2017, **117**, 9524-9593.

55.   X. Shi, H. Xiao, H. Azarabadi, J. Song, X. Wu, X. Chen and K. S. Lackner, *Angew. Chem. Int. Ed.*, 2020, **59**, 6984-7006.

56.   Q.-W. Song, Z.-H. Zhou and L.-N. He, *Green Chem.*, 2017, **19**, 3707-3728.

57.   D. Brilman and R. Veneman, *Energy Procedia*, 2013, **37**, 6070-6078.

58.   E. M. Kutorglo, J. Kovačovič, D. Trunov, F. Hassouna, A. Fučíková, D. Kopecký, I. Sedlářová and M. Šoóš, *Chem. Eng. J.*, 2020, **388**, 124308.

59.   M. Senthilkumaran, C. Saravanan, V. Sethuraman, P. Puthiaraj and P. M. Mareeswaran, *Eur. Polym. J.*, 2020, **124**, 109477.

60.   Y. Wang, H. Wang, T. C. Zhang, S. Yuan and B. Liang, *J. Power Sources*, 2020, **472**, 228610.

61.   J. Wang and Y. Zhang, *Green Chem.*, 2016, **18**, 5248-5253.

62.   J. Kou and L.-B. Sun, *J. Mater. Chem. A*, 2016, **4**, 17299-17307.

63.   R. Muhammad, P. Rekha and P. Mohanty, *RSC Adv.*, 2016, **6**, 17100-17105.

64.   A. Yassin, M. Trunk, F. Czerny, P. Fayon, A. Trewin, J. Schmidt and A. Thomas, *Adv. Funct. Mater.*, 2017, **27**, 1700233.

65.   B. Chang, S. Zhang, H. Yin and B. Yang, *Appl. Surf. Sci.*, 2017, **412**, 606-615.

66.   A. Rehman and S.-J. Park,   *Macromol. Res.*, 2017, **25**, 1035-1042.

67.   J. Du, L. Liu, L. Zhang, Y. Yu, Y. Zhang and A. Chen, *J. Renew. Sustain. Energy*, 2017, **9**, 064901.

68.   J.-R. Song, W.-G. Duan and D.-P. Li, *Molecules*, 2018, **23**, 1732.

69.   Y. Zhang, L. Liu, P. Zhang, J. Wang, M. Xu, Q. Deng, Z. Zeng and S. Deng, *Chem. Eng. J.*, 2019, **355**, 309-319.

70.   J. Yang, J. Dai, J. He, L. Wang, A. Xie and Y. Yan, *J. Porous Mater.*, 2020, 1-9.

71.   Y. H. Abdelmoaty, T.-D. Tessema, F. A. Choudhury, O. M. El-Kadri and H. M. El-Kaderi, *ACS Appl. Mater. Interfaces*, 2018, **10**, 16049-16058.

72.   R. Walczak, A. Savateev, J. Heske, N. V. Tarakina, S. Sahoo, J. D. Epping, T. D. Kühne, B. Kurpil, M. Antonietti and M. Oschatz, *Sustain. Energy & Fuels*, 2019, **3**, 2819-2827.

73.   Z. Wang, N. Goyal, L. Liu, D. C. Tsang, J. Shang, W. Liu and G. Li, *Chem. Eng. J.*, 2020, 125376.

74.   N. Song, T. Ma, T. Wang, Z. Li, H. Yao and S. Guan, *J. Colloid Interface Sci.*, 2020.

75.   I. A. Principe and A. J. Fletcher, *Adsorption*, 2020, 1-13.

76.   E. Dooris, C. A. McAnally, E. J. Cussen, A. R. Kennedy and A. J. Fletcher, *Crystals*, 2016, **6**, 14.

77.   J. Wang, Y. Lin, Q. Yue, K. Tao, C. Kong and L. Chen, *RSC Adv.*, 2016, **6**, 53017-53024.

78.   K. A. Forrest, T. Pham and B. Space, *Phys. Chem. Chem. Phys.*, 2017, **19**, 29204-29221.

79. P. Das and S. K. Mandal, *Chem. Mater.*, 2019, **31**, 1584-1596.
80. Y. Zhi, P. Shao, X. Feng, H. Xia, Y. Zhang, Z. Shi, Y. Mu and X. Liu, *J. Mater. Chem. A*, 2018, **6**, 374-382.
81. J. E. Crooks and J. P. Donnellan, *J. Chem. Soc., Perkin trans. 1*, 1989, 331-333.
82. D. Guo, H. Thee, C. Y. Tan, J. Chen, W. Fei, S. Kentish, G. W. Stevens and G. da Silva, *Energy Fuels*, 2013, **27**, 3898-3904.
83. J. v. Holst, S. R. Kersten and K. J. Hogendoorn, *J. Chem. Eng. Data .* 2008, **53**, 1286-1291.
84. E. S. Hamborg, J. P. Niederer and G. F. Versteeg, *J. Chem. Eng. Data .* 2007, **52**, 2491-2502.
85. A. F. Ciftja, A. Hartono and H. F. Svendsen, *Energy Procedia*, 2013, **37**, 1597-1604.
86. U. E. Aronu, A. F. Ciftja, I. Kim and A. Hartono, *Energy Procedia*, 2013, **37**, 233-240.
87. C. A. Seipp, N. J. Williams, M. K. Kidder and R. Custelcean, *Angew. Chem. Int. Ed.*, 2017, **129**, 1062-1065.
88. R. Custelcean, N. J. Williams, K. A. Garrabrant, P. Agullo, F. M. Brethomé, H. J. Martin and M. K. Kidder, *Ind. Eng. Chem. Res.*, 2019, **58**, 23338-23346.
89. J. Thiele and E. Dralle, *Justus Liebieg's Ann. Chem.*, 1898, **302**, 275-299.
90. R. Custelcean, N. Williams, K. Garrabrant, C. Seipp and F. Brethome, CO_2 separation by crystallization of guanidinium carbonates, 2019.
91. R. Custelcean, *Chem. Commun.*, 2020.
92. R. Custelcean, N. J. Williams and C. A. Seipp, Google Patents2020.
93. A. Barbarini, R. Maggi, A. Mazzacani, G. Mori, G. Sartori and R. Sartorio, *Tetrahedron Lett.*, 2003, **44**, 2931-2934.
94. Z.-Z. Yang, Y.-N. Zhao, L.-N. He, J. Gao and Z.-S. Yin, *Green Chem.*, 2012, **14**, 519-527.
95. D. Wei-Li, J. Bi, L. Sheng-Lian, L. Xu-Biao, T. Xin-Man and A. Chak-Tong, *J. Mol. Catal. A Chem.*, 2013, **378**, 326-332.
96. X. Wang, Y. N. Lim, C. Lee, H. Y. Jang and B. Y. Lee, *Eur. J. Org. Chem.*, 2013, **2013**, 1867-1871.
97. R. Nicholls, S. Kaufhold and B. N. Nguyen, *Catal. Sci. Technol.*, 2014, **4**, 3458-3462.
98. C. Villiers, J. P. Dognon, R. Pollet, P. Thuéry and M. Ephritikhine, *Angew. Chem.*, 2010, **122**, 3543-3546.
99. J. Ma, X. Zhang, N. Zhao, A. S. Al-Arifi, T. Aouak, Z. A. Al-Othman, F. Xiao, W. Wei and Y. Sun, *J. Mol. Catal. A Chem.*, 2010, **315**, 76-81.
100. E. R. Pérez, M. O. da Silva, V. C. Costa, U. P. Rodrigues-Filho and D. W. Franco, *Tetrahedron Lett.*, 2002, **43**, 4091-4093.
101. E. R. Pérez, R. H. Santos, M. T. Gambardella, L. G. de Macedo, U. P. Rodrigues-Filho, J.-C. Launay and D. W. Franco, *J. Org. Chem.*, 2004, **69**, 8005-8011.
102. D. J. Heldebrant, P. G. Jessop, C. A. Thomas, C. A. Eckert and C. L. Liotta, *J. Org. Chem.*, 2005, **70**, 5335-5338.
103. F. S. Pereira, D. L. da Silva Agostini, R. D. do Espírito Santo, E. R. deAzevedo, T. J. Bonagamba, A. E. Job and E. R. P. González, *Green Chem.*, 2011, **13**, 2146-2153.
104. F. S. Pereira, E. R. deAzevedo, E. F. da Silva, T. J. Bonagamba, D. L. da Silva Agostíni, A. Magalhaes, A. E. Job and E. R. P. Gonzalez, *Tetrahedron*, 2008, **64**, 10097-10106.

105. E. A. Prasetyanto, M. B. Ansari, B.-H. Min and S.-E. Park, *Catal. Today*, 2010, **158**, 252-257.

106. C. Rether, W. Sicking, R. Boese and C. Schmuck, *Beilstein Journal of Organic Chemistry*, 2010, **6**, 8.

107. L. F. Wilm, M. Das, D. Janssen-Müller, C. Mück-Lichtenfeld, F. Glorius and F. Dielmann, *Angew. Chem. Int. Ed.*, 2022, **61**, e202112344.

108. M. T. Ho, G. W. Allinson and D. E. Wiley, *Ind. Eng. Chem. Res.*, 2008, **47**, 4883-4890.

109. S. Y. Lee and S. J. Park, *Ind. Eng. Chem. Res.*, 2015, **23**, 1-11.

110. Y. Jiao, A. J. Du, Z. H. Zhu, V. Rudolph and S. C. Smith, *J. Mater. Chem.*, 2010, **20**, 10426-10430.

111. Q. Sun, M. Wang, Z. Li, A. J. Du and D. J. Searles, *J. Phys. Chem. C*, 2014, **118**, 2170-2177.

112. K. B. Lee and S. Sircar, *Aiche J.*, 2008, **54**, 2293-2302.

113. G. Ferey, C. Serre, T. Devic, G. Maurin, H. Jobic, P. L. Llewellyn, G. De Weireld, A. Vimont, M. Daturi and J. S. Chang, *Chem. Soc. Rev.*, 2011, **40**, 550-562.

114. R. Tenne, *Adv. Mater.*, 1995, **7**, 965-+.

115. Q. Sun, Z. Li, D. J. Searles, Y. Chen, G. Q. Lu and A. J. Du, *J. Am. Chem. Soc.*, 2013, **135**, 8246-8253.

116. T. S. Zhao, Q. Wang, Y. Kawazoe and P. Jena, *Carbon*, 2018, **132**, 249-256.

117. N. Martín, *Chem. Commun.*, 2006, 2093-2104.

118. P. D. W. Boyd and C. A. Reed, *Accounts Chem. Res.*, 2005, **38**, 235-242.

119. T. Hasobe, H. Imahori, P. V. Kamat and S. Fukuzumi, *J. Am. Chem. Soc.*, 2003, **125**, 14962-14963.

120. Y. Zhang, D. Wang and W. Wang, *Comput. Theor. Chem.*, 2018, **1128**, 56-59.

121. S. Osuna, M. Swart and M. Sola, *Phys. Chem. Chem. Phys.*, 2011, **13**, 3585-3603.

122. J. Cioslowski and K. Raghavachari, *J. Chem. Phys.*, 1993, **98**, 8734-8741.

123. L. Dunsch and S. F. Yang, *Phys. Chem. Chem. Phys.*, 2007, **9**, 3067-3081.

124. A. Krachmalnicoff, R. Bounds, S. Mamone, S. Alom, M. Concistre, B. Meier, K. Kouril, M. E. Light, M. R. Johnson, S. Rols, A. J. Horsewill, A. Shugai, U. Nagel, T. Room, M. Carravetta, M. H. Levitt and R. J. Whitby, *Nat. Chem.*, 2016, **8**, 953-957.

125. K. Kurotobi and Y. Murata, *Science*, 2011, **333**, 613-616.

126. K. Komatsu, M. Murata and Y. Murata, *Science*, 2005, **307**, 238-240.

127. X. Wu and X. Lu, *J. Am. Chem. Soc.*, 2007, **129**, 2171-2177.

128. R. E. Estrada-Salas and A. A. Valladares, *Theochem-J. Mol. Struct.*, 2008, **869**, 1-5.

129. K. Lee, H. Song and J. T. Park, *Accounts Chem. Res.*, 2003, **36**, 78-86.

130. S. Vidal, J. Marco-Martínez, S. Filippone and N. Martín, *Chem. Commun.*, 2017, **53**, 4842-4844.

131. C. Z. Li, C. C. Chueh, H. L. Yip, F. Ding, X. Li and A. K. Y. Jen, *Adv. Mater.*, 2013, **25**, 2457-2461.

132. J. Cioslowski and A. Nanayakkara, *J. Chem. Phys.*, 1992, **96**, 8354-8362.

133. B. Gao, J. X. Zhao, Q. H. Cai, X. G. Wang and X. Z. Wang, *J. Phys. Chem. A*, 2011, **115**, 9969-9976.

134. F. Gao, G. L. Zhao, S. Z. Yang and J. J. Spivey, *J. Am. Chem. Soc.*, 2013, **135**, 3315-3318.

135. Q. Sun, M. Wang, Z. Li, Y. Y. Ma and A. J. Du, *Chem. Phys. Lett.*, 2013, **575**, 59-66.

136. Y. Jiao, Y. Zheng, S. C. Smith, A. J. Du and Z. H. Zhu, *ChemSusChem*, 2014, **7**, 435-441.
137. S. W. de Silva, A. J. Du, W. Senadeera and Y. T. Gu, *Beilstein J. Nanotechnol.*, 2014, **5**, 413-418.
138. S. Ralser, A. Kaiser, M. Probst, J. Postler, M. Renzler, D. K. Bohme and P. Scheier, *Phys. Chem. Chem. Phys.*, 2016, **18**, 3048-3055.
139. S. Wang, S. M. Mahurin, S. Dai and D. E. Jiang, *ACS Appl. Mater. Interfaces*, 2021, **13**, 17511-17516.
140. J. Heath, S. O'brien, Q. Zhang, Y. Liu, R. Curl, F. Tittel and R. Smalley, *J. Am. Chem.Soc.*, 1985, **107**, 7779-7780.
141. A. J. Stone and D. J. Wales, *Chem. Phys. Lett.*, 1986, **128**, 501-503.
142. A. L. Balch and M. M. Olmstead, *Chem. Rev.*, 1998, **98**, 2123-2166.
143. Y. Wang, D. Tománek and R. S. Ruoff, *Chem. Phys. Lett.*, 1993, **208**, 79-85.
144. A. A. Popov and L. Dunsch, *Chem. Eur. J.*, 2009, **15**, 9707-9729.
145. J. Cioslowski, *J. Am. Chem. Soc.*, 1991, **113**, 4139-4141.
146. P. Ravinder and V. Subramanian, *J. Phys. Chem. A*, 2011, **115**, 11723-11733.
147. C. Ramachandran and N. Sathyamurthy, *Chem. Phys. Lett.*, 2005, **410**, 348-351.
148. O. Shameema, C. Ramachandran and N. Sathyamurthy, *J. Phys. Chem. A*, 2006, **110**, 2-4.
149. O. V. de Oliveira and A. da Silva Gonçalves, *Comput. Chem.*, 2014, **2**, 51.
150. Y. Garcia-Rodeja, M. Sola, F. M. Bickelhaupt and I. Fernandez, *Chem. Eur. J.*, 2017.
151. T. A. Murphy, T. Pawlik, A. Weidinger, M. Höhne, R. Alcala and J.-M. Spaeth, *Phys. Rev. Lett.*, 1996, **77**, 1075.
152. C. Knapp, N. Weiden, H. Kass, K.-P. Dinse, B. Pietzak, M. Waiblinger and A. Weidinger, *Mol. Phys.*, 1998, **95**, 999-1004.
153. E. Dietel, A. Hirsch, B. Pietzak, M. Waiblinger, K. Lips, A. Weidinger, A. Gruss and K.-P. Dinse, *J. Am. Chem. Soc.*, 1999, **121**, 2432-2437.
154. A. A. Popov, S. Yang and L. Dunsch, *Chem. Rev*, 2013, **113**, 5989-6113.
155. J. López-Andarias, A. Bauzá, N. Sakai, A. Frontera and S. Matile, *Angew. Chem. Int. Ed.*, 2018, **130**, 11049-11053.
156. J. López-Andarias, A. Frontera and S. Matile, *J. Am. Chem.Soc.*, 2017, **139**, 13296-13299.
157. J. Lopez-Andarias, A. Frontera and S. Matile, *J. Am. Chem. Soc.*, 2017, **139**, 13296-13299.
158. E. C. Escudero-Adán, A. Bauzá, L. P. Hernández-Eguía, F. Würthner, P. Ballester and A. Frontera, *Crystengcomm*, 2017, **19**, 4911-4919.
159. Y. Matsuo and E. Nakamura, *Chem. Rev.*, 2008, **108**, 3016-3028.
160. Y. Matsuo, Y. Kuninobu, A. Muramatsu, M. Sawamura and E. Nakamura, *Organometallics*, 2008, **27**, 3403-3409.
161. Q.-L. Yan, M. Gozin, F.-Q. Zhao, A. Cohen and S.-P. Pang, *Nanoscale*, 2016, **8**, 4799-4851.
162. J. M. Hawkins, A. Meyer, T. A. Lewis, S. Loren and F. J. Hollander, *Science*, 1991, **252**, 312-313.
163. P. J. Fagan, J. C. Calabrese and B. Malone, *Science*, 1991, **252**, 1160-1162.
164. P. J. Fagan, J. C. Calabrese and B. Malone, *Accounts Chem. Res.*, 1992, **25**, 134-142.

165. A. L. Balch, V. J. Catalano, J. W. Lee, M. M. Olmstead and S. R. Parkin, *J. Am. Chem. Soc.*, 1991, **113**, 8953-8955.

166. R. S. Koefod, M. F. Hudgens and J. R. Shapley, *J. Am. Chem.Soc.*, 1991, **113**, 8957-8958.

167. V. V. Bashilov, P. V. Petrovskii, V. I. Sokolov, S. Lindeman, I. A. Guzey and Y. T. Struchkov, *Organometallics*, 1993, **12**, 991-992.

168. B. Chase and P. J. Fagan, *J. Am. Chem. Soc.*, 1992, **114**, 2252-2256.

169. S. A. Lerke, B. Parkinson, D. H. Evans and P. J. Fagan, *J. Am. Chem. Soc.*, 1992, **114**, 7807-7813.

170. T. Pradeep, G. Kulkarni, K. Kannan, T. G. Row and C. Rao, *J. Am. Chem.Soc.*, 1992, **114**, 2272-2273.

171. M. N. Bengough, D. M. Thompson, M. C. Baird and G. D. Enright, *Organometallics*, 1999, **18**, 2950-2952.

172. D. M. Thompson, M. Bengough and M. C. Baird, *Organometallics*, 2002, **21**, 4762-4770.

173. C. M. Alvarez, R. J. Angelici, A. Sygula, R. Sygula and P. W. Rabideau, *Organometallics*, 2003, **22**, 624-626.

174. C. J. Cramer, *Essentials of computational chemistry: theories and models*, John Wiley & Sons, 2013.

175. A. R. Leach and A. R. Leach, *Molecular modelling: principles and applications*, Pearson education, 2001.

176. T. Schlick, *Molecular modeling and simulation: an interdisciplinary guide: an interdisciplinary guide*, Springer Science & Business Media, 2010.

177. H. F. Schaefer III, *J. Mol. Struct. (Theochem)*, 2001, **573**, 129-137.

178. E. Lewars, *Computational chemistry*, 2003.

179. S. R. Gadre, S. A. Kulkarni, C. H. Suresh and I. H. Shrivastava, *Chem. Phys. Lett.*, 1995, **239**, 273-281.

180. W. Thiel, *Tetrahedron*, 1988, **44**, 7393-7408.

181. J. J. Stewart, *Rev. Comput. Chem.*, 1990, **1**, 45-81.

182. A. D. MacKerell Jr, *J. Comput. Chem.*, 2004, **25**, 1584-1604.

183. J. W. Ponder and D. A. Case, *Adv Protein Chem*, 2003, **66**, 27-85.

184. A. K. Rappé and C. J. Casewit, *Molecular mechanics across chemistry*, University Science Books, 1997.

185. U. Dinur and A. T. Hagler, *Rev. Comput. Chem.*, 1991, **2**, 99-164.

186. J. Thyssen, T. Fleig and H. J. A. Jensen, *J. Chem. Phys.*, 2008, **129**, 034109.

187. R. A. Friesner, Ab initio quantum chemistry: Methodology and applications, 2005.

188. E. Schrödinger, *E. Ann. Phys*, 1926, **79**, 361-376.

189. A. Szabo and N. S. Ostlund, *Modern quantum chemistry: introduction to advanced electronic structure theory*, Courier Corporation, 2012.

190. D. R. Hartree, The wave mechanics of an atom with a non-Coulomb central field. Part I. Theory and methods, 1928.

191. J. C. Slater, *Phys. Rev.*, 1930, **35**, 210.

192. D. C. Young, *Computational Chemistry: A Practical Guide for Applying Techniques to Real World Problems*, Wiley-Interscience, New York, 2001.

193. I. Shavitt, *Mol. Phys.*, 1998, **94**, 3-17.
194. R. J. Bartlett and M. Musiał, *Rev. Mod. Phys.*, 2007, **79**, 291.
195. E. K. Gross and R. M. Dreizler, *Density functional theory*, Springer Science & Business Media, 2013.
196. J. F. Dobson, G. Vignale and M. P. Das, *Electronic density functional theory: recent progress and new directions*, 2013.
197. W. Kohn, A. D. Becke and R. G. Parr, *J. Phys. Chem.*, 1996, **100**, 12974-12980.
198. W. Kohn, *Rev. Mod. Phys.* , 1999, **71**, 1253.
199. P. Hohenberg and W. Kohn, *Phys. Rev.*, 1964, **136**, B864.
200. W. Kohn and L. J. Sham, *Phys. Rev.*, 1965, **140**, A1133.
201. W. Koch and M. C. Holthausen, *A chemist's guide to density functional theory*, John Wiley & Sons, 2015.
202. M. Orio, D. A. Pantazis and F. Neese, *Photosynth. Res.*, 2009, **102**, 443-453.
203. L. H. Thomas, The calculation of atomic fields, 1927.
204. E. Fermi, *Rend. Accad. Naz. Lincei*, 1927, **6**, 32.
205. M. Gell-Mann and K. A. Brueckner, *Phys. Rev.*, 1957, **106**, 364.
206. J. C. Slater, *Phys. Rev.*, 1951, **81**, 385.
207. A. D. Becke, *Phys. Rev. A*, 1988, **38**, 3098.
208. J. P. Perdew, *Phys. Rev. B*, 1986, **33**, 8822.
209. R. Peverati and D. G. Truhlar, *Phil. Trans. R. Soc. A*, 2014, **372**, 20120476.
210. Y. Zhao and D. G. Truhlar, *J. Chem. Phys.*, 2006, **125**, 194101.
211. Y. Zhao, N. E. Schultz and D. G. Truhlar, *J. Chem. Phys.*, 2005, **123**, 161103.
212. Y. Zhao, N. E. Schultz and D. G. Truhlar,

J. Chem. Theory Comput. , 2006, **2**, 364-382.
213. R. Peverati and D. G. Truhlar, *J. Chem. Theory Comput.* , 2012, **8**, 2310-2319.
214. J. P. Perdew and K. Schmidt, Jacob's ladder of density functional approximations for the exchange-correlation energy, 2001.
215. N. Mardirossian and M. Head-Gordon, *Phys. Chem. Chem. Phys.*, 2014, **16**, 9904-9924.
216. J. P. Perdew, A. Ruzsinszky, J. Tao, V. N. Staroverov, G. E. Scuseria and G. I. Csonka, *J. Chem. Phys.*, 2005, **123**, 062201.
217. N. Mardirossian and M. Head-Gordon, *Mol. Phys.*, 2017, **115**, 2315-2372.
218. L. C. Allen and A. M. Karo, *Rev. Mod. Phys.*, 1960, **32**, 275-285.
219. J. C. Slater, *Phys. Rev.*, 1930, **36**, 57-64.
220. E. Besalú and R. Carbó-Dorca, *J. Math. Chem.*, 2011, **49**, 1769-1784.
221. I. Shavitt and M. Karplus, *J. Chem. Phys.*, 1965, **43**, 398-414.
222. Y. Sakai, H. Tatewaki and S. Huzinaga, *J. Comput. Chem.*, 1981, **2**, 100-107.
223. R. F. Stewart and W. J. Hehre, *J. Chem. Phys.*, 1970, **52**, 5243-5247.
224. H. Tatewaki and S. Huzinaga, *J. Chem. Phys.*, 1979, **71**, 4339-4348.
225. W. J. Hehre, R. F. Stewart and J. A. Pople, *J. Chem. Phys.*, 1969, **51**, 2657-2664.
226. J. B. Collins, P. von R. Schleyer, J. S. Binkley and J. A. Pople, *J. Chem. Phys.*, 1976, **64**, 5142-5151.
227. E. R. Davidson and D. Feller, *Chem. Rev.*, 1986, **86**, 681-696.
228. R. Ditchfield, W. J. Hehre and J. A. Pople, *J. Chem. Phys.* , 1971, **54**, 724-728.

229.   S. R. Gadre and P. K. Bhadane, *J. Chem. Phys.*, 1997, **107**, 5625-5626.

230.   J. G. Hill, *Int. J. Quantum Chem.*, 2013, **113**, 21-34.

231.   P. J. Hay and W. R. Wadt, *J. Chem. Phys.*, 1985, **82**, 270-283.

232.   F. Jensen, *Introduction to computational chemistry*, John wiley & sons, 2017.

233.   P. J. Hay and W. R. Wadt, *J. Chem. Phys.*, 1985, **82**, 270-283.

234.   T. R. Cundari and W. J. Stevens, *J. Chem. Phys.*, 1993, **98**, 5555-5565.

235.   M. Dolg, in *Theor. Comput. Chem.*, ed. P. Schwerdtfeger, Elsevier. 2002, vol. 11, pp. 793-862.

236.   C. E. Check, T. O. Faust, J. M. Bailey, B. J. Wright, T. M. Gilbert and L. S. Sunderlin, *J. Phys. Chem. A*, 2001, **105**, 8111-8116.

237.   R. Krishnan, J. S. Binkley, R. Seeger and J. A. Pople, *J. Chem. Phys.*, 1980, **72**, 650-654.

238.   M. J. Frisch, J. A. Pople and J. S. Binkley, *J. Chem. Phys.*, 1984, **80**, 3265-3269.

239.   F. B. Van Duijneveldt, J. G. van Duijneveldt-van de Rijdt and J. H. van Lenthe, *Chem. Rev.*, 1994, **94**, 1873-1885.

240.   M. Born and J. R. Oppenheimer, *Ann. Phys.*, 1927.

241.   H. B. Schlegel, *Wiley Interdiscip. Rev. Comput. Mol. Sci.*, 2011, **1**, 790-809.

242.   M. L. Kouwizjer and P. D. Grootenhuis, *J. Phys. Chem.*, 1995, **99**, 13426-13436.

243.   S. S. Shaik, H. B. Schlegel and S. Wolfe, *Theoretical aspects of physical organic chemistry*, Wiley, 1992.

244.   A. Matsuura, H. Sato, W. Sotoyama, A. Takahashi and M. Sakurai, *J. Mol. Struct. (Theochem)*, 2008, **860**, 119-127.

245.   J. Baker, *J. Comput. Chem.*, 1986, **7**, 385-395.

246.   J. Baker and F. Chan, *J. Comput. Chem.*, 1996, **17**, 888-904.

247.   H. B. Schlegel, *J. Comput. Chem.*, 1982, **3**, 214-218.

248.   S. M. Bachrach, *Annual Reports Section" B"(Organic Chemistry)*, 2009, **105**, 398-420.

249.   T. W. de Lima, A. Caliri, F. L. B. da Silva, R. Tinós, G. Travieso, I. N. da Silva, P. S. Lopes, E. M. de Souza, A. C. B. Delbem and V. Bonatto, in *Evolutionary Computation*, IntechOpen. 2009.

250.   C. J. Cramer and D. G. Truhlar, *Chem. Rev.*, 1999, **99**, 2161-2200.

251.   J. Tomasi, B. Mennucci and R. Cammi, *Chem. Rev.*, 2005, **105**, 2999-3094.

252.   J. Thar, S. Zahn and B. Kirchner, *J Phys Chem B*, 2008, **112**, 1456.

253.   A. T. Brunger and P. D. Adams, *Acc. Chem. Res.*, 2002, **35**, 404-412.

254.   D. C. Young, *Computational Chemistry: A Practical Guide for Applying Techniques to Real-World Problems*, Wiley-Interscience, New York, 2001.

255.   J. B. Foresman, T. A. Keith, K. B. Wiberg, J. Snoonian and M. J. Frisch, *J Phys Chem*, 1996, **100**, 16098-16104.

256.   R. Skyner, J. McDonagh, C. Groom, T. Van Mourik and J. Mitchell, *Phys. Chem. Chem. Phys.*, 2015, **17**, 6174-6191.

257.   S. Miertuš, E. Scrocco and J. Tomasi, *Chem. Phys.*, 1981, **55**, 117-129.

258.   J. Tomasi, E. Cancès, C. S. Pomelli, M. Caricato, G. Scalmani, M. J. Frisch, R. Cammi, M. V. Basilevsky, G. N. Chuev and B. Mennucci, in *Continuum Solvation Models in Chemical Physics*, John Wiley & Sons, Ltd. 2007, pp. 1-123.

259.   E. S. Gwee, Z. L. Seeger, D. R. Appadoo, B. R. Wood and E. I. Izgorodina, *ACS omega*, 2019, **4**, 5254-5269.

260. C. P. Kelly, C. J. Cramer and D. G. Truhlar, *J. Phys. Chem. A*, 2006, **110**, 2493-2499.
261. F. Eckert, M. Diedenhofen and A. Klamt, *Mol. Phys.*, 2010, **108**, 229-241.
262. S. Hamad, S. Lago and J. Mejias, *J. Phys. Chem. A*, 2002, **106**, 9104-9113.
263. I. Topol, G. Tawa, S. Burt and A. Rashin, *J. Chem. Phys.*, 1999, **111**, 10998-11014.
264. A. Okur and C. Simmerling, *Annu Rep Comput Chem*, 2006, **2**, 97-109.
265. R. F. Bader, *Accounts of Chemical Research*, 1985, **18**, 9-15.
266. R. F. Bader, *Accounts of Chemical Research*, 1975, **8**, 34-40.
267. R. F. W. Bader, *Acc. Chem. Res*, 1985, **18**, 9-15.
268. R. F. W. Bader, ed. *Atoms in Molecules: A Quantum Theory*, Clarendon Press,Oxford, UK, 1990.
269. R. F. W. Bader, *Atoms in Molecules*, John Wiley & Sons, Ltd, 2002.
270. T. Keith, *Google Scholar There is no corresponding record for this reference*.
271. E. Scrocco and J. Tomasi, *Adv. Quantum Chem.*, 1978, **11**, 115–193.
272. E. Scrocco and J. Tomasi, The electrostatic molecular potential as a tool for the interpretation of molecular properties, Berlin, Heidelberg, 1973.
273. J. S. Murray and P. Politzer, *Wiley Interdiscip. Rev.: Comput. Mol. Sci.*, 2011, **1**, 153-163.
274. S. R. Gadre and C. Suresh, *J. Org. Chem.*, 1997, **62**, 2625-2627.
275. C. K. Bagdassarian, V. L. Schramm and S. D. Schwartz, *J. Am. Chem. Soc.*, 1996, **118**, 8825-8836.
276. C. I. Bayly, P. Cieplak, W. Cornell and P. A. Kollman, *J. Phys. Chem.* , 1993, **97**, 10269-10280.
277. B. Pullman, D. Perahia and D. Cauchy, *Nucleic Acids Res.*, 1979, **6**, 3821-3830.
278. A. Pullman and B. Pullman, *Q. Rev. Biophys.*, 1981, **14**, 289-380.
279. R. Lavery and B. Pullman, *Int. J. Quantum Chem.*, 1981, **20**, 259-272.
280. R. Lavery and B. Pullman, *Nucleic Acids Res.*, 1981, **9**, 4677-4688.
281. S. Chidangil, M. K. Shukla and P. C. Mishra, *Mol. Model. Annu.*, 1998, **4**, 250-258.
282. B. Pullman, *Int. J. Quantum Chem. Quantum Biol. Symp.*, 1990, **17**, 81–92.
283. P. Politzer, L. Abrahmsen and P. Sjoberg, *J. Am. Chem. Soc.*, 1984, **106**, 855-860.
284. F. A. Bulat, A. Toro-Labbe, T. Brinck, J. S. Murray and P. Politzer, *J. Mol. Model.*, 2010, **16**, 1679-1691.
285. P. Politzer, J. S. Murray and T. Clark, *Phys. Chem. Chem. Phys.*, 2013, **15**, 11178-11189.
286. P. Politzer, P. R. Laurence and K. Jayasuriya, *Environ. Health. Persp.*, 1985, **61**, 191-202.
287. P. Politzer and J. S. Murray, *J. Mol. Struct.*, 1996, **376**, 419-424.
288. S. R. Gadre and R. N. Shirsat, *Electrostatics of Atoms and Molecules*, Universities Press, Hyderabad, 2000.
289. S. R. Gadre, S. S. Pundlik, A. C. Limaye and A. P. Rendell, *Chem. Commun.*, 1998, **31**, 573–574.
290. S. R. Gadre, S. A. Kulkarni and I. H. Shrivastava, *J. Chem. Phys.*, 1992, **96** 5253-5260.
291. S. Gadre, K. Babu and A. Rendell, *J. Phys. Chem. A*, 2000, **104**, 8976-8982.
292. R. K. Pathak and S. R. Gadre, *J. Chem. Phys.*, 1990, **93**, 1770-1773.
293. S. R. Gadre and I. H. Shrivastava, *J. Chem. Phys.*, 1991, **94**, 4384-4390.
294. S. R. Gadre, S. Bapat and I. Shrivastava, *Comput. Chem.*, 1991, **15**, 203-206.

295. S. R. Gadre, C. Koelmel and I. H. Shrivastava, *Inorg. Chem.*, 1992, **31**, 2279-2281.
296. S. R. Gadre, S. A. Kulkarni and I. H. Shrivastava, *J. Chem. Phys.*, 1992, **96**, 5253-5260.
297. S. E. Wheeler and K. N. Houk, *J. Am. Chem. Soc.*, 2009, **131**, 3126-3127.
298. S. E. Wheeler and K. N. Houk, *J. Chem. Theory Comput.*, 2009, **5**, 2301-2312.
299. S. E. Wheeler and K. N. Houk, *J. Phys. Chem. A*, 2010, **114**, 8658-8664.
300. S. E. Wheeler, *J. Am. Chem. Soc.*, 2011, **133**, 10262-10274.
301. S. E. Wheeler, *Acc. Chem. Res.*, 2013, **46**, 1029-1038.
302. B. Galabov and P. Bobadova-Parvanova, *J. Phys. Chem. A*, 1999, **103**, 6793-6799.
303. B. Galabov and P. Bobadova-Parvanova, *J. Mol. Struct.*, 2000, **550**, 93-98.
304. B. Galabov, S. Ilieva, G. Koleva, W. D. Allen, H. F. Schaefer III and P. von R. Schleyer, *Wiley Interdiscip. Rev. Computat. Mol. Sci.*, 2013, **3**, 37-55.
305. F. B. Sayyed and C. H. Suresh, *Tetrahedron Lett.*, 2009, **50**, 7351-7354.
306. C. H. Suresh, P. Alexander, K. P. Vijayalakshmi, P. K. Sajith and S. R. Gadre, *Phys. Chem. Chem. Phys.*, 2008, **10**, 6492-6499.
307. F. B. Sayyed and C. H. Suresh, *New J. Chem.*, 2009, **33**, 2465-2471.
308. F. B. Sayyed, C. H. Suresh and S. R. Gadre, *J. Phys. Chem. A*, 2010, **114**, 12330-12333.
309. P. K. Sajith and C. H. Suresh, *Inorg. Chem.*, 2012, **51**, 967-977.
310. F. B. Sayyed and C. H. Suresh, *J. Phys. Chem. A*, 2011, **115**, 9300-9307.
311. F. B. Sayyed and C. H. Suresh, *J. Phys. Chem. A*, 2011, **115**, 5660-5664.
312. F. B. Sayyed and C. H. Suresh, *J. Phys. Chem. A*, 2012, **116**, 5723-5732.
313. N. Mohan, C. H. Suresh, A. Kumar and S. R. Gadre, *Phys. Chem. Chem. Phys.*, 2013, **15**, 18401-18409.
314. N. Mohan and C. H. Suresh, *J. Phys. Chem. A*, 2014, **118**, 1697-1705.
315. K. P. Vijayalakshmi and C. H. Suresh, *New J. Chem.*, 2010, **34**, 2132-2138.
316. C. H. Suresh and S. R. Gadre, *J. Org. Chem.*, 1999, **64**, 2505-2512.
317. C. H. Suresh and N. Koga, *Inorg. Chem.*, 2002, **41**, 1573-1578.
318. C. H. Suresh, *Inorg. Chem.*, 2006, **45**, 4982-4986.
319. J. Mathew, T. Thomas and C. H. Suresh, *Inorg. Chem.*, 2007, **46**, 10800-10809.
320. J. Mathew and C. H. Suresh, *Inorg. Chem.*, 2010, **49**, 4665-4669.
321. J. Mathew and C. H. Suresh, *Organometallics*, 2011, **30**, 1438-1444.
322. J. Mathew and C. H. Suresh, *Organometallics*, 2011, **30**, 3106-3112.

Formation of Large Clusters of CO_2 Around Anions: DFT Study Reveals Cooperative CO_2 Adsorption
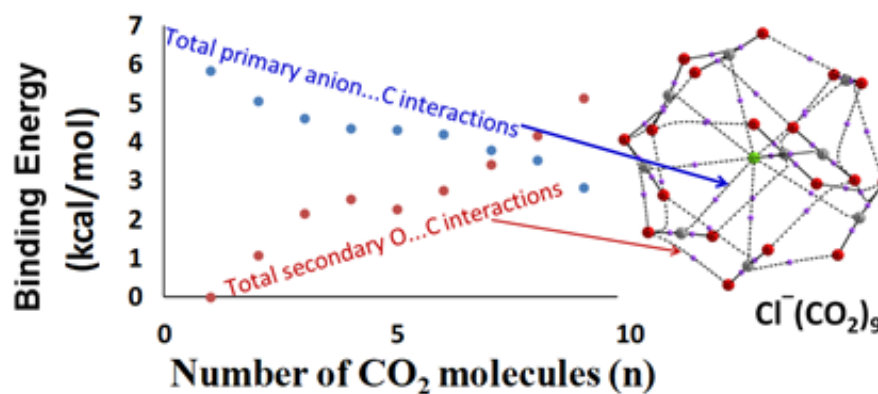
Formation of Large Clusters of CO_2 Around Anions: DFT Study Reveals Cooperative CO_2 Adsorption

2.1 Abstract

Structure and energetics of the interaction of CO_2 molecules with anions F^-, Cl^-, Br^-, CN^-, NC^-, OH^-, ClO^-, NH_2^-, and NO_2^-, have been studied at the M06L/6–311++G** level of density functional theory. The maximum number of CO_2 molecules (n_{max}) adsorbed by the anions to saturate the first shell of coordination varies from 8 – 12 in different complexes. The anion$\cdots CO_2$ distance (d_{int}) in $F^-(CO_2)$, $NC^-(CO_2)$, $ClO^-(CO_2)$, $HO^-(CO_2)$ and $H_2N^-(CO_2)$ is 1.533, 1.527, 1.468, 1.456, and 1.470 Å, respectively which indicates covalent bond formation between carbon and the anion which is confirmed from the binding energy (E_b) values of these complexes -29.0, -14.7, -23.2, -41.7, and -48.1 kcal/mol, respectively. The Cl^-, Br^-, CN^- and NO_2^- interact always non-covalently with the carbon center of CO_2 with d_{int} in the range of 2.5 – 2.9 Å. With the adsorption of each CO_2, an average increment of 5.9 to 6.7 kcal/mol is observed in the magnitude of E_b value of the complexes. The binding energy per CO_2 ($E_{b/CO2}$) is nearly a constant for all the noncovalent complexes, even up to n_{max} number of CO_2 adsorbed. Though the primary anion$\cdots CO_2$ interaction gets weaker with the increasing size of CO_2 cluster, a steady increase in the secondary $O\cdots C$ interaction between adsorbed CO_2 molecules helps the systems to maintain a constant value for $E_{b/CO2}$. The electron density data of noncovalent bond critical points in quantum theory of atoms in molecules (QTAIM) analysis are used to partition the total binding energy data in to primary anion$\cdots C$ and secondary $O\cdots C$ interactions. Further, the multicenter charge delocalization in the anionic complexes is explained using the molecular electrostatic potential (MESP) analysis. The study proves that anions possess a remarkable ability to interact with a large number of CO_2 molecules due to cooperativity resulting from the secondary $O\cdots C$ interactions which compensate for the weakening of the primary anion$\cdots C$ interactions. This property of the anion-CO_2 interactions can be exploited for developing anionic or anion-incorporated materials for CO_2 storage.

2.2 Introduction

Cost effective carbon dioxide (CO_2) capture and storage (CCS)[1-8] techniques have to be developed for the isolation, extraction, and storage of CO_2 emitted from various sources especially from fossil fuel based power generation to alleviate the emission of CO_2 into the atmosphere. For storing CO_2, it must interact with the storage materials. A covalent interaction can lead to chemisorption while a noncovalent interaction can lead to physisorption.[9] Though CO_2 is electrically neutral, strong electrostatic interactions can develop with charged species due to their polarizability.[10] The theoretical[6, 11-16] and experimental[17-29] studies on the interactions between CO_2 and halide anions have been a field of interest for a long time. Spears and Ferguson studied $F(CO_2)^-$ both experimentally and theoretically, and found that electrostatic calculations were insufficient to describe the covalent character of C–F bond.[30, 31] McMahon and Larson, explained the bonding in $F(CO_2)^-$ complex as covalent between F and C to suggest the formation of fluoroformate anion FCO_2^- and that in $Cl(CO_2)^-$ complex as electrostatic, using the ion cyclotron resonance (ICR) technique.[32] Semiempirical studies by Ault has given a planar C_{2v} symmetric structure for the fluoroformate anion, which was later confirmed from the *ab initio* calculations by Hiraoka *et al.*[33,34] Arnold and co-workers studied the geometry of the X^-/CO_2 clusters (X = I, Br, Cl, and F) at the SCF and Møller–Plesset (MP2 and MP4) levels of theory.[35] They also obtained the solvation energetics using the negative ion photoelectron spectroscopy, as an expansion of the work by Markovich *et al.*[36,37] The structure and energetics of the CO_2 – halide (Br^-, I^- and Cl^-) interactions were also studied by Pathak.[38-40] In addition to the inorganic anions[41], the energetics as well as the spectral properties of the CO_2 clusters of organic anions (Py^-)[42] and metal anions: Au,[43-45] Ag,[45, 46] Cu[45, 47]and, Ni[48, 49] have been studied by various research groups.

Very recently, in a series of papers, Della and Suresh have reported DFT studies on the interactive behaviour of H_2 molecules with a large variety of anions and showed that anions possess a unique ability to interact with a large number of H_2 molecules.[50-53] Their studies also revealed the cooperativity of intermolecular

dihydrogen interactions in the cluster formation. Though many theoretical as well as experimental studies have been reported for the anion-CO_2 interactions, a systematic study focusing on the energetics of the formation of clusters of CO_2 around anions has not been reported yet. The present study addresses this topic using density functional theory and also elaborates the nature of anion-CO_2 bonding - covalent versus noncovalent and cooperativity of interactions. The selected anions are F^-, Cl^-, Br^-, CN^-, NO_2^-, OH^-, ClO^-, NC^-, and NH_2^-.

2.2.1 Computational Methods

All the calculations have been done using Gaussian 16 quantum chemistry package[54] at M06L/6-311++G** level of density functional theory (DFT).[55, 56] Selection of this method is based on a previous benchmark study which recommends this as the best method to calculate the geometry and binding energy of noncovalent dimers to the accuracy close to CCSD.[57,50] Since all complexes are anionic in nature, the diffuse functions in the basis set are essential to describe the wave function. All the clusters discussed here are taken in their gaseous state at standard conditions of temperature (298.1 K) and pressure (1.0 atm). Presence of all real frequencies in the vibrational analysis is confirmed for all the optimized geometries. The geometry of $X^-(CO_2)_n$ for n =1 to n = n_{max} are obtained for $X^- = F^-$, Cl^-, Br^-, CN^-, NO_2^-, OH^-, ClO^-, NC^-, and NH_2^- where n_{max} stands for the maximum number of CO_2 molecules that can be accommodated into the first coordination shell of the anion. Saturation of the first coordination shell is confirmed by locating the structure of $X^-(CO_2)_{n_{max}+1}$ wherein at least one of the anion$\cdots$C distance is significantly larger than the rest. For systems containing up to five CO_2 molecules, several configurations are optimized and among them the most stable $X^-(CO_2)_n$ is reported here. Based on such configurations, higher clusters are constructed by maximizing the O$\cdots$C interactions between adsorbed CO_2 molecules. The interaction energies of the complexes are calculated using the supermolecule approach. For any two interacting subsystems A and B, the binding energy (E_b) of the supermolecule AB is calculated as;

$$E_b = E_{AB} - E_A - E_B \qquad\qquad\qquad\qquad (Eq.\ 2.1)$$

where, E_A , E_B and E_{AB} stand for the energy of systems A (anion), B (n CO_2 molecules) and AB ($X^-(CO_2)_n$ cluster), respectively.[58-61] The zero-point corrected energy of the systems is used for the calculation of E_b values. Further, E_b is incorporated with the correction for the basis set superposition error (BSSE)[62-65] using the counterpoise (CP) approach of Boys and Bernardi.[66, 67]

Bader's quantum theory of atoms in molecules (QTAIM) analysis, based on the electron density (ρ) distribution is carried out, using AIMAll package, to visualize the bond paths and to locate the bond critical points (BCPs). Atom–atom interactions are distinguished as covalent and noncovalent interactions based on the electron densities at the respective BCPs (ρ_b) as well as from the sign of the corresponding Laplacian ($\nabla^2\rho_b$). The sum of electron density at the BCPs ($\Sigma\rho_b$) and the sign of Laplacian of electron density ($\nabla^2\rho_b$) are also analyzed for all the complexes. The MESP topographical analysis is carried out on all the complexes at M06L/6-311++G** level of theory to understand the intermolecular interactions and the delocalization of the electron density from the anion to the adsorbed CO_2 molecules. Further, a benchmark set of calculations is done on representative cases using B3LYP-D3, BP86-D3, wB97XD levels in conjunction with the basis set 6-311++G**.

2.3   Results and discussion

2.3.1 Structure and energetics

The optimized structures of the $X^-(CO_2)$ of all the anions are given in Figure 2.1. In all the cases, 'C' of CO_2 interacts with the anion and the distance of interaction (d_{int}) gives a quick assessment of the strength of interaction. The d_{int} of $F^-(CO_2)$, $NC^-(CO_2)$, $ClO^-(CO_2)$, $HO^-(CO_2)$ and $H_2N^-(CO_2)$ is 1.533, 1.527, 1.468, 1.456, and 1.470 Å, respectively which indicates the formation of a covalent bond between carbon and the anion and the resulting systems are the carboxylate anions of fluoroformic acid (FCOO$^-$), cyano formic acid (NCCOO$^-$), hypochloro

formic acid (ClOCOO⁻), carbonic acid (HOCOO⁻) and carbamic acid (H₂NCOO⁻). The OCO bond angle (θ) in FCOO⁻, NCCOO⁻, ClOCOO⁻, HOCOO⁻ and H₂NCOO⁻ is 138.9, 133.1, 137.3, 133.3 and 130.9° respectively which is 40 – 50° smaller than the OCO angle in CO_2.
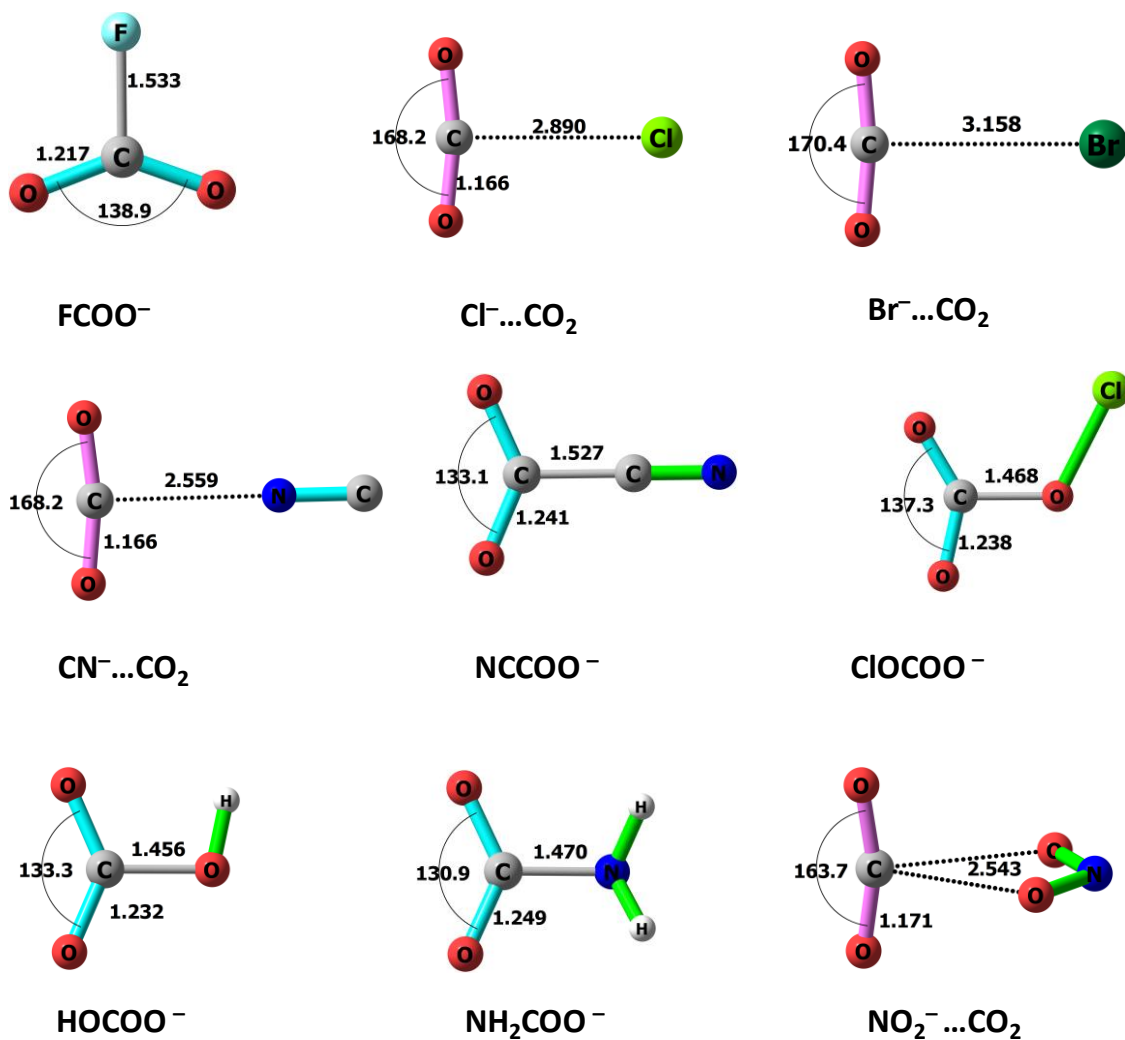
Figure 2.1 Optimized structures of X⁻(CO_2) with their d_{int} (Å) and θ (°) at M06L/6-311++G** level of theory.

Further, CO bond elongates from 1.161 Å in CO_2 to 1.217 - 1.249 Å in the carboxylates. This shows the structural deformation in CO_2 resulting from the strong interaction with the anion. Anions Cl⁻, Br⁻, CN⁻ and NO₂⁻ interacts non-covalently with the carbon of CO_2 as d_{int} 2.5 – 2.9 Å seen in Cl⁻(CO_2), Br⁻(CO_2),

$CN^-(CO_2)$ and $NO_2^-(CO_2)$ is significantly higher than the typical covalent bond distances. In these systems, reduction in θ due to noncovalent bond formation is 10 - 18° and the CO bond elongation is 0.005- 0.027 Å.
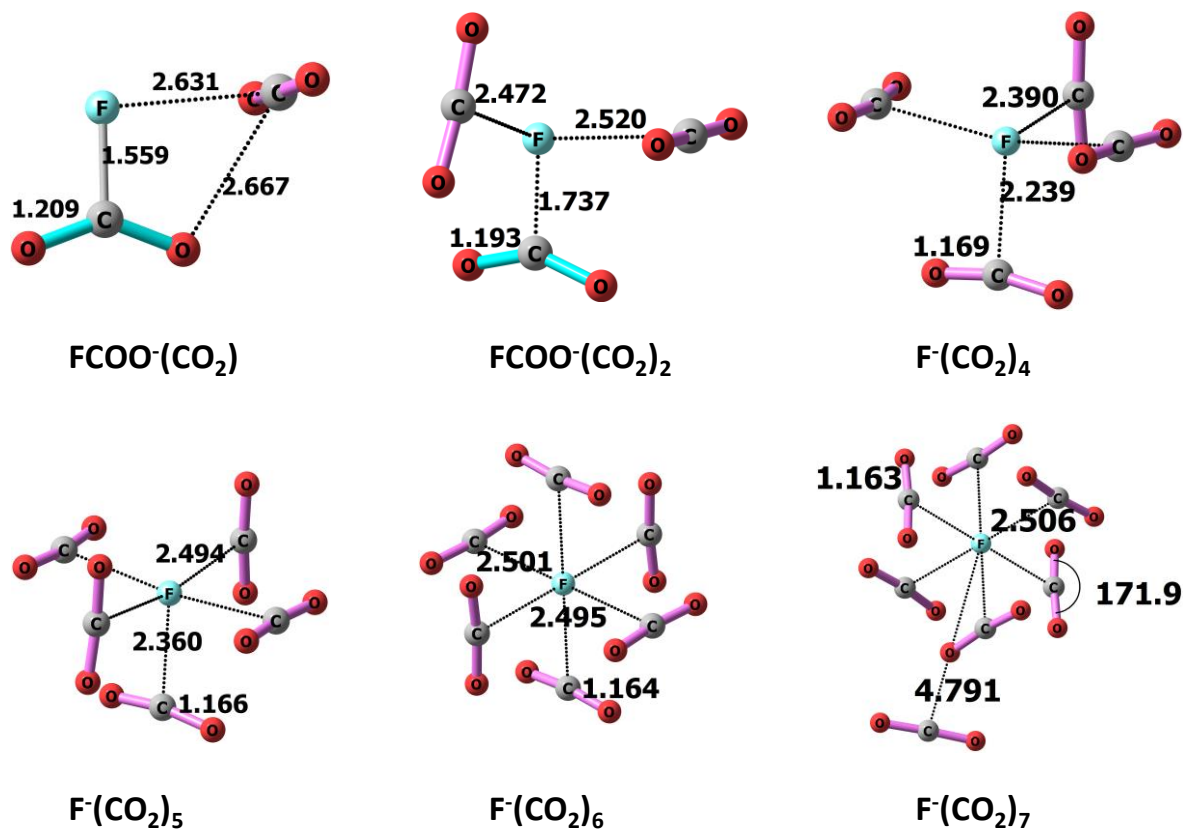
Figure 2.2 Optimized structures of CO_2 complexes of F^- with their d_{int} (Å) and θ (°)at M06L/6-311++G** level.

The interaction of F^- and CO_2 leading to the formation of $FCOO^-$ has been previously reported.[32, 33] Binding energy (E_b) for the covalent bond formation (bond energy) in $FCOO^-$ is -29.0 kcal/mol. The $FCOO^-$ retains the carboxylate form even when a second CO_2 molecule interacts with it. The second CO_2 interacts non-covalently with the fluoroformate anion through $F \cdots CO_2$ and $O \cdots CO_2$ interactions (Figure 2.2). The resulting complex $FCOO^-(CO_2)$ has F-C distance 1.559 Å which is 0.026 Å higher than the F-C distance of $FCOO^-$ (Figure 2.1). Interaction from a third CO_2 molecule further increases the F-C distance to 1.737 Å which suggests

substantial loss of covalent character for this bond. In fact the carboxylate anionic form disappears when four or more CO_2 molecules interact with F^- and they can be represented as $F^-(CO_2)_n$ where n > 3. The strong covalent F-C interaction in $FCOO^-$ breaks up due to the combined noncovalent interaction from four or more CO_2 molecules as the shortest F-C distance in $F^-(CO_2)_4$, $F^-(CO_2)_5$, and $F^-(CO_2)_6$ is 2.239, 2.364, and 2.496 Å, respectively (Figure 2.2). In the case of $F^-(CO_2)_7$, the seventh CO_2 interacts at a distance 4.791 Å from the F^- suggesting that the first coordination shell of F^- is saturated with six CO_2 molecules. The shell and half-shell formations of solvent molecules (CO_2) around anions such as I_2^-, IBr^-, and ICN^- have been observed theoretically as well as experimentally by Lineberger[63, 68] and Neumark groups.[69-71]

Table 2.1 ZPE and BSSE corrected E_b and $E_{b/CO2}$, in kcal/mol, for the CO_2 complexes of F^- at M06L/6-311++G** level.

Complex	Reaction	E_b	$E_{b/CO2}$
$FCOO^-$	$F^- + CO_2$	-29.0	-29.0
$FCOO^-(CO_2)$	$FCOO^- + CO_2$	-7.9	-7.9
$FCOO^-(CO_2)_2$	$FCOO^- + 2CO_2$	-14.3	-7.2
$F^-(CO_2)_4$	$F^- + 4CO_2$	-52.4	-13.1
$F^-(CO_2)_5$	$F^- + 5CO_2$	-61.0	-12.2
$F^-(CO_2)_6$	$F^- + 6CO_2$	-71.3	-11.9
$F^-(CO_2)_7$	$F^- + 7CO_2$	-74.6	-10.7

The E_b values of $F^-(CO_2)_n$ complexes given in Table 2.1 suggest that once the coordination shell is saturated at n = 6, further interaction from a CO_2 in the second shell can only bring an additional stabilization of 3.3 kcal/mol which is 7.0 kcal/mol lower than that observed for n = 5 to n = 6 step. The binding energy per CO_2 ($E_{b/CO2}$) for n > 3 can be considered as a measure of the noncovalent $F^-\cdots C$ bond strength as such complexes show only noncovalent bonds whereas $E_{b/CO2}$ for n = 2

and n = 3 corresponds to the noncovalent binding energy of CO_2 with fluoroformate anion while that for n = 1 gives the F-C covalent bond strength. The E_{b/CO_2} -11.9 kcal/mol observed for the saturated complex $F^-(CO_2)_6$ indicates the high probability for the formation of such a complex in the gas phase. The E_{b/CO_2} data in Table 2.1 suggests that the noncovalent interaction between F^- and CO_2 is significantly stronger than that between $FCOO^-$ and CO_2 which can be attributed to the higher charge concentration in the smaller sized F^- than $FCOO^-$.

Table 2.2 ZPE- and BSSE- corrected E_b and E_{b/CO_2}, in kcal/mol, for the CO_2 complexes of NC^-, ClO^-, OH^-, and NH_2^-, at M06L/6-311++G** level.

n	$NCCOO^-(CO_2)_n$		$ClOCOO^-(CO_2)_n$		$HOCOO^-(CO_2)_n$		$H_2NCOO^-(CO_2)_n$	
	E_b	E_{b/CO_2}	E_b	E_{b/CO_2}	E_b	E_{b/CO_2}	E_b	E_{b/CO_2}
0	-14.7	-14.7	-23.2	-23.2	-41.7	-41.7	-48.1	-48.1
1	-5.9	-5.9	-6.3	-6.3	-5.6	-5.6	-8.9	-8.9
2	-12.8	-6.4	-11.6	-5.8	-13.2	-6.6	-16.5	-8.3
3	-19.0	-6.3	-17.0	-5.7	-20.5	-6.8	-20.6	-6.9
4	-24.9	-6.2	-21.7	-5.4	-23.8	-6.0	-30.2	-7.6
5	-29.1	-5.8	-28.3	-5.7	-36.9	-7.4	-33.8	-6.8
6	-34.0	-5.7	-28.6	-4.8	-36.2	-6.0	-34.4	-5.7
7	-37.8	-5.4	-37.3	-5.3	-48.1	-6.9	-47.0	-6.7
8	-42.0	-5.3	-38.1	-4.8	-53.8	-6.7	-49.7	-6.2
9	-46.7	-5.2	-41.8	-4.6	-59.1	-6.6	-54.9	-6.1
10	-51.9	-5.2	-46.4	-4.6	-63.7	-6.4	-60.2	-6.0
11	-57.9	-5.3	-56.4	-5.1	-67.3	-6.1	-62.2	-5.7

E_b value for the covalent bond formation (bond energy) in $FCOO^-$, $NCCOO^-$, $ClOCOO^-$, $HOCOO^-$ and H_2NCOO^- is found to be -29.0, -14.7, -23.2, -41.7, and -48.1 kcal/mol, respectively whereas E_b -6.9, -5.6, -7.1, and -11.6 kcal/mol observed for

Cl$^-$(CO$_2$), Br$^-$(CO$_2$), CN$^-$(CO$_2$) and NO$_2$$^-$(CO$_2$), respectively indicate noncovalent bond formation between the anion and CO$_2$.

Table 2.3 ZPE- and BSSE- corrected E$_b$ and E$_{b/CO2}$ in kcal/mol, for the CO$_2$ complexes of Cl$^-$, Br$^-$, CN$^-$, and NO$_2$$^-$, at M06L/6-311++G** level.

n	Cl$^-$		Br$^-$		CN$^-$		O$_2$N$^-$	
	E$_b$	E$_{b/CO2}$	E$_b$	E$_{b/CO2}$	E$_b$	E$_{b/CO2}$	E$_b$	E$_{b/CO2}$
1	-6.9	-6.9	-5.6	-5.6	-7.1	-7.1	-11.6	-11.6
2	-14.0	-7.0	-11.5	-5.8	-13.8	-6.9	-17.7	-8.8
3	-21.7	-7.2	-18.4	-6.1	-20.0	-6.7	-24.1	-8.0
4	-28.7	-7.2	-24.6	-6.2	-26.4	-6.6	-30.2	-7.5
5	-35.7	-7.1	-30.3	-6.1	-32.4	-6.5	-36.1	-7.2
6	-42.2	-7.0	-36.2	-6.0	-39.6	-6.6	-40.4	-6.7
7	-49.3	-7.0	-42.7	-6.1	-44.3	-6.3	-44.2	-6.3
8	-57.1	-7.1	-49.7	-6.2	-51.0	-6.4	-53.1	-6.6
9	-60.1	-6.7	-55.0	-6.1	-	-	-	-

In NCCOO$^-$, ClOCOO$^-$, HOCOO$^-$ and H$_2$NCOO$^-$, the initially formed bond with CO$_2$, *viz*. C-C, O-C, O-C and N-C respectively is retained in the system even for the fully saturated coordination state of these anions with CO$_2$. The optimized structures of NCCOO$^-$(CO$_2$)$_n$, ClOCOO$^-$(CO$_2$)$_n$, HOCOO$^-$(CO$_2$)$_n$ and H$_2$NCOO$^-$(CO$_2$)$_n$ are shown in Figure 2.3 for the highest n (n$_{max}$). The n$_{max}$ is found to be 11 for NCCOO$^-$, ClOCOO$^-$, HOCOO$^-$ and H$_2$NCOO$^-$. The NC-C, HO-C and H$_2$N-C bonds of NCCOO$^-$, HOCOO$^-$ and H$_2$NCOO$^-$, respectively showed contraction in bond length, *viz*. 1.527 to 1.503 Å for NCCOO$^-$, 1.474 to 1.401 Å for HOCOO$^-$, and 1.470 to 1.420 Å for H$_2$NCOO$^-$ when the number of coordinated CO$_2$ molecules changed from n = 1 to n = n$_{max}$. This is an unexpected result as the opposite trend is seen in the case of FCOO$^-$. However, in the case of ClOCOO$^-$, ClO-C bond length increased from 1.468

to 1.507 Å. The change in bond length is not substantial here which indicates the retention of the covalent character of the bond in the saturated complexes.
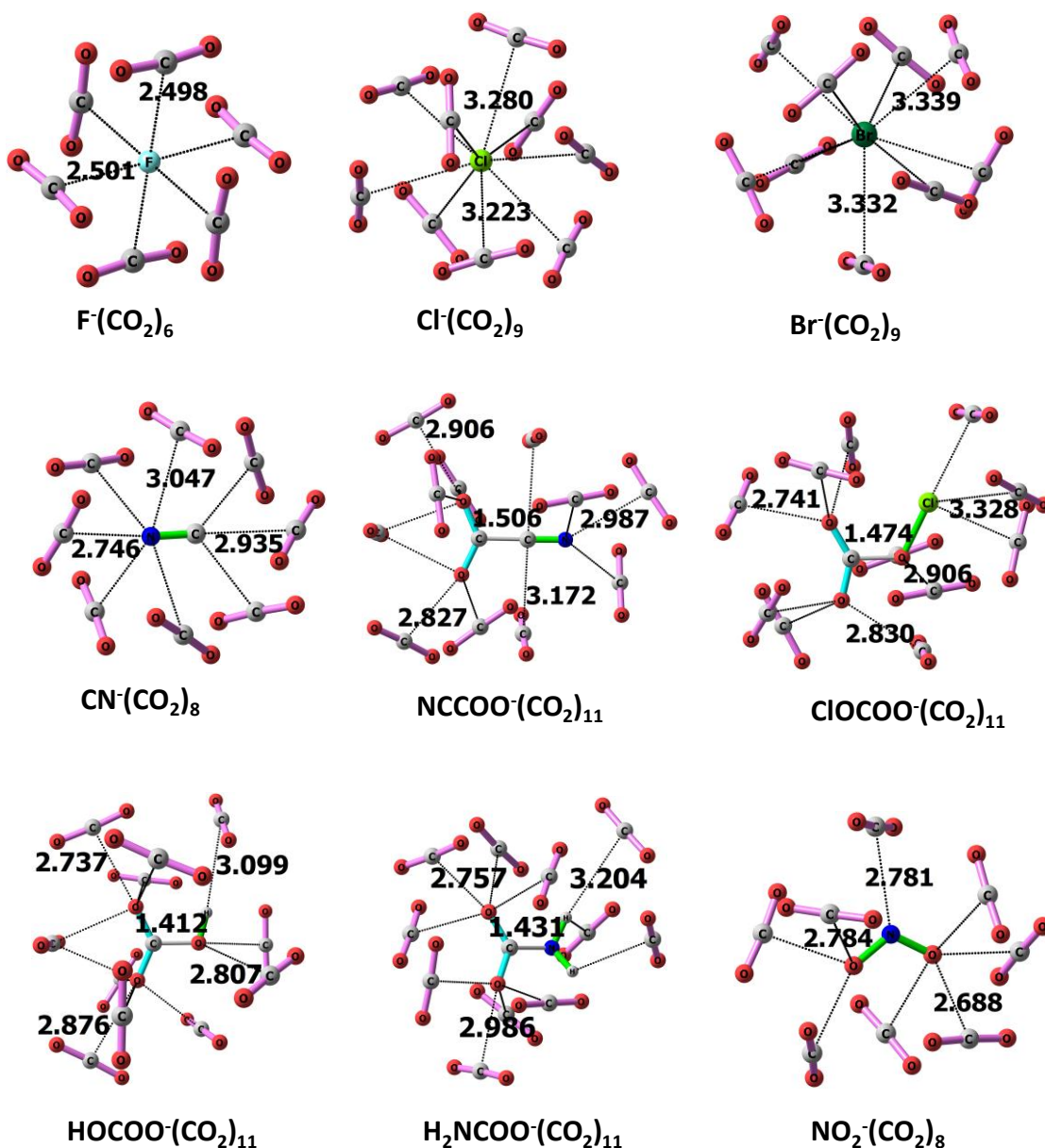
Figure 2.3 Optimized structures of $X^-(CO_2)_{nmax}$ (X^- = NCCOO$^-$, ClOCOO$^-$, HOCOO$^-$, H$_2$NCOO$^-$, Cl$^-$, Br$^-$, CN$^-$ and NO$_2^-$) with representative d_{int} (Å) at M06L/6-311++G** level of theory.

The E_b values for NCCOO$^-$, ClOCOO$^-$, HOCOO$^-$ and H$_2$NCOO$^-$ are given in Table 2.2. The highest magnitude in E_b is observed for H$_2$NCOO$^-(CO_2)_n$ which shows an average increase 7.6 kcal/mol with the addition of each CO_2 molecule. For each CO_2

adsorbed on the anion, on an average E_b becomes more negative by 6.5, 6.3 and 8.8 kcal/mol for the complexes $NCCOO^-(CO_2)_n$ $ClOCOO^-(CO_2)_n$ and $HOCOO^-(CO_2)_n$, respectively.

In $Cl^-(CO_2)_n$, $Br^-(CO_2)_n$, $CN^-(CO_2)_n$ and $NO_2^-(CO_2)_n$, always noncovalent bond formation is observed between the anion and CO_2 for all n values. Structure of these complexes for $n = n_{max}$ is given in Figure 2.3. The n_{max} is 9 for Cl^- and Br^- and 8 for CN^- and NO_2^-. On an average, the anion-CO_2 distance in $Cl^-(CO_2)_n$, $Br^-(CO_2)_n$, $CN^-(CO_2)_n$ and $NO_2^-(CO_2)_n$ is in the range 2.888 -3.241, 3.158 - 3.546, 2.559 -3.260, and 2.109 -3.366 Å, respectively. These data indicate a decrease in noncovalent interaction strength as n changes from 1 to n_{max}. In the case of $Cl^-(CO_2)_n$, E_b (Table 2.3) improves by 6.7 kcal/mol with the addition of each CO_2 molecule; this effect is 6.2, 6.3, and 5.9 kcal/mol, respectively for $Br^-(CO_2)_n$, $CN^-(CO_2)_n$, and $NO_2^-(CO_2)_n$.

Table 2.4 ZPE- and BSSE- corrected ΔG_b and $\Delta G_{b/CO2}$, in kcal/mol, for the CO_2 complexes of NC^-, ClO^-, OH^-, and NH_2^-, at M06L/6-311++G** level.

n	$NCCOO^-(CO_2)_n$		$ClOCOO^-(CO_2)_n$		$HOCOO^-(CO_2)_n$		$H_2NCOO^-(CO_2)_n$	
	ΔG_b	$\Delta G_{b/CO2}$	ΔG_b	$\Delta G_{b/CO2}$	ΔG_b	$\Delta G_{b/CO2}$	ΔG_b	$\Delta G_{b/CO2}$
0	-6.9	-6.9	-15.0	-15.0	-34.7	-34.7	-40.2	-40.2
1	1.6	1.6	1.3	1.3	0.4	0.4	-0.4	-0.4
2	3.4	1.7	5.2	2.6	1.9	0.9	-0.3	-0.2
3	5.9	2.0	7.0	2.3	4.2	1.4	4.4	1.5
4	9.9	2.5	12.5	3.1	9.3	2.3	4.4	1.1
5	13.5	2.7	14.7	2.9	6.7	1.3	8.6	1.7
6	19.0	3.2	23.4	3.9	14.7	2.5	18.8	3.1
7	25.9	3.7	25.0	3.6	14.2	2.0	15.5	2.2
8	31.8	4.0	32.2	4.0	18.6	2.3	20.9	2.6
9	35.5	3.9	39.6	4.4	22.6	2.5	25.0	2.8
10	39.3	3.9	42.4	4.2	28.8	2.9	30.5	3.1
11	43.4	3.9	41.4	3.8	33.6	3.1	36.0	3.3

Some of the small $X^-(CO_2)_n$ clusters ($n \leq 3$) show negative ΔG values for anions such as H_2NCOO^-, Cl^-, Br^-, CN^-, and NO_2^- while a medium sized cluster (4 – 6 CO_2 molecules) gives positive ΔG values, 1 - 10 kcal/mol and large clusters show values above 10 kcal/mol (Tables 2.4 and 2.5). The negative entropy is the decisive factor as the $T\Delta S$ (T = 298 K) contribution per every CO_2 molecule adsorbed in the system is ~8.00 kcal/mol. In the case of a realistic system consisting of anions and their counter cations, the adsorption can take place only by overcoming the strong columbic interaction between the ions. Our results suggest that anionic or electron rich systems have high tendency to adsorb CO_2 molecules and among the studied anions, F^- has the highest ability.

Table 2.5 ZPE- and BSSE-corrected ΔG_b and $\Delta G_{b/CO2}$, in kcal/mol, for the CO_2 complexes of Cl^-, Br^-, CN^-, NO_2^-, and F^- at M06L/6-311++G** level.

n	Cl^-		Br^-		CN^-		O_2N^-		F^-	
	ΔG_b	$\Delta G_{b/CO2}$	ΔG_b	$\Delta G_{b/CO2}$	ΔG_b	$\Delta G_{b/CO2}$	ΔG_b	$\Delta G_{b/CO2}$	ΔG_b	$\Delta G_{b/CO2}$
1	-2.4	-2.4	-1.2	-1.2	-1.4	-1.4	-3.8	-3.8	-23.4	-23.4
2	-2.6	-1.3	-0.2	-0.1	-0.7	-0.3	-2.2	-1.1	0.1	0.0
3	-0.4	-0.1	2.2	0.7	0.2	0.1	-1.1	-0.4	2.1	0.7
4	1.7	0.4	5.3	1.3	5.3	1.3	2.0	0.5	-22.0	-5.5
5	3.8	0.8	8.7	1.7	8.0	1.6	5.1	1.0	-19.6	-3.9
6	5.7	0.9	11.9	2.0	9.4	1.6	11.1	1.9	-19.7	-3.3
7	7.8	1.1	14.4	2.1	12.7	1.8	17.8	2.5	-14.4	-2.1
8	9.4	1.2	18.2	2.3	17.2	2.1	16.8	2.1	-	-
9	15.6	1.7	28.3	3.1	-	-	-	-	-	-

We also carried out a benchmark study on a representative case, $Cl^-(CO_2)_n$ using dispersion effect included methods, *viz.* B3LYP-D3, BP86-D3, and wB97XD in conjunction with basis set 6-311++G**. In Table 2.6, E_b values computed using these methods are compared with M06L/6-311++G** data. All the methods give similar E_b data apart from the slight enhancement of ~1 kcal/mol observed in the average $E_{b/CO2}$ for B3LYP-D3 and BP86-D3. M06L method is thoroughly benchmarked in a previous study and also previous studies showed that it yields reliable results for anionic systems.[50-53] Rest of the study is conducted using M06L/6-311++G** method.

Table 2.6 Benchmark study for the representative case, $Cl^-(CO_2)_n$ complexes with the basis set 6-311++G**. ZPE and BSSE corrected E_b values are given in kcal/mol.

n	B3LYP-D3	BP86-D3	wB97XD	M06L
1	-7.7	-7.0	-6.2	-6.9
2	-15.3	-12.5	-12.3	-14.0
3	-23.3	-18.2	-18.6	-21.7
4	-30.9	-23.3	-24.5	-28.7
5	-38.4	-28.5	-30.6	-35.7
6	-45.5	-33.3	-36.1	-42.2
7	-53.4	-38.3	-41.6	-49.3
8	-61.6	-43.6	-47.2	-57.1
9	-66.9	-45.4	-49.9	-60.1

2.3.2 QTAIM analysis

The QTAIM molecular plots of the anionic clusters at n_{max} are given in Figure 2.4. The dotted lines indicate the bond paths and purple spheres represent the BCPs. In addition to the interactions between the anionic center and the CO_2, secondary O···C interactions arise between adsorbed CO_2 molecules, as indicated by the presence of BCPs between O and C. According to Koch and Popelier criterion[72, 73], for a noncovalent interaction, ρ_b falls in the range 0.002 – 0.040 au

and $\nabla^2\rho_b$ is positive, typically in the range 0.024 – 0.139 au Although negative $\nabla^2\rho_b$ values generally indicate covalent interactions, there are exceptions such as the charge-shift bonds proposed by Shaik *et al.*[74] Such bonds are marked by the BCPs with large value for the third eigenvalue of the Hessian (λ_3) than the other two (λ_1 and λ_2).[75] Also the parallel principal axis of the ellipsoid aligned with the eigen vectors is smaller than the perpendicular one (c < a, b) and are obtained as, a = $|\nabla\rho|/|\lambda_1|$, b = $|\nabla\rho|/|\lambda_2|$, and c = $|\nabla\rho|/|\lambda_3|$ (assuming that all the critical points are rank three, i.e., $\lambda_i \neq 0$, for i = 1-3).

Table 2.7 $\Sigma\rho_b$ values (au) of $X^-...CO_2$ bond in complexes at the M06L/6-311++G** level of theory.

n	F^-	Cl^-	Br^-	CN^-	NO_2^-	$NCCOO^-$	$ClOCOO^-$	$HOCOO^-$	H_2NCOO^-
1	0.176	0.016	0.012	0.021	0.043	0.016	0.022	0.019	0.067
2	0.029	0.035	0.028	0.037	0.068	0.039	0.045	0.04	0.089
3	0.055	0.058	0.05	0.051	0.081	0.064	0.061	0.088	0.102
4	0.139	0.078	0.069	0.074	0.102	0.088	0.078	0.107	0.12
5	0.169	0.093	0.085	0.094	0.119	0.096	0.106	0.14	0.124
6	0.205	0.118	0.103	0.117	0.145	0.121	0.123	0.14	0.131
7	0.215	0.143	0.127	0.131	0.155	0.15	0.144	0.181	0.177
8	-	0.174	0.147	0.165	0.183	0.165	0.166	0.201	0.191
9	-	0.202	0.164	-	-	0.193	0.215	0.223	0.224
10	-	-	-	-	-	0.209	0.233	0.257	0.265
11	-	-	-	-	-	0.229	0.252	0.278	0.290

In all the cases studied here, Koch-Popelier criterion on ρ_b is valid for all the noncovalent interactions (Table 2.7) and the sign of $\nabla^2\rho$ is positive whereas the covalent bonds, *viz.* F-C in $FCOO^-$, NC-C in $NCCOO^-$, ClO-C in $ClOCOO^-$, HO-C in $HOCOO^-$ and H_2N-C in H_2NCOO^- show large ρ_b and negative $\nabla^2\rho$ values. In the case

of (FCOO$^-$)(CO$_2$)$_n$, the ordered pair of (ρ_b, $\nabla^2\rho_b$) for the shortest F-C interaction is (0.1756, -0.0285) for n = 0, (0.1648, 0.0251) for n = 1, (0.1072, 0.1983) for n = 2, and (0.0339, 0.1078) for n = 3. For FCOO$^-$, the F-C bond is completely covalent in nature as indicated by the large ρ_b and negative $\nabla^2\rho_b$ values. For FCOO$^-$(CO$_2$) and FCOO$^-$(CO$_2$)$_2$, ρ_b falls in the covalent range while the positive $\nabla^2\rho_b$ indicates the possibility of charge-shift bonding. For instance, the shortest F-C interaction seen in FCOO$^-$(CO$_2$) is marked by the eigenvalues -0.2928, -0.2808 and 0.5987 and the values of principal axes a, b and c of the ellipsoids aligned with the eigenvectors are 0.5412, 0.5644 and 0.2646, respectively. Here $|\lambda_3| > |\lambda_1|$, $|\lambda_2|$ and c < a, b which support the formation of charge-shift bond. Similar is the case of FCOO$^-$(CO$_2$)$_2$. Upon addition of the fourth CO$_2$, the existing covalent F-C interaction disappears and the noncovalent complex F$^-$(CO$_2$)$_4$ forms with ρ_b and $\nabla^2\rho_b$ in the prescribed range.
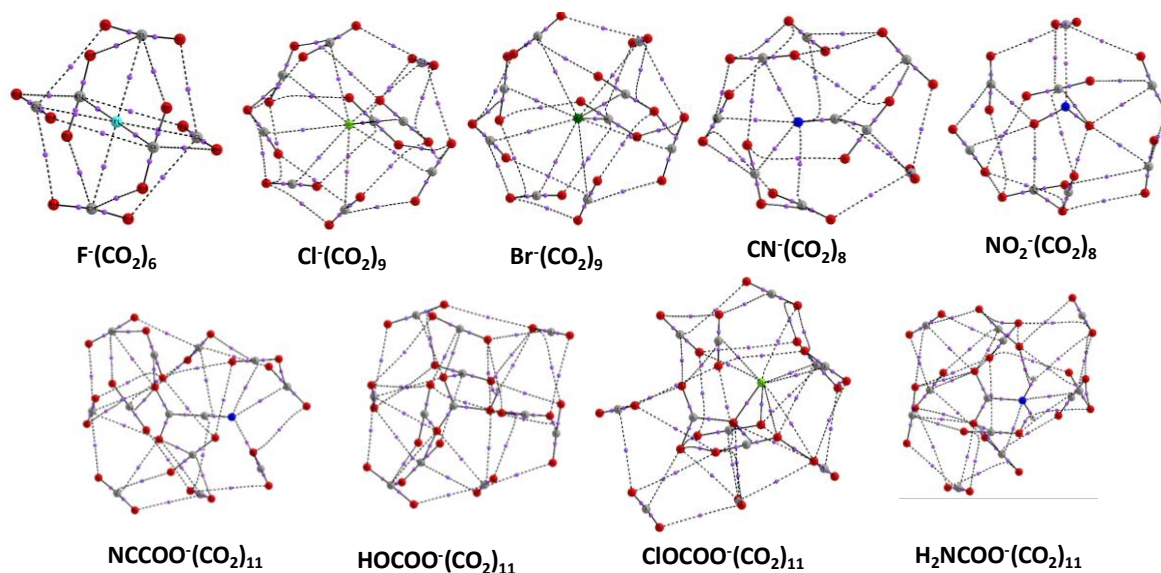
Figure 2.4 QTAIM bond critical points (purple dots) and bond paths (dotted lines) of X$^-$ (CO$_2$)$_{nmax}$ complexes at the M06L/6-311++G** level.

Unlike FCOO$^-$, the interaction of 'n' number of CO$_2$ with NCCOO$^-$, ClOCOO$^-$, HOCOO$^-$ and H$_2$NCOO$^-$ does not change the covalent character of the initially

formed anion-carbon bond as ρ_b and $\nabla^2\rho_b$ in all these cases show values in the range 0.2134 – 0.2852 au for the former and (-0.2837) – (-0.7866) au for the latter.

(a)

(b)
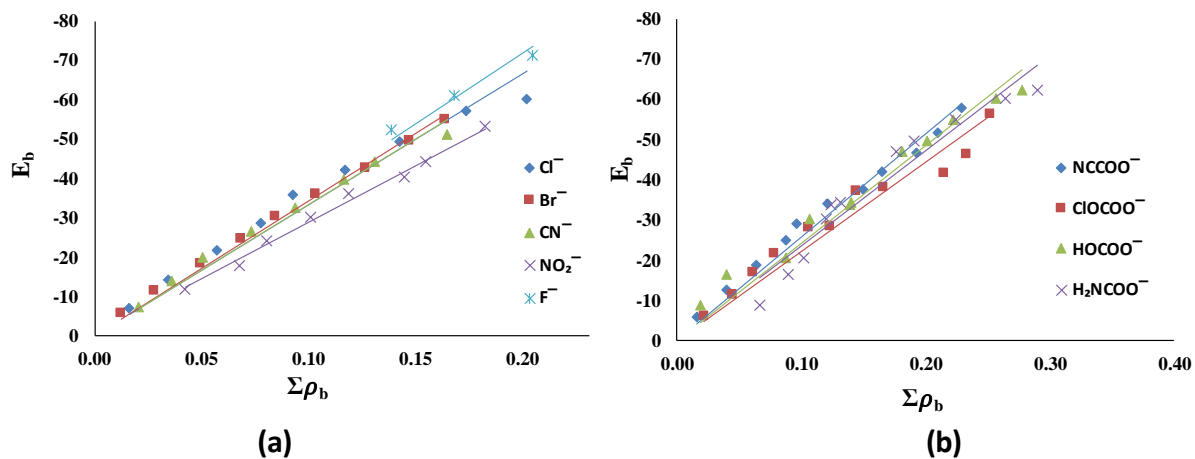
Figure 2.5 (a) and (b) Correlation between E_b (kcal/mol) and $\Sigma\rho_b$ (au) of $X^-(CO_2)_n$ complexes at the M06L/6-311++G** level.

Table 2.8 Slope (m) and correlation coefficient (R) of the plots between E_b and $\Sigma\rho_b$ of $X^-(CO_2)_n$ complexes at the M06L/6-311++G** level.

Anion	Slope (m)	Correlation coefficient (R)
F^-	358.67	0.9678
Cl^-	332.34	0.9801
Br^-	342.76	0.9969
CN^-	332.64	0.9902
NO_2^-	288.44	0.9959
$NCCOO^-$	256.85	0.9878
$ClOCOO^-$	221.78	0.9667
$HOCOO^-$	254.24	0.9933
H_2NCOO^-	235.63	0.9668

Table 2.9 $\Sigma\rho_1$ values (au) of $X^-\cdots CO_2$ bond in complexes at the M06L/6-311++G** level of theory.

n	F^-	Cl^-	Br^-	CN^-	NO_2^-	$NCCOO^-$	$ClOCOO^-$	$HOCOO^-$	H_2NCOO^-
1	0.176	0.016	0.012	0.021	0.043	0.016	0.022	0.019	0.067
2	0.014	0.045	0.022	0.031	0.068	0.039	0.044	0.034	0.089
3	0.038	0.039	0.031	0.039	0.075	0.052	0.054	0.081	0.090
4	0.113	0.049	0.039	0.048	0.089	0.065	0.061	0.085	0.102
5	0.110	0.061	0.050	0.058	0.094	0.074	0.080	0.110	0.086
6	0.117	0.071	0.056	0.068	0.083	0.085	0.088	0.097	0.068
7	-	0.075	0.064	0.076	0.115	0.095	0.081	0.125	0.125
8	-	0.080	0.075	0.079	0.114	0.097	0.105	0.141	0.122
9	-	0.072	0.070	-	-	0.110	0.124	0.145	0.151
10	-	-	-	-	-	0.129	0.142	0.131	0.160
11	-	-	-	-	-	0.116	0.147	0.138	0.141

Table 2.10 $\Sigma\rho_2$ values (au) of $X^-\cdots CO_2$ bond in complexes at the M06L/6-311++G** level of theory.

n	F^-	Cl^-	Br^-	CN^-	NO_2^-	$NCCOO^-$	$ClOCOO^-$	$HOCOO^-$	H_2NCOO^-
1	0	0	0	0	0	0	0	0	0
2	0.015	0.006	0.006	0.006	0.000	0.000	0.001	0.006	0.000
3	0.017	0.018	0.019	0.012	0.006	0.012	0.007	0.007	0.011
4	0.027	0.029	0.029	0.025	0.013	0.023	0.017	0.022	0.018
5	0.059	0.032	0.035	0.036	0.025	0.022	0.026	0.030	0.038
6	0.088	0.047	0.048	0.049	0.062	0.036	0.035	0.043	0.063
7	-	0.068	0.062	0.055	0.040	0.056	0.063	0.056	0.052
8	-	0.094	0.072	0.086	0.069	0.068	0.061	0.061	0.068
9	-	0.130	0.094	-	-	0.083	0.091	0.078	0.074
10	-	-	-	-	-	0.081	0.091	0.126	0.105
11	-	-	-	-	-	0.113	0.105	0.140	0.149

The value of ρ_b is often used as a measure of the strength of the corresponding noncovalent bonding interaction while the sum of ρ_b ($\Sigma\rho_b$) can be indicative of the total stabilizing influence of the noncovalent interactions. The $\Sigma\rho_b$ values presented in Table 2.7 for all the anions show a strong linear correlation with the total binding energy E_b (Figure 2.5). The slope of the correlation plot (intercept is zero) can be used as a measure of the noncovalent binding affinity of the anions to CO_2 molecules (Table 2.8). The decreasing order of the slope is $F^- >$ $Br^- > CN^- > Cl^- > NO_2^- > NCCOO^- > HOCOO^- > H_2NCOO^- > ClOCOO^-$ and suggests that F^- has the highest and $ClOCOO^-$ has the lowest affinity towards CO_2.

For all the anions, a linear increase in E_b is observed with respect to the number of CO_2 adsorbed. For example, E_b for $Cl^-(CO_2)$ is -6.9 kcal/mol while that for $Cl^-(CO_2)_9$ is -60.1 kcal/mol; the stabilizing effect is more than nine times. The $E_{b/CO2}$ is nearly a constant for most of the anions. The steady increase in E_b with each CO_2 adsorbed can be regarded as one of the most remarkable feature of the anion-CO_2 interaction. With the addition of each CO_2, the noncovalent anion....C binding distance (d_{int}) steadily increases. For instance, in the case of $Cl^-(CO_2)_n$, for n = 1, d_{int} is 2.888 Å and it increases to 3.241Å for n = 9. Such a distance feature may suggest a diminishing trend for $E_{b/CO2}$ with increase in the number of adsorbed CO_2. In order to explain the observed steady value of $E_{b/CO2}$, the combined effect of primary anion...C interactions and secondary O···C interactions has to be evaluated. Hence $\Sigma\rho_b$ is divided in to two parts, one for anion···C noncovalent interactions ($\Sigma\rho_1$) (Table 2.9) and the other for O···C secondary interactions between adsorbed CO_2 molecules ($\Sigma\rho_2$) (Table 2.10). The correlation plots in Figure 2.5 suggest,

$$E_b = m\ \Sigma\rho_b = m\ (\Sigma\rho_1 + \Sigma\rho_2) \hspace{3cm} \text{(Eq. 2.2)}$$

Hence, total anion...C binding energy,

$$E_1 = m\ \Sigma\rho_1 \hspace{3cm} \text{(Eq. 2.3)}$$

and total O...C binding energy,

$$E_2 = m\ \Sigma\rho_2 \hspace{3cm} \text{(Eq.2.4)}$$

Table 2.11 E_{1/CO_2} (kcal/mol) of $X^-\cdots CO_2$ bond in complexes at the M06L/6-311++G** level of theory.

n	F^-	Cl^-	Br^-	CN^-	NO_2^-	$NCCOO^-$	$ClOCOO^-$	$HOCOO^-$	H_2NCOO^-
1	-65.9	-5.8	-4.5	-7.6	-13.4	-4.6	-5.3	-5.2	-17.4
2	-2.6	-5.1	-4.1	-5.5	-10.6	-5.7	-5.4	-4.7	-11.7
3	-4.8	-4.6	-3.8	-4.7	-7.8	-5.0	-4.4	-7.5	-7.8
4	-10.6	-4.4	-3.6	-4.4	-7.0	-4.7	-3.8	-6.0	-6.7
5	-8.2	-4.3	-3.6	-4.1	-5.9	-4.3	-4.0	-6.1	-4.5
6	-7.3	-4.2	-3.4	-4.1	-4.3	-4.1	-3.6	-4.5	-3.0
7	-	-3.8	-3.4	-3.9	-5.2	-3.9	-2.9	-5.0	-4.6
8	-	-3.5	-3.5	-3.6	-4.5	-3.5	-3.2	-4.9	-4.0
9	-	-2.8	-2.9	-	-	-3.5	-3.4	-4.5	-4.4
10	-	-	-	-	-	-3.7	-3.5	-3.7	-4.2
11	-	-	-	-	-	-3.0	-3.3	-3.5	-3.3

Table 2.12 E_{2/CO_2} (kcal/mol) of $X^-\cdots CO_2$ bond in complexes at the M06L/6-311++G** level of theory.

n	F^-	Cl^-	Br^-	CN^-	NO_2^-	$NCCOO^-$	$ClOCOO^-$	$HOCOO^-$	H_2NCOO^-
1	0.0	0.0	0.0	0.0	0.0	0.0	0.0	0.0	0.0
2	-2.7	-1.1	-1.0	-1.1	0.0	0.0	0.2	0.8	0.0
3	-2.1	-2.2	-2.3	-1.4	-0.6	-1.1	-0.6	-0.7	-1.0
4	-2.5	-2.5	-2.7	-2.3	-1.0	-1.7	-1.1	-1.5	-1.2
5	-4.4	-2.3	-2.6	-2.6	-1.6	-1.3	-1.3	-1.7	-2.0
6	-5.5	-2.8	-2.9	-3.0	-3.2	-1.7	-1.4	-2.0	-2.7
7	-	-3.4	-3.3	-2.8	-1.8	-2.3	-2.2	-2.2	-1.9
8	-	-4.2	-3.3	-3.9	-2.7	-2.4	-1.9	-2.1	-2.2
9	-	-5.1	-3.8	-	-	-2.7	-2.5	-2.4	-2.1
10	-	-	-	-	-	-2.3	-2.3	-3.5	-2.7
11	-	-	-	-	-	-3.0	-2.4	-3.6	-3.5

The $E_{1/CO2}$ and $E_{2/CO2}$ data presented in Table 2.11 and Table 2.12, respectively suggest that the contribution from the anion⋯C interaction is decreasing while that due to O⋯C interaction is increasing with increase in the number of adsorbed CO_2 molecules (Figure 2.6). The interactions compensate for the weakening of primary interactions in large clusters. In fact, in large clusters, secondary interactions dominate over the primary interactions and the sum of both interactions per CO_2 adsorbed maintains a constant value. The E_1 and E_2 data clearly suggest that cooperativity between the adsorbed CO_2 molecules is very high leading to the formation of large clusters. Here cooperativity means that adsorption of a CO_2 molecule promotes the adsorption of yet another CO_2 due to enhancement in the secondary interaction and such a process continues till the primary coordination shell of the anion is saturated. Many of the secondary O...C interactions among the adsorbed CO_2 molecules are showing tetrel bond characteristics, arising from the electron density donation from the oxygen lone pairs to the carbon centers.[76-79]
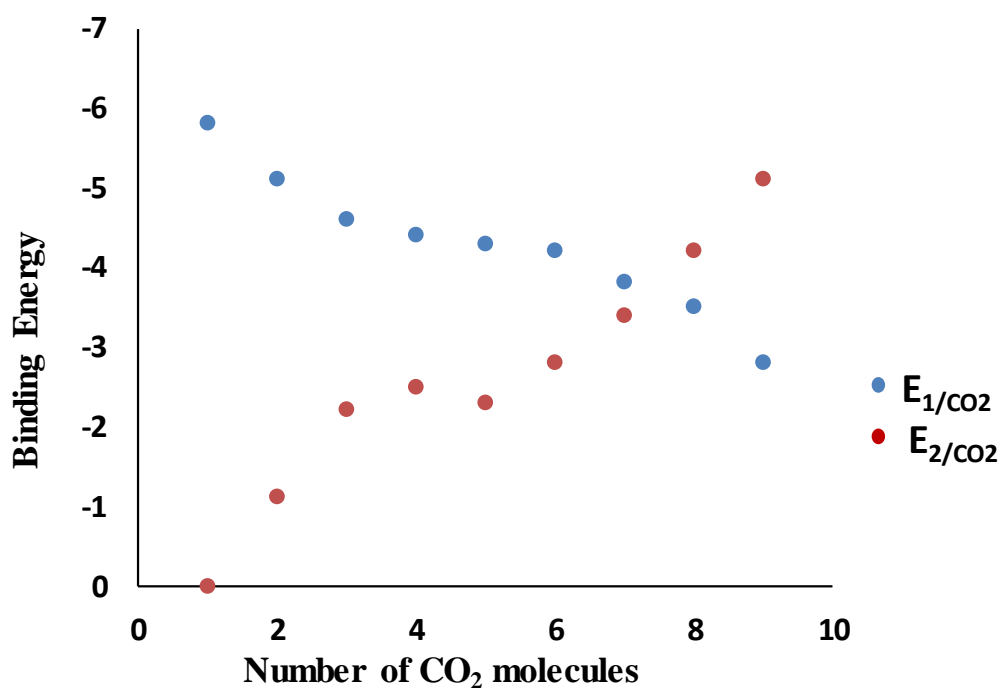
Figure 2.6 Correlation plot for $E_{1/CO2}$ and $E_{2/CO2}$ vs number of CO_2 molecules (n) for $Cl^-(CO_2)_n$ at M06L/6-311++G** level.

2.3.3 MESP analysis

According to Gadre-Pathak theorem, an anion or an anionic complex can be characterized by locating a negative-valued MESP surface that engulfs the whole system.[80] Analysis of such a surface is useful in understanding the delocalized nature of the extra electron in the system. It is expected that as the size of the CO_2 cluster increases, the delocalization increases leading to a decrease in the magnitude of the value of the MESP surface that engulfs the whole system (V_{max}). This can be illustrated using a representative case, $Br^-(CO_2)_n$ for which the most negative-valued isosurface engulfing the whole complex is given in Figure 2.7. For every anion…C noncovalent interaction, some amount of electron density gets transferred from the anion to the CO_2 whereas the secondary O⋯C interactions lead to further reorganization of the electron density.

| -0.0932 | -0.0887 | -0.0875 | -0.0847 |
| $Br^-(CO_2)$ | $Br^-(CO_2)_2$ | $Br^-(CO_2)_3$ | $Br^-(CO_2)_4$ |

| -0.0837 | -0.0801 | -0.0790 | -0.0799 | -0.0784 |
| $Br^-(CO_2)_5$ | $Br^-(CO_2)_6$ | $Br^-(CO_2)_7$ | $Br^-(CO_2)_8$ | $Br^-(CO_2)_9$ |
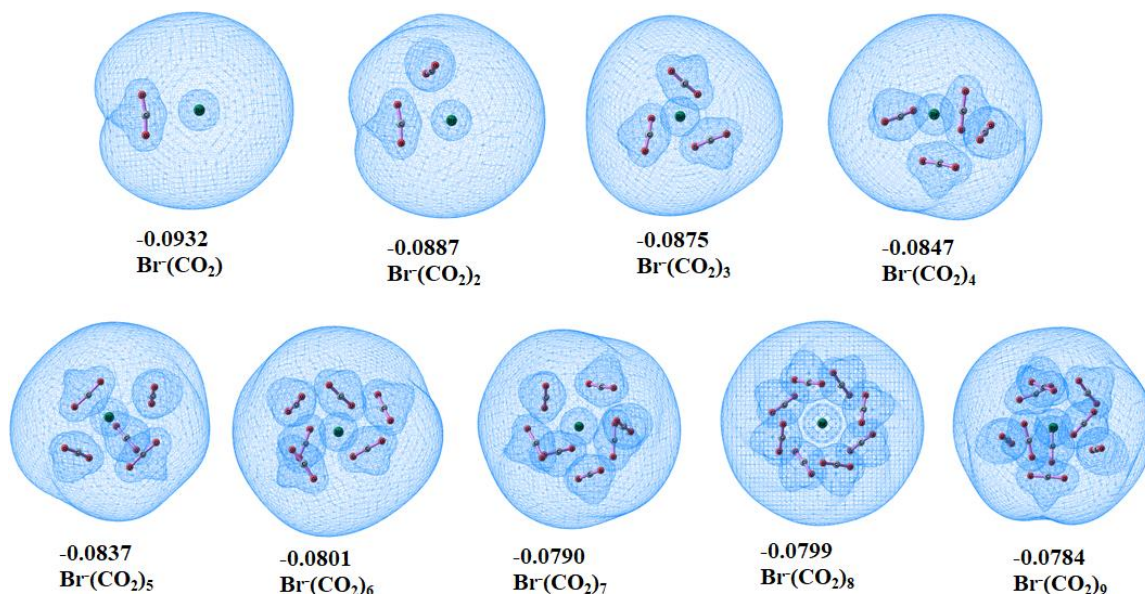
Figure 2.7 MESP of CO_2 complexes of Br^- at the M06L/6-311++G** level. The minimum value of MESP that engulfs the whole anion (V_{max}) is depicted in au.

The charge delocalization from anionic center to the surrounding solvent shell in anionic clusters of CO_2 had been observed in the spectroscopic studies by the Neumark[35, 69], Bowen[81] and Weber[5, 44, 82] groups. The Lineberger group also reported the redistribution of the negative charge on anion towards the solvent shell

surrounding it in their works on solvent mediated charge distribution in anionic clusters.[83-85] In our study, we observed a gradual decrease in the negative character of V_{max} with increase in the size of the cluster. However, marginal irregularities in this trend are observed in some cases due to structural differences.
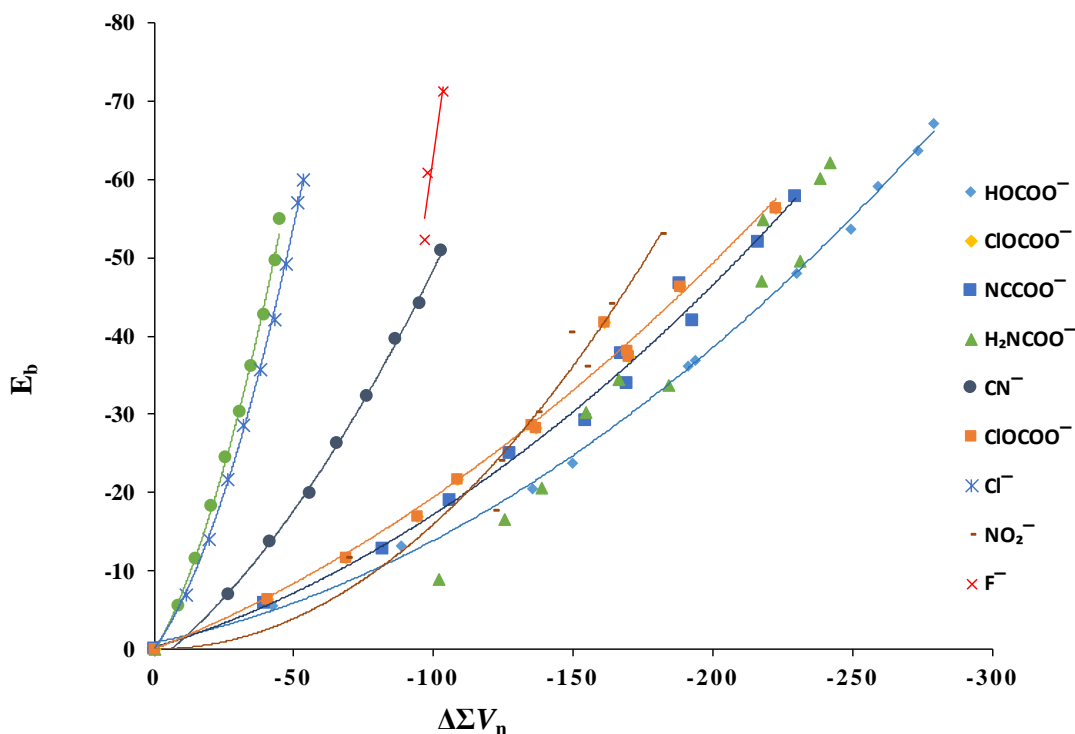
Figure 2.8 Correlation between E_b and $\Sigma(\Delta V_n)$ of $X^-(CO_2)_n$ complexes at the M06L/6-311++G** level.

Previous studies by Suresh *et al.* have shown that analysis of MESP at the nucleus (V_n) of intermolecularly interacting atoms in molecules can give insight in to the strength of interactions.[51, 52] In the present study, the donation of electron density from the anion to CO_2 suggest a decrease in the magnitude of V_n at every atoms of the anion. The change in MESP due to complexation with CO_2 at every atom of the anion (ΔV_n) is computed to obtain the total change in MESP ($\Sigma(\Delta V_n)$) for the anion (Table 2.13). The negative character of $\Sigma(\Delta V_n)$ decreases steadily with increase in the number of CO_2 adsorbed. Also the strong correlations are observed between $\Sigma(\Delta V_n)$ and E_b. Though the correlation appears linear for most of the data, a second degree polynomial is the best fitting for the data (Figure 2.8) wherein the correlation

coefficients fall in the range 0.9817 to 0.9995. The case of F^- is not included because of its unique nature the covalent to noncovalent transformation as cluster size increases - and the availability of only three noncovalent points.

Table 2.13 $\Sigma(\Delta V_n)$ in $X^-(CO_2)_n$ complexes at the M06L/6-311++G** level of theory.

n	F^-	Cl^-	Br^-	CN^-	NO_2^-	$NCCOO^-$	$ClOCOO^-$	$HOCOO^-$	H_2NCOO^-
1	-122.6	-11.6	-8.4	-26.4	-69.2	-39.5	-40.7	-42.2	-102.0
2	-131.2	-19.5	-15.0	-41.5	-121.9	-82.0	-68.9	-88.2	-125.6
3	-117.1	-26.0	-20.3	-55.6	-124.0	-105.9	-94.0	-135.2	-138.7
4	-97.0	-31.8	-25.4	-65.2	-137.0	-127.7	-108.5	-149.4	-154.7
5	-98.0	-37.8	-30.5	-76.2	-154.3	-154.3	-136.8	-193.7	-184.1
6	-103.3	-43.1	-34.7	-86.5	-149.0	-169.4	-135.3	-191.2	-166.1
7	-	-47.2	-39.1	-95.2	-163.4	-167.3	-169.8	-230.0	-217.4
8	-	-51.2	-43.6	-102.8	-181.7	-193.0	-169.3	-249.5	-231.2
9	-	-53.4	-44.7	-	-	-188.1	-161.1	-258.9	-218.0
10	-	-	-	-	-	-216.5	-188.3	-273.5	-238.6
11	-	-	-	-	-	-229.8	-222.6	-279.0	-241.7

2.4 Conclusions

The interactive behaviour of mono atomic and polyatomic anions with large number of CO_2 molecules has been studied using M06L/6-311++G** level DFT. In case of F^-, ClO^-, HO^- and H_2N^- anions, the interaction of a CO_2 leads to the formation of the corresponding carboxylate anion, $viz.$ $FCOO^-$, $ClOCOO^-$, $HOCOO^-$ and H_2NCOO^- due to the formation of anion-C covalent bond. With the intake of more than three CO_2 molecules, anion-C covalent bond observed for F^- changes to a noncovalent interaction while the rest of the anions retain the initially formed covalent bond and produce the noncovalent CO_2 complexes of the carboxylate anions. In case of

CN^-, the C end of the anion interacting with CO_2 leads to the formation of anion-C covalent bond and further uptake of CO_2 is accounted by the corresponding carboxylate anion $NCCOO^-$. If the interaction of first CO_2 is on the N end of the anion, noncovalent anion···C interaction occurs and further uptake of CO_2 gives noncovalent complex. In case of Cl^-, Br^-, and NO_2^-, only noncovalent complex formation is observed. The energetics data of the anion-CO_2 noncovalent complexes show that the anions maintain almost a constant value of $E_{b/CO2}$ with increasing number of CO_2 molecules. In addition to the anion···C noncovalent interactions, the secondary O···C interactions between adsorbed CO_2 molecules contribute significantly to the stability of the clusters, which is confirmed by finding strong correlation between the binding energy data and electron density data of noncovalent bond critical points in QTAIM analysis. As the CO_2 cluster size increases around the anion, the total effect of secondary O···C interactions increases while that of primary anion···C interaction decreases. A steady value of $E_{b/CO2}$ is observed in almost all anions because the reduction in primary interactions is compensated by increase in secondary interactions. MESP analysis is found to be very useful for assessing the delocalization of the extra electron in the system through the network of adsorbed CO_2 molecules. All anions show a steady decrease in the negative character of MESP at the nuclei as the cluster size increases. The MESP data correlates well with the binding energy data through a second degree polynomial equation. This study demonstrates the remarkable ability of anions to bind with several molecules of CO_2 and such a character of the anion is attributed to the cooperativity in secondary O···C interactions which gives significant stabilizing effect on the complex even though primary anion···C interactions decreases with increasing number of CO_2 adsorbed.

2.5 References

1. S. Solomon, D. Qin, M. Manning, Z. Chen, M. Marquis, K. B. Averyt, M. Tignor and H. L. Miller, *Contribution of working group I to the fourth assessment report of the intergovernmental panel on climate change, 2007*, 2007.

2.   R. E. Hester and R. M. Harrison, *Carbon capture: sequestration and storage*, Royal Society of Chemistry, , 2010.

3.   M. Ramdin, T. W. de Loos and T. J. Vlugt, *Ind. Eng. Chem. Res.*, 2012, **51**, 8149-8177.

4.   I. C. Change, *The Assessment Report*, 2013.

5.   J. M. Weber, *Int. Rev. Phys. Chem.*, 2014, **33**, 489-519.

6.   G. B. Damas, A. B. Dias and L. T. Costa, *J. Phys. Chem. B*, 2014, **118**, 9046-9064.

7.   I. P. o. C. Change, *Climate Change 2014–Impacts, Adaptation and Vulnerability: Regional Aspects*, Cambridge University Press, , 2014.

8.   I. P. O. C. CHANGE, *Climate Change 2014, Mitigation of Climate Change, Working Group III Contribution to the Fifth Assessment Report of the Intergovernmental Panel on Climate Change*, 2014.

9.   M. Younas, M. Sohail, L. Leong, M. J. Bashir and S. Sumathi, *Int. J. Environ. Sci. Technol.*, 2016, **13**, 1839-1860.

10.   M. Lewis, Z. Wu and R. Glaser, *J. Phys. Chem. A*, 2000, **104**, 11355-11361.

11.   H.-J. Fan and C.-W. Liu, *Chem. Phys. Lett.*, 1999, **300**, 351-358.

12.   B. Bhargava and S. Balasubramanian, *Chem. Phys. Lett.*, 2007, **444**, 242-246.

13.   B. Bhargava, M. Saharay and S. Balasubramanian, *Bull. Mater. Sci.*, 2008, **31**, 327-334.

14.   K. M. Gupta and J. Jiang, *J. Phys. Chem. C*, 2014, **118**, 3110-3118.

15.   J. X. Mao, J. A. Steckel, F. Yan, N. Dhumal, H. Kim and K. Damodaran, *Phys. Chem. Chem. Phys.*, 2016, **18**, 1911-1917.

16.   A. R. Shaikh, H. Karkhanechi, E. Kamio, T. Yoshioka and H. Matsuyama, *J. Phys. Chem. C*, 2016, **120**, 27734-27745.

17.   X. Zhang, X. Zhang, H. Dong, Z. Zhao, S. Zhang and Y. Huang, *Energy Environ. Sci.*, 2012, **5**, 6668-6681.

18.   A. P. Hallenbeck and J. R. Kitchin, *Ind. Eng. Chem. Res.*, 2013, **52**, 10788-10794.

19.   J. Wang, L. Huang, R. Yang, Z. Zhang, J. Wu, Y. Gao, Q. Wang, D. O'Hare and Z. Zhong, *Energy Environ. Sci.*, 2014, **7**, 3478-3518.

20.   A. Sanna, M. Uibu, G. Caramanna, R. Kuusik and M. Maroto-Valer, *Chem. Soc. Rev.*, 2014, **43**, 8049-8080.

21.   A. Goeppert, M. Czaun, J.-P. Jones, G. S. Prakash and G. A. Olah, *Chem. Soc. Rev.*, 2014, **43**, 7995-8048.

22.   N. Hollingsworth, S. Taylor, M. T. Galante, J. Jacquemin, C. Longo, K. B. Holt, N. H. de Leeuw and C. Hardacre, *Angew. Chem. Int. Ed.*, 2015, **54**, 14164-14168.

23.   D. Chen, X. Zhang and A. F. Lee, *J. Mater. Chem. A*, 2015, **3**, 14487-14516.

24.   M. Marszewski, S. Cao, J. Yu and M. Jaroniec, *Mater. Horiz.*, 2015, **2**, 261-278.

25.   A. Otto, T. Grube, S. Schiebahn and D. Stolten, *Energy Environ. Sci.*, 2015, **8**, 3283-3297.

26.   G. A. Ozin, *Adv. Mater.*, 2015, **27**, 1957-1963.

27.   J. Kothandaraman, A. Goeppert, M. Czaun, G. A. Olah and G. S. Prakash, *J. Am.Chem. Soc.*, 2016, **138**, 778-781.

28.   X. Chang, T. Wang and J. Gong, *Energy Environ. Sci.*, 2016, **9**, 2177-2196.

29.   I. H. Arellano, S. H. Madani, J. Huang and P. Pendleton, *Chem. Eng. J.*, 2016, **283**, 692-702.

30.   K. Spears, *J. Chem. Phys.*, 1972, **57**, 1850-1858.

31.   K. G. Spears and E. Ferguson, *J. Chem. Phys.*, 1973, **59**, 4174-4183.

32. J. Larson and T. McMahon, *J. Am. Chem. Soc.*, 1985, **107**, 766-773.
33. B. S. Ault, *Inorg. Chem.*, 1982, **21**, 756-759.
34. K. Hiraoka, S. Mizuse and S. Yamabe, *J. Chem. Phys.*, 1987, **87**, 3647-3652.
35. D. W. Arnold, S. E. Bradforth, E. H. Kim and D. M. Neumark, *J. Chem. Phys.*, 1995, **102**, 3493-3509.
36. G. Markovich, R. Giniger, M. Levin and O. Cheshnovsky, *Z. Phy. D*, 1991, **20**, 69-72.
37. D. W. Arnold, S. E. Bradforth, E. H. Kim and D. M. Neumark, *J. Chem. Phys.*, 1995, **102**, 3510-3518.
38. A. K. Pathak, *ChemPhysChem*, 2011, **12**, 2641-2645.
39. A. K. Pathak, *J. Chem. Phys.*, 2012, **136**, 234306.
40. A. K. Pathak, *J. Phys. Chem. A*, 2016, **120**, 9776-9781.
41. L. Sheps, E. M. Miller and W. C. Lineberger, *J. Chem. Phys.*, 2009, **131**, 064304.
42. M. Z. Kamrath, R. A. Relph and M. A. Johnson, *J. Am. Chem. Soc.*, 2010, **132**, 15508-15511.
43. A. D. Boese, H. Schneider, A. N. Glöß and J. M. Weber, *J. Chem. Phys.*, 2005, **122**, 154301.
44. B. J. Knurr and J. M. Weber, *J. Am. Chem. Soc.*, 2012, **134**, 18804-18808.
45. X. Zhang, E. Lim, S. K. Kim and K. H. Bowen, *J. Chem. Phys.*, 2015, **143**, 174305.
46. B. J. Knurr and J. M. Weber, *J. Phys. Chem. A*, 2013, **117**, 10764-10771.
47. B. J. Knurr and J. M. Weber, *J. Phys. Chem. A*, 2014, **118**, 10246-10251.
48. B. J. Knurr and J. M. Weber, *J. Phys. Chem. A*, 2014, **118**, 8753-8757.
49. G. Liu, S. M. Ciborowski, Z. Zhu, Y. Chen, X. Zhang and K. H. Bowen, *Phys. Chem. Chem. Phys.*, 2019.
50. T. D. Della and C. H. Suresh, *Phys. Chem. Chem. Phys.*, 2016, **18**, 14588-14602.
51. T. D. Della and C. H. Suresh, *ACS Omega*, 2017, **2**, 4505-4513.
52. T. D. Della and C. H. Suresh, *Phys. Chem. Chem. Phys.*, 2017, **19**, 5830-5838.
53. T. D. Della and C. H. Suresh, *Phy. Chem. Chem. Phys.*, 2018, **20**, 6227-6235.
54. M. J. Frisch, G. W. Trucks, H. B. Schlegel, G. E. Scuseria, M. A. Robb, J. R. Cheeseman, G. Scalmani, V. Barone, G. A. Petersson, H. Nakatsuji, X. Li, M. Caricato, A. V. Marenich, J. Bloino, B. G. Janesko, R. Gomperts, B. Mennucci, H. P. Hratchian, J. V. Ortiz, A. F. Izmaylov, J. L. Sonnenberg, D. Williams-Young, F. Ding, F. Lipparini, F. Egidi, J. Goings, B. Peng, A. Petrone, T. Henderson, D. Ranasinghe, V. G. Zakrzewski, J. Gao, N. Rega, G. Zheng, W. Liang, M. Hada, M. Ehara, K. Toyota, R. Fukuda, J. Hasegawa, M. Ishida, T. Nakajima, Y. Honda, O. Kitao, H. Nakai, T. Vreven, K. Throssell, J. A. Montgomery Jr., J. E. Peralta, F. Ogliaro, M. J. Bearpark, J. J. Heyd, E. N. Brothers, K. N. Kudin, V. N. Staroverov, T. A. Keith, R. Kobayashi, J. Normand, K. Raghavachari, A. P. Rendell, J. C. Burant, S. S. Iyengar, J. Tomasi, M. Cossi, J. M. Millam, M. Klene, C. Adamo, R. Cammi, J. W. Ochterski, R. L. Martin, K. Morokuma, O. Farkas, J. B. Foresman and D. J. Fox, *Gaussian 16 Rev. A.03*, Gaussian, Inc., Wallingford CT, 2016.
55. Y. Zhao and D. G. Truhlar, *J. Chem. Phys.*, 2006, **125**, 194101.
56. Y. Zhao and D. G. Truhlar, *Acc. Chem. Res.*, 2008, **41**, 157-167.
57. K. Remya and C. H. Suresh, *J. Comput. Chem.*, 2013, **34**, 1341-1353.
58. S.-Y. Chang, H. Weinstein and D. Chou, *Chem. Phys. Lett.*, 1976, **42**, 145-150.
59. L. C. G. Freitas, R. L. Longo and A. M. Simas, *J. Chem. Soc. Faraday Trans.*, 1992, **88**, 189-193.

60.	M. C. Daza, J. Dobado, J. M. Molina, P. Salvador, M. Duran and J. L. Villaveces, *J. Chem. Phys.*, 1999, **110**, 11806-11813.

61.	R. J. Wheatley, A. S. Tulegenov and E. Bichoutskaia, *Int. Rev. Phys. Chem.*, 2004, **23**, 151-185.

62.	S. F. Boys and F. d. Bernardi, *Mol. Phys.*, 1970, **19**, 553-566.

63.	V. Vorsa, S. Nandi, P. J. Campagnola, M. Larsson and W. Lineberger, *J. Chem. Phys.*, 1997, **106**, 1402-1410.

64.	C. D. Sherrill, T. Takatani and E. G. Hohenstein, *J. Phys. Chem. A*, 2009, **113**, 10146-10159.

65.	P. Hobza and K. Müller-Dethlefs, *Non-covalent interactions: theory and experiment*, Royal Society of Chemistry, , 2010.

66.	A. Halkier, W. Klopper, T. Helgaker, P. Jo/rgensen and P. R. Taylor, *J. Chem. Phys.*, 1999, **111**, 9157-9167.

67.	C. D. Sherrill, *School of Chemistry and Biochemistry, Georgia Institute of Technology*, 2010.

68.	A. Sanov and W. C. Lineberger, *Phys. Chem. Chem. Phys.*, 2004, **6**, 2018-2032.

69.	M. T. Zanni, B. J. Greenblatt and D. M. Neumark, *J. Chem. Phys.*, 1998, **109**, 9648-9651.

70.	B. J. Greenblatt, M. T. Zanni and D. M. Neumark, *J. Chem. Phys.*, 2000, **112**, 601-612.

71.	T. Lenzer, I. Yourshaw, M. R. Furlanetto, N. L. Pivonka and D. M. Neumark, *J. Chem. Phys.*, 2001, **115**, 3578-3589.

72.	U. Koch and P. L. Popelier, *J. Phys. Chem.*, 1995, **99**, 9747-9754.

73.	P. Popelier, *J. Phys. Chem. A*, 1998, **102**, 1873-1878.

74.	S. Shaik, D. Danovich, W. Wu and P. C. Hiberty, *Nat. Chem.*, 2009, **1**, 443.

75.	H. J. Bohórquez, R. J. Boyd and C. F. Matta, *J. Phys. Chem. A*, 2011, **115**, 12991-12997.

76.	L. M. Azofra and S. Scheiner, *J. Chem. Phys.*, 2015, **142**, 034307.

77.	S. Yourdkhani, T. Korona and N. L. Hadipour, *J. Comput. Chem.*, 2015, **36**, 2412-2428.

78.	I. Alkorta, J. Elguero and J. E. Del Bene, *J.Phys. Chem. A*, 2017, **121**, 8017-8025.

79.	M. Liu, Q. Li and S. Scheiner, *Phys, Chem. Chem. Phys.*, 2017, **19**, 5550-5559.

80.	S. R. Gadre and R. N. Shirsat, *Electrostatics of atoms and molecules*, Universities Press, , 2000.

81.	J. D. Graham, A. M. Buytendyk, Y. Wang, S. K. Kim and K. H. Bowen Jr, *J. Chem. Phys.*, 2015, **142**, 234307.

82.	M. C. Thompson, J. Ramsay and J. M. Weber, *J. Phys. Chem. A*, 2017, **121**, 7534-7542.

83.	L. Sheps, E. M. Miller, S. Horvath, M. A. Thompson, R. Parson, A. B. McCoy and W. C. Lineberger, *Science*, 2010, **328**, 220-224.

84.	L. Sheps, E. M. Miller, S. Horvath, M. A. Thompson, R. Parson, A. B. McCoy and W. C. Lineberger, *J. Chem. Phys.*, 2011, **134**, 184311.

85.	J. P. Martin, A. S. Case, Q. Gu, J. P. Darr, A. B. McCoy and W. C. Lineberger, *J. Chem. Phys.*, 2013, **139**, 064315.

Chapter 3

Part A

Guanidine as a Strong CO$_2$ Adsorbent: A DFT Study on Cooperative CO$_2$ Adsorption

Part B

Demarcating Noncovalent and Covalent Bond Territories: Imine-CO$_2$ Complexes and Cooperative CO$_2$ Capture
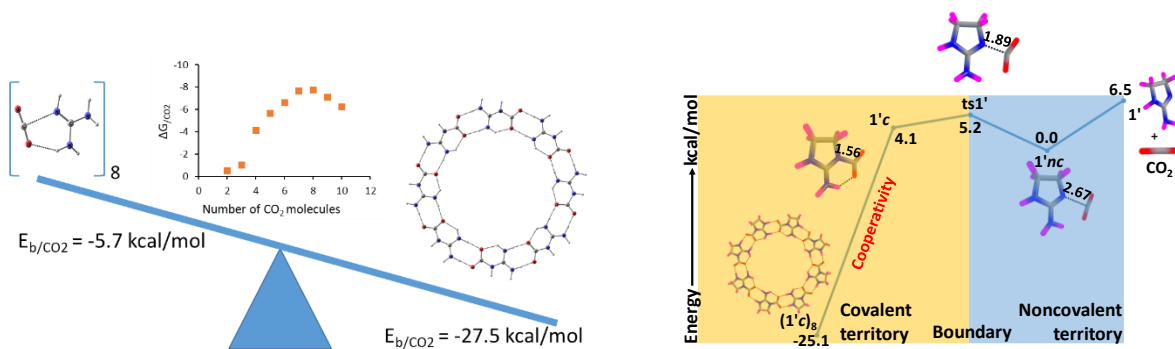
Part A: Guanidine as a Strong CO_2 Adsorbent: A DFT Study on Cooperative CO_2 Adsorption

3.1 Abstract

Among the various carbon capture and storage (CCS) technologies, direct air capture (DAC) of CO_2 by engineered chemical reactions on suitable adsorbents has attained more attention in recent times. Guanidine (G) is one of such promising adsorbent molecules for CO_2 capture. Recently Lee et al. reported the binding energy (E_b) -5.5 kcal/mol for the G···CO_2 complex at CCSD(T)/CBS level which was one of the best noncovalent interaction observed for CO_2 among several functional molecules. Here we show that the noncovalent G···CO_2 complex can transform to a strongly interacting G-CO_2 covalent complex under the influence of multiple G and CO_2. The study conducted at M06-2X /6-311++G** level density functional theory shows E_b = -5.7 kcal/mol for G···CO_2 with N···C distance 2.688 Å while almost a five-fold increase in E_b (-27.5 kcal/mol) is observed for the (G-CO_2)$_8$ cluster wherein the N-C distance is 1.444 Å. All the (G-CO_2)$_n$ clusters (n = 2 – 10) show strong N-CO_2 covalent interaction with N-C distance gradually decreasing from 1.479 Å for n = 2 to 1.444 Å for n = 8 $\cong$ 9, 10. The N-CO_2 bonding gives (G$^+$)-(CO_2^-) zwitterion character for G-CO_2 and the charge-separated units preferred a cyclic arrangement in (G-CO_2)$_n$ clusters due to the support of three strong intermolecular O···HN hydrogen bonds from every CO_2. The O···HN interaction also enhances with an increase in the size of the cluster up to n = 8. The high E_b is attributed to the large cooperativity associated with the N-CO_2 and O···HN interactions. The quantum theory of atoms in molecules (QTAIM) analysis confirms the nature and strength of such interactions and also finds that the total binding energy is directly related to the sum of the electron density at the bond critical points of N-CO_2 and O···HN interactions. Further, molecular electrostatic potential analysis shows that the cyclic cluster is stabilized due to the delocalization of charges accumulated on the (G$^+$)-(CO_2^-) zwitterion *via* multiple

O···HN interactions. The cyclic $(G-CO_2)_n$ cluster formation is a highly exergonic process which reveals the high CO_2 adsorption capability of guanidine.

3.2 Introduction

The balance of the planetary climate is facing a major challenge from calamitous increase in global temperatures resulting from the increased emission of various anthropogenic greenhouse gases (GHG), most importantly CO_2.[1] To reduce atmospheric CO_2 concentration and thereby to manage the long-run risks of persistent climate changes it has become highly important to remove CO_2 from the air faster than nature does.[2, 3] Though a lot of research activities are going on in this area of carbon capture and storage (CCS), still we need better sequestration methods, a long term exploratory research effort for the development of air capture along with other direct methods for the active removal of CO_2 from the atmosphere.[4, 5] One promising approach among various negative emissions technologies (NETs) which aim at reducing the atmospheric CO_2 concentration is direct air capture (DAC), a process that removes CO_2 from the air by engineered chemical reactions.[6-10] In 1999 Lackner *et al*. familiarized the concept of capturing CO_2 from air for climate change mitigation.[11] This hurled a discussion on whether DAC is an important and viable option for reducing greenhouse gas levels or not.[12-18] DAC stands different from other NET methods, owing to its use of abiogenic means of removing CO_2 from the atmosphere.[19] Since the overall atmospheric concentration of CO_2 is very low, the absorbents should have very strong binding affinity and good selectivity against other components in air like water. Another important challenge in the DAC is the regeneration of the sorbent and the energy spent in these regeneration processes.

Several experimental and theoretical studies have been carried out to understand the binding interaction of CO_2 with different molecules. Alkhabbaz *et al*. evaluated CO_2 adsorption performance of aminosilica adsorbents prepared by the impregnation of guanidinylated poly(allylamine) (GPAA) into silica mesocellular foam supports. From the CO_2 adsorption-desorption cycling

experiments they found that the GPAA adsorbents have a better stability and regenerability at higher temperatures, making this class of materials suited for temperature swing cycles operating in a higher temperature regime than traditional aminosilica adsorbents based on PEI.[20] Wang *et al.* synthesized polybenzoxazine-based polymer sphere as CO_2 adsorbent and reported that the nitrogen content of the carbon adsorbent is a booster for CO_2 adsorption capacity at low pressures.[21] In this material the porous carbon spheres contain intrinsic nitrogen-containing groups. Sabet-Sarvestani *et al.* studied the role of four guanidine based supper bases 1,8-diazabicyclo[5.4.0]undec-7-ene (DBU), 1,5-diazabicyclo[4.3.0]non-5-ene (DBN) 1,1,3,3-tetramethylguanidine (TMG), and 1,5,7-triazabicyclo[4.4.0]dec-5-ene (MTBD) in the conversion of carbon dioxide and 2-aminobenzonitrile to quinazoline-2,4(1H, 3H)-diones.[22] But the triazabicyclo derivative of guanidine incorporated mesoporous silica nanoparticles (MCM) has shown a weak adsorption capacity for CO_2 compared to the other modified versions of MCM.[23] Aqueous solution of 2,6-pyridinebis(iminoguanidine), PyBIG was found to be an efficient absorbent to be employed in the DAC process, owing to the low aqueous solubility of the carbonate salt, $(PyBIGH_2)(CO_3)(H_2O)_4$ even in the very low concentration of CO_2 in the air.[24, 25] A mild heating at 120°C is sufficient for the regeneration of the PyBIG sorbent, which then can be reused in another DAC cycle. Thus the overall process remains as an energy efficient DAC technology. Custelcean *et al.* studied the chemical bonding and intermolecular interactions in the highly insoluble carbonate salt of a 2,6-pyridine-bis(iminoguanidine), within the framework of the QTAIM based on the experimental electron density derived from X-ray diffraction data obtained at 20 K.[26] They also patented guanidine compounds for carbon dioxide capture (US10583387B2).[27] Though first reported in 1898 by the German chemist Johannes Thiele[28], iminoguanidines are grabbing more attention in the last five years due to its high recognition abilities towards hydrophilic oxyanions through strong and complementary hydrogen bonding from the guanidinium groups.

Cooperativity originating from the long-range interactions between two identical or different sites lead various important implications for many systems,

including ligand–receptor binding,[29] catalysis,[30-33] and CO_2 adsorption[34-37] through the tuning of these cooperative interactions. In 2001, Schmuck demonstrated self-assembling of 2-(guanidiniocarbonyl)-pyrrole-4-carboxylate zwitterion into oligomeric structures in DMSO due to ion pairing between the carboxylate function and the guanidinium group of neighboring monomers resulting in one-dimensional assemblies.[38] Cooperative interactions enhance the CO_2 adsorption enthalpy with the CO_2-binding energy of a functional group.[39] In 2017, Steinhardt *et al.* reported cooperative CO_2 absorption in solution phase system comprising bidentate guanidine and bidentate alcohol at ambient temperature.[40] Cooperative adsorption of gases by porous frameworks permits more efficient gas uptake and removal than the more usual non-cooperative (Langmuir-type) adsorption.[41] In the case of CO_2 capture by amines, the higher degrees of amination will not be necessarily favorable as excessive clustering of amine groups can interfere with CO_2 binding. This was clearly demonstrated by Vaidhyanathan *et al.* through combined experiment and simulation methods that cooperative interactions between CO_2 molecules contribute significantly to binding energies and sorbents with pores that bind higher aggregates of CO_2 will significantly enhance heats of adsorption.[42] Recently, Kim *et al.* reported a family of robust tetraamine-functionalized frameworks that retain cooperativity, leading to the potential for exceptional efficiency in capturing CO_2 under the extreme conditions relevant to natural gas flue emissions.[43] Very recently, Hosseini *et al.* investigated the ability of sphingosine kinase inhibitor (SphKI) with multiple reaction including guanidine and oxadiazole groups to bind CO_2 using symmetry-adapted perturbation theory and a non-covalent interaction approach.[44] The strongest binding energy between SphKI and CO_2 is a -12.9 kcal/mol, in complex C1, indicating that guanidine in the polar head plays an important role in CO_2 capture.

In 2015, Lee and co-workers reported a study on the interaction of CO_2 with various functional molecules using density functional theory (DFT) and wavefunction methods.[45] They suggested guanidine as one of the molecules having strong interaction with CO_2 and the reported binding energy 5.5 kcal/mol at

CCSD(T)/CBS method was better than that of many functional molecules. Though their study showed a high affinity for guanidine towards CO_2, the binding energy suggests only a weak noncovalent interaction and may not be sufficient enough to explain the strong adsorption capability of guanidine as such an association process is always accompanied by entropy loss. A free energy lowering would be expected for an association process when the binding energy for a two body interaction is typically around 8 – 10 kcal/mol. Here a systematic study is proposed for analyzing both noncovalent and covalent interaction possibilities of guanidine (G) molecules with CO_2 molecules. The cooperativity involved in the CO_2 binding of the guanidine molecules is revealed in the study to suggest guanidine as a promising adsorbent for CO_2 capture. Most of the reported works involves the cooperativity in the adsorption of CO_2 molecules onto the material surface.[37, 41, 43, 46-48] This study will focus on the molecular level analysis of the interaction between the CO_2 and G molecule and the cooperativity involved in the stabilization of their large cluster.

3.2.1 Computational methods

All the geometry optimizations are carried out at the M06-2X/6-311++G** level of DFT using Gaussian 16 suite of programs.[49] M06-2X functional is regarded as one of the best methods for modelling intermolecular noncovalent interactions.[50] The vibrational frequency analysis has been carried out on all optimized geometries which confirms the energy minima nature of them with all real frequencies. The interaction energies of the guanidine-CO_2 complexes are calculated using the supermolecule approach. For any two interacting subsystems A and B, stabilization energy or the binding energy (E_b) of the supermolecule C is calculated using the equation;

$$E_b = E_C - E_A - E_B \qquad\qquad (Eq.\ 3.1)$$

E_A, E_B, and E_C represent zero-point energy (ZPE)-corrected energy of G, CO_2 and guanidine-CO_2 complex, respectively. Further, correction for the basis set superposition error (BSSE)[51-54] is made by the counterpoise (CP) approach of Boys and Bernardi.[55, 56] Similarly free energy change and enthalpy change at standard

temperature and pressure (STP) associated with the interaction is calculated using supermolecule approach. Further the entropy change involved in G···CO_2 clustering is also calculated.

Atom–atom interactions are distinguished as covalent and noncovalent interactions based on the electron densities at the respective BCPs (ρ_b) as well as from the sign of the corresponding Laplacian ($\nabla^2\rho_b$) from the Bader's QTAIM analysis using AIMAll package. The sum of electron density at the BCPs ($\Sigma\rho_b$) and the sign of Laplacian of electron density ($\nabla^2\rho_b$) are also analyzed for all the complexes. Molecular electrostatic potential (MESP) analysis is carried out on all the complexes at M06-2X/6-311++G** level of theory to understand the charge delocalization across the G and CO_2 units in the clusters. Further, a benchmark set of calculations is done on a representative case using B3LYP, B3LYP-D3, BP86-D3, M06-2X-D3 and wB97XD levels in conjunction with the basis set 6-311++G**. The D3 stands for Grimme's dispersion correction.

3.3 Results and discussion

The interaction of the molecule G with molecules of CO_2 has been studied through the structure and energetics parameters. Figure 3.1 gives the representative structures of the optimized geometries of $G(CO_2)_n$ clusters. The binding energy, E_b of first molecule of CO_2 with sp^2 hybridized (imine) N atom of G is -5.7 kcal/mol (Table 3.1). With the increase in the number of CO_2 molecules, total E_b value increases. Additional CO_2 molecules are also found to be interacting with the imine N atom of G. The distance of interaction (d_{int}) of CO_2 with the imine N of G increases from 2.688 Å in $G(CO_2)$ to an average value 2.930 Å in $G(CO_2)_4$, which indicates a decrease in the strength of interaction of each CO_2 with the imine N. However, the $E_{b/CO2}$ values given in Table 3.1 shows that with the increasing number of molecules of CO_2, the value of $E_{b/CO2}$ for $G(CO_2)_n$ systems are found to be comparable from n = 3. The phenomenon of maintaining a similar of $E_{b/CO2}$ could be due to additional stabilizations other than the N···CO_2 interactions. To understand the additional stabilizations in the $G(CO_2)_n$ systems we carried out the QTAIM analysis.
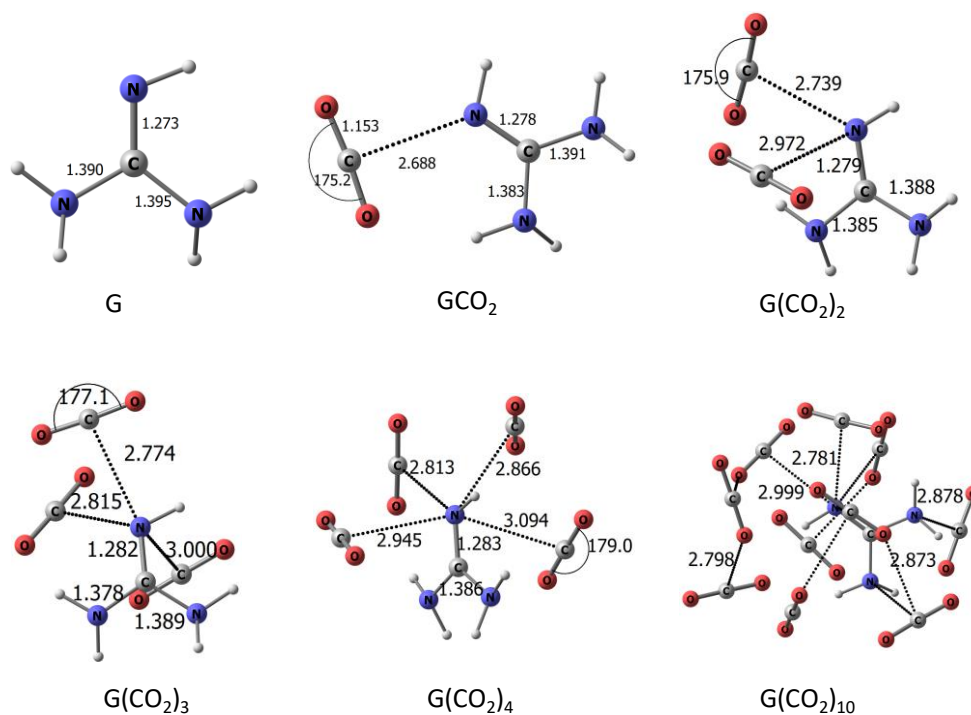
Figure 3.1 Optimized geometries of $G(CO_2)_n$ complexes with their d_{int} (Å), and OCO angle, θ (°) at M06-2X/6-311++G**.
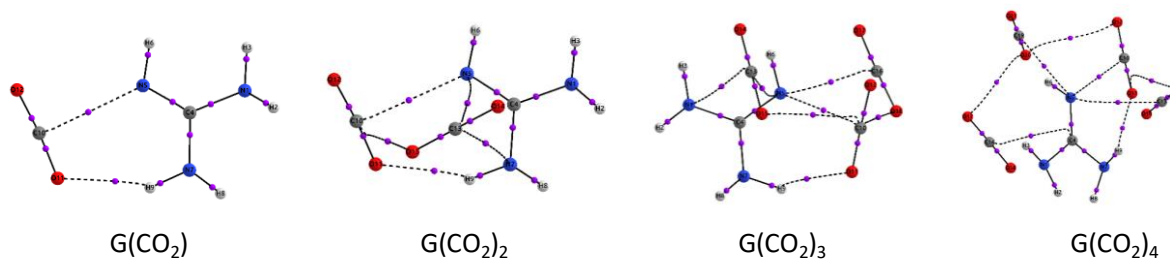
Figure 3.2 QTAIM plots of $G(CO_2)_n$ complexes for n = 1 to 4 at M06-2X/6-311++G**.

The QTAIM plot of $G(CO_2)$ shows BCP for imino(N)···CO_2 interaction with ρ_b value 0.0165 au as well as BCP for NH···OCO interaction with ρ_b value 0.0121 au. In all other case, the N···CO_2 and NH···OCO interactions are observed for at least one CO_2 molecule. Further, multiple N···CO_2 interactions are identified in many cases through the location of BCPs. In addition to N···CO_2 and NH···OCO interactions, all $G(CO_2)_n$ clusters with n > 1 showed (Figure 3.2) BCPs between the adsorbed CO_2 molecules, indicating the presence of secondary O···C interactions.

As n increases, multiple O···C interactions occurs in $G(CO_2)_n$ clusters, leading to significant cooperative stabilization of the cluster. This kind of cooperative stabilizations were already reported for the clustering of CO_2 around anions.[57]

Table 3.1 ZPE and BSSE corrected E_b, ΔG, $E_{b/CO2}$ and $\Delta G_{/CO2}$ (kcal/mol) of $G(CO_2)_n$ complexes at M06-2X/6-311++G** level.

n	E_b	$E_{b/CO2}$	ΔG	$\Delta G_{/CO2}$	ΔH	$T\Delta S$
1	-5.7	-5.7	2.3	2.3	-5.5	-7.8
2	-10.3	-5.2	6.8	3.4	-9.9	-16.7
3	-14.1	-4.7	11.5	3.8	-13.3	-24.8
4	-18.4	-4.6	16.7	4.2	-17.4	-34.1
5	-21.6	-4.3	20.9	4.2	-20.2	-41.1
6	-26.6	-4.4	25.7	4.3	-25.2	-50.9
7	-31.9	-4.6	31.6	4.5	-30.3	-61.9
8	-35.2	-4.4	37.3	4.7	-33.3	-70.6
9	-38.9	-4.3	43.9	4.9	-36.9	-80.8
10	-43.6	-4.4	49.0	4.9	-41.5	-90.5

Though the imine N···CO_2 interactions become weaker with increasing value of n, due to the additional stabilization from the O···C interactions, $E_{b/CO2}$ maintains a steady value around -4.4 kcal/mol even up to n = 10. The OCO bond angle, θ shows a small change, 3 - 5° from free CO_2 molecule indicating that the G···CO_2 interaction does not make any significant structural deformation on CO_2. Also on the free energy scale, the clustering of CO_2 around G is found to be an endergonic process (Table 3.1). This is due to the large decrease in entropy associated with the clustering. The energy data in Table 3.1 clearly suggest that a spontaneous formation of $G(CO_2)_n$ system is impossible at standard temperature and pressure (STP) conditions for any value of n. In order to further assess the affinity of CO_2 to bind with G, the G···G interaction has to be addressed.
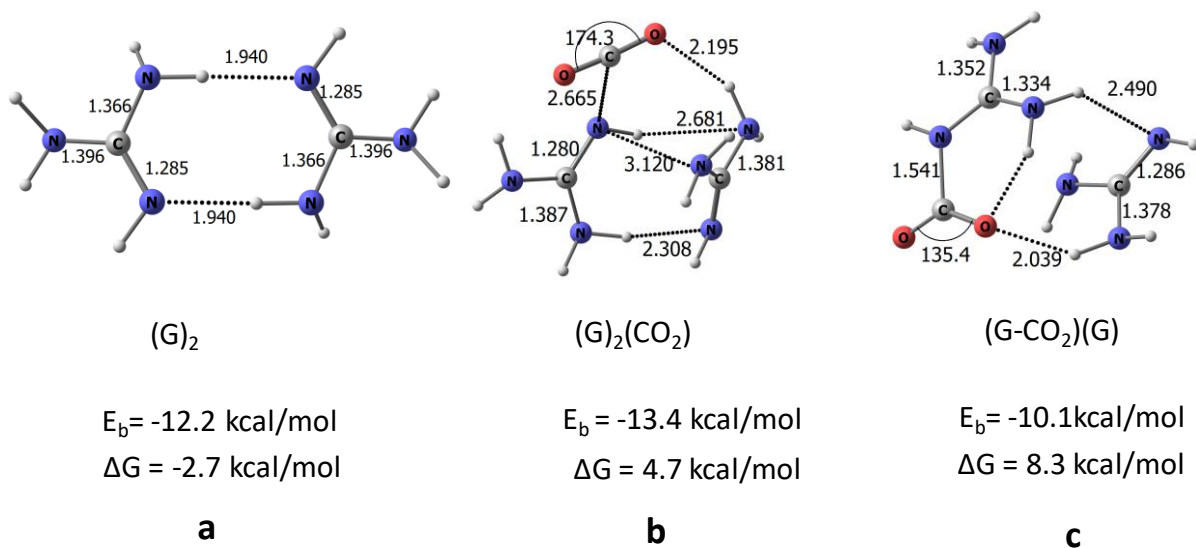
Figure 3.3 Optimized geometries with respective E_b values of $(G)_2$, $(G)_2CO_2$ and $(G\text{-}CO_2)(G)$ complexes with their d_{int} (Å), θ (°) and E_b and ΔG values at M06-2X/6-311++G**.

The guanidine dimer $((G)_2)$ shown in Figure 3.3a shows two amino to imino NH···H hydrogen bond interactions, resulting to E_b -12.2 kcal/mol. Such a dimer formation is spontaneous as ΔG -2.7 kcal/mol indicates an exergonic process. This result also suggests that G···CO_2 interaction would be inadequate to break the G···G interaction to make G···CO_2 complex. Hence the interaction of CO_2 with $(G)_2$ is considered. Two configurations are obtained for $(G)_2$···CO_2 complex; the first one designated as $(G)_2(CO_2)$ is depicted in Figure 3.3b and the second one designated as $(G\text{-}CO_2)(G)$ is given in Figure 3.3c. Compared to $(G)_2$, the E_b of $(G)_2(CO_2)$ is enhanced by 1.2 kcal/mol whereas that of $(G\text{-}CO_2)(G)$ is decreased by 2.1 kcal/mol. In both the cases, insertion of CO_2 occurs to the NH···H hydrogen bond of $(G)_2$. In $(G)_2(CO_2)$, the N···C distance 2.665 Å indicates a weak noncovalent bond whereas the N-C distance 1.541 Å in $(G\text{-}CO_2)(G)$ indicates the formation of a strong coordination bond. Also formation of the N-C coordination bond changes the linear OCO to a bent OCO with angle 135.4°. Hereafter, the use of hyphen in the notation G-CO_2 would indicate a coordinate N-C bond formation. Both the complexations involve positive ΔG values and are less likely to occur at STP.
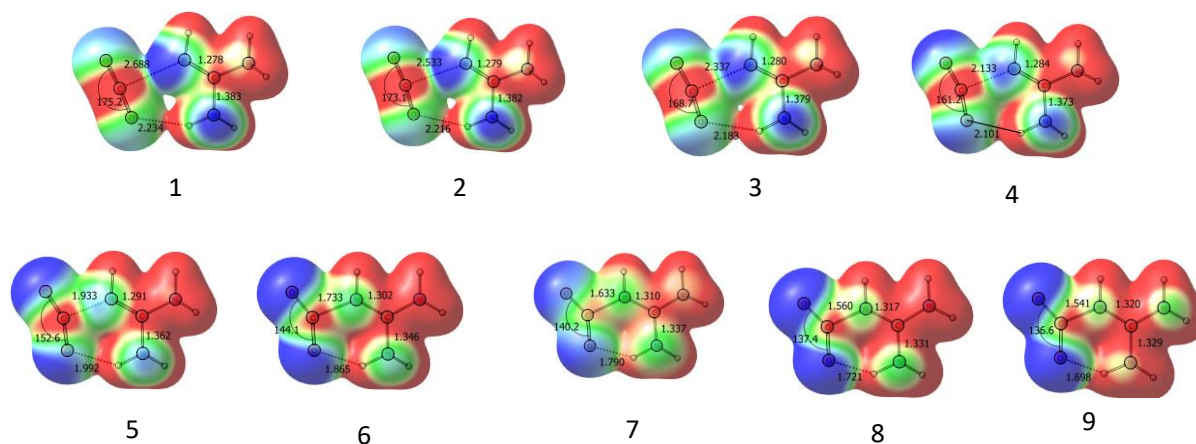
Figure 3.4 MESP topographic plots for the G-CO$_2$ unit with their d$_{int}$ (Å), and θ (°) at various N-C distances of interaction at M06-2X/6-311++G** at isosurface value = 0.01 au.
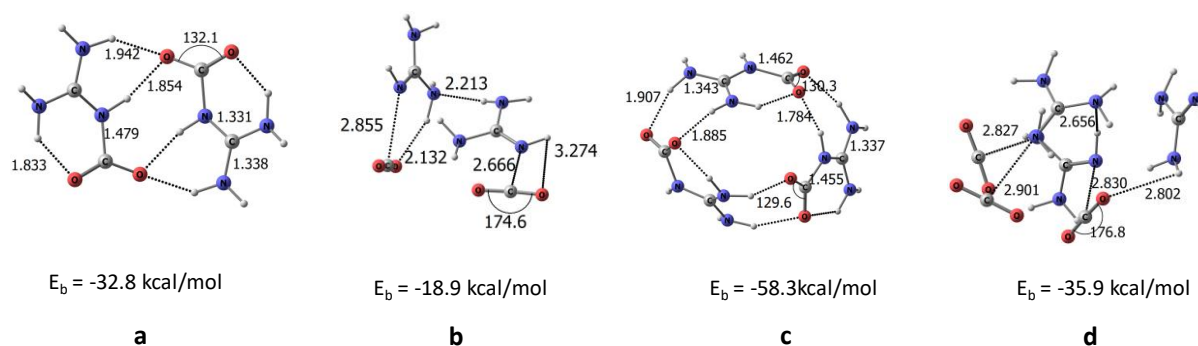
Figure 3.5 Optimized geometries of (G-CO$_2$) dimer and (G-CO$_2$) trimer complexes with their d$_{int}$ (Å), θ (°) and their respective ZPE- and BSSE corrected E$_b$ values.

The G-CO$_2$ portion of (G-CO$_2$)(G) given in Figure 3.3c can be regarded as guanidinium carboxylate zwitterion (G$^+$)-(CO$_2^-$) and a unique aspect of this structure is that it cannot exist independently. Compared to G···CO$_2$ noncovalent interaction, the N-C bond formation in G-CO$_2$ leads to charge transfer from imine N to the O centers of CO$_2$. The transformation of the G···CO$_2$ interaction from noncovalent to a highly charge separated (G$^+$)-(CO$_2^-$) interaction can happen only when the accumulated charges are utilized for developing further interactions. Figure 3.4 depicts the + and – charge accumulation when (G)(CO$_2$) is changed to G-

CO_2 in terms of MESP plots on isodensity surface for configurations optimized for various N-C distances. In the noncovalent $G(CO_2)$ with $N \cdots C$ distance 2.688 Å, the imine N atom shows charge concentration (dark blue region on N) due to its lone pair. A clear shift of the electron cloud from G to CO_2 is evident when the distance of interaction gradually changes to the covalent distance 1.541 Å (the last configuration in Figure 3.4). This zwitterion configuration $(G^+)-(CO_2^-)$ is clear from the MESP plot which shows charge concentration on the O centers (dark blue) and charge depletion on the guanidinium portion (red region).

Although $(G^+)-(CO_2^-)$ zwitterion structure does not exist, we consider the possibility of dimer formation of such a structure to derive additional stabilizing interactions. Surprisingly, the zwitterion dimer (Figure 3.5a) is an energy minimum and corresponds to a total stabilization of -32.8 kcal/mol (complexation energy for two G's with two CO_2). Also the complexation leads to a free energy lowering by 1.00 kcal/mol. Compared to the zwitterion dimer, the noncovalent dimer $(G)_2(CO_2)_2$ (Figure 3.5b) gives a complexation energy -18.9 kcal/mol and the process is endergonic by 7.9 kcal/mol. The N-C bond length of zwitterion dimer is 1.479 Å which is 0.062 Å shorter than $G-CO_2(G)$ complex and indicates the improved interaction between G and CO_2 in the presence of the zwitterion than the simple G. The zwitterion species interact through better complimentary electrostatic interactions than that involving neutral species. In zwitterion dimer, strong interactions arise due to the large number of inter- and intramolecular H-bonds, which cooperatively induces the binding of the activated G unit with the CO_2 molecule.

The complimentary hydrogen bond interactions as seen in the zwitterion dimer can be extended to higher order clusters. For instance, in the zwitterion trimer (Figure 3.5c), the binding energy is further enhanced to -58.3 kcal/mol with free energy lowering by 3.1 kcal/mol. Here, formation of the corresponding noncovalent trimer (Figure 3.5d) can be regarded as unlikely due to the highly endergonic character (14.1 kcal/mol). The optimized geometries of $(G-CO_2)_n$ clusters (n = 4 - 10) are given in Figure 3.6 and the E_b and ΔG values for all the

clusters are listed in Table 2. A cyclic growth pattern is emerged for these higher order clusters.

Table 3.2 ZPE and BSSE corrected E_b, $E_{b/CO2}$, ΔG, and, $\Delta G_{/CO2}$ (kcal/mol) of $(G-CO_2)_n$ complexes at M06-2X/6-311++G** level.

n	E_b	$E_{b/CO2}$	ΔG	$\Delta G_{/CO2}$
1	-5.7	-5.7	2.3	2.3
2	-32.8	-16.4	-1.0	-0.5
3	-58.3	-19.4	-3.1	-1
4	-93.4	-23.4	-16.6	-4.1
5	-126.6	-25.3	-28.3	-5.7
6	-158.8	-26.5	-39.7	-6.6
7	-191.5	-27.4	-53.8	-7.7
8	-219.9	-27.5	-62.2	-7.8
9	-244.4	-27.2	-64.0	-7.1
10	-265	-26.5	-62.6	-6.3

The cyclic structure enables the participation of all the O centers for intermolecular hydrogen bond interaction with the NH bonds (O⋯HN interaction). In such structures, the positively charged guanidine portion is nicely poised for complementary interaction from the negatively charged carboxylate group leading to the formation of multiple hydrogen bonds and delocalization of the accumulated charges on each (G^+)-(CO_2^-). For n = 4 – 7, the $(G-CO_2)_n$ shows a bowl like shape. The bowl depth is the maximum for n = 4 (2.890 Å) and it rapidly decreases to 2.508 Å for n = 5. For n = 6 and 7, the bowl depth further decreases to 1.947 Å and 1.013 Å, respectively indicating the tendency towards planarization as n increases. Almost a planar structure is observed for n = 8 and this structure showed the highest binding energy. Beyond n = 8, the structure tends to distort from planarity. Also the N-C distance shows a decreasing trend as n goes from 4 – 8 indicating that the planarization enhances the stability of the complex. Also the bond angle of

O⋯HN interaction gradually increases from 145.2^0 for n = 2 to the highest value 178.5^0 for n = 8 and thereafter, the O⋯HN decreases. It is clear that the highest strength for the hydrogen bond is provided by geometrically preferred linear arrangement of the atoms of O⋯HN interaction which is achieved at the most planar configuration, n = 8.
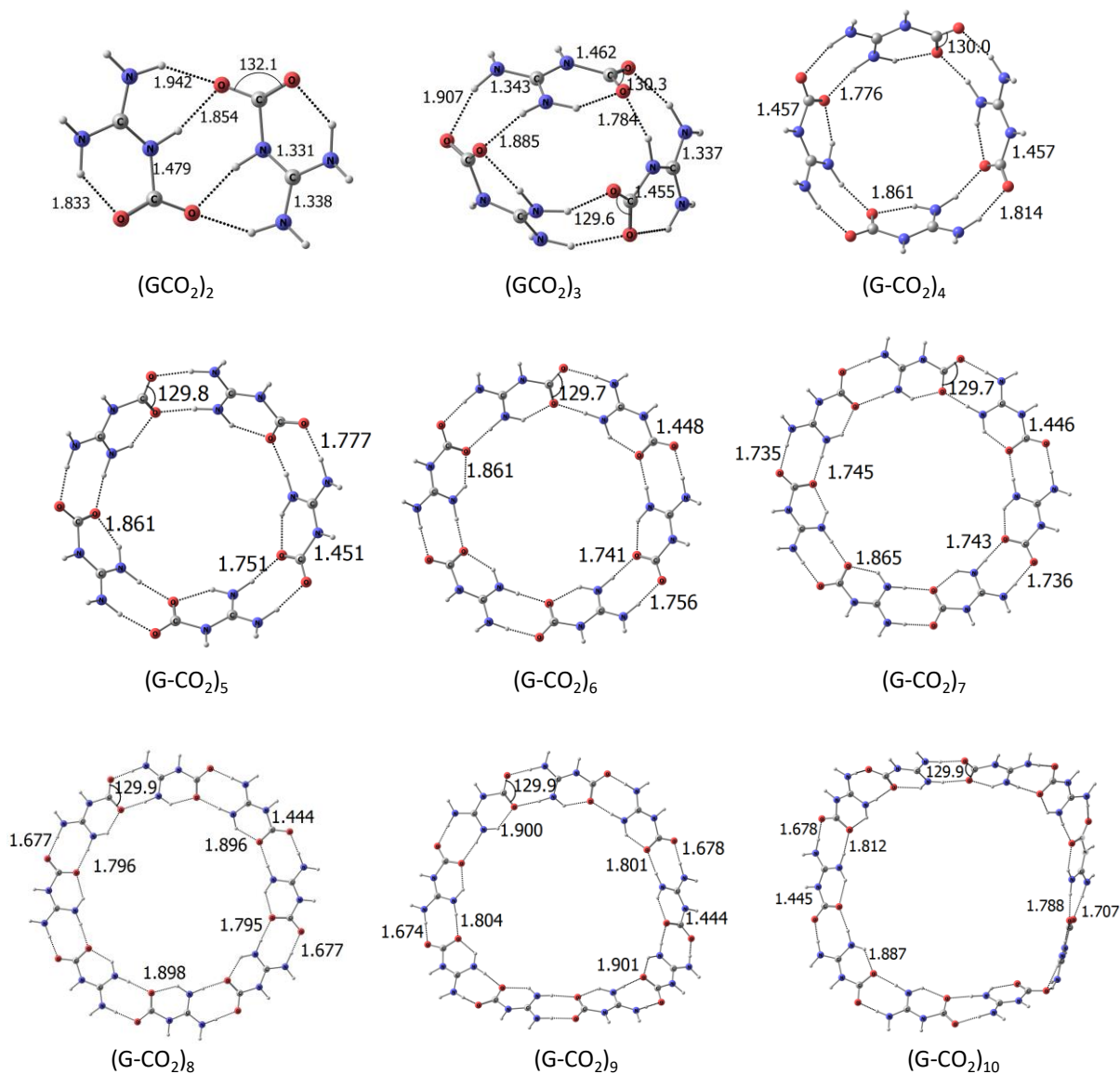
Figure 3.6 Optimized geometries of $(G-CO_2)_n$ complexes at M06-2X/6-311++G** level for n= 4 to 10.

Recently, Bijina and Suresh used MESP analysis to derive the positive cooperativity in a large variety of intermolecular trimer complexes.[58] Always the trimer showed a better bonding scenario than the dimer due positive cooperativity

arising from the electron donor-acceptor nature of the interactions. Here in (G-CO_2)$_n$ clusters, G units donates N-lone pair electrons to CO_2 and the resulting (G$^+$)-(CO_2^-) zwitterion structures are assembled in a cyclic fashion due to complementary electrostatic interactions and positive cooperativity. Recently, Wang *et al.* observed the formation of zwitterionic guanidinium/carboxylate salts derived from amino acids through the bonding of carboxylate to the guanidine N–H bonds.[59] Also formation of self-assembly of 2-(guanidiniocarbonyl)-pyrrole-4-carboxylate mediated *via* intermolecular ion pairing between the carboxylate of one and the guanidinium group of another molecule was reported by Schmuck.[38] The linear growth pattern for (G-CO_2)$_n$ clusters is found to yield higher energy structures.
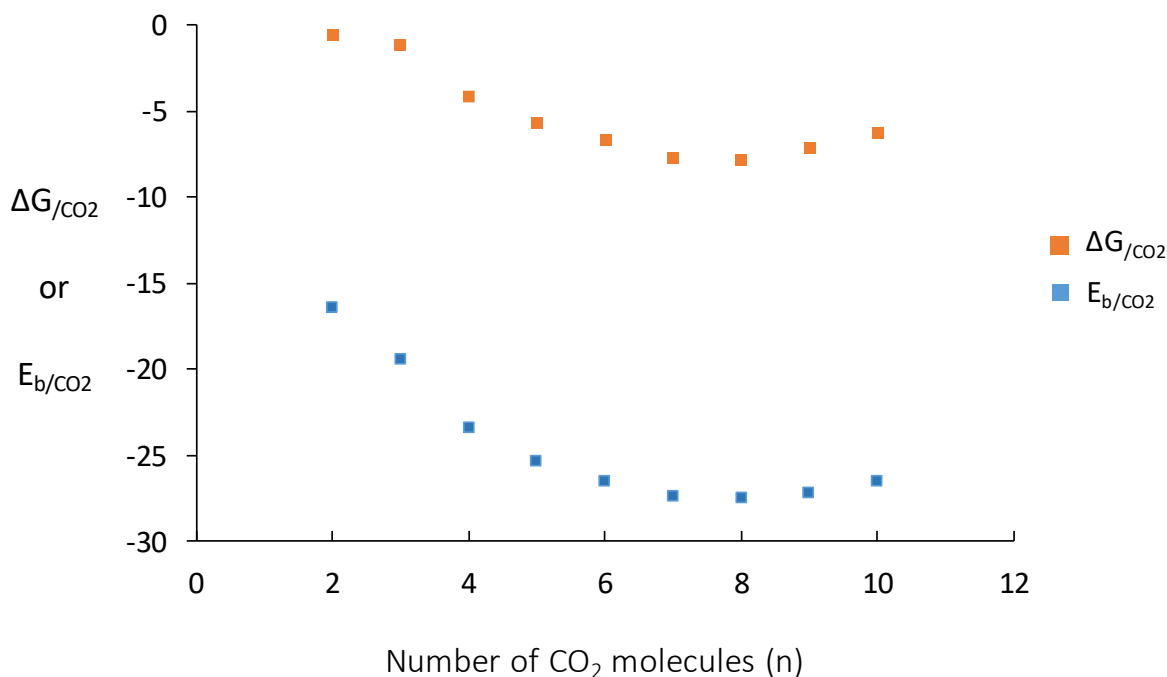
Figure 3.7 Plot showing the enhancement in E_{b/CO_2} and $\Delta G_{/CO_2}$ (kcal/mol) with increase in the number of (G-CO_2) units.

Figure 3.7 shows the variation of E_{b/CO_2} and $\Delta G_{/CO_2}$ with the number of (G-CO_2)$_n$ units. All cases show negative $\Delta G_{/CO_2}$ which increases as n increases and reaches to the best at n = 8 (Table 3.2). Similarly, E_{b/CO_2} shows the increasing stability of the complex as 'n' increases. Larger clusters are thus associated with

higher degree of cooperativity in the CO_2 adsorption. The $(G-CO_2)_8$ cluster appears as the most stable and beyond n = 8, the stability of the complexes show a decreasing trend.

3.3.1 NMR analysis

Formation of (G^+)-(CO_2^-) zwitterion structures is also observed in the NMR analysis of the $(G-CO_2)_n$ clusters (Table 3.3) as indicated by the presence of peaks corresponding to carboxylate group (COO^-). NMR calculations are carried out for the $(G-CO_2)_n$ complexes and the reference compound TMS to obtain the magnetic shielding value (σ) of the C nucleus. Nuclear magnetic resonance (NMR) analysis has been carried out using the Gauge-Independent Atomic Orbital (GIAO) method[60] at M06-2X/6-311++G** level. The calculated magnetic shielding value (σ) is converted into a chemical shift (δ) by calculating the magnetic shielding of the reference compound,[61] trimethyl silane (TMS) as,

$$\delta_{nucl} = \sigma_{ref} - \sigma_{nucl} \qquad \text{(Eq. 3.2)}$$

where δ_{nucl} is the chemical shift of the nucleus under study (here C of CO_2), σ_{ref} is the calculated shielding of TMS, and σ_{nucl} is the calculated shielding of the C.

Table 3.3. Average δ values of C nucleus of the CO_2 molecules in $(G-CO_2)_n$ complexes at M062X/6-311++G** level.

System	δ (ppm)	System	δ (ppm)
CO_2	139	$(G-CO_2)_6$	169
$G(CO_2)$	140	$(G-CO_2)_7$	169
$(G-CO_2)_2$	164	$(G-CO_2)_8$	170
$(G-CO_2)_3$	168	$(G-CO_2)_9$	170
$(G-CO_2)_4$	168	$(G-CO_2)_{10}$	170
$(G-CO_2)_5$	169	-	-

From theses δ values are calculated using the equation 3.2. The δ value observed for the CO_2 is 139 ppm. The values observed for the G-CO_2 is 140 ppm which is comparable to that of CO_2. (G-CO_2)$_2$ onwards the δ value is found to have a large jump to 160 ppm and the value slightly increases to 164 ppm for (G-CO_2)$_3$ and beyond this δ value remains almost same 168 – 170 ppm towards the larger clusters. Higher δ values shows the transformation of the C nuclei of CO_2 to the anionic nature in the zwitterion, (G$^+$)-(CO$_2^-$). This δ value is in the range that is observed for the carbamate group, which again shows the formation of carbamate through the N-C covalent interaction.[62-65] The constant nature of the δ value beyond n = 5 again shows that the nature of the electronic environment around the C nucleus remains same in higher clusters, which was also visible in the E_b value of the (G-CO_2)$_n$ clusters, where a constant value of E_{b/CO_2} was observed for the higher clusters.

3.3.2 QTAIM analysis

The QTAIM molecular plots of a representative set of (G-CO_2)$_n$ clusters (n = 2, 4, 6, and 8) are given in Figure 3.8. The dotted lines indicate the bond paths for O...HN interactions and the purple spheres represent the BCPs. According to Koch and Popelier criterion[66, 67], for noncovalent interactions, ρ_b falls in the range 0.002 – 0.040 au and $\nabla^2\rho_b$ is positive, typically in the range 0.024 – 0.139 au. The average values of ρ_b ($\rho_{b.avg}$) for the O...HN noncovalent interactions as well as for the N-C covalent interactions are given in Table 3.4. For (G-CO_2)$_n$ clusters, Koch-Popelier criterion on ρ_b is valid for all the O...HN noncovalent interactions (Table 3.4) and the sign of $\nabla^2\rho_b$ is positive whereas the N-C covalent bonds show large ρ_b and negative $\nabla^2\rho_b$ values. As the cluster size increases, the $\rho_{b.avg}$ of the N-C covalent interactions increases up to n = 8 while with further increase in the cluster size, it decreases. The value of ρ_b is often used as a measure of the strength of the interaction while the sum of ρ_b ($\Sigma\rho_b$) for O...HN and N-C interactions can be indicative of the total stabilizing influence in the cluster.[57, 68] The $\Sigma\rho_b$ values show a strong linear correlation with the total binding energy, E_b (Figure 3.9) indicating

that reorganization of the electron density along the O...HN and N-C bonding regions is stabilizing the cluster.

(G-CO$_2$)$_2$　　　　(G-CO$_2$)$_4$　　　　(G-CO$_2$)$_6$　　　　(G-CO$_2$)$_8$
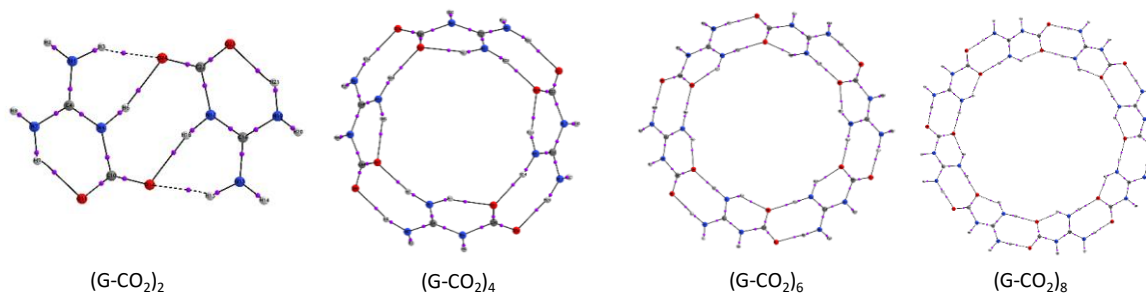
Figure 3.8 QTAIM molecular plots of (G-CO$_2$)$_n$ clusters for n = 2, 4, 6,and 8.

Table 3.4 QTAIM parameters of the noncovalent interactions and N-C covalent interactions in (G-CO$_2$)$_n$ clusters. The values are given in au.

System	N-C interaction		O···HN interaction		$\Sigma\rho_b$
	$\rho_{b.avg}$	$\nabla^2\rho_{b.avg}$	$\rho_{b.avg}$	$\nabla^2\rho_{b.avg}$	
G(CO$_2$)	0.014	0.054	0.017	0.060	0.045
(G-CO$_2$)$_2$	0.031	0.115	0.244	-0.580	0.671
(G-CO$_2$)$_3$	0.027	0.102	0.252	-0.626	1.000
(G-CO$_2$)$_4$	0.034	0.126	0.256	-0.654	1.438
(G-CO$_2$)$_5$	0.036	0.129	0.259	-0.672	1.841
(G-CO$_2$)$_6$	0.037	0.131	0.261	-0.680	2.237
(G-CO$_2$)$_7$	0.038	0.131	0.262	-0.685	2.628
(G-CO$_2$)$_8$	0.030	0.102	0.263	-0.690	2.830
(G-CO$_2$)$_9$	0.038	0.127	0.263	-0.689	3.378
(G-CO$_2$)$_{10}$	0.036	0.126	0.262	-0.683	3.707
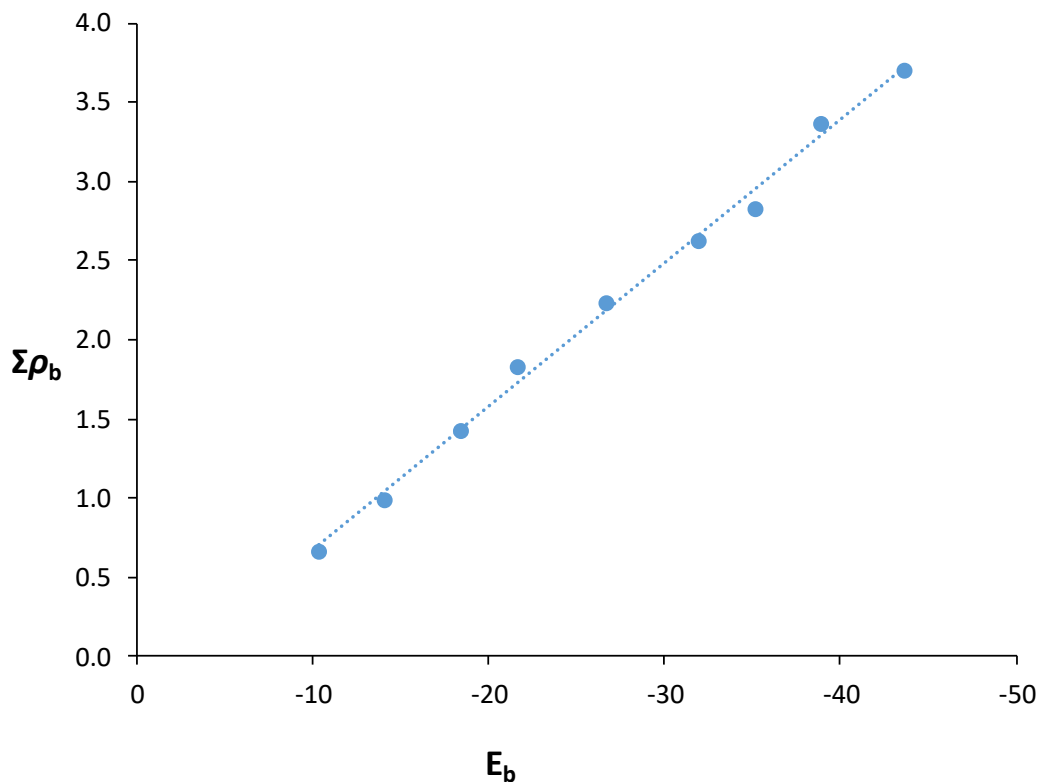
Figure 3.9 Correlation between $\Sigma\rho_b$ in au and E_b in kcal/mol for $(G-CO_2)_n$ clusters

3.3.3 MESP analysis

The MESP plots of $(G-CO_2)_n$ clusters ($n \geq 2$) are given in Figure 3.10, for every $G-CO_2$ covalent interaction, some amount of electron density gets transferred from G to the CO_2 whereas the additional $O{\cdots}H$ noncovalent interactions lead to further reorganization of the electron density. As observed from Figure 3.4, the electron density was initially concentrated mostly on the N atom of G molecule but the N-C covalent interaction transfers the charge to the CO_2 unit. Accordingly, an increase in the negative potential on the O centers is observed, which is reflected as an enhancement in the minimum potential (V_{min}) at the O atoms. The electron rich O centers show attractive interactions with the electron deficient H-N bonds on another $G-CO_2$.
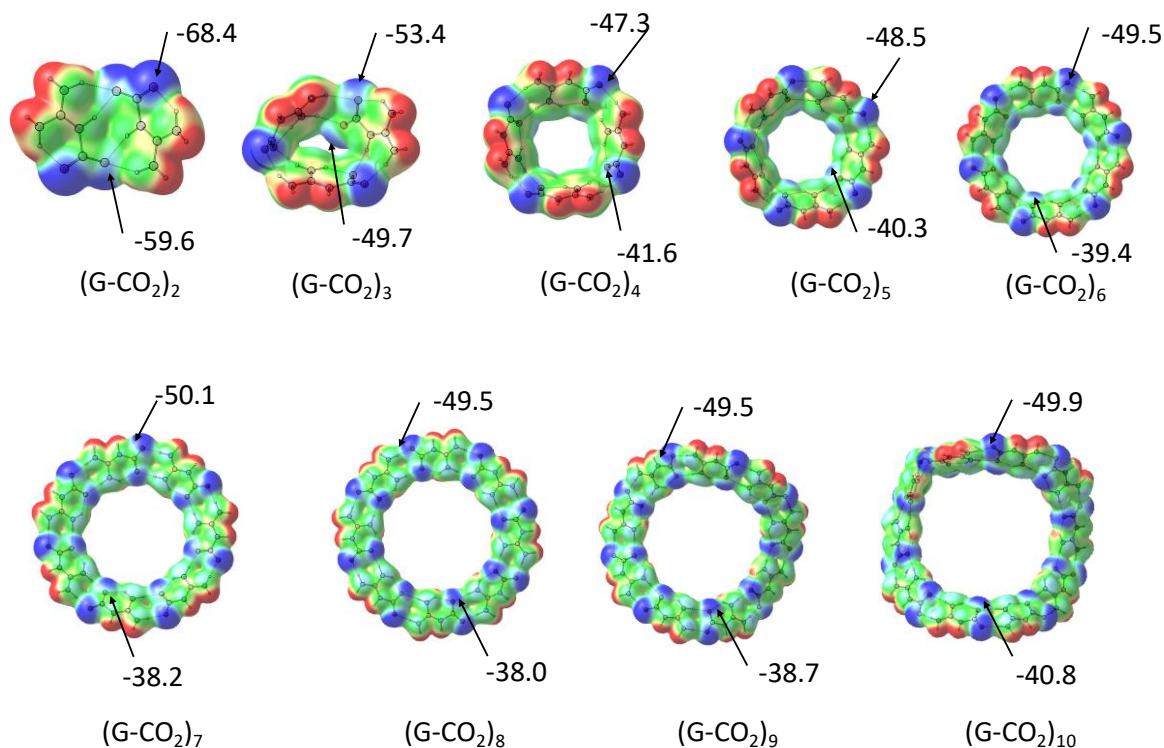
Figure 3.10 MESP plotted on isodensity surface of value 0.006 au for $(G\text{-}CO_2)_n$ complexes. The V_{min} and V_{min}' values in kcal/mol at M06-2X/6-311++G** level is also depicted. Color coding (-0.05 ▬▬▬▬ 0.05) indicates the most electron rich (blue) to most electron deficient (red) regions.

The cyclic arrangement of the $G\text{-}CO_2$ in the cluster leads to the formation of maximum $O\cdots HN$ interactions. The O atoms at the outer edge of the cyclic structures interact with one H-N bond and show more negative MESP minimum (V_{min}) than the O atoms at the inner edge (V_{min}') interacting with two H-N bonds. Both the V_{min} and V_{min}' values are in linear correlation (Figure 3.11) with the E_b values indicating that the total binding energy is directly proportional to the ability of the systems to undergo electron delocalization. Also it suggests that the cooperativity from the neighbouring $G\text{-}CO_2$ units is very effective in dispersing the charge separation in the $(G^+)\text{-}(CO_2^-)$ zwitterion units.
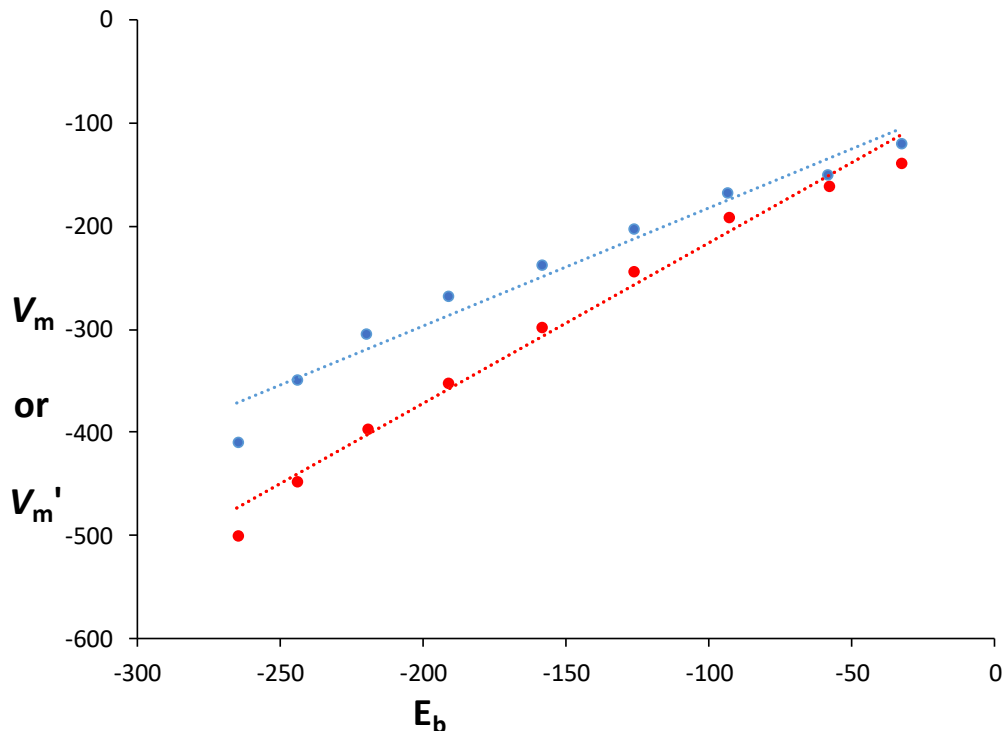
Figure 3.11 Correlation between V_{min} and V_{min}' with E_b. The values are given in kcal/mol.

3.3.4 Benchmark study

A benchmark study on $(G-CO_2)_n$ clusters is carried out using B3LYP and the dispersion included methods, *viz.* B3LYP-D3, BP86-D3, M06-2X-D3 and wB97XD in conjunction with basis set 6-311++G**. The ΔG data computed using these methods are compared with the M06-2X/6-311++G** data in Table 3.5. All except B3LYP give similar trend for ΔG and E_b meaning that the dispersion effect is very important to derive the structure and energetics of $(G-CO_2)_n$ clusters. The intrinsic dispersion effects integrated within M06-2X gives results similar to that obtained with other dispersion correction incorporated methods. Positive ΔG value observed for $G-CO_2$ in all the methods indicates that G alone cannot show a strong binding with CO_2 while the positive cooperativity generated from $(G^+)-(CO_2^-)$ zwitterionic units in the cluster strengthens the N-C interaction. The magnitude of ΔG values becomes more negative with increasing values of n which can be easily understood from the $\Delta G_{/CO2}$ values. The ΔG is the most negative for n = 8, indicating

the higher probability of formation of such closed ring structures of CO_2 complexes of G.

Table 3.5 BSSE and ZPE corrected ΔG (kcal/mol) for $(G-CO_2)_n$ complexes using different methods with dispersion correction in conjunction with basis set 6-311++G**.

n	B3LYP		B3LYP-D3		M06-2X-D3		BP86-D3		wB97XD	
	E_b	ΔG	E_b	ΔG	E_b	ΔG	E_b	ΔG	E_b	ΔG
1	-3.1	4.4	-5.3	2.4	-3.5	4.4	-4.9	2.8	-4.7	3.0
2	-19.8	11.8	-28.9	2.7	-33.4	-1.6	-34.1	-2.3	-32.1	-0.3
3	-35.8	19.8	-54.3	1.2	-60.1	-4.9	-62.5	-6.7	-58.3	-2.6
4	-67.2	10.9	-89.2	-11.3	-95.7	-19.1	-99.0	-20.9	-94.9	-16.9
5	-94.3	5.4	-120.9	-21.5	-129.1	-30.8	-132.7	-33.1	-128.4	-28.8
6	-120.2	0.6	-151.6	-31.1	-161.5	-42.4	-165.4	-44.9	-160.7	-40.1
7	-145.5	-5.2	-182.1	-42.3	-193.9	-56.1	-197.5	-58.2	-192.7	-52.8
8	-168.8	-9.9	-209.6	-50	-223.8	-69.4	-226.4	-66.6	-222.3	-63.6
9	-186.3	-3.7	-232.7	-50.2	-248.2	-67.7	-252.1	-69.3	-246.6	-64.0

3.4 Conclusions

The interactive behaviour of guanidine (G) with CO_2 molecules has been studied using M06-2X/6-311++G** level of DFT. G interacts with CO_2 molecules through noncovalent as well as covalent interactions. As reported by Lee *et al.*[45] we also observed noncovalent interaction between G and CO_2, with E_b -5.7 kcal/mol . However, the application of G for CO_2 capture suggested better interaction possibilities, which was revealed through the systematic study on the $G(CO_2)_n$ and $(G-CO_2)_n$ clusters. For the purely noncovalent $G(CO_2)_n$ complexes, E_b values improved with n and maintained a constant value of E_b $/_{CO2}$ beyond n = 3. But all these were associated with a positive ΔG value, which indicated the endergonic nature of the formation of $G(CO_2)_n$ complexes. However in the analysis

of $(G-CO_2)_n$ clusters, a pattern of cyclic cluster growth has been observed through the formation of the zwitterion, $(G^+)-(CO_2^-)$ which involves strong N-C covalent interaction. The interaction between the zwitterion units also increased with n and the most stable cluster was observed for n = 8, with $E_{b/CO2}$ of -27.5 kcal/mol. In addition to the N-C covalent interactions, the O···HN noncovalent interactions between $G-CO_2$ units contribute significantly to the stability of the large cyclic clusters, which is confirmed by the strong correlation between the binding energy data and electron density data of bond critical points in QTAIM analysis. MESP analysis also supported the N-C covalent bonding and the delocalization of charges of the zwitterion $(G^+)-(CO_2^-)$ through complementary O···HN hydrogen bonding interactions. Further, as the cluster size increases, the cooperative effect of O···HN and N-C interactions increases leading to a steady enhancement in E_b. This study illustrates the remarkable influence of cooperativity in the stabilization of the large cyclic structure formations of $G-CO_2$ units with zwitterion character. The study on the influence of dispersion effects using different DFT methods showed that for n > 2, the clusters formation is exergonic and the most stable cluster is observed at n = 8. The exergonic character observed for the $(G-CO_2)_8$ cluster formation demands an experimental verification and we urge the experimentalists to suggest a synthetic strategy for it. The high affinity of guanidine towards CO_2 cannot be justified by the weak G···CO_2 noncovalent interaction whereas the exergonic formation of zwitterionic $(G-CO_2)_n$ clusters suggests the high CO_2 adsorption capability of guanidine. Another advantage is the desorption of CO_2 from the most stable $(G-CO_2)_8$ cluster is feasible by mild heating due to the moderate value of the G···CO_2 dissociation energy and favorable entropy for the endergonic process. These theoretical results suggest G as a promising adsorbent for CO_2 capture.

Part B: Demarcating Noncovalent and Covalent Bond Territories: Imine-CO_2 Complexes and Cooperative CO_2 Capture

3.5 Abstract

Chemical bond territory is rich with covalently bonded molecules wherein a strong bond is formed by equal or unequal sharing of a quantum of electrons. The noncovalent version of the bonding scenarios expands the chemical bonding territory to a weak domain wherein the interplay of electrostatic, π-effects, dipole-dipole, dipole-induced dipole, induced dipole-induced dipole interactions, and hydrophobic effects occur. Here, we study both the covalent and noncovalent interactive behavior of cyclic and acyclic imine-based functional molecules (XN) with CO_2. All parent XN systems preferred the formation of noncovalent (***nc***) complex XN···CO_2 while more saturated such systems (XN') produced both nc and covalent (***c***) complex XN'$^+$−$(CO_2)^-$. In all such cases, crossover from nc to c complex is clearly demarcated with the identification of a transition state (**ts**). The complexes XN'···CO_2 and XN'$^+$−$(CO_2)^-$ are bond stretch isomers and they define the weak and strong bonding territories, respectively while the **ts** appears as the demarcation point of the two territories. Cluster formation of XN with CO_2 reinforces the interaction between them and all become covalent clusters of general formula $(XN^+-(CO_2)^-)_n$. The positive cooperativity associated with the NH···OC hydrogen bond formation between any two XN'$^+$−$(CO_2)^-$ units strengthened the N-C coordinate covalent bond and led to massive stabilization of the cluster. For instance, the stabilizing interaction between the XN unit with CO_2 is increased from 2 - 7 kcal/mol range in monomer complex to 14 – 31 kcal/mol range for the octamer cluster $(XN'^+-(CO_2)^-)_8$. The cooperativity effect compensates for the large reduction in the entropy of cluster formation. Several imine systems showed the exergonic formation of the cluster and are predicted as potential candidates for CO_2 capture and conversion.

3.6 Introduction

The chemical bond is regarded as one of the fundamental territories of chemistry, populated by a large variety of covalent (nonpolar), ionic (polar) and metallic bonds.[69] Advanced quantum mechanical studies have led to electron density (ρ) based descriptions of bonding between pairs of atoms, while new bonding features unearthed from such studies provided accurate interpretations of structure and reactivity of molecules and materials. According to IUPAC, a covalent bond refers to the region of relatively high electron density between nuclei which arises at least partly from sharing of electrons and gives rise to an attractive force and characteristic internuclear distance.[70] A more sophisticated view suggests that covalent bonding involves synergism between several interactions, including the intricate interplay of interatomic and intra-atomic interactions. Electrostatic attraction, exchange (Pauli) repulsion, and further factors contribute to the intricate combination that yields a chemical bond.[71] Covalent bonding interaction in the purest form is proposed in the case of homonuclear diatomic species while a degree of polarization in the bond may develop when hetero atoms are involved which gives some ionic bond characteristics. The covalent bond energy typically ranges from 40 to 100 kcal/mol for the single bonds involving main block elements *viz.* B, C, N, O, etc. The energy decomposition analysis (EDA)[69, 72] and natural bond orbital (NBO)[73, 74] analysis are powerful theoretical tools for the study of bonding situations. The EDA studies by Frenking *et al.* have contributed immensely to the understanding and explaining of the chemical bond in terms of quasiclassical electrostatic interactions, Pauli repulsion and attractive orbital interactions.[75-83]

Although the covalent bond is intimately connected with equal or unequal sharing of a quantum of electrons, the noncovalent version of the bonding scenarios arises often in molecular assemblies.[84] Such interactions refers to almost any interaction weaker than a covalent bond, typically less than 15 kcal/mol. The chemical bonding landscape expands greatly with the advent of noncovalent interactions such as electrostatic (ionic, hydrogen and halogen bonds), π-effects

(π-π interactions, cation-π and anion-π interactions), van der Waals forces (dipole-dipole interactions, dipole-induced dipole interactions, and induced dipole-induced dipole interactions), and hydrophobic effects.[85] One of the most thoroughly studied noncovalent interaction is the hydrogen bond.[86-89] As per the IUPAC definition, the form of association between an electronegative atom and a hydrogen atom attached to a second, relatively electronegative atom is considered as the hydrogen bond.[70, 90] Though the concept of bond energy seems to be one means of making the distinction between covalent and noncovalent bonds, unfortunately, things are not always very straightforward. There are a number of different interactions with bond energies in the standard noncovalent range, but through a systematic strengthening of the interactions, for instance, *via*, appropriate modifications of substituents, they can advance into the energy range normally reserved for covalent bonds. Jemmis *et al.* explained possible formation of a relatively 'strong bond' without much covalent bonding character *via* the example of the halogen bond which shortens and strengthens the bridge bond of [1.1.1]propellane and the open form of [2.2.2]propellane.[91] Very recently Dereka *et al.* illustrated the crossover of the hydrogen bonding into covalent bonding interaction in terms of the H···F/H-F interactions in bifluoride anion [F-H-F]⁻.[92] Also recently Scheiner *et al.* observed that slight modifications in the electronic environment of the substrate can lead to strengthening of the tetrel bonding interactions.[93] Though these studies suggest the possibility of crossover of interacting molecular systems from noncovalent to covalent bonding territory, a clear demarcation of the bonding territories is yet to be established.

Bader's quantum theory of atoms in molecules (QTAIM) topology analysis of electron density (ρ) has been effectively used for the interpretation of both the covalent and noncovalent bonding interactions.[94-97] In the Bader analysis, atom–atom interactions are distinguished as covalent and noncovalent based on the minimum value of ρ on bond paths (bond critical point (BCP)), as well as from the sign of the corresponding Laplacian ($\nabla^2\rho_b$). According to Koch and Popelier[66, 98], for a non-covalent interaction, ρ at BCP (ρ_b) falls in the range 0.002 – 0.040 au and $\nabla^2\rho_b$ is positive, typically in the range 0.024 – 0.139 au. Although negative $\nabla^2\rho_b$

values generally indicate covalent interactions, there are exceptions to this such as the charge-shift bonds proposed by Shaik *et al.*[99,100]

DFT M06-2X/6-311++G** study on the interactive behavior of CO_2 with guanidine (G) has shown that noncovalently interacting G$\cdots CO_2$ can transform to a strongly interacting G-CO_2 covalent complex under the influence of multiple G and CO_2 units.[101] The five-fold increase in binding energy observed in the (G-CO_2)$_8$ cluster was attributed to large cooperativity associated with the (G$^+$)-(CO_2^-) zwitterion nature of G-CO_2. The reinforcement of the interaction observed for the guanidine-carbon dioxide system from weak noncovalent to strong covalent nature has inspired us to perform the present research. Here we examine the noncovalent-covalent transformation behavior as a general phenomenon in chemical bond territory and also locate the crossover point for such transformations. The boundary crossing occurs with a slight variation in the electronic structure through the promotion of positive cooperativity in the interactions.

3.6.1 Computational methods

The M06-2X/6-311++G**, a robust DFT method for modelling intermolecular noncovalent interactions, as implemented in the Gaussian 16 suite of programs is used for locating all minimum energy (XN)(CO_2) structures and transition state geometries (XN corresponds to an N-heterocyclic or N-rich acyclic molecule containing at least one imine functionality).[49, 101, 102] The zero-point energy (ZPE)-corrected binding energy (E$_b$) between XN and CO_2 is calculated using the supermolecule approach as

$$E_b = E_{(XN)(CO2)} - E_{XN} - E_{CO2} + E_{bsse} \qquad \text{(Eq. 3.3)}$$

where E$_{bsse}$ corresponds to the basis set superposition error[51-54] as per the counterpoise (CP) approach of Boys and Bernardi.[56, 103] Similarly the free energy change (ΔG) and enthalpy change (ΔH) at standard temperature and pressure (STP) associated with the complex formation are also computed using

supermolecule approach. The deformation energy (E_{def}) for the XN–CO_2 interaction is calculated as,

$$E_{def} = E_{def-XN} + E_{def-CO2} = (E_{XN} - E_{XN*}) + (E_{CO2} - E_{CO2*}) \qquad (Eq.\ 3.4)$$

where E_{XN*} and E_{CO2*} are the energies of the deformed XN-unit and deformed CO_2 in the complex, respectively.

Further, QTAIM, molecular electrostatic potential (MESP) and nuclear magnetic resonance (NMR) analyses have been carried out for all (XN)(CO_2) complexes with the M06-2X/6-311++G** method. The Gauge-Independent Atomic Orbital (GIAO) method is used to derive NMR data.[60][104]

3.7 Results and discussion

For the (XN)(CO_2) complexes studied here, the imino XN systems are designated as **1** - **7** and **1'** – **7'**. The **1** - **7** molecules contain a CC or NN or CN double bond adjacent to the imino nitrogen whereas **1'** – **7'** are made by changing such a double bond to a single bond (Figure 3.12). This change in structure assures that in terms of its electron rich character, the lone pair bearing imino nitrogen in the 'non-primed' structures is slightly different from that in the 'primed' structures. Since the imino N-lone pair is used as the two electron donor to CO_2, an assessment on the electronic feature of this center is made from the MESP minimum (V_{min}) corresponding to this lone pair. Compared to XN, the more saturated systems (XN') showed higher negative character for the V_{min}, indicating that XN' has better interaction ability than XN with CO_2 (Table 3.6). Two classifications are made for the optimized (XN)(CO_2) complexes (Figure 3.12), *viz.* (i) noncovalent (***nc***) XN···CO_2 complexes wherein the imino N to CO_2 interaction occurs at a distance 2.63 to 2.78 Å which is far greater than a covalent bond distance and (ii) covalent (***c***) XN–CO_2 complexes which are characterized by imino N-CO_2 coordinate covalent bond with N-C distance in the range 1.55 – 1.65 Å. Hereafter, the '***nc***' or '***c***' notation is used along with the number notation to specify the nature of the complex.
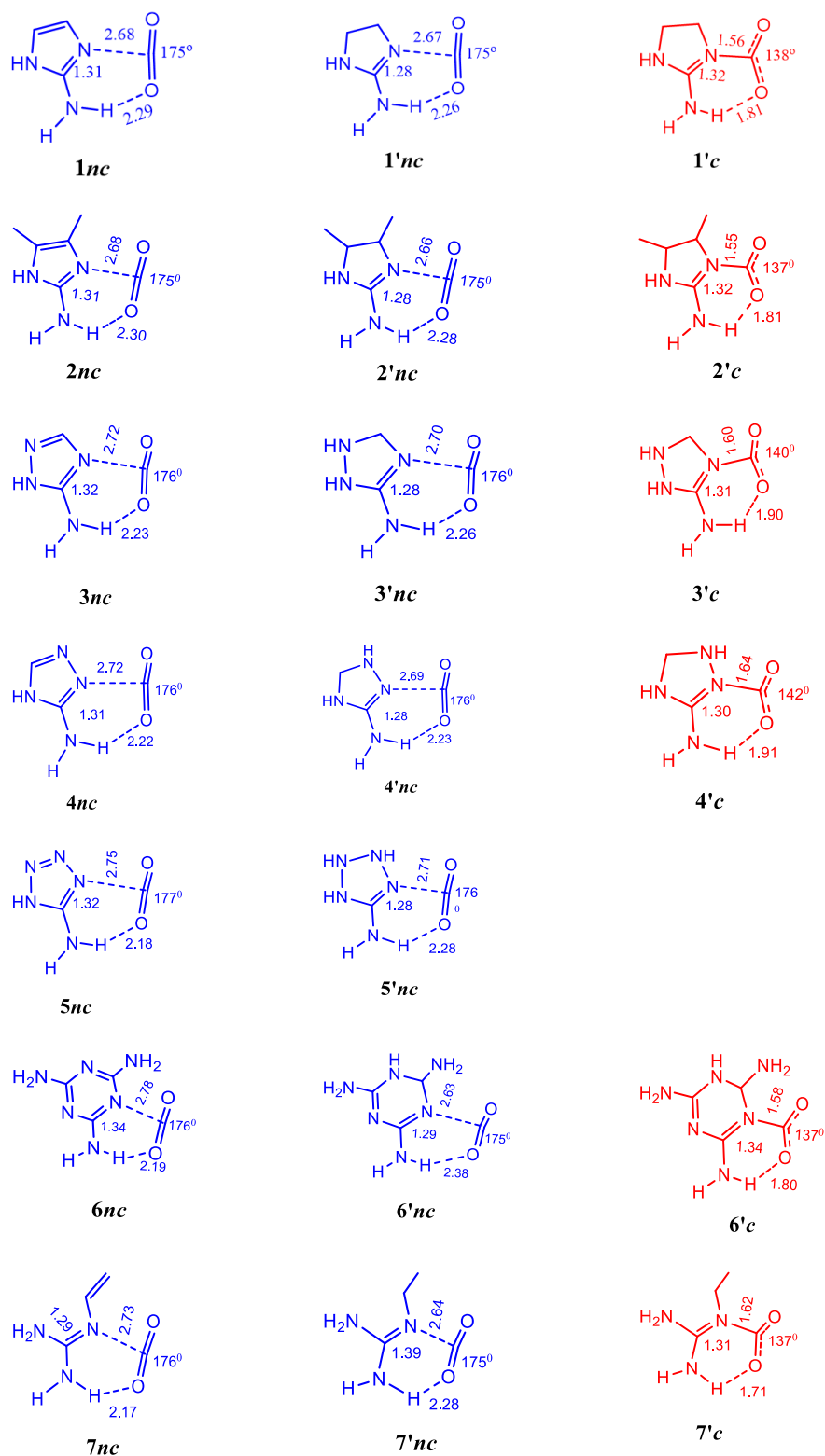
Figure 3.12 Geometry parameters of optimized $(XN)(CO_2)$ complexes in the *nc* (blue) and *c* (red) bond regimes. Distances in Å and angles in degrees.

The O···H distance in the range 2.17 to 2.30 Å observed for **nc** complexes suggest very weak interactions, whereas the similar interaction seen in the **c** complexes is expected to be stronger due to shorter O···H distances in the range 1.70 to 1.91 Å (Figure 3.12). Except **5'**, all other primed structures show the formation of both **nc** and **c** complexes while the non-primed structures show only the formation of **nc** complexes. This suggests that electron-rich XN' have the ability to force a covalent bond formation with the CO_2.

Table 3.6 V_{min} values in kcal/mol for all N-heterocyclic and N-rich acyclic molecules at M06-2X/6-311++G** level.

Notation	V_{min}
1 & **1'**	-67.5 & -71.1
2 & **2'**	-70.5 & -71.5
3 & **3'**	-58.7 & -63.4
4 & **4'**	-66.7 & -66.9
5 & **5'**	-55.8 & -57.9
6 & **6'**	-54.8 & -68.6
7 & **7'**	-63.5 & -69.3

The E_b data given in Table 3.7 suggests that **nc** complexes of primed structures lie lower in energy than the **c** complexes. A net destabilization of 2.4 kcal/mol is found for both **3'c** and **4'c**, while the rest show stabilization with respect to infinitely separate XN or XN' and CO_2. On the free energy scale, due to loss of entropy, the complex formation appears endergonic for all, by 1.5 – 12.4 kcal/mol. Although a strong N–C bond is formed in the **c** complexes, it does not guarantee high stabilization for the complex. The reason for this can be attributed to the large deformation induced on CO_2; around 38 – 46° deviation for the OCO bond angle and significant elongation of the CO bond distance. Since $E_{def-CO2}$ for the

c complexes is high, in the range 36.7 to 49.5 kcal/mol (Table 3.7), the N−C bond energy has to be higher or close to $E_{def-CO2}$ to attain net stabilization. The intramolecular NH···OCO interaction also contributes to the stabilization of the *c* complexes. In the case of *nc* complexes, E_{def} is ≤ 0.6 kcal/mol and suggests that E_b is almost fully accounted by the N···C noncovalent interaction. E_{def-XN} is negligible for *nc* complexes while this quantity for *c* complexes is ~14 % of the total deformation energy E_{def}.
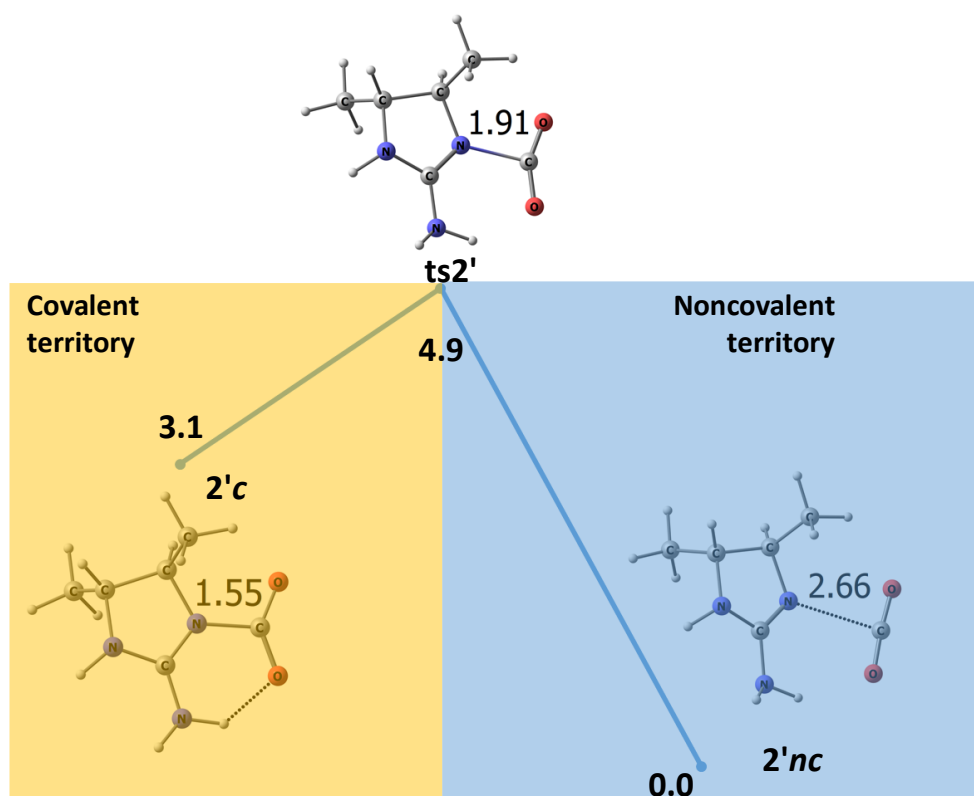
Figure 3.13 XN−CO₂, XN···CO₂ and the transition state for their interconversion. Bond lengths in Å and ZPE-corrected relative energy in kcal/mol.

For the primed structures, the noncovalent and covalent regions of bond formation can be demarcated by identifying a transition state (**ts**) for their interconversion. The transition states **ts1'** – **ts7'** are located for **1'nc** – **7'nc** conversion to **1'c** – **7'c**. The energy profile in Figure 3.13 depicts the conversion of **2'nc** to **2'c** *via* **ts2'** and the results for the other systems are given in Figure 3.14.

The **ts2'** appears as a demarcation point between the noncovalent and covalent realms of bond formation which takes place at the N···C distance 1.91 Å. Below this distance, covalent character develops between the N and C atoms.

Table 3.7 Energy parameters (kcal/mol) for (XN)(CO$_2$) complexes at M06-2X/6-311++G** level.

Notation	E_b	ΔG	$E_{def\text{-}XN}$	$E_{def\text{-}CO2}$
1*nc*	-5.6	2.5	0.1	0.4
1'*nc*, 1'*c*	-6.0, -2.4	1.9, 7.8	0.1, 6.6	0.5, 39.6
2*nc*	-6.0	2.3	0.1	0.4
2'*nc*, 2'*c*	-6.3, -3.7	1.9, 6.8	0.1, 6.7	0.5, 40.9
3*nc*	-5.4	2.7	0.1	0.3
3'*nc*, 3'*c*	-5.6, 2.4	2.2, 12.2	0.1, 5.2	0.4, 34.9
4*nc*	-5.3	2.7	0.1	0.4
4'*nc*, 4'*c*	-5.4, 2.4	2.4, 12.4	0.1, 5.0	0.3, 31.6
5*nc*	-5.1	3.0	0.1	0.3
5'*nc*	-5.1	2.8	0.1	0.3
6*nc*	-6.4, -2.0	1.7	0.1, 8.1	0.3, 41.0
6'*nc*, 6'*c*	-6.9	1.5, 8.6	0.1	0.5
7*nc*	-5.9, -1.1	2.4	0.2, 6.9	0.4, 39.5
7'*nc*, 7'*c*	-5.2	3.2, 9.2	0.1	0.5

ts1'

5.2

ts2'

4.9

ts3'

8.3

ts4'

8.9

ts6'

6.3

ts7'

5.0

Figure 3.14 Optimized geometries and ZPE-corrected relative energy (kcal/mol) for the transition states with respect to $(XN)(CO_2)$ *nc* complexes M06-2X/6-311++G** level. Bond distance in Å and angles in degree.

2'*nc*

ts2'

2'*c*
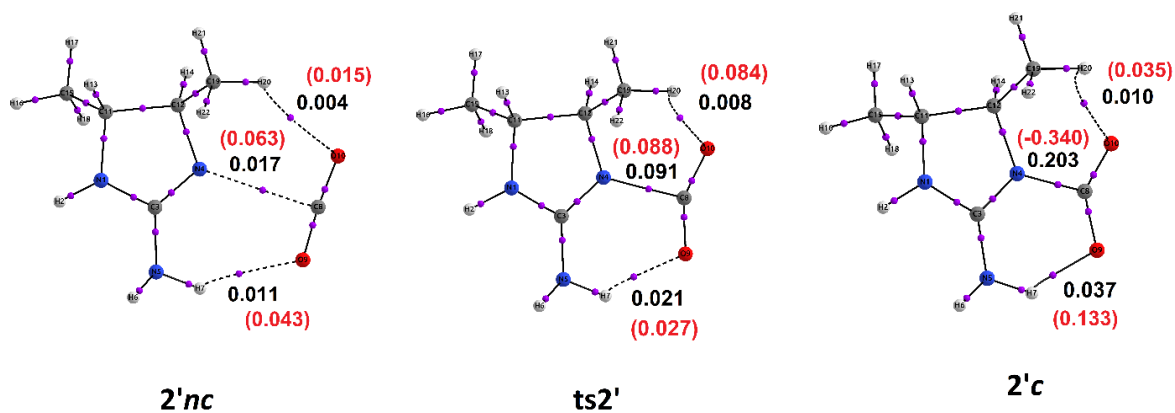
Figure 3.15 QTAIM molecular graph of **2'*nc***, **ts2'** and **2'*c***. Values in black and red colors are ρ_b and $\nabla^2\rho_b$ in au.

132

3.7.1 QTAIM analysis

The QTAIM analysis using the molecular graph in Figure 3.15, $\nabla^2\rho_b$ plots (Figure 3.16) and QTAIM data (Tables 3.8 & 3.9) can clearly demarcate the bonding territories of $(XN)(CO_2)$ complexes. The molecular graph is characterized by bond paths for N-C/N⋯C and NH⋯OCO interactions. The covalent N-C bond is established from the high value of electron density at the bond critical point (ρ_b) and high negative values of $\nabla^2\rho_b$, whereas noncovalent complexes show very small ρ_b and small positive $\nabla^2\rho_b$ values (Figure 3.15).

Table 3.8 QTAIM parameters for the N-C/N⋯C bond of $(XN)(CO_2)$ complexes at M06-2X/6-311++G** level. All the values are given in au.

Notation	ρ_b	$\nabla^2\rho_b$	V_b	G_b	H_b	$|V_b|/G_b$
1nc	0.017	0.061	-0.012	0.014	0.002	0.888
1'nc	0.017	0.062	-0.013	0.014	0.001	0.897
1'c	0.200	-0.319	-0.282	0.101	-0.181	2.789
2nc	0.017	0.062	-0.012	0.014	0.001	0.893
2'nc	0.018	0.063	-0.013	0.014	0.001	0.900
2'c	0.203	-0.340	-0.291	0.103	-0.188	2.825
3nc	0.015	0.058	-0.011	0.013	0.002	0.872
3'nc	0.016	0.059	-0.012	0.013	0.002	0.883
3'c	0.182	-0.221	-0.241	0.093	-0.148	2.593
4nc	0.016	0.058	-0.011	0.013	0.002	0.873
4'nc	0.016	0.061	-0.012	0.014	0.002	0.882
4'c	0.172	-0.167	-0.222	0.090	-0.132	2.463
5nc	0.014	0.055	-0.010	0.012	0.002	0.857
5'nc	0.015	0.058	-0.011	0.013	0.002	0.868
6nc	0.014	0.051	-0.010	0.011	0.001	0.875
6'nc	0.019	0.067	-0.014	0.016	0.001	0.921
6'c	0.195	-0.291	-0.261	0.094	-0.167	2.774
7nc	0.015	0.055	-0.011	0.012	0.001	0.885
7'nc	0.019	0.065	-0.014	0.015	0.001	0.915
7'c	0.181	-0.220	-0.226	0.085	-0.140	2.644

The $\nabla^2\rho_b$ plots for **2'nc**, **ts2'** and **2'c** (Figure 3.16) give positive, positive and negative values, respectively at the N-C/N···C bonding region. Hence, as per QTAIM criteria, the transition state lies in the noncovalent territory, very close to the border with the covalent territory. The values of local kinetic (G_b), potential (V_b) and total electron (H_b) energy densities at the bond critical points are given in Tables 3.8 for the N-C/N···C interaction and Table 3.9 for NH···OCO interaction. In the **c** complexes, $|V_b| > 2G_b$ and negative H_b values confirm the covalent nature of N-C interactions while NH···OCO and N···C interactions (in **nc** complexes) show $|V_b| < G_b$ and positive H_b which confirm their noncovalent nature.[105, 106]

Table 3.9 QTAIM parameters for the NH···OCO bond of $(XN)(CO_2)$ complexes at M06-2X/6-311++G** level. All the values are given in au.

Notation	ρ_b	$\nabla^2\rho_b$	V_b	G_b	H_b	$|V_b|/G_b$
1nc	0.011	0.042	-0.007	0.009	0.002	0.811
1'nc	0.012	0.045	-0.008	0.009	0.002	0.992
1'c	0.037	0.132	-0.032	0.033	0.000	0.800
2nc	0.011	0.041	-0.007	0.009	0.002	0.808
2'nc	0.011	0.043	-0.007	0.009	0.002	0.802
2'c	0.037	0.133	-0.033	0.033	0.000	0.928
3nc	0.012	0.048	-0.008	0.010	0.002	0.807
3'nc	0.012	0.045	-0.008	0.010	0.002	0.900
3'c	0.030	0.116	-0.025	0.027	0.002	0.787
4nc	0.013	0.050	-0.008	0.010	0.002	0.813
4'nc	0.011	0.042	-0.007	0.009	0.002	0.991
4'c	0.027	0.105	-0.021	0.024	0.002	1.073
5nc	0.014	0.055	-0.009	0.012	0.002	0.798
5'nc	0.011	0.043	-0.007	0.009	0.002	0.980
6nc	0.013	0.052	-0.008	0.011	0.002	0.804
6'nc	0.009	0.034	-0.006	0.007	0.001	0.810
6'c	0.037	0.142	-0.034	0.035	0.001	0.805
7nc	0.014	0.056	-0.009	0.012	0.002	0.808
7'nc	0.011	0.043	-0.007	0.009	0.002	0.806
7'c	0.046	0.158	-0.046	0.043	-0.003	0.809

The QTAIM molecular graphs as well as the identification of **ts1'** – **ts7'** for the interconversion of **1'nc** – **7'nc** to **1'c** – **7'c** suggest that *nc* and the corresponding *c* complexes differ only in the length of bonds. They can be regarded as bond stretch isomers (BSI) as per the criteria proposed by Hoffmann *et al.*[107, 108] An unambiguous experimental validation of the existence of genuine BSI in chemistry[109-114] is yet to be furnished,[115] while the present results give a beautiful illustration of this concept and also ascertains that BSI connects two contrasting bonding territories.

| 2' *nc* | ts2' | 2' *c* |
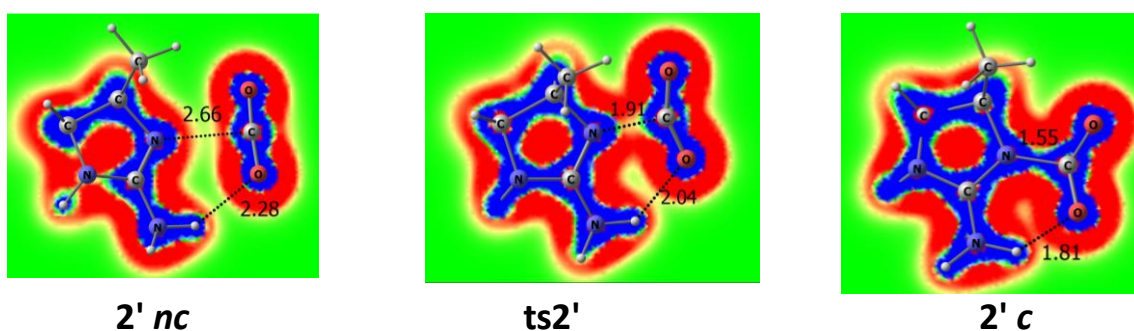
Figure 3.16 The Laplacian of the electron density plotted on a plane that passes through the N-CO$_2$ bonded region. Red and blue colors indicate positive and negative regions, respectively. The bond lengths are given in Å.

3.7.2 NMR analysis

The formation of the XN$^+$–(CO$_2$)$^-$ zwitterion in the *c* complexes is verified using the NMR analysis of the (XN)(CO$_2$) complexes with TMS as the reference compound to obtain the NMR chemical shift values. The δ value calculated for the C atom of CO$_2$ in noncovalent XN$\cdots$CO$_2$ complexes is 140 ppm which is very close to that of CO$_2$. The covalent adduct XN-CO$_2$ shows δ in the range 153 to 160 ppm and the substantial change in δ compared to noncovalent complex suggests the transformation of CO$_2$ to COO$^-$. Also this range of δ is close to the value of a carbamate and hence confirm the transformation of CO$_2$ into (CO$_2$)$^-$ in the *c* complexes (Table 3.10).

Table 3.10 The δ values for C of CO_2 in $(XN)(CO_2)$ complexes at M06-2X/6-311++G** level.

Notation	δ (ppm)	Notation	δ (ppm)
CO_2	139	**4'nc**, **4'c**	140, 149
1nc	140	**5nc**	140
1'nc, **1'c**	140, 155	**5'nc**	140
2nc	140	**6nc**	140
2'nc, **2'c**	140, 155	**6'nc**, **6'c**	140, 156
3nc	140	**7nc**	140
3'nc, **3'c**	140, 151	**7'nc**, **7'c**	140, 153
4nc	140	-	-

3.7.3 MESP analysis

The MESP plots given in Figure 3.17 are useful to distinguish the *nc* and *c* covalent formations in $(XN)(CO_2)$ complexes. For example, the **2nc** and **2'nc** complexes show the characteristic electron deficient C center of CO_2 in the MESP plot as a red strip around the C center. In contrast, the coordinate covalent N–C bond formed in **2'c** leads to accumulation of large negative MESP around the O centers of CO_2 (blue region around O centers) as well as large positive MESP over the imine molecule (red regions). The MESP analysis suggests that the characteristic electronic features of both imine and CO_2 are nearly unaffected by the *nc* bond formation whereas the chemical nature of both the molecules drastically change in the *c* complex due to the development of $XN^+-(CO_2)^-$ zwitterion character.
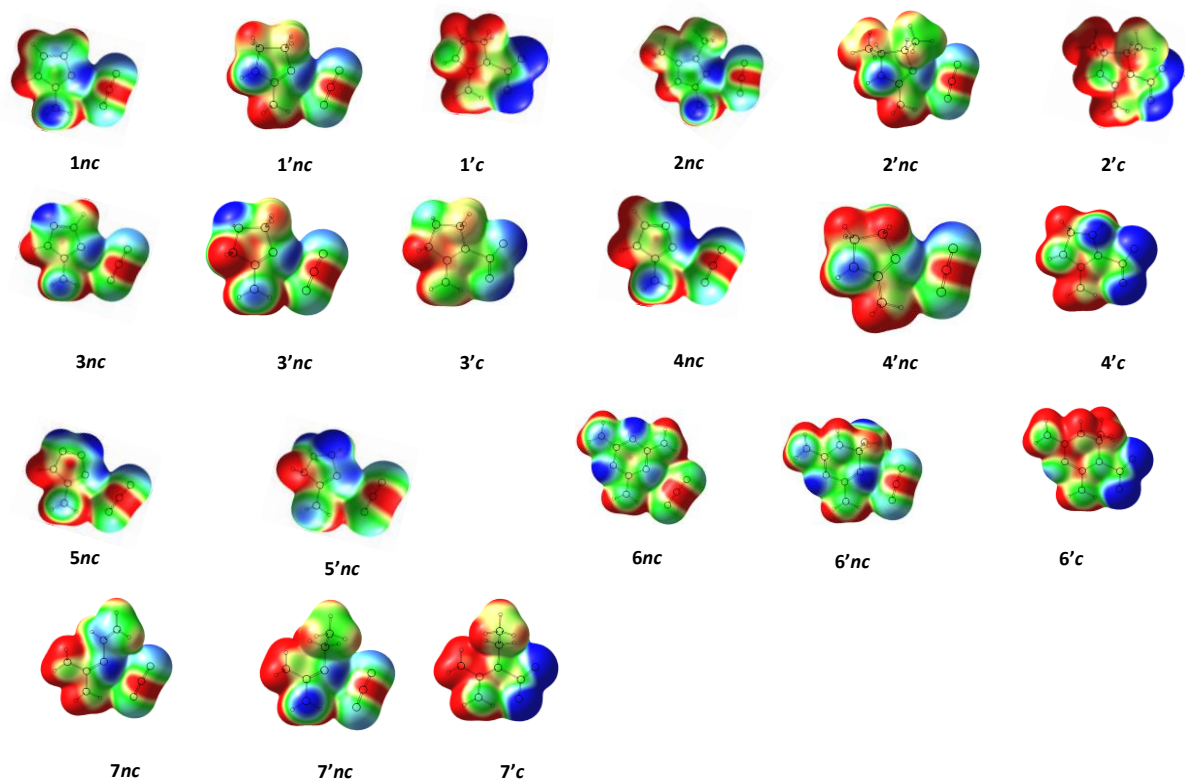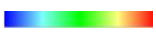
Figure 3.17 MESP textured on to 0.005 au electron density isosurface (the color code ▬▬▬▬▬▬ from blue to red is -0.05 au 0.05 au).

1	**CH₃CN…1**	**CH₃CN…1⁺–(CO₂)⁻**
(a)	**(b)**	**(c)**
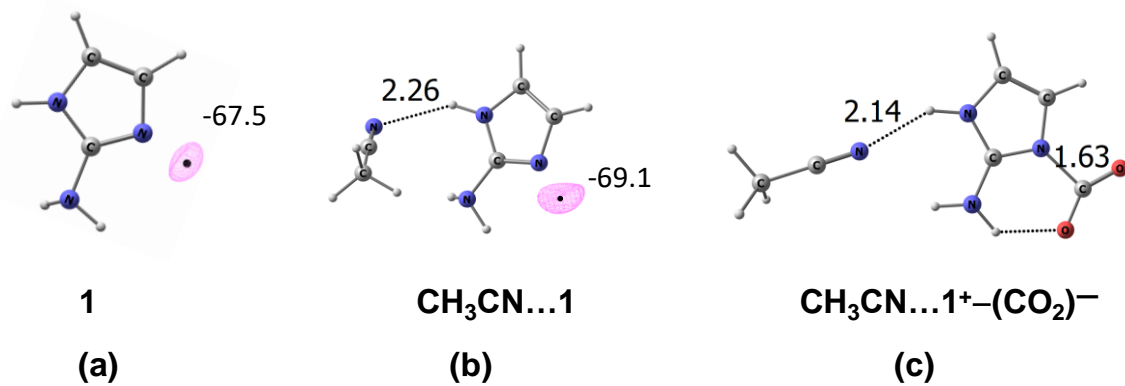
Figure 3.18 The MESP minimum (kcal/mol) of (a) imine **1,** (b) hydrogen-bonded **1** with CH_3CN and (c) covalent complex of **1** with CO_2 in presence of CH_3CN. The distances in Å.

The higher electron rich character of XN' over XN (as per the V_{min} data given in Table 3.6) is previously invoked to explain the ability of the XN' to yield **c** complex with CO_2. The data in Figure 3.18 show that XN can also yield a **c** complex if it comes under the influence of a hydrogen bond with a solvent molecule such as acetonitrile. For instance, the hydrogen bond in $CH_3CN\cdots\mathbf{1}$ slightly enhances the negative character of V_{min} at the lone pair region of imine N-center. Such a small variation in the electronic feature of **1** promotes the formation of covalent bond between **1** and CO_2. In other words, $CH_3CN\cdots\mathbf{1}^+-(CO_2)^-$ exists as a minimum on the potential energy surface while $\mathbf{1}^+-(CO_2)^-$ does not. Formation of $CH_3CN\cdots\mathbf{1}^+-(CO_2)^-$ explains a hitherto unknown phenomenon in chemical bonding theory – formation of a covalent bond due to the influence of a noncovalent bond. Formation of the complex $\mathbf{1c}\cdots\mathbf{1}$ (Figure 3.19) can also be regarded as an example for this scenario because **1c** does not exist if **1** is removed from $\mathbf{1c}\cdots\mathbf{1}$.
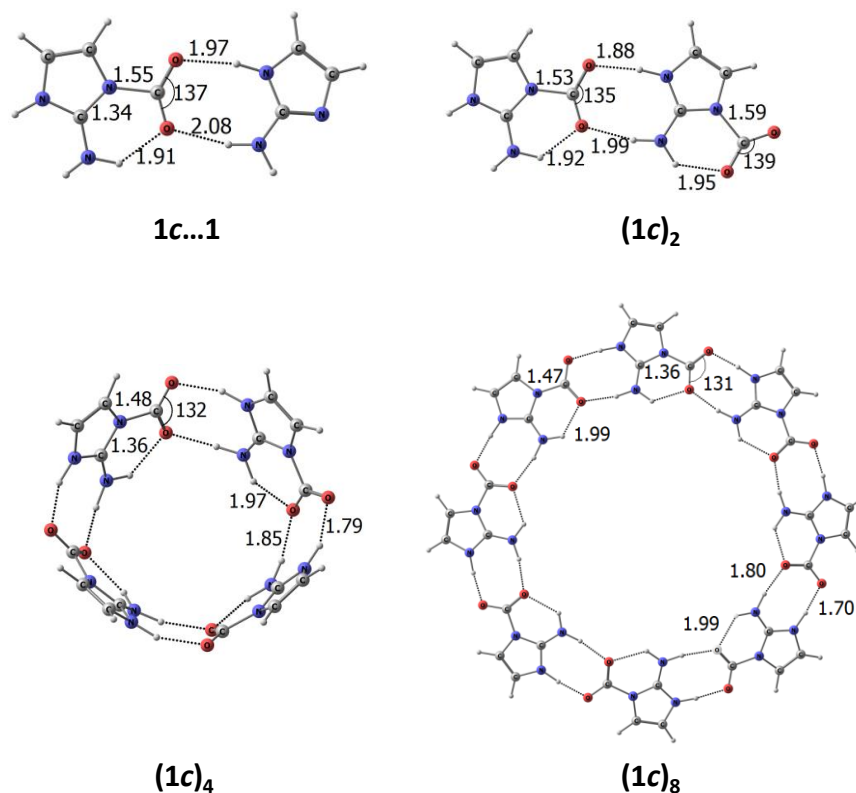
Figure 3.19 Molecular complexes and clusters of **1** with CO_2 at M06-2X/6-311++G** level. Distances in Å and angles in degrees.

Table 3.11 Energy parameters (kcal/mol) for molecular complexes and clusters of 1H-imidazol-2-amine with CO_2 at M06-2X/6-311++G** level.

Notation	E_b	ΔG	$E_{b/CO2}$	$\Delta G_{/CO2}$
1nc	-5.6	2.5	-5.6	2.5
1c···**1**	-7.7	12.3	-7.7	12.3
(**1**c)$_2$	-11.0	19.9	-5.5	9.9
(**1**c)$_4$	-77.4	1.7	-19.4	0.4
(**1**c)$_8$	-189.2	-25.8	-23.7	-3.2

1c..**1**   (**1**c)$_2$

(**1**c)$_4$ (**1**c)$_8$
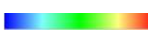
Figure 3.20 MESP for CO_2 clusters of **1** textured on to 0.005 au electron density isosurface (color code ▬▬▬▬▬ from blue to red is -0.05 au 0.05 au).

Table 3.12 Energy parameters (kcal/mol) for $(XN^+-(CO_2)^-)_8$ clusters at M06-2X/6-311++G** level.

Notation	E_b	ΔG	$E_{b/CO2}$	$\Delta G_{/CO2}$
$(1c)_8$	-189.2	-25.8	-23.7	-3.2
$(1'c)_8$	-243.5	-80	-30.4	-10
$(2c)_8$	-191.4	-29.9	-23.9	-3.7
$(2'c)_8$	-247	-82.2	-30.9	-10.3
$(3c)_8$	-136.9	26.6	-17.1	3.3
$(3'c)_8$	-168.6	-6.4	-21.1	-0.8
$(4c)_8$	-188.7	-22.1	-23.6	-2.8
$(4'c)_8$	-191.4	-27.5	-23.9	-3.4
$(5c)_8$	-116.7	47.8	-14.6	6
$(5'c)_8$	-165.2	-1.5	-20.7	-0.2
$(7c)_8$	-170.3	-3.3	-21.3	-0.4
$(7'c)_8$	-219.1	-53.9	-27.4	-6.7

Further, the binding energy per CO_2 ($E_{b/CO2}$) for the energy minimum **1nc**, -5.6 kcal/mol, is enhanced to -7.7 kcal/mol for **1c···1** which can be attributed to the NH···OC hydrogen bond interactions between **1c** and **1**. Similarly, the higher order clusters $(1c)_2$, $(1c)_4$ and $(1c)_8$ (Figure 3.19) show a steady improvement in binding energy per CO_2 ($E_{b/CO2}$) due to the NH···OC interactions between adjacent **1c** pairs (Table 3.11). The most stable $(1c)_8$ has $E_{b/CO2}$ -23.7 kcal/mol and most importantly, this cluster formation is exergonic by -3.2 kcal/mol as per the free energy change per CO_2 ($\Delta G_{/CO2}$). As the cluster size increases, a decreasing trend in both N-C bond distance and OCO angle is observed which indicates the increasing covalent character of the N–C bond in higher order clusters. The NH···OC interaction leads to the delocalization of the accumulated negative charge on the deformed CO_2 unit which in turn improves the donating power of the imine lone pair (Figure 3.20) to yield only the covalent complex.
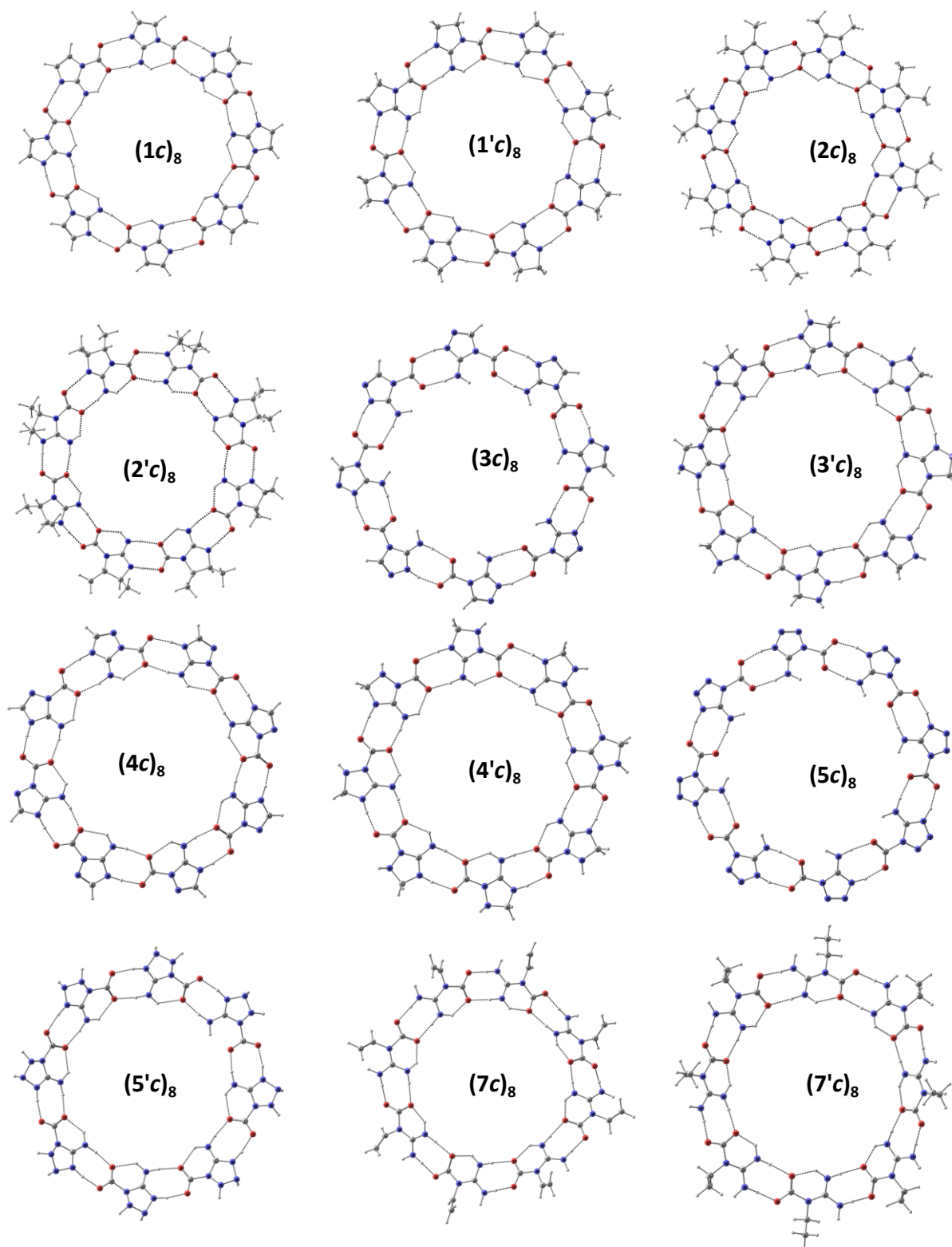
Figure 3.21 Optimized geometries of $((XN)(CO_2))_8$ clusters at M06-2X/6-311++G** level.

These observations are valid for complexes of all other non-primed and primed $(XN)(CO_2)$ systems, except **6** and **6'**. In all such octamer clusters, the $XN^+–(CO_2)^-$ units adopt nearly a planar arrangement (Figure 3.21). Unlike other systems, **6** and **6'** cannot operate through double NH⋯OC interactions to support higher order clusters. The cooperativity effect is very high for the octamer cluster, and this can be verified from the tremendous increase in the magnitude of $E_{b/CO2}$ data (Table 3.21) compared to that of the monomer $(XN)(CO_2)$ complexes.
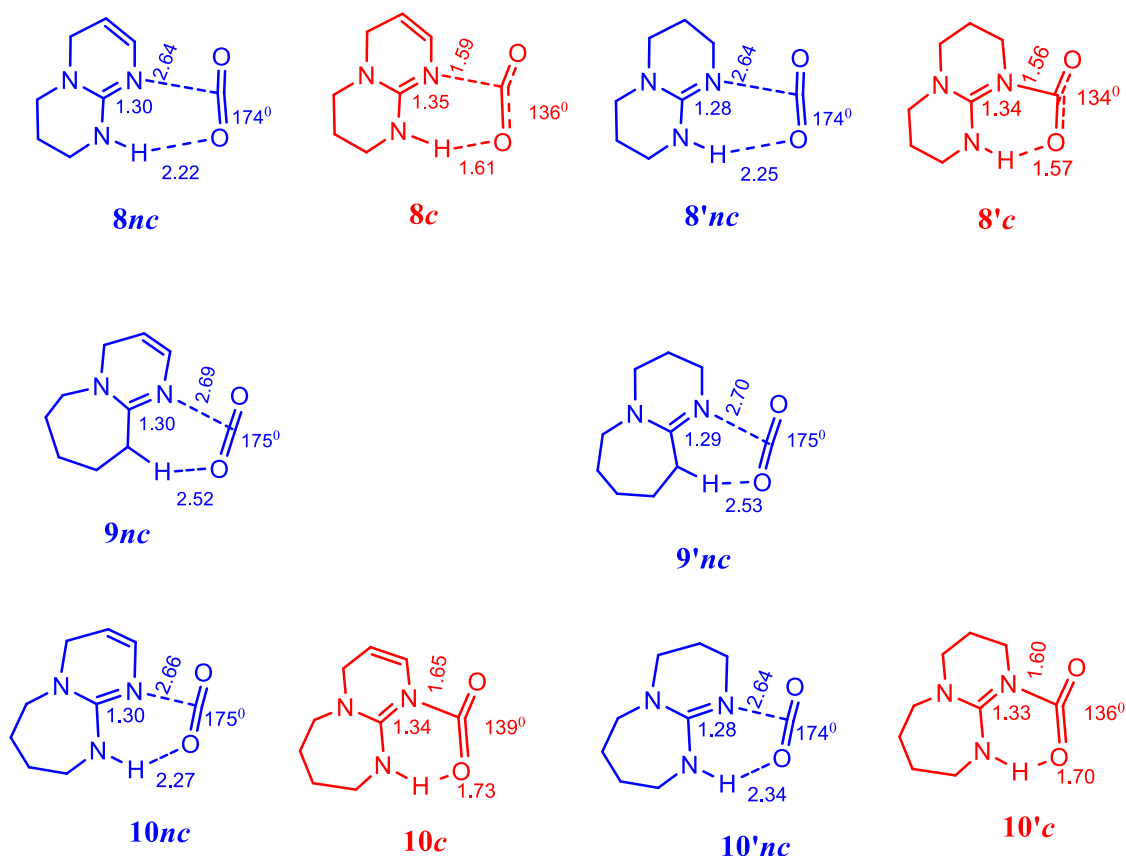
Figure 3.22 Geometry parameters of optimized $(XN)(CO_2)$ complexes in the *nc* (blue) and *c* (red) bond regimes. Distances in Å and angles in degrees.

The interaction of CO_2 with guanidine and related compounds in the process of CO_2 capture and conversion has been investigated from the past two decades. The 1,5,7-triazabicyclo [4.4.0]dec-5-ene (TBD), 7-methyl-1,5,7-triazabicyclo[4.4.0]dec-5-ene (MTBD), tetramethylguanidine (TMG), and 1,8-

diazabicyclo[5.4.0]undec-7-ene (DBU) are few important guanidine derivatives widely studied for CO_2 capture.[116-118] Hence we also studied the interaction of the experimentally proven imine systems like TBD, DBU and their derivatives with CO_2 molecule (Figure 3.22). TBD (**8'**) and its unsaturated version (**8**) have given ***nc*** complex as the minimum energy structure and ***c*** complex as a higher energy isomer (Table 3.13). In the case of DBU derivatives, **9'** and its unsaturated version, **9** have given only ***nc*** complexes with CO_2 while **10** & **10'** have given both ***nc*** and ***c*** complexes. Similar to **6** and **6'**, a planar arrangement of the zwitterion units to support higher order clusters is difficult for these imine systems due to the possibility of only one NH⋯OC interaction between adjacent units. These results suggest that in comparison to the molecular systems based on TBD or DBU, the molecular design patterns similar to the imines **1** - **7** and **1'**- **7'** are more efficient for CO_2 adsorption.

Table 3.13 Energy parameters (kcal/mol) for (XN)(CO_2) complexes at M06-2X/6-311++G** level.

Notation	E_b	ΔG
8*nc*, 8*c*	-6.5, -3.0	1.8, 6.9
8'*nc*, 8'*c*	-6.5, -5.7	1.6, 4.3
9*nc*	-5.4	2.7
9'*nc*	-5.6	2.7
10*nc*, 10*c*	-6.1, -0.3	2.1, 9.8
10'*nc*, 10'*c*	-6.4, -3.4	1.5, 7.0

3.7.4 Cooperativity effect

The formation of the octamer complex with only noncovalent interactions is also analyzed for the imine molecule **1**. One of the possible configurations of the octamer cluster is optimized by selecting a starting structure containing several

N···CO$_2$ noncovalent interactions. This structure after 417 optimization cycles converged to a configuration (**1nc**)$_8$ with several imine···imine noncovalent interactions (Figure 3.23) instead of N···CO$_2$ interactions. This shows that the imine-imine NH···N hydrogen bond is stronger than imine···CO$_2$ and CO$_2$···CO$_2$ noncovalent interactions.

(1)$_8$

$E_b = E_{(1)8} - 8*E_{(1)}$

$= -120.6$ kcal/mol

$+$

(CO$_2$)$_8$

$E_b = E_{(CO2)8} - 8* E_{CO2}$

$= -25.5$ kcal/mol

$E_{rea} = E_{(1nc)8} - E_{(CO2)8} - E_{(1)8}$

$= -24.3$ kcal/mol

$E_{rea} = E_{(1c)8} - E_{(CO2)8} - E_{(1)8}$

$= -73.4$ kcal/mol

(1nc)$_8$

$E_b = E_{(1nc)8} - 8*E_{(1)} - 8* E_{CO2}$

$= -170.4$ kcal/mol

(1c)$_8$

$E_b = E_{(1c)8} - 8*E_{(1)} - 8* E_{CO2}$
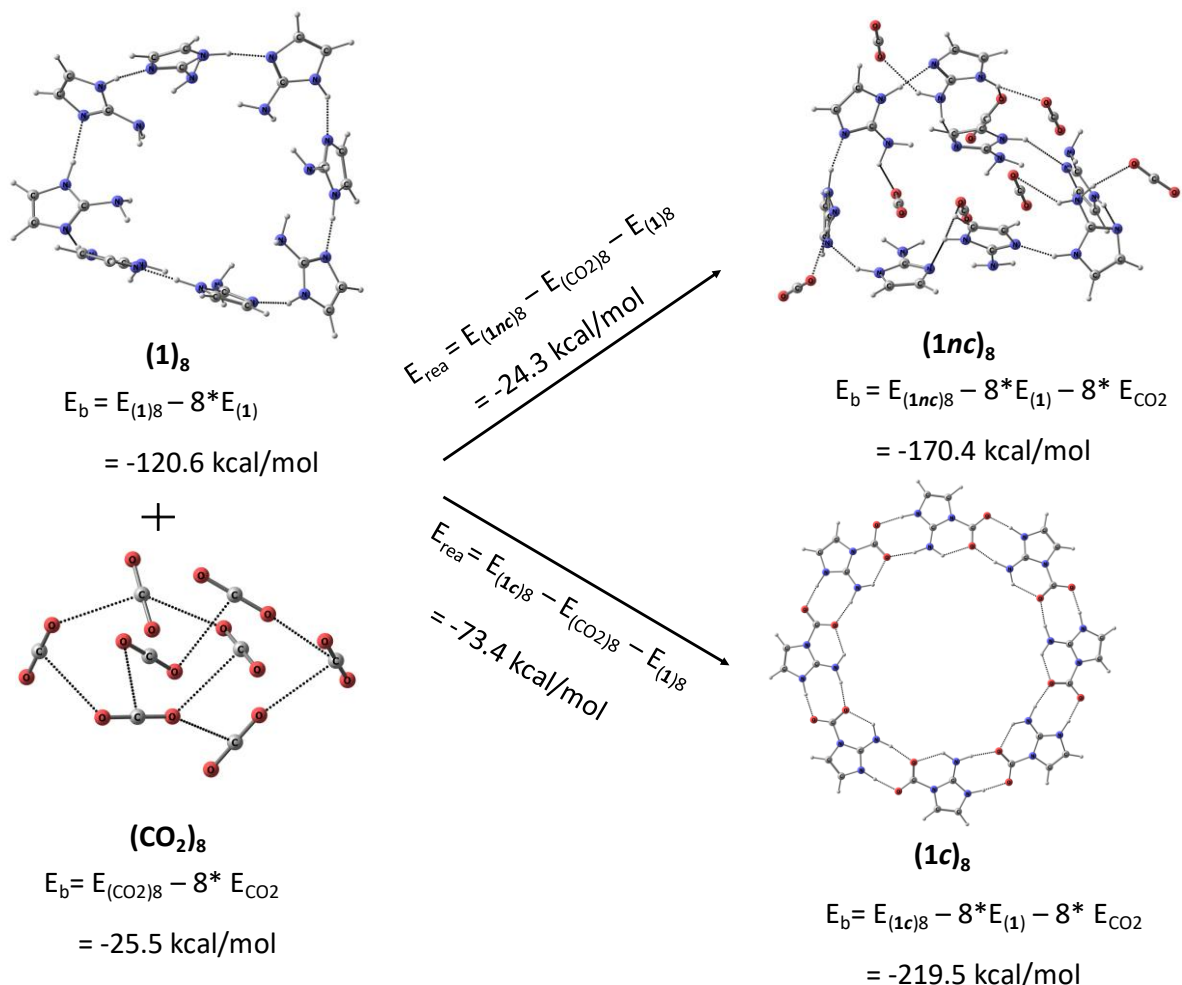
$= -219.5$ kcal/mol

Figure 3.23 Octamer clusters of imine **1**, CO$_2$ and imine-CO$_2$ systems. The binding energy (E$_b$) and the energy of formation (E$_{rea}$) are given in kcal/mol.

The E$_b$ data for the formation of imine cluster (**1**)$_8$ -120.6 kcal/mol and that of (CO$_2$)$_8$ cluster [119] -25.5 kcal/mol support this point. Also the E$_b$ -170.4 kcal/mol observed for (**1nc**)$_8$ indicates that its formation from (**1**)$_8$ and (CO$_2$)$_8$ is exothermic by 24.3 kcal/mol. The E$_b$ of (**1c**)$_8$ is 49.1 kcal/mol higher in magnitude than (**1nc**)$_8$ suggesting that the additional stabilization of the former is due to sixteen NH···OC

intermolecular interactions (between **1c**) and eight NH⋯OC intramolecular interactions (Figure 3.23). The transformation of NH⋯OC intermolecular interactions to N⋯HOC interactions *via* the proton transfer from N to O is also modelled for (**1c**)$_4$. This reaction will generate the cluster of the carboxylic acid derivative of the N-heterocycle (Figure 3.24). Such a cluster is 23.1 kcal/mol less stable than (**1c**)$_4$. However, in the case of octamer, all attempts to optimize the acid cluster have converged to the zwitterionic cluster (**1c**)$_8$. These results suggest that the captured CO_2 by **1** is preserved in the cluster with anionic character and the system resists the conversion of the CO_2 to the acid.

(1c)$_4$

SCF Energy = -1880.6308 au
Relative Energy = 0.0 kcal/mol

Carboxylic acid derivative of **(1c)$_4$**

SCF Energy = -1880.5939 au
Relative Energy = 23.1 kcal/mol
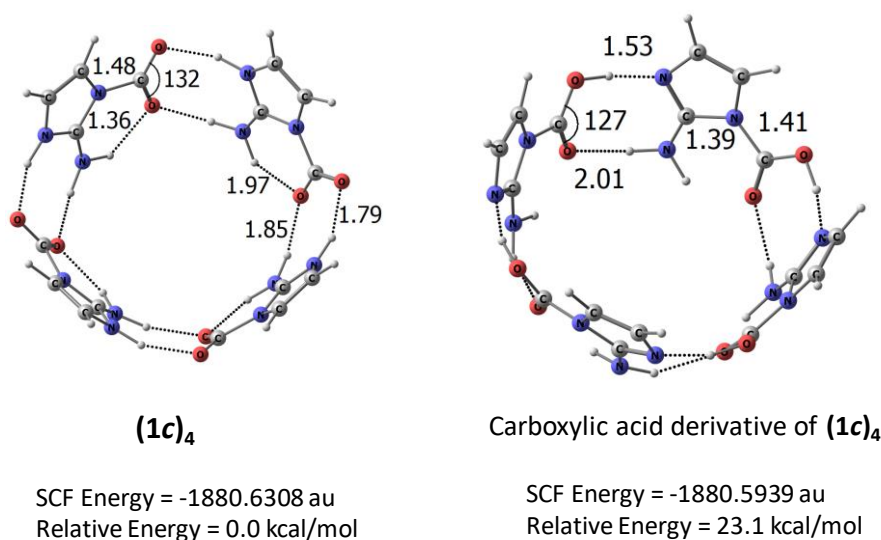
Figure 3.24 Optimized geometries of (**1c**)$_4$ and the corresponding carboxylic acid derivative of the N-heterocycle tetramer. Distances in Å and angles in degrees.

The (**1c**)$_8$ cluster, a zwitterionic $(XN^+-(CO_2)^-)_8$ system composed of several inter- and intramolecular NH⋯OC interactions is expected to show large positive cooperativity. Although (**1c**)$_8$ is composed of zwitterion units $XN^+-(CO_2)^-$ (**1c*** - the geometry of **1c** in the cluster), the stable form of the monomer is the **nc** complex **1nc**. The sum of the difference between the energy of **1nc** and the energy of each unit of $XN^+-(CO_2)^-$ in (**1c**)$_8$ can be considered as the deformation energy ($E_{def-oct}$) associated with the octamer formation. The $E_{def-oct}$ 118.0 kcal/mol suggests that changing the structure from **1nc** to **1c*** requires 14.75 kcal/mol energy per

monomer. The NH⋯OC intramolecular interaction in $1c^*$ is also accounted here. The conversion of eight $1nc$ to $(1c)_8$ is exothermic by -165.6 kcal/mol meaning that the total stabilizing interaction (E_S) in the cluster due to the eight deformed species $1c^*$ is -283.6 kcal/mol (Scheme 3.1). The pairwise interaction energy (E_p) between each pair of $1c^*$ in the octamer is also calculated (Table 3.14) which showed stabilizing interaction for every pair. The adjacent pairs showed the highest stabilization -25.9 kcal/mol due to two NH⋯OC interactions while the rest of the pairs showed E_p in the range -0.5 to -2.2 kcal/mol. The total pairwise interaction energy ΣE_p is found to be -232.3 kcal/mol which is 51.2 kcal/mol less in magnitude compared to E_S which can be attributed as the positive cooperativity effect (18%) due to the octamer assembly. Thus it is clear that in addition to the pairwise interaction energy or the hydrogen bonding energy, a substantial degree of cooperativity effect is involved in the stabilization of the octamer complex. (CO_2) complexes.

$$E_{con} = E_{(1c)8} - 8*E_{nc}$$

$$= -165.6 \text{ kcal/mol}$$

$$E_{def-oct} = 8*[E_{1c^*} - E_{1nc}]$$

$$= 118.0 \text{ kcal/mol}$$

$1nc$ $1c^*$

$$E_S = E_{con} - E_{def-oct}$$

$$= -283.5 \text{ kcal/mol}$$

$1c^{*1}$ $1c^{*8}$ $1c^{*2}$ $1c^{*7}$ $1c^{*3}$ $1c^{*8}$ $1c^{*4}$ E_p

$(1c)_8$

$$\Sigma E_p = \sum_{j>i=1}^{8} (E_{1c*ij} - 2*E_{1c^*})$$

$$= -219.5 \text{ kcal/mol}$$
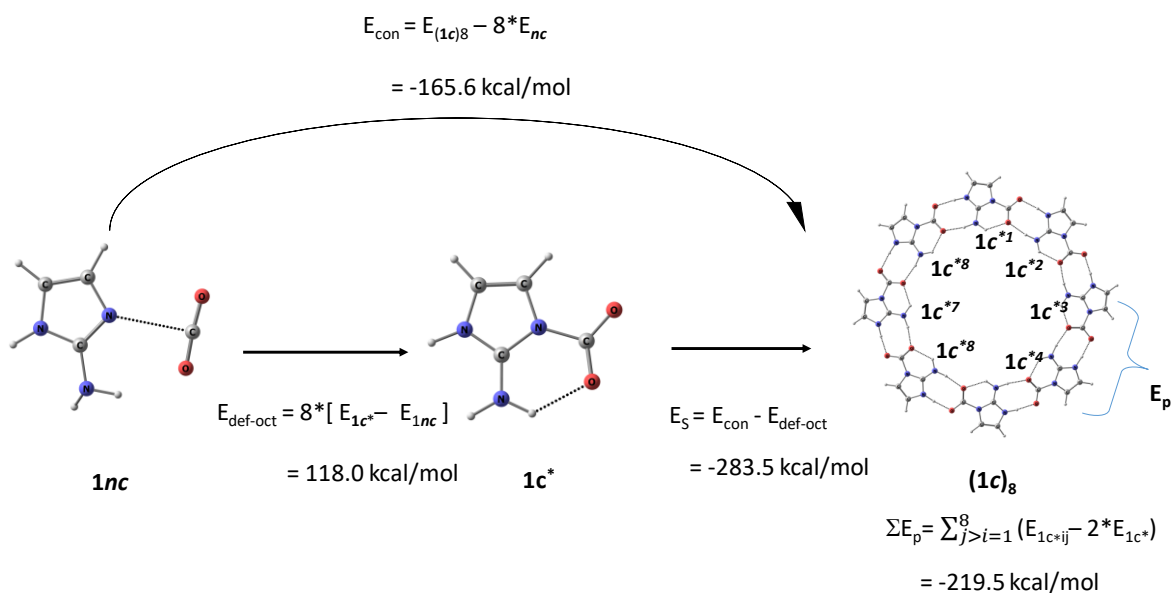
Scheme 3.1 Schematic representation of the stabilizing factors of the octamer complex $(1c)_8$. $1c^{*1}$, $1c^{*2}$, ..., and $1c^{*8}$ are the 1st, 2nd ...and 8th $XN^+-(CO_2)^-$ unit respectively.

Table 3.14 Pairwise interaction energies, E_p (kcal/mol) of the octamer complex $(1c)_8$.

Pair	E_p	Pair	E_p
1, 2	-25.9	3, 5	-0.5
1, 3	-2.2	3, 6	-25.9
1, 4	-0.7	3, 7	-2.2
1, 5	-2.2	3, 8	-0.7
1, 6	-0.7	4, 5	-25.9
1, 7	-0.5	4, 6	-2.2
1, 8	-25.9	4, 7	-25.9
2, 3	-25.9	4, 8	-2.2
2, 4	-0.5	5, 6	-0.7
2, 5	-0.7	5, 7	-2.2
2, 6	-2.2	5, 8	-25.9
2, 7	-0.7	6, 7	-25.9
2, 8	-2.2	6, 8	-0.5
3, 4	-0.7	7, 8	-0.7

The negative entropy factor associated with the cluster formation (assembly of sixteen molecular units) is easily overcome by the thermodynamic stabilization due to high positive cooperativity in many cases and the process becomes exergonic in nature for the octamer complexes except **3c** and **5c**. Among the different octamer clusters studied, **1'**, **2'**, and **7'** show the best E_{b/CO_2} and they are proposed as promising systems for cooperative CO_2 capture and conversion.

3.8 Conclusions

This research has shown that the interaction of imine systems XN with CO_2 results in the formation of XN···CO_2 complexes in the noncovalent territory. With a slight improvement in the electronic density of the imine lone pair, the more saturated XN' systems showed N-C bonding interactions in the covalent territory to yield zwitterionic $XN^+–(CO_2)^-$ complexes. This zwitterionic complex is identified as the bond stretch isomer of XN···CO_2. The bond stretch isomerism occurs through a **ts** which is proposed as the boundary crossing point for the noncovalent and covalent bond territories. The zwiterionic $(XN^+–(CO_2)^-)_n$ cluster formation is observed for all types of XN imines, wherein both intra- and intermolecular NH···OC noncovalent interactions provided additional stabilization to the cluster. These cooperative interactions enhance the N-C coordinate covalent bond, and the cluster is devoid of any N···C noncovalent interactions. Transforming eight XN···CO_2 systems to one covalent octamer cluster $(XN^+–(CO_2)^-)_8$ led to a five-fold increase in the binding energy which is attributed to the large cooperativity effect associated with N-C covalent and NH···OC noncovalent interactions whereas the corresponding noncovalent cluster $(XN···CO_2)_8$ showed significantly lower binding energy than the covalent cluster. The pairwise interaction energy for each monomer pair in the covalent cluster is stabilizing in nature while the total stabilization of the cluster exceeded the total pairwise interaction energy by 18 % (51.2 kcal/mol) which is nearly same as the energy difference between the noncovalent and covalent octamer clusters. This result proves that the covalent cluster formation is truly driven by positive cooperativity. Moreover, many XN systems showed exergonic nature for the cluster formation up to octamer. The favorable energetics and the carboxylate character developed for CO_2 in the zwitterionic clusters suggest that many XN systems are highly promising molecules for CO_2 capture.

Though the noncovalent to covalent boundary crossing problem is addressed only for the imines and CO_2 combinations, one may visualize that many such noncovalent to covalent bonding territory crossovers may have happened

during the origin of life when small molecules were reacted to give larger ones. A noteworthy example is the formation of $CH_3CN \cdots \mathbf{1}^+-(CO_2)^-$ complex which explains a hitherto unknown phenomenon in chemical bonding theory – formation of a covalent bond due to the influence of a noncovalent bond. The previous studies on the transformation of the weak hydrogen or tetrel bonds into strong covalent bonds also support this crossover trend in chemical bonding. The transition state (**ts**) structures identified in this study stand as the demarcating point for such a crossover from weak noncovalent to strong covalent bonding territory.

3.9   References

1.   I. P. o. C. Change, *Climate Change 2014–Impacts, Adaptation and Vulnerability: Regional Aspects*, Cambridge University Press, , 2014.
2.   J. C. Stephens and D. W. Keith, *Clim. Change*, 2008, **90**, 217.
3.   D. W. Keith, *Science*, 2009, **325**, 1654-1655.
4.   D. W. Keith, M. Ha-Duong and J. K. Stolaroff, *Clim. Change*, 2006, **74**, 17-45.
5.   P. Agreement, Paris agreement, 2015.
6.   K. S. Lackner, S. Brennan, J. M. Matter, A.-H. A. Park, A. Wright and B. Van Der Zwaan, *Proc. Natl. Acad. Sci. U.S.A.*, 2012, **109**, 13156-13162.
7.   E. S. Sanz-Perez, C. R. Murdock, S. A. Didas and C. W. Jones, *Chem. Rev.*, 2016, **116**, 11840-11876.
8.   D. W. Keith, G. Holmes, D. S. Angelo and K. Heidel, *Joule*, 2018, **2**, 1573-1594.
9.   S. Brandani, *Energy Environ.*, 2012, **23**, 319-328.
10.   D. Sarewitz and R. Nelson, *Nature*, 2008, **456**, 871-872.
11.   K. Lackner, H.-J. Ziock and P. Grimes, *Carbon dioxide extraction from air: Is it an option?*, Los Alamos National Lab., NM (US)1999.
12.   F. S. Zeman and K. S. Lackner, *World Resour. Rev.*, 2004, **16**, 157-172.
13.   K. S. Lackner and S. Brennan, *Clim. Change*, 2009, **96**, 357-378.
14.   G. Chichilnisky and P. Eisenberger, *Nature*, 2009, **459**, 1053-1053.
15.   T. M. McDonald, W. R. Lee, J. A. Mason, B. M. Wiers, C. S. Hong and J. R. Long, *J. Am. Chem. Soc.*, 2012, **134**, 7056-7065.
16.   O. S. Board, E. National Academies of Sciences and Medicine, *Negative emissions technologies and reliable sequestration: A research agenda*, National Academies Press, 2019.
17.   Y. Yuan, H. You and L. Ricardez-Sandoval, *Chin. J. Chem. Eng.*, 2019, **27**, 1554-1565.
18.   K. S. Lackner, *Science*, 2003, **300**, 1677-1678.
19.   X. Shi, H. Xiao, H. Azarabadi, J. Song, X. Wu, X. Chen and K. S. Lackner, *Angew. Chem. Int. Ed.*, 2020, **59**, 6984-7006.
20.   M. A. Alkhabbaz, R. Khunsupat and C. W. Jones, *Fuel*, 2014, **121**, 79-85.

21. S. Wang, W.-C. Li, L. Zhang, Z.-Y. Jin and A.-H. Lu, *J. Mater. Chem. A*, 2014, **2**, 4406-4412.
22. H. Sabet-Sarvestani, H. Eshghi and M. Izadyar, *Struct. Chem.*, 2017, **28**, 675-686.
23. T. C. dos Santos, S. Bourrelly, P. L. Llewellyn, J. W. d. M. Carneiro and C. M. Ronconi, *Phys. Chem. Chem. Phys.*, 2015, **17**, 11095-11102.
24. C. A. Seipp, N. J. Williams, M. K. Kidder and R. Custelcean, *Angew. Chem. Int. Ed.*, 2017, **56**, 1042-1045.
25. F. M. Brethomé, N. J. Williams, C. A. Seipp, M. K. Kidder and R. Custelcean, *Nat. Energy*, 2018, **3**, 553-559.
26. C. G. Gianopoulos, Z. Chua, V. V. Zhurov, C. A. Seipp, X. Wang, R. Custelcean and A. A. Pinkerton, *IUCrJ*, 2019, **6**, 56-65.
27. R. Custelcean, N. J. Williams and C. A. Seipp, Google Patents2020.
28. J. Thiele and E. Dralle, *Justus Liebieg's Ann. Chem.*, 1898, **302**, 275-299.
29. J.-M. Wurtz, W. Bourguet, J.-P. Renaud, V. Vivat, P. Chambon, D. Moras and H. Gronemeyer, *Nat. Struct. Biol.*, 1996, **3**, 87-94.
30. R. G. Konsler, J. Karl and E. N. Jacobsen, *J. Am. Chem. Soc.*, 1998, **120**, 10780-10781.
31. N. A. Brunelli, K. Venkatasubbaiah and C. W. Jones, *Chem. Mater*, 2012, **24**, 2433-2442.
32. V. Lyaskovskyy and B. de Bruin, *Acs Catal.*, 2012, **2**, 270-279.
33. C. Song, Y. Chu, M. Wang, H. Shi, L. Zhao, X. Guo, W. Yang, J. Shen, N. Xue and L. Peng, *J. Catal*, 2017, **349**, 163-174.
34. M. Caplow, *J. Am. Chem. Soc.*, 1968, **90**, 6795-6803.
35. P. Danckwerts, *Chem. Eng. Sci.*, 1979, **34**, 443-446.
36. T. L. Donaldson and Y. N. Nguyen, *Ind. Eng.*, 1980, **19**, 260-266.
37. I. Dovgaliuk, F. Nouar, C. Serre, Y. Filinchuk and D. Chernyshov, *Chem. Eur. J.*, 2017, **23**, 17714-17720.
38. C. Schmuck, *Tetrahedron*, 2001, **57**, 3063-3067.
39. M. Saleh, H. M. Lee, K. C. Kemp and K. S. Kim, *ACS Appl. Mater. Interfaces*, 2014, **6**, 7325-7333.
40. R. Steinhardt, S. C. Hiew, H. Mohapatra, D. Nguyen, Z. Oh, R. Truong and A. Esser-Kahn, *ACS Cent. Sci.*, 2017, **3**, 1271-1275.
41. J. Kundu, J. F. Stilck, J.-H. Lee, J. B. Neaton, D. Prendergast and S. Whitelam, *Phys. Rev. Lett.*, 2018, **121**, 015701.
42. R. Vaidhyanathan, S. S. Iremonger, G. K. Shimizu, P. G. Boyd, S. Alavi and T. K. Woo, *Angew. Chem. Int. Ed.*, 2012, **124**, 1862-1865.
43. E. J. Kim, R. L. Siegelman, H. Z. Jiang, A. C. Forse, J.-H. Lee, J. D. Martell, P. J. Milner, J. M. Falkowski, J. B. Neaton and J. A. Reimer, *Science*, 2020, **369**, 392-396.
44. S. T. Hosseini, H. Raissi and M. Pakdel, *New J. Chem.*, 2020, **44**, 7771-7779.
45. H. M. Lee, I. S. Youn, M. Saleh, J. W. Lee and K. S. Kim, *Phys. Chem. Chem. Phys.*, 2015, **17**, 10925-10933.
46. J. D. Martell, P. J. Milner, R. L. Siegelman and J. R. Long, *Chem. Sci.*, 2020, **11**, 6457-6471.
47. V. Y. Mao, P. J. Milner, J. H. Lee, A. C. Forse, E. J. Kim, R. L. Siegelman, C. M. McGuirk, L. B. Porter-Zasada, J. B. Neaton and J. A. Reimer, *Angew. Chem. Int. Ed.*, 2020, **59**, 19468-19477.

48. R. L. Siegelman, T. M. McDonald, M. I. Gonzalez, J. D. Martell, P. J. Milner, J. A. Mason, A. H. Berger, A. S. Bhown and J. R. Long, *J. Am. Chem. Soc.*, 2017, **139**, 10526-10538.
49. M. J. Frisch, G. W. Trucks, H. B. Schlegel, G. E. Scuseria, M. A. Robb, J. R. Cheeseman, G. Scalmani, V. Barone, G. A. Petersson, H. Nakatsuji, X. Li, M. Caricato, A. V. Marenich, J. Bloino, B. G. Janesko, R. Gomperts, B. Mennucci, H. P. Hratchian, J. V. Ortiz, A. F. Izmaylov, J. L. Sonnenberg, D. Williams-Young, F. Ding, F. Lipparini, F. Egidi, J. Goings, B. Peng, A. Petrone, T. Henderson, D. Ranasinghe, V. G. Zakrzewski, J. Gao, N. Rega, G. Zheng, W. Liang, M. Hada, M. Ehara, K. Toyota, R. Fukuda, J. Hasegawa, M. Ishida, T. Nakajima, Y. Honda, O. Kitao, H. Nakai, T. Vreven, K. Throssell, J. A. Montgomery Jr., J. E. Peralta, F. Ogliaro, M. J. Bearpark, J. J. Heyd, E. N. Brothers, K. N. Kudin, V. N. Staroverov, T. A. Keith, R. Kobayashi, J. Normand, K. Raghavachari, A. P. Rendell, J. C. Burant, S. S. Iyengar, J. Tomasi, M. Cossi, J. M. Millam, M. Klene, C. Adamo, R. Cammi, J. W. Ochterski, R. L. Martin, K. Morokuma, O. Farkas, J. B. Foresman and D. J. Fox, *Gaussian 16 Rev. A.03*, Gaussian, Inc., Wallingford CT, **2016**.
50. Y. Zhao and D. G. Truhlar, *Theoretical Chemistry Accounts*, 2008, **120**, 215-241.
51. S. F. Boys and F. d. Bernardi, *Mol. Phys.*, 1970, **19**, 553-566.
52. P. Hobza and K. Müller-Dethlefs, *Non-covalent interactions: theory and experiment*, Royal Society of Chemistry, , Cambridge, 2010.
53. Ł. Mentel and E. Baerends, *J. Chem. Theory Comput.*, 2013, **10**, 252-267.
54. C. D. Sherrill, T. Takatani and E. G. Hohenstein, *J. Phys. Chem. A*, 2009, **113**, 10146-10159.
55. C. D. Sherrill, *School of Chemistry and Biochemistry, Georgia Institute of Technology*, 2010.
56. A. Halkier, W. Klopper, T. Helgaker, P. Jo/rgensen and P. R. Taylor, *J. Chem. Phys.*, 1999, **111**, 9157-9167.
57. S. Anila and C. H. Suresh, *Phys. Chem. Chem. Phys.*, 2019, **21**, 23143-23153.
58. P. V. Bijina and C. H. Suresh, *J. Phys. Chem. A*, 2020, **124**, 2231-2241.
59. W. Wang, J. Gu, X. Zou, W. Tong and H. Gong, *Tetrahedron Lett.*, 2015, **56**, 2684-2687.
60. R. Ditchfield, *Mol. Phys.*, 1974, **27**, 789-807.
61. L. B. Casabianca, *Magn. Reson. Chem*, 2020.
62. Q. Yang, M. Bown, A. Ali, D. Winkler, G. Puxty and M. Attalla, *Energy Procedia*, 2009, **1**, 955-962.
63. J. Seravalli and S. W. Ragsdale, *Biochemistry*, 2008, **47**, 6770-6781.
64. T. M. Abbott, G. W. Buchanan, P. Kruus and K. C. Lee, *Canadian Journal of Chemistry*, 1982, **60**, 1000-1006.
65. C. Perinu, B. Arstad and K.-J. Jens, *Energy Procedia*, 2013, **37**, 7310-7317.
66. U. Koch and P. L. Popelier, *J. Phys. Chem.*, 1995, **99**, 9747-9754.
67. P. Popelier, *J. Phys. Chem. A*, 1998, **102**, 1873-1878.
68. T. D. Della and C. H. Suresh, *Phys. Chem. Chem. Phys.*, 2017, **19**, 5830-5838.
69. G. Frenking and S. Shaik, *The chemical bond: fundamental aspects of chemical bonding*, John Wiley & Sons, Germany, 2014.
70. A. D. McNaught and A. Wilkinson, *Compendium of chemical terminology*, Blackwell Science Oxford, U.K., 1997.

71. L. L. Zhao, S. Pan, N. Holzmann, P. Schwerdtfeger and G. Frenking, *Chem. Rev.*, 2019, **119**, 8781-8845.
72. L. L. Zhao, M. von Hopffgarten, D. M. Andrada and G. Frenking, *Wiley Interdiscip. Rev.-Comput. Mol. Sci.*, 2018, **8**, 37.
73. C. R. Landis, R. P. Hughes and F. Weinhold, *Organometallics*, 2015, **34**, 3442-3449.
74. F. Weinhold, C. R. Landis and E. D. Glendening, *Int. Rev. Phys. Chem.*, 2016, **35**, 399-440.
75. C. Esterhuysen and G. Frenking, *Theor. Chem. Acc.*, 2004, **111**, 381-389.
76. M. Lein and G. Frenking, *Theory and applications of computational chemistry: the first 40 years*, Elsevier, Amsterdam, 2005.
77. A. Kovacs, C. Esterhuysen and G. Frenking, *Chem. Eur. J.*, 2005, **11**, 1813-1825.
78. C. Esterhuysen and G. Frenking, *Theor. Chem. Acc.*, 2005, **113**, 294-294.
79. A. Krapp, F. M. Bickelhaupt and G. Frenking, *Chem. Eur. J.*, 2006, **12**, 9196-9216.
80. G. Frenking and A. Krapp, *J. Comput. Chem.*, 2007, **28**, 15-24.
81. L. L. Zhao, M. Hermann, W. H. E. Schwarz and G. Frenking, *Nat. Rev. Chem.*, 2019, **3**, 48-63.
82. S. Pan and G. Frenking, *Molecules*, 2021, **26**, 14.
83. L. Zhao, M. Zhi and G. Frenking, *Int. J. Quantum Chem.*, 2021, e26773.
84. S. Shaik, *J. Comput. Chem.*, 2007, **28**, 51-61.
85. S. Scheiner, *J. Chem. Phys.*, 2020, **153**, 140901.
86. S. Scheiner, *Hydrogen bonding: a theoretical perspective*, Oxford University Press, New York, 1997.
87. G. Gilli and P. Gilli, *The nature of the hydrogen bond: outline of a comprehensive hydrogen bond theory*, Oxford University Press, Oxford, 2009.
88. D. Bodesheim, G. Kieslich, M. Johnson and K. T. Butler, *J. Phys. Chem. Lett.*, 2020, **11**, 3495-3500.
89. P. A. Hunt, *Top. Curr. Chem.*, 2017, **375**, 22.
90. J. M. Berg, J. L. Tymoczko and L. Stryer, *New York: Freeman and Company: New York*, 2002.
91. J. Joy, E. Akhil and E. D. Jemmis, *Phys. Chem. Chem. Phys.*, 2018, **20**, 25792-25798.
92. B. Dereka, Q. Yu, N. H. Lewis, W. B. Carpenter, J. M. Bowman and A. Tokmakoff, *Science*, 2021, **371**, 160-164.
93. N. Liu, X. Xie, Q. Li and S. Scheiner, *ChemPhysChem*, 2021, **22**, 2305-2312.
94. R. F. Bader, *Atoms in molecules: a quantum theory, International series of monographs on chemistry*, Oxford University Press, Oxford, 1990.
95. P. L. A. Popelier, F. Aicken and S. O'Brien, *Atoms in molecules*, Prentice Hall Manchester, 2000.
96. M. Jabłoński and M. Palusiak, *J. Phys. Chem. A*, 2010, **114**, 2240-2244.
97. H. J. Bohórquez, R. J. Boyd and C. F. Matta, *J. Phys. Chem. A*, 2011, **115**, 12991-12997.
98. P. Popelier, *J. Phys. Chem. A*, 1998, **102**, 1873-1878.
99. S. Shaik, D. Danovich, W. Wu and P. C. Hiberty, *Nat. Chem.*, 2009, **1**, 443.
100. H. J. Bohórquez, R. J. Boyd and C. F. Matta, *J. Phys. Chem. A*, 2011, **115**, 12991-12997.
101. S. Anila and C. H. Suresh, *Phys. Chem. Chem. Phys.*, 2021, **23**, 13662-13671.
102. Y. Zhao and D. G. Truhlar, *Theor. Chem. Acc.*, 2008, **120**, 215-241.

103. C. D. Sherrill, ed. G. I. o. T. School of Chemistry and Biochemistry, Georgia Institute of Technology**2010**.
104. L. B. Casabianca, *Magn. Reson. Chem.*, 2020, **58**, 611-624.
105. G. V. Gibbs, D. Cox, T. D. Crawford, K. M. Rosso, N. Ross and R. Downs, *J. Chem. Phys.*, 2006, **124**, 084704.
106. P. S. V. Kumar, V. Raghavendra and V. Subramanian, *J. Chem. Sci.*, 2016, **128**, 1527-1536.
107. W. D. Stohrer and R. Hoffmann, *J. Am. Chem. Soc.*, 1972, **94**, 779-786.
108. W. D. Stohrer and R. Hoffmann, *J. Am. Chem. Soc.*, 1972, **94**, 1661-1668.
109. Y. Jean, A. Lledos, J. K. Burdett and R. Hoffmann, *J. Am. Chem. Soc.*, 1988, **110**, 4506-4516.
110. G. Parkin, *Chem. Rev.*, 1993, **93**, 887-911.
111. M.-M. Rohmer, A. Strich, M. Bénard and J.-P. Malrieu, *J. Am. Chem. Soc.*, 2001, **123**, 9126-9134.
112. R. Clérac, F. A. Cotton, L. M. Daniels, K. R. Dunbar, C. A. Murillo and X. Wang, *Inorg. Chem.*, 2001, **40**, 1256-1264.
113. P. Comba, M. Kerscher, M. Merz, V. Müller, H. Pritzkow, R. Remenyi, W. Schiek and Y. Xiong, *Chem. Eur. J.*, 2002, **8**, 5750-5760.
114. J. A. Labinger, *C. R. Chim.*, 2002, **5**, 235-244.
115. F. P. Di Nicola, M. Lanzi, F. Marchetti, G. Pampaloni and S. Zacchini, *Dalton Trans.*, 2015, **44**, 12653-12659.
116. F. S. Pereira, E. R. deAzevedo, E. F. da Silva, T. J. Bonagamba, D. L. da Silva Agostíni, A. Magalhaes, A. E. Job and E. R. P. Gonzalez, *Tetrahedron*, 2008, **64**, 10097-10106.
117. D. J. Heldebrant, P. G. Jessop, C. A. Thomas, C. A. Eckert and C. L. Liotta, *J. Org. Chem.*, 2005, **70**, 5335-5338.
118. C. Rether, W. Sicking, R. Boese and C. Schmuck, *Beilstein J. Org. Chem.*, 2010, **6**, 3.
119. S. D. Yeole, N. Sahu and S. R. Gadre, *Phys. Chem. Chem. Phys.*, 2012, **14**, 7718-7723.

Chapter 4

Part A

Imidazolium-fulleride Ionic Liquids – A DFT Prediction

Part B

Polyanionic Cyano-fulleride for CO_2 capture

$IM^+...\ (C_{60}H)^-$

anion

dianion

trianion

hexaanion

tetraanion

pentaanion
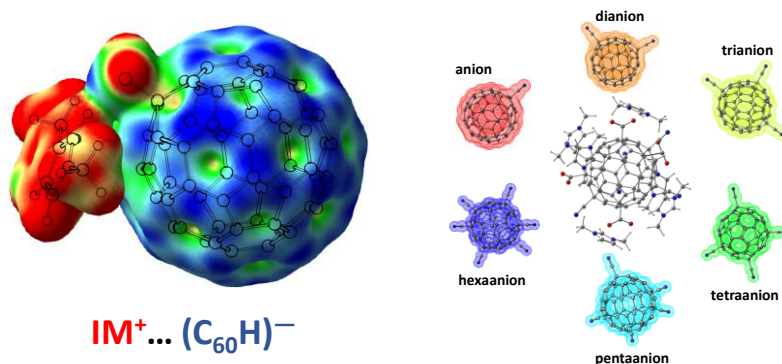
Part A: Imidazolium-fulleride Ionic Liquids – A DFT Prediction

4.1 Abstract

Ionic liquids (ILs) exhibit tunable physicochemical properties due to the flexibility in selecting their cation–anion combination from a large pool of ions. The size of ions controls the properties of ILs in the range from ionic to molecular and thus large ions play an important role in regulating the melting temperature and viscosity. Here we show that the exohedral addition of anionic X^- moieties to C_{60} (X = H, F, OH, CN, NH_2, and NO_2) is thermodynamically a viable process to create large X-fulleride anions $(C_{60}X)^-$. The addition of X^- to C_{60} is modelled by locating the transition state for the reaction between C_{60} and 1,3-dimethyl-2X-Imidazole (IMX) at M06L/6-311++G**//M06L/6-31G** level. The reaction yielded the ion-pair complex $IM^+\cdots(C_{60}X)^-$ for X = H, F, OH, CN, NH_2, and NO_2 and the ordered pair of (activation free energy in kcal/mol, reaction free energy in kcal/mol) is found to be (14.5, 1.1), (6.1, 3.1), (16.7, 2.3), (14.7, -7.9), (27.9, 0.5) and (11.9, 12.4), respectively. The low barrier of the reactions suggests their feasibility. The reaction is slightly endergonic for X = H, F, OH, and NH_2 while X = CN show a significant exergonic character. The X-fulleride formation is not observed when X = Cl and Br. The ion-pair interactions ($E_{ion-pair}$) observed for $IM^+\cdots(C_{60}X)^-$ ranges from -64.0 to -73.0 kcal/mol which is substantially lower ($\sim$10 %) than the typically reported values for imidazolium-based ionic liquids such as $[EMIm]^+[trz]^-$, $[EMIm]^+[dc]^-$, $[EMIm]^+[dtrz]^-$, and $[EMIm]^+[NH_2tz]^-$. Quantum theory of atoms in molecule (QTAIM) analysis showed that C-X bonding in $(C_{60}X)^-$ is covalent while that in $(IM^+\cdots X^-)\cdots C_{60}$ (for X = Cl and Br) is noncovalent. Further, molecular electrostatic potential (MESP) analysis showed that the X-fulleride could behave as a large spherical anion due to the delocalization of the excess electron in the system over the entire carbon framework. The large anionic character of the X-fulleride is also revealed by the identification of several close lying local energy minima for the $IM^+\cdots(C_{60}X)^-$ ion-pair. The low $E_{ion-pair}$ value, significant contribution of

dispersion to $E_{ion-pair}$ and spherical nature of the anion predict low melting and highly viscous IL formation from X-fullerides and imidazolium cation.

4.2 Introduction

Ionic liquids (ILs) are low melting point salts, which, by definition, melt below 100 °C and are found to be useful as solvents in organic synthesis and extraction processes.[1, 2] Theoretical methods to predict the properties of proposed cation–anion combinations before synthesis are useful in designing novel ILs to better meet the needs of particular applications by altering the combinations of cations and anions. Bernard *et al.* have shown the variation of trends in thermodynamic and transport properties of ionic liquids (ILs) with their ion-pair binding energy.[3] The high viscosity is one of the major limitation commonly encountered in the performance of ionic liquids when used as electrolytes in electrochemical devices.[4] Cyano-functionalized anions produce some of the most fluid and conductive ionic liquids with low melting temperatures and low viscosities.[5-7] Wide range of studies have been carried out on imidazolium-based ILs owing to their excellent properties of stability, flexibility in molecular design, ease of synthesis and adaptability to multiple functions.[8] The 1-ethyl-3-methylimidazolium cation ([EMIm]$^+$) is well studied and tends to form low viscous liquids with a large number of anions.[9-11]

Tuning the ion-pair interactions in ILs is one of the important strategies adopted in the designing of new ionic liquids. The size of ions also has the control in regulating the properties of ILs ranging from ionic to molecular.[7] Lowering the melting point is directly related to lowering the viscosity of the ILs, which in turn is influenced by the electrostatic interaction forces between the ions in the salts.[12] Since these interactions are mostly electrostatic in nature, the strength of interaction decreases with increase in the local-minimum distance and this could be easily achieved by increasing the size of the ions. Thus large ions are of great interest in this particular aspect. Though, it is quite difficult to lower the viscosity of the ILs, large ions are certainly effective in lowering the melting temperature and viscosity.[13]

Compared to other all carbon allotropes, the discovery of C_{60} fullerene has transfigured the chemistry of carbon.[14-22] Maciel *et al.* studied solvation of the C_{60} in ionic liquids by molecular dynamics simulations and the spatial distributions revealed different patterns for the solvation of the C_{60}.[23] Later García *et al.* analysed the solvation of C_{60} fullerene by 24 different ionic liquids belonging to the imidazolium, piperazinium, and cholinium families using classic molecular dynamics simulations and density functional theory (DFT) methods.[24, 25] They extended the theoretical investigation to study the interaction of other carbon nanostructures with ionic liquids.[26, 27] In 2015 Campisciano *et al.* synthesized and characterized a series of fullerene–ionic-liquid hybrids in which the fullerene-malonate derivatives are synthesized and substituted with number of IL moieties to form new fullerene–ionic-liquid hybrids.[28] They also applied this new fullerene derivative-conjugate for the immobilization of palladium nanoparticles through ion exchange followed by reduction with sodium borohydride. Chaban *et al.* theoretically investigated the concept of solvating fullerenes using room-temperature ionic liquids (RTILs) which opened a new direction to obtain well-dispersed fullerene containing systems by comparing a range of common molecular solvents and novel ionic solvents to the RTIL, 1-butyl-3-methylimidazolium tetrafluoroborate ($[BMIm]^+[BF_4]^-$).[29] In another work they observed that the imidazolium ionic liquid helps to disperse fullerenes in water.[30] Both theoretical[31-35] and experimental[36-39] studies on endohedral[32, 40-43] as well as exohedral[14, 44, 45] modifications on the fullerene cage has been done to generate the new materials of interest. According to the DFT and Born–Oppenheimer molecular dynamics (BOMD) calculations by Ravinder and Subramanian, the stability of the endohedral fullerenes depends on the size of both the anion and the fullerene cage.[46] BOMD simulations by Chaban *et al.* suggested novel C_{60}–RTILs systems on the basis of the systematically positive effective electrostatic charge developed on the C_{60} fullerene *via* the electronic polarization on C_{60} fullerene by imidazolium-based RTILs.[47] They also studied the possibility of using fullerene-based systems for medicinal applications and CO_2 capture.[48, 49] Salehzadeh *et al.* also showed that the interaction energy of -62.5 to -79.2 kcal/mol for the encapsulation of halides within the fullerenes at the MP2/6-311++G** level.[50] As an extension to the study on the influence of the encapsulation of anion inside the C_{60} fullerene cage on its exohedral

reactivity, García-Rodeja *et al.* studied the Diels–Alder reaction between 1,3-cyclohexadiene and M@C_{60} (M= Li^+, Na^+, K^+, Be^{2+}, Mg^{2+}, Al^{3+}, and Cl^-).[51] They reported a significant enhancement in Diels–Alder reactivity for systems having an endohedral cation, whereas a decrease in reactivity is observed when an anion is encapsulated in the C_{60} cage. They also studied the Bingel Hirsch (BH) addition of ethyl bromomalonate over a series of ion encapsulated M@C_{60} (M= Li^+, Na^+, K^+, Mg^{2+}, Ca^{2+}, and Cl^-) and found that K^+@C_{60} is the one that leads to the fastest BH reaction, while Cl^-@C_{60} gave the slowest reaction.[52]

All the previous studies are either on the confinement of the encapsulated species inside the cage or on the binding interactions of the fullerene cage with the functional moieties. Though Campisciano *et al.* reported fullerene derivative incorporated IL, the use of fullerene systems either in the cationic or anionic form is not yet reported for the development of ILs. In a recent study using DFT methods, Suresh *et al.* have shown that anion encapsulated endohedral fullerenes behave as closed shell anions and are represented as (X@C_{60})$^-$.[53] Apart from the endohedral modifications on fullerenes, the exohedral changes also have influence on the chemical reactivity and properties of the C_{60} cage. The present study explores the idea that a large-sized anion, characterized by the spherical distribution of the negative charge could be effectively utilized for designing new ion-pair combinations to develop novel ILs. Here the interaction of the X-fullerides ((C_{60}X)$^-$) with imidazolium cation (IM$^+$) has been studied for X = H, F, Cl, Br, OH, CN, NH_2, and NO_2 and the feasibility of formation of such an anion⋯ cation complexes is also evaluated by modelling the transition state for the reaction between 1,3-dimethyl-2X-Imidazole (IMX) and C_{60}.

4.2.1 Computational methods

All the calculations have been carried out at the M06L/6-311++G**//M06L/6-31G** level of DFT[54-57] using the Gaussian 16 suite of programs[58]. The vibrational frequency analysis has been done to confirm the optimized geometries as true energy minima. Previous benchmark study reported that M06L method is a robust method for calculating the geometry and interaction energy of noncovalent dimers.[59] Further, recent

studies benchmarked some of the dispersion corrected methods[60, 61] for anionic fullerene systems and found that M06L is a reliable method.[53] The energy of the reaction between 1,3-dimethyl-2X-Imidazole (IMX) and C_{60} (E_{rea}) is calculated as

$$E_{rea} = E_2 - E_1 \qquad \text{(Eq. 4.1)}$$

where E_1 and E_2 stand for the zero-point energy (ZPE)-corrected energy of reactant complex ($C_{60}\cdots IMX$) and the product $(IM^+)\cdots(C_{60}X)^-$ ion-pair complex, respectively. The free energy (G_{rea}) associated with the reaction is also calculated in a similar fashion.

The ion-pair binding energy ($E_{ion\text{-}pair}$) is calculated as

$$E_{ion\text{-}pair} = E_2 - (E_3 + E_4) \qquad \text{(Eq. 4.2)}$$

where, E_3 and E_4 stand for the ZPE-corrected energy of $(C_{60}X)^-$ and IM^+, respectively. In the case of Cl^- and Br^-, $IM^+\cdots X^-$ ion-pair is found to interact noncovalently with C_{60} to form the $(IM^+\cdots X^-)\cdots C_{60}$ complex. Here the noncovalent interaction energy (E_{noncov}) of C_{60} with $IM^+\cdots X^-$ is calculated as

$$E_{noncov} = E_7 - (E_5 + E_6) \qquad \text{(Eq. 4.3)}$$

where E_5, E_6 and E_7 stand for the ZPE-corrected energy of C_{60}, $IM^+\cdots X^-$ and $(IM^+\cdots X^-)\cdots C_{60}$, respectively. The energy for dissociation (E_d) of each $(C_{60}X)^-$ into C_{60} and anion X^- is calculated as

$$E_d = (E_5 + E_8) - E_3 \qquad \text{(Eq. 4.4)}$$

where E_8 is the ZPE-corrected energy of the anion X^-. The free energy associated with the dissociation reaction (G_d) is also calculated in a similar fashion.

MESP analysis has been carried out to analyse the intermolecular interactions and charge delocalization in complexes.[62-64] Bader's quantum theory of atoms in molecules (QTAIM) analysis, based on the electron density (ρ) distribution is carried out using AIMAll package.

4.3   Results and discussion

The imidazolium cation is one of the most frequently encountered cationic species in ionic liquids. Here we look at the possibility of the reaction between neutral 1,3-dimethyl-2X-Imidazole (IMX) and C_{60} (Scheme 4.1), for X = H, F, Cl, Br, OH, CN, NH_2, and NO_2. Two possible outcomes of this reaction are shown in Scheme 4.1, *viz.* the formation of the ion-pair $IM^+\cdots(C_{60}X)^-$ or formation of the $(IM^+\cdots X^-)\cdots C_{60}$ complex.
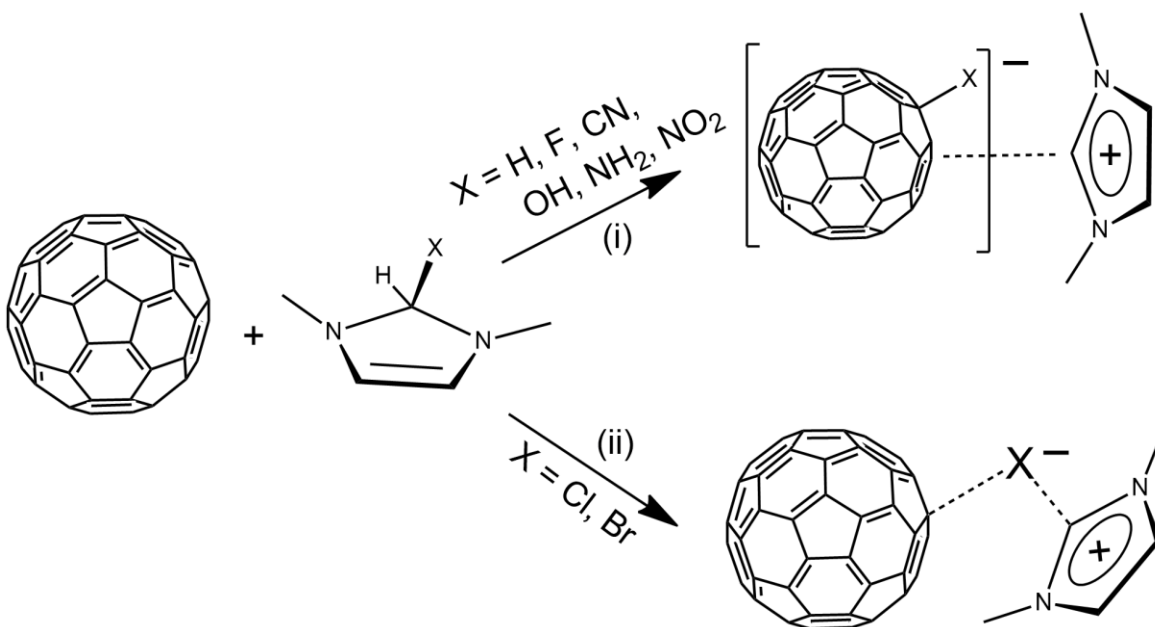
Scheme 4.1 Two possible outcomes of the reaction between IMX and C_{60}.

Among the different anions in this study, H^-, F^-, CN^-, OH^-, NH_2^- and NO_2^- are observed to follow the reaction pathway (i) while the anions Cl^- and Br^- follow the reaction pathway (ii). The X-fullerides $(C_{60}X)^-$ formed in pathway (i) shows C-X covalent bonding interaction and suggests that the anionic charge is delocalized over the whole carbon framework. Thus $(C_{60}X)^-$ can be considered as a large anion and it interacts with IM^+ for electrostatic stabilization to form the ion-pair $IM^+\cdots(C_{60}X)^-$. In $(IM^+\cdots X^-)\cdots C_{60}$, C_{60} interacts noncovalently with the ion-pair $IM^+\cdots X^-$.
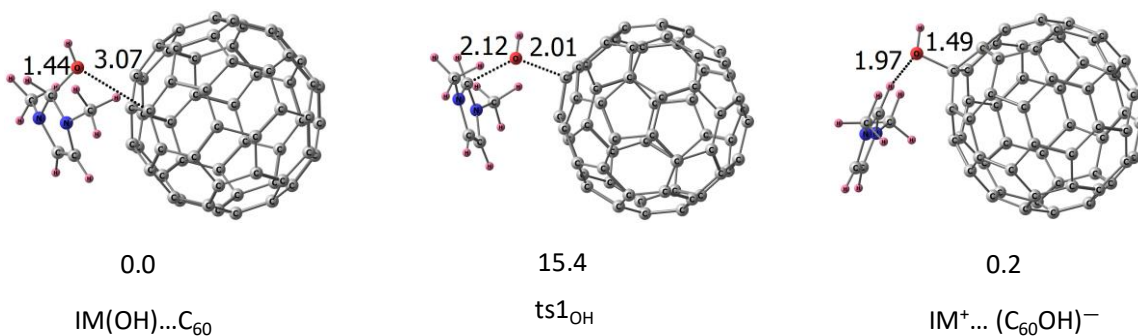
Figure 4.1 Optimized geometries of reactant, transition state and product for the reaction between IM(OH) and C_{60} at M06L/6-31G** level with their local-minimum distance in Å. Relative ZPE-corrected energies in kcal/mol at M06L/6-311++G**//M06L/6-31G** level are also depicted.
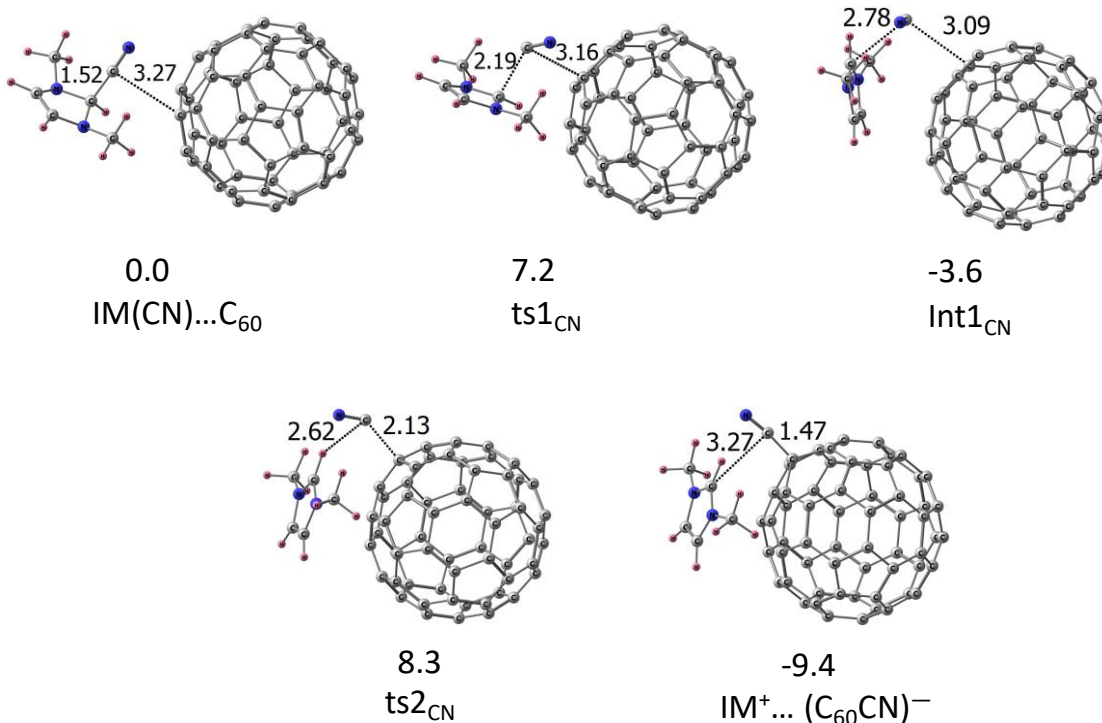
Figure 4.2 Optimized geometries of reactant, transition states and product for the reaction between IM(CN) and C_{60} at M06L/6-31G** level with their local-minimum distances in Å. Relative ZPE-corrected energies in kcal/mol at M06L/6-311++G**//M06L/6-31G** level is also depicted.

Optimized geometries of reactant complex, transition state and product of a representative case (X = OH) for pathway (i) is given in Figure 4.1. Here the binding energy for the van der Waals complex IM(OH)···C_{60} is 7.7 kcal/mol and it passes through the transition state ts1$_{OH}$ to yield the ion-pair complex IM$^+$···(C_{60}OH)$^-$. The structure of ts1$_{OH}$ shows the C-OH bond breaking of IMX at 2.12 Å as well as the initiation of C-OH bond formation on fullerene at 2.01 Å. The E_{rea} for IM$^+$···(C_{60}OH)$^-$ formation is 0.2 kcal/mol, slightly endothermic, and requires the activation energy (E_{act}) 15.4 kcal/mol which is surmountable at room temperature.

Table 4.1 ZPE-corrected $E_{ion-pair}$, $G_{ion-pair}$, E_{rea}, G_{rea} E_{act} and G_{act} values (kcal/mol) of IM$^+$(C_{60}X)$^-$ systems at the M06L/6-311++G**//M06L/6-31G** level.

System	$E_{ion-pair}$	$G_{ion-pair}$	E_{rea}	G_{rea}	E_{act}	G_{act}
IM$^+$···(C_{60}H)$^-$	-64.0	-52.1	-0.03	1.1	11.8	14.5
IM$^+$···(C_{60}F)$^-$	-71.8	-59.1	0.3	3.1	4.7	6.1
IM$^+$···(C_{60}OH)$^-$	-72.0	-58.9	0.2	2.3	15.4	16.7
IM$^+$···(C_{60}CN)$^-$	-69.6	-57.1	-9.4	-7.9	11.9	14.7
IM$^+$···(C_{60}NH$_2$)$^-$	-73.0	-61.3	-0.6	0.5	24.7	27.9
IM$^+$···(C_{60}NO$_2$)$^-$	-71.0	-57.7	8.8	12.4	7.0	11.9

Figure 4.2 shows the energy profile for the reaction between C_{60} and IM(CN) which is slightly different from that of C_{60} and IM(OH) as it takes place in two steps. Here the C-CN distance 3.62 Å in ts1$_{CN}$ suggests that a fully cleaved CN$^-$ from IMX will be reacting on C_{60} through the formation of an intermediate, Int1$_{CN}$. In Int1$_{CN}$, the C_{60}···CN and IM···CN distances are 3.09 and 2.78 Å, respectively. In the second step, the C_{60}-CN bond formation occurs by passing through the transition state ts2$_{CN}$ wherein the C-CN distance is 2.13 Å. The ts1$_{CN}$ suggests E_{act} 7.2 kcal/mol for the formation of Int1$_{CN}$ at -3.6 kcal/mol while ts2$_{CN}$ requires E_{act} 11.9 kcal/mol to yield the product. The intermediate

Int1$_{CN}$ can be represented as (IM$^+$···CN$^-$)···C$_{60}$. The product IM$^+$···(C$_{60}$CN)$^-$ formation is exothermic by 9.4 kcal/mol. The energetic parameters including the free energy parameters are given in Table 4.1.

Optimized structures of IM$^+$···(C$_{60}$X)$^-$ ion-pairs for X = H, F, NH$_2$, and NO$_2$ are given in Figure 4.3, along with the local-minimum distances. The first four structures show covalent bond formation between C$_{60}$ and X which is evident from the C-H, C-F, C-NH$_2$ and C-NO$_2$ distances 1.11, 1.55, 1.51, 1.68 Å, respectively whereas the nearest distance from X to IM$^+$ indicates either a weak noncovalent interaction (for X = H) or a hydrogen bond interaction as observed in the previous cases of X = OH or CN. All these ion-pairs have E$_{ion\text{-}pair}$ value ranging from -64.0 to -73.0 kcal/mol (Table 4.1).

IM$^+$... (C$_{60}$H)$^-$ **IM$^+$... (C$_{60}$F)$^-$** **IM$^+$... (C$_{60}$NH$_2$)$^-$**

IM$^+$... (C$_{60}$NO$_2$)$^-$ **(IM$^+$...Cl$^-$)...C$_{60}$** **(IM$^+$...Br$^-$)...C$_{60}$)**
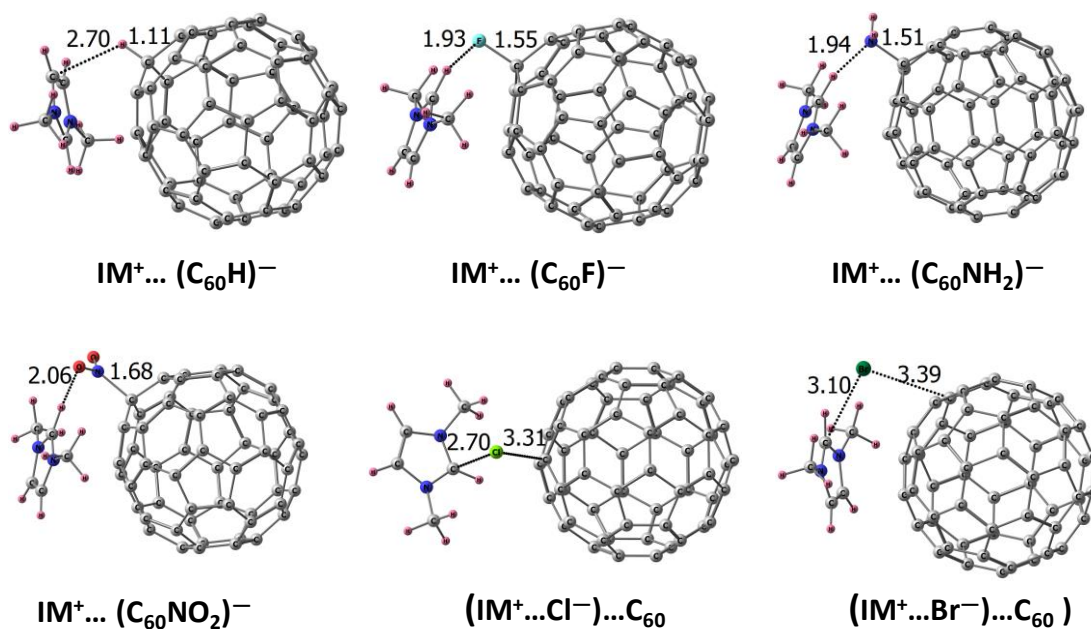
Figure 4.3 Optimized geometries of the IM$^+$···(C$_{60}$X)$^-$ ion-pairs for X = H, F, NH$_2$, NO$_2$, Cl, and Br at M06L/6-31G** level with their local-minimum distances (Å).

For Cl$^-$ and Br$^-$, the IMX compound itself exists as ion-pair IM$^+$···X$^-$. The IM$^+$···X$^-$ ion-pair interacts weakly with C$_{60}$ to form the noncovalent (IM$^+$···X$^-$)···C$_{60}$ complexes (Figure 4.3). This is reflected in the large local-minimum distance between C$_{60}$ and IM$^+$···X$^-$, *viz.* 3.31 Å and 3.39 Å for X = Cl and X = Br, respectively. E$_{noncov}$ observed for C$_{60}$

with IM$^+$···Cl$^-$ and IM$^+$···Br$^-$ is -9.3 and -9.9 kcal/mol, respectively. Also note that in (IM$^+$···X$^-$)···C$_{60}$, the interaction energy between IM$^+$ and (X$^-$···C$_{60}$) is -82.4 and -80.2 kcal/mol for X = Cl and X = Br, respectively.

4.3.1 MESP features

Figure 4.4 represents the MESP mapped on the isodensity surface 0.01 au for C$_{60}$, C$_{60}^{\bullet-}$, and X-fullerides. The dark blue pattern observed for MESP of C$_{60}^{\bullet-}$ and X-fullerides indicates very similar electron rich nature of the carbon framework while the pale green surface seen for C$_{60}$ indicates relatively high electron deficiency.

-0.9	-63.4	-72.2	-93.3 -68.1	-103.5 -71.4
C$_{60}$	C$_{60}^{\bullet-}$	(C$_{60}$H)$^-$	(C$_{60}$F)$^-$	(C$_{60}$OH)$^-$

-101.2 -70.7	-116.5 -71.5	-95.8 -65.8	-119.5 -50.8	-105.3 -51.6
(C$_{60}$CN)$^-$	(C$_{60}$NH$_2$)$^-$	(C$_{60}$NO$_2$)$^-$	Cl$^-$...C$_{60}$	Br$^-$...C$_{60}$
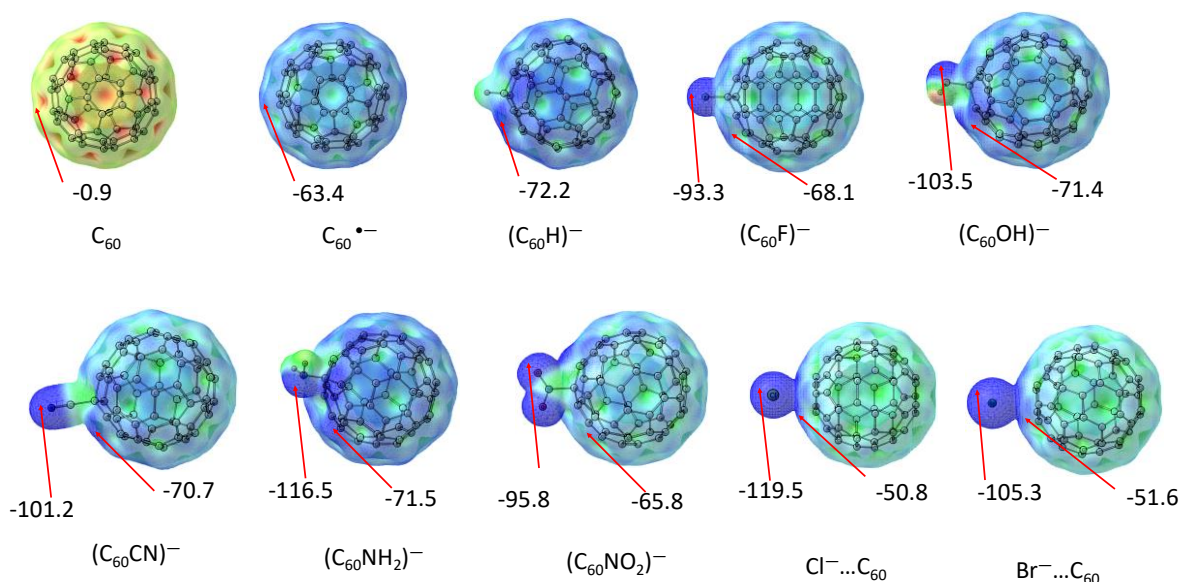
Figure 4.4 MESP topographic plots for the exohedral fullerides at the M06L/6-311++G**//M06L/6-31G** level with the V_{m1} (kcal/mol) on the right side and V_{m2} (kcal/mol) left side at isosurface value = 0.01 au.

Further, a quantification of the MESP feature is available from the most negative MESP value (V_{min}) on the fullerene cage (V_{m1}) as well as from the most negative MESP value on the X group (V_{m2}). The V_{m1} of (C$_{60}$X)$^-$ species (X = H, F, CN, OH, NH$_2$ and NO$_2$) lies in the range -65.8 to -72.2 kcal/mol and that of Cl$^-$···C$_{60}$ and Br$^-$···C$_{60}$ is -50.8 and -51.6 kcal/mol, respectively (Table 4.2). The magnitude of V_{m1} of (C$_{60}$X)$^-$ is higher than that of C$_{60}^{\bullet-}$ which suggests that the carbon cage of X-fulleride would behave as an electron rich

anionic cage. On the basis of the magnitude of V_{m1}, the anionic nature of the X- fulleride can be assessed[65] as $(C_{60}H)^- > (C_{60}NH_2)^- > (C_{60}OH)^- > (C_{60}CN)^- > (C_{60}F)^- > (C_{60}NO_2)^-$. The strength of the C-X bond of the fulleride can be acertained from C-X dissociation energies (Table 4.2) the is found to be proportional to the anionic character of the fulleride (Figure 4.5).

Table 4.2 Most negative MESP values and dissociation energetics in kcal/mol for exohedral fullerides at M06L/6-311++G**//M06L/6-31G** level.

System	V_{m1}	V_{m2}	E_d	G_d
$(C_{60}H)^-$	-72.2	-	97	90.9
$(C_{60}F)^-$	-68.1	-93.3	56.8	48.7
$(C_{60}OH)^-$	-71.4	-103.5	73.5	64.5
$(C_{60}CN)^-$	-70.7	-101.2	48.3	38
$(C_{60}NH_2)^-$	-71.5	-116.5	86.5	76.4
$(C_{60}NO_2)^-$	-65.8	-95.8	33.5	22.4
$Cl^-\cdots C_{60}$	-50.8	-119.5	24.4	18.8
$Br^-\cdots C_{60}$	-51.6	-105.3	22.7	16.7

The V_{m2} value indicates the nature of the negative MESP around the lone pair bearing X group in $(C_{60}X)^-$ as X = H is devoid of such a minimum. If X^- alone is analyzed for V_m data one may notice that the observed values, viz. -188.4, -240.3, -186.0, -241.5, -237.6, and -186.4, for X = H, F, CN, OH, NH2 and NO2, respectively is much more negative (~54%) than the V_{m2} observed for the corresponding $(C_{60}X)^-$, while a deviation of an average 31% is observed in the V_m data of X = Cl and Br. This feature supports that the excess electron in the system is delocalized over the entire carbon cage of the X-fulleride and it would behave as a large spherical anion. A negative-valued MESP isosurface engulfing the whole carbon cage has been located in each X-fulleride (Figure 4.6) which also illustrates the anionic character of the carbon cage. [62, 66]
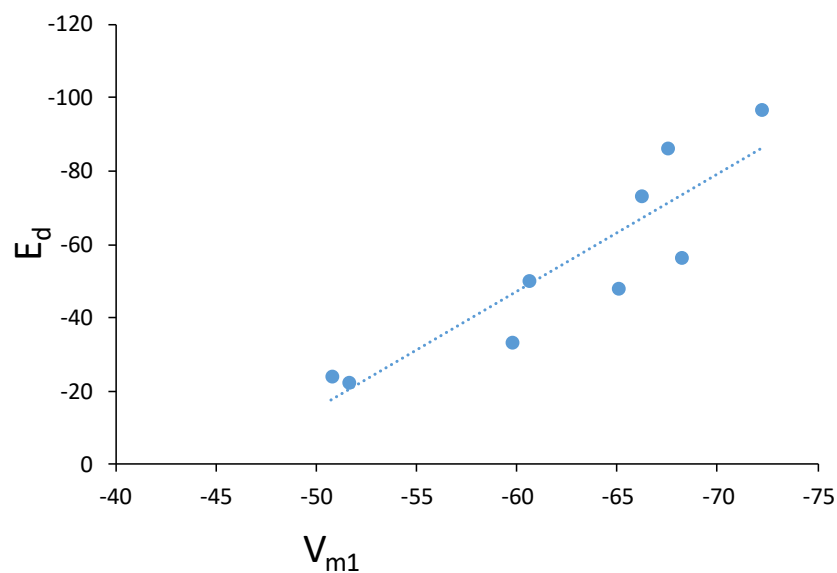
Figure 4.5 Correlation between V_{m1} (kcal/mol) and E_d (kcal/mol) of exohedral fullerides at the M06L/6-311++G**//M06L/6-31G** level.

$(C_{60}H)^-$	$(C_{60}F)^-$	$(C_{60}OH)^-$	$(C_{60}CN)^-$
-0.0645	-0.0802	-0.0602	-0.0782

$(C_{60}NH_2)^-$	$(C_{60}NO_2)^-$	$Cl^-...C_{60}$	$Br^-...C_{60}$
-0.0575	-0.0770	-0.1126	-0.0853
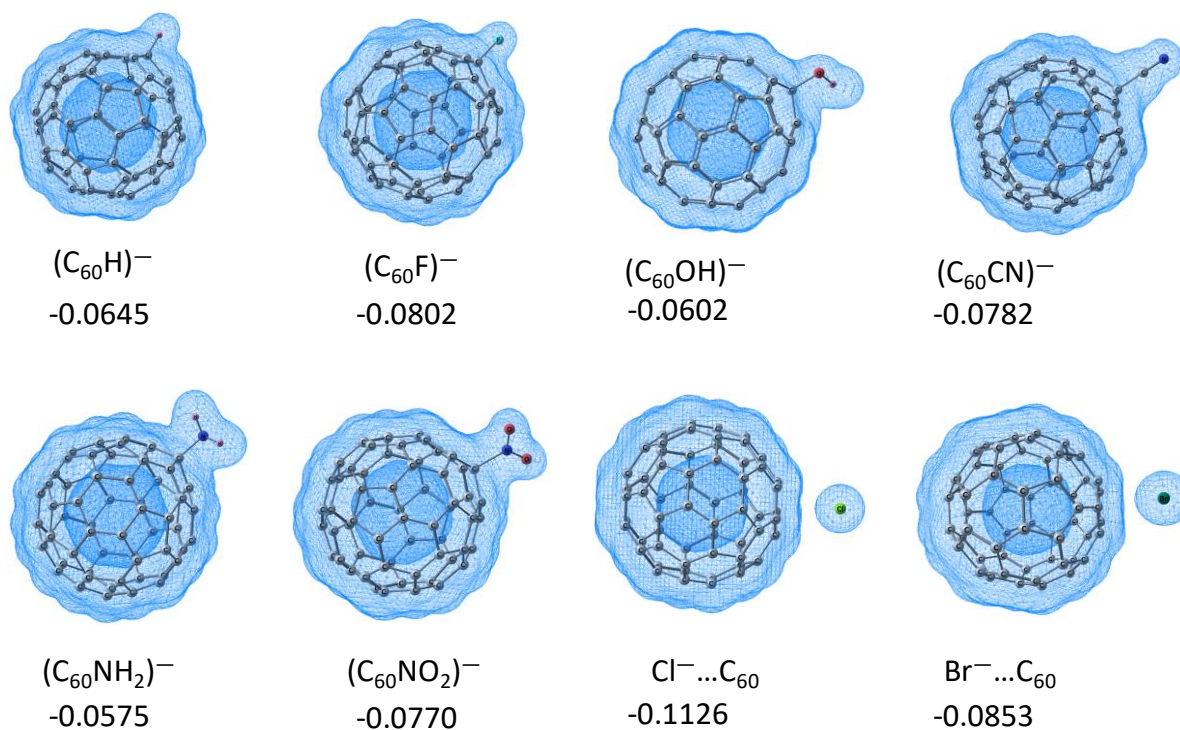
Figure 4.6 MESP of exohedral fullerides that engulfs the whole anion at M06L/6-311++G**//M06L/6-31G** level. The value of the MESP surface that engulfs the whole anion is also depicted in au.

4.3.2 Energy minimum structures of $IM^+\cdots(C_{60}X)^-$ ion-pair

The $IM^+\cdots(C_{60}X)^-$ ion-pair systems (X = H, F, CN, OH, NH$_2$ and NO$_2$) show multiple energy minima wherein the location of cation is nearly randomized. This indicates that anionic character is distributed all over the carbon framework of the fulleride and the cation could approach to the anion from any direction for a substantial stabilization. A representative case of $IM^+\cdots(C_{60}OH)^-$ ion-pair is given in Figure 4.7. Among these structures, IM^+ located close to the 'OH' region of the $(C_{60}OH)^-$ is found to be the most stable (structure i), with the ion-pair energy of -72.0 kcal/mol. Also the least stable structure is the one showing the farthest distance between OH region and cation (structure v) having the ion-pair energy of -59.0 kcal/mol. The energy difference between the two extreme structures is 13.0 kcal/mol.

-72.0	-71.2	-68.3
(i)	(ii)	(iii)

-59.9	-59.0
(iv)	(v)
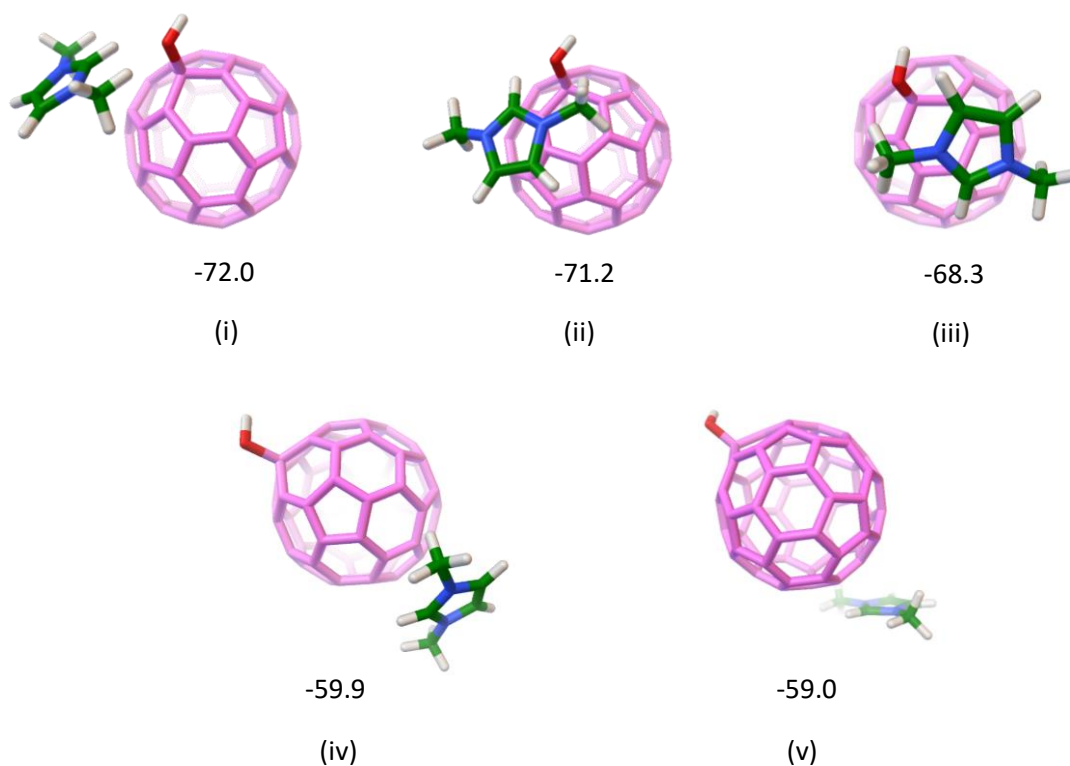
Figure 4.7 Geometries of $IM^+\cdots(C_{60}OH)^-$ ion-pair optimized at the M06L/6-31G** level with IM^+ at various positions around the fullerene cage. ZPE-corrected ion-pair binding energies in kcal/mol is also depicted.
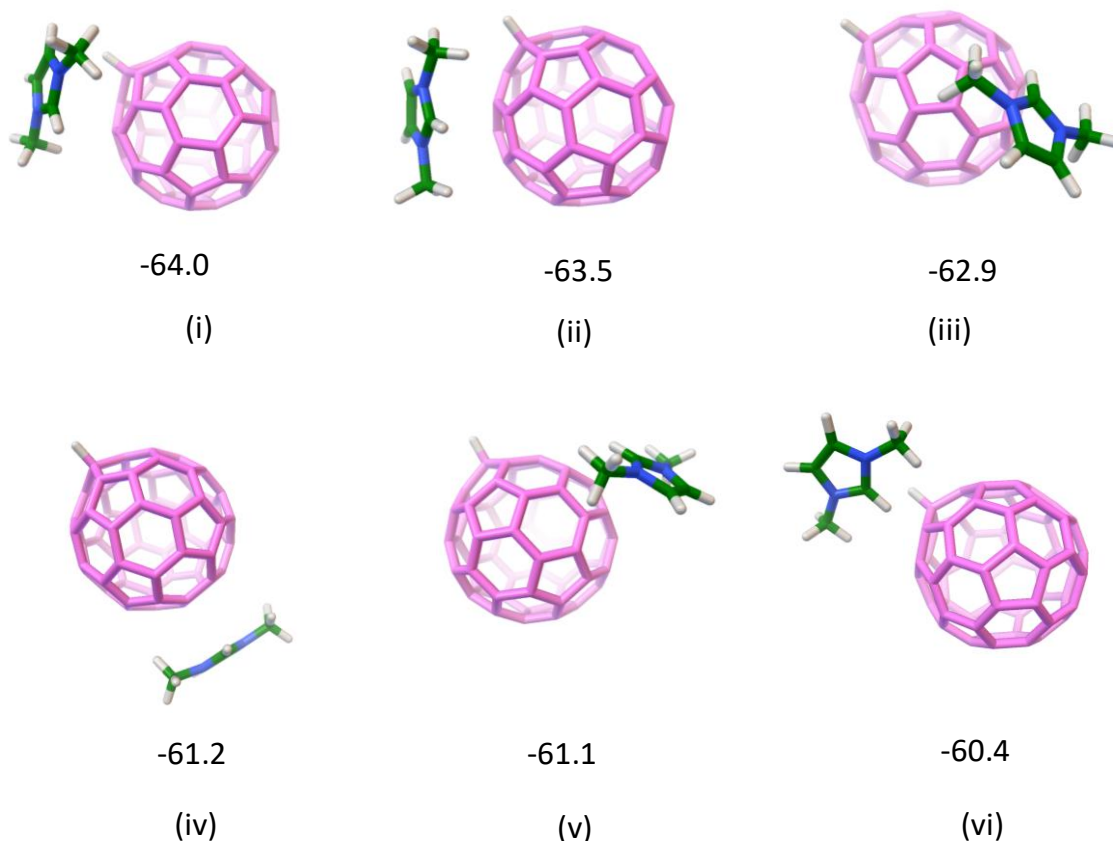
Figure 4.8 Geometries of $IM^+\cdots(C_{60}H)^-$ ion-pair optimized at the M06L/6-31G** level with IM^+ at various positions around the fullerene cage. ZPE-corrected ion-pair binding energies in kcal/mol is also depicted.

Another representative example $IM^+\cdots(C_{60}H)^-$ ion-pair shows six local minima wherein IM^+ is located at various positions around the fullerene cage. Here also the interaction is observed to be the best when IM^+ is facing the cage from the direction of H (structure (i) in Figure 4.8) which is 3.6 kcal/mol superior in ion-pair binding than the least stable structure (vi). The positioning of the cation on the fullerene cage is very random and such energetically close lying multiple minima indicates smooth delocalization of the anionic charge. Also such minima suggest that the movement of the cation from one minimum position to another is nearly barrier less and the whole potential energy surface would behave like a slippery one. The presence of different minima has been identified in other $IM^+\cdots(C_{60}X)^-$ ion-pair systems as well. This slippery nature of the ion-pair interactions makes the $IM^+\cdots(C_{60}X)^-$ complexes a suitable

candidate for developing ILs for lubricant applications. The viscous nature of the ILs owing to the large spherical nature of the anion also supports ability of the ILs to act as lubricants.

4.3.3 QTAIM features

The electron densities at BCPs (ρ_b), Laplacian ($\nabla^2 \rho_b$), and total electron energy density (H_b) obtained from the QTAIM analysis are used to analyse the C-X interaction in $(C_{60}X)^-$. For X = H, F, CN, OH, NH$_2$ and NO$_2$, ρ_b value in the range of 0.1636 to 0.2592 au and negative $\nabla^2\rho_b$ and H_b values are observed for the C-X interaction in $(C_{60}X)^-$ indicating the covalent character of their C-X bonding interaction. The ρ_b values of 0.0093 au and 0.0092 au, respectively for X = Cl and Br along with positive $\nabla^2\rho_b$ and H_b values and suggests weak noncovalent nature of the C...X interaction in $(IM^+ \cdots X^-) \cdots C_{60}$ complexes. The QTAIM plots of the complexes and their QTAIM data are given in Figure 4.9 and Tables 4.3 & 4.4.

Table 4.3 QTAIM parameters (au) of exohedral fullerides at the M06L/6-311++G**//M06L/6-31G** level.

System	Bond	ρ_b	$\nabla^2 \rho_b$	H_b
$(C_{60}H)^-$	C-H	0.2651	-0.8441	-0.2557
$(C_{60}F)^-$	C-F	0.2131	-0.1983	-0.2463
$(C_{60}OH)^-$	C-O	0.2423	-0.4899	-0.2949
$(C_{60}CN)^-$	C-C	0.2600	-0.6755	-0.2459
$(C_{60}NH_2)^-$	C-N	0.2542	-0.6226	-0.2583
$(C_{60}NO_2)^-$	C-N	0.1777	-0.1957	-0.1241
$(C_{60}Cl)^-$	C...Cl	0.0125	0.0448	0.0022
$(C_{60}Br)^-$	C...Br	0.0152	0.0471	0.0018

| (C_{60}H)^- | (C_{60}F)^- | (C_{60}OH)^- | (C_{60}CN)^- |

| (C_{60}NH_2)^- | (C_{60}NO_2)^- | Cl^-...C_{60} | Br^-...C_{60} |
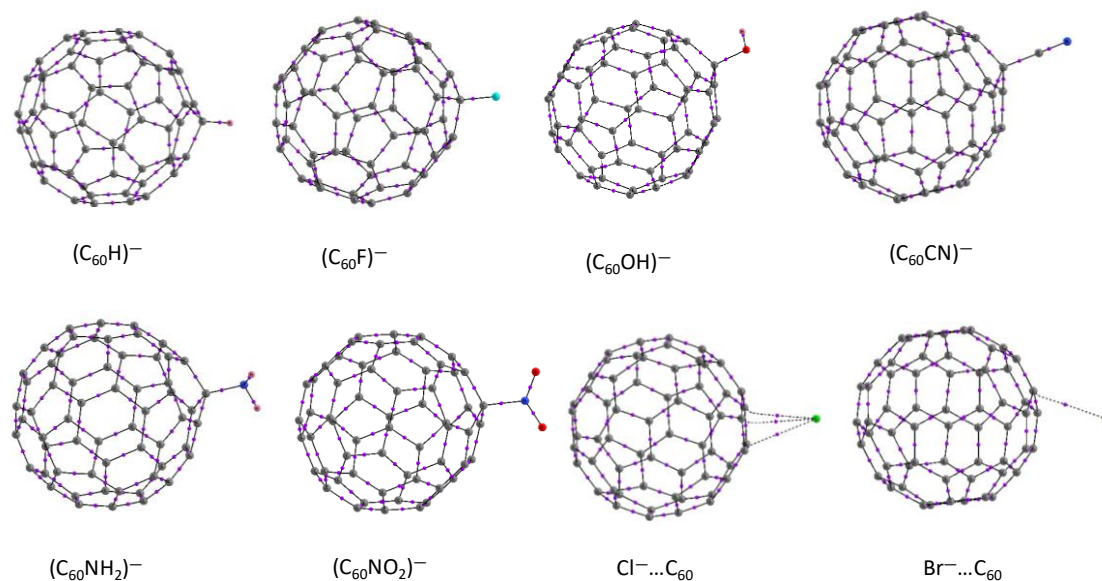
Figure 4.9 QTAIM plots of exohedral fulleride.

Table 4.4 QTAIM parameters (au) of $IM^+\cdots(C_{60}X)^-$ systems at the M06L/6-311++G**//M06L/6-31G** level.

System	Bond	ρ_b	$\nabla^2 \rho_b$	H_b
$IM^+\cdots(C_{60}H)^-$	C-H	0.2627	-0.8293	-0.2526
$IM^+\cdots(C_{60}F)^-$	C-F	0.1636	-0.0260	-0.1229
$IM^+\cdots(C_{60}OH)^-$	C-O	0.2193	-0.3854	-0.2422
$IM^+\cdots(C_{60}CN)^-$	C-C	0.2592	-0.6719	-0.2502
$IM^+\cdots(C_{60}NH_2)^-$	C-N	0.2419	-0.5631	-0.2411
$IM^+\cdots(C_{60}NO_2)^-$	C-N	0.1647	-0.1388	-0.1074
$(IM^+\cdots Cl^-)\cdots C_{60}$	C$\cdots$Cl	0.0093	0.0295	0.0387
$(IM^+\cdots Br^-)\cdots C_{60}$	C$\cdots$Br	0.0092	0.0290	0.0382

4.3.4 Benchmark study

To analyze the influence of dispersion effects on the ion-pair interactions we also carried out a benchmark study on the $IM^+\cdots(C_{60}X)^-$ complexes, using dispersion included methods, *viz.* wB97XD, BP86-D3, M06-2X, and B3LYP-D3, in conjunction with basis set 6-311++G**. The $E_{ion-pair}$ data computed using these methods are compared with M06L/6-311++G** data in Table 4.5. All these dispersion methods give similar trend in the $E_{ion-pair}$ values. The intrinsic dispersion effects integrated within M06L gives results similar to that methods with the dispersion correction, with a slight deviation of 0 - 4 kcal/mol.

Table 4.5 $E_{ion-pair}$ (kcal/mol) for $IM^+\cdots(C_{60}X)^-$ complexes using different methods in conjunction with basis set 6-311++G**.

System	wB97XD	BP86-D3	M06-2X	M06L	B3LYP-D3	B3LYP
$IM^+\cdots(C_{60}H)^-$	-68.3	-68.6	-65.7	-64.5	-66.0	-53.9
$IM^+\cdots(C_{60}F)^-$	-75.7	-76.1	-72.8	-72.8	-73.9	-61.7
$IM^+\cdots(C_{60}OH)^-$	-76.1	-76.2	-74.2	-73.3	-73.9	-61.6
$IM^+\cdots(C_{60}CN)^-$	-74.3	-73.9	-71.9	-70.5	-71.5	-58.3
$IM^+\cdots(C_{60}NH_2)^-$	-78.3	-77.5	-75.6	-73.9	-75.0	-62.4
$IM^+\cdots(C_{60}NO_2)^-$	-75.3	-75.3	-73.8	-71.8	-73.1	-59.1

Further, the influence of dispersion effects is brought out from the $E_{ion-pair}$ values calculated at B3LYP/6-311++G** level – a method without any dispersion correction. At this level the $E_{ion-pair}$ ranges from -53.9 to -62.4 kcal/mol, which is ~15 -20% kcal/mol lower than that observed for the dispersion included methods. The high dispersion effect also supports the charge delocalization involved in the interaction between the X-

fullerides and IM^+. ILs based on conjugated rings or bulkier anions with multiple noncovalent interaction sites are also expected to have a significant contribution from dispersion forces to their $E_{ion\text{-}pair}$ values that clearly influence their thermodynamic and transport properties.[67] The theoretical studies by Bernard *et al.* have illustrated that the ratio of total ion-pair binding energy and its dispersion energy component correlates well with the melting point of IL.[3] The $E_{ion\text{-}pair}$ values for the $IM^+\cdots(C_{60}X)^-$ complexes are significantly lower in magnitude than that observed for the ion-pairs of imidazolium-based ILs reported in the literature, *viz.*, -80.6, -87.3, -96.3, and -96.9 kcal/mol for $[EMIm]^+[trz]^-$, $[EMIm]^+[dc]^-$, $[EMIm]^+[dtrz]^-$, and $[EMIm]^+[NH_2tz]^-$, respectively.[68] The lower $E_{ion\text{-}pair}$ values observed for $IM^+\cdots(C_{60}\,X)^-$ as well as the significant dispersion contribution to the interaction suggest that these ion-pairs are expected to result in the formation of one of lowest melting category of ILs.[3, 67]

4.4 Conclusion

DFT analysis of the reaction between C_{60} and IMX, studied at M06L/6-311++G**//M06L/6-31G** level has shown the facile formation of $IM^+\cdots(C_{60}X)^-$ ion-pair for X = H, F, OH, CN, NH_2, and NO_2. The reaction showed exothermic character for X = H, CN, and NH_2 while X = F, OH, and NO_2 showed endothermic character. Also among all the reactions studied, high exergonic nature is observed for X = CN. The energetics of the reaction strongly support the possibility of the development of X-fulleride-based $IM^+\cdots(C_{60}X)^-$ ion-pair systems. Such systems are characterized by significantly lower $E_{ion\text{-}pair}$ values than that of the ion-pairs of known ionic liquids.[68] For X = Cl and Br, fulleride formation is not observed as the system remained in the noncovalent state, $(IM^+\cdots X^-)\cdots C_{60}$. The benchmark study using different DFT methods, *viz.* wB97XD, BP86-D3, M06-2X, B3LYP-D3, and B3LYP has shown that the results derived using M06L method are reliable. The MESP analysis of all the $(C_{60}X)^-$ complexes has shown that the excess electron in the system is no longer concentrated on X, but distributed almost evenly over the whole carbon cage. This analysis also supports that the anionic character on X is transferred to the whole fullerene cage and the X-fulleride system $(C_{60}X)^-$ would behave as a large anion. Unlike $(C_{60}{}^{\bullet-})$ anion, the closed shell system $(C_{60}X)^-$ is expected

to be stable for developing novel ILs. Further, the anionic nature of the carbon cage is found to be increasing with increase in the strength of the C-X covalent bonding interaction. This bonding assures that the pi-space of the unsaturated 59 carbon atoms is defined by sixty electrons.

The identification of many local minimum structures in a narrow energy range for $IM^+\cdots(C_{60}X)^-$ ion-pair indicates a slippery potential energy surface for the system which also supports that such large spherical anions are useful for the development of highly viscous ILs.[8, 69] As per the study by Bernard *et al.*, the low magnitude of $E_{ion\text{-}pair}$ and its high dispersion contribution propose the formation low melting IL for imidazolium-based X-fulleride $IM^+\cdots(C_{60}X)^-$ systems. We predict that such ILs would show properties suitable for designing novel lubricants, halogen-free green ILs and low melting materials for space applications.[70-74]

Part B: Polyanionic Cyano-fullerides for CO_2 Capture

4.5 Abstract

The reaction of C_{60} fullerene with 'n' molecules (n = 1 to 6) of 1,3-dimethyl-2,3-dihydro-2-cyano-imidazole (IMCN) results in the exothermic formation of imidazolium cation-polyanionic fulleride complexes, $(IM^+)_n \cdots ((C_{60}(CN)_n)^{n-})$. The binding energy of IM^+ with $(C_{60}(CN)_n)^{n-}$ in the imidazolium-fulleride ionic complexes increased from -69.6 kcal/mol for n = 1 to -202.9 kcal/mol for n = 6. The energetics of the complex formation and cation-anion interaction energy data suggest the formation of imidazolium-fulleride ionic liquid (IL) systems. Further, the dimer formation of such ionic complexes showed more endergonic nature due to multiple cooperative electrostatic interactions between oppositely charged species and suggested improved energetics for higher order clusters. The molecular electrostatic potential (MESP) analysis has revealed that the extra 'n' electrons in the ionic complex as well as that in the bare $(C_{60}(CN)_n)^{n-}$ are delocalized mainly on the unsaturated carbon centers of the fullerene unit while the CN groups remain as a neutral unit. The MESP minimum (V_{min}) values of $(C_{60}(CN)_n)^{n-}$ on the carbon cage have shown that addition of each CN^- unit on the cage enhances the negative character of V_{min} by ~54.7 kcal/mol. This enhancement in MESP is comparable to the enhancement observed when one electron is added to C_{60} to produce $C_{60}^{\bullet-}$ (-62.5 kcal/mol) and suggests that adding 'n' CN^- groups to fullerene cage is equivalent to supplying 'n' electrons to the carbon cage. Also the high capacity of fullerene cage to hold several electrons can be attributed to the spherical delocalization of them on to the electron deficient carbon cage. The interactive behavior of CO_2 molecules with $(IM^+)_n \cdots (C_{60}(CN)_n)^{n-}$ systems showed that the interaction becomes stronger from -2.3 kcal/mol for n = 1 to -18.6 kcal/mol for n = 6. From the trianionic fulleride onwards, the $C \cdots CO_2$ noncovalent (**nc**) interaction changes to $C–CO_2$ covalent (**c**) interaction with the

development of carboxylate character on the adsorbed CO_2. These results prove that cyano-fullerides are promising candidates for CO_2 capture.

4.6   Introduction

Besides the amine scrubbing,[75, 76] contemporary research on CO_2 capture focuses on adsorption using dry adsorbent systems. Adsorption is a separation technology with the potential to reduce the cost of post-combustion capture (PCC).[77] The process of capturing CO_2 using a dry adsorbent involves selective separation of CO_2 based on gas–solid interactions. In general, universal dry adsorbents such as activated carbons and molecular sieves are used in packed columns.[78] Though metal organic frameworks (MOFs) have emerged as solid CO_2 adsorbent materials due to their tunable chemical and physical properties, still there is a growing interest for metal free carbon-based/nitrogen-rich materials for gas adsorption.[79-86] Carbon-based nanomaterials such as fullerene, carbon nanotubes, graphene, and hetero-fullerenes[87] offer excellent thermal and chemical stability as CO_2 adsorbents.[88-90] Fullerenes, the class of hollow-spherical molecules comprising of only C atoms varying in number,[91] exhibit low reduction potentials and strong electron acceptor properties.[92, 93] Matile *et al.* have shown that the MESP surface of C_{60} is overall positive with highly localized areas of positive potential, a bit like the dimples on a golf ball.[94, 95] Zhang *et al.* have shown that the inner cavities of many fullerenes and carbon nanotubes are the regions of positive electrostatic potential, and are electron-withdrawing in character.[19] Many theoretical[96, 97] and experimental[98-100] studies have been carried out on endohedral[101-103] as well as exohedral[91, 104, 105] modifications on the fullerene cage. In the case of endohedral fullerenes, the encapsulated species influence the reactivity. Apart from these endohedral modifications on fullerenes the exohedral changes also have influence on the chemical reactivity and properties of the C_{60} cage.[106, 107] Their electronic properties such as the complexation energy, ionization potentials, and the stability concerning internal electron transfer can be determined by the electrostatic potential at the cage center.[108]

Fullerene based systems have been used as adsorbent for various gases. B. Gao *et al.*[109] studied CO_2 adsorption on calcium decorated C_{60} fullerene and F. Gao *et*

al.[110] studied O_2 adsorption on nitrogen-doped fullerene. Sun *et al.* showed that chemical interactions between boron–carbon nanotubes (B₂CNT) and CO_2 can be enhanced by introducing extra electrons to the system.[88,111] They explained that the enhanced interactions are due to the Lewis acidity of CO_2, which prefers to accept electrons. Further, Jiao *et al.* proved the enhanced interaction of CO_2 with adsorbent materials by electron injection.[112] de Silva *et al.* investigated the CO_2 adsorption on BC_{59} fullerene and showed that negatively charged BC_{59} fullerene exhibits a stronger interaction with CO_2 than the neutral BC_{59} fullerene.[113] For neutral BC_{59} fullerene the interaction with CO_2 molecule was physical which changed to a substantial chemical interaction with CO_2 in the case of charged BC_{59}. In 2016 Ralser *et al.* have shown, both experimentally and theoretically, that the adsorption of CO_2 is sensitive to charge on a capturing carbonaceous surface model.[114] Very recently Wang *et al.* proposed a design of the graphene/ionic liquid (GIL) composite materials for gas separation by opening up the interlayer space between graphene sheets by intercalated ions of different sizes.[115] Their density functional theory (DFT) and Monte Carlo simulations suggested a new strategy to achieve tunable pore sizes via the graphene/IL composites for highly selective CO_2/N_2 and CO_2/CH_4 adsorption.

Our recent studies have shown the anionic nature of endohedral as well as exohedral fullerides and their strong η^5 coordinating ability.[116, 117] Another very recent study from us has revealed the formation of X-fulleride based ionic liquids (ILs) from the reaction of 1,3-dimethyl-2X-Imidazole (IMX) and C_{60} to give $IM^+\cdots(C_{60}X)^-$ ion-pair complexes for X = H, F, OH, CN, NH₂, and NO₂.[118] The ion-pair binding energies obtained for these complexes were in the range of -64.0 to -73.0 kcal/mol, which is significantly lower than the known imidazolium-based ILs. Herein, we propose the formation of polyanionic fullerides and their ionic complexes with imidazolium cations (IM^+).

Recently Lawrence *et al.* has reported the synthesis of hexaanionic fulleride complex {(^{Ar}nacnac)Mg}₆(C_{60})$^{6-}$ wherein ^{Ar}nacnac represents a bidentate ligand HC(MeCNAr)₂ for various Ar, *viz.* 2,6-iPr₂C₆H₃, 2,6-Et₂C₆H₃, 2,4,6-Me₃C₆H₂, and 2,6-Me₂C₆H₃.[119] This study also provided strong theoretical support to the formation of the hexaanion (C_{60})$^{6-}$ as a cation-π complex formed with six (^{Ar}nacnac)Mg$^+$. The hexaanion is

formed as a result of the electron transfer from the ligated Mg to C_{60}. In the present approach, we are investigating a reaction leading to the breakup of IMCN as IM^+ and CN^- and the subsequent transfer of the CN^- to the carbon cage of C_{60} through a covalent bond formation. Essentially, this reaction also transfers one electron to the fullerene cage when one CN^- is added to it. The electronic structure of the polyanionic fullerides are investigated using the MESP analysis. Further, these ionic complexes have been analyzed for their application in CO_2 capture.

4.6.1 Computational methods

All calculations have been carried out at the M06L/6-311++G**//M06L/6-31G** level of DFT using the Gaussian 16 suite of programs.[58] The vibrational frequency analysis has been done to confirm the optimized geometries as the energy minima. The M06L is regarded as a robust DFT method in overall performance for the optimization of organometallic, inorganic systems and for the study of noncovalent interactions especially for moderate-sized and large systems. [54, 55, 59, 66] A recent benchmark study from our group has shown the accuracy of this method in calculating the interaction energy of anionic fullerene systems for Grimme's dispersion correction.[60, 61, 118] The reaction of 'n' times 1,3-dimethyl-2,3-dihydro-2-cyano-imidazole (IMCN) with C_{60} yields the ion pair complex $(IM^+)_n \cdots (C_{60}(CN)_n)^{n-}$.
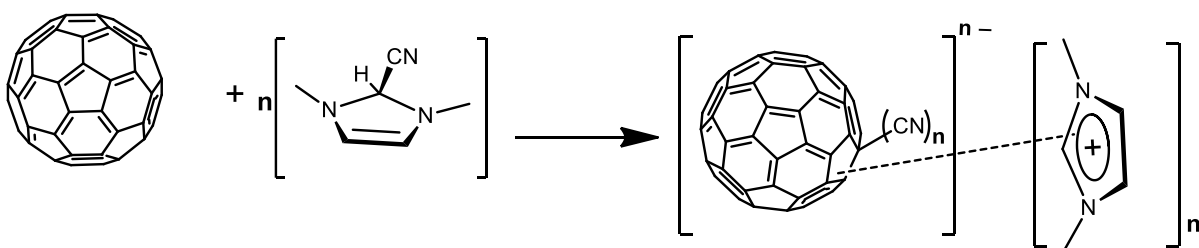
Scheme 4.2 Reaction of C_{60} with 'n' times IMCN to give polyanionic fulleride complex, $(IM^+)_n \cdots ((C_{60}(CN)_n)^{n-})$.

The feasibility of such a reaction (Scheme 1) is evaluated from the energy of the reaction (E_{rea}) calculated as,

$$E_{rea} = E_3 - (E_2 + E_1) \hspace{2cm} \text{(Eq. 4.5)}$$

where E_1, E_2 and E_3 stand for the zero-point energy (ZPE)-corrected energy of C_{60}, 'n' times IMCN and the ionic complex, $(IM^+)_n \cdots (C_{60}(CN)_n)^{n-}$, respectively. Here the ZPE-correction obtained from M06L/6-31G** level is added to the single point energy calculated at M06L/6-311++G** level. The free energy change (G_{rea}) associated with the reaction is also calculated in a similar fashion.

Further, the influence of solvent effects on the complexation of fulleride has been studied at M06L/SMD/6-311++G**//M06L/6-31G** level. Here SMD stands for the solvation model based on density (SMD) approach, a self-consistent reaction field (SCRF) method as implemented in Gaussian 16. The selected solvent for SMD calculation is dichloromethane (DCM). The solvation incorporated energy of the reaction (E'_{rea}) of each complex is calculated using equation;

$$E'_{rea} = E'_3 - (E'_2 + E'_1) \qquad \text{(Eq. 4.6)}$$

where E'_1, E'_2 and E'_3 stand for the zero-point energy (ZPE)-corrected energy of C_{60}, 'n' times IMCN and the ionic complex, $(IM^+)_n \cdots (C_{60}(CN)_n)^{n-}$, respectively. The ZPE-correction is obtained from M06L/6-31G** level. Similarly, the free energy change (G'_{rea}) associated with the reaction is also calculated.

The binding energy (E_b) for the ionic complex $(IM^+)_n \cdots (C_{60}(CN)_n)^{n-}$ is calculated as

$$E_b = E_3 - (E_4 + E_5) \qquad \text{(Eq. 4.7)}$$

where E_4 and E_5 stand for the ZPE-corrected energy of $(C_{60}(CN)_n)^{n-}$ and 'n' times IM^+, respectively. Further, the interaction of imidazolium cation-polyanionic fulleride complex with CO_2 has been studied and the binding energy of CO_2 with each imidazolium cation-polyanionic fulleride complex (ΔE) is calculated using the supermolecule approach,

$$\Delta E = E_6 - (E_7 + E_3) \qquad \text{(Eq. 4.8)}$$

where E_6 and E_7 stand for the ZPE-corrected energy of the CO_2 complex of the imidazolium -polyanionic fulleride complex and 'n' CO_2 respectively.

MESP analysis has been carried out to analyze the intermolecular interactions and charge delocalization in the fulleride complexes.

4.7 Results and discussion

4.7.1 Formation of imidazolium cation-polyanionic fulleride complexes

The previous study on the $IM^+\cdots(C_{60}X)^-$ ion-pair complex formation for X = H, F, OH, CN, NH$_2$, and NO$_2$, has shown that the formation of $IM^+\cdots(C_{60}CN)^-$ ion-pair is exergonic in nature.

$[(IM^+)\cdots((C_{60}CN)^-)]$ $\qquad$ $[(IM^+)_2\cdots((C_{60}(CN)_2)^{2-})]$ $\qquad$ $[(IM^+)_3\cdots((C_{60}(CN)_3)^{3-})]$

$[(IM^+)_4\cdots((C_{60}(CN)_4)^{4-})]$ $\qquad$ $[(IM^+)_5\cdots((C_{60}(CN)_5)^{5-})]$ $\qquad$ $[(IM^+)_6\cdots((C_{60}(CN)_6)^{6-})]$
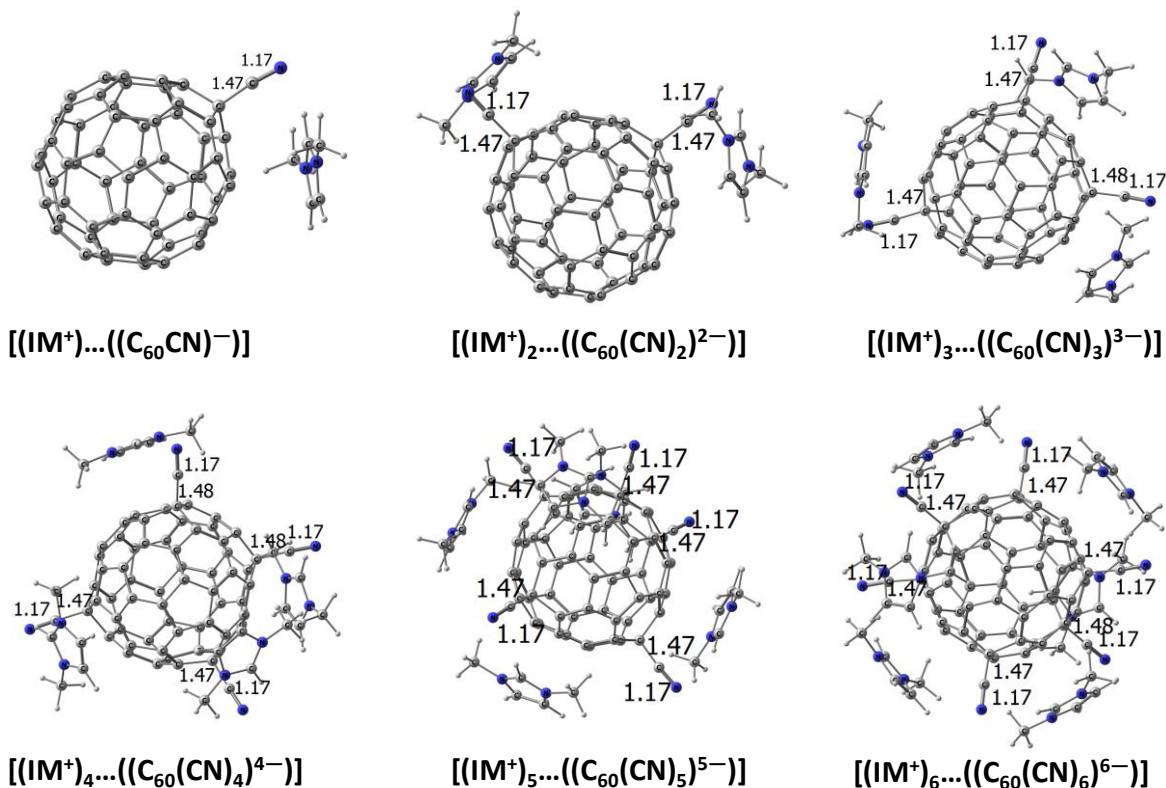
Figure 4.10 The optimized geometries of the $(IM^+)_n\cdots((C_{60}(CN)_n)^{n-})$ complexes for n = 1 to 6 at M06L/6-31G** level. The distances are given in Å.
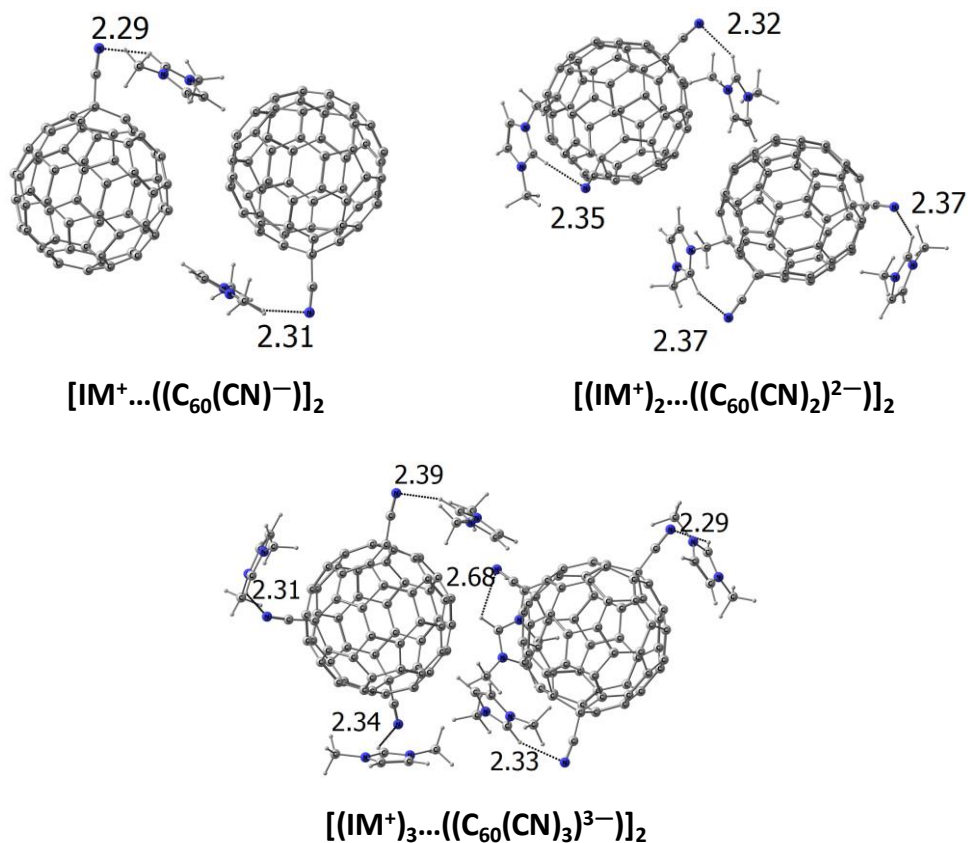
Figure 4.11 The optimized geometry of dimers of $(IM^+)_n \cdots ((C_{60}(CN)_n)^{n-})$ for $n = 1$ to 3 at M06L/6-31G** level. The distances are given in Å.

In the present study, formation of $(IM^+)_n \cdots ((C_{60}(CN)_n)^{n-})$ given in Scheme 4.2 is studied for $n = 1$ to 6. For $n > 1$, among the several isomeric structures possible for $C_{60}(CN)_n{}^{n-}$, only one is examined here (Figure 4.10). In such structures, close proximity of CN centers is avoided. Similar structural parameters are observed for these imidazolium cation-polyanionic fulleride complexes from $n = 1$ to 6, which is reflected in the C–N and C–CN distances, 1.17 and 1.47 Å respectively. Further, the bond lengths of sp^2–sp^2 C–C bonds and sp^3–sp^2 C–C bonds of the carbon cage remain consistent for $(IM^+)_n \cdots ((C_{60}(CN)_n)^{n-})$ complexes, from $n = 1$ to 6 (Table 4.6). Also the reaction is exothermic for all values of n. The energy of the reaction, E_{rea}, in Table 4.7, shows an increasing exothermic character from $n = 1$ to 6. The free energy change associated with the ionic complex formation (G_{rea}), in Table 4.7, suggests that the reaction is exergonic for $n = 1$ to 6 and shows an increasing exergonic character from $n = 1$ to 3 while this trend

reverses beyond n = 3. The free energy change associated with the ionic complex formation (G_{rea}), in Table 4.7, suggests that the reaction is exergonic for n = 1, slightly endergonic for n = 2 and 3 and in general, the endergonic nature increases with 'n'.

Table 4.6 The sp^2—sp^2 C—C and sp^3—sp^2 C—C bond lengths of the carbon cage in Å at M06L/6-31G** level.

System	sp^3—sp^2 C—C	sp^2—sp^2 C—C
$(C_{60}(CN))^-$	1.54	1.43
$(C_{60}(CN)_2)^{2-}$	1.54	1.43
$(C_{60}(CN)_3)^{3-}$	1.54	1.43
$(C_{60}(CN)_4)^{4-}$	1.54	1.43
$(C_{60}(CN)_5)^{5-}$	1.54	1.43
$(C_{60}(CN)_6)^{6-}$	1.55	1.43
$IM^+\cdots((C_{60}(CN)^-)$	1.54	1.43
$(IM^+)_2\cdots((C_{60}(CN)_2)^{2-})$	1.54	1.43
$(IM^+)_3\cdots((C_{60}(CN)_3)^{3-})$	1.54	1.43
$(IM^+)_4\cdots((C_{60}(CN)_4)^{4-})$	1.54	1.43
$(IM^+)_5\cdots((C_{60}(CN)_5)^{5-})$	1.54	1.43
$(IM^+)_6\cdots((C_{60}(CN)_6)^{6-})$	1.54	1.43

Due to the spherical distribution of the anionic charge, the interaction between multiple $(IM^+)_n\cdots((C_{60}(CN)_n)^{n-})$ complexes are expected to give additional stabilization which may enhance the exergonic feasibility of the

reaction. For instance, the E_{rea} and G_{rea} for the dimer $[IM^+\cdots((C_{60}(CN)^-)]_2$ are -48.4 kcal/mol and -10.5 kcal/mol, respectively (Figure 4.11). Compared to monomer formation, exothermicity of the dimer formation is improved by 33.7 kcal/mol which can be attributed to the cooperative electrostatic interaction among the charged species. In the case of $(IM^+)_2\cdots((C_{60}(CN)_2)^{2-})$, the dimer (Figure 4.11) formation is exergonic (-1.9 kcal/mol) while the dimer, $[(IM^+)_3\cdots((C_{60}(CN)_3)^{3-})]_2$, formation of the trianionic fulleride complex is endergonic, but better than $(IM^+)_3\cdots((C_{60}(CN)_3)^{3-})$ formation by 1.7 kcal/mol. Further improvement in energetics is expected for higher order clusters due to multiple electrostatic interactions between oppositely charged species.

Table 4.7 The energetics (kcal/mol) of the formation of $(IM^+)_n\cdots((C_{60}(CN)_n)^{n-})$ at M06L/6-311++G**//M06L/6-31G** level.

Reactants	System	E_{rea}	G_{rea}
$IMCN + C_{60}$	$IM^+\cdots((C_{60}(CN)^-)$	-14.7	-2.6
$2(IMCN) + C_{60}$	$(IM^+)_2\cdots((C_{60}(CN)_2)^{2-})$	-23.4	1.7
$3(IMCN) + C_{60}$	$(IM^+)_3\cdots((C_{60}(CN)_3)^{3-})$	-28.1	9.2
$4(IMCN) + C_{60}$	$(IM^+)_4\cdots((C_{60}(CN)_4)^{4-})$	-23.7	27.1
$5(IMCN) + C_{60}$	$(IM^+)_5\cdots((C_{60}(CN)_5)^{5-})$	-24.3	40.5
$6(IMCN) + C_{60}$	$(IM^+)_6\cdots((C_{60}(CN)_6)^{6-})$	-18.7	59.8
$2(IMCN)+ 2(C_{60})$	$[IM^+\cdots((C_{60}(CN)^-)]_2$	-48.4	-10.5
$4(IMCN)+ 2(C_{60})$	$[(IM^+)_2\cdots((C_{60}(CN)_2)^{2-})]_2$	-65.9	-1.9
$6(IMCN)+ 2(C_{60})$	$[(IM^+)_3\cdots((C_{60}(CN)_3)^{3-})]_2$	-85.3	7.5
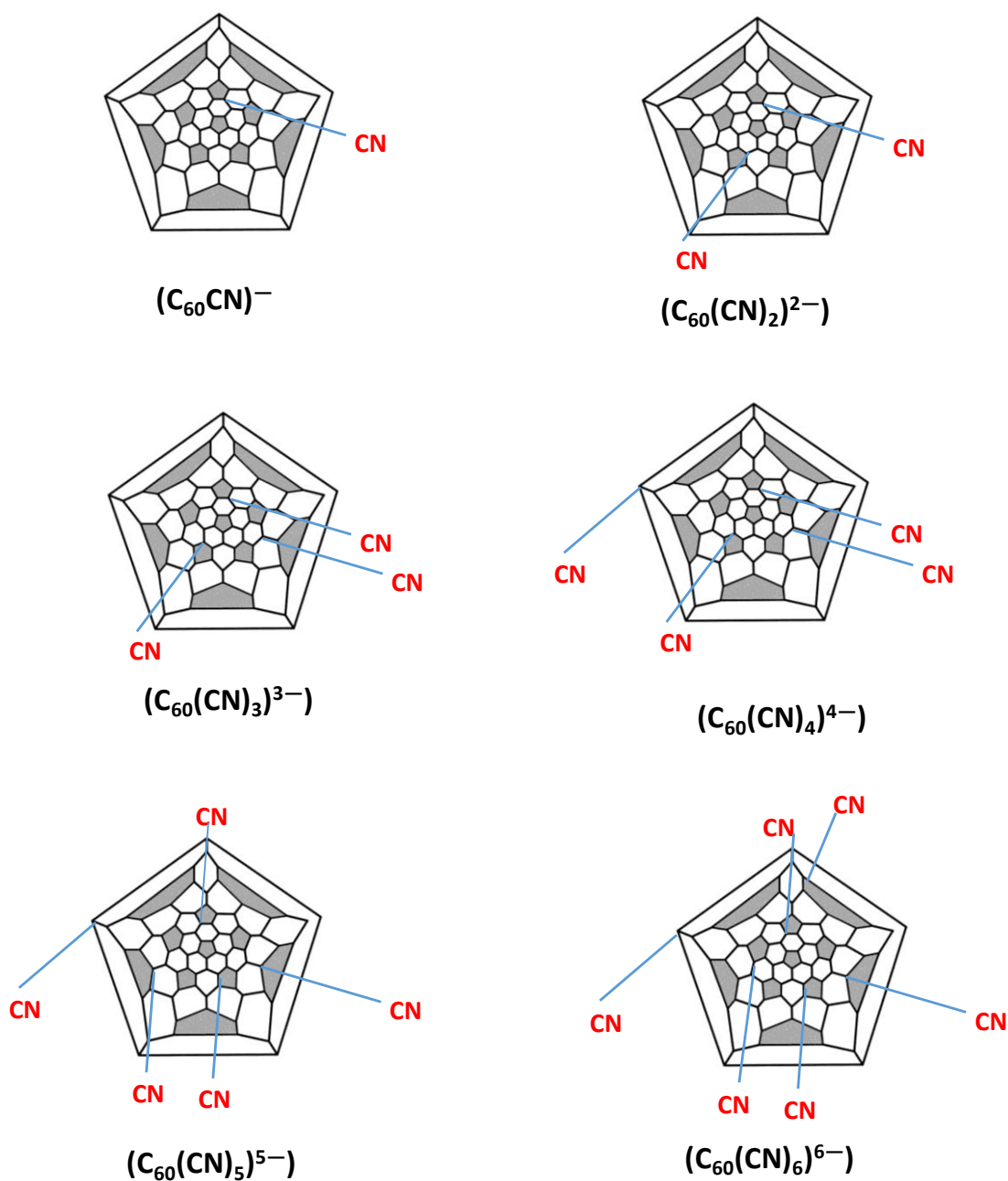
Figure 4.12 The Schlegel diagram indicating the position of CN units.

To understand more about the electronic features of the fulleride anion, we optimized the bare fulleride anions, $((C_{60}(CN)_n)^{n-})$, by removing the IM^+ cations from the respective ionic complexes in Figure 4.10. The Schlegel diagram indicating the position of CN units is given in Figure 4.12. The structural features of these fulleride polyanions (Figure 4.13) are very similar that of the fulleride structures optimized in

presence of the counter cations (complexes in Figure 4.10). The optimized geometries of the fulleride polyanions, given Figure 4.12, show that from n = 1 to 6, both the C–N bond and C–CN bond lengths show only an increase of 0.01 Å, while the sp^2–sp^2 C–C and sp^3–sp^2 C–C bond lengths of the carbon cage remain consistent with that of the ionic complexes (Table 4.6).

(C$_{60}$CN)$^-$ **(C$_{60}$(CN)$_2$)$^{2-}$**   **(C$_{60}$(CN)$_3$)$^{3-}$**

(C$_{60}$(CN)$_4$)$^{4-}$ **(C$_{60}$(CN)$_5$)$^{5-}$**   **(C$_{60}$(CN)$_6$)$^{6-}$**
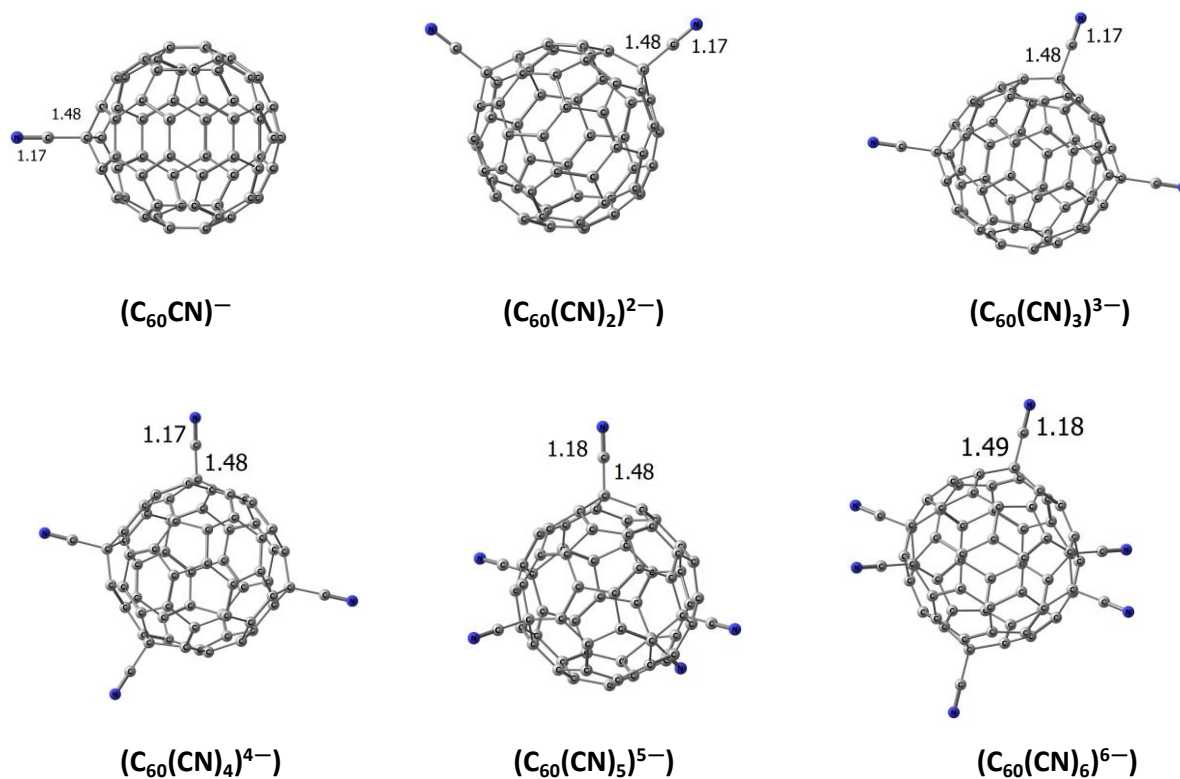
Figure 4.13 The optimized geometries of the C$_{60}$(CN)$_n$)$^{n-}$ anions for n = 1 to 6 at M06L/6-31G** level. The distances are given in Å.

4.7.2 Effect of solvation

The solvation effect-incorporated energy of reactions (E'$_{rea}$) are given in Table 4.8. For all the cases, E'$_{rea}$ data show high exothermic character compared to the gas phase E$_{rea}$ values (Table 4.7). As a result, all the reactions become exergonic in terms of G'$_{rea}$ values. This remarkable change in the energetics of the reaction in presence of solvent can be attributed to the highly anionic character of the fulleride which leads to strong electrostatic interactions with the solvent medium. These energetics strongly support the formation of fulleride ionic complexes from the reaction of fullerene and IMCN.

Table 4.8 The energetics (kcal/mol) of the formation of $(IM^+)_n \cdots ((C_{60}(CN)_n)^{n-})$ in DCM solvent at M06L/SMD/6-311++G**//M06L/6-31G** level.

System	E'_{rea}	G'_{rea}
$IM^+ \cdots ((C_{60}(CN)^-)$	-29.3	-17.2
$(IM^+)_2 \cdots ((C_{60}(CN)_2)^{2-})$	-52.5	-27.4
$(IM^+)_3 \cdots ((C_{60}(CN)_3)^{3-})$	-69.9	-32.6
$(IM^+)_4 \cdots ((C_{60}(CN)_4)^{4-})$	-76.2	-25.4
$(IM^+)_5 \cdots ((C_{60}(CN)_5)^{5-})$	-83.5	-18.6
$(IM^+)_6 \cdots ((C_{60}(CN)_6)^{6-})$	-84.0	-5.5
$[IM^+ \cdots ((C_{60}(CN)^-)]_2$	-65.0	-27.0
$[(IM^+)_2 \cdots ((C_{60}(CN)_3)^{2-})]_2$	-111.2	-47.2
$[(IM^+)_3 \cdots ((C_{60}(CN)_3)^{3-})]_2$	-150.4	-57.6

4.7.3 MESP features

MESP analysis is very useful to interpret the electron rich character of a molecular system. For instance, the inherent electron deficient nature of the C_{60} molecule is reflected in the very small negative value observed for its MESP minimum value on the fullerene cage (V_{min-on}), -0.9 kcal/mol. Similarly, the electron rich character of the radical anion, $C_{60}^{\bullet-}$ is visible from the large negative V_{min-on} value, -63.4 kcal/mol as well asfrom the spin density distribution (Figure 4.14). In the case of acetonitrile (CH_3CN), nitrogen lone pair region is the most electron rich and the MESP minimum at this region (V_{min-CN}) is -52.4 kcal/mol whereas for the anion, CN^-, V_{min-CN} becomes highly negative, -184.6 kcal/mol. In the case of cyano-fullerides, the MESP minimum on the fullerene cage (V_{min-on}), inside the fullerene cage (V_{min-in}), and on the CN unit (V_{min-CN}) are evaluated to assess their electron rich character.

$$C_{60}{}^{\bullet-}$$
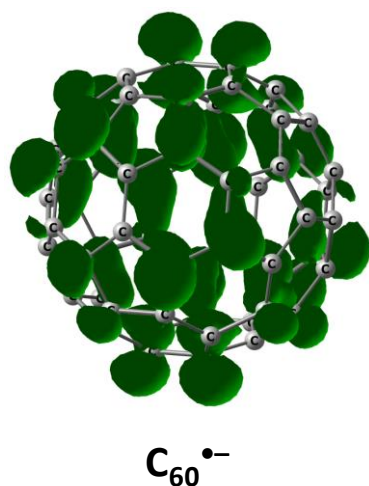
Figure 4.14 The spin density distribution over $C_{60}{}^{\bullet-}$ at M06L/6-311++G(d,p)//M06L/6-31G(d,p) level (isosurface value = 0.001 au).
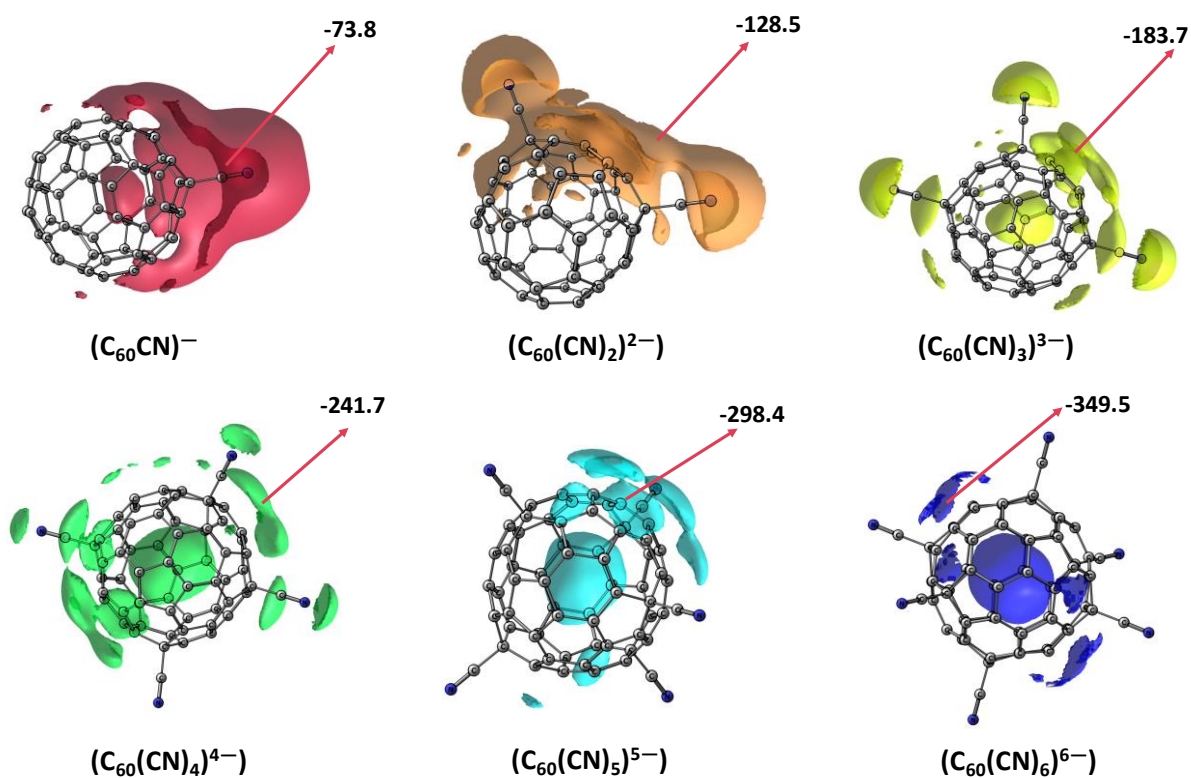
Figure 4.15 MESP isosurface plotted for $((C_{60}(CN)_n)^{n-})$ fullerides. The $V_{\text{min-on}}$ values are given in kcal/mol. The colour of isosurface is varied from red to blue as the MESP value becomes more negative.

The data in Table 4.9 indicate that the fullerene cage of $(C_{60}(CN))^-$ is slightly more electron rich than $C_{60}{}^{•-}$ and this electronic feature, V_{min-on}, improves by ~54.7 kcal/mol with addition of each CN^- unit on the cage. Similarly, V_{min-in} changes by ~57.7 kcal/mol with addition of CN^- on the cage. The V_{min-CN} of mono-, di-, and tri-anionic cyano fullerides shows more negative value than their V_{min-on} and V_{min-in} values whereas tetra-, penta-, and hexa-anionic fullerides exhibit more negative MESP on carbon cage than the CN unit. The analysis of these MESP data clearly suggest that with the addition of each CN^- unit on the carbon cage, its electron rich character increases significantly, particularly on the carbon cage, both interior and exterior due to the delocalization of the extra electrons derived from the CN^- units (Figure 4.15).

| $(C_{60}CN)^-$ | $(C_{60}(CN)_2)^{2-})$ | $(C_{60}(CN)_3)^{3-})$ |
| -50.3 | -105.5 | -158.1 |

| $(C_{60}(CN)_4)^{4-})$ | $(C_{60}(CN)_5)^{5-})$ | $(C_{60}(CN)_6)^{6-})$ |
| -210.7 | -257.0 | -308.9 |
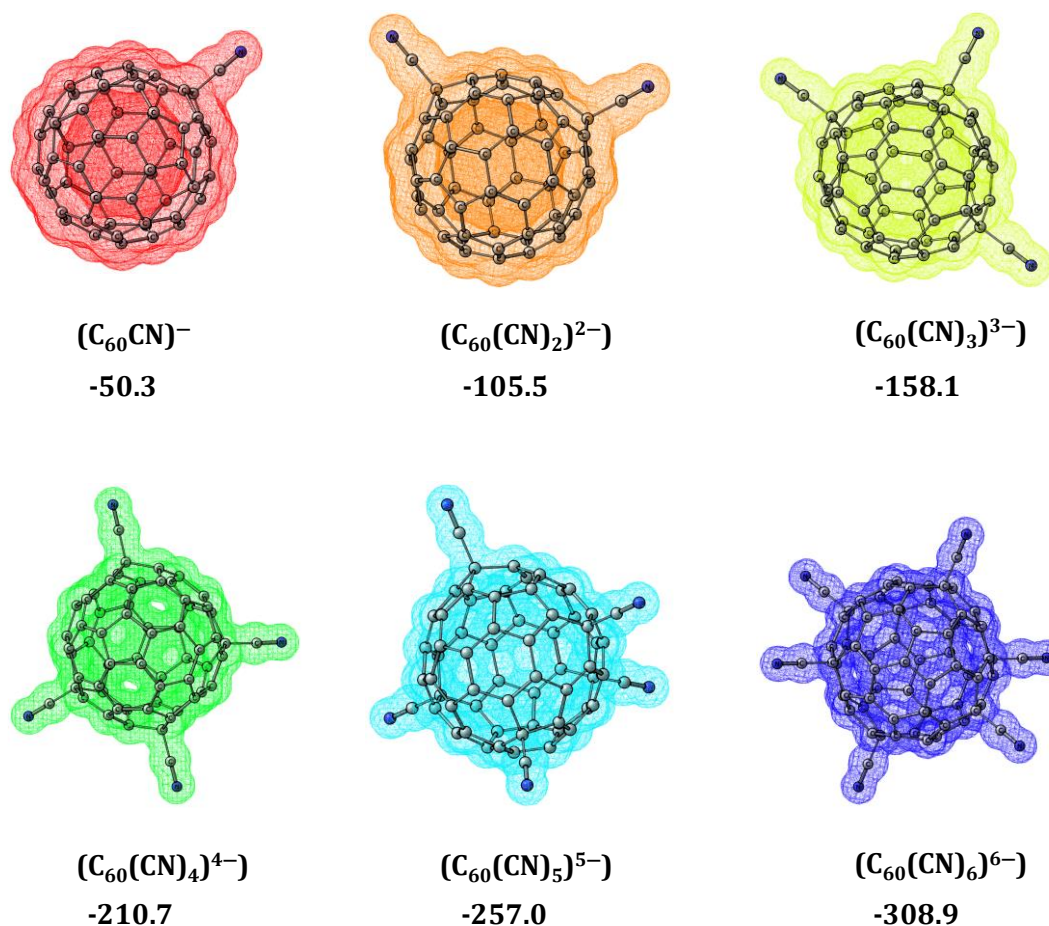
Figure 4.16 MESP surfaces of $(C_{60}(CN)_n)^{n-}$ for n = 1 to 6, that engulfs the whole anion at M06L/6-311++G(d,p)//M06L/6-31G(d,p) level. The minimum value of MESP that engulfs the whole anion in kcal/mol is also depicted.
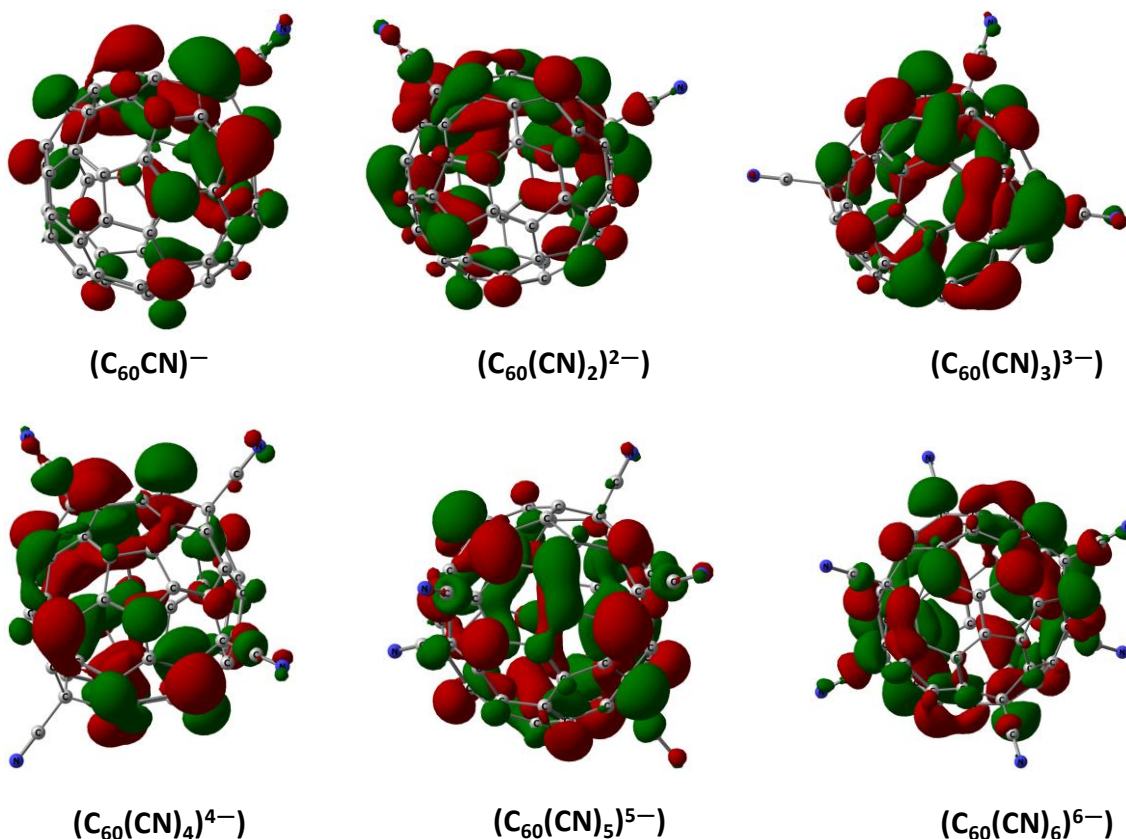
Figure 4.17 HOMO plots of $(C_{60}(CN)_n)^{n-}$ for n = 1 to 6 at M06L/6-311++G**//M06L/6-31G** level (isosurface value = 0.02 au).

According to Gadre-Pathak theorem, for any negative charged system, there exists a surface which passes through all the negative valued critical points (the directional negative valued minimum along any arbitrary direction).[120] Identification of such an engulfing MESP surface is useful for assessing the delocalized distribution of the extra electron/s in the cyano fullerides . Such a surface corresponds to the lowest negative MESP or the highest MESP value (V_{max}). The V_{max} of mono-, di-, tri-, tetra-, penta- and hexa-anionic cyano fulleries is -50.3, -103.9, -158.1, -210.7, -257.0, and -308.9 kcal/mol respectively (Figure 4.16). The magnitude of V_{max} jumps by ~-51.7 kcal/mol with the addition of each CN^- on the fullerene cage indicating polyanionic character of the systems. The distribution of the highest occupied molecular orbital (HOMO) over the fullerene carbon framework (Figure 4.17) also supports the delocalization of the additional electrons and the anionic nature of the whole carbon cage. Recent

experimental and theoretical study by Lawrence *et al.* on the hexaanionic fulleride (C_{60}^{6-}) complexes of magnesium shows that such highly anionic systems of fullerides are possible.[119]

Table 4.9 The minimum MESP at M06L/6-311++G**//M06L/6-31G** level. The values are given in kcal/mol.

System	V_{min-on}	V_{min-in}	V_{min-CN}
CN^-	--	--	-184.6
CH_3CN	--	--	-52.4
C_{60}	-0.9	--	--
$C_{60}^{\bullet-}$	-63.4	-53.2	--
$(C_{60}(CN))^-$	-73.8	-61.1	-104.7
$(C_{60}(CN)_2)^{2-}$	-128.5	-115.1	-147.7
$(C_{60}(CN)_3)^{3-}$	-183.7	-175.5	-193.3
$(C_{60}(CN)_4)^{4-}$	-241.7	-235.3	-240.3
$(C_{60}(CN)_5)^{5-}$	-298.4	-296.2	-284.5
$(C_{60}(CN)_6)^{6-}$	-347.5	-349.5	-327.9
$IM^+\cdots((C_{60}(CN)^-)$	-13.2	--	-35.9
$(IM^+)_2\cdots((C_{60}(CN)_2)^{2-})$	-26.1	-11.2	-46.1
$(IM^+)_3\cdots((C_{60}(CN)_3)^{3-})$	-40.4	-24.3	-51.6
$(IM^+)_4\cdots((C_{60}(CN)_4)^{4-})$	-43.1	-30.1	-56.9
$(IM^+)_5\cdots((C_{60}(CN)_5)^{5-})$	-44.5	-54.0	-60.4
$(IM^+)_6\cdots((C_{60}(CN)_6)^{6-})$	-50.9	-58.4	-64.2

Anions interact with cations to achieve charge neutrality and the formation of the ionic complexes, $(IM^+)_n \cdots ((C_{60}(CN)_n)^{n-})$, is more realistic than the existence of bare anions. Figure 4.18 shows the MESP distribution in $(IM^+)_n \cdots ((C_{60}(CN)_n)^{n-})$ systems. Compared to bare anions, the charge neutralization effect in the ionic complexes is clearly visible in the small magnitude of MESP values, V_{min-on}, V_{min-in} and V_{min-CN} (Tables 4.9 & 4.10). Even for the complex of hexaanionic system, $(IM^+)_6 \cdots ((C_{60}(CN)_6)^{6-})$, these parameters are distributed in the range -50.9 to -64.2 kcal/mol which is comparable to the MESP values observed $C_{60}{}^{\bullet-}$. For the complexes of mono- and dianionic systems, V_{min-CN} values are less negative than that of CH_3CN while the trianionic complex shows a V_{min-CN} value comparable to that of CH_3CN. The hexaanionic system shows the highest negative V_{min-CN} value -64.2 kcal/mol which is more negative than CH_3CN by 11.8 kcal/mol. This data clearly suggests that with the addition of each CN^- unit, the electron rich character of both the carbon cage and CN unit increases.

Table 4.10 The binding energy of $(IM^+)_n \cdots (C_{60}(CN)_n)^{n-}$ at M06L/6-311++G**//M06L/6-31G** level. All the values are given in kcal/mol.

System	E_b	G_b	$E_{b/IM+}$	$G_{b/IM+}$
$IM^+ \cdots ((C_{60}(CN)^-)$	-69.6	-57.1	-69.6	-57.1
$(IM^+)_2 \cdots ((C_{60}(CN)_2)^{2-})$	-192.8	-166.9	-96.4	-83.4
$(IM^+)_3 \cdots ((C_{60}(CN)_3)^{3-})$	-369.2	-330.8	-123.1	-110.3
$(IM^+)_4 \cdots ((C_{60}(CN)_4)^{4-})$	-597.9	-545.6	-149.5	-136.4
$(IM^+)_5 \cdots ((C_{60}(CN)_5)^{5-})$	-885.1	-818.3	-177.0	-163.7
$(IM^+)_6 \cdots ((C_{60}(CN)_6)^{6-})$	-1217.3	-1136.6	-202.9	-189.4
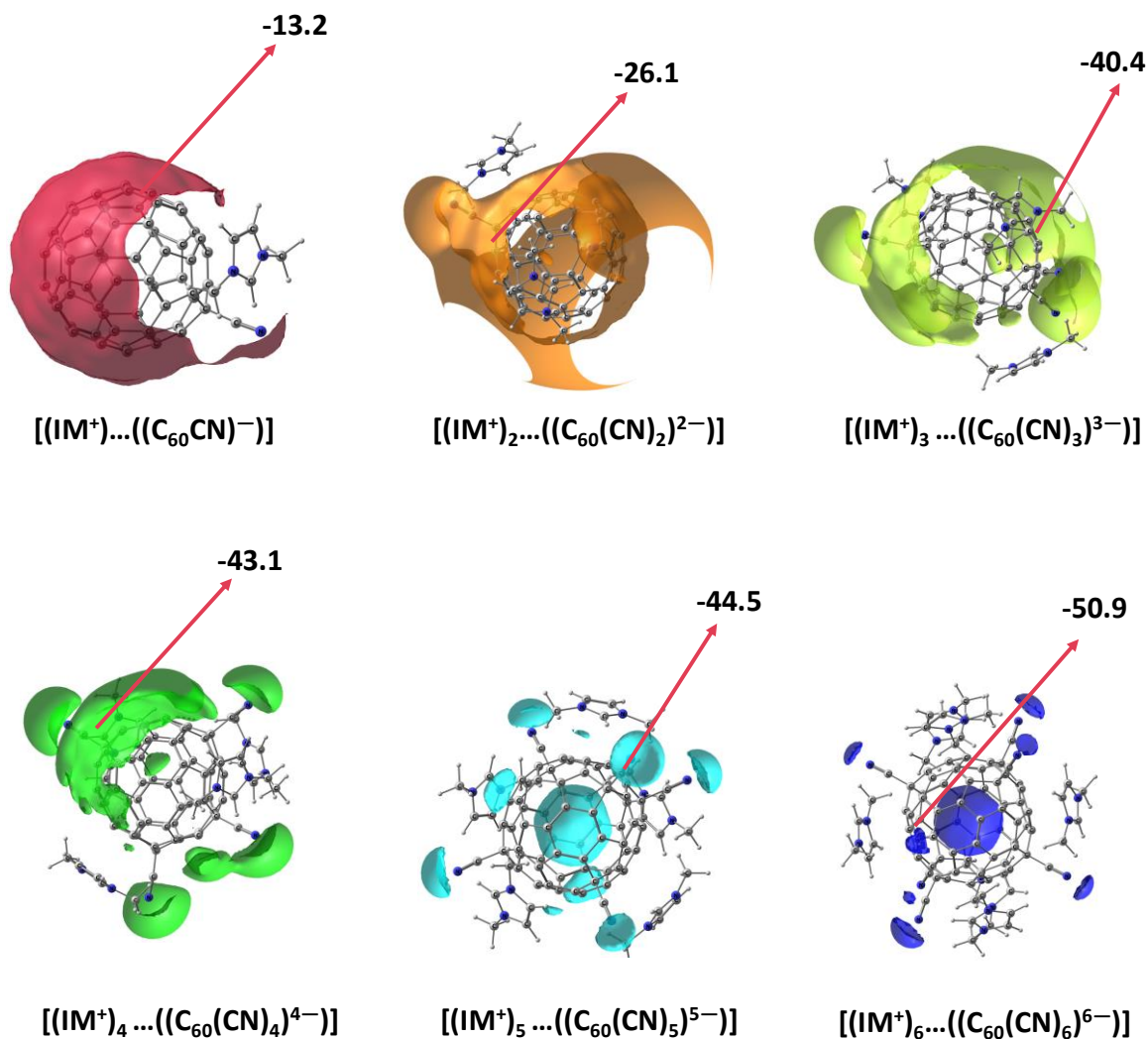
Figure 4.18 MESP isosurface plotted for $(IM^+)_n \cdots ((C_{60}(CN)_n)^{n-})$ complexes. The $V_{\text{min-on}}$ values are given in kcal/mol. The colour of isosurface is varied from red to blue to indicate the enhancement in MESP negative character.

The ionic interaction energy of the cyano-fullerides with 'n' number of IM^+ is depicted in Table 4.10. The interaction of $(C_{60}(CN)^-$ with IM^+ cation gives the binding energy (E_b) of -69.6 kcal/mol. As observed from the MESP analysis, addition of each CN^- on the C_{60} cage improves its electron rich character and thus in the ionic complexes of polyanionic fullerides, interaction with multiple IM^+ gives very large magnitudes of E_b values. For instance, in hexaanionic fulleride complex, the E_b -1217.3 kcal/mol suggests that on an average, interaction energy per IM^+ cation is -202.9 kcal/mol. Such a large

value of interaction energy can be attributed to the huge electron rich nature observed for the bare fullerides. This argument is also supported by the strong linear correlation (correlation coefficient, R = 0.9997) obtained between V_{min-on} values of the bare fulleride anions and $E_{b/IM+}$ values (Figure 4.19). With each CN^- addition on the carbon cage, the MESP values become more negative by ~54.7 kcal/mol and the $E_{b/IM+}$ values are observed to be stronger by ~26.7 kcal/mol. Higher the negative charge, stronger is the ionic interactions and thus more energy is required to dissociate the IM^+ cations from the $(IM^+)_n \cdots (C_{60}(CN)_n)^{n-}$ complexes.
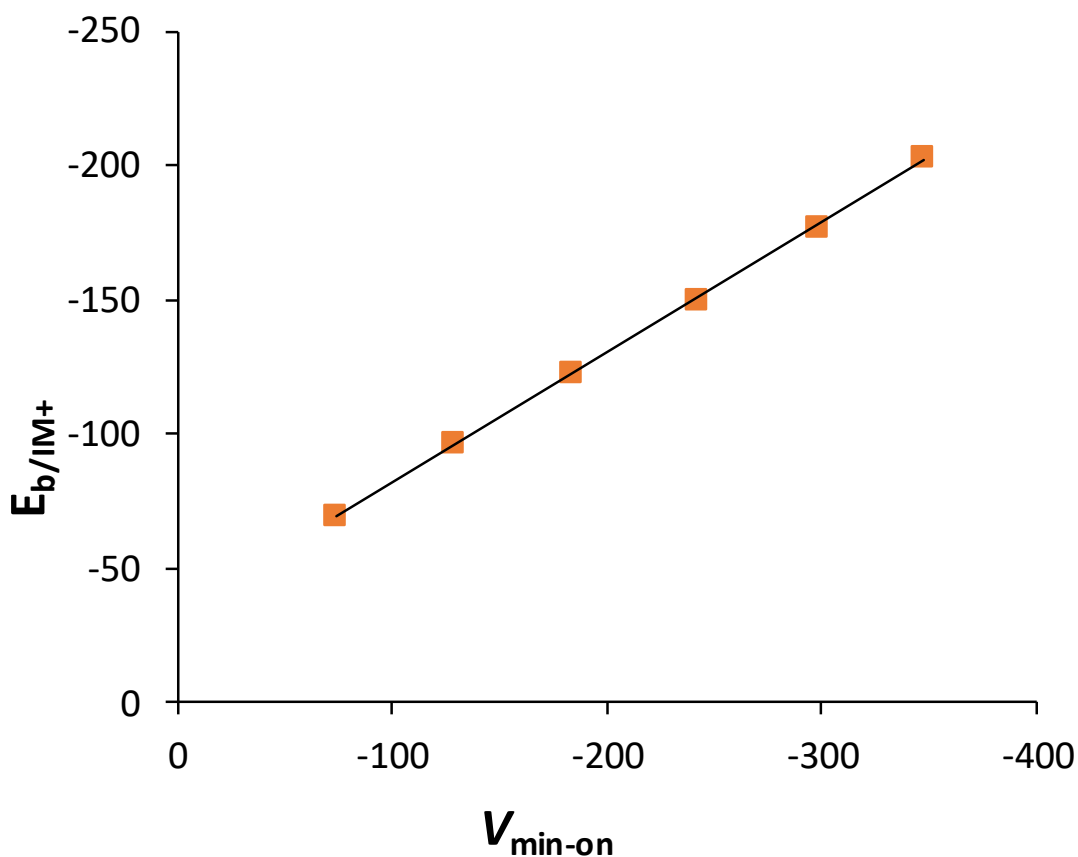
Figure 4.19 Correlation between V_{min-on} of $(C_{60}(CN)_n)^{n-}$ and $E_{b/IM+}$ of $(IM^+)_n \cdots ((C_{60}(CN)_n)^{n-})$ ion pair. All values are given in kcal/mol.

4.7.4 CO$_2$ capture by polyanionic fulleride complexes

All the imidazolium cation-polyanionic fulleride complexes are analyzed for their possible interactions with CO$_2$ molecule *via* the carbon cage and the CN center. Figure 4.18 gives the optimized structures of such CO$_2$ complexes of $[(IM^+)_n \cdots ((C_{60}(CN)_n)^{n-})]$. The ion-pair, $IM^+ \cdots ((C_{60}(CN)^-)$, shows noncovalent (*nc*) complex formation with CO$_2$ either through the carbon cage (**1nc**) or *via* the CN group on the fulleride (**1'nc**). The **1'nc** is more stable than **1nc** by 2.1 kcal/mol. In the case of the ionic complex, $[(IM^+)_n \cdots ((C_{60}(CN)_n)^{n-})]$, for n > 1, the interaction with the CO$_2$ is observed only through the carbon cage. Also, for n = 1 and 2, the imidazolium- fulleride complex gives only *nc* complex with CO$_2$ whereas from n = 3 onwards, the it gives both *nc* and covalent (*c*) complex with the CO$_2$. In '*c*' complexes, the C–C bond formation between C of CO$_2$ and fullerene carbon is evident from the C–C distance in the range 1.54 Å to 1.60 Å whereas the noncovalent C$\cdots$C interaction distance is in the range   3.15 Å to 3.29 Å (Figure 4.20).

Table 4.11 Energetics of CO$_2$ complexes of $[(IM^+)_n \cdots ((C_{60}(CN)_n)^{n-})]$ complexes in kcal/mol.

n	ΔE	ΔG
1nc	-2.3	4.6
1'nc	-4.4	2.8
2nc	-4.7	4.4
3nc	-5.0	4.6
3c	-3.6	9.0
4nc	-5.7	1.7
4c	-16.1	-4.0
5nc	-5.8	2.7
5c	-16.5	-4.3
6nc	-7.2	1.8
6c	-18.6	-6.3
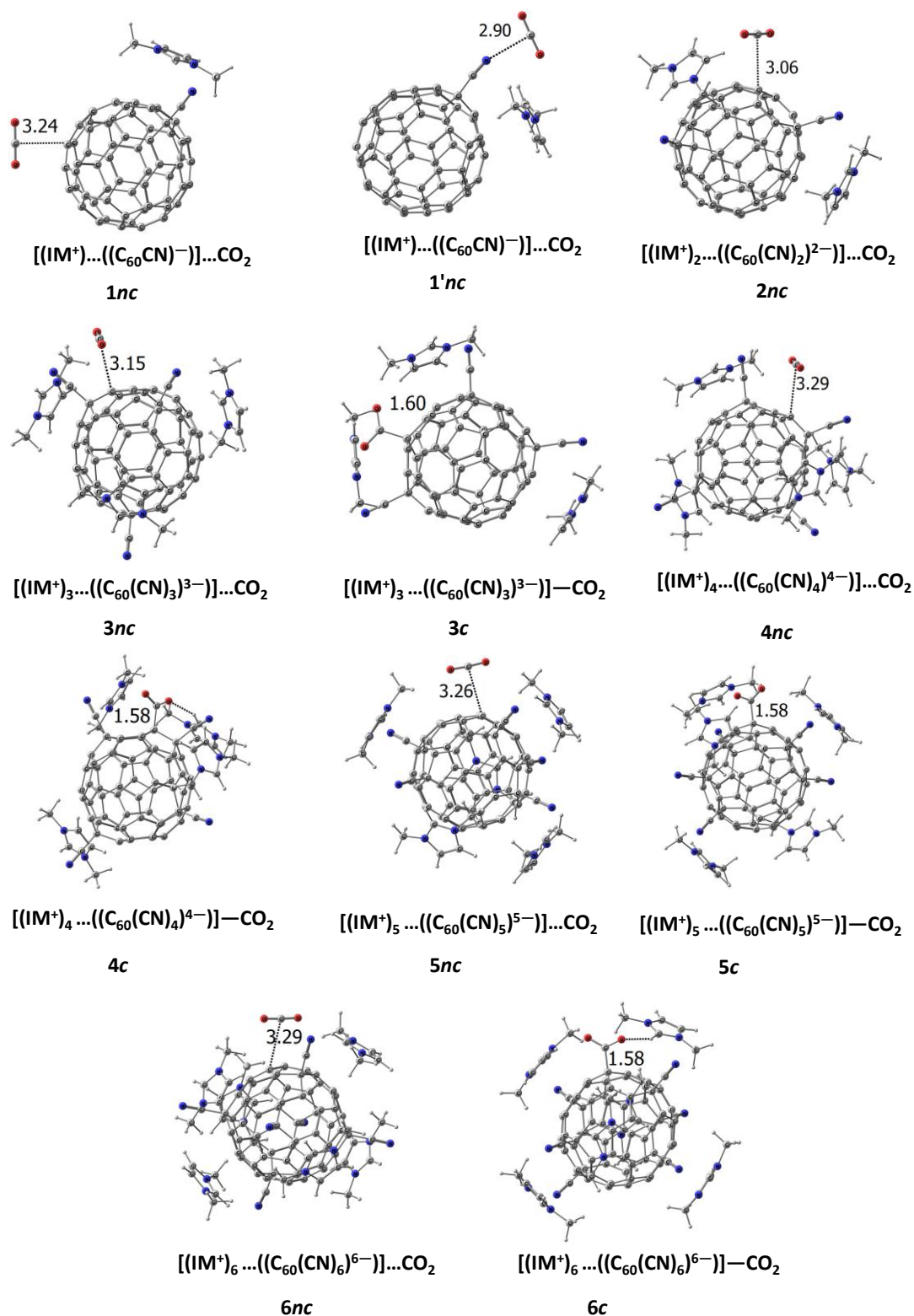
Figure 4.20 Optimized geometries of CO_2 complexes of $[(IM^+)_n \cdots ((C_{60}(CN)_n)^{n-})]$ complexes, for n = 1 to 6 at M06L/6-31G** level. Distances are in Å.

$[(IM^+)_6 \cdots ((C_{60}(CN)_6)^{6-})] - (CO_2)_2$
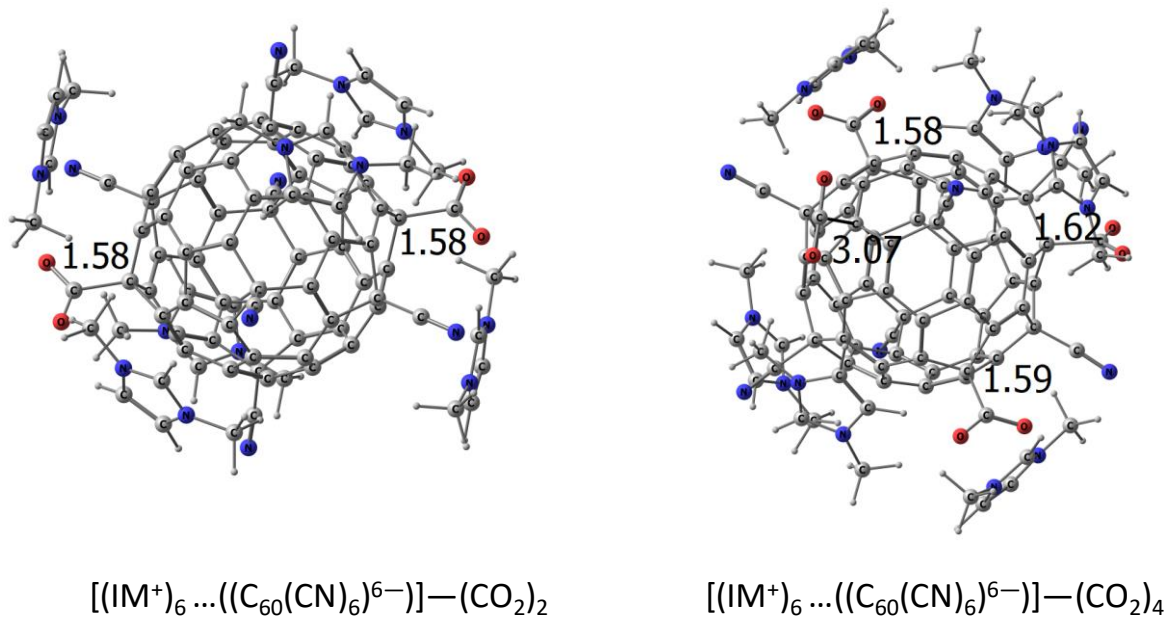
$[(IM^+)_6 \cdots ((C_{60}(CN)_6)^{6-})] - (CO_2)_4$

Figure 4.21 The optimized geometries of $[(IM^+)_6 \cdots ((C_{60}(CN)_6)^{6-})] - (CO_2)_2$ and $[(IM^+)_6 \cdots ((C_{60}(CN)_6)^{6-})] - (CO_2)_4$ at M06L/6-31G** level. The distances are given in Å.

This C–CO$_2$ covalent bonding directs the charge transfer from the fullerene cage to the CO$_2$ and thereby transforms CO$_2$ into the carboxylate anion. Though the covalent interaction facilitates the formation of a strong C–C bond, the large structural deformation occurs on CO$_2$ weakens its CO double bonds resulting to an overall stabilization which is ~10.8 kcal/mol better than **nc** complex formation for n = 4, 5 and 6 (Table 4.11). The imidazolium -polyanionic fulleride complex of trianionic fulleride with CO$_2$ is an exception to this observation wherein, **3nc** is more stable than **3c** by 1.4 kcal/mol which can be attributed to the formation weak C–C bond of distance 1.60 Å in the later.

The interaction of multiple CO$_2$ molecules with the complex, $(IM^+)_6\cdots((C_{60}(CN)_6)^{6-})$ is also investigated (Figure 4.21). The attempt to optimize $(IM^+)_6\cdots((C_{60}(CN)_6)^{6-})$ with two CO$_2$ has shown that both CO$_2$ molecules have covalent interactions with the carbon cage with the interaction energy per CO$_2$ ($\Delta E_{/CO2}$) of -18.5 kcal/mol. The optimization with four CO$_2$ molecules has shown that the complex has covalent interaction with three

of CO_2 and a noncovalent interaction with the fourth CO_2 molecule with the $\Delta E_{/CO2}$ of -11.1 kcal/mol respectively. These results show the capability of such polyanionic fulleride complexes to hold more number of CO_2 molecules and are predicted as potential candidates for CO_2 capture.

4.8 Conclusions

The DFT study at M06L/6-311++G(d,p)//M06L/6-31G(d,p) level has shown the exothermic formation of imidazolium-polyanionic fulleride complexes, $(IM^+)_n\cdots(C_{60}(CN)_n)^{n-}$, for n = 1 to 6, from the reaction of 'n' IMCN and C_{60}. The incorporation of solvent effects (in DCM) has shown that the formation of such ionic complexes is exergonic in nature. Further, the dimer formation of such ionic complexes is also found to be exergonic due to multiple cooperative electrostatic interactions between oppositely-charged species. The MESP analysis using surface plots and topology parameters V_{min} and V_{max} clearly brought out the delocalization features of the extra electron/s over the carbon cage of the fulleride. Addition of each CN^- unit on the fullerene cage leads to substantial increase in the electron rich character of the C_{60} cage in terms of V_{min-on} value which is comparable to the enhancement in V_{min-on} value when one electron is added to C_{60}. The anionic to polyanionic character developed for the C_{60} cage due to the addition of each CN^- unit substantially improves its electrostatic interaction with IM^+ units. Parallel to the study by Lawrence *et al.,* this study also show that highly charged anionic fullerides are possible due to the extensive delocalization of the anionic charges through the entire molecule. In C_{60}, the scenario of sixty π-electrons delocalized over ninety C–C bonds suggests electron deficient nature of its carbon centers and offers large room on the carbon cage for the delocalization of the negative charge and makes the fulleride more capable of holding additional electrons, which is further confirmed from the consistent structural parameters observed for the fullerides and their imidazolium complexes form n = 1 to 6.

The fulleride complexes of IM^+ show both noncovalent (***nc***) and covalent (***c***) interactive behavior with CO_2. The high anionic nature of the polyanionic fullerides lead to covalent interactions between CO_2 and the carbon cage resulting to the formation of

carboxylate anion. The imidazolium-fulleride systems are proposed as potent CO_2 adsorbents owing to their tendency to interact with several CO_2 molecules with moderate binding energy. Mild exergonic character of the adsorption of CO_2 observed for many fulleride systems also suggest that its desorption is not an energetically demanding process. Anionic functionalization of even larger fullerenes could be considered as a promising strategy to design new functional materials for CO_2 capture.

4.9   References

1.   P. Wasserscheid and T. Welton, *Ionic liquids in synthesis*, John Wiley & Sons, 2008.
2.   K. N. Marsh, J. A. Boxall and R. Lichtenthaler, *Fluid Ph. Equilibria*, 2004, **219**, 93-98.
3.   U. L. Bernard, E. I. Izgorodina and D. R. MacFarlane, *J. Phys. Chem. C*, 2010, **114**, 20472-20478.
4.   G. Pandey and S. Hashmi, *Bull. Mater. Sci.*, 2013, **36**, 729-733.
5.   K. B. Dhungana, L. F. Faria, B. Wu, M. Liang, M. C. Ribeiro, C. J. Margulis and E. W. Castner Jr, *J. Chem. Phys.*, 2016, **145**, 024503.
6.   D. Weingarth, I. Czekaj, Z. Fei, A. Foelske-Schmitz, P. J. Dyson, A. Wokaun and R. Koetz, *J. Electrochem. Soc.*, 2012, **159**, H611.
7.   M. Marszalek, Z. Fei, D.-R. Zhu, R. Scopelliti, P. J. Dyson, S. M. Zakeeruddin and M. Grätzel, *Inorg. Chem.*, 2011, **50**, 11561-11567.
8.   F. Zhou, Y. Liang and W. Liu, *Chem. Soc. Rev.*, 2009, **38**, 2590-2599.
9.   M. Galiński, A. Lewandowski and I. Stępniak, *Electrochim. Acta*, 2006, **51**, 5567-5580.
10.   I. Kuusik, M. Berholts, J. Kruusma, V. Kisand, A. Tõnisoo, E. Lust and E. Nõmmiste, *RSC Adv.*, 2018, **8**, 30298-30304.
11.   I. Kuusik, M. Berholts, J. Kruusma, A. Tõnisoo, E. Lust, E. Nõmmiste and V. Kisand, *RSC Adv.*, 2019, **9**, 33140-33146.
12.   J. Garche, C. Dyer, P. Moseley, Z. Ogumi, D. Rand and B. Scrosati, in *Encyclopedia of electrochemical power sources,* 2009, vol. 1, 154-155.
13.   H. Spohr and G. Patey, *J. Chem. Phys.*, 2008, **129**, 064517.
14.   N. Martín, *Chem. Commun.*, 2006, 2093-2104.
15.   P. D. Boyd and C. A. Reed, *Acc. Chem. Res.*, 2005, **38**, 235-242.
16.   E. Nakamura and H. Isobe, *Acc. Chem. Res.*, 2003, **36**, 807-815.
17.   Y. Rubin, S. Khan, D. I. Freedberg and C. Yeretzian, *J. Am. Chem. Soc.*, 1993, **115**, 344-345.
18.   R. Taylor and D. R. Walton, *Nature*, 1993, **363**, 685-693.
19.   Y. Zhang, D. Wang and W. Wang, *Comput. Theor. Chem.*, 2018, **1128**, 56-59.
20.   J. López-Andarias, A. Bauzá, N. Sakai, A. Frontera and S. Matile, *Angew. Chem.*, 2018, **130**, 11049-11053.
21.   J. López-Andarias, A. Frontera and S. Matile, *J. Am. Chem. Soc.*, 2017, **139**, 13296-13299.
22.   C. Sikorska, *Phys. Chem. Chem. Phys.*, 2016, **18**, 18739-18749.

23. C. Maciel and E. E. Fileti, *Chem. Phys. Lett.*, 2013, **568**, 75-79.
24. G. García, M. Atilhan and S. Aparicio, *J. Phys. Chem. B*, 2014, **118**, 11330-11340.
25. G. García, M. Atilhan and S. Aparicio, *J. Phys. Chem. B*, 2015, **119**, 12224-12237.
26. C. Herrera, R. Alcalde, G. Garcia, M. Atilhan and S. Aparicio, *J. Phys. Chem. C*, 2015, **119**, 27080-27094.
27. G. García, M. Atilhan and S. Aparicio, *J. Phys. Chem. B*, 2015, **119**, 10616-10629.
28. V. Campisciano, V. La Parola, L. F. Liotta, F. Giacalone and M. Gruttadauria, *Chem. Eur. J.*, 2015, **21**, 3327-3334.
29. V. V. Chaban, C. Maciel and E. E. Fileti, *J. Solution Chem.*, 2014, **43**, 1019-1031.
30. E. E. Fileti and V. V. Chaban, *J. Phys. Chem. Lett.*, 2014, **5**, 1795-1800.
31. S. Osuna, M. Swart and M. Solà, *Phys. Chem. Chem. Phys.*, 2011, **13**, 3585-3603.
32. Y. Wang, D. Tománek and R. S. Ruoff, *Chem. Phys. Lett.*, 1993, **208**, 79-85.
33. J. Cioslowski and K. Raghavachari, *J. Chem. Phys.*, 1993, **98**, 8734-8741.
34. A. A. Popov and L. Dunsch, *Chem. Eur. J.*, 2009, **15**, 9707-9729.
35. E. D. Jemmis, G. Subramanian, G. N. Sastry, G. Mehta, R. N. Shirsat and S. R. Gadre, *J. Chem. Soc., Perkin Trans. 2*, 1996, **11**, 2343-2346.
36. L. Dunsch and S. Yang, *Phys. Chem. Chem. Phys.*, 2007, **9**, 3067-3081.
37. A. Krachmalnicoff, R. Bounds, S. Mamone, S. Alom, M. Concistrè, B. Meier, K. Kouřil, M. E. Light, M. R. Johnson and S. Rols, *Nat. Chem.*, 2016, **8**, 953-957.
38. K. Kurotobi and Y. Murata, *Science*, 2011, **333**, 613-616.
39. E. C. Escudero-Adán, A. Bauzá, L. P. Hernández-Eguía, F. Würthner, P. Ballester and A. Frontera, *CrystEngComm*, 2017, **19**, 4911-4919.
40. X. Wu and X. Lu, *J. Am. Chem. Soc.*, 2007, **129**, 2171-2177.
41. R. E. Estrada-Salas and A. A. Valladares, *J. Mol. Struct. THEOCHEM*, 2008, **869**, 1-5.
42. K. Komatsu, M. Murata and Y. Murata, *Science*, 2005, **307**, 238-240.
43. J. Cioslowski and A. Nanayakkara, *J. Chem. Phys.*, 1992, **96**, 8354-8362.
44. A. L. Balch and M. M. Olmstead, *Chem. Rev.*, 1998, **98**, 2123-2166.
45. K. Lee, H. Song and J. T. Park, *Acc. Chem. Res.*, 2003, **36**, 78-86.
46. P. Ravinder and V. Subramanian, *J. Phys. Chem. A*, 2011, **115**, 11723-11733.
47. V. V. Chaban and E. E. Fileti, *Phys. Chem. Chem. Phys.*, 2015, **17**, 15739-15745.
48. N. A. Andreeva and V. V. Chaban, *J. Chem. Thermodyn.*, 2018, **116**, 1-6.
49. V. V. Chaban, E. E. Fileti and T. Malaspina, *Comput. Theor. Chem.*, 2016, **1083**, 7-11.
50. S. Salehzadeh, F. Yaghoobi and M. Bayat, *Comput. Theor. Chem.*, 2014, **1034**, 73-79.
51. Y. Garcia-Rodeja, M. Sola, F. M. Bickelhaupt and I. Fernandez, *Chem. Eur. J.*, 2017, **23**, 11030.
52. P. Besalú Sala, J. M. Luis Luis and M. Solà i Puig, *Chem. Eur. J.*, 2020.
53. T. D. Della and C. H. Suresh, *Phys. Chem. Chem. Phys.*, 2018, **20**, 24885-24893.
54. Y. Zhao and D. G. Truhlar, *J. Chem. Phys.*, 2006, **125**, 194101.
55. Y. Zhao and D. G. Truhlar, *Acc. Chem. Res.*, 2008, **41**, 157-167.
56. S. Zahn, D. R. MacFarlane and E. I. Izgorodina, *Phys. Chem. Chem. Phys.*, 2013, **15**, 13664-13675.
57. D. Wu and D. G. Truhlar, *J. Chem. Theory Comput.*, 2021.
58. M. J. Frisch, G. W. Trucks, H. B. Schlegel, G. E. Scuseria, M. A. Robb, J. R. Cheeseman, G. Scalmani, V. Barone, G. A. Petersson, H. Nakatsuji, X. Li, M. Caricato, A. V. Marenich,

J. Bloino, B. G. Janesko, R. Gomperts, B. Mennucci, H. P. Hratchian, J. V. Ortiz, A. F. Izmaylov, J. L. Sonnenberg, D. Williams-Young, F. Ding, F. Lipparini, F. Egidi, J. Goings, B. Peng, A. Petrone, T. Henderson, D. Ranasinghe, V. G. Zakrzewski, J. Gao, N. Rega, G. Zheng, W. Liang, M. Hada, M. Ehara, K. Toyota, R. Fukuda, J. Hasegawa, M. Ishida, T. Nakajima, Y. Honda, O. Kitao, H. Nakai, T. Vreven, K. Throssell, J. A. Montgomery Jr., J. E. Peralta, F. Ogliaro, M. J. Bearpark, J. J. Heyd, E. N. Brothers, K. N. Kudin, V. N. Staroverov, T. A. Keith, R. Kobayashi, J. Normand, K. Raghavachari, A. P. Rendell, J. C. Burant, S. S. Iyengar, J. Tomasi, M. Cossi, J. M. Millam, M. Klene, C. Adamo, R. Cammi, J. W. Ochterski, R. L. Martin, K. Morokuma, O. Farkas, J. B. Foresman and D. J. Fox, *Gaussian 16 Rev. A.03*, Gaussian, Inc., Wallingford CT, 2016.

59.   K. Remya and C. H. Suresh, *J. Comput. Chem.*, 2013, **34**, 1341-1353.
60.   S. Grimme, *J. Comput. Chem.*, 2006, **27**, 1787-1799.
61.   S. Grimme, J. Antony, S. Ehrlich and H. Krieg, *J. Chem. Phys.*, 2010, **132**, 154104.
62.   S. R. Gadre and R. N. Shirsat, *Electrostatics of atoms and molecules*, Universities Press, 2000.
63.   P. Politzer and D. G. Truhlar, *Chemical applications of atomic and molecular electrostatic potentials: reactivity, structure, scattering, and energetics of organic, inorganic, and biological systems*, Springer Science & Business Media, 2013.
64.   J. S. Murray and K. Sen, *Molecular electrostatic potentials: concepts and applications*, Elsevier, 1996.
65.   S. Anila and C. H. Suresh, *Phys. Chem. Chem. Phys.*, 2021, **23**, 13662-13671.
66.   S. Anila and C. H. Suresh, *Phys. Chem. Chem. Phys.*, 2019, **21**, 23143-23153.
67.   E. I. Izgorodina, D. Golze, R. Maganti, V. Armel, M. Taige, T. J. Schubert and D. R. MacFarlane, *Phys. Chem. Chem. Phys.*, 2014, **16**, 7209-7221.
68.   E. Thomas, K. P. Vijayalakshmi and B. K. George, *RSC Adv.*, 2015, **5**, 71896-71902.
69.   S. Seki, T. Kobayashi, Y. Kobayashi, K. Takei, H. Miyashiro, K. Hayamizu, S. Tsuzuki, T. Mitsugi and Y. Umebayashi, *J. Mol. Liq.*, 2010, **152**, 9-13.
70.   M. Cai, Q. Yu, W. Liu and F. Zhou, *Chem. Soc. Rev.*, 2020, **49**, 7753–7818.
71.   C. Ye, W. Liu, Y. Chen and L. Yu, *Chem. Commun.*, 2001, 2244-2245.
72.   G. Mordukhovich, J. Qu, J. Y. Howe, S. Bair, B. Yu, H. Luo, D. J. Smolenski, P. J. Blau, B. G. Bunting and S. Dai, *Wear*, 2013, **301**, 740-746.
73.   Y. Xia, Z. Wang and Y. Song, *Ind. Lubr. Tribol.*, 2014, **66**, 443–451.
74.   N. Dörr, A. Merstallinger, R. Holzbauer, V. Pejaković, J. Brenner, L. Pisarova, J. Stelzl and M. Frauscher, *Tribol. Lett.*, 2019, **67**, 1-18.
75.   G. T. Rochelle, *Science*, 2009, **325**, 1652-1654.
76.   K. Gottschling, L. Stegbauer, G. Sayasci, N. A. Prisco, Z. J. Berkson, C. Ochsenfeld, B. F. Chmelka and B. V. Lotsch, *Chem. Mat.*, 2019, **31**, 1946-1955.
77.   M. T. Ho, G. W. Allinson and D. E. Wiley, *Ind. Eng. Chem. Res.*, 2008, **47**, 4883-4890.
78.   S. Y. Lee and S. J. Park, *J. Ind. Eng. Chem.*, 2015, **23**, 1-11.
79.   K. B. Lee and S. Sircar, *Aiche J.*, 2008, **54**, 2293-2302.
80.   Y. Jiao, A. J. Du, Z. H. Zhu, V. Rudolph and S. C. Smith, *J. Mater. Chem.*, 2010, **20**, 10426-10430.
81.   G. Ferey, C. Serre, T. Devic, G. Maurin, H. Jobic, P. L. Llewellyn, G. De Weireld, A. Vimont, M. Daturi and J. S. Chang, *Chem. Soc. Rev.*, 2011, **40**, 550-562.

82. Q. Sun, M. Wang, Z. Li, A. J. Du and D. J. Searles, *J. Phys. Chem. C*, 2014, **118**, 2170-2177.
83. T. C. dos Santos, S. Bourrelly, P. L. Llewellyn, J. W. d. M. Carneiro and C. M. Ronconi, *Phys. Chem. Chem. Phys.*, 2015, **17**, 11095-11102.
84. C. A. Seipp, N. J. Williams, M. K. Kidder and R. Custelcean, *Angew. Chem. Int. Ed.*, 2017, **56**, 1042-1045.
85. R. Custelcean, N. J. Williams and C. A. Seipp, Google Patents2020.
86. S. Anila and C. H. Suresh, *Phys. Chem. Chem. Phys.*, 2021, **23**, 13662-13671.
87. R. Tenne, *Adv. Mater.*, 1995, **7**, 965-995.
88. Q. Sun, Z. Li, D. J. Searles, Y. Chen, G. Q. Lu and A. J. Du, *J. Am. Chem. Soc.*, 2013, **135**, 8246-8253.
89. S. Liu, H. B. Yang, X. Su, J. Ding, Q. Mao, Y. Q. Huang, T. Zhang and B. Liu, *J. Energy Chem.*, 2019, **36**, 95-105.
90. T. S. Zhao, Q. Wang, Y. Kawazoe and P. Jena, *Carbon*, 2018, **132**, 249-256.
91. N. Martin, *Chem. Commun.*, 2006, 2093-2104.
92. P. D. W. Boyd and C. A. Reed, *Acc. Chem. Res.*, 2005, **38**, 235-242.
93. T. Hasobe, H. Imahori, P. V. Kamat and S. Fukuzumi, *J. Am. Chem. Soc.*, 2003, **125**, 14962-14963.
94. J. Lopez-Andarias, A. Frontera and S. Matile, *J. Am. Chem. Soc.*, 2017, **139**, 13296-13299.
95. E. C. Escudero-Adan, A. Bauza, L. P. Hernandez-Eguia, F. Wurthner, P. Ballester and A. Frontera, *Crystengcomm*, 2017, **19**, 4911-4919.
96. S. Osuna, M. Swart and M. Sola, *Phys. Chem. Chem. Phys.*, 2011, **13**, 3585-3603.
97. J. Cioslowski and K. Raghavachari, *J. Chem. Phys.*, 1993, **98**, 8734-8741.
98. L. Dunsch and S. F. Yang, *Phys. Chem. Chem. Phys.*, 2007, **9**, 3067-3081.
99. K. Kurotobi and Y. Murata, *Science*, 2011, **333**, 613-616.
100. A. Krachmalnicoff, R. Bounds, S. Mamone, S. Alom, M. Concistre, B. Meier, K. Kouril, M. E. Light, M. R. Johnson, S. Rols, A. J. Horsewill, A. Shugai, U. Nagel, T. Room, M. Carravetta, M. H. Levitt and R. J. Whitby, *Nat. Chem.*, 2016, **8**, 953-957.
101. K. Komatsu, M. Murata and Y. Murata, *Science*, 2005, **307**, 238-240.
102. X. Wu and X. Lu, *J. Am. Chem. Soc.*, 2007, **129**, 2171-2177.
103. R. E. Estrada-Salas and A. A. Valladares, *Theochem-J. Mol. Struct.*, 2008, **869**, 1-5.
104. A. L. Balch and M. M. Olmstead, *Chem. Rev.*, 1998, **98**, 2123-2165.
105. K. Lee, H. Song and J. T. Park, *Acc. Chem. Res.*, 2003, **36**, 78-86.
106. S. Vidal, J. Marco-Martinez, S. Filippone and N. Martin, *Chem. Commun.*, 2017, **53**, 4842-4844.
107. C. Z. Li, C. C. Chueh, H. L. Yip, F. Z. Ding, X. S. Li and A. K. Y. Jen, *Adv. Mater.*, 2013, **25**, 2457-2461.
108. J. Cioslowski and A. Nanayakkara, *J. Chem. Phys.*, 1992, **96**, 8354-8362.
109. B. Gao, J. X. Zhao, Q. H. Cai, X. G. Wang and X. Z. Wang, *J. Phys. Chem. A*, 2011, **115**, 9969-9976.
110. F. Gao, G. L. Zhao, S. Z. Yang and J. J. Spivey, *J. Am. Chem. Soc.*, 2013, **135**, 3315-3318.
111. Q. Sun, M. Wang, Z. Li, Y. Y. Ma and A. J. Du, *Chem. Phys. Lett.*, 2013, **575**, 59-66.
112. Y. Jiao, Y. Zheng, S. C. Smith, A. J. Du and Z. H. Zhu, *ChemSusChem*, 2014, **7**, 435-441.

113. S. W. de Silva, A. J. Du, W. Senadeera and Y. T. Gu, *Beilstein J. Nanotechnol.*, 2014, **5**, 413-418.

114. S. Ralser, A. Kaiser, M. Probst, J. Postler, M. Renzler, D. K. Bohme and P. Scheier, *Phys. Chem. Chem. Phys.*, 2016, **18**, 3048-3055.

115. S. Wang, S. M. Mahurin, S. Dai and D. E. Jiang, *ACS Appl. Mater. Interfaces*, 2021, **13**, 17511-17516.

116. S. Anila and C. H. Suresh, *Phys. Chem. Chem. Phys.*, 2021, **23**, 3646-3655.

117. S. Anila and C. H. Suresh, *J. Comput. Chem.*, 2022, **1**.

118. S. Anila and C. H. Suresh, *Phys. Chem. Chem. Phys.*, 2021, **23**, 20086-20094.

119. S. R. Lawrence, C. A. Ohlin, D. B. Cordes, A. M. Slawin and A. Stasch, *Chem. Sci.*, 2019, **10**, 10755-10764.

120. R. K. Pathak and S. R. Gadre, *J. Chem. Phys.*, 1990, **93**, 1770-1773.

Chapter 5

Part A

Endo- and Exohedral Chloro-fullerides as η^5 ligands: A DFT study on the first-row transition metal complexes

Part B

Fulleride-metal η^5 sandwich and multi-decker sandwich complexes
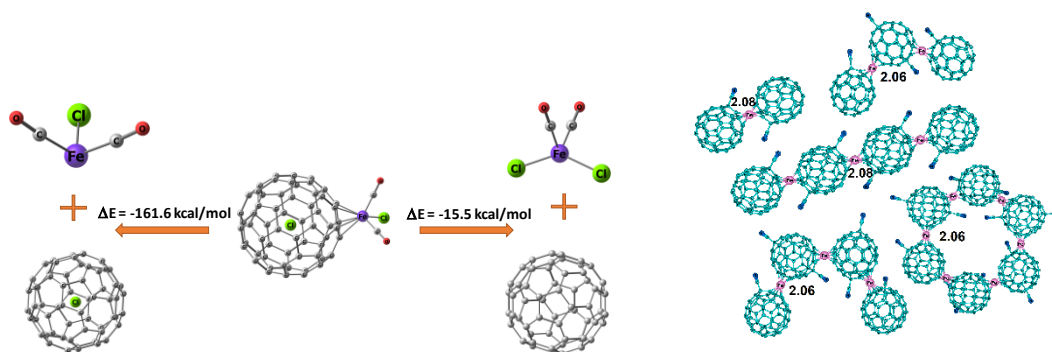
Part A: Endo- and Exohedral Chloro-fullerides as η^5 Ligands: A DFT Study on the First-row Transition Metal Complexes

5.1 Abstract

C_{60} fullerene coordinates to transition metals in η^2-fashion through its C-C bond at [6,6] ring fusion whereas other coordination modes η^3, η^4, η^5 and η^6 are rarely observed. The coordination power of C_{60} to transition metals is weak owing to the inherent π-electron deficiency on each C-C bond as 60 electrons get delocalized over 90 bonds. The encapsulation of Cl^- by C_{60} describes a highly exothermic reaction and the resulting $Cl^-@C_{60}$ behaves as a large anion. Similarly, the exohedral chloro-fulleride Cl^-C_{60} acts as an electron-rich ligand towards metal coordination. A comparison of the coordinating ability of $Cl^-@C_{60}$ and Cl^-C_{60} with that of Cp^- ligand is done for early to late transition metals of the first row using M06L/6-31G**level of density functional theory. The binding energy (E_b) for the formation of endohedral $(Cl^-@C_{60})(ML_n)^+$ and exohedral $(Cl^-C_{60})(ML_n)^+$ complexes by the chloro-fulleride ligands ranges from -116 to -170 kcal/mol and -111 to -173 kcal/mol, respectively. Variation in E_b is also assessed for the effect of solvation by o-dichlorobenzene using self-consistent reaction field method which showed 69 - 88 % reduction in binding affinity owing to more stabilization of the cationic and anionic fragments in solvent compared to the neutral product complex. For each $(Cl^-@C_{60})(ML_n)^+$ and $(Cl^-C_{60})(ML_n)^+$ complex, the energetics for the transformation to C_{60} and ML_nCl is evaluated which showed exothermic character for all endohedral and exohedral Co(I) and Ni(II) complexes. The rest of exohedral complexes, viz. the Sc(I), Ti(II), Ti(IV), V(I), Cr(II), Mn(I), Fe(II) and Cu(I), systems showed endothermic value in the range 2 - 35 kcal/mol. The anionic modification makes the C_{60} unit a strong η^5 ligand similar to Cp^- for cationic transition metal fragments. The bulky anionic nature and strong coordination ability of chloro-fulleride ligands suggest new design strategies for organometallic catalysts.

5.2 Introduction

The C_{60} fullerene has been reported as η^2–type ligand for several transition metal complexes whereas other possible coordination modes such as η^3, η^4, η^5 and η^6 have been rarely observed.[1-6] Hawkins *et al.*[7] were the first to demonstrate the η^2 coordination of C_{60} to the C_{60}-osmium tetroxide adduct $C_{60}(OsO_4)$(4-tert-butylpyridine)$_2$ wherein the C-C bond at the 6-6 ring fusion coordinates to the metal for bond formation. Afterwards complexes of Pt(0)[8, 9], Ir(I)[10, 11], Pd(I)[12-14] with C_{60} as a ligand connected in η^2 format to the metal centre were isolated. Baird *et al.* made stable anionic complexes of the type $A[Mn(CO)_4(\eta^2\text{-}C_{60})]$, (A = Na, bis(triphenylphosphoranylidene) ammonium).[15, 16] Organometallic polymer of fullerene containing polymetallic linkages has been reported wherein the metal centre gets bonded to C_{60} in η^2 fashion.[17-19] The heterogeneous reaction of the palladium or platinum–η^2-fullerene polymer with P ligands (tertiary phosphines or tertiary phosphites) in solution, gives the complexes $C_{60}ML_2$.[20-22]

$$Mn(CO)_4(\eta^2C_{60})\qquad Fe(Cp)(\eta^5C_{60}Me_5)\qquad RuCl(CO)_2(\eta^5C_{60}Me_5)$$
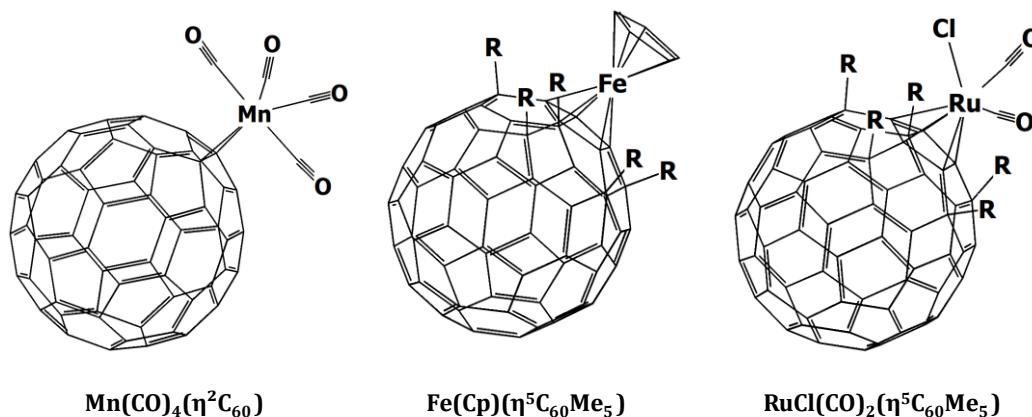
Figure 5.1 A representative set of fullerene-metal complexes

The η^3, η^4, η^5 or η^6 coordination of C_{60} is rarely observed in organometallic chemistry because the spherically delocalized distribution of 60-π electrons over 90 C-C bonds gives rise to significant reduction in π-electron density over each C-C bond compared to a localized C-C double bond. Hence the C-C bond of fullerene at the 6-6 ring fusion can show reactivity similar to electron deficient olefins.[23, 24] Chemists have achieved disruption in the 60-π electron conjugation by saturating five α positions

around a 5-membered ring of C_{60}. The reported η^5-fullerene metal complexes formed with such modified fullerenes are called pseudofullerenes (Figure 5.1). Nakamura group gave an experimental validation for the existence of η^5-C_{60} pseudofullerene-organometallic complexes.[25-28] The ferrocene/pseudofullerene hybrid molecule has been synthesized by Sawamura *et al.* in the singlet ground-state through the use of suitably modified fullerene derivatives (pseudofullerene) that can act as a 6π-electron donor ligand to the 6d electron Fe(II).[27] Toganoh *et al.* reported the reactivity profile of group VI metal complexes of η^5-pentamethyl C_{60} fullerene ligand (pseudofullerene) in a variety of oxidation states, from II to VI.[29] Theoretical studies also predicted the stability of the pseudofullerene bis(η^5-fullerenyl-R_5)Fe, an analogue of ferrocene.[30-33]

Using DFT PBE calculations, Stankevich *et al.* identified η^3- π-hapticity for allyl type derivatives of C_{60} fullerene ($C_{60}R_3$ (R = H, F, Cl, Br)) with Ni and Co.[34] The possibility of the formation of η^4-π-complexes of C_{60} with a Fe(CO)$_3$ species was analysed by Chistyakov and Stankevich through DFT calculations.[35] The stability of η^4-π-complexes of C_{60} with Fe(CO)$_3$ unit has been related to the attachment of four (or six) hydrogen atoms to C_{60} to form "butadiene"-or "fulvalene"-type derivatives. Alvarez *et al.* studied the coordination of C_{60} as well as that of corannulene bucky bowls to the metal fragments and reported that despite of very similar structural features, their preferences for metal coordination are completely different.[36] Using a two-laser vaporization method, the η^6 coordination of C_{60} with Sc to Co was observed by Nagao *et al.*[37] Peng *et al.* observed the η^6 coordination of C_{60} in the complex $C_{60}RuCp(R)_5$ by mass spectroscopy data.[38] Using orbital compatibility arguments, Jemmis *et al.* proposed that due to the splayed out distribution of the π-orbitals of the five- and six-membered rings of C_{60}, an effective η^5/η^6 bonding interaction is difficult for it with a metal fragment. To overcome this and to achieve strong μ-6 coordination, they suggested the use of metal fragments with highly diffuse frontier orbitals such as C_3H_3Co and C_3H_3Rh.[39-41] Recently, theoretical study by Molina *et al.* suggested η^6- coordination for C_{60} with the metals Cr(0) and Ru(II) in sandwich-type complexes.[42] The molybdenum organometallic derivative of C_{60} with the polysubstitution of fluorine atoms, prepared by Taylor and co-workers appeared as η^6-coordinated due to strong distortion in the C_{60} sphere.[43]

Endohedral fullerene (EF) formed by encapsulating atoms, ions, or small molecules inside the cage, show electronic structures different from their parent empty cage, and thus have many applications in the fields of materials science and biomedical applications. Using Hartree-Fock theory, Cioslowski and co-workers theoretically predicted that upon encapsulation of atoms, ions, and molecules with C_{60}, there are almost no changes in the cage structure.[44] Inspired by this work, several experimental and theoretical investigations have been directed towards understanding the properties of a large variety of EFs.[45-47] Most of the theoretical studies were on the confinement and stabilization of the species encapsulated into the endohedral cavity. The encapsulated species, atom or the molecule was found to occupy the centre of the cage cavity. Sathyamurthy and co-workers have studied the structural and electronic confinement of molecules: HF, H_2O, NH_3, and CH_4 inside fullerene.[48, 49] Weidinger *et al.* developed EFs with nitrogen[50] or phosphorus[51] atoms by bombarding C_{60} with nitrogen ions from a conventional plasma discharge ion source. Similarly, $N@C_{70}$, $N_2@C_{70}$,[52] and $P@C_{60}$ were also synthesized using this ion implantation method.[53] Ravinder and Subramanian reported the study on endohedral complexes of halides such as F^-, Cl^-, and Br^- with C_{30}, C_{32}, C_{34}, C_{36}, C_{60}, and C_{70} molecules at B3LYP/6-311+G* level of theory and they also reported the structure and stability of OH and CN inside the C_{60} and C_{70}.[54] Campbell *et al.* used ion bombardment to implant alkali metal ions (especially Li^+) into C_{60}, but the characterization of the final products was difficult.[46] The $Li@C_{60}$ produced by ion bombardment was isolated by Sawa, Tobita and co-workers in the form of its cationic salt, $[Li^+@C_{60}](SbCl_6)$.[55] A detailed investigation of the electronic and structural properties of $M@C_{60}$ (where M = H_2O, Li^+, Na^+, K^+, Be^{2+}, Mg^{2+}, and Ca^{2+}) by Oliveira and Gonçalves, using quantum chemical calculations at the DFT/B3LYP/6-31G** level has shown that energy gap calculated for the endohedral fullerenes based on the HOMO and LUMO energy difference is less than that of pure C_{60}.[56] Tuning of exohedral reactivity of fullerenes by the encapsulation of ions inside the cage is highly important. Garcia-Rodeja *et al.* found that Diels-Alder (DA) reactions between 1,3-cyclohexadiene and ion-encapsulated fullerenes of the type $M@C_{60}$ (M=Li^+, Na^+, K^+, Cl^-) proceed concertedly via highly synchronous transition states, and thus resemble the corresponding process involving the parent C_{60} fullerene. Systems having an endohedral cation has shown a

clear enhancement towards the DA reactions, whereas the behaviour of those with anionic compounds was the opposite.[57]

Although the literature shows evidence for the formation of η^5/η^6- fullerene – organometallic complexes, a synthetically viable strategy for promoting such a coordination behavior is available only for pseudo fullerenes. Recent studies from our group on EFs showed that anions such as F^-, Cl^-, Br^-, OH^-, NH_2^-, NO_2^-, CN^-, and ClO^- interacts strongly with the interior of the fullerene cage leading to significant stabilization of the EFs.[58] Further, such EFs show electron rich behavior on the carbon surface which is similar to the electron rich character of the radical anion $C_{60}^{\bullet-}$. The complexes such as $F^-@C_{60}$, $Cl^-@C_{60}$, $Br^-@C_{60}$, $OH^-@C_{60}$, $NH_2^-@C_{60}$, $NO_2^-@C_{60}$, $CN^-@C_{60}$ and $ClO^-@C_{60}$ behaved like large anions. Frontier molecular orbital (FMO) analysis along with the molecular electrostatic potential (MESP) analysis and quantum theory of atoms in molecules (QTAIM) analysis proved that the electron rich character of the carbon framework of $X^-@C_{60}$ resembles very close to that of the radical anion $C_{60}^{\bullet-}$. This study also suggested that $X^-@C_{60}$ systems has the closed shell nature which gives high chemical stability, compared to the radical anion $C_{60}^{\bullet-}$. Here we consider the possibility of $Cl^-@C_{60}$ as a strongly coordinating η^5/η^6–ligand to transition metal complexes. Also for more realistic application, we consider the exohedral version of such systems, $Cl^-C_{60}ML_n$, the coordination of a chloro-fulleride with a transition metal fragment.

5.2.1 Computational methods

All the geometry optimizations in this study are carried out at the M06L/6-31G** level of DFT using Gaussian 16 suite of programs.[59] The vibrational frequency analysis has been carried out on optimized geometries which confirms the energy minima nature with all real frequencies. The binding energy (coordination energy) of each transition metal complex is calculated using the equation;

$$E_b = E_{TM} - (E_X + E_Y) \qquad\qquad (Eq.\ 5.1)$$

where E_{TM}, E_X and E_Y stand for the zero-point energy (ZPE)-corrected energy of the transition metal complex, the ligand X and metal fragment Y, respectively.

Further, the influence of solvent effects on the complexation of anion incorporated fullerene moiety with metal fragments has been studied using self-consistent reaction field (SCRF) method using the solvation model based on density (SMD) approach. The selected solvent for SMD calculation is o-dichlorobenzene (ODCB). Here Single point calculations are carried out for the complexes with the solvent at M06L/6-311++G** level of theory. The solvation incorporated binding energy (E_{bs}) of each complex is calculated using equation;

$$E_{bs} = E_{TMs} - (E_{Xs} + E_{Ys}) \hspace{3cm} (Eq.\ 5.2)$$

where E_{TMs}, E_{Xs} and E_{Ys} stand for energy of the transition metal complex, the ligand X and metal fragment Y, respectively obtained from the SCRF calculations.

The energy of dissociation (E_r) of the transition metal complex into the corresponding metal halide and C_{60} is calculated as;

$$E_r = E_{TM} - (E_A + E_B) \hspace{3cm} (Eq.\ 5.3)$$

where E_{TM}, E_A and E_B stand for the zero-point energy (ZPE)-corrected energy of the transition metal complex, C_{60} (A) and metal halide (B), respectively.

5.3 Results and discussion

5.3.1 Complexes of [Mn(CO)$_3$]$^+$

The anionic cyclopentadienyl ligand (Cp$^-$), being highly versatile and potential six-electron donor, is one of the most frequently encountered η^5 ligands in organometallic chemistry. Here we consider the Cl$^-$ incorporated endohedral fullerene, Cl$^-$@C$_{60}$ or its exohedral version, Cl$^-$C$_{60}$ as an anionic ligand similar to Cp$^-$. The initial assessment of the η^5 as well as η^6 coordination of Cl$^-$@C$_{60}$ and Cl$^-$C$_{60}$ is carried out by complexing them with the metal fragment [Mn(CO)$_3$]$^+$. The cationic manganese tricarbonyl system is a good choice for this study as the corresponding Cp$^-$ complex Mn(CO)$_3$(Cp) is well documented in the literature with crystal structure.[60, 61] Figure 5.2 gives the optimised geometries of [Mn(CO)$_3$]$^+$ in different coordination fashions.

Mn(CO)₃(Cp)   **[Mn(CO)₃(η⁵ -C₆₀)]⁺**   **Mn(CO)₃(η⁵-(Cl⁻@C₆₀))**   **Mn(CO)₃(η⁵-(Cl⁻C₆₀))**

[Mn(CO)₃(η⁶ -C₆₀)]⁺   **Mn(CO)₃(η⁶-(Cl⁻@C₆₀))**   **Mn(CO)₃(η⁶-(Cl⁻C₆₀))**
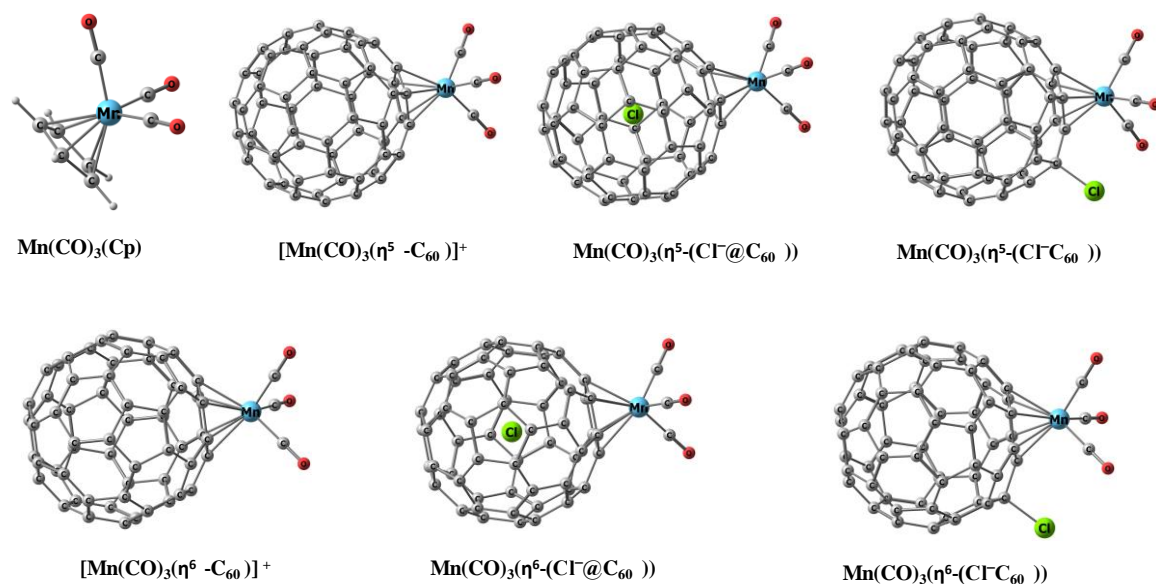
Figure 5.2 Optimised geometries of Mn(CO)₃ complexes at M06L/6-31G**.

Some of the major structural parameters of the complexes depicted in Figure 5.2 are given in Table 5.1. The distance between Mn and the centre of the five or six membered ring is labelled as d_1, d_2 represents Mn-CO distance and d_3 gives the C-O distance. The values of d_1, d_2 and d_3 observed in Mn(CO)₃(Cp) complex are found to be 1.74, 1.78, and 1.16 Å, respectively, which is in agreement with the corresponding crystal structure data, *viz.* 1.77, 1.79, and 1.16 Å. When Cp⁻ ligand is replaced by the anion encapsulated endohedral fullerene [Cl⁻@C₆₀] and exohedral fullerene [Cl⁻C₆₀], CO ligands remain mostly unaffected, as indicated by almost same values of d_2 and d_3 for the η⁵ and η⁶ cases whereas the d_1 values fall in the range 1.85 – 1.88 Å suggest a significant increase compared to d_1 value of the corresponding Cp-complex. The C-Cl distance observed in the exohedral complex in η⁵ and η⁶ coordination modes were 1.87 and 1.94 Å respectively, which is longer than the normal C-Cl distance found in the sp³ hybridised C compounds like CH₃Cl (1.78 Å). This shows that the η⁵ coordination mode is making stronger C-Cl interaction than corresponding η⁶ mode of coordination. In the case of the endohedral complexes, the C-Cl distance observed in η⁵ and η⁶ is 3.54 Å, which is nearly half of the diameter of the C₆₀ molecule (7.07 Å) and suggests that Cl⁻ is at the centre of the fullerene cage. The complexes [Mn(CO)₃(η⁵-C₆₀)]⁺ and [Mn(CO)₃(η⁶-C₆₀)]⁺ showed d_1, d_2 and d_3 values very similar to that of the anionic fullerene derivatives. It is clear that the

relative stability of the complexes cannot be correctly inferred from the distance parameters.

Table 5.1 Structural parameters (Å), vibrational frequency of CO symmetric stretching (cm^{-1}) and E_b (kcal/mol) values of the Mn-complexes at M06L/6-31G**.

Complex	d_1	d_2	d_3	d_4	$\bar{v}_{CO}$
Mn(CO)$_3$Cp	1.74	1.79	1.16	-	2103
[Mn(CO)$_3$(η^5-C$_{60}$)]$^+$	1.86	1.80	1.16	-	2133
[Mn(CO)$_3$(η^6-C$_{60}$)]$^+$	1.85	1.80	1.15	-	2139
Mn(CO)$_3$(η^5-(Cl$^-$@C$_{60}$))	1.85	1.79	1.16	3.54	2111
Mn(CO)$_3$(η^6-(Cl$^-$@C$_{60}$))	1.85	1.79	1.16	3.55	2115
Mn(CO)$_3$(η^5-Cl$^-$C$_{60}$)	1.85	1.79	1.16	1.87	2112
Mn(CO)$_3$(η^6-Cl$^-$C$_{60}$)	1.88	1.79	1.16	1.94	2122

IR vibrational frequency analysis of these complexes (Table 5.1) shows that the carbonyl symmetric stretching frequencies ($\bar{v}_{CO}$) of the complexes are higher than that of the reference complex, Mn(CO)$_3$(Cp). The C-O vibrational frequency increases in the order, Cp$^-$ < (Cl$^-$@C$_{60}$) < (Cl$^-$C$_{60}$) < C$_{60}$. Higher degree of back-bonding from the Mn centre to CO ligand in the complex Mn(CO)$_3$(Cp) results in the lowest observed $\bar{v}_{CO}$ of ~2103 cm^{-1} whereas the coordination of [Mn(CO)$_3$]$^+$ to fullerene either in η^5 or η^6 fashion gives the largest $\bar{v}_{CO}$, 2133 - 2139 cm^{-1} due to the weak back-bonding. Also between η^5 and η^6 coordination, 4 - 10 cm^{-1} lower value of $\bar{v}_{CO}$ is observed for the former indicating the higher preference of such a coordination for fullerene units with [Mn(CO)$_3$]$^+$.

Table 5.2 E_b (kcal/mol) values of various complexation possibilities of the Mn-complexes at M06L/6-311++G**// M06L/6-31G**.

Complex	Complexation reaction	E_b
$Mn(CO)_3Cp$	$[Mn(CO)_3]^+ + Cp^-$	-263.9
$(Mn(CO)_3)^+(\eta^5\text{-}C_{60})$	$[Mn(CO)_3]^+ + (\eta^5\text{-}C_{60})$	-81.1
$(Mn(CO)_3)^+(\eta^6\text{-}C_{60})$	$[Mn(CO)_3]^+ + (\eta^6\text{-}C_{60})$	-78.8
$Cl^-@C_{60}$	$C_{60} + Cl^-$	-52.2
Cl^-C_{60}	$C_{60} + Cl^-$	-25.6
$(Mn(CO)_3)^+(\eta^5\text{-}(Cl^-@C_{60}))$	$[Mn(CO)_3]^+ + Cl^-@C_{60}$	-160.5
$(Mn(CO)_3)^+(\eta^6\text{-}(Cl^-@C_{60}))$	$[Mn(CO)_3]^+ + Cl^-@C_{60}$	157.0
$(Mn(CO)_3)^+(\eta^5\text{-}(Cl^-C_{60}))$	$[Mn(CO)_3]^+ + Cl^-C_{60}$	-165.3
$(Mn(CO)_3)^+(\eta^6\text{-}(Cl^-C_{60}))$	$[Mn(CO)_3]^+ + Cl^-C_{60}$	-149.1

The energetics of various complexation possibilities are presented in Table 5.2. The separation of $Mn(CO)_3Cp$ to ionic fragments $Mn(CO_3)^+$ and Cp^- is energy demanding with E_b -263.9 kcal/mol. The η^5 coordination of C_{60} with $Mn(CO_3)^+$ is exothermic by 81.1 kcal/mol while the η^6 coordination is weaker by 2.3 kcal/mol. The endohedral complexation of Cl^- with fullerene is exothermic by 52.2 kcal/mol whereas its exohedral complexation is exothermic by 25.6 kcal/mol. The dissociation of the complex $[(Mn(CO)_3)^+(\eta^5\text{-}(Cl^-C_{60})]$ into the fragments $[MnCO_3]^+$ and $Cl^-@C_{60}$ requires energy 160.5 kcal/mol. In the case of the exohedral complex $[(Mn(CO)_3)^+(\eta^5\text{-}(Cl^-C_{60})]$, E_b for the fragmentation $(Mn(CO)_3)^+$ and Cl^-C_{60} is -165.3 kcal/mol, which is higher than the respective endohedral variant by 4.8 kcal/mol. In $Cl^-–C_{60}$, the interaction distance of Cl^- with the nearest five carbon atoms ranges from 3.10 Å - 3.14 Å which indicates that fullerene is having only a weak non-covalent interaction with Cl^- whereas the C—Cl distance 1.87 Å observed in $(Mn(CO)_3)^+(\eta^5\text{-}(Cl^-C_{60}))$ suggests strong covalent interaction between the atoms. The preferred positon for exohedral bonding of Cl- to the fullerene is

the α-carbon, with respect to the η^5-coordinated five-membered ring as observed from the different possible variations in the exohedral structures. In the case of η^6 - coordination, the E_b values observed for the complexes are less than the corresponding η^5-complexes (Table 5.1). The difference is 3.5 kcal/mol for $Cl^-@C_{60}$, whereas in the case of Cl^-C_{60}, the difference is of 16.2 kcal/mol.

The energy data on different complexation possibilities clearly suggest that the anionic endohedral as well as exohedral variants of the fullerene molecule with Cl^- are capable of coordinating with the metal fragments to give stable η^5 and η^6 complexes. Although not as strong as the Cp^- ligands, the endohedral or exohedral modification on the fullerene with anion improves the E_b by almost double compared to bare fullerene-metal interaction. The anion incorporation makes the carbon centers of fullerene electron rich and the whole system behaves as a large anion for a strong coordination with the metal fragment. Since η^5- complex is more stable than η^6-varient, it tested for other metal complexes and only the former is studied for other metal centers.

5.3.2 Complexes of first row transition metals

The strong η^5-type coordinating ability of $Cl^-@C_{60}$ and Cl^-C_{60} observed for tricarbonyl manganese complex could be validated for other transition metals. In order to do this, the study is extended to the organometallic complexes of the first row transition metals: Sc, Ti, V, Cr, Mn, Fe, Co, Ni, and Cu. X-ray structures of complexes of these metals containing Cp^- or a substituted Cp^- (Cp^{-*}) have been reported in the literature. Two or three complexes of each of the first row transition metals are discussed here with mostly the carbonyl ligand or trialkyl amine and trialkyl phosphine ligand. The optimized structures of selected such complexes ($CpML_n$) from the literature (Cp^{-*} is replaced with Cp^-) are shown in Figure 5.3.

The E_b value of $CpML_n$ for Cp^- dissociation is in the range -196 to -275 kcal/mol (Table 5.3). E_b values varies with respect to the nature of the metal centre and the associated ligands. The Cp – metal interaction is the weakest for the early and late transition metals such as Sc, Cu and Ni while the middle transition metals such as Cr and Fe show the strongest interaction. In all these complexes, if Cp^- is replaced with C_{60} for

an η^5 coordination with the metal center, the corresponding cationic complexes, $[C_{60}ML_n]^+$ show E_b in the range -52 to -88 kcal/mol (Table 5.3).
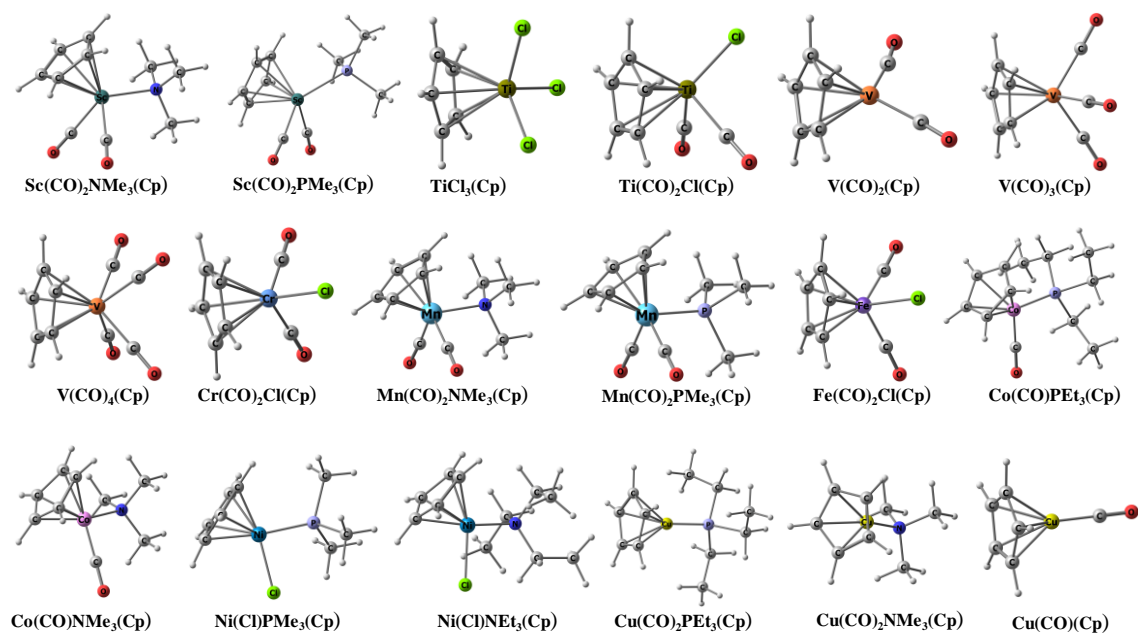
Figure 5.3 Optimised structures of transition metal complexes of Cp⁻ at M06L/6-31G**.

Figure 5.4 gives the optimized geometries of $(Cl^-@C_{60})(ML_n)^+$. Here $Cl^-@C_{60}$ behaves as a large anionic ligand to provide six electrons to metal center through the η^5 coordination. The E_b is in the range -116 to -171 kcal/mol which is 63 to 98 kcal/mol better than $[C_{60}ML_n]^+$ complexes. Compared to early and late transition metals, the middle ones showed higher interaction with $Cl^-@C_{60}$. In all $(Cl^-@C_{60})(ML_n)^+$ cases, Cl^- is trapped deep inside the fullerene moiety (close to the center) and a direct covalent interaction of Cl with fullerene carbon or metal center can be ruled out. The significant enhancement in the binding energy between $Cl^-@C_{60}$ and M compared to C_{60} and M can be interpreted as solely due to the through space electronic influence of Cl^- on the metal. In effect, $Cl^-@C_{60}$ acts as a large anion[58] due to the significant transfer of the extra negative charge density on the Cl^- to the whole fullerene C atoms leading to six electron coordination power for $Cl^-@C_{60}$ towards the metal center. In essence, the ligation from the Cl^- incorporated fullerene unit through the five membered ring could be considered as an interaction similar to between Cp⁻ and metal in organometallic complexes.

Table 5.3 ZPE corrected- E_b of the transition metal complexes for L = Cp⁻, L = C_{60}, L= Cl⁻@C_{60}, and L = Cl⁻C_{60} at M06L/6-311++G**//M06L/6-31G** level.

Metal	Ligands	E_b (kcal/mol)			
		L = Cp⁻	L= C_{60}	L= Cl⁻@C_{60}	L= C_{60}⁻Cl⁻
Sc (I)	CO, CO, NMe₃, L	-194.3	-52.3	-115.9	-118.2
Sc (I)	CO, CO, PMe₃, L	-195.5	-52.0	-116.8	-111.3
Sc (I)	4CO, L	-216.7	-56.5	-129.4	-131.9
Ti (II)	CO, CO, Cl⁻, L	-248.8	-73.7	-152.3	-155.4
Ti (IV)	3 Cl⁻, L	-255.9	-73.0	-155.2	-161.4
V (I)	CO, CO, L	-247.9	-77.1	-153.1	-157.7
V (I)	CO, CO, CO, L	-251.6	-76.5	-154.5	-158.0
V (I)	4CO, L	-256.2	-76.8	-156.6	-160.5
Cr (II)	CO, CO, Cl⁻, L	-221.3	-87.7	-170.0	-173.4
Mn (I)	CO, CO, NMe₃, L	-224.8	-61.1	-132.3	-134.6
Mn (I)	CO, CO, PMe₃, L	-235.2	-67.9	-139.8	-142.2
Fe (II)	CO, CO, Cl⁻, L	-267.1	-79.3	-161.6	-168.9
Fe (II)	CO, CO, Br, L	-264.5	-78.3	-159.6	-166.8
Co (I)	CO, NMe₃, L	-221.3	-70.8	-138.1	-144.6
Co (I)	CO, PEt₃, L	-223.0	-69.0	-136.3	-139.2
Ni (II)	PMe₃, Cl, L	-230.8	-78.9	-149.2	-153.3
Ni (II)	NMe₃, Cl, L	-208.4	-58.4	-129.5	-135.2
Cu (I)	CO, L	-235.8	-83.1	-156.0	-156.2
Cu (I)	NMe₃, L	-200.1	-76.7	-139.4	-134.8
Cu (I)	PEt₃, L	-198.2	-68.9	-131.4	-127.3
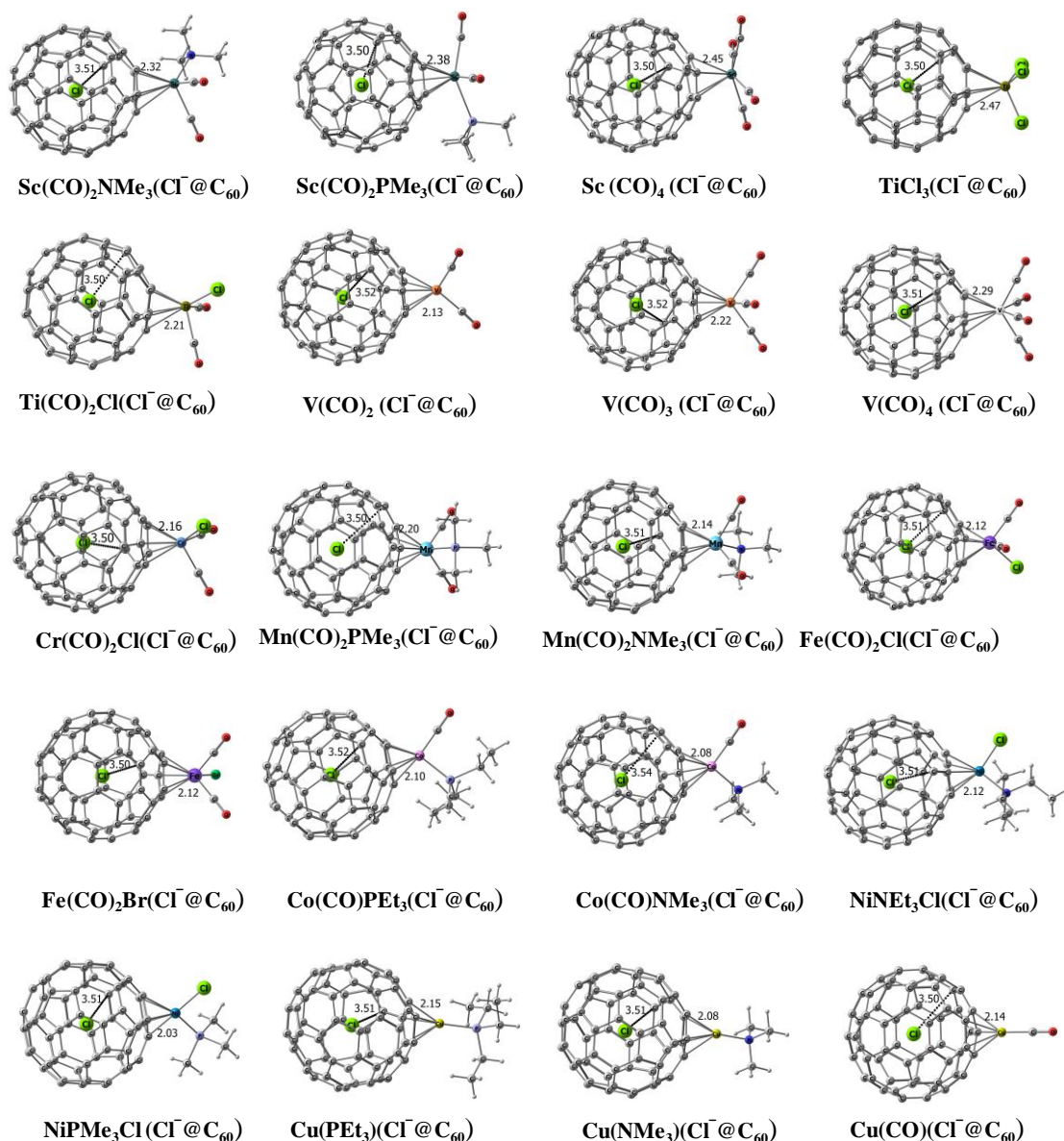
Figure 5.4 Optimised structures of transition metal complexes of $Cl^-@C_{60}$ at M06L/6-31G** level.

The optimized geometries of $(Cl^-C_{60})(ML_n)^+$ complexes are given in Figure 5.5. The E_b values of the complexes are in the range -111 to -169 kcal/mol. Strong η^5 coordination is observed for the ligand with all the metal fragments except $[Sc(CO)_2PMe_3]^+$, $[CuNMe_3]^+$ and $[TiCl_3]^+$. In the case of $[Sc(CO)_2PMe_3]^+$ and $[CuNMe_3]^+$, a bond formation of Cl^- with the α- carbon is not observed. All attempts to optimize such structures give the complexes C_{60}–$Sc(CO)_2PMe_3Cl$ and C_{60}–$CuNMe_3Cl$ respectively. The

($Cl^{-}C_{60}$)(ML_n)$^+$ complex of [$Sc(CO)_2PMe_3$]$^+$ and [$CuNMe_3$]$^+$ given in Figure 5.5 shows the bonding of Cl^{-} at the β-carbon and the coordination of fullerene to Sc and Cu is η^5 type. Similarly in the case of [$TiCl_3$]$^+$, the non-bonded $C_{60}\cdots TiCl_4$ is formed when the optimization is attempted for ($Cl^{-}C_{60}$)($TiCl_3$)$^+$ with Cl^{-} at the α-position. Also, the optimization of the complex with Cl^{-} at the β-position yields the structure given in Figure 5.5 wherein the fullerene part shows η^1 coordination with Ti. When the Cl^{-} is connected diametrically opposite to the metal coordination, η^5 complex of [($Cl^{-}C_{60}$)($TiCl_3$)$^+$] is obtained. The η^1 and η^5 complexes of Ti are higher in energy compared to the non-bonded neutral complex by 41.8 and 65.1 kcal/mol, respectively (Figure 5.6).
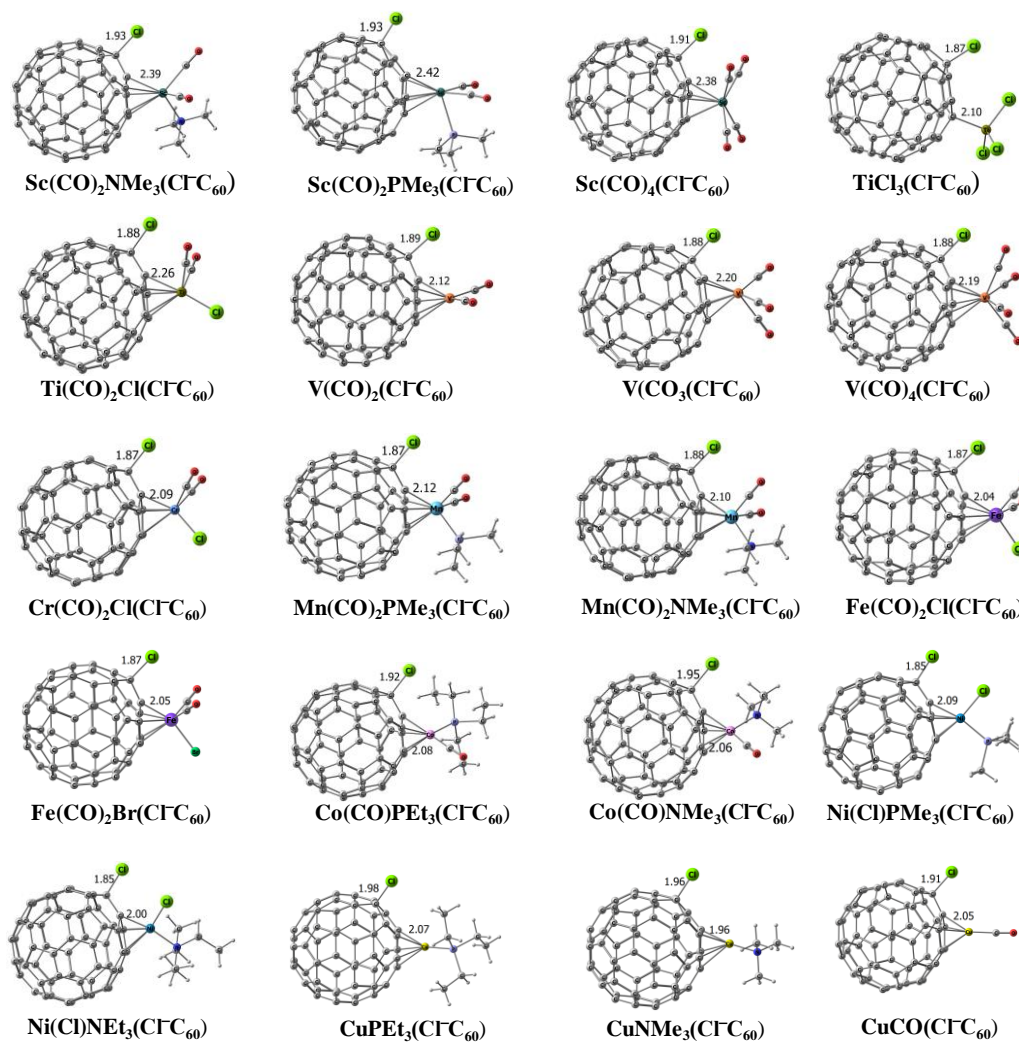
Figure 5.5 Optimised structures of transition metal complexes of $Cl^{-}C_{60}$ at M06L/6-31G** level.

C$_{60}$...TiCl4 **TiCl$_3$(Cl⁻C$_{60}$)_β** **TiCl$_3$(Cl⁻C$_{60}$)_η**
E$_{rel}$ = 41.8 kcal/mol **E$_{rel}$ = 65.1 kcal/mol**
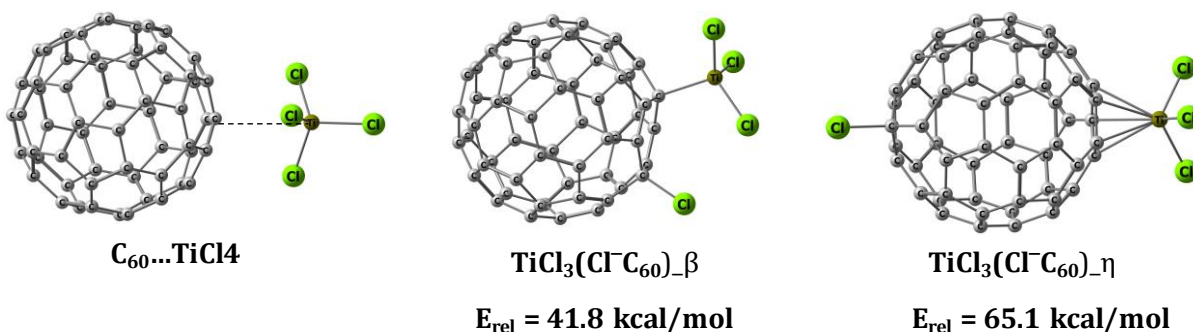
Figure 5.6 Optimized geometries of $[(Cl⁻C_{60})TiCl_3]$ with Cl⁻ at α, β, and diametrically opposite to metal coordination (η) position at M06L/6-31G** level. The difference in their SCF energies (E$_{rel}$)are given in kcal/mol.

The trend observed for E$_b$ (Table 5.3) for exohedral fullerene complexes (Figure 5.5) is very similar to that of endohedral complexes (Figure 5.4) and between them only small variations in E$_b$ is observed. The C-Cl bond formation is well evident in all the exohedral complexes as their bond distance falls in the range 1.87 to 2.47 Å. Compared to the C-Cl distance observed for Cl⁻C$_{60}$, 46 % reduction in the bond parameter is observed for the exohedral complex and suggests that strong electrostatic interaction between Cl⁻ and (C$_{60}$ML$_n$)⁺ forces the bond formation.

5.3.3 Effect of solvation

All the complexes discussed above are studied for the influence of the solvent ODCB on the complexation. The solvation effect incorporated binding energy (E$_{bs}$) values of are given in Table 5.4. For all the cases, E$_{bs}$ data show a large decrease compared to the gas phase value E$_b$. For example, E$_{bs}$ of CpML$_n$ complexes are in the range -40.3 to -122.7 kcal/mol, which is ~150 kcal/mol lower than the corresponding E$_b$. Similarly, E$_{bs}$ of (C$_{60}$)(ML$_n$)⁺, (Cl⁻@C$_{60}$)(ML$_n$)⁺ and (Cl⁻C$_{60}$)(ML$_n$)⁺ decreased, but to a lesser extent than the CpML$_n$ complexes. Among (C$_{60}$)(ML$_n$)⁺, (Cl⁻@C$_{60}$)(ML$_n$)⁺ and (Cl⁻C$_{60}$)(ML$_n$)⁺, the endohedral variant is the most stabilized with E$_{bs}$ in the range -2.5 to -47.5 kcal/mol followed by the exohedral complexes. Among all, the best tendency to complex formation is observed for Mn, Fe, Co, and Ni complexes.

Table 5.4 E_{bs} of the transition metal complexes for L = Cp^-, L = C_{60}, L= $Cl^-@C_{60}$, and L = Cl^-C_{60} at M06L/SMD/6-311++G**//M06L/6-311++G** level using ODCB as the solvent.

Metal	Ligands	E_{bs} (kcal/mol)			
		L =Cp^-	L = $Cl^-@C_{60}$	L = Cl^-C_{60}	L =C_{60}
Sc (I)	CO, CO, NMe$_3$, L	-52.2	-6.9	-0.2	-2.4
Sc (I)	CO, CO, PMe$_3$, L	-51.6	-7.7	9.0	-3.4
Sc (I)	4CO, L	-68.36	-13.01	-6.8	-2.8
Ti (II)	CO, CO, Cl$^-$, L	-85.1	-16.6	-13.4	-2.3
Ti (IV)	3Cl$^-$, L	-107.7	-33.8	-33.1	-17.2
V (I)	CO, CO, L	-80.0	-14.2	-10.2	-2.2
V (I)	CO, CO, CO, L	-89.5	-20.7	-16.0	-7.1
V (I)	4CO, L	-98.2	-24.7	-22.3	-10.2
Cr (II)	CO, CO, Cl$^-$, L	-122.7	-47.5	-45.9	-31.2
Mn (I)	CO, CO, CO, L	-102.4	-24.9	-15.4	-10.5
Mn (I)	CO, CO, NMe$_3$, L	-80.2	-15.3	-10.0	-4.8
Mn (I)	CO, CO, PMe$_3$, L	-89.2	-21.2	-15.7	-10.1
Fe (II)	CO, CO, Cl$^-$, L	-120.6	-39.0	-40.9	-22.1
Fe (II)	CO, CO, Br$^-$, L	-129.3	-48.1	-49.2	-31.8
Co (I)	CO, NMe$_3$, L	-81.3	-26.2	-21.8	-17.6
Co (I)	CO, PEt$_3$, L	-89.9	-30.8	-25.1	-22.1
Ni (II)	PMe$_3$, Cl$^-$, L	-89.1	-34.7	-30.0	-24.6
Ni (II)	NMe$_3$, Cl$^-$, L	-80.9	-26.3	-25.4	-14.5
Cu (I)	CO, L	-50.7	-2.5	6.7	7.2
Cu (I)	NMe$_3$, L	-40.3	-12.2	-0.7	-5.9
Cu (I)	PEt$_3$, L	-43.4	-9.1	-6.0	-2.8

5.3.4 Chloro-fulleride complex to fullerene and metal chloride

Assuming that the known systems C_{60} and ML_nCl reacts to give $(Cl^-C_{60})(ML_n)^+$ or $(Cl^-@C_{60})(ML_n)^+$, the energy the reaction (E_r) can be used as a parameter to assess the stability of $(Cl^-C_{60})(ML_n)^+$ and $(Cl^-@C_{60})(ML_n)^+$ complexes.

Table 5.5 ZPE corrected-reaction energy (E_r) and solvation included reaction energy (E_{rs}) in kcal/mol for the complexes $(Cl^-@C_{60})(ML_n)^+$ and $(Cl^-C_{60})(ML_n)^+$ into corresponding ML_nCl and C_{60}.

Metal	ligands	E_r		E_{rs}	
		$L = Cl^-@C_{60}$	$L = Cl^-C_{60}$	$L = Cl^-@C_{60}$	$L = Cl^-C_{60}$
Sc (I)	CO, CO, NMe₃, L	-0.2	24.1	-3.9	27.7
Sc (I)	CO, CO, PMe₃, L	-4.3	27.8	-12.7	28.8
Sc (I)	4CO, L	-0.1	24.1	-4.1	27.0
Ti (II)	CO, CO, Cl⁻, L	-2.8	21.9	-3.9	24.0
Ti (IV)	3Cl⁻, L	14.3	34.7	10.6	36.2
V (I)	CO, CO, L	-12.8	9.2	-4.6	24.2
V (I)	CO, CO, CO, L	-9.8	13.3	-6.6	22.9
V (I)	4CO, L	-8.1	14.5	-9.3	17.9
Cr (II)	CO, CO, Cl⁻, L	-14.7	8.4	-12.8	13.6
Mn (I)	CO, CO, CO, L	-12.8	11.5	-7.7	22.5
Mn (I)	CO, CO, NMe₃, L	-16.8	7.4	-10.7	19.5
Mn (I)	CO, CO, PMe₃, L	-15.5	3.8	-11.7	11.3
Fe (II)	CO, CO, Cl⁻, L	-17.5	1.9	-12.2	11.5
Fe (II)	CO, CO, Br⁻, L	-26.4	-6.3	-11.7	17.5
Co (I)	CO, NMe₃, L	-28.0	-4.3	-12.2	18.3
Co (I)	CO, PEt₃, L	-24.0	-1.5	-4.3	25.2
Ni (II)	PMe₃, Cl⁻, L	-24.1	-3.3	-5.6	20.1
Ni (II)	NMe₃, Cl⁻, L	-19.5	6.8	7.3	41.2
Cu (I)	CO, L	-27.8	3.3	3.4	39.7
Cu (I)	NMe₃, L	-25.5	5.2	0.3	28.3

The E_r data in gas phase and solvent phase (E_s) are given in Table 5.5 For the endohedral cases, E_r is negative (exothermic) indicating the favourability of the formation of coordinated complex over fullerene and metal chloride. The endohedral character is found only for exohedral systems of Co(I) and Ni(II). Also the endohedral complexes always showed higher stability than the exohedral variant. This is because the interaction of Cl^- with the interior surface of C_{60} is significantly more stabilizing in character than its exohedral interaction with C_{60}. The E_s data show that solvent effect is improving the coordination property of the endohedral Sc(I), Ti(I), Ti(IV) and one of the V(I) systems whereas for the rest of the systems and for exohedral complexes, the solvation effect has a diminishing effect on the coordination properties. The diminished coordination power in solvent is the highest for the late transition metals such as Co(I), Ni(II) and Cu(I) complexes.

5.4 Conclusions

Endohedral and exohedral chloro-fullerides are capable of interacting with the metal fragments to give different transition metal complexes in the η^5 and η^6 coordination modes. $Cl^-@C_{60}$ is found to be stable in the isolated as well as in the complexed form, whereas Cl^-C_{60} is found to have the covalent C-Cl interaction only in the presence of the counter cationic metallic fragment. The η^5 complex was more stabilized than the corresponding η^6 variant in the studied representative case of $[Mn(CO)_3L]$ (L= C_{60}, $Cl^-@C_{60}$ and Cl^-C_{60}). The E_b data clearly showed the superior coordinating ability of $Cl^-@C_{60}$ and Cl^-C_{60} in comparison with C_{60} for all the metallic complexes from Sc to Cu. The effect of solvation on the complexation of chloro-fulleride with metal fragments studied with SCRF method has shown a similar trend in energetics as that of the gaseous state but with a reduced value for binding energy. This is because in the ligands $Cl^-@C_{60}$ and Cl^-C_{60}, the negative charge is no longer on Cl atom alone but delocalized over all the carbon atoms. The chloro-fulleride behaves as bulky anion with the ability to coordinate strongly with transition metals. Among the different metals, Mn, Fe, Co, and Ni are found to have significantly higher values of both E_b and E_{bs}. The endohedral chloro-fulleride showed higher coordination ability than the exohedral one. The E_r data indicate that by

220

reacting fullerene with a transition metal chloride, formation of chloro-fulleride incorporated transition metal complex can be achieved. Such a reaction is exothermic for endohedral systems and mostly endothermic for the exohedral complex. All these facts thus accentuate the possibility of the anionic form of the fullerene molecule to act as a large anionic ligand in organometallic complexes. The large size (~0.7 nm in diameter), high chemical stability, large specific surface area, good electrical conductivity and unique three-dimensional structure of the fullerene unit in ligands: $Cl^-@C_{60}$ and Cl^-C_{60}, makes them suitable for designing complexes with specific catalytic activities. The steric bulkiness of the ligand helps in stabilizing the metals in their incomplete electronic states like 12-, 14- and 16-electrons by preventing the metal centre from further ligation.

Part B: Fulleride-metal η⁵ Sandwich and Multi-decker Sandwich Complexes

5.5 Abstract

The $(C_{60}CN)^-$ formed by the reaction of CN^- with fullerene shows high electron rich character, very similar to $C_{60}^{\bullet-}$, and it behaves as a large anion. Similar to Cp^-, the bulky anion, $(C_{60}CN)^-$, acts as a strong η^5 ligand towards transition metal centers. Previous studies on η^5 coordination of fullerene cage are reported for pseudo fullerenes whereas the present study deals with sandwich complexes of $(C_{60}CN)^-$ with Fe(II), Ru(II), Cr(II), Mo(II), and Ni(II) and multi-decker sandwich complexes of CN–fullerides with Fe(II). The structural parameters of these complexes and the corresponding Cp^- complexes showed very close resemblance. Analysis of the metal-to-carbon bonding molecular orbitals showed that sandwich complex $[Fe(\eta^5\text{-}(C_{60}CN)^-)_2]$ exhibit bonding features very similar to that of ferrocene. Also, a 6-fold decrease in the band gap energy is observed for $[Fe(\eta^5\text{-}(C_{60}CN)^-)_2]$ compared to ferrocene. The energy of dissociation (ΔE) of the ligand $(C_{60}CN)^-$ from $[Fe(\eta^5\text{-}(C_{60}CN)^-)_2]$ is slightly lower than the ΔE of a Cp^* ligand from a ferrocene derivative wherein each cyclopentadienyl unit is substituted with four tertiary butyl groups. The $(C_{60}CN)^-$ ligand behaved as one of the bulkiest ligands in the chemistry of sandwich complexes. Further, the coordinating ability of the dianion, $(C_{60}(CN)_2)^{2-}$ is evaluated which showed strong coordination ability simultaneously with two metal centers leading to the formation of multi-decker sandwich and pearl-necklace type polymeric structures.

5.6 Introduction

Independent researches by Pauson and Kealy and by Miller and co-workers led to the accidental discovery of the biscyclopentadienyl complex of iron, $[Fe(C_5H_5)_2]$, called ferrocene,[62, 63] which established the concept of pπ-dπ complexes.[33] The electronic structure of ferrocene was solved independently by Fischer[64] and Woodward and Wilkinson[65, 66] as a 6d-electron Fe(II) atom sandwiched between a pair of 6π-electron

aromatic pentagonal carbon arrays (cyclopentadienyl anion = Cp−).[67] The X-ray crystallography by Eiland and Pepinski confirmed the sandwich-type configuration of ferrocene.[68] Later Dunitz and Orgel explained the high stability of ferrocene with molecular orbital theory.[69] This discovery of ferrocene opened up a completely new gateway to the organometallic chemistry of sandwich complexes, commonly known as metallocenes.[70-72] The applications of metallocenes are based on their behavior as reducing agents, antioxidants, and as excellent organic carriers of iron in high concentration and are also used as a catalyst for various organic reactions.[73]

The tuning of the properties of sandwich complexes is achieved through modifying the Cp− ligand by different alkyl substitution resulting to the synthesis of various bulky sandwich complexes.[74-76] Further, the five membered ring of a fullerene cage has been considered as a replacement for Cp− ligand for developing new set of sandwich complexes. Ravinder and Subramanian reported a DFT study on the structure and stability of fullerene based endohedral sandwich complexes.[77] Previous theoretical studies predicted the formation of Cp-type π-complexes of fullerene derivatives, for example, the fullerene analogue of ferrocene, bis(η^5-fullerenyl-R_5)Fe.[30-32, 78, 79] Here 'R' substituted five α-carbon centers around the five-membered ring were saturated which created pure Cp− character and such modified fullerene derivatives are known as 'pseudo fullerenes'.[5] Nakamura group gave an experimental validation for the existence of ferrocene-type singlet ground state configurations of η^5-pseudo fullerene complexes of Fe(II), Ru(II).[25-28, 80, 81] They also synthesized group 6 metal complexes of the η^5-pentamethyl[60]fullerene.[82] Muhammad *et al.* theoretically studied the diradical character and nonlinear optical properties of buckyferrocenes by suitably modifying the pseudo fullerene fragments.[83]

All the studies on sandwich complexes developed with fullerene derivatives have utilized a five-membered ring surrounded with saturated carbon centers for η^5 coordination whereas a ferrocene analogue of fullerene C_{60} is not yet reported. Although C_{60} is capable of forming compounds in various coordination forms such as η^2, η^3, η^4, η^5 and η^6, most of the experimental studies were focused on the η^2 mode of coordination towards the metal. Owing to the conjugated π-electron cloud, a simple η^5 coordination

from five-membered ring or η^6 coordination from six-membered ring appeared difficult which can be attributed to the electron deficient character of the fullerene cage. The unique properties of fullerene such as low reduction potentials and strong electron acceptor nature make it a potential source of new materials or chemotherapeutic agents.[84-89] This has instigated several theoretical[90-96] and experimental[97-99] studies on endohedral[91, 100-102] as well as exohedral[103-106] modifications on the fullerene cage to generate the new materials of interest.[107-110]

Shortly after the bulk synthesis of C_{60}, different kinds of fullerene polymers have been synthesized, including the so-called "pearl necklace", or main-chain, structures, in which the fullerene molecules are joined together with short bridging groups, and the "charm bracelet", or side-chain, polymers, where the fullerenes dangle from the backbone of existing polymers.[111-113] Organometallic C_{60} polymers was an area of significant interest and in 1992 Nagashima and co-workers synthesised the first example of such a polymer with pearl-necklace structure.[114, 115] Recently, Leng *et al.* have reported spontaneously self-assembled -C_{60}-Ru-C_{60}- polymeric chains as spherical particles. Their DFT calculations showed that the metal Ru exhibited the η^2 to η^6 modes of coordination with the C_{60} and the stable configuration was observed to possess the η^2 mode of coordination and a stabilization of 86 kcal/mol was observed for C_{60}-Ru-C_{60}.[116] Organometallic C_{60} polymers may have potential applications in catalysis,[115] electrochemistry,[117] and other areas.[118] The extended sandwich structures (triple-deckers, tetra-deckers *etc.*) containing d-transition metals are well established and literature also gives reports on the multi-decker sandwich complexes of f-elements with sterically demanding ligands.[119-121] However, such multi-decker sandwich complexes containing fulleride ligands are not reported yet.

Recently, in a study using the M06L/6-311++G**//M06L/6-31G** level of DFT, we have shown that both endohedral and exohedral chloro-fullerides act as an η^5 ligand similar to Cp$^-$ with cationic transition metal fragments.[122] This study also revealed that in comparison to the simple C_{60}, the chloro-fullerides act as bulky anionic ligands in η^5 or η^6 mode of coordination. The binding energy observed for the complexes of chloro-fullerides (110 – 160 kcal/mol) was twice than that of the complexes formed by C_{60} (50 -

90 kcal/mol). The encapsulation of an anion in the fullerene cage is very difficult to accomplish while the exohedral modification of fullerene cage has been found to be a possible way to obtain the anionic fullerene derivatives. Very recently, DFT studies predicted the exothermic formation of anionic exohedral fullerides (X-fullerides, X = H, F, OH, CN, NH_2 and NO_2) from C_{60} and an X-substituted imidazolium (IMX) compound.[123] The X-fullerides showed the delocalised distribution of the extra electron on the fullerene cage. As a result, compared to fullerene, the C_{60} cage of fulleride showed high electron rich character very similar to C_{60} anion. Further, the proposed mechanism of formation $IM^+(C_{60}X)^-$ ion-pairs from C_{60} and 1,3-dimethyl-2X-Imidazole (IMX) supported the formation of low melting imidazolium-fulleride ionic liquids. Among the different reactions, the formation of $IM^+(C_{60}CN)^-$ was the most exergonic. Considering the electron rich character of the X-fullerides, here we explore the η^5 coordination tendency of them towards the formation of sandwich complexes. The $(C_{60}CN)^-$ is selected as the η^5 ligand for different transition metals *viz*. Fe, Ru, Cr, Mo and Ni. Further, $(C_{60}(CN)_2)^{2-}$ dianion species is considered for developing extended structures of fulleride-sandwich complexes.

5.6.1 Computational methods

All calculations have been carried out at the M06L/6-311++G**//M06L/6-31G** level of density functional theory[124-126] using the Gaussian16 suite of programs[127]. M06L functional has been suggested as the best method in overall performance for organometallic, and noncovalent interactions.[124] The vibrational frequency analysis has been done to confirm the optimized geometries as the true energy minima. A mixed basis set is used for the complexes of Ru amd Mo where LANL2DZ basis set is used for defining transition metal Ru and Mo while 6-31G** and 6-311++G** basis sets are used for other atoms in optimization and singlepoint calculations respectively. The energy required to dissociate one of the ligands from the sandwich complex (ΔE) is calculated using the supermolecule approach.

$$\Delta E = E_3 - (E_1 + E_2) \qquad\qquad (Eq.\ 5.4)$$

where E_1, E_2 and E_3 stand for the zero-point energy (ZPE)-corrected energy of the organometallic fragment, $(C_{60}CN)^-$ and sandwich complex, respectively. Here the ZPE-correction obtained from M06L/6-31G** level is added to the single point energy calculated at M06L/6-311++G** level. The free energy change (ΔG) associated with the reaction is also calculated in a similar fashion.

$$\Delta G = G_3 - (G_1 + G_2) \hspace{2cm} \text{(Eq. 5.5)}$$

where G_1, G_2 and G_3 stand for corrected free energy of the organometallic fragment, $(C_{60}CN)^-$ and sandwich complex, respectively.

MESP topology analysis is performed on ligands and complexes to locate their most negative-valued point, a (3, +3) critical point, also known as V_{min}.[128] Atom–atom interactions could be characterized as covalent or noncovalent, based on the electron densities at the respective BCPs (ρ_b) as well as from the sign of the corresponding Laplacian ($\nabla^2\rho_b$). Further, natural bond orbitals (NBO) analysis, as implemented in Gaussian 16 is used for understanding the charge transfer from ligand to metal centre.

5.7 Results and discussion

Figure 5.7 shows the optimized geometries of the sandwich complexes of Fe(II) *viz.* [Fe(η^5- Cp)$_2$], [Fe(η^5-C$_5$(t-Bu)$_3$)$_2$], [Fe(η^5-(C$_{60}$CN)$^-$)(η^5- Cp)] and [Fe(η^5-(C$_{60}$CN)$^-$)$_2$] which are labelled as **1**, **2**, **3**, and **4** respectively with the shortest Fe–C distance (d_1) and longest Fe–C distance (d_2) with each ligand in Å. The stable conformation of the ferrocene molecule has the Cp$^-$ rings in the eclipsed configuration[129] with the average Fe–C bond length of 2.01 Å and a distance of 1.60 Å is observed between the Fe atom and centre of the Cp$^-$ ring (d_3) which are in agreement with the experimental values.[130, 131] In the [Fe(η^5-C$_5$(t-Bu)$_3$)$_2$] complex, three H atoms on each Cp$^-$ ring is substituted with bulky tertiary butyl (t-Bu) groups. This bulky ferrocene derivative has d_3 1.65 Å which is comparable with the experimental observation.[132] This increase in the Fe–C bond length and Fe–Cp$^-$ distance (d_3) is due to steric influence from the bulky substituents on the Cp ring. The replacement of one of the Cp$^-$ with (C$_{60}$CN)$^-$ gives the hybrid complex **3**, with d_3 1.59 Å towards Cp$^-$ ligand, is very similar to that of the ferrocene molecule while d_3

1.65 Å towards the fulleride indicates that this ligand is bulkier than the $C_5(t\text{-}Bu)_{33}$) ligand. As observed in the case of the ferrocene, the pentagonal ring of the $(C_{60}CN)^-$ unit is in eclipsed conformation with the Cp^- ligand. Replacement of both the Cp^- rings with two $(C_{60}CN)^-$ units gives the complex **4**, with d_3 1.66 Å. These results confirm that the sandwich complexes of $(C_{60}CN)^-$ with Fe(II) is analogues to ferrocene.

Fe(η^5-C$_5$H$_5$)$_2$

ΔE = -237.9 kcal/mol

1

Fe(η^5-C$_5$(t-Bu)$_3$)$_2$

ΔE = -192.8 kcal/mol

2

Fe(η^5-C$_5$H$_5$)(η^5-C$_{60}$CN$^-$)

ΔE = -151.8 kcal/mol

3

Fe(η^5-C$_{60}$CN$^-$))$_2$

ΔE = -145.8 kcal/mol

4

Fe(η^5-C$_5$(t-Bu)$_4$)$_2$

ΔE = -159.7 kcal/mol

5
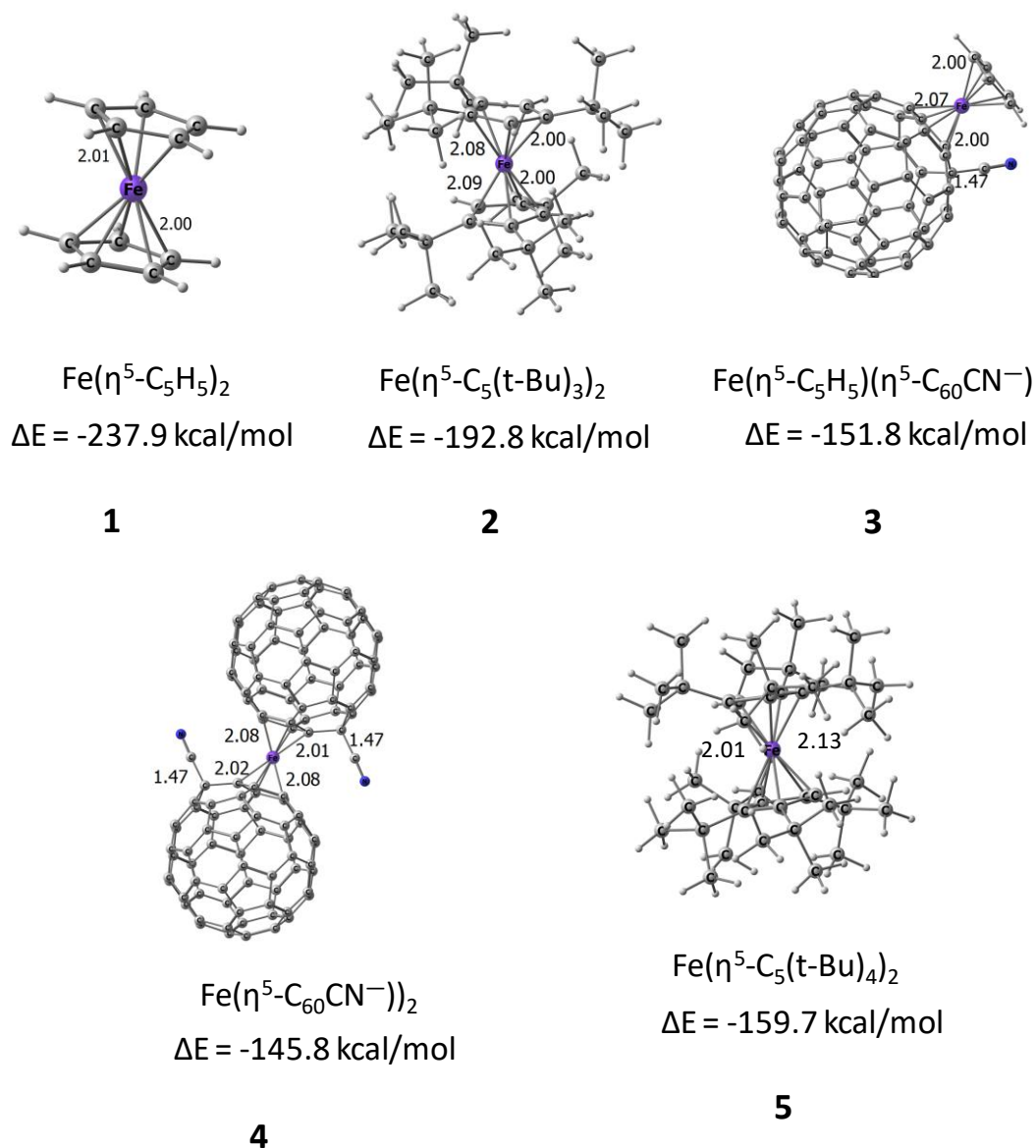
Figure 5.7 Optimized geometries of the sandwich complexes with their bond lengths in Å unit. The ligand dissociation energy ΔE of these complexes, at M06L/6-311++G**//M06L/6-31G** level, is also depicted in kcal/mol.

The energy required to dissociate one of the Cp⁻ ligands (ΔE) from complex **1** is -237.9 kcal/mol whereas the same observed for the $C_5(t\text{-Bu})_3$ ligand is -192.8 kcal/mol (Figure 5.7). The ΔE for the $(C_{60}CN)^-$ ligand in the complexes **3** and **4** is -151.8 and -145.8 kcal/mol, respectively. The lower range of ΔE for the fulleride complexes can be attributed to the bulky nature of the fulleride ligand; in fact, the data support it as one of the bulkiest ligands in organometallic chemistry. Hence we also studied the ferrocene derivative of tetra substituted Cp⁻ ligand, **5**, $[Fe(\eta^5\text{-}C_5(t\text{-Bu})_4)_2]$. A penta-substitution on the Cp⁻ ring with t-Bu appears was not possible due to spatial congestions from several methyl groups. Though the structural parameters of complex **5** is not available in the literature, the DFT study has shown that the d_3 is 1.69 Å and the ΔE -159.7 kcal/mol is very close to that of the complexes **3** and **4**.

We also studied the η^6 coordination of the $(C_{60}CN)^-$ ligand in the complex **3** and **4**. The slightly inferior ΔE values -137.1 and -130.0 kcal/mol, respectively for the complex **3** and **4** in η^6 coordination clearly illustrates the preference for the η^5 coordination in sandwich complexes.

5.7.1 MESP analysis

The electron rich sites characterized by (3, +3) critical points are often referred as MESP minimum, V_{min}. Figure 5.8 gives the MESP plots and V_{min} values of the ligands Cp⁻, $(C_5(t\text{-Bu})_3)^-$, $(C_{60}CN)^-$, and their sandwich complexes *viz.* **1**, **2**, **3** and **4**. Both Cp⁻ ligand and $(C_5(t\text{-Bu})_3)^-$ show high negative V_{min} (intense blue region) over the five-membered ring whereas $(C_{60}CN)^-$ shows lower magnitude for V_{min} which can be attributed to the delocalization of the extra electron over the 59 sp^2 hybridized carbon centers. The electron delocalization feature is also displayed using the minimum value of MESP that engulfs the whole anion (Figure 5.9).[133] Up on coordination with the metal center, a drastic reduction in the magnitude of negative MESP occurs for both Cp⁻ and $(C_5(t\text{-Bu})_3)^-$ in the corresponding metallocenes while $(C_{60}CN)^-$ show only positive potential (except for the lone pair region of CN unit).
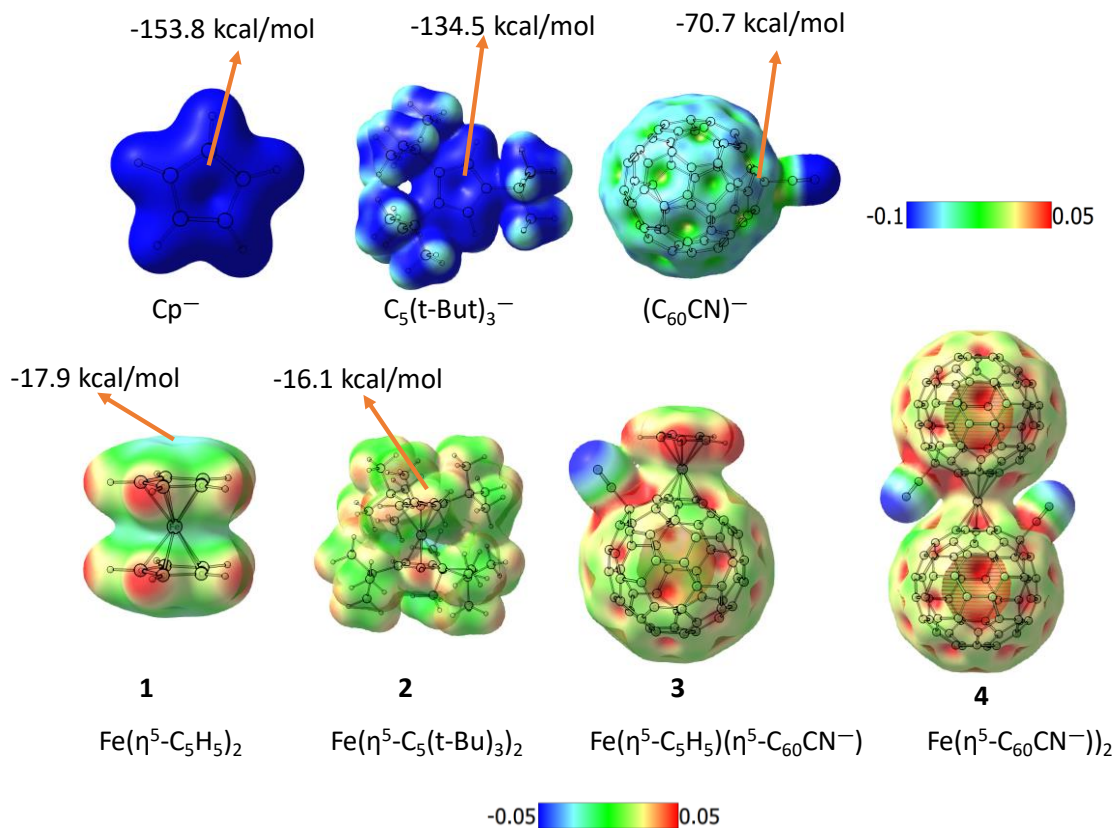
Figure 5.8 MESP of ligands and complexes plotted on isodensity surface 0.005 au, at M06L/6-311++G**//M06L/6-31G** level DFT. MESP value at a (3, +3) critical point, V_{min} is also depicted.
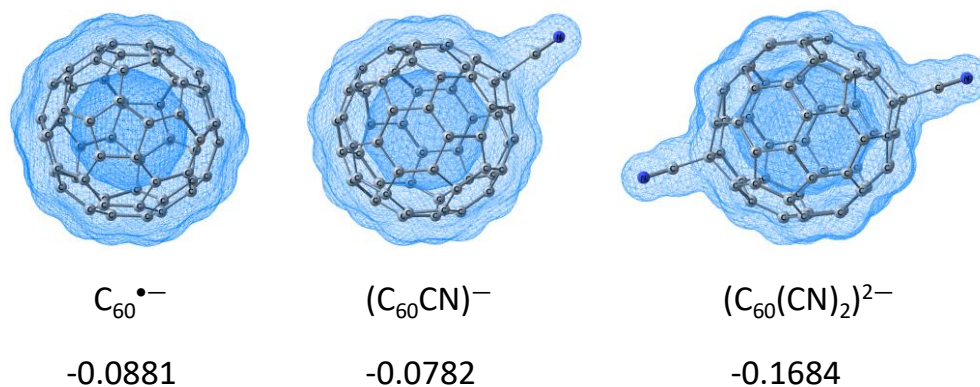
Figure 5.9 MESP of $C_{60}{}^{\bullet-}$, $(C_{60}CN)^-$ and $(C_{60}(CN)_2)^{2-}$ that engulfs the whole anion at M06L/6-311++G**//M06L/6-31G** level. The minimum value of MESP that engulfs the whole anion in au is also depicted.

The observed change in MESP can be attributed to the strong electron donating η^5-coordination of the ligands with the metal center which leads to charge transfer from the ligand to the metal. The five-membered ring adjacent to the CN substitution is identified as the most strongly coordinating η^5-region due to the appearance of the highest negative MESP features over there.

5.7.2 NBO analysis

The NBO natural charge observed for Fe(II) center is -0.52, -0.42, -0.40, -0.29 and -0.28 for **1**, **2**, **3**, **4** and **5**, respectively (Table 5.6). This data suggests that the charge transfer is maximum in ferrocene while both fulleride-sandwich complex **4** and the highly substituted ferrocene derivative **5** show similar but diminished charge transfer features which can be attributed to the high steric effect in both the cases.

Table 5.6 The natural charge (au) on Fe(II) and the average Fe-C BO distance (Å) at M06L/6-311++G**//M06L/6-31G** level.

System	Natural charge on Fe(II)	Avg. Fe-C BO distance
1	-0.52	0.46
2	-0.42	0.44
3	-0.40	0.45
4	-0.29	0.43
5	-0.28	0.41

5.7.3 Molecular orbital analysis

A few important bonding molecular orbitals (MOs) of the sandwich compounds, ferrocene and **4,** are given in Figure 5.10. The MO diagram shows the significant 'd'-orbital nature of the typical doubly degenerate HOMO (HOMO$_a$ and HOMO$_b$) for ferrocene. The HOMO-2 orbital also shows high 'd' orbital character with minimum interactions from the Cp$^-$ ligands. Significant overlap between Cp$^-$ orbitals is seen in the

degenerate HOMO-3$_a$ and HOMO-3$_b$ and they represent the pπ-pπ interactions in ferrocene. The degenerate HOMO-5$_a$ and HOMO-5$_b$ represent the dπ-pπ interactions between metal and ligand orbitals.
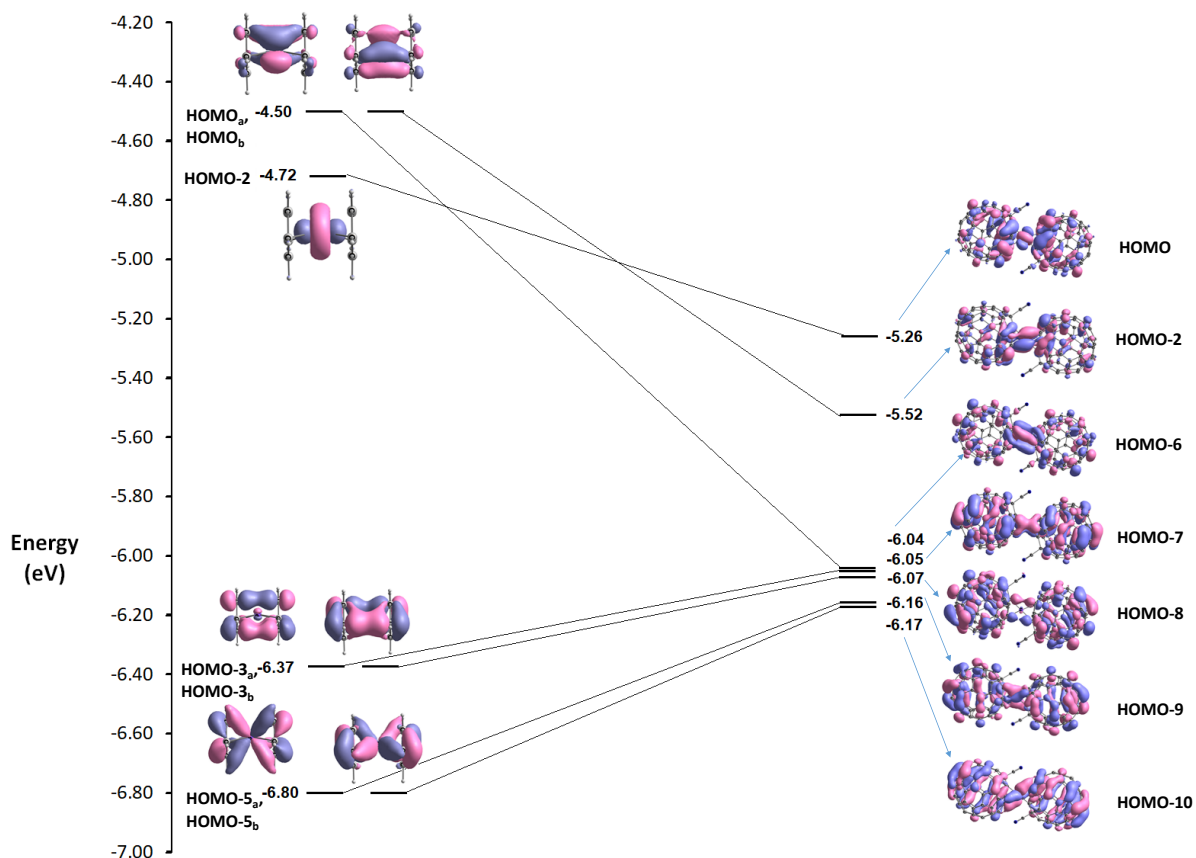
Figure 5.10 Molecular orbital correlation diagram for ferrocene (left, isosurface = 0.04 au) and complex **4** (isosurface = 0.015 au), at M06L/6-311++G**//M06L/6-31G** level DFT.

In comparison with ferrocene, a similar case of bonding scenario is observed in complex **4** as well, but the energy levels show significant variations which can be attributed to the bulky nature and lower symmetry of the $(C_{60}CN)^-$) than Cp$^-$ ligand. The HOMO of **4** has high metal 'd' orbital character and it resembles to the HOMO-2 of ferrocene. This MO is more stabilized in **4** than ferrocene. The HOMO-2 and HOMO-6 of **4** are similar to the degenerate HOMO$_a$ and HOMO$_b$ of ferrocene and are more stabilized

in **4**. The orbitals HOMO-7, HOMO-8, HOMO-9 and HOMO-10 are analogous to HOMO-3$_a$, HOMO-3$_b$, HOMO-5$_a$ and H-5$_b$ of ferrocene, respectively. Though the bonding features appear to be similar in these four MOs, they are slightly destabilized in comparison with that of ferrocene. The LUMO of ferrocene is at 0.95 eV which makes the HOMO – LUMO band gap at 3.54 eV. In complex **4,** LUMO appears at -4.71 eV which indicates high stabilization, resulting to a very low band gap 0.55 eV. The lower band gap exhibited by fulleride sandwich complex than ferrocene can be attributed the weaker interactions between the ligands arising from their steric effects.[79] Compared to ferrocene, **2** and **5** also show lower band gap, 3.09 and 2.54 eV, respectively.

5.7.4 QTAIM analysis

The nature of coordination of fulleride with metal is confirmed from the QTAIM BCP analysis (Figure 5.11). The BCPs of the Fe−C bonding interactions show positive Laplacian of electron density ($\nabla^2\rho_b$) values while negative values are observed for total electron energy density (H) (Table 5.7). Thus these interactions can be considered as closed shell interactions with partial covalent nature.[134]
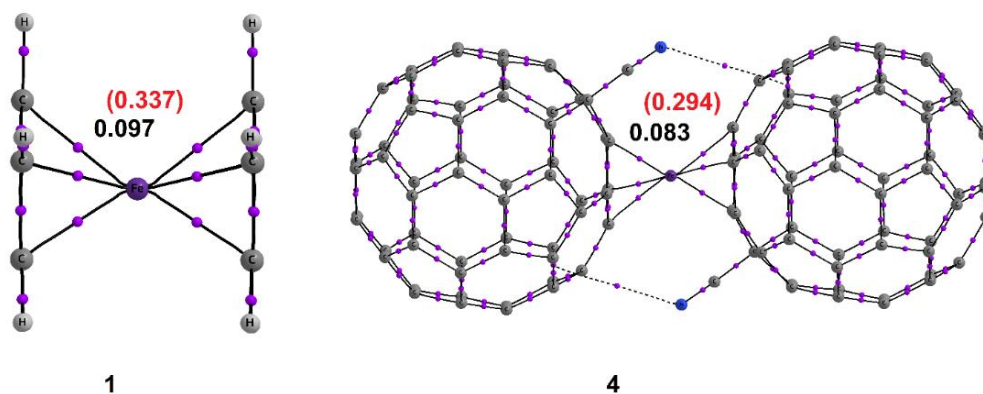
Figure 5.11 QTAIM molecular graph of complexes **1** and **4**. Values in black and red colors are ρ_b and $\nabla^2\rho_b$ in au.

Previous studies analyzed the bonding in ferrocene and different derivatives of it for understanding the contributions of electrostatic and covalent interactions.[129, 135, 136] Frenking *et al.* showed that the Fe−C bonding interactions in ferrocene is from 53 – 58 %

electrostatic attraction and the rest is from covalent interactions. The $\nabla^2\rho_b$ plots in Figure 4 and also those given in Figure 5.12 show that the Fe−C bonding interactions in both ferrocene and fulleride-sandwich complexes are very similar.

1

0.097
0.337
-0.026

2

0.094
0.301
-0.025

3

0.093
0.318
-0.024

4

0.083
0.294
-0.019

-0.3 [ ] 0.3
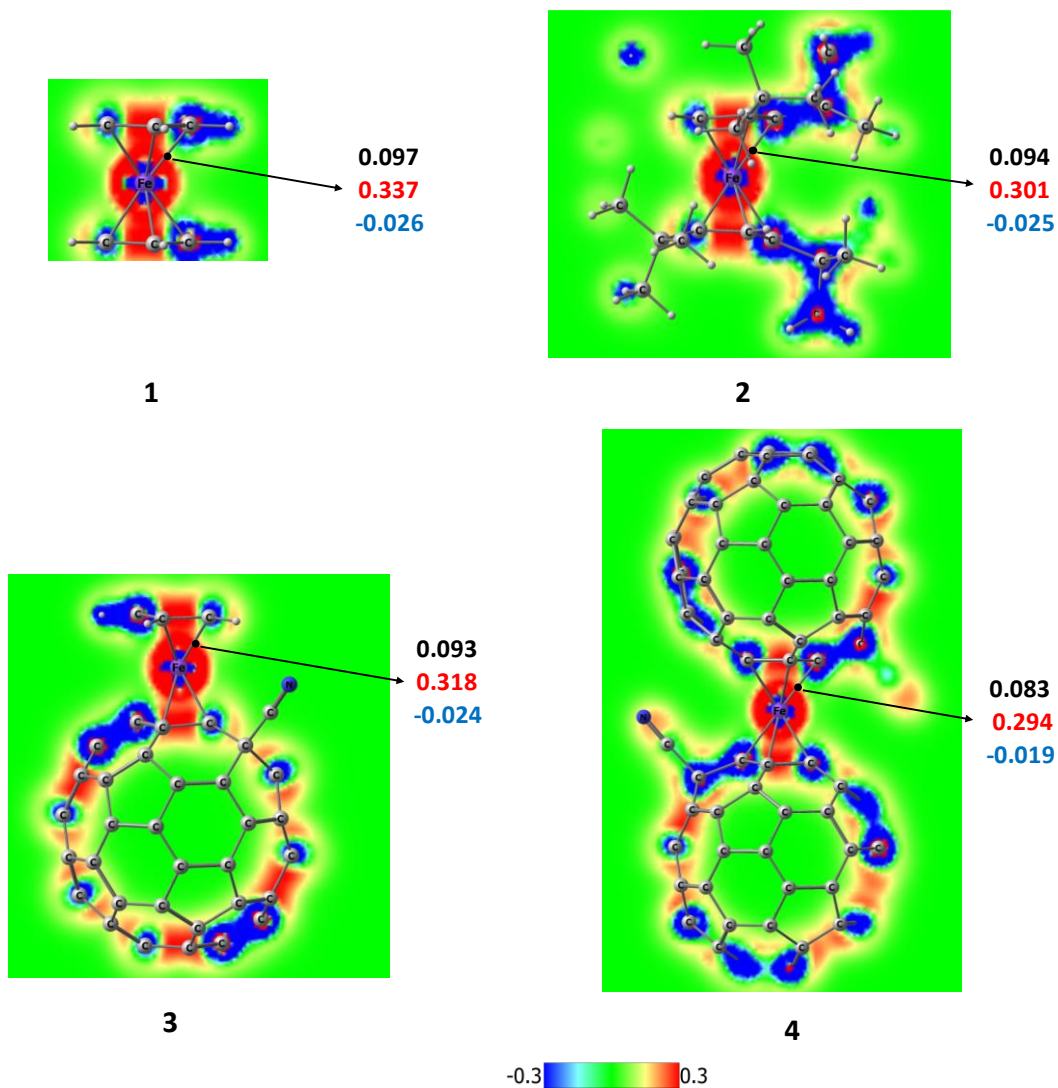
Figure 5.12 $\nabla^2\rho_b$ values plotted on a plane passing through one of the Fe-C bond for complexes **1**, **2**, **3**, and **4**. The red and blue regions indicate the noncovalent and covalent bonding regimes. The BCP for the Fe−C bonding is indicated with ρ_b (black), $\nabla^2\rho_b$ (red) and H_b (blue) values in au.

The red to blue variation in $\nabla^2\rho_b$ plot indicates the noncovalent to covalent changes in the bonding interactions. As observed from the ρ_b and $\nabla^2\rho_b$ values, the

strength of the Fe–C bonding interactions in complex **4** is slightly weaker than that of **1** (Figure 5.12), which is reflected in the more intense red region in the $\nabla^2\rho_b$ plot of **1** than **4**. Also the total electron energy density (H_b) values show the most negative character in the complex **1**, and it decreases in the order **1**, **2**, **3**, **5**, and **4**. Hence, compared to ferrocene a reduced degree of covalent character is expected in the case of fulleride-sandwich complex **4**, which can be attributed to the high steric effects from the fulleride ligand.

Table 5.7 The average values of ρ_b, $\nabla^2\rho_b$ and H on the bond critical points (BCPs) of Fe-C bonding interactions at M06L/6-311++G** level. The values are given in au.

System	Avg. ρ_b	Avg. $\nabla^2\rho_b$	Avg. H_b
1	0.0973	0.3371	-0.0259
2	0.0936	0.3008	-0.0246
3	0.0932	0.3177	-0.0241
4	0.0830	0.2942	-0.0187
5	0.0852	0.2669	-0.0206

5.7.5 Sandwich complexes of other metals

Similar to ferrocene, Ru(II) also gives the stable 18 electron sandwich complex Ru(η^5-(C_{60}CN)$^-$)$_2$ (Figure 5.13) with an average Ru–C bond length 2.24 Å which is higher than the corresponding value 2.19 Å in ruthenocene.[137] For Cr(II) and Mo(II), the sandwich complexes exhibit 16-electron configuration with average metal-carbon distance 2.16 and 2.32 Å, respectively which agree well with the corresponding experimental values of their Cp$^-$ complex. [138] [139] Experimental studies show that Cp$^-$ complexes of Mo(II) often undergoes either further coordination with additional two ligands (Cl$^-$ or H$^-$) or dimerizes to a stable 18-electron configuration. Here the bulky fulleride ligands may prevent the metal centers from further coordination to yield the 16-electron complex. In the case of Ni(II), the [Ni(η^5-(C_{60}CN)$^-$)$_2$] complex has 20-electron

configuration with average Ni-C distance 2.16 Å which is in good agreement with the corresponding Cp⁻ complex.[140]

$Ru(\eta^5\text{-}C_{60}CN^-)_2$
ΔE = -135.7 kcal/mol

$Cr(\eta^5\text{-}C_{60}CN^-)_2$
ΔE = -134.1 kcal/mol

$Mo(\eta^5\text{-}C_{60}CN^-)_2$
ΔE= -127.9 kcal/mol

$Ni(\eta^5\text{-}C_{60}CN^-)_2$
ΔE = -126.3 kcal/mol
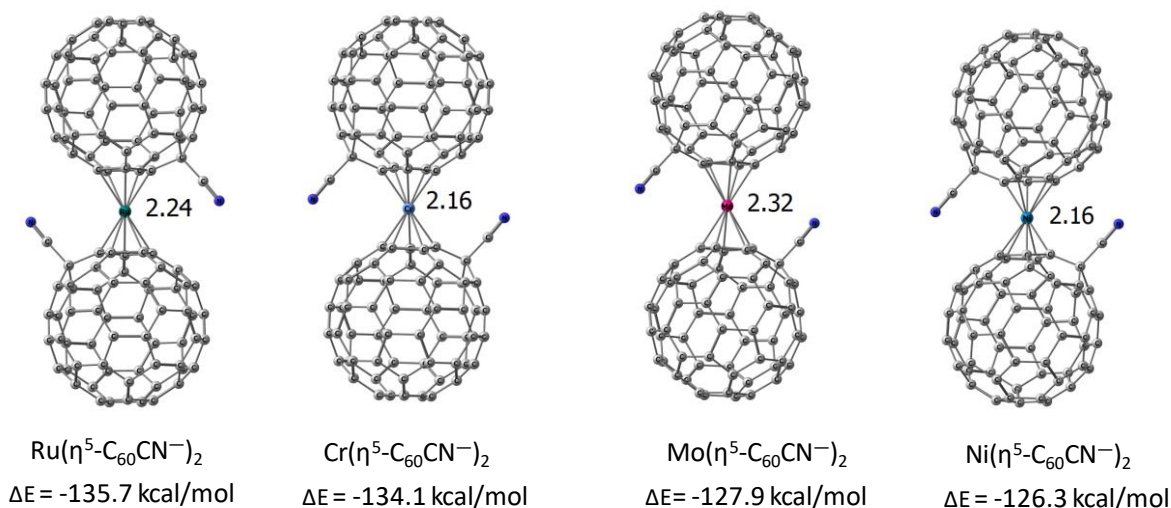
Figure 5.13 Optimized geometries of the sandwich complexes of Ru(II), Cr(II), Mo(II), and Ni(II) with the shortest metal–C bond length in Å unit. The ΔE values are also depicted in kcal/mol.

The energy required to dissociate of one $(C_{60}CN)^-$ ligand from the sandwich complex (ΔE) is calculated for each case. The ΔE of $[Ru(\eta^5\text{-}(C_{60}CN)^-)_2]$ is found to be -135.7 kcal/mol which is 10 kcal/mol lower than that of Fe-complex **4**. The decrease in the magnitude of ΔE can be attributed to the slightly inferior Ru–C interactions owing to the larger size of the Ru atom. Similarly, the ΔE value of Cr(II) complex is higher in magnitude than that of Mo(II) by about 6 kcal/mol. The 20-electron fulleride-sandwich complex, $[Ni(\eta^5\text{-}(C_{60}CN)^-)_2]$ has ΔE -126.3 kcal/mol, which indicates that Ni–C interactions are slightly weaker than those in 16- and 18-electron complexes. Similar to the Fe(II) complexes, these complexes also prefer the η^5 coordination mode over the η^6. For instance $Cr(\eta^5\text{-}(C_{60}CN)^-)_2$ is more stable than the corresponding η^6 complex by 11.1 kcal/mol.

5.7.6 Multi-decker sandwich complexes

The exohedral addition of two CN⁻ to the fullerene cage can create a dianion $((C_{60}(CN)_2)^{2-})$. The energetics of the reaction of two molecules of 1,3-dimethyl-2,3-

dihydro -2- cyano-imidazole (IMCN) and C_{60} (Scheme 5.1) suggests that formation of the imidazolium complex of the dianionic fulleride $(C_{60}(CN)_2)^{2-}$ is exothermic by 23.3 kcal/mol and the corresponding free energy change (ΔG) is 0.7 kcal/mol. The dianionic character of $(C_{60}(CN)_2)^{2-}$ suggests the utilization of two pentagonal units for making η^5 coordination with metal centers. Moreover, large number of such fullerides may assemble in presence of cationic metal centers to form polymeric metallocenes. Recent report by Leng *et al.* on the formation of nanoclusters of C_{60} in presence of Ru and their DFT modelling of one-dimensional -C_{60}-Ru-C_{60}- and other bulk structures suggested favorable η^2 type interactions between metal center and C_{60}. Here we modelled five polymeric structures, viz. **6**, **7**, **8**, **9** and **10** (Figure 5.14) wherein multiple Fe(II) centers exist in ferrocene-type sandwich configuration with Cp units of fulleride cage. The **6** and **8** are made by two $(C_{60}CN)^-$ and one $(C_{60}(CN)_2)^{2-}$, **7** and **9** are made by two $(C_{60}CN)^-$ and two $(C_{60}(CN)_2)^{2-}$ while **10**, a cyclic sandwich polymeric structure is made with six $(C_{60}(CN)_2)^{2-}$ units.
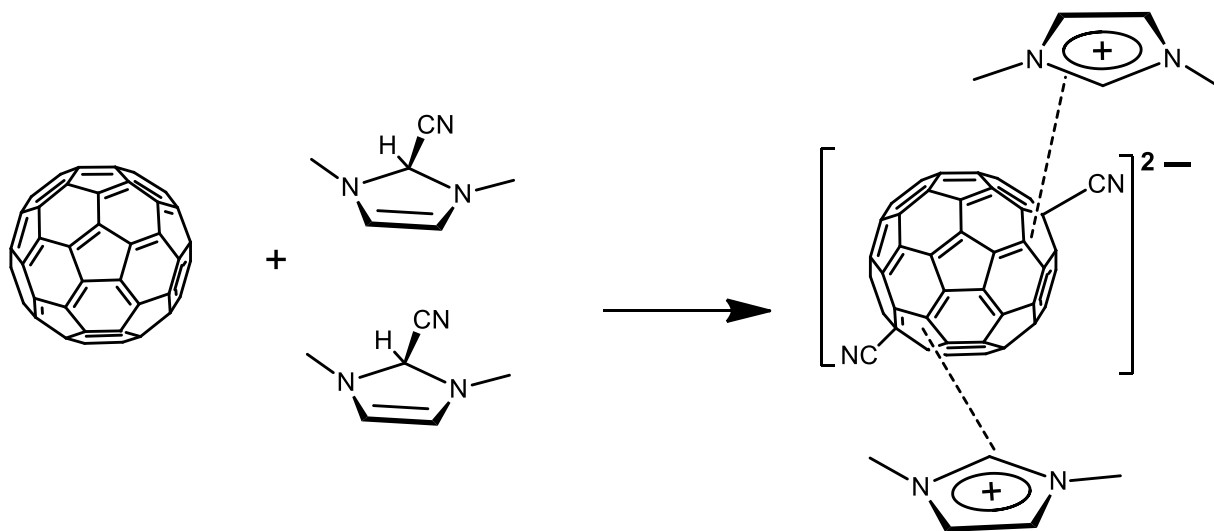
Scheme 5.1 Reaction of C_{60} with IMCN to give dianionic fulleride.
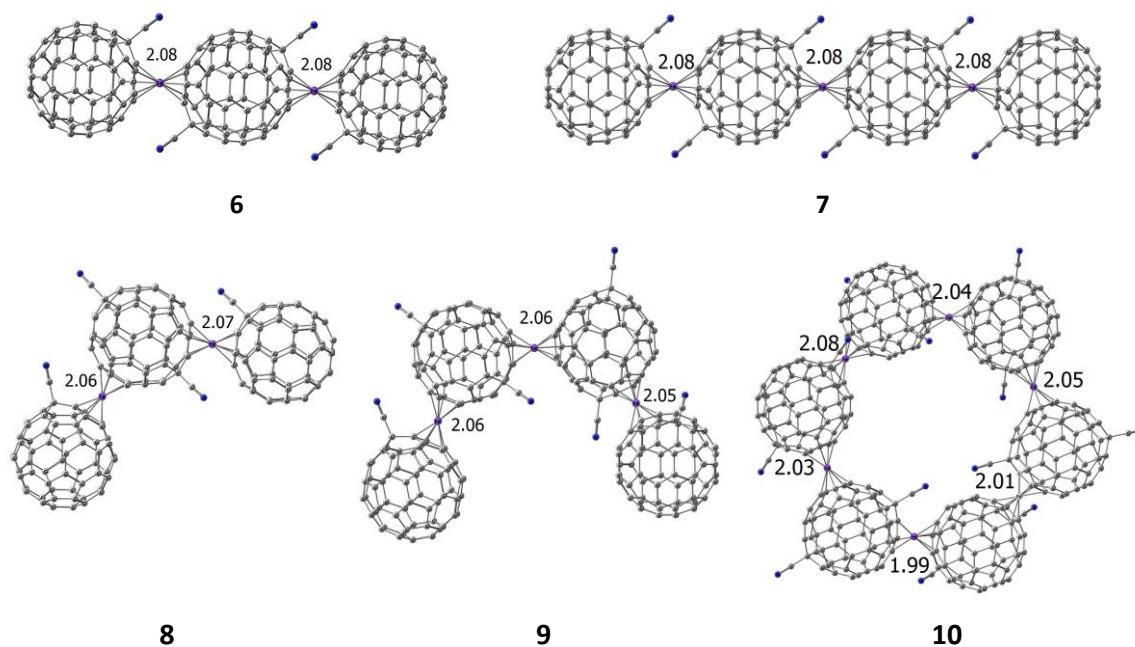
Figure 5.14 Optimized geometry of sandwich fulleride polymer complexes of Fe(II) at M06L/6-31G** level.

Further, the strength of the η^5 coordination in the multi-decker sandwich/polymeric complexes is analyzed by dissociating them into Fe(II) and the corresponding fullerides. The dissociation scheme of each complex is given in Table 5.8. In each case, the total energy of dissociation (ΔE_{total}), the free energy change (ΔG_{total}) and the dissociation energy per Fe(II) ($\Delta E_{/Fe(II)}$) are calculated (Table 5.8). Ferrocene has the highest magnitude for $\Delta E_{/Fe(II)}$, -735.4 kcal/mol. The tertiary butyl (t-Bu) substituted derivatives **2** and **5** have lower magnitude of $\Delta E_{/Fe(II)}$ than ferrocene and the value further decreases in complex **4**. The linear pearl-necklace type polymer **6** and **7** have $\Delta E_{/Fe(II)}$ -587.5 and -597.6 kcal/mol, which are better than the sandwich complex [Fe(η^5-($C_{60}CN$)$^-$)$_2$], **4**. Compared to the multi-decker linear sandwich complexes **6** and **7**, their corresponding angular isomers **8** and **9** show slightly lower $\Delta E_{/Fe(II)}$. Further, $\Delta E_{/Fe(II)}$ shows better values when moving from normal sandwich to triple-decker to tetra-decker systems. The complex **10** is a cyclic hexamer structure, similar to a closed pearl-necklace polymer, composed of six Fe(II) and six units of ($C_{60}(CN)_2$)$^{2-}$. The complete

fragmentation of the polymer to constituent units gives $\Delta E_{/Fe(II)}$ -303.0 kcal/mol indicating that dianionic fulleride has higher coordination ability than the anionic fullerides. On the free energy scale, all the reactions given in Table 1 appear exergonic in nature. Despite the decreased entropy factor, the hexamer **10** formation from dianionic fullerides appears highly feasible in terms of both ΔE and ΔG terms. Also the trend in $\Delta E_{/Fe(II)}$ shows that the energetics is better for the formation of the higher order structures **7** and **9** than **6** and **8**, respectively.

Table 5.8 The dissociation pattern in each sandwich complex, the total energy of dissociation (ΔE_{total}), the dissociation energy per Fe(II) ($\Delta E_{/Fe(II)}$) and the free energy change (ΔG_{total}). Value in kcal/mol at M06L/6-311++G**//M06L/6-31G** level DFT.

Complex	Dissociation	ΔE_{total}	$\Delta E_{/Fe(II)}$	ΔG_{total}
1	$Fe^{2+} + 2Cp^-$	-735.4	-735.4	-224.9
2	$Fe^{2+} + 2(C_5(t\text{-}Bu)_3)^-$	-711.5	-711.5	-176.8
3	$Fe^{2+} + Cp^- + (C_{60}CN)^-$	-649.3	-649.3	-138.4
4	$Fe^{2+} + 2(C_{60}CN)^-$	-556.7	-556.7	-132.2
5	$Fe^{2+} + 2(C_5(t\text{-}Bu)_4)^-$	-683.3	-683.3	-140.1
6	$2Fe^{2+} + 2(C_{60}CN)^- + (C_{60}(CN)_2)^{2-}$	-1174.9	-587.5	-174.9
7	$3Fe^{2+} + 2(C_{60}CN)^- + 2(C_{60}(CN)_2)^{2-}$	-1792.9	-597.6	-189.7
8	$2Fe^{2+} + 2(C_{60}CN)^- + (C_{60}(CN)_2)^{2-}$	-1161.5	-580.8	-168.8
9	$3Fe^{2+} + 2(C_{60}CN)^- + 2(C_{60}(CN)_2)^{2-}$	-1768.6	-589.5	-182.0
10	$6Fe^{2+} + 6(C_{60}(CN)_2)^{2-}$	-3635.5	-605.9	-594.0

5.8 Conclusions

Similar to ferrocene, the η^5 coordinated sandwich complexes have been observed for the metals Fe(II), Ru(II), Cr(II), Mo(II) and Ni(II) with the $(C_{60}CN)^-$ ligand. The structural parameters of these fulleride sandwich complexes are comparable to those of the corresponding Cp^- sandwich complexes. The η^5 coordination mode of $(C_{60}CN)^-$ is preferred over η^6 coordination. The MESP analysis showed the delocalized anionic nature of the ligand $(C_{60}CN)^-$. Further, upon coordination with the metal center, a drastic decrease in the negative character of the MESP is observed in the complex which indicated strong η^5 mode of coordination of the ligand. The MO analysis has shown that the η^5 Fe—C bonding features of $[Fe(\eta^5\text{-}(C_{60}CN)^-)_2]$ is very similar to that of ferrocene. The similarity in the metal–ligand bonding as well as the covalent-noncovalent nature of the Fe-C bonding interactions is further confirmed from the QTAIM analysis.

The coordination ability of dianionic fulleride, $(C_{60}(CN)_2)^{2-}$ with metal centers is better than the anionic fullerides. Also $(C_{60}(CN)_2)^{2-}$ can simultaneously utilize two of its five-membered rings to develop η^5 coordination with metal centers which lead to the formation of multi-decker sandwich complexes and pearl-necklace type polymers. The growth patterns of the complexes in both linear and bent directions as well as formation of cyclic structures are found to be energetically feasible. The analysis of $\Delta E_{/\eta5}$ values of each multi-decker system has shown that the energetics is favorable for the formation of polymeric structures. The highest magnitude of $\Delta E_{/Fe(II)}$ is observed for the closed pearl-necklace structure composed of dianionic fulleride and Fe(II) centers. These results clearly suggest that CN–fullerides are very bulky and versatile η^5 ligands which can be utilized for the development of hitherto unknown multi-decker sandwich and pearl-necklace type polymeric structures.

5.9 References

1. J. Heath, S. O'brien, Q. Zhang, Y. Liu, R. Curl, F. Tittel and R. Smalley, *J. Am. Chem.Soc.*, 1985, **107**, 7779-7780.
2. A. J. Stone and D. J. Wales, *Chem. Phys. Lett.*, 1986, **128**, 501-503.

3. D. L. Lichtenberger, L. L. Wright, N. E. Gruhn and M. E. Rempe, *Synth. Met.*, 1993, **59**, 353-367.
4. D. L. Lichtenberger, L. L. Wright, N. E. Gruhn and M. E. Rempe, *J. Organomet. Chem.*, 1994, **478**, 213-221.
5. V. Sokolov, *Russ. J. Coord. Chem.*, 2007, **33**, 711-724.
6. F. Liu and S. Yang, *Encyclopedia of Inorganic and Bioinorganic Chemistry*, 2014.
7. J. M. Hawkins, A. Meyer, T. A. Lewis, S. Loren and F. J. Hollander, *Science*, 1991, **252**, 312-313.
8. P. J. Fagan, J. C. Calabrese and B. Malone, *Science*, 1991, **252**, 1160-1162.
9. P. J. Fagan, J. C. Calabrese and B. Malone, *Accounts Chem. Res.*, 1992, **25**, 134-142.
10. A. L. Balch, V. J. Catalano, J. W. Lee, M. M. Olmstead and S. R. Parkin, *J. Am. Chem. Soc.*, 1991, **113**, 8953-8955.
11. R. S. Koefod, M. F. Hudgens and J. R. Shapley, *J. Am. Chem.Soc.*, 1991, **113**, 8957-8958.
12. V. V. Bashilov, P. V. Petrovskii, V. I. Sokolov, S. Lindeman, I. A. Guzey and Y. T. Struchkov, *Organometallics*, 1993, **12**, 991-992.
13. B. Chase and P. J. Fagan, *J. Am. Chem. Soc.*, 1992, **114**, 2252-2256.
14. S. A. Lerke, B. Parkinson, D. H. Evans and P. J. Fagan, *J. Am. Chem. Soc.*, 1992, **114**, 7807-7813.
15. M. N. Bengough, D. M. Thompson, M. C. Baird and G. D. Enright, *Organometallics*, 1999, **18**, 2950-2952.
16. D. M. Thompson, M. Bengough and M. C. Baird, *Organometallics*, 2002, **21**, 4762-4770.
17. P. J. Fagan, J. C. Calabrese and B. Malone, *J. Am. Chem. Soc.*, 1991, **113**, 9408-9409.
18. A. V. Usatov, S. M. Peregudova, L. I. Denisovich, E. V. Vorontsov, L. E. Vinogradova and Y. N. Novikov, *J. Organomet. Chem.*, 2000, **599**, 87-96.
19. A. L. Balch, L. Hao and M. M. Olmstead, *Angew. Chem. Int. Ed Engl.*, 1996, **35**, 188-190.
20. F. J. Brady, D. J. Cardina and M. Domin, *J. Organomet. Chem.*, 1995, **491**, 169-172.
21. H. Nagashima, Y. Kato, H. Yamaguchi, E. Kimura, T. Kawanishi, M. Kato, Y. Saito, M. Haga and K. Itoh, *Chem. Lett.*, 1994, **23**, 1207-1210.
22. H. Nagashima, A. Nakaoka, Y. Saito, M. Kato, T. Kawanishi and K. Itoh, *Chem. Comm.*, 1992, 377-379.
23. P. Fowler and A. Ceulemans, *J. Phys. Chem.* , 1995, **99**, 508-510.
24. A. L. Balch and M. M. Olmstead, *Chem. Rev*, 1998, **98**, 2123-2166.
25. M. Sawamura, H. Iikura and E. Nakamura, *J. Am. Chem. Soc.*, 1996, **118**, 12850-12851.
26. M. Sawamura, H. Iikura, A. Hirai and E. Nakamura, *J. Am. Chem. Soc.*, 1998, **120**, 8285-8286.
27. M. Sawamura, Y. Kuninobu, M. Toganoh, Y. Matsuo, M. Yamanaka and E. Nakamura, *J. Am. Chem. Soc.*, 2002, **124**, 9354-9355.
28. Y. Matsuo and E. Nakamura, *Chem. Rev.*, 2008, **108**, 3016-3028.
29. M. Toganoh, Y. Matsuo and E. Nakamura, *J. Am. Chem. Soc.*, 2003, **125**, 13974-13975.
30. A. Chistyakov and L. Stankevich, *Russ. Chem. Bull.*, 1996, **45**, 2294-2301.
31. J. A. López and C. Mealli, *J. Organomet. Chem.*, 1994, **478**, 161-171.

32.   A. Chistyakov, I. Stankevich and N. Gambaryan, *Russ. Chem. Bull.*, 1995, **44**, 828-831.
33.   E. Nakamura, *Pure Appl. Chem.*, 2003, **75**, 427-434.
34.   I. Stankevich and A. Chistyakov, *Russ. Chem. Bull.*, 2003, **52**, 1272-1279.
35.   A. Chistyakov and I. Stankevich, *Russ. Chem. Bull.*, 2002, **51**, 230-239.
36.   C. M. Alvarez, R. J. Angelici, A. Sygula, R. Sygula and P. W. Rabideau, *Organometallics*, 2003, **22**, 624-626.
37.   S. Nagao, T. Kurikawa, K. Miyajima, A. Nakajima and K. Kaya, *J. Phys. Chem. A*, 1998, **102**, 4495-4500.
38.   I. J. Mavunkal, Y. Chi, S.-M. Peng and G.-H. Lee, *Organometallics*, 1995, **14**, 4454-4456.
39.   E. Jemmis and M. Manoharan, *Curr. Sci.*, 1999, **76**, 1122-1126.
40.   E. D. Jemmis, M. Manoharan and P. K. Sharma, *Organometallics*, 2000, **19**, 1879-1887.
41.   E. D. Jemmis, P. Parameswaran and A. Anoop, *Int. J. Quantum Chem.*, 2003, **95**, 810-815.
42.   B. Molina, L. Pérez-Manríquez and R. Salcedo, *J. Mol. Model*, 2017, **23**, 171.
43.   M. D. Francis, O. V. Boltalina, J. F. Nixon and R. Taylor, *Fuller. Nanotub.*, 2003, **11**, 115-120.
44.   J. Cioslowski, *J. Am. Chem. Soc.*, 1991, **113**, 4139-4141.
45.   T. Pradeep, G. Kulkarni, K. Kannan, T. G. Row and C. Rao, *J. Am. Chem. Soc.*, 1992, **114**, 2272-2273.
46.   E. Campbell, R. Tellgmann, N. Krawez and I. Hertel, *J. Phys. Chem. Solids* 1997, **58**, 1763-1769.
47.   F. Pichierri, V. Kumar and Y. Kawazoe, *Chem. Phys. Lett.*, 2005, **406**, 341-344.
48.   C. Ramachandran and N. Sathyamurthy, *Chem. Phys. Lett.*, 2005, **410**, 348-351.
49.   O. Shameema, C. Ramachandran and N. Sathyamurthy, *J. Phys. Chem. A*, 2006, **110**, 2-4.
50.   T. A. Murphy, T. Pawlik, A. Weidinger, M. Höhne, R. Alcala and J.-M. Spaeth, *Phys. Rev. Lett.*, 1996, **77**, 1075.
51.   C. Knapp, N. Weiden, H. Kass, K.-P. Dinse, B. Pietzak, M. Waiblinger and A. Weidinger, *Mol. Phys.*, 1998, **95**, 999-1004.
52.   E. Dietel, A. Hirsch, B. Pietzak, M. Waiblinger, K. Lips, A. Weidinger, A. Gruss and K.-P. Dinse, *J. Am. Chem. Soc.*, 1999, **121**, 2432-2437.
53.   A. A. Popov, S. Yang and L. Dunsch, *Chem. Rev.*, 2013, **113**, 5989-6113.
54.   P. Ravinder and V. Subramanian, *J. Phys. Chem. A*, 2011, **115**, 11723-11733.
55.   S. Aoyagi, E. Nishibori, H. Sawa, K. Sugimoto, M. Takata, Y. Miyata, R. Kitaura, H. Shinohara, H. Okada and T. Sakai, *Nat. Chem.*, 2010, **2**, 678-683.
56.   O. V. d. Oliveira and A. d. S. Gonçalves, *Computational Chemistry*, 2014, **2**, 51.
57.   Y. Garcia-Rodeja, M. Sola, F. M. Bickelhaupt and I. Fernandez, *Chem. Eur. J.*, 2017.
58.   T. D. Della and C. H. Suresh, *Phys. Chem. Chem. Phys.*, 2018, **20**, 24885-24893.
59.   M. J. Frisch, G. W. Trucks, H. B. Schlegel, G. E. Scuseria, M. A. Robb, J. R. Cheeseman, G. Scalmani, V. Barone, G. A. Petersson, H. Nakatsuji, X. Li, M. Caricato, A. V. Marenich, J. Bloino, B. G. Janesko, R. Gomperts, B. Mennucci, H. P. Hratchian, J. V. Ortiz, A. F. Izmaylov, J. L. Sonnenberg, D. Williams-Young, F. Ding, F. Lipparini, F. Egidi, J. Goings, B. Peng, A. Petrone, T. Henderson, D. Ranasinghe, V. G. Zakrzewski,

J. Gao, N. Rega, G. Zheng, W. Liang, M. Hada, M. Ehara, K. Toyota, R. Fukuda, J. Hasegawa, M. Ishida, T. Nakajima, Y. Honda, O. Kitao, H. Nakai, T. Vreven, K. Throssell, J. A. Montgomery Jr., J. E. Peralta, F. Ogliaro, M. J. Bearpark, J. J. Heyd, E. N. Brothers, K. N. Kudin, V. N. Staroverov, T. A. Keith, R. Kobayashi, J. Normand, K. Raghavachari, A. P. Rendell, J. C. Burant, S. S. Iyengar, J. Tomasi, M. Cossi, J. M. Millam, M. Klene, C. Adamo, R. Cammi, J. W. Ochterski, R. L. Martin, K. Morokuma, O. Farkas, J. B. Foresman and D. J. Fox, *Gaussian 16 Rev. A.03*, Gaussian, Inc., Wallingford CT, 2016.

60. P. J. Fitzpatrick, Y. Le Page, J. Sedman and I. S. Butler, *Inorg. Chem.*, 1981, **20**, 2852-2861.
61. M. Kawano, Y. Kobayashi, T. Ozeki and M. Fujita, *J. Am. Chem.Soc.*, 2006, **128**, 6558-6559.
62. T. Kealy and P. Pauson, *Nature*, 1951, **168**, 1039-1040.
63. S. Miller, J. Tebboth and J. Tremaine, *J. Chem. Soc., Perkin trans. 2*, 1952.
64. E. O. Fischer and W. Pfab, *Z. Naturforsch. B*, 1952, **7**, 377-379.
65. G. Wilkinson, M. Rosenblum, M. Whiting and R. Woodward, *J. Am. Chem. Soc.*, 1952, **74**, 2125-2126.
66. R. Woodward, M. Rosenblum and M. Whiting, *J. Am. Chem. Soc.*, 1952, **74**, 3458-3459.
67. H. Werner, *Angew. Chem. Int. Ed.*, 2012, **51**, 6052-6058.
68. P. F. Eiland and R. Pepinsky, *J. Am. Chem. Soc.*, 1952, **74**, 4971-4971.
69. J. Dunitz and L. Orgel, *Nature*, 1953, **171**, 121-122.
70. G. Wilkinson, *J. Am. Chem. Soc.*, 1952, **74**, 6146-6147.
71. G. Wilkinson, P. Pauson and F. Cotton, *J. Am. Chem. Soc.*, 1954, **76**, 1970-1974.
72. G. Wilkinson and J. Birmingham, *J. Am. Chem. Soc.*, 1954, **76**, 4281-4284.
73. M. Rausch, M. Vogel and H. Rosenberg, *J. Chem. Educ.*, 1957, **34**, 268.
74. M. Roemer, D. Heinrich, Y. K. Kang, Y. K. Chung and D. Lentz, *Organometallics*, 2012, **31**, 1500-1510.
75. B. Kashyap and P. Phukan, *RSC Adv.*, 2013, **3**, 15327-15336.
76. A. Paul, R. Borrelli, H. Bouyanfif, S. Gottis and F. Sauvage, *ACS Omega*, 2019, **4**, 14780-14789.
77. P. Ravinder and V. Subramanian, *Comput. Theor. Chem.*, 2012, **998**, 106-112.
78. E. D. Jemmis and M. Manoharan, *Curr. Sci.*, 1999, **76**, 1122-1126.
79. H. S. Kang, *J. Comput. Chem.*, 2007, **28**, 594-600.
80. M. Toganoh, Y. Matsuo and E. Nakamura, *J. Am. Chem. Soc.*, 2003, **125**, 13974-13975.
81. Y. Matsuo, Y. Kuninobu, S. Ito and E. Nakamura, *Chem. Lett.*, 2004, **33**, 68-69.
82. Y. Matsuo, A. Iwashita and E. Nakamura, *Organometallics*, 2008, **27**, 4611-4617.
83. S. Muhammad, S. Ito, M. Nakano, R. Kishi, K. Yoneda, Y. Kitagawa, M. Shkir, A. Irfan, A. R. Chaudhry, S. AlFaify, A. Kalam and A. G. Al-Sehemi, *Phys. Chem. Chem. Phys.*, 2015, **17**, 5805-5816.
84. P. J. Fagan, P. J. Krusic, D. H. Evans, S. A. Lerke and E. Johnston, *J. Am. Chem. Soc.*, 1992, **114**, 9697-9699.
85. F. Wudl, *Acc. Chem. Res.*, 1992, **25**, 157-161.
86. R. Taylor and D. R. Walton, *Nature*, 1993, **363**, 685-693.
87. E. Nakamura and H. Isobe, *Acc. Chem. Res.*, 2003, **36**, 807-815.

88.   T. Hasobe, H. Imahori, P. V. Kamat and S. Fukuzumi, *J. Am. Chem. Soc.*, 2003, **125**, 14962-14963.
89.   P. D. Boyd and C. A. Reed, *Acc. Chem. Res.*, 2005, **38**, 235-242.
90.   J. Cioslowski and K. Raghavachari, *J. Chem. Phys.*, 1993, **98**, 8734-8741.
91.   Y. Wang, D. Tománek and R. S. Ruoff, *Chem. Phys. Lett.*, 1993, **208**, 79-85.
92.   A. A. Popov and L. Dunsch, *Chem. Eur. J.*, 2009, **15**, 9707-9729.
93.   S. Osuna, M. Swart and M. Sola, *Phys. Chem. Chem. Phys.*, 2011, **13**, 3585-3603.
94.   Y. Zhang, D. Wang and W. Wang, *Comput. Theor. Chem.*, 2018, **1128**, 56-59.
95.   M. Alipour and K. Kargar, *J. Comput. Chem.*, 2020, **41**, 1912-1920.
96.   B. S. Tan, R. F. Peng, H. B. Li, B. Jin, S. J. Chu and X. P. Long, *J. Comput. Chem.*, 2010, **31**, 2233-2237.
97.   L. Dunsch and S. Yang, *Phys. Chem. Chem. Phys.*, 2007, **9**, 3067-3081.
98.   K. Kurotobi and Y. Murata, *Science*, 2011, **333**, 613-616.
99.   A. Krachmalnicoff, R. Bounds, S. Mamone, S. Alom, M. Concistrè, B. Meier, K. Kouřil, M. E. Light, M. R. Johnson and S. Rols, *Nat. Chem.*, 2016, **8**, 953-957.
100.   K. Komatsu, M. Murata and Y. Murata, *Science*, 2005, **307**, 238-240.
101.   X. Wu and X. Lu, *J. Am. Chem. Soc.*, 2007, **129**, 2171-2177.
102.   R. E. Estrada-Salas and A. A. Valladares, *J. Mol. Struct. THEOCHEM*, 2008, **869**, 1-5.
103.   A. L. Balch and M. M. Olmstead, *Chem. Rev.*, 1998, **98**, 2123-2166.
104.   K. Lee, H. Song and J. T. Park, *Accounts Chem. Res.*, 2003, **36**, 78-86.
105.   J. López-Andarias, A. Bauzá, N. Sakai, A. Frontera and S. Matile, *Angew. Chem.*, 2018, **130**, 11049-11053.
106.   J. López-Andarias, A. Frontera and S. Matile, *J. Am. Chem. Soc.*, 2017, **139**, 13296-13299.
107.   K. Fujiwara, Y. Murata, T. S. Wan and K. Komatsu, *Tetrahedron*, 1998, **54**, 2049-2058.
108.   P. Sofou, Y. Elemes, E. Panou-Pomonis, A. Stavrakoudis, V. Tsikaris, C. Sakarellos, M. Sakarellos-Daitsiotis, M. Maggini, F. Formaggio and C. Toniolo, *Tetrahedron*, 2004, **60**, 2823-2828.
109.   A. Hirsch, *Phys. Status Solidi B*, 2006, **243**, 3209-3212.
110.   J. Yang, K. Wang, J. Driver, J. Yang and A. R. Barron, *Org. Biomol. Chem.*, 2007, **5**, 260-266.
111.   F. Giacalone and N. Martin, *Chem. Rev.*, 2006, **106**, 5136-5190.
112.   P. Ravi, S. Dai, C. Wang and K. C. Tam, *J. Nanosci. Nanotechnol.*, 2007, **7**, 1176-1196.
113.   E. Grądzka, M. Wysocka-Żołopa and K. Winkler, *Adv. Energy Mater.*, 2020, **10**, 2001443.
114.   H. Nagashima, A. Nakaoka, Y. Saito, M. Kato, T. Kawanishi and K. Itoh, *Chem. Commun.*, 1992, 377-379.
115.   H. Nagashima, A. Nakaoka, S. Tajima, Y. Saito and K. Itoh, *Chem. Lett.*, 1992, **21**, 1361-1364.
116.   F. Leng, I. Gerber, P. Lecante, W. Bacsa, J. Miller, J. Gallagher, S. Moldovan, M. Girleanu, M. Axet and P. Serp, *RSC Adv.*, 2016, **6**, 69135-69148.
117.   E. Brancewicz, E. Grądzka and K. Winkler, *J. Solid State Electrochem.*, 2013, **17**, 1233-1245.
118.   P. J. Harris, *C*, 2020, **6**, 71.

119. T. Kurikawa, Y. Negishi, F. Hayakawa, S. Nagao, K. Miyajima, A. Nakajima and K. Kaya, *J. Am. Chem. Soc.*, 1998, **120**, 11766-11772.
120. F. T. Edelmann, *New J. Chem.*, 2011, **35**, 517-528.
121. T. N. Gribanova, R. M. Minyaev and V. I. Minkin, *Phys. Chem. Chem. Phys.*, 2012, **14**, 14803-14809.
122. S. Anila and C. H. Suresh, *Phys. Chem. Chem. Phys.*, 2021, **23**, 3646-3655.
123. S. Anila and C. H. Suresh, *Phys. Chem. Chem. Phys.*, 2021, **23**, 20086-20094.
124. Y. Zhao and D. G. Truhlar, *J. Chem. Phys.*, 2006, **125**, 194101.
125. Y. Zhao and D. G. Truhlar, *Acc. Chem. Res.*, 2008, **41**, 157-167.
126. S. Zahn, D. R. MacFarlane and E. I. Izgorodina, *Phys. Chem. Chem. Phys.*, 2013, **15**, 13664-13675.
127. M. J. Frisch, G. W. Trucks, H. B. Schlegel, G. E. Scuseria, M. A. Robb, J. R. Cheeseman, G. Scalmani, V. Barone, G. A. Petersson, H. Nakatsuji, X. Li, M. Caricato, A. V. Marenich, J. Bloino, B. G. Janesko, R. Gomperts, B. Mennucci, H. P. Hratchian, J. V. Ortiz, A. F. Izmaylov, J. L. Sonnenberg, D. Williams-Young, F. Ding, F. Lipparini, F. Egidi, J. Goings, B. Peng, A. Petrone, T. Henderson, D. Ranasinghe, V. G. Zakrzewski, J. Gao, N. Rega, G. Zheng, W. Liang, M. Hada, M. Ehara, K. Toyota, R. Fukuda, J. Hasegawa, M. Ishida, T. Nakajima, Y. Honda, O. Kitao, H. Nakai, T. Vreven, K. Throssell, J. A. Montgomery Jr., J. E. Peralta, F. Ogliaro, M. J. Bearpark, J. J. Heyd, E. N. Brothers, K. N. Kudin, V. N. Staroverov, T. A. Keith, R. Kobayashi, J. Normand, K. Raghavachari, A. P. Rendell, J. C. Burant, S. S. Iyengar, J. Tomasi, M. Cossi, J. M. Millam, M. Klene, C. Adamo, R. Cammi, J. W. Ochterski, R. L. Martin, K. Morokuma, O. Farkas, J. B. Foresman and D. J. Fox, *Gaussian 16 Rev. A.03*, 2016, Gaussian, Inc., Wallingford CT, .
128. S. R. Gadre, C. H. Suresh and N. Mohan, *Molecules*, 2021, **26**, 3289.
129. V. M. Rayón and G. Frenking, *Organometallics*, 2003, **22**, 3304-3308.
130. A. Haaland and J. Nilsson, *Acta Chem. Scand.*, 1968, **22**, 2653-2670.
131. A. Haaland, *Acc. Chem. Res.*, 1979, **12**, 415-422.
132. C. A. P. Goodwin, M. J. Giansiracusa, S. M. Greer, H. M. Nicholas, P. Evans, M. Vonci, S. Hill, N. F. Chilton and D. P. Mills, *Nat. Chem.*, 2021, **13**, 243-248.
133. R. K. Pathak and S. R. Gadre, *J. Chem. Phys.*, 1990, **93**, 1770-1773.
134. G. Golding Sheeba, D. Usha, M. Amalanathan, M. Sony Michael Mary and H. MarshanRobert, *Spectrosc. Lett.*, 2021, **54**, 419-436.
135. J. Frunzke, M. Lein and G. Frenking, *Organometallics*, 2002, **21**, 3351-3359.
136. V. Y. Lee, R. Kato, A. Sekiguchi, A. Krapp and G. Frenking, *J. Am. Chem. Soc.*, 2007, **129**, 10340-10341.
137. M. Nakada, T. Kuwabara, S. Furukawa, M. Hada, M. Minoura and M. Saito, *Chem. Sci.*, 2017, **8**, 3092-3097.
138. K. R. Flower and P. B. Hitchcock, *J. Organomet. Chem.*, 1996, **507**, 275-277.
139. K. Prout, T. S. Cameron, R. A. Forder, S. R. Critchley, B. Denton and G. V. Rees, *Acta Crystallogr. B*, 1974, **30**, 2290-2304.
140. P. Seiler and J. D. Dunitz, *Acta Crystallogr. B*, 1980, **36**, 2255-2260.

Abstract

Name of the Student: Ms. Anila Sebastian	Registration No.: 10CC17A39007
Faculty of Study: Chemical Sciences	Year of Submission: 2022
AcSIR academic centre/CSIR Lab: CSIR–National Institute for Interdisciplinary Science and Technology (NIIST)	Name of the Supervisor: Dr. C. H. Suresh

Title of the thesis: Density Functional Theory Studies on Transition Metal Fulleride Complexes and CO_2 Capture by Anions, Fullerides, and N-rich Molecular Systems

---

Carbon dioxide capture and storage (CCS) has been a hot topic of discussion for past few decades. CO_2 capture and storage depends on the CO_2 interaction with the storage materials. A covalent interaction can lead to chemisorption while a non-covalent interaction can lead to physisorption. Recent studies have shown that the nitrogen (N)-rich and carbonaceous molecular systems play an essential role in the CO_2 capture. The thesis focuses on the interaction of CO_2 with different anionic and N-rich molecular systems using density functional theory (DFT).

The first part of **Chapter 1** provides a brief account of various CO_2 capture and storage techniques and important theoretical and experimental works on the capability of fullerene based systems to act as an organometallic η^5 ligand. In **part B**, an overview of computational chemistry and methodologies employed in the thesis are included.

Chapter 2 demonstrates the substantial affinity of the anions such as F^-, Cl^-, Br^-, OH^-, NH_2^-, NO_2^-, CN^-, and ClO^- to bind with a large number of CO_2 molecules. The remarkable ability of the anions to interact with a large number of CO_2 molecules is due to the cooperativity resulting from the secondary O...C interactions which compensate for the weakening of the primary anion...C interactions as the cluster size increases.

Chapter 3 is divided into two parts. **Part A** shows the substantial affinity of guanidine (G) to bind with a large number of CO_2 molecules through the (G^+)-(CO_2^-) zwitterion *via* multiple O...HN interactions. In part B, the study is extended to varoius cyclic/acyclic imine based functional molecules (XN) for their CO_2 binding affinities. Formation of only noncovalent (**nc**) XN...CO_2 complexes is observed for a group of imines while more saturated imines (XN') produced both **nc** and covalent (**c**) complex XN'^+−$(CO_2)^-$. Also noncovalent and covalent bonding territories are clearly demarcated with the identification of a transition state (**ts**) as the crossover point.

In **chapter 4**, **Part A** demonstrates that the exohedral addition of anionic X^- moieties to C_{60} (X = H, F, OH, CN, NH_2, and NO_2) is thermodynamically a viable process to create large X-fulleride anions $(C_{60}X)^-$ by locating the transition state for the reaction between C_{60} and 1,3-dimethyl-2X-Imidazole (IMX). In **Part B** the formation of imidazolium-based ionic complexes of polyanionic fullerides, $(IM^+)_n...(C_{60}(CN)_n)^{n-}$ from the reaction of C_{60} fullerene with 'n' molecules of 1,3-dimethyl-2,3-dihydro-2-cyano-imidazole (IMCN) is demonstrated. The $(IM^+)_n...(C_{60}(CN)_n)^{n-}$ ion-pair systems showed strong interactions with CO_2 molecules.

Chapter 5 is divided into two parts. **Part A** shows the coordinating ability of endohedral and exohedral chloro-fullerides to acts as η^5-ligands towards various metal centres *viz.* Sc(I), Ti(II), Ti(IV), V(I), Cr(II), Mn(I), Fe(II) and Cu(I). **Part B** illustrates that similar to Cp^-, the bulky anion, $(C_{60}CN)^-$, acts as a strong η^5 ligand to form sandwich complexes with Fe(II), Ru(II), Cr(II), Mo(II), and Ni(II). Further, the coordinating ability of the dianion, $(C_{60}(CN)_2)^{2-}$ is evaluated which showed strong coordination ability simultaneously with two metal centers leading to the formation of multi-decker sandwich and pearl-necklace type polymeric structures.

List of the publications emanating from the thesis work

1. **Anila, Sebastian**, and Cherumuttathu H. Suresh, Formation of large clusters of CO_2 around anions: DFT study reveals cooperative CO_2 adsorption, *Phys. Chem. Chem. Phys.* 2019, *21*, 23143-23153.

2. **Anila, Sebastian**, and Cherumuttathu H. Suresh, Endo-and exohedral chloro-fulleride as η^5 ligands: a DFT study on the first-row transition metal complexes, *Phys. Chem. Chem. Phys.* 2021, *23*, 3646-3655.

3. **Anila, Sebastian**, and Cherumuttathu H. Suresh, Guanidine as a strong CO_2 adsorbent: a DFT study on cooperative CO_2 adsorption, *Phys. Chem. Chem. Phys.* 2021, *23*, 13662-13671.

4. **Anila, Sebastian**, and Cherumuttathu H. Suresh, Imidazolium–fulleride ionic liquids–a DFT prediction, *Phys. Chem. Chem. Phys.* 2021, *23*, 20086-20094. [HOT ARTICLE]

5. **Anila, Sebastian**, and Cherumuttathu H. Suresh, Fulleride-metal η^5 sandwich and multi-decker sandwich complexes: A DFT prediction, *J. Comput. Chem.* 2022. *https://doi.org/10.1002/jcc.26860*.

6. **Anila, Sebastian**, Cherumuttathu H. Suresh, and Henry F. Schaefer III, Demarcating noncovalent and covalent bond territories: Imine-CO_2 complexes and cooperative CO_2 capture, [Just accepted in *J. Phys. Chem. A* 2022. *https://doi.org/10.1021/acs.jpca.2c03221*

7. **Anila, Sebastian**, and Cherumuttathu H. Suresh, Polyanionic cyano-fullerides for CO_2 capture: A DFT Prediction, [Communicated].

Contributions to academic conferences

1. Presented a poster entitled "*Carbon dioxide interaction with typical anions: DFT study reveals formation of large clusters*" at the International Conference on Advanced Chemical and Structural Biology (ICACSB 2019), organized at Ponnaiyah Ramajayam Institute of Science and Technology (PRIST), Manamai campus, Chennai, 19-21 February, 2019.

   Abstract: Structure and energetics of the interaction of CO_2 molecules with anions F^-, Cl^-, Br^-, CN^-, NC^-, OH^-, ClO^-, NH_2^-, and NO_2^-, have been studied at the M06L/6–311++G** level of density functional theory. In all the cases, C of CO_2 interacts with the anion. The maximum number of CO_2 molecules (n_{max}) absorbed by the anions to saturate the first shell of coordination varies from 8 – 12 in different complexes. The distance of interaction (d_{int}) of $F^-(CO_2)$, $NC^-(CO_2)$, ClO^- (CO_2), $HO^-(CO_2)$ and $H_2N^-(CO_2)$ is 1.533, 1.527, 1.468, 1.456, and 1.470 Å, respectively which indicates covalent bond formation between carbon and the interacting atom in the anion which is confirmed from the interaction energy (E_{int}) values of these complexes -29.8, -16.4, -24.4, -45.3, and -53.0 kcal/mol, respectively. However, the Cl^-, Br^-, CN^- and NO_2^- interact non-covalently with the carbon center of CO_2 with the d_{int} in the range of 2.5 – 2.9 Å. With the adsorption of each CO_2, an average increment of 5.2 – 7.2 kcal/mol is observed in the E_{int} value of the complexes. Secondary O...C interactions and the resulting stabilizations are explored from the quantum theory of atoms in molecules (QTAIM) parameters. Further, the multicenter charge delocalization in the anionic complexes is explained using the molecular electrostatic potential (MESP) analysis. The study proves that anions possess a remarkable ability to interact with a large number of CO_2 molecules which leads to significant stabilization of the complex. This property can be employed for CO_2 sequestration.

2. Presented a poster entitled "*Formation of large clusters of CO_2 around anions: DFT study reveals cooperative CO_2 adsorption*", at the National Conference on New Frontiers in Chemistry – From Fundamentals to Applications (NFCFA2019) organized at BITS Pilani, K K Birla Goa Campus, Goa, 20-22 December, 2019.

Abstract: Structure and energetics of the interaction of CO_2 molecules with anions F^-, Cl^-, Br^-, CN^-, NC^-, OH^-, ClO^-, NH_2^-, and NO_2^-, have been studied at the M06L/6−311++G** level of density functional theory. The maximum number of CO_2 molecules (n_{max}) adsorbed by the anions to saturate the first shell of coordination varies from 8 – 12 in different complexes. The anion...CO_2 distance (d_{int}) in $F^-(CO_2)$, $NC^-(CO_2)$, $ClO^-(CO_2)$, $HO^-(CO_2)$ and $H_2N^-(CO_2)$ is 1.533, 1.527, 1.468, 1.456, and 1.470 Å, respectively which indicates covalent bond formation between carbon and the anion which is confirmed from the interaction energy (E_{int}) values of these complexes 29.0, 14.7, 23.2, 41.7, and 48.1 kcal/mol, respectively. The Cl^-, Br^-, CN^- and NO_2^- interact always non-covalently with the carbon center of CO_2 with d_{int} in the range of 2.5 – 2.9 Å. With the adsorption of each CO_2, an average increment of 5.9 – 6.7 kcal/mol is observed in the E_{int} value of the complexes. The E_{int} per CO_2 ($E_{int/CO2}$) is nearly a constant for all the non-covalent complexes, even up to n_{max} number of CO_2 adsorbed. Though the primary anion...CO_2 interaction gets weaker with the increasing size of CO_2 cluster, a steady increase in the secondary O...C interaction between adsorbed CO_2 molecules helps the systems to maintain a constant value for $E_{int/CO2}$. The electron density data of non-covalent bond critical points in quantum theory of atoms in molecules (QTAIM) analysis are used to partition the total interaction energy data in to primary anion...C and secondary O...C interactions. Further, the multicenter charge delocalization in the anionic complexes is explained using the molecular electrostatic potential (MESP) analysis. The study proves that anions possess a remarkable ability to interact with a large number of CO_2 molecules due to cooperativity resulting from the secondary O...C interactions which compensate for the weakening of the primary anion...C interactions. This property of the anion-CO_2 interactions can be exploited for developing anionic or anion-incorporated materials for CO_2 storage.

3. Presented a Poster entitled "*Guanidine as a strong CO_2 adsorbent: A DFT study on cooperative CO_2 adsorption*" the Theoretical Chemistry Symposium (TCS), IISER Kolkata, 12-14 December, 2021.

Abstract: Among the various carbon capture and storage (CCS) technologies, direct air capture (DAC) of CO_2 by engineered chemical reactions on suitable adsorbents has attained more attention in recent times. Guanidine (G) is one of such promising adsorbent molecules for CO_2 capture. Here we show that the noncovalent G...CO_2 complex can transform to a strongly interacting G-CO_2 covalent complex under the influence of multiple G and CO_2. The study conducted at M06-2X /6-311++G** level density functional theory shows ΔE = -5.7 kcal/mol for G...CO_2 with N...C distance 2.688 Å while almost a five-fold increase in ΔE (-27.5 kcal/mol) is observed for the (G-CO_2)$_8$ cluster wherein the N-C distance is 1.444 Å. All the (G-CO_2)$_n$ clusters (n = 2 – 10) show strong N-CO_2 covalent interaction with N-C distance gradually decreasing from 1.479 Å for n = 2 to 1.444 Å for n = 8 $\cong$ 9, 10. The N-CO_2 bonding gives (G$^+$)-(CO$_2^-$) zwitterion character for G-CO_2 and the charge-separated units preferred a cyclic arrangement in (G-CO_2)$_n$ clusters due to the support of three strong intermolecular O...HN hydrogen bonds from every CO_2. The O...HN interaction also enhances with an increase in the size of the cluster up to n = 8. The high ΔE is attributed to the large cooperativity associated with the N-CO_2 and O...HN interactions. The quantum theory of atoms in molecules (QTAIM) analysis confirms the nature and strength of such interactions and also finds that the total interaction energy is directly related to the sum of the electron density at the bond critical points of N-CO_2 and O...HN interactions. Further, molecular electrostatic potential analysis shows that the cyclic cluster is stabilized due to the delocalization of charges accumulated on the (G$^+$)-(CO$_2^-$) zwitterion via multiple O...HN interactions. The cyclic (G-CO_2)$_n$ cluster formation is a highly exergonic process which reveals the high CO_2 adsorption capability of guanidine.

SCI Publications

Formation of large clusters of CO_2 around anions: DFT study reveals cooperative CO_2 adsorption†

Sebastian Anila[ab] and Cherumuttathu H. Suresh [ID] *[ab]

The structure and energetics of the interaction of CO_2 molecules with anions F^-, Cl^-, Br^-, CN^-, NC^-, OH^-, ClO^-, NH_2^-, and NO_2^-, have been studied at the M06L/6-311++G** level of density functional theory. The maximum number of CO_2 molecules (n_{max}) adsorbed by the anions to saturate the first shell of coordination varies from 8 to 12 in different complexes. The anion$\cdots CO_2$ distance (d_{int}) in $F^-(CO_2)$, $NC^-(CO_2)$, $ClO^-(CO_2)$, $HO^-(CO_2)$ and $H_2N^-(CO_2)$ is 1.533, 1.527, 1.468, 1.456, and 1.470 Å, respectively, which indicates covalent bond formation between carbon and the anion, which is confirmed from the interaction energy (E_{int}) values of these complexes 29.0, 14.7, 23.2, 41.7, and 48.1 kcal mol^{-1}, respectively. The Cl^-, Br^-, CN^- and NO_2^- interact always non-covalently with the carbon center of CO_2 with d_{int} in the range of 2.5–2.9 Å. With the adsorption of each CO_2, an average increment of 5.9–6.7 kcal mol^{-1} is observed in the E_{int} value of the complexes. The E_{int} per CO_2 (E_{int/CO_2}) is nearly a constant for all the non-covalent complexes, even up to n_{max} number of CO_2 adsorbed. Though the primary anion$\cdots CO_2$ interaction gets weaker with the increasing size of the CO_2 cluster, a steady increase in the secondary $O\cdots C$ interaction between adsorbed CO_2 molecules helps the systems to maintain a constant value for E_{int/CO_2}. The electron density data of non-covalent bond critical points in quantum theory of atoms in molecules (QTAIM) analysis are used to partition the total interaction energy data into primary anion$\cdots C$ and secondary $O\cdots C$ interactions. Furthermore, the multicenter charge delocalization in the anionic complexes is explained using the molecular electrostatic potential (MESP) analysis. This study proves that the anions possess a remarkable ability to interact with a large number of CO_2 molecules due to cooperativity resulting from the secondary $O\cdots C$ interactions which compensate for the weakening of the primary anion$\cdots C$ interactions. This property of the anion–CO_2 interactions can be exploited for developing anionic or anion-incorporated materials for CO_2 storage.

^{a} *Chemical Sciences and Technology Division, CSIR-National Institute for*
Interdisciplinary Science and Technology, Thiruvananthapuram, Kerala, 695 019,
India. E-mail: sureshch@niist.res.in, sureshch@gmail.com; Tel: +91-471-2515472
^{b} *Academy of Scientific and Innovative Research (AcSIR), Ghaziabad 201002, India*
† Electronic supplementary information (ESI) available: Optimized geometries, relevant tables, figures, *etc.* See DOI: 10.1039/c9cp03348c

Introduction

Cheap and effective carbon dioxide (CO_2) capture and storage (CCS)[1–8] techniques have to be developed for the isolation, extraction, and storage of CO_2 emitted from various sources, especially from fossil fuel-based power generation, to alleviate the emission of CO_2 into the atmosphere. For storing CO_2, it must interact with the storage materials. A covalent interaction can lead to chemisorption while a non-covalent interaction can lead to physisorption.[9] Though CO_2 is electrically neutral, strong electrostatic interactions can develop with charged species due to their polarizability.[10] The theoretical[6,11–16] and experimental[17–29] studies on the interactions between CO_2 and

halide ions (anions) have been a field of interest for a long time. Spears and Ferguson studied $F(CO_2)^-$ both experimentally and theoretically, and found that electrostatic calculations were insufficient to describe the covalent character of the C–F bond.[30,31] McMahon and Larson explained the bonding in $F(CO_2)^-$ complexes as covalent between F and C to suggest the formation of fluoroformate anion FCO_2^- and that in $Cl(CO_2)^-$ complexes as electrostatic, using the ion cyclotron resonance (ICR) technique.[32] Semi-empirical studies by Ault have given a planar C_{2v} symmetry structure for the fluoroformate anion, which was later confirmed from the *ab initio* calculations by Hiraoka *et al.*,[33,34] and Arnold and co-workers studied the geometry of the X^-/CO_2 clusters (X = I, Br, Cl, and F) at the SCF and Møller–Plesset (MP2 and MP4) levels of theory.[35] They also obtained the solvation energetics using negative ion photoelectron spectroscopy, as an expansion of the work by Markovich *et al.*[36,37] The structure and energetics of the CO_2–halide (Br^-, I^- and Cl^-) interactions were also studied by Pathak.[38–40] In addition to the inorganic anions,[41] the energetics as well as the spectral properties of the CO_2 clusters of organic anions

(Py^-)[42] and metal anions, namely Au,[43–45] Ag,[45,46] Cu[45,47] and Ni,[48,49] have been studied by various research groups.

Very recently, in a series of papers, Della and Suresh have reported a systematic study on the interactive behaviour of H_2 molecules with a large variety of anions and showed that anions possess a unique ability to interact with a large number of H_2 molecules.[50–53] Their studies also revealed the cooperativity of intermolecular dihydrogen interactions in the cluster formation. Though many theoretical and experimental studies have been reported for anion–CO_2 interactions, a systematic study focusing on the energetics of the formation of clusters of CO_2 around anions has not been reported yet. The present study addresses this topic using density functional theory and also elaborates on the nature of anion–CO_2 bonding – covalent *versus* non-covalent and cooperativity of interactions. The selected anions are F^-, Cl^-, Br^-, CN^-, NO_2^-, OH^-, ClO^-, NC^-, and NH_2^-.

Computational methods

All the calculations have been done using the Gaussian 16 quantum chemistry package[54] at the M06L/6-311++G** level of density functional theory (DFT).[55,56] Selection of this method is based on a previous benchmark study which recommends this as the best method to calculate the geometry and interaction energy of non-covalent dimers to an accuracy close to CCSD.[50,57] Since all complexes are anionic, the diffuse functions in the basis set are essential to describe the wave function. All the clusters discussed here are taken in their gaseous state at standard conditions of temperature (298.1 K) and pressure (1.0 atm). The presence of all real frequencies in the vibrational analysis is confirmed for all the optimized geometries. The geometry of $X^-(CO_2)_n$ for $n = 1$ to $n = n_{max}$ are obtained for $X^- = F^-$, Cl^-, Br^-, CN^-, NO_2^-, OH^-, ClO^-, NC^-, and NH_2^- where n_{max} stands for the maximum number of CO_2 molecules that can be accommodated into the first coordination shell of the anion. Saturation of the first coordination shell is confirmed by locating the structure of $X^-(CO_2)_{n_{max}+1}$ wherein at least one of the anion$\cdots$C distances is significantly larger than the rest. For systems containing up to five CO_2 molecules, several configurations are optimized (Table S15, ESI†) and among them the most stable $X^-(CO_2)_n$ is reported here. Based on such configurations, higher clusters are constructed by maximizing the O$\cdots$C interactions between adsorbed CO_2 molecules. The interaction energies of the complexes are calculated using the super-molecule approach. For any two interacting subsystems A and B, stabilization energy or the energy of interaction (E_{int}) of the super-molecule AB is calculated as

$$\Delta E = E_A + E_B - E_{AB} \qquad (1)$$

where, E_A, E_B and E_{AB} stand for the energy of systems A (anion), B (nCO_2 molecules) and AB ($X^-(CO_2)_n$ cluster), respectively.[58–61] The zero-point corrected energy of the systems is used for the calculation of E_{int} values. Furthermore, E_{int} is incorporated with the correction for the basis set superposition error (BSSE)[62–65] using the counterpoise (CP) approach of Boys and Bernardi.[66,67]

Bader's quantum theory of atoms in molecules (QTAIM) analysis, based on the electron density (ρ) distribution is carried out to get deep insight into the covalent and non-covalent interactions present in the complexes as well as to understand the cooperativity of the interactions. The QTAIM plots contain bond paths, which are lines connecting the bonded nuclei through the distributed locally maximal electron density and the corresponding bond critical points.[68–70] The AIMAll package has been used to visualize the bond paths and to locate the bond critical points (BCPs) in the QTAIM analysis.[71] Atom–atom interactions are distinguished as covalent and non-covalent interactions based on the electron densities at the respective BCPs (ρ_b) as well as from the sign of the corresponding Laplacian ($\nabla^2\rho$). The sum of electron density at the BCPs ($\Sigma\rho_b$) and the sign of the Laplacian of electron density ($\nabla^2\rho$) are also analyzed for all the complexes.

Molecular electrostatic potential (MESP) is a real physical property which is directly related to the electron density function $\rho(\mathbf{r})$.[72] MESP at any point $\mathbf{r}$ in space, $V(\mathbf{r})$ is defined by the equation:

$$V(\mathbf{r}) = \sum_A^N \frac{Z_A}{|\mathbf{r} - \mathbf{R}_A|} - \int \frac{\rho(\mathbf{r}')d^3r'}{|\mathbf{r} - \mathbf{r}'|} \qquad (2)$$

where Z_A is the charge on the nucleus located at a distance $\mathbf{R}_A$, $\rho(\mathbf{r}')$ is the electron density and $\mathbf{r}'$ is a dummy integration variable.[72,73] The MESP topographical analysis is carried out on all the complexes at the M06L/6-311++G** level of theory to understand the intermolecular interactions[73–75] and the delocalization of the electron density from the anion to the adsorbed CO_2 molecules. Furthermore, a benchmark set of calculations is done on representative cases using the B3LYP-D3, BP86-D3, and wB97XD levels in conjunction with the basis set 6-311++G**. The D3 stands for Grimme's dispersion correction.[76]

Results and discussion

Structure and energetics

The optimized structures of the $X^-(CO_2)$ of all the anions are given in Fig. 1. In all the cases, C of CO_2 interacts with the anion and the distance of interaction (d_{int}) gives a quick assessment of the strength of interaction. The d_{int} of $F^-(CO_2)$, $NC^-(CO_2)$, $ClO^-(CO_2)$, $HO^-(CO_2)$ and $H_2N^-(CO_2)$ is 1.533, 1.527, 1.468, 1.456, and 1.470 Å, respectively, which indicates the formation of a covalent bond between carbon and the anion and the resulting systems are the carboxylate anions of fluoroformic acid ($FCOO^-$), cyano formic acid ($NCCOO^-$), hypochloro formic acid ($ClOCOO^-$), carbonic acid ($HOCOO^-$) and carbamic acid (H_2NCOO^-), respectively. The OCO bond angles (θ) in $FCOO^-$, $NCCOO^-$, $ClOCOO^-$, $HOCOO^-$ and H_2NCOO^- are 138.9, 133.1, 137.3, 133.3 and 130.9°, respectively, which are 40–50° smaller than the OCO angle in CO_2. Furthermore, the CO bond elongates from 1.161 Å in CO_2 to 1.217–1.249 Å in the carboxylates. This shows the structural deformation in CO_2 resulting from the strong interaction with the anion. Anions Cl^-, Br^-, CN^- and
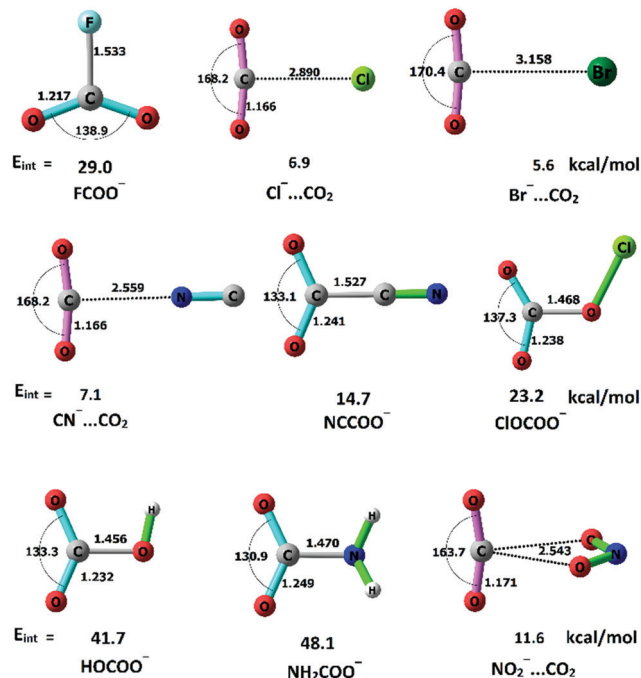
Fig. 1 Optimized structures of $X^-(CO_2)$ with their d_{int} (Å), θ (°) and interaction energy (kcal mol^{-1}) at the M06L/6-311++G** level of theory.

NO_2^- interact non-covalently with the carbon of CO_2 as d_{int} 2.5–2.9 Å seen in $Cl^-(CO_2)$, $Br^-(CO_2)$, $CN^-(CO_2)$ and $NO_2^-(CO_2)$ is significantly higher than the typical covalent bond distances. In these systems, the reduction in θ due to non-covalent bond formation is 10–18° and the CO bond elongation is 0.005–0.027 Å.

The interaction of F^- and CO_2 leading to the formation of $FCOO^-$ has been previously reported.[32,33] The interaction energy (E_{int}) for the covalent bond formation (bond energy) in $FCOO^-$ is 29.0 kcal mol^{-1}. The $FCOO^-$ retains the carboxylate form even when a second CO_2 molecule interacts with it. The second CO_2 interacts non-covalently with the fluoroformate anion through $F\cdots CO_2$ and $O\cdots CO_2$ interactions (Fig. 2). The resulting complex $FCOO^-(CO_2)$ has F–C distance 1.559 Å which is 0.026 Å higher than the F–C distance of $FCOO^-$ (Fig. 1). Interaction from a third CO_2 molecule further increases the F–C distance to 1.737 Å which suggests substantial loss of covalent character for this bond. In fact the carboxylate anionic form disappears when four or more CO_2 molecules interact with F^- and they can be represented as $F^-(CO_2)_n$ where $n > 3$. The strong covalent F–C interaction in $FCOO^-$ breaks up due to the combined non-covalent interaction from four or more CO_2 molecules as the shortest F–C distance in $F^-(CO_2)_4$, $F^-(CO_2)_5$, and $F^-(CO_2)_6$ is 2.239, 2.364, and 2.496 Å, respectively (Fig. 2). In the case of $F^-(CO_2)_7$, the seventh CO_2 interacts at a distance 4.791 Å from the F^- suggesting that the first coordination shell of F^- is saturated with six CO_2 molecules (Fig. 2). The shell and half-shell formations of solvent molecules (CO_2) around anions such as I_2^-, IBr^-, and ICN^- have been observed theoretically as well as experimentally by the Lineberger[63,77] and Neumark groups.[78–80]

The E_{int} values of the $F^-(CO_2)_n$ complexes given in Table 1 suggest that once the coordination shell is saturated at $n = 6$,
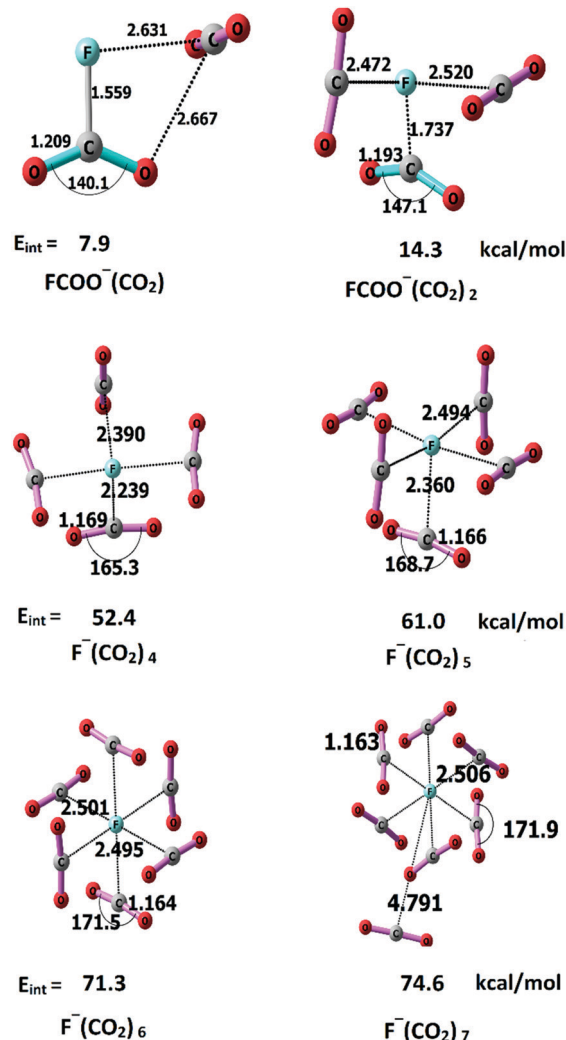
Fig. 2 Optimized structures of CO_2 complexes of F^- with their d_{int} (Å), θ (°) and E_{int} (kcal mol^{-1}) at M06L/6-311++G**.

Table 1 ZPE- and BSSE-corrected E_{int} and E_{int/CO_2}, in kcal mol^{-1}, for the CO_2 complexes of F^- at the M06L/6-311++G** level

Complex	Reaction	E_{int}	E_{int/CO_2}
$FCOO^-$	$F^- + CO_2$	29.0	29.0
$FCOO^-(CO_2)$	$FCOO^- + CO_2$	7.9	7.9
$FCOO^-(CO_2)_2$	$FCOO^- + 2CO_2$	14.3	7.2
$F^-(CO_2)_4$	$F^- + 4CO_2$	52.4	13.1
$F^-(CO_2)_5$	$F^- + 5CO_2$	61.0	12.2
$F^-(CO_2)_6$	$F^- + 6CO_2$	71.3	11.9
$F^-(CO_2)_7$	$F^- + 7CO_2$	74.6	10.7

further interaction from a CO_2 in the second shell can only bring an additional stabilization of 3.3 kcal mol^{-1} which is 7.0 kcal mol^{-1} lower than that observed for the $n = 5$ to $n = 6$ step. The interaction energy per CO_2 (E_{int/CO_2}) for $n > 3$ can be considered as a measure of the non-covalent $F^-\cdots C$ bond strength as such complexes show only non-covalent bonds whereas E_{int/CO_2} for $n = 2$ and $n = 3$ corresponds to the non-covalent interaction energy of CO_2 with a fluoroformate anion while that for $n = 1$ gives the F–C covalent bond strength.
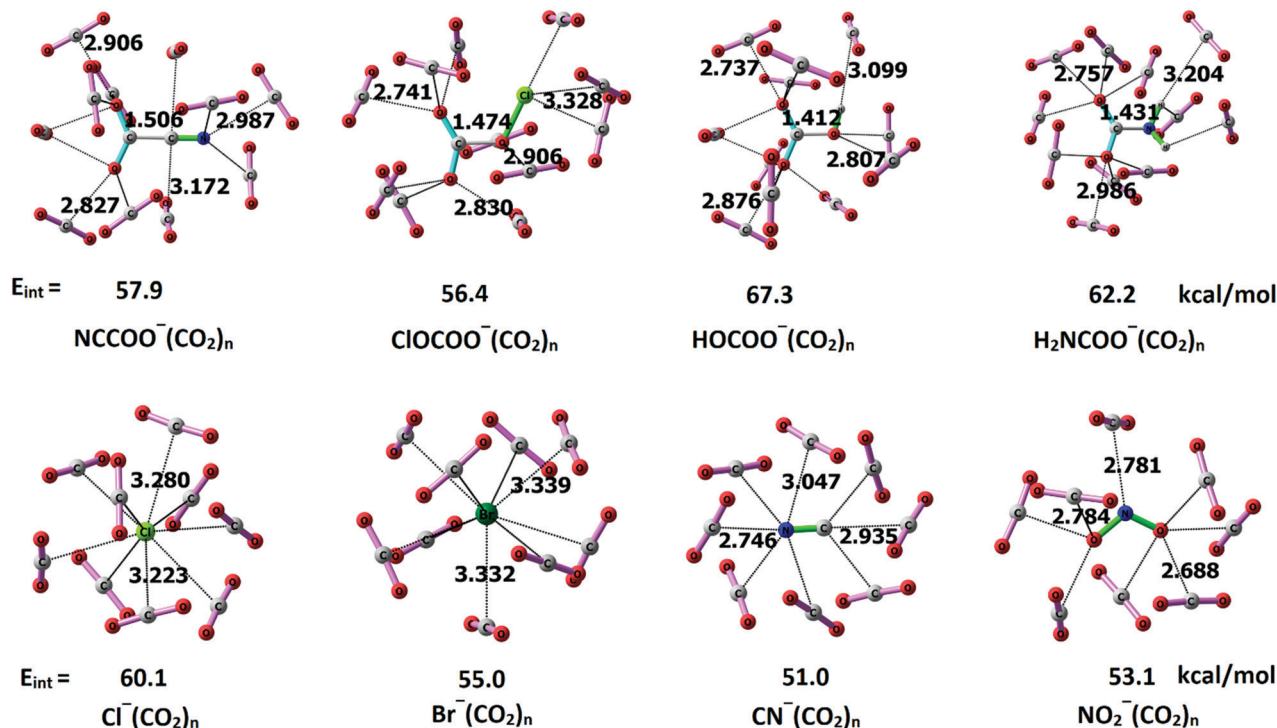
Fig. 3 Optimised structures of $X^-(CO_2)_{n_{max}}$ (X^- = $NCCOO^-$, $ClOCOO^-$, $HOCOO^-$, H_2NCOO^-, Cl^-, Br^-, CN^- and NO_2^-) with representative d_{int} (Å) and E_{int} (kcal mol^{-1}) at the M06L/6-311++G** level of theory.

The E_{int/CO_2} 11.9 kcal mol^{-1} observed for the saturated complex $F^-(CO_2)_6$ indicates the high probability for the formation of such a complex in the gas phase. The E_{int/CO_2} data in Table 1 also suggest that the non-covalent interaction between F^- and CO_2 is significantly stronger than that between $FCOO^-$ and CO_2 which can be attributed to the higher charge concentration in the smaller sized F^- than that in $FCOO^-$.

The interaction energy (E_{int}) for the covalent bond formation (bond energy) in $FCOO^-$, $NCCOO^-$, $ClOCOO^-$, $HOCOO^-$ and H_2NCOO^- is found to be 29.0, 14.7, 23.2, 41.7, and 48.1 kcal mol^{-1}, respectively, whereas E_{int} 6.9, 5.6, 7.1, and 11.6 kcal mol^{-1} observed for $Cl^-(CO_2)$, $Br^-(CO_2)$, $CN^-(CO_2)$ and $NO_2^-(CO_2)$, respectively, indicates non-covalent bond formation between the anion and CO_2.

In $NCCOO^-$, $ClOCOO^-$, $HOCOO^-$ and H_2NCOO^-, the initially formed bond with CO_2, *viz.* C–C, O–C, O–C and N–C, respectively, is retained in the system even for the fully saturated coordination state of these anions with CO_2. The optimised structures of $NCCOO^-(CO_2)_n$, $ClOCOO^-(CO_2)_n$, $HOCOO^-(CO_2)_n$ and $H_2NCOO^-(CO_2)_n$ are shown in Fig. 3 for the highest n (n_{max}) and the rest are given in the ESI.† The n_{max} is found to be 11 for $NCCOO^-$, $ClOCOO^-$, $HOCOO^-$ and H_2NCOO^-. The NC–C, HO–C and H_2N–C bonds of $NCCOO^-$, $HOCOO^-$ and H_2NCOO^-, respectively, showed contraction in bond length, *viz.* 1.527 to 1.503 Å for $NCCOO^-$, 1.474 to 1.401 Å for $HOCOO^-$, and 1.470 to 1.420 Å for H_2NCOO^- when the number of coordinated CO_2 molecules changed from $n = 1$ to $n = n_{max}$. This is an unexpected result as the opposite trend is seen in the case of $FCOO^-$. However, in the case of $ClOCOO^-$, the ClO–C bond length increased from 1.468 to 1.507 Å. The change in bond length is

not substantial here which indicates the retention of the covalent character of the bond in the saturated complexes.

The E_{int} values for $NCCOO^-$, $ClOCOO^-$, $HOCOO^-$ and H_2NCOO^- are given in Table 2. The highest magnitude in E_{int} is observed for $H_2NCOO^-(CO_2)_n$ which shows an average increase of 7.6 kcal mol^{-1} with the addition of each CO_2 molecule (Table 2). For each CO_2 adsorbed on the anion, on average E_{int} becomes more negative by 6.5, 6.3 and 8.8 kcal mol^{-1} for the complexes $NCCOO^-(CO_2)_n$ $ClOCOO^-(CO_2)_n$ and $HOCOO^-(CO_2)_n$, respectively.

In $Cl^-(CO_2)_n$, $Br^-(CO_2)_n$, $CN^-(CO_2)_n$ and $NO_2^-(CO_2)_n$, always non-covalent bond formation is observed between the anion and CO_2 for all n values. Structures of these complexes for

Table 2 ZPE- and BSSE-corrected E_{int} and E_{int/CO_2}, in kcal mol^{-1}, for the CO_2 complexes of NC^-, ClO^-, OH^-, and NH_2^-, at the M06L/6-311++G** level

	$NCCOO^-(CO_2)_n$		$ClOCOO^-(CO_2)_n$		$HOCOO^-(CO_2)_n$		$H_2NCOO^-(CO_2)_n$	
n	E_{int}	E_{int/CO_2}	E_{int}	E_{int/CO_2}	E_{int}	E_{int/CO_2}	E_{int}	E_{int/CO_2}
0	14.7	14.7	23.2	23.2	41.7	41.7	48.1	48.1
1	5.9	5.9	6.3	6.3	5.6	5.6	8.9	8.9
2	12.8	6.4	11.6	5.8	13.2	6.6	16.5	8.3
3	19.0	6.3	17.0	5.7	20.5	6.8	20.6	6.9
4	24.9	6.2	21.7	5.4	23.8	6.0	30.2	7.6
5	29.1	5.8	28.3	5.7	36.9	7.4	33.8	6.8
6	34.0	5.7	28.6	4.8	36.2	6.0	34.4	5.7
7	37.8	5.4	37.3	5.3	48.1	6.9	47.0	6.7
8	42.0	5.3	38.1	4.8	53.8	6.7	49.7	6.2
9	46.7	5.2	41.8	4.6	59.1	6.6	54.9	6.1
10	51.9	5.2	46.4	4.6	63.7	6.4	60.2	6.0
11	57.9	5.3	56.4	5.1	67.3	6.1	62.2	5.7

Table 3 ZPE- and BSSE-corrected E_{int} and E_{int/CO_2} in kcal mol^{-1}, for the CO_2 complexes of Cl$^-$, Br$^-$, CN$^-$, and NO$_2^-$, at the M06L/6-311++G** level

n	Cl$^-$		Br$^-$		CN$^-$		O$_2$N$^-$	
	E_{int}	E_{int/CO_2}	E_{int}	E_{int/CO_2}	E_{int}	E_{int/CO_2}	E_{int}	E_{int/CO_2}
1	6.9	6.9	5.6	5.6	7.1	7.1	11.6	11.6
2	14.0	7.0	11.5	5.8	13.8	6.9	17.7	8.8
3	21.7	7.2	18.4	6.1	20.0	6.7	24.1	8.0
4	28.7	7.2	24.6	6.2	26.4	6.6	30.2	7.5
5	35.7	7.1	30.3	6.1	32.4	6.5	36.1	7.2
6	42.2	7.0	36.2	6.0	39.6	6.6	40.4	6.7
7	49.3	7.0	42.7	6.1	44.3	6.3	44.2	6.3
8	57.1	7.1	49.7	6.2	51.0	6.4	53.1	6.6
9	60.1	6.7	55.0	6.1	—	—	—	—

$n = n_{max}$ are given in Fig. 3. The n_{max} is 9 for Cl$^-$ and Br$^-$ and 8 for CN$^-$ and NO$_2^-$. On average, the anion–CO$_2$ distance in Cl$^-$(CO$_2$)$_n$, Br$^-$(CO$_2$)$_n$, CN$^-$(CO$_2$)$_n$ and NO$_2^-$(CO$_2$)$_n$ is in the range of 2.888–3.241, 3.158–3.546, 2.559–3.260, and 2.109–3.366 Å, respectively (ESI†). These data indicate a decrease in non-covalent interaction strength as n changes from 1 to n_{max}. In the case of Cl$^-$(CO$_2$)$_n$, E_{int} (Table 3) improves by 6.7 kcal mol^{-1} with the addition of each CO$_2$ molecule; this effect is 6.2, 6.3, and 5.9 kcal mol^{-1}, respectively, for Br$^-$(CO$_2$)$_n$, CN$^-$(CO$_2$)$_n$, and NO$_2^-$(CO$_2$)$_n$.

Some of the small X$^-$(CO$_2$)$_n$ clusters ($n \leq 3$) show negative ΔG values for anions such as H$_2$NCOO$^-$, Cl$^-$, Br$^-$, CN$^-$, and NO$_2^-$ while a medium sized cluster (4–6 CO$_2$ molecules) gives positive ΔG values, 1–10 kcal mol^{-1} and large clusters show values above 10 kcal mol^{-1} (Tables S6 and S7, ESI†). The negative entropy is the decisive factor as the $T\Delta S$ (T = 298 K) contribution per every CO$_2$ molecule adsorbed in the system is $\sim$8.00 kcal mol^{-1}. In the case of a realistic system consisting of anions and the counter cations, the adsorption can take place only by overcoming the strong coulombic interaction between the ions. Our results suggest that anionic or electron rich systems have high tendency to adsorb CO$_2$ molecules and among the studied anions, F$^-$ has the highest ability.

We also carried out a benchmark study on a representative case, Cl$^-$(CO$_2$)$_n$ using dispersion effect-included methods, viz. B3LYP-D3, BP86-D3, and wB97XD in conjunction with basis set 6-311++G**. In Table 4, E_{int} values computed using these methods are compared with M06L/6-311++G** data. All the methods give similar E_{int} data apart from the slight enhancement

Table 4 Benchmark study for the representative case, Cl$^-$ (CO$_2$)$_n$ complexes with the basis set 6-311++G**. ZPE- and BSSE-corrected E_{int} values are given in kcal mol^{-1}

n	B3LYP-D3	BP86-D3	wB97XD	M06L
1	7.7	7.0	6.2	6.9
2	15.3	12.5	12.3	14.0
3	23.3	18.2	18.6	21.7
4	30.9	23.3	24.5	28.7
5	38.4	28.5	30.6	35.7
6	45.5	33.3	36.1	42.2
7	53.4	38.3	41.6	49.3
8	61.6	43.6	47.2	57.1
9	66.9	45.4	49.9	60.1

of $\sim$1 kcal mol^{-1} observed in the average E_{int/CO_2} for B3LYP-D3 and BP86-D3 (ESI†). The M06L method was thoroughly bench-marked in a previous study and also previous studies showed that it yields reliable results for anionic systems.[50–53] The rest of the study is conducted using the M06L/6-311++G** method.

Quantum theory of atoms in molecule (QTAIM) analysis

The QTAIM molecular plots of the anionic clusters at n_{max} are given in Fig. 4. The dotted lines indicate the bond paths and purple spheres represent the BCPs. In addition to the inter-actions between the anionic center and the CO$_2$, secondary O$\cdots$C interactions arise between adsorbed CO$_2$ molecules, as indicated by the presence of BCPs between O and C. According to the Koch and Popelier criterion,[81,82] for a non-covalent interaction, ρ_b falls in the range of 0.002–0.040 a.u. and $\nabla^2\rho$ is positive, typically in the range of 0.024–0.139 a.u. Although negative $\nabla^2\rho$ values generally indicate covalent interactions, there are exceptions such as the charge-shift bonds proposed by Shaik et al.[83] Such bonds are marked by the BCPs with larger value for the third eigenvalue of the Hessian (λ_3) than those of the other two (λ_1 and λ_2).[70] Also the parallel principal axis of the ellipsoid aligned with the eigenvectors is smaller than the perpendicular one ($c < a, b$) and is obtained as, $a = |\nabla\rho|/|\lambda_1|$, $b = |\nabla\rho|/|\lambda_2|$, and $c = |\nabla\rho|/|\lambda_3|$ (assuming that all the critical points are rank three, i.e., $\lambda_i \neq 0$, for $i = 1$–3).

In all the cases studied here, the Koch–Popelier criterion on ρ_b is valid for all the non-covalent interactions (Table 5) and the sign of $\nabla^2\rho$ is positive whereas the covalent bonds, viz. F–C in FCOO$^-$, NC–C in NCCOO$^-$, ClO–C in ClOCOO$^-$, HO–C in HOCOO$^-$ and H$_2$N–C in H$_2$NCOO$^-$ show large ρ_b and negative $\nabla^2\rho$ values. In the case of (FCOO$^-$)(CO$_2$)$_n$, the ordered pair of (ρ_b, $\nabla^2\rho$) for the shortest F–C interaction is (0.1756, $-$0.0285) for $n = 0$, (0.1648, 0.0251) for $n = 1$, (0.1072, 0.1983) for $n = 2$, and (0.0339, 0.1078) for $n = 3$. For FCOO$^-$, the F–C bond is completely covalent in nature as indicated by the large ρ_b and negative $\nabla^2\rho$ values. For FCOO$^-$(CO$_2$) and FCOO$^-$(CO$_2$)$_2$, ρ_b falls in the covalent range while the positive $\nabla^2\rho$ indicates the possibility of charge-shift bonding. For instance, the shortest F–C interaction seen in FCOO$^-$(CO$_2$) is marked by the eigenvalues $-$0.2928, $-$0.2808 and 0.5987 and the values of principal axes a, b and c of the ellipsoids aligned with the eigenvectors are 0.5412, 0.5644 and 0.2646, respectively. Here $|\lambda_3| > |\lambda_{1,2}|$ and $c < a, b$, which supports the formation of a charge-shift bond. Similar is the case of FCOO$^-$(CO$_2$)$_2$. Upon addition of the fourth CO$_2$, the existing covalent F–C interaction disappears and the non-covalent complex F$^-$(CO$_2$)$_4$ forms with ρ_b and $\nabla^2\rho$ in the prescribed range.

Unlike FCOO$^-$, the interaction of 'n' number of CO$_2$ with NCCOO$^-$, ClOCOO$^-$, HOCOO$^-$ and H$_2$NCOO$^-$ does not change the covalent character of the initially formed anion–carbon bond as ρ_b and $\nabla^2\rho$ in all these cases show values in the range of 0.2134–0.2852 a.u. for the former and ($-$0.2837)–($-$0.7866) a.u. for the latter.

The value of ρ_b is often used as a measure of the strength of the corresponding non-covalent bonding interaction while the sum of ρ_b ($\Sigma\rho_b$) can be indicative of the total stabilizing
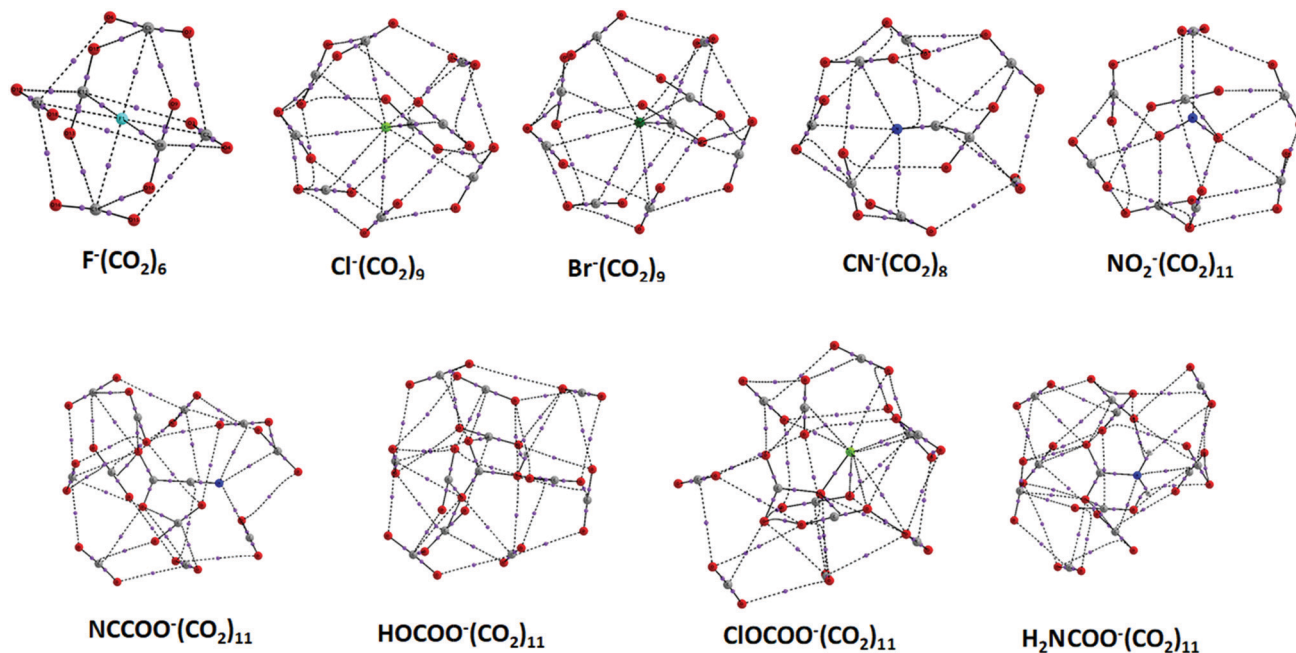
Fig. 4 QTAIM bond critical points (purple dots) and bond paths (dotted lines) of X^- $(CO_2)_{nmax}$ complexes at the M06L/6-311++G** level.

Table 5 $\Sigma\rho_b$ values (a.u.) of the $X^-\cdots CO_2$ bond in complexes at the M06L/6-311++G** level of theory

n	F^-	Cl^-	Br^-	CN^-	NO_2^-	$NCCOO^-$	$ClOCOO^-$	$HOCOO^-$	H_2NCOO^-
1	0.1755	0.0164	0.0122	0.0210	0.0427	0.0160	0.0216	0.0186	0.0669
2	0.0285	0.0347	0.0278	0.0366	0.0679	0.0394	0.0448	0.0395	0.0894
3	0.0549	0.0575	0.0495	0.0509	0.0806	0.0639	0.0605	0.0879	0.1017
4	0.1389	0.0777	0.0686	0.0736	0.1015	0.0879	0.0784	0.1070	0.120
5	0.1685	0.0930	0.0847	0.0938	0.1192	0.0957	0.1058	0.1396	0.1242
6	0.2050	0.1176	0.1034	0.1169	0.1450	0.1207	0.1227	0.1403	0.1312
7	0.2153	0.1427	0.1268	0.1314	0.1550	0.1501	0.1438	0.1812	0.1768
8	—	0.1740	0.1473	0.1648	0.1826	0.1648	0.1655	0.2013	0.1908
9	—	0.2023	0.1638	—	—	0.1929	0.2148	0.2225	0.2243
10	—	—	—	—	—	0.2094	0.2327	0.2567	0.2647
11	—	—	—	—	—	0.2288	0.2520	0.2780	0.2902

influence of the non-covalent interactions. The $\Sigma\rho_b$ values presented in Table 5 for all the anions show a strong linear correlation with the total interaction energy E_{int} (Fig. 5). The slope of the correlation plot (intercept is zero) can be used as a measure of the non-covalent binding affinity of the anions to CO_2 molecules (Table S11, ESI†). The decreasing order of the slope is $F^- > Br^- > CN^- > Cl^- > NO_2^- > NCCOO^- > HOCOO^- > H_2NCOO^- > ClOCOO^-$ and suggests that F^- has the highest and $ClOCOO^-$ has the lowest affinity towards CO_2.

For all the anions, a linear increase in E_{int} is observed with respect to the number of CO_2 adsorbed. For example, E_{int} for $Cl^-(CO_2)$ is 6.9 kcal mol^{-1} while that for $Cl^-(CO_2)_9$ is 60.1 kcal mol^{-1}; the stabilizing effect is more than nine times. The E_{int/CO_2} is nearly a constant for most of the anions. The steady increase in E_{int} with each CO_2 adsorbed can be regarded as one of the most remarkable features of the anion–CO_2 interaction. With the addition of each CO_2, the non-covalent anion$\cdots$C binding distance (d_{int}) steadily increases. For instance, in the case of $Cl^-(CO_2)_n$, for $n = 1$, d_{int} is 2.888 Å and it increases to

3.241 Å for $n = 9$. Such a distance feature may suggest a diminishing trend for E_{int/CO_2} with increase in the number of adsorbed CO_2. In order to explain the observed steady value of E_{int/CO_2}, the combined effect of primary anion$\cdots$C interactions and secondary O$\cdots$C interactions has to be evaluated. Hence, $\Sigma\rho_b$ is divided into two parts, one for anion$\cdots$C non-covalent interactions ($\Sigma\rho_1$) (Table S12, ESI†) and the other for O$\cdots$C secondary interactions between adsorbed CO_2 molecules ($\Sigma\rho_2$) (Table S13, ESI†). The correlation plots in Fig. 5 suggest,

$$E_{int} = m\Sigma\rho_b = m(\Sigma\rho_1 + \Sigma\rho_2) \quad (3)$$

Hence, total anion$\cdots$C interaction energy,

$$E_1 = m\Sigma\rho_1 \quad (4)$$

and total O$\cdots$C interaction energy,

$$E_2 = m\Sigma\rho_2 \quad (5)$$

The E_1 and E_2 data presented in Tables 6 and 7, respectively, suggest that the contribution from the anion$\cdots$C interaction is
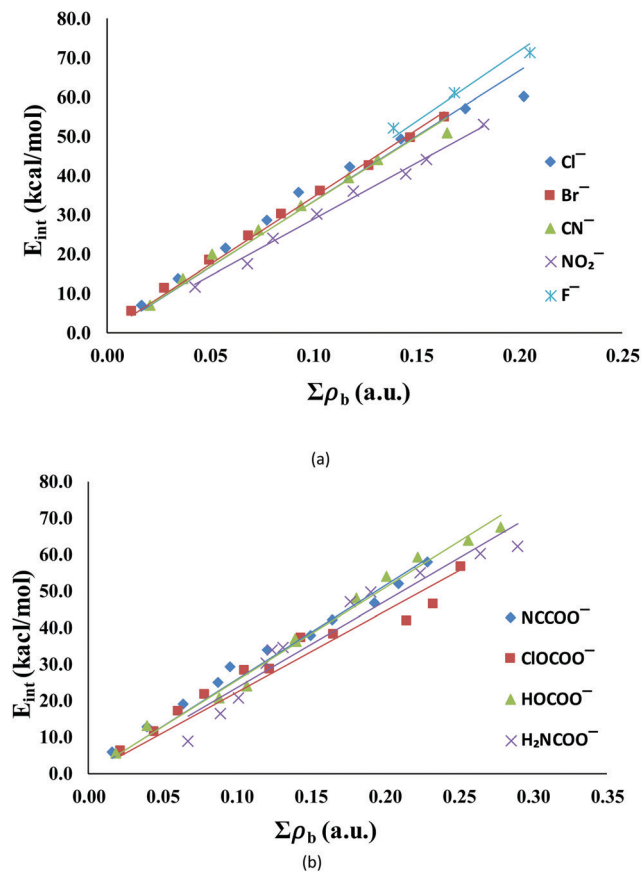
Fig. 5 (a and b) Correlations between E_{int} and $\Sigma\rho_b$ of $X^-(CO_2)_n$ complexes at the M06L/6-311++G** level.

decreasing while that due to O···C interaction is increasing with increase in the number of adsorbed CO_2 molecules (Fig. 6). The primary interaction energy is found to be inversely proportional to d_{int} (Fig. S3, ESI†). The increase in secondary interactions compensates for the weakening of primary interactions in large clusters. In fact, in large clusters, secondary interactions dominate over the primary interactions and the sum of both interactions per CO_2 adsorbed maintains a constant value. The E_1 and E_2 data clearly suggest that cooperativity between the adsorbed CO_2 molecules is very high leading to the formation of large clusters. Here cooperativity means that adsorption of a CO_2 molecule promotes the adsorption of yet another CO_2 due to enhancement in the secondary interaction and such a process continues until the primary coordination shell of the anion is saturated. Many of the secondary O···C interactions among the adsorbed CO_2 molecules are showing tetrel bond characteristics, arising from the electron density donation from the oxygen lone pairs to the carbon centers.[84–87]

Molecular electrostatic potential analysis

According to the Gadre–Pathak theorem, an anion or an anionic complex can be characterized by locating a negative-valued MESP surface that engulfs the whole system.[73] Analysis of such a surface is useful in understanding the delocalized nature of the extra electron in the system. It is expected that as the size of the CO_2 cluster increases, the delocalization increases leading to a decrease in the magnitude of the MESP minimum (V_m). This can be illustrated using a representative case, $Br^-(CO_2)_n$, for which the most negative-valued isosurface engulfing the whole complex is given in Fig. 7. For every anion···C

Table 6 E_{1/CO_2} (kcal mol^{-1}) of the $X^-\cdots CO_2$ bond in complexes at the M06L/6-311++G** level of theory

n	F^-	Cl^-	Br^-	CN^-	NO_2^-	$NCCOO^-$	$ClOCOO^-$	$HOCOO^-$	H_2NCOO^-
1	65.9	5.8	4.5	7.6	13.4	4.6	5.3	5.2	17.4
2	2.6	5.1	4.1	5.5	10.6	5.7	5.4	4.7	11.7
3	4.8	4.6	3.8	4.7	7.8	5.0	4.4	7.5	7.8
4	10.6	4.4	3.6	4.4	7.0	4.7	3.8	6.0	6.7
5	8.2	4.3	3.6	4.1	5.9	4.3	4.0	6.1	4.5
6	7.3	4.2	3.4	4.1	4.3	4.1	3.6	4.5	3.0
7	—	3.8	3.4	3.9	5.2	3.9	2.9	5.0	4.6
8	—	3.5	3.5	3.6	4.5	3.5	3.2	4.9	4.0
9	—	2.8	2.9	—	—	3.5	3.4	4.5	4.4
10	—	—	—	—	—	3.7	3.5	3.7	4.2
11	—	—	—	—	—	3.0	3.3	3.5	3.3

Table 7 E_{2/CO_2} (kcal mol^{-1}) of the $X^-\cdots CO_2$ bond in complexes at the M06L/6-311++G** level of theory

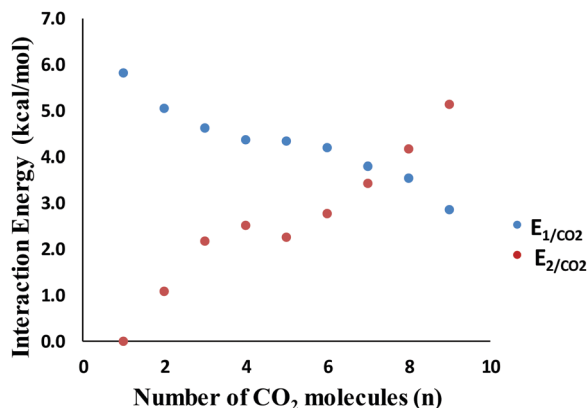| n	F^-	Cl^-	Br^-	CN^-	NO_2^-	$NCCOO^-$	$ClOCOO^-$	$HOCOO^{--}$	H_2NCOO^-
1	0.0	0.0	0.0	0.0	0.0	0.0	0.0	0.0	0.0
2	2.7	1.1	1.0	1.1	0.0	0.0	0.2	0.8	0.0
3	2.1	2.2	2.3	1.4	0.6	1.1	0.6	0.7	1.0
4	2.5	2.5	2.7	2.3	1.0	1.7	1.1	1.5	1.2
5	4.4	2.3	2.6	2.6	1.6	1.3	1.3	1.7	2.0
6	5.5	2.8	2.9	3.0	3.2	1.7	1.4	2.0	2.7
7	—	3.4	3.3	2.8	1.8	2.3	2.2	2.2	1.9
8	—	4.2	3.3	3.9	2.7	2.4	1.9	2.1	2.2
9	—	5.1	3.8	—	—	2.7	2.5	2.4	2.1
10	—	—	—	—	—	2.3	2.3	3.5	2.7
11	—	—	—	—	—	3.0	2.4	3.6	3.5

Fig. 6 Correlation plots for E_{1/CO_2} and E_{2/CO_2} vs. number of CO_2 molecules (n) for $Cl^-(CO_2)_n$ at the M06L/6-311++G(d,p) level.

non-covalent interaction, some amount of electron density gets transferred from the anion to the CO_2 whereas the secondary $O\cdots C$ interactions lead to further reorganization of the electron density.

The charge delocalization from the anionic center to the surrounding solvent shell in anionic clusters of CO_2 has been observed in the spectroscopic studies by the Neumark,[35,78] Bowen[88] and Weber[5,44,89] groups. The Lineberger group also reported the redistribution of the negative charge on the anion towards the solvent shell surrounding it in their works on solvent mediated charge distribution in anionic clusters.[90–92] In our study, we observed a gradual decrease in the negative character of V_m with increase in the size of the cluster. However, marginal irregularities in this trend are observed in some cases due to structural differences (ESI†).

Previous studies by Suresh *et al.* have shown that analysis of MESP at the nucleus (V_n) of intermolecularly interacting atoms in molecules can give insight into the strength of interactions.[51,52] In the present study, the donation of electron density from the anion to the CO_2 suggests a decrease in the magnitude of V_n at every atom of the anion. The change in MESP due to complexation with CO_2 at every atom of the anion (ΔV_n) is computed to obtain the total change in MESP ($\Sigma(\Delta V_n)$) for the anion (Table 8). The negative character of $\Sigma(\Delta V_n)$ decreases steadily with increase in the number of CO_2 adsorbed. Also strong correlations are
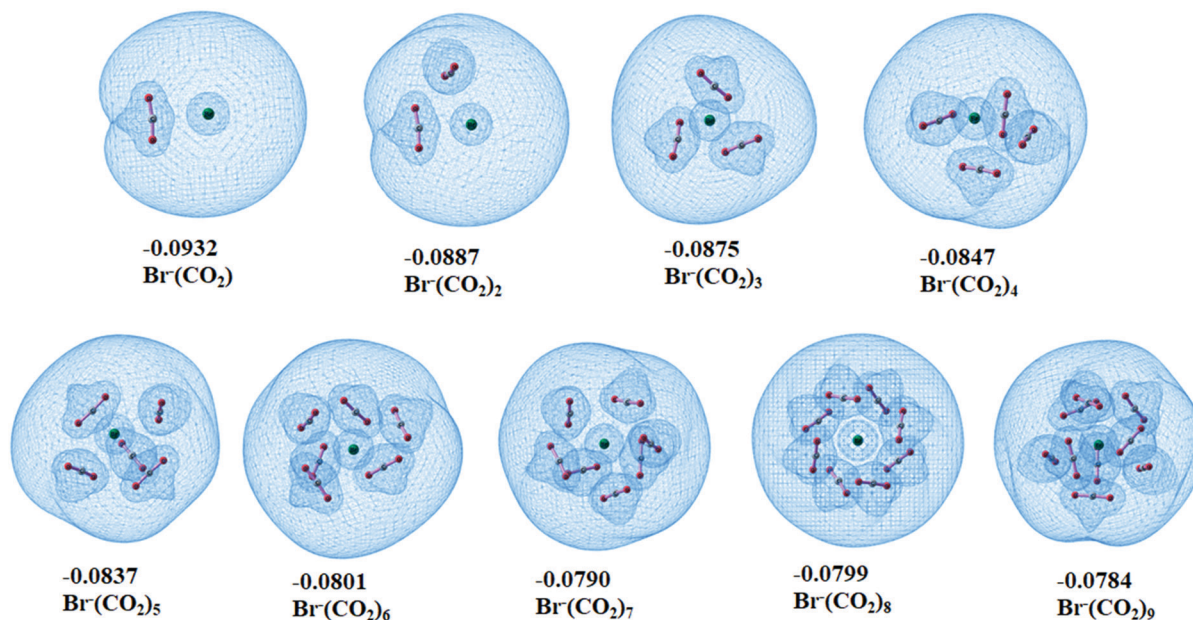
Fig. 7 MESPs of CO_2 complexes of Br^- at the M06L/6-311++G** level. The minimum value of MESP that engulfs the whole anion (V_m) is also depicted in a.u.

Table 8 $\Sigma(\Delta V_n)$ in $X^-(CO_2)_n$ complexes at the M06L/6-311++G** level of theory

n	F^-	Cl^-	Br^-	CN^-	NO_2^-	$NCCOO^-$	$ClOCOO^-$	$HOCOO^-$	H_2NCOO^-
1	−122.6	−11.6	−8.4	−26.4	−69.2	−39.5	−40.7	−42.2	−102.0
2	−131.2	−19.5	−15.0	−41.5	−121.9	−82.0	−68.9	−88.2	−125.6
3	−117.1	−26.0	−20.3	−55.6	−124.0	−105.9	−94.0	−135.2	−138.7
4	−97.0	−31.8	−25.4	−65.2	−137.0	−127.7	−108.5	−149.4	−154.7
5	−98.0	−37.8	−30.5	−76.2	−154.3	−154.3	−136.8	−193.7	−184.1
6	−103.3	−43.1	−34.7	−86.5	−149.0	−169.4	−135.3	−191.2	−166.1
7	—	−47.2	−39.1	−95.2	−163.4	−167.3	−169.8	−230.0	−217.4
8	—	−51.2	−43.6	−102.8	−181.7	−193.0	−169.3	−249.5	−231.2
9	—	−53.4	−44.7	—	—	−188.1	−161.1	−258.9	−218.0
10	—	—	—	—	—	−216.5	−188.3	−273.5	−238.6
11	—	—	—	—	—	−229.8	−222.6	−279.0	−241.7

Fig. 8 Correlations between E_{int} and $\Sigma(\Delta V_n)$ of $X^-(CO_2)_n$ complexes at the M06L/6-311++G** level.

observed between $\Sigma(\Delta V_n)$ and E_{int}. Though the correlation appears linear for most of the data, a second degree polynomial is the best fitting for the data (Fig. 8) wherein the correlation coefficients fall in the range of 0.9817 to 0.9995. The case of F^- is not included, because of its unique nature where the covalent to non-covalent transformation increases as cluster size increases – and the availability of only three non-covalent points.

Conclusions

The interactive behaviour of mono atomic and polyatomic anions with large number of CO_2 molecules has been studied using the M06L/6-311++G** level DFT. In the case of F^-, ClO^-, HO^- and H_2N^- anions, the interaction of a CO_2 leads to the formation of the corresponding carboxylate anion, $viz.$ $FCOO^-$, $ClOCOO^-$, $HOCOO^-$ and H_2NCOO^- due to the formation of an anion–C covalent bond. With the intake of more than three CO_2 molecules, the anion–C covalent bond observed for F^- changes to a non-covale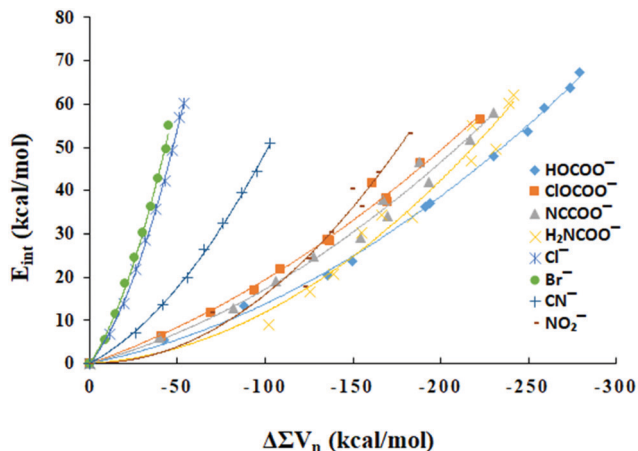nt interaction while the rest of the anions retain the initially formed covalent bond and produce the non-covalent CO_2 complexes of the carboxylate anions. In the case of CN^-, the C end of the anion interacting with CO_2 leads to the formation of an anion–C covalent bond and further uptake of CO_2 is accounted for by the corresponding carboxylate anion $NCCOO^-$. If the interaction of the first CO_2 is on the N end of the anion, non-covalent anion···C interaction occurs and further uptake of CO_2 gives a non-covalent complex. In the case of Cl^-, Br^-, and NO_2^-, only non-covalent complex formation is observed. The energetics data of the anion–CO_2 non-covalent complexes show that the anions maintain almost a constant value of E_{int/CO_2} with increasing number of CO_2 molecules. In addition to the anion···C non-covalent interactions, the secondary O···C interactions between adsorbed CO_2 molecules contribute significantly to the stability of the clusters, which is confirmed by finding strong correlation between the interaction energy data and electron density data of non-covalent bond critical points in the QTAIM analysis. As the CO_2 cluster size increases around the anion, the total effect

of secondary O···C interactions increases while that of primary anion···C interaction decreases. A steady value of E_{int/CO_2} is observed in almost all anions because the reduction in primary interactions is compensated by increase in secondary interactions. The MESP analysis is found to be very useful for assessing the delocalization of the extra electron in the system through the network of adsorbed CO_2 molecules. All anions show a steady decrease in the negative character of MESP at the nuclei as the cluster size increases. The MESP data correlate well with the interaction energy data through a second degree polynomial equation. This study demonstrates the remarkable ability of anions to bind with several molecules of CO_2 and such a character of the anion is attributed to the cooperativity in secondary O···C interactions, which gives a significant stabilizing effect on the complex even though primary anion···C interactions decrease with increasing number of CO_2 adsorbed.

Conflicts of interest

There are no conflicts to declare.

Acknowledgements

References

1 S. Solomon, D. Qin, M. Manning, Z. Chen, M. Marquis, K. B. Averyt, M. Tignor and H. L. Miller, *Contribution of working group I to the fourth assessment report of the intergovernmental panel on climate change*, Cambridge University Press, Cambridge, 2007.

2 R. E. Hester and R. M. Harrison, *Carbon capture: sequestration and storage*, Royal Society of Chemistry, 2010.

3 M. Ramdin, T. W. de Loos and T. J. Vlugt, *Ind. Eng. Chem. Res.*, 2012, **51**, 8149–8177.

4 I. C. Change, *The Assessment Report*, 2013.

5 J. M. Weber, *Int. Rev. Phys. Chem.*, 2014, **33**, 489–519.

6 G. B. Damas, A. B. Dias and L. T. Costa, *J. Phys. Chem. B*, 2014, **118**, 9046–9064.

7 I. P. o. C. Change, *Climate Change 2014-Impacts, Adaptation and Vulnerability: Regional Aspects*, Cambridge University Press, 2014.

8 I. P. O. C. Change, *Climate Change 2014, Mitigation of Climate Change, Working Group III Contribution to the Fifth Assessment Report of the Intergovernmental Panel on Climate Change*, Cambridge University Press, Cambridge, 2014.

9 M. Younas, M. Sohail, L. Leong, M. J. Bashir and S. Sumathi, *Int. J. Environ. Sci. Technol.*, 2016, **13**, 1839–1860.

10 M. Lewis, Z. Wu and R. Glaser, *J. Phys. Chem. A*, 2000, **104**, 11355–11361.

11 H.-J. Fan and C.-W. Liu, *Chem. Phys. Lett.*, 1999, **300**, 351–358.

12 B. Bhargava and S. Balasubramanian, *Chem. Phys. Lett.*, 2007, **444**, 242–246.

13 B. Bhargava, M. Saharay and S. Balasubramanian, *Bull. Mater. Sci.*, 2008, **31**, 327–334.

14 K. M. Gupta and J. Jiang, *J. Phys. Chem. C*, 2014, **118**, 3110–3118.

15 J. X. Mao, J. A. Steckel, F. Yan, N. Dhumal, H. Kim and K. Damodaran, *Phys. Chem. Chem. Phys.*, 2016, **18**, 1911–1917.

16 A. R. Shaikh, H. Karkhanechi, E. Kamio, T. Yoshioka and H. Matsuyama, *J. Phys. Chem. C*, 2016, **120**, 27734–27745.

17 X. Zhang, X. Zhang, H. Dong, Z. Zhao, S. Zhang and Y. Huang, *Energy Environ. Sci.*, 2012, **5**, 6668–6681.

18 A. P. Hallenbeck and J. R. Kitchin, *Ind. Eng. Chem. Res.*, 2013, **52**, 10788–10794.

19 J. Wang, L. Huang, R. Yang, Z. Zhang, J. Wu, Y. Gao, Q. Wang, D. O'Hare and Z. Zhong, *Energy Environ. Sci.*, 2014, **7**, 3478–3518.

20 A. Sanna, M. Uibu, G. Caramanna, R. Kuusik and M. Maroto-Valer, *Chem. Soc. Rev.*, 2014, **43**, 8049–8080.

21 A. Goeppert, M. Czaun, J.-P. Jones, G. S. Prakash and G. A. Olah, *Chem. Soc. Rev.*, 2014, **43**, 7995–8048.

22 N. Hollingsworth, S. Taylor, M. T. Galante, J. Jacquemin, C. Longo, K. B. Holt, N. H. de Leeuw and C. Hardacre, *Angew. Chem., Int. Ed.*, 2015, **54**, 14164–14168.

23 D. Chen, X. Zhang and A. F. Lee, *J. Mater. Chem. A*, 2015, **3**, 14487–14516.

24 M. Marszewski, S. Cao, J. Yu and M. Jaroniec, *Mater. Horiz.*, 2015, **2**, 261–278.

25 A. Otto, T. Grube, S. Schiebahn and D. Stolten, *Energy Environ. Sci.*, 2015, **8**, 3283–3297.

26 G. A. Ozin, *Adv. Mater.*, 2015, **27**, 1957–1963.

27 J. Kothandaraman, A. Goeppert, M. Czaun, G. A. Olah and G. S. Prakash, *J. Am. Chem. Soc.*, 2016, **138**, 778–781.

28 X. Chang, T. Wang and J. Gong, *Energy Environ. Sci.*, 2016, **9**, 2177–2196.

29 I. H. Arellano, S. H. Madani, J. Huang and P. Pendleton, *Chem. Eng. J.*, 2016, **283**, 692–702.

30 K. Spears, *J. Chem. Phys.*, 1972, **57**, 1850–1858.

31 K. G. Spears and E. Ferguson, *J. Chem. Phys.*, 1973, **59**, 4174–4183.

32 J. Larson and T. McMahon, *J. Am. Chem. Soc.*, 1985, **107**, 766–773.

33 B. S. Ault, *Inorg. Chem.*, 1982, **21**, 756–759.

34 K. Hiraoka, S. Mizuse and S. Yamabe, *J. Chem. Phys.*, 1987, **87**, 3647–3652.

35 D. W. Arnold, S. E. Bradforth, E. H. Kim and D. M. Neumark, *J. Chem. Phys.*, 1995, **102**, 3493–3509.

36 G. Markovich, R. Giniger, M. Levin and O. Cheshnovsky, *Z. Phys. D*, 1991, **20**, 69–72.

37 D. W. Arnold, S. E. Bradforth, E. H. Kim and D. M. Neumark, *J. Chem. Phys.*, 1995, **102**, 3510–3518.

38 A. K. Pathak, *ChemPhysChem*, 2011, **12**, 2641–2645.

39 A. K. Pathak, *J. Chem. Phys.*, 2012, **136**, 234306.

40 A. K. Pathak, *J. Phys. Chem. A*, 2016, **120**, 9776–9781.

41 L. Sheps, E. M. Miller and W. C. Lineberger, *J. Chem. Phys.*, 2009, **131**, 064304.

42 M. Z. Kamrath, R. A. Relph and M. A. Johnson, *J. Am. Chem. Soc.*, 2010, **132**, 15508–15511.

43 A. D. Boese, H. Schneider, A. N. Glöß and J. M. Weber, *J. Chem. Phys.*, 2005, **122**, 154301.

44 B. J. Knurr and J. M. Weber, *J. Am. Chem. Soc.*, 2012, **134**, 18804–18808.

45 X. Zhang, E. Lim, S. K. Kim and K. H. Bowen, *J. Chem. Phys.*, 2015, **143**, 174305.

46 B. J. Knurr and J. M. Weber, *J. Phys. Chem. A*, 2013, **117**, 10764–10771.

47 B. J. Knurr and J. M. Weber, *J. Phys. Chem. A*, 2014, **118**, 10246–10251.

48 B. J. Knurr and J. M. Weber, *J. Phys. Chem. A*, 2014, **118**, 8753–8757.

49 G. Liu, S. M. Ciborowski, Z. Zhu, Y. Chen, X. Zhang and K. H. Bowen, *Phys. Chem. Chem. Phys.*, 2019, **21**, 10955–10960.

50 T. D. Della and C. H. Suresh, *Phys. Chem. Chem. Phys.*, 2016, **18**, 14588–14602.

51 T. D. Della and C. H. Suresh, *ACS Omega*, 2017, **2**, 4505–4513.

52 T. D. Della and C. H. Suresh, *Phys. Chem. Chem. Phys.*, 2017, **19**, 5830–5838.

53 T. D. Della and C. H. Suresh, *Phys. Chem. Chem. Phys.*, 2018, **20**, 6227–6235.

54 M. J. Frisch, G. W. Trucks, H. B. Schlegel, G. E. Scuseria, M. A. Robb, J. R. Cheeseman, G. Scalmani, V. Barone, G. A. Petersson, H. Nakatsuji, X. Li, M. Caricato, A. V. Marenich, J. Bloino, B. G. Janesko, R. Gomperts, B. Mennucci, H. P. Hratchian, J. V. Ortiz, A. F. Izmaylov, J. L. Sonnenberg, D. Williams-Young, F. Ding, F. Lipparini, F. Egidi, J. Goings, B. Peng, A. Petrone, T. Henderson, D. Ranasinghe, V. G. Zakrzewski, J. Gao, N. Rega, G. Zheng, W. Liang, M. Hada, M. Ehara, K. Toyota, R. Fukuda, J. Hasegawa, M. Ishida, T. Nakajima, Y. Honda, O. Kitao, H. Nakai, T. Vreven, K. Throssell, J. A. Montgomery Jr., J. E. Peralta, F. Ogliaro, M. J. Bearpark, J. J. Heyd, E. N. Brothers, K. N. Kudin, V. N. Staroverov, T. A. Keith, R. Kobayashi, J. Normand, K. Raghavachari, A. P. Rendell, J. C. Burant, S. S. Iyengar, J. Tomasi, M. Cossi, J. M. Millam, M. Klene, C. Adamo, R. Cammi, J. W. Ochterski, R. L. Martin, K. Morokuma, O. Farkas, J. B. Foresman and D. J. Fox, *Gaussian 16 Rev. B.01*, Gaussian, Inc., Wallingford, CT, 2016.

55 Y. Zhao and D. G. Truhlar, *J. Chem. Phys.*, 2006, **125**, 194101.

56 Y. Zhao and D. G. Truhlar, *Acc. Chem. Res.*, 2008, **41**, 157–167.

57 K. Remya and C. H. Suresh, *J. Comput. Chem.*, 2013, **34**, 1341–1353.

58 S.-Y. Chang, H. Weinstein and D. Chou, *Chem. Phys. Lett.*, 1976, **42**, 145–150.

59 L. C. G. Freitas, R. L. Longo and A. M. Simas, *J. Chem. Soc., Faraday Trans.*, 1992, **88**, 189–193.

60 M. C. Daza, J. Dobado, J. M. Molina, P. Salvador, M. Duran and J. L. Villaveces, *J. Chem. Phys.*, 1999, **110**, 11806–11813.

61 R. J. Wheatley, A. S. Tulegenov and E. Bichoutskaia, *Int. Rev. Phys. Chem.*, 2004, **23**, 151–185.

62 S. F. Boys and F. d. Bernardi, *Mol. Phys.*, 1970, **19**, 553–566.

63 V. Vorsa, S. Nandi, P. J. Campagnola, M. Larsson and W. Lineberger, *J. Chem. Phys.*, 1997, **106**, 1402–1410.

64 C. D. Sherrill, T. Takatani and E. G. Hohenstein, *J. Phys. Chem. A*, 2009, **113**, 10146–10159.

65 P. Hobza and K. Müller-Dethlefs, *Non-covalent interactions: theory and experiment*, Royal Society of Chemistry, 2010.

66 A. Halkier, W. Klopper, T. Helgaker, P. Jøgensen and P. R. Taylor, *J. Chem. Phys.*, 1999, **111**, 9157–9167.

67 C. D. Sherrill, *School of Chemistry and Biochemistry*, Georgia Institute of Technology, 2010.

68 R. F. Bader, *Atoms in molecules: a quantum theory, International series of monographs on chemistry*, Oxford University Press, Oxford, vol. 22, 1990.

69 M. Jabłoński and M. Palusiak, *J. Phys. Chem. A*, 2010, **114**, 2240–2244.

70 H. J. Bohórquez, R. J. Boyd and C. F. Matta, *J. Phys. Chem. A*, 2011, **115**, 12991–12997.

71 T. Keith, *TK Gristmill Software*, Overland Park, KS, 2014.

72 P. Politzer and D. G. Truhlar, *Chemical applications of atomic and molecular electrostatic potentials: reactivity, structure, scattering, and energetics of organic, inorganic, and biological systems*, Springer Science & Business Media, 2013.

73 S. R. Gadre and R. N. Shirsat, *Electrostatics of atoms and molecules*, Universities Press, 2000.

74 N. Mohan and C. H. Suresh, *J. Phys. Chem. A*, 2014, **118**, 1697–1705.

75 P. V. Bijina and C. H. Suresh, *J. Chem. Sci.*, 2016, **128**, 1677–1686.

76 N. Tasinato and S. Grimme, *Phys. Chem. Chem. Phys.*, 2015, **17**, 5659–5669.

77 A. Sanov and W. C. Lineberger, *Phys. Chem. Chem. Phys.*, 2004, **6**, 2018–2032.

78 M. T. Zanni, B. J. Greenblatt and D. M. Neumark, *J. Chem. Phys.*, 1998, **109**, 9648–9651.

79 B. J. Greenblatt, M. T. Zanni and D. M. Neumark, *J. Chem. Phys.*, 2000, **112**, 601–612.

80 T. Lenzer, I. Yourshaw, M. R. Furlanetto, N. L. Pivonka and D. M. Neumark, *J. Chem. Phys.*, 2001, **115**, 3578–3589.

81 U. Koch and P. L. Popelier, *J. Phys. Chem.*, 1995, **99**, 9747–9754.

82 P. Popelier, *J. Phys. Chem. A*, 1998, **102**, 1873–1878.

83 S. Shaik, D. Danovich, W. Wu and P. C. Hiberty, *Nat. Chem.*, 2009, **1**, 443.

84 L. M. Azofra and S. Scheiner, *J. Chem. Phys.*, 2015, **142**, 034307.

85 S. Yourdkhani, T. Korona and N. L. Hadipour, *J. Comput. Chem.*, 2015, **36**, 2412–2428.

86 I. Alkorta, J. Elguero and J. E. Del Bene, *J. Phys. Chem. A*, 2017, **121**, 8017–8025.

87 M. Liu, Q. Li and S. Scheiner, *Phys. Chem. Chem. Phys.*, 2017, **19**, 5550–5559.

88 J. D. Graham, A. M. Buytendyk, Y. Wang, S. K. Kim and K. H. Bowen Jr, *J. Chem. Phys.*, 2015, **142**, 234307.

89 M. C. Thompson, J. Ramsay and J. M. Weber, *J. Phys. Chem. A*, 2017, **121**, 7534–7542.

90 L. Sheps, E. M. Miller, S. Horvath, M. A. Thompson, R. Parson, A. B. McCoy and W. C. Lineberger, *Science*, 2010, **328**, 220–224.

91 L. Sheps, E. M. Miller, S. Horvath, M. A. Thompson, R. Parson, A. B. McCoy and W. C. Lineberger, *J. Chem. Phys.*, 2011, **134**, 184311.

92 J. P. Martin, A. S. Case, Q. Gu, J. P. Darr, A. B. McCoy and W. C. Lineberger, *J. Chem. Phys.*, 2013, **139**, 064315.

ROYAL SOCIETY
OF CHEMISTRY

Check for updates

Endo- and exohedral chloro-fulleride as η⁵ ligands: a DFT study on the first-row transition metal complexes†

Sebastian Anila[ab] and Cherumuttathu H. Suresh [ID] *[ab]

C_{60} fullerene coordinates to transition metals in η^2-fashion through its C–C bond at the 6-6 ring fusion site, whereas other coordination modes η^3, η^4, η^5 and η^6 are rarely observed. The coordination power of C_{60} to transition metals is weak owing to the inherent π-electron deficiency on each C–C bond as 60 electrons get delocalized over 90 bonds. The encapsulation of Cl^- by C_{60} describes a highly exothermic reaction and the resulting $Cl^-@C_{60}$ behaves as a large anion. Similarly, the exohedral chloro-fulleride Cl^-C_{60} acts as an electron-rich ligand towards metal coordination. A comparison of the coordinating ability of $Cl^-@C_{60}$ and Cl^-C_{60} with that of the Cp^- ligand is done for early to late transition metals of the first row using the M06L/6-31G** level of density functional theory. The binding energy (E_b) for the formation of endohedral $(Cl^-@C_{60})(ML_n)^+$ and exohedral $(Cl^-C_{60})(ML_n)^+$ complexes by the chloro-fulleride ligands ranges from -116 to -170 kcal mol^{-1} and from -111 to -173 kcal mol^{-1}, respectively. Variation in E_b is also assessed for the effect of solvation by *o*-dichlorobenzene using a self-consistent reaction field method which showed 69–88% reduction in the binding affinity owing to more stabilization of the cationic and anionic fragments in the solvent compared to the neutral product complex. For each $(Cl^-@C_{60})(ML_n)^+$ and $(Cl^-C_{60})(ML_n)^+$ complex, the energetics for the transformation to C_{60} and ML_nCl is evaluated which showed exothermic character for all endohedral and exohedral Co(I) and Ni(II) complexes. The rest of the exohedral complexes, *viz.* Sc(I), Ti(II), Ti(IV), V(I), Cr(II), Mn(I), Fe(II) and Cu(I) systems showed endothermic values in the range 2–35 kcal mol^{-1}. The anionic modification makes the C_{60} unit a strong η^5 ligand similar to Cp^- for cationic transition metal fragments. The bulky anionic nature and strong coordination ability of chloro-fulleride ligands suggest new design strategies for organometallic catalysts.

Introduction

C_{60} fullerene has been reported as an η^2-type ligand for several transition metal complexes, whereas other possible coordination modes such as η^3, η^4, η^5 and η^6 have been rarely observed.[1–6] Hawkins *et al.*[7] were the first to demonstrate the η^2 coordination of C_{60} to the C_{60}–osmium tetroxide adduct $C_{60}(OsO_4)(4\text{-}tert\text{-}butylpyridine)_2$ wherein the C–C bond at the 6-6 ring fusion site coordinates to the metal for bond formation. Afterwards, the complexes of Pt(0),[8,9] Ir(I),[10,11] Pd(I)[12–14] with C_{60} as a ligand connected in the η^2 format to the metal centre were isolated. Baird *et al.* made stable anionic complexes of the type $A[Mn(CO)_4(\eta^2\text{-}C_{60})]$ (A = Na, bis(triphenylphosphoranylidene)

ammonium).[15,16] The organometallic polymer of fullerene containing polymetallic linkages has been reported wherein the metal centre gets bonded to C_{60} in an η^2 fashion.[17–19] The heterogeneous reaction of the palladium or platinum–η^2-fullerene polymer with P ligands (tertiary phosphines or tertiary phosphites) in solution affords the complexes $C_{60}ML_2$.[20–22]

The η^3, η^4, η^5 or η^6 coordination of C_{60} is rarely observed in organometallic chemistry because the spherically delocalized distribution of 60-π electrons over 90 C–C bonds gives rise to significant reduction in the π-electron density over each C–C bond compared to a localized C–C double bond. Hence, the C–C bond of fullerene at the 6-6 ring fusion site can show reactivity similar to electron deficient olefins.[23,24] Chemists have achieved disruption in the 60-π electron conjugation by saturating five α positions around a 5-membered ring of C_{60}. The reported η^5-fullerene metal complexes formed with such modified fullerenes are called pseudofullerenes (Fig. 1). The Nakamura group gave an experimental validation for the existence of η^5-C_{60} pseudofullerene–organometallic complexes.[25–28] The ferrocene/pseudofullerene hybrid molecule has been

ᵃ Chemical Sciences and Technology Division, CSIR – National Institute for Interdisciplinary Science and Technology, Thiruvananthapuram, Kerala, 695 019, India. E-mail: sureshch@niist.res.in, sureshch@gmail.com; Tel: +91 471 2515472
ᵇ Academy of Scientific and Innovative Research (AcSIR), Ghaziabad 201002, India
† Electronic supplementary information (ESI) available: Optimized geometries, relevant tables, figures, *etc.* See DOI: 10.1039/d0cp05612j
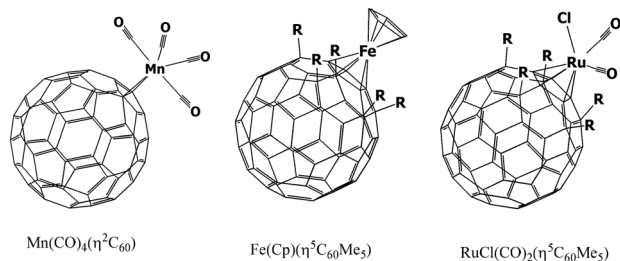
Fig. 1 A representative set of fullerene–metal complexes.

synthesized by Sawamura *et al.* in the singlet ground-state through the use of suitably modified fullerene derivatives (pseudofullerene) that can act as a 6π-electron donor ligand to the 6d electron Fe(II).[27] Toganoh *et al.* reported the reactivity profile of group VI metal complexes of the η[5]-pentamethyl C_{60} fullerene ligand (pseudofullerene) in a variety of oxidation states, from II to VI.[29] Theoretical studies also predicted the stability of the pseudofullerene bis(η[5]-fullerenyl-R_5)Fe, an analogue of ferrocene.[30–33]

Using DFT PBE calculations, Stankevich *et al.* identified η[3]-π-hapticity for allyl type derivatives of C_{60} fullerene ($C_{60}R_3$ (R = H, F, Cl, Br)) with Ni and Co.[34] The possibility of formation of η[4]-π-complexes of C_{60} with a Fe(CO)$_3$ species was analysed by Chistyakov and Stankevich through DFT calculations.[35] The stability of η[4]-π-complexes of C_{60} with the Fe(CO)$_3$ unit has been related to the attachment of four (or six) hydrogen atoms to C_{60} to form "butadiene"-or "fulvalene"-type derivatives. Alvarez *et al.* studied the coordination of C_{60} as well as that of corannulene bucky bowls to the metal fragments and reported that despite the very similar structural features, their preferences for metal coordination are completely different.[36] Using a two-laser vaporization method, the η[6] coordination of C_{60} with Sc to Co was observed by Nagao *et al.*[37] Peng *et al.* observed the η[6] coordination of C_{60} in the complex $C_{60}RuCp(R)_5$ by mass spectroscopy data.[38] Using orbital compatibility arguments, Jemmis *et al.* proposed that due to the splayed out distribution of the π-orbitals of the five- and six-membered rings of C_{60}, an effective η[5]/η[6] bonding interaction is difficult for it with a metal fragment. To overcome this and to achieve strong η[6] coordination, they suggested the use of metal fragments with highly diffused frontier orbitals such as C_3H_3Co and C_3H_3Rh.[39–41] Recently, a theoretical study by Molina *et al.* suggested η[6]-coordination for C_{60} with the metals Cr(0) and Ru(II) in sandwich-type complexes.[42] The molybdenum organometallic derivative of C_{60} with the polysubstitution of fluorine atoms, prepared by Taylor and co-workers, appeared as η[6]-coordinated due to the strong distortion in the C_{60} sphere.[43]

Endohedral fullerenes (EFs) formed by encapsulating atoms, ions, or small molecules inside the cage show electronic structures different from their parent empty cage, and thus have many applications in the fields of materials science and biomedical applications. Using Hartree–Fock theory, Cioslowski and co-workers theoretically predicted that upon encapsulation of atoms, ions, and molecules with C_{60}, there are almost no changes in the cage structure.[44] Inspired by this work, several

experimental and theoretical investigations have been directed towards understanding the properties of a large variety of EFs.[45–47] Most of the theoretical studies were on the confinement and stabilization of the species encapsulated into the endohedral cavity. The encapsulated species, atom or molecule was found to occupy the centre of the cage cavity. Sathyamurthy and co-workers studied the structural and electronic confinement of molecules: HF, H_2O, NH_3, and CH_4 inside fullerene.[48,49] Weidinger *et al.* developed EFs with nitrogen[50] or phosphorus[51] atoms by bombarding C_{60} with nitrogen ions from a conventional plasma discharge ion source. Similarly, N@C_{70}, N_2@C_{70},[52] and P@C_{60} were also synthesized using this ion implantation method.[53] Ravinder and Subramanian reported the study on endohedral complexes of halides such as F^-, Cl^-, and Br^- with C_{30}, C_{32}, C_{34}, C_{36}, C_{60}, and C_{70} molecules at the B3LYP/6-311+G* level of theory and they also reported the structure and stability of OH and CN inside the C_{60} and C_{70}.[54] Campbell *et al.* used ion bombardment to implant alkali metal ions (especially Li^+) into C_{60}, but the characterization of the final products was difficult.[46] Li@C_{60} produced by ion bombardment was isolated by Sawa, Tobita and co-workers in the form of its cationic salt, [Li^+@C_{60}](SbCl$_6$).[55] A detailed investigation of the electronic and structural properties of M@C_{60} (where M = H_2O, Li^+, Na^+, K^+, Be^{2+}, Mg^{2+}, and Ca^{2+}) by Oliveira and Gonçalves, using quantum chemical calculations at the DFT/B3LYP/6-31G** level, has shown that the energy gap calculated for the endohedral fullerenes based on the HOMO and LUMO energy difference is less than that of pure C_{60}.[56] Tuning of the exohedral reactivity of fullerenes by the encapsulation of ions inside the cage is highly important. Garcia-Rodeja *et.al* found that Diels–Alder (DA) reactions between 1,3-cyclohexadiene and ion-encapsulated fullerenes of the type M@C_{60} (M = Li^+, Na^+, K^+, Cl^-) proceed concertedly *via* highly synchronous transition states, and thus resemble the corresponding process involving the parent C_{60} fullerene. Systems having an endohedral cation has shown a clear enhancement towards the DA reactions, whereas the behaviour of those with anionic compounds was the opposite.[57]

Although the literature shows evidence for the formation of η[5]/η[6]-fullerene–organometallic complexes, a synthetically viable strategy for promoting such a coordination behavior is available only for pseudo fullerenes. Recent studies from our group on EFs showed that anions such as F^-, Cl^-, Br^-, OH^-, NH_2^-, NO_2^-, CN^-, and ClO^- interact strongly with the interior of the fullerene cage leading to significant stabilization of the EFs.[58] Further, such EFs show electron rich behavior on the carbon surface, which is similar to the electron rich character of the radical anion $C_{60}^{\bullet-}$. The complexes such as F^-@C_{60}, Cl^-@$C_{60}Br^-$@$C_{60}OH^-$@C_{60}, NH_2^-@C_{60}, NO_2^-@C_{60}, CN^-@C_{60} and ClO^-@C_{60} behaved like large anions. Frontier molecular orbital (FMO) analysis along with the molecular electrostatic potential (MESP) analysis and quantum theory of atoms in molecules (QTAIM) analysis proved that the electron rich character of the carbon framework of X^-@C_{60} resembles very close to that of the radical anion $C_{60}^{\bullet-}$. This study also suggested that X^-@C_{60} systems have a closed shell nature which gives high chemical stability, compared to the radical

This journal is © the Owner Societies 2021

Phys. Chem. Chem. Phys., 2021, **23**, 3646–3655 | **3647**

anion $C_{60}^{\bullet-}$. Here we consider the possibility of $Cl^-@C_{60}$ as a strongly coordinating η^5/η^6-ligand to transition metal complexes. Also for more realistic application, we consider the exohedral version of such systems, $Cl^-C_{60}ML_n$, the coordination of a chloro-fulleride with a transition metal fragment.

Computational methods

All the geometry optimizations in this study are carried out at the M06L/6-31G** level of DFT using the Gaussian 16 suite of programs.[59] Zhao and Truhlar suggested the M06L functional as the best method in the overall performance for organometallic, inorganometallic and noncovalent interactions.[60] Previously, a benchmark study by Remya and Suresh showed that the M06L method is a robust method for calculating the structure and energetics of even very weakly interacting complexes.[61] Also a recent study from our group has showed that the M06L method gives reliable results for anionic fullerene systems.[55] Vibrational frequency analysis has been carried out on optimized geometries which confirms the energy minima nature with all real frequencies. The binding energy (coordination energy) of each transition metal complex is calculated using the equation,

$$E_b = E_{TM} - (E_X + E_Y) \tag{1}$$

where E_{TM}, E_X and E_Y stand for the zero-point energy (ZPE)-corrected energy of the transition metal complex, the ligand X and metal fragment Y, respectively.

Further, the influence of solvent effects on the complexation of the anion incorporated fullerene moiety with metal fragments has been studied using the self-consistent reaction field (SCRF) method using the solvation model based on the density (SMD) approach. The selected solvent for SMD calculation is o-dichlorobenzene (ODCB). Here single point calculations are carried out for the complexes with the solvent at the M06L/6-311++G** level of theory. The solvation incorporated binding energy (E_{bs}) of each complex is calculated using the equation,

$$E_{bs} = E_{TMs} - (E_{Xs} + E_{Ys}) \tag{2}$$

where E_{TMs}, E_{Xs} and E_{Ys} stand for the energy of the transition metal complex, the ligand X and the metal fragment Y, respectively, obtained from the SCRF calculations.

The energy of dissociation (E_r) of the transition metal complex into the corresponding metal halide and C_{60} is calculated as,

$$E_r = E_{TM} - (E_A + E_B) \tag{3}$$

where E_{TM}, E_A and E_B stand for the zero-point energy (ZPE)-corrected energy of the transition metal complex, C_{60} (A) and metal halide (B), respectively.

Results and discussion

Complexes of $[Mn(CO)_3]^+$

The anionic cyclopentadienyl ligand (Cp^-), being highly versatile and a potential six-electron donor, is one of the most frequently encountered η^5 ligands in organometallic chemistry. Here, we consider the Cl^- incorporated endohedral fullerene, $Cl^-@C_{60}$ or its exohedral version, Cl^-C_{60} as an anionic ligand similar to Cp^-. The initial assessment of η^5 as well as η^6 coordination of $Cl^-@C_{60}$ and Cl^-C_{60} is carried out by complexing them with the metal fragment $[Mn(CO)_3]^+$. The cationic manganese tricarbonyl system is a good choice for this study as the corresponding Cp^- complex $Mn(CO)_3(Cp)$ is well documented in the literature with the crystal structure (ESI,† Fig. S1).[62,63] Fig. 2 shows the optimised geometries of $[Mn(CO)_3]^+$ in different coordination fashions.

Some of the major structural parameters of the complexes depicted in Fig. 2 are given in Table 1. The distance between Mn and the centre of the five or six membered ring is labelled as d_1, d_2 represents Mn–CO distance and d_3 represents the C–O distance. The values of d_1, d_2 and d_3 observed in the $Mn(CO)_3(Cp)$ complex are found to be 1.74, 1.78 and 1.16 Å, respectively, which is in agreement with the corresponding
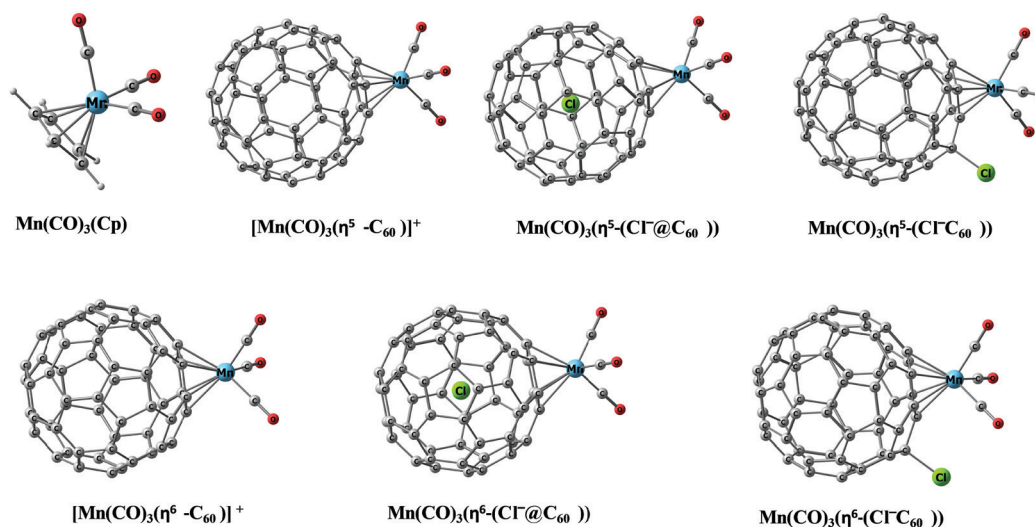

Fig. 2 Optimised geometries of $Mn(CO)_3$ complexes.

3648 | *Phys. Chem. Chem. Phys.*, 2021, **23**, 3646–3655

This journal is © the Owner Societies 2021

Table 1 Structural parameters (Å), vibrational frequency of CO symmetric stretching (cm^{-1}) and E_b (kcal mol^{-1}) values of the Mn-complexes

Complex	d_1	d_2	d_3	d_4	$\bar{\nu}_{CO}$
Mn(CO)$_3$Cp	1.74	1.79	1.16	—	2103
[Mn(CO)$_3$(η^5-C$_{60}$)]$^+$	1.86	1.80	1.16	—	2133
[Mn(CO)$_3$(η^6-C$_{60}$)]$^+$	1.85	1.80	1.15	—	2139
Mn(CO)$_3$(η^5-(Cl$^-$@C$_{60}$))	1.85	1.79	1.16	3.54	2111
Mn(CO)$_3$(η^6-(Cl$^-$@C$_{60}$))	1.85	1.79	1.16	3.55	2115
Mn(CO)$_3$(η^5-Cl$^-$C$_{60}$)	1.85	1.79	1.16	1.87	2112
Mn(CO)$_3$(η^6-Cl$^-$C$_{60}$)	1.88	1.79	1.16	1.94	2122

Table 2 E_b (kcal mol^{-1}) values of various complexation possibilities of the Mn-complexes

Complex	Complexation reaction	E_b
Mn(CO)$_3$Cp	[Mn(CO)$_3$]$^+$ + Cp$^-$	−263.9
(Mn(CO)$_3$)$^+$(η^5-C$_{60}$)	[Mn(CO)$_3$]$^+$ + (η^5-C$_{60}$)	−81.1
(Mn(CO)$_3$)$^+$(η^6-C$_{60}$)	[Mn(CO)$_3$]$^+$ + (η^6-C$_{60}$)	−78.8
Cl$^-$@C$_{60}$	C$_{60}$ + Cl$^-$	−52.2
Cl$^-$C$_{60}$	C$_{60}$ + Cl$^-$	−25.6
(Mn(CO)$_3$)$^+$(η^5-(Cl$^-$@C$_{60}$))	[Mn(CO)$_3$]$^+$ + Cl$^-$@C$_{60}$	−160.5
(Mn(CO)$_3$)$^+$(η^6-(Cl$^-$@C$_{60}$))	[Mn(CO)$_3$]$^+$ + Cl$^-$@C$_{60}$	157.0
(Mn(CO)$_3$)$^+$(η^5-(Cl$^-$C$_{60}$))	[Mn(CO)$_3$]$^+$ + Cl$^-$C$_{60}$	−165.3
(Mn(CO)$_3$)$^+$(η^6-(Cl$^-$C$_{60}$))	[Mn(CO)$_3$]$^+$ + Cl$^-$C$_{60}$	−149.1

crystal structure data, *viz.* 1.77, 1.79, and 1.16 Å. When the Cp$^-$ ligand is replaced by the anion encapsulated endohedral fullerene [Cl$^-$@C$_{60}$] and exohedral fullerene [Cl$^-$C$_{60}$], the CO ligands remain mostly unaffected, as indicated by the almost same values of d_2 and d_3 for the η^5 and η^6 cases, whereas the d_1 values that fall in the range of 1.85–1.88 Å suggest a significant increase compared to the d_1 value of the corresponding Cp-complex. The C–Cl distances observed in the exohedral complex in η^5 and η^6 coordination modes were 1.87 and 1.94 Å, respectively, which is longer than the normal C–Cl distance found in the sp^3 hybridised C compounds like CH$_3$Cl (1.78 Å). This shows that the η^5 coordination mode is making stronger C–Cl interaction than the corresponding η^6 mode of coordination. In the case of the endohedral complexes, the C–Cl distance observed in η^5 and η^6 is 3.54 Å, which is nearly half of the diameter of the C$_{60}$ molecule (7.07 Å) and suggests that Cl$^-$ is at the centre of the fullerene cage. The complexes [Mn(CO)$_3$(η^5-C$_{60}$)]$^+$ and [Mn(CO)$_3$(η^6-C$_{60}$)]$^+$ showed d_1, d_2 and d_3 values very similar to those of the anionic fullerene derivatives. It is clear that the relative stability of the complexes cannot be correctly inferred from the distance parameters.

IR vibrational frequency analysis of these complexes (Table 1) shows that the carbonyl symmetric stretching frequencies ($\bar{\nu}_{CO}$) of the complexes are higher than that of the reference complex, Mn(CO)$_3$(Cp). The C–O vibrational frequency increases in the order, Cp$^-$ < (Cl$^-$@C$_{60}$) < (Cl$^-$C$_{60}$) < C$_{60}$. The higher degree of back-bonding from the Mn centre to the CO ligand in the complex Mn(CO)$_3$(Cp) results in the lowest observed $\bar{\nu}_{CO}$ of ∼2103 cm^{-1}, whereas the coordination of [Mn(CO)$_3$]$^+$ to fullerene either in η^5 or η^6 fashion gives the largest $\bar{\nu}_{CO}$, 2133–2139 cm^{-1} due to the weak back-bonding. Also between η^5 and η^6 coordination, a 4–10 cm^{-1} lower value of $\bar{\nu}_{CO}$ is observed for the former indicating the higher preference of such a coordination for fullerene units with [Mn(CO)$_3$]$^+$.

The energetics of various complexation possibilities are presented in Table 2. The separation of Mn(CO)$_3$Cp to ionic fragments Mn(CO$_3$)$^+$ and Cp$^-$ is energy demanding with E_b −263.9 kcal mol^{-1}. The η^5 coordination of C$_{60}$ with Mn(CO$_3$)$^+$ is exothermic by 81.1 kcal mol^{-1}, while the η^6 coordination is weaker by 2.3 kcal mol^{-1}. The endohedral complexation of Cl$^-$ with fullerene is exothermic by 52.2 kcal mol^{-1}, whereas its exohedral complexation is exothermic by 25.6 kcal mol^{-1}. The dissociation of the complex [(Mn(CO)$_3$)$^+$(η^5-(Cl$^-$C$_{60}$))] into the fragments [MnCO$_3$]$^+$ and Cl$^-$@C$_{60}$ requires energy 160.5 kcal mol^{-1}. In the case of the exohedral complex

[(Mn(CO)$_3$)$^+$(η^5-(Cl$^-$C$_{60}$))], E_b for the fragmentation (Mn(CO)$_3$)$^+$ and Cl$^-$C$_{60}$ is −165.3 kcal mol^{-1}, which is higher than the respective endohedral variant by 4.8 kcal mol^{-1}. In Cl$^-$–C$_{60}$, the interaction distance of Cl$^-$ with the nearest five carbon atoms ranges from 3.10 to 3.14 Å which indicates that fullerene has only a weak non-covalent interaction with Cl$^-$, whereas the C–Cl distance 1.87 Å observed in (Mn(CO)$_3$)$^+$(η^5-(Cl$^-$C$_{60}$)) suggests strong covalent interaction between the atoms. The preferred positon for exohedral bonding of Cl$^-$ to the fullerene is the α-carbon, with respect to the η^5-coordinated five-membered ring as observed from the different possible variations in the exohedral structures (ESI,† Fig. S2). In the case of η^6-coordination, the E_b values observed for the complexes are less than the corresponding η^5-complexes (Table 1). The difference is 3.5 kcal mol^{-1} for Cl$^-$@C$_{60}$, whereas in the case of Cl$^-$C$_{60}$, the difference is 16.2 kcal mol^{-1}.

The energy data on different complexation possibilities clearly suggest that the anionic endohedral as well as exohedral variants of the fullerene molecule with Cl$^-$ are capable of coordinating with the metal fragments to form stable η^5 and η^6 complexes. Although not as strong as the Cp$^-$ ligands, the endohedral or exohedral modification on the fullerene with the anion improves the E_b by almost double compared to the bare fullerene–metal interaction. The anion incorporation makes the carbon centers of fullerene electron rich and the whole system behaves as a large anion for a strong coordination with the metal fragment. Since the η^5-complex is more stable than the η^6-varient, it tested for other metal complexes (ESI,† Fig. S7), and only the former is studied for other metal centers.

Complexes of the first row transition metals

The strong η^5-type coordinating ability of Cl$^-$@C$_{60}$ and Cl$^-$C$_{60}$ observed for the tricarbonyl manganese complex could be validated for other transition metals. In order to do this, the study is extended to the organometallic complexes of the first row transition metals: Sc, Ti, V, Cr, Mn, Fe, Co, Ni, and Cu. X-ray structures of the complexes of these metals containing Cp$^-$ or a substituted Cp$^-$ (Cp$^-$*) have been reported in the literature (ESI†). Two or three complexes of each of the first row transition metals are discussed here with mostly the carbonyl ligand or trialkyl amine and the trialkyl phosphine ligand. The optimized structures of selected such complexes (CpML$_n$) from the literature (Cp$^-$* is replaced with Cp$^-$) are shown in Fig. 3.
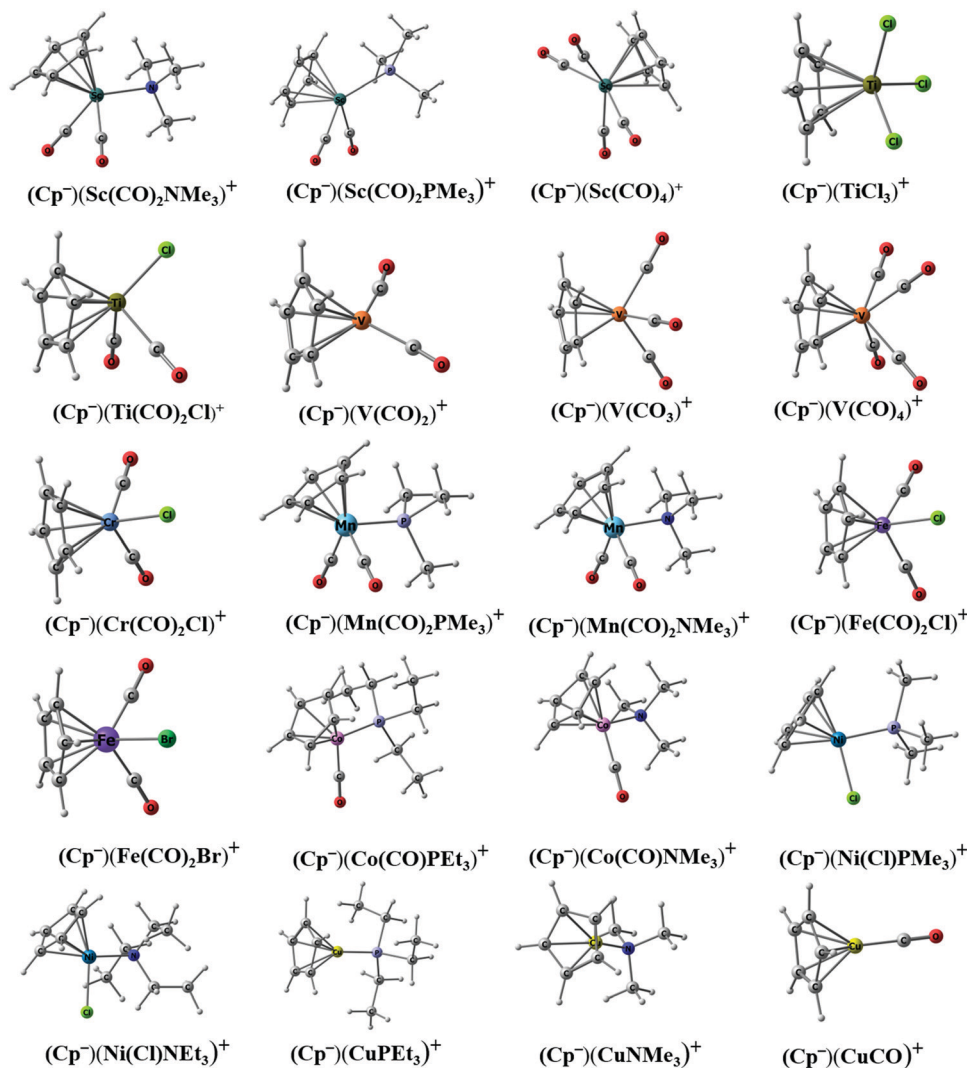
Fig. 3 Optimised structures of transition metal complexes of Cp⁻ at M06L/6-31G**.

The E_b values of CpML$_n$ for Cp⁻ dissociation are in the range from −196 to −275 kcal mol⁻¹ (Table 3). E_b values vary with respect to the nature of the metal centre and the associated ligands. The Cp–metal interaction is the weakest for the early and late transition metals such as Sc, Cu and Ni, while the middle transition metals such as Cr and Fe show the strongest interaction. In all these complexes, if Cp⁻ is replaced with C$_{60}$ for an η⁵ coordination with the metal center, the corresponding cationic complexes, [C$_{60}$ML$_n$]⁺ show E_b in the range −52 to −88 kcal mol⁻¹ (Table 3).

Fig. 4 shows the optimized geometries of (Cl⁻@C$_{60}$)(ML$_n$)⁺. Here Cl⁻@C$_{60}$ behaves as a large anionic ligand to provide six electrons to the metal center through the η⁵ coordination. E_b is in the range −116 to −171 kcal mol⁻¹ which is 63 to 98 kcal mol⁻¹ better than [C$_{60}$ML$_n$]⁺ complexes. Compared to early and late transition metals, the middle ones showed higher interaction with Cl⁻@C$_{60}$. In all the (Cl⁻@C$_{60}$)(ML$_n$)⁺ cases, Cl⁻ is trapped deep inside the fullerene moiety (close to the center) and a direct covalent interaction of Cl with fullerene carbon or the metal center can be ruled out. The significant enhancement in

the interaction energy between Cl⁻@C$_{60}$ and M compared to C$_{60}$ and M can be interpreted as solely due to the through space electronic influence of Cl⁻ on the metal. In effect, Cl⁻@C$_{60}$ acts as a large anion[58] due to the significant transfer of the extra negative charge density on the Cl⁻ to the whole fullerene C atoms leading to six electron coordination power for Cl⁻@C$_{60}$ towards the metal center. In essence, the ligation from the Cl⁻ incorporated fullerene unit through the five membered ring could be considered as an interaction similar to between Cp⁻ and metals in organometallic complexes.

The optimized geometries of (Cl⁻C$_{60}$)(ML$_n$)⁺ complexes are given in Fig. 5. The E_b values of the complexes are in the range from −111 to −169 kcal mol⁻¹. Strong η⁵ coordination is observed for the ligand with all the metal fragments except [Sc(CO)$_2$PMe$_3$]⁺, [CuNMe$_3$]⁺ and [TiCl$_3$]⁺. In the case of [Sc(CO)$_2$PMe$_3$]⁺ and [CuNMe$_3$]⁺, the bond formation of Cl⁻ with the α-carbon is not observed. All attempts to optimize such structures give the complexes C$_{60}$–Sc(CO)$_2$PMe$_3$Cl and C$_{60}$–CuNMe$_3$Cl, respectively. The (Cl⁻C$_{60}$)(ML$_n$)⁺ complex of [Sc(CO)$_2$PMe$_3$]⁺ and [CuNMe$_3$]⁺ given in Fig. 5 shows the

3650 | *Phys. Chem. Chem. Phys.*, 2021, **23**, 3646–3655

This journal is © the Owner Societies 2021

Table 3 ZPE corrected-E_b of the transition metal complexes for L = Cp⁻, L = C_{60}, L = Cl⁻@C_{60}, and L = Cl⁻C_{60} at the M06L/6-31G** level

Label	Metal	Ligands	E_b (kcal mol⁻¹)			
			L = Cp⁻	L = C_{60}	L = Cl⁻@C_{60}	L = C_{60}⁻Cl⁻
1	Sc(I)	CO, CO, NMe₃, L	−194.3	−52.3	−115.9	−118.2
2	Sc(I)	CO, CO, PMe₃, L	−195.5	−52.0	−116.8	−111.3
3	Sc(I)	4CO, L	−216.7	−56.5	−129.4	−131.9
4	Ti(II)	CO, CO, Cl⁻, L	−248.8	−73.7	−152.3	−155.4
5	Ti(IV)	3Cl⁻, L	−255.9	−73.0	−155.2	−161.4
6	V(I)	CO, CO, L	−247.9	−77.1	−153.1	−157.7
7	V(I)	CO, CO, CO, L	−251.6	−76.5	−154.5	−158.0
8	V(I)	4CO, L	−256.2	−76.8	−156.6	−160.5
9	Cr(II)	CO, CO, Cl⁻, L	−221.3	−87.7	−170.0	−173.4
10	Mn(I)	CO, CO, NMe₃, L	−224.8	−61.1	−132.3	−134.6
11	Mn(I)	CO, CO, PMe₃, L	−235.2	−67.9	−139.8	−142.2
12	Fe(II)	CO, CO, Cl⁻, L	−267.1	−79.3	−161.6	−168.9
13	Fe(II)	CO, CO, Br, L	−264.5	−78.3	−159.6	−166.8
14	Co(I)	CO, NMe₃, L	−221.3	−70.8	−138.1	−144.6
15	Co(I)	CO, PEt₃, L	−223.0	−69.0	−136.3	−139.2
16	Ni(II)	PMe₃, Cl, L	−230.8	−78.9	−149.2	−153.3
17	Ni(II)	NMe₃, Cl, L	−208.4	−58.4	−129.5	−135.2
18	Cu(I)	CO, L	−235.8	−83.1	−156.0	−156.2
19	Cu(I)	NMe₃, L	−200.1	−76.7	−139.4	−134.8
20	Cu(I)	PEt₃, L	−198.2	−68.9	−131.4	−127.3

bonding of Cl⁻ at the β-carbon and the coordination of fullerene to Sc and Cu is η⁵ type. Similarly in the case of [TiCl₃]⁺, the non-bonded $C_{60} \cdots TiCl_4$ is formed when the optimization is attempted for (Cl⁻C_{60})(TiCl₃)⁺ with Cl⁻ at the α-position. Also, the optimization of the complex with Cl⁻ at the β-position yields the structure given in Fig. 5, wherein the fullerene part shows η¹ coordination with Ti. When the Cl⁻ is connected diametrically opposite to the metal coordination, the η⁵ complex of (Cl⁻C_{60})(TiCl₃)⁺ is obtained. The η¹ and η⁵ complexes of Ti are higher in energy compared to the non-bonded neutral complex by 41.8 and 65.1 kcal mol⁻¹, respectively (ESI,† Fig. S4).

The trend observed for E_b (Table 3) for exohedral fullerene complexes (Fig. 5) is very similar to that of endohedral complexes (Fig. 4) and between them only small variations in E_b are observed. The C–Cl bond formation is well evident in all the exohedral complexes as their bond distance falls in the range 1.87 to 2.47 Å. Compared to the C–Cl distance observed for Cl⁻C_{60}, 46% reduction in the bond parameter is observed for the exohedral complex and suggests that strong electrostatic interaction between Cl⁻ and ($C_{60}ML_n$)⁺ forces the bond formation.
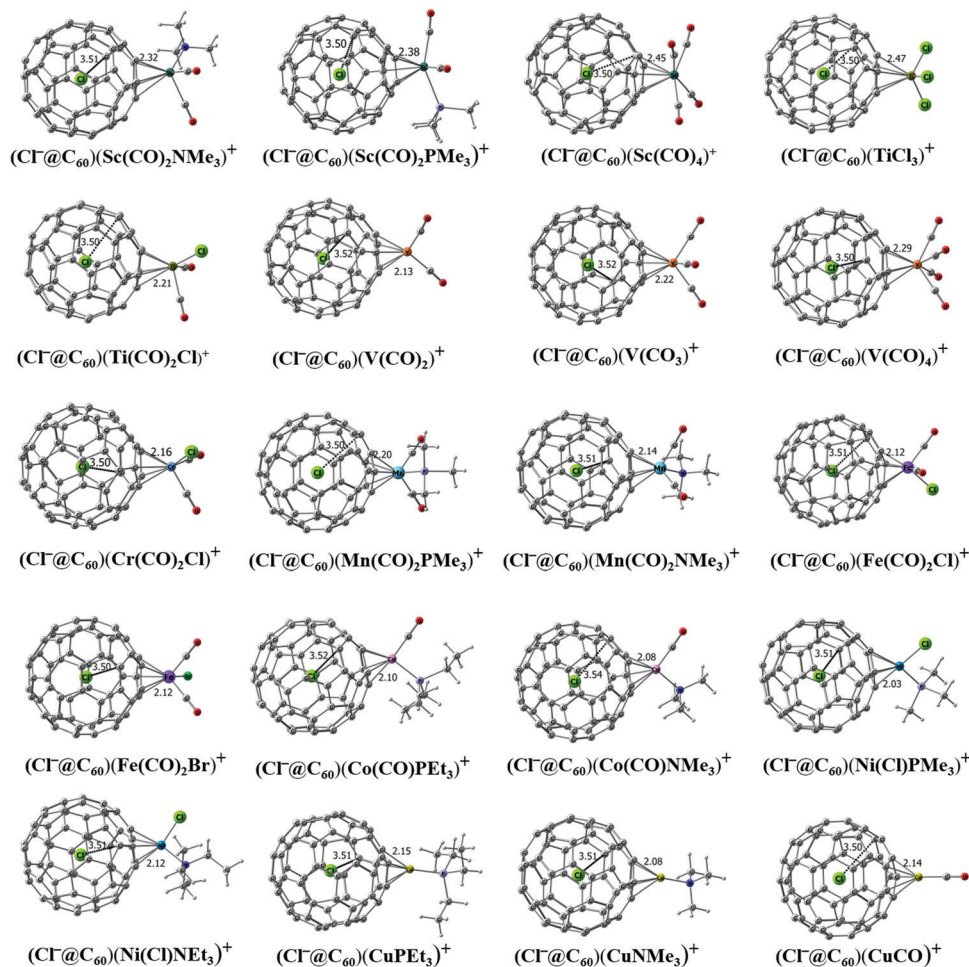

Fig. 4 Optimised structures of transition metal complexes of Cl⁻@C_{60} at the M06L/6-31G** level.

This journal is © the Owner Societies 2021
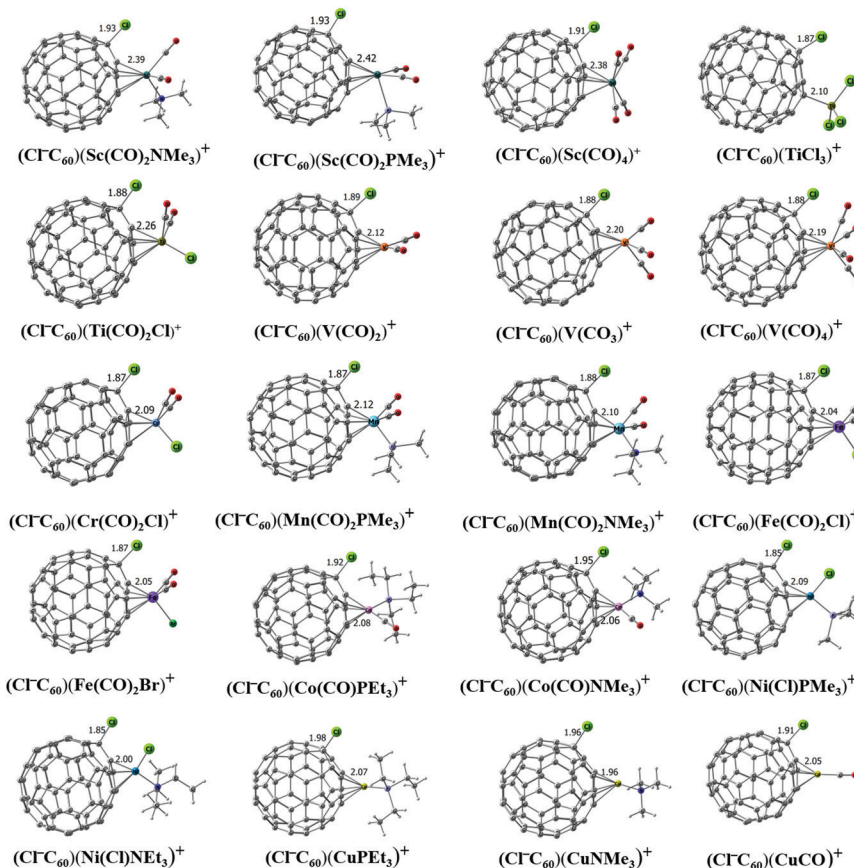
Phys. Chem. Chem. Phys., 2021, **23**, 3646–3655 | **3651**

Fig. 5 Optimised structures of transition metal complexes of the Cl^-C_{60} at the M06L/6-31G** level.

Effect of solvation

All the complexes discussed above are studied for the influence of the solvent ODCB on the complexation. The solvation effect incorporated binding energy (E_{bs}) values are given in Table 4. For all the cases, E_{bs} data show a large decrease compared to the gas phase value E_b. For example, E_{bs} of $CpML_n$ complexes are in the range from −40.3 to −122.7 kcal mol^{-1}, which is ~150 kcal mol^{-1} lower than the corresponding E_b. Similarly, the E_{bs} of $(C_{60})(ML_n)^+$, $(Cl^-@C_{60})(ML_n)^+$ and $(Cl^-C_{60})(ML_n)^+$ decreased, but to a lesser extent than the $CpML_n$ complexes. Among $(C_{60})(ML_n)^+$, $(Cl^-@C_{60})(ML_n)^+$ and $(Cl^-C_{60})(ML_n)^+$, the endohedral variant is the most stabilized with E_{bs} in the range from −2.5 to −47.5 kcal mol^{-1} followed by the exohedral complexes. Among all, the best tendency to complex formation is observed for Mn, Fe, Co, and Ni complexes.

Chloro-fulleride complex to fullerene and metal chloride

Assuming that the known systems C_{60} and ML_nCl react to form $(Cl^-C_{60})(ML_n)^+$ or $(Cl^-@C_{60})(ML_n)^+$, the energy of the reaction (E_r) can be used as a parameter to assess the stability of $(Cl^-C_{60})(ML_n)^+$ and $(Cl^-@C_{60})(ML_n)^+$ complexes. The E_r data in the gas phase and the solvent phase (E_s) are given in Table 5. For the endohedral cases, E_r is negative (exothermic) indicating the favourability of the formation of the coordinated complex over fullerene and metal chloride. The endohedral character is

Table 4 E_{bs} of the transition metal complexes for L = Cp⁻, L = C_{60}, L = $Cl^-@C_{60}$, and L = Cl^-C_{60} at the M06L/6-311++G** level using ODCB as the solvent

Metal	Ligands	E_{bs} (kcal mol^{-1})			
		L = Cp⁻	L = Cl⁻@C$_{60}$	L = Cl⁻C$_{60}$	L = C$_{60}$
Sc(I)	CO, CO, NMe$_3$, L	−52.2	−6.9	−0.2	−2.4
Sc(I)	CO, CO, PMe$_3$, L	−51.6	−7.7	9.0	−3.4
Sc(I)	4CO, L	−68.36	−13.01	−6.8	−2.8
Ti(II)	CO, CO, Cl⁻, L	−85.1	−16.6	−13.4	−2.3
Ti(IV)	3Cl⁻, L	−107.7	−33.8	−33.1	−17.2
V(I)	CO, CO, L	−80.0	−14.2	−10.2	−2.2
V(I)	CO, CO, CO, L	−89.5	−20.7	−16.0	−7.1
V(I)	4CO, L	−98.2	−24.7	−22.3	−10.2
Cr(II)	CO, CO, Cl⁻, L	−122.7	−47.5	−45.9	−31.2
Mn(I)	CO, CO, CO, L	−102.4	−24.9	−15.4	−10.5
Mn(I)	CO, CO, NMe$_3$, L	−80.2	−15.3	−10.0	−4.8
Mn(I)	CO, CO, PMe$_3$, L	−89.2	−21.2	−15.7	−10.1
Fe(II)	CO, CO, Cl⁻, L	−120.6	−39.0	−40.9	−22.1
Fe(II)	CO, CO, Br⁻, L	−129.3	−48.1	−49.2	−31.8
Co(I)	CO, NMe$_3$, L	−81.3	−26.2	−21.8	−17.6
Co(I)	CO, PEt$_3$, L	−89.9	−30.8	−25.1	−22.1
Ni(II)	PMe$_3$, Cl⁻, L	−89.1	−34.7	−30.0	−24.6
Ni(II)	NMe$_3$, Cl⁻, L	−80.9	−26.3	−25.4	−14.5
Cu(I)	CO, L	−50.7	−2.5	6.7	7.2
Cu(I)	NMe$_3$, L	−40.3	−12.2	−0.7	−5.9
Cu(I)	PEt$_3$, L	−43.4	−9.1	−6.0	−2.8

found only for exohedral systems of Co(I) and Ni(II). Also the endohedral complexes always showed higher stability than the

3652 | Phys. Chem. Chem. Phys., 2021, 23, 3646–3655

This journal is © the Owner Societies 2021

Table 5 ZPE corrected-reaction energy (E_r) and solvation included reaction energy (E_{rs}) in kcal mol^{-1} for the complexes $(Cl^-@C_{60})(ML_n)^+$ and $(Cl^-C_{60})(ML_n)^+$ into the corresponding ML_nCl and C_{60} at the M06L/6-31G** level

Metal	Ligands	E_r		E_{rs}	
		L = $Cl^-@C_{60}$	L = Cl^-C_{60}	L = $Cl^-@C_{60}$	L = Cl^-C_{60}
Sc(I)	CO, CO, NMe$_3$, L	−0.2	24.1	−3.9	27.7
Sc(I)	CO, CO, PMe$_3$, L	−4.3	27.8	−12.7	28.8
Sc(I)	4CO, L	−0.1	24.1	−4.1	27.0
Ti(II)	CO, CO, Cl$^-$, L	−2.8	21.9	−3.9	24.0
Ti(IV)	3Cl$^-$, L	14.3	34.7	10.6	36.2
V(I)	CO, CO, L	−12.8	9.2	−4.6	24.2
V(I)	CO, CO, CO, L	−9.8	13.3	−6.6	22.9
V(I)	4CO, L	−8.1	14.5	−9.3	17.9
Cr(II)	CO, CO, Cl$^-$, L	−14.7	8.4	−12.8	13.6
Mn(I)	CO, CO, CO, L	−12.8	11.5	−7.7	22.5
Mn(I)	CO, CO, NMe$_3$, L	−16.8	7.4	−10.7	19.5
Mn(I)	CO, CO, PMe$_3$, L	−15.5	3.8	−11.7	11.3
Fe(II)	CO, CO, Cl$^-$, L	−17.5	1.9	−12.2	11.5
Fe(II)	CO, CO, Br$^-$, L	−26.4	−6.3	−11.7	17.5
Co(I)	CO, NMe$_3$, L	−28.0	−4.3	−12.2	18.3
Co(I)	CO, PEt$_3$, L	−24.0	−1.5	−4.3	25.2
Ni(II)	PMe$_3$, Cl$^-$, L	−24.1	−3.3	−5.6	20.1
Ni(II)	NMe$_3$, Cl$^-$, L	−19.5	6.8	7.3	41.2
Cu(I)	CO, L	−27.8	3.3	3.4	39.7
Cu(I)	NMe$_3$, L	−25.5	5.2	0.3	28.3

exohedral variant. This is because the interaction of Cl$^-$ with the interior surface of C$_{60}$ is significantly more stabilizing in character than its exohedral interaction with C$_{60}$. The E_s data show that the solvent effect is improving the coordination properties of the endohedral Sc(I), Ti(I), and Ti(IV) and one of the V(I) systems, whereas for the rest of the systems and for the exohedral complexes, the solvation effect has a diminishing effect on the coordination properties. The diminished coordination power in solvent is the highest for the late transition metals such as Co(I), Ni(II) and Cu(I) complexes.

Conclusions

Endohedral and exohedral chloro-fullerides are capable of interacting with metal fragments to give different transition metal complexes in η^5 and η^6 coordination modes. Cl$^-@C_{60}$ is found to be stable in the isolated as well as in the complexed form, whereas Cl$^-C_{60}$ is found to have the covalent C–Cl interaction only in the presence of a counter cationic metallic fragment. The η^5 complex was more stabilized than the corresponding η^6 variant in the studied representative case of [Mn(CO)$_3$L] (L = C$_{60}$, Cl$^-@C_{60}$ and Cl$^-C_{60}$). The E_b data clearly showed the superior coordinating ability of Cl$^-@C_{60}$ and Cl$^-C_{60}$ in comparison with C$_{60}$ for all the metallic complexes from Sc to Cu. The effect of solvation on the complexation of chloro-fulleride with metal fragments studied with the SCRF method has shown a similar trend in energetics to that of the gaseous state but with a reduced value for binding energy. This is because in the ligands Cl$^-@C_{60}$ and Cl$^-C_{60}$, the negative charge is no longer on the Cl atom alone but delocalized over all the carbon atoms. The chloro-fulleride behaves as a bulky

anion with the ability to coordinate strongly with transition metals. Among the different metals, Mn, Fe, Co, and Ni are found to have significantly higher values of both E_b and E_{bs}. The endohedral chloro-fulleride showed higher coordination ability than the exohedral one. The E_r data indicate that by reacting fullerene with a transition metal chloride, the formation of a chloro-fulleride incorporated transition metal complex can be achieved. Such a reaction is exothermic for endohedral systems and mostly endothermic for the exohedral complex. All these facts thus accentuate the possibility of the anionic form of the fullerene molecule to act as a large anionic ligand in organometallic complexes. The large size (~ 0.7 nm in diameter), high chemical stability, large specific surface area, good electrical conductivity and unique three-dimensional structure of the fullerene unit in ligands Cl$^-@C_{60}$ and Cl$^-C_{60}$, makes them suitable for designing complexes with specific catalytic activities. The steric bulkiness of the ligand helps in stabilizing the metals in their incomplete electronic states like 12-, 14- and 16-electrons by preventing the metal centre from further ligation.

Conflicts of interest

There are no conflicts to declare.

Acknowledgements

References

1 J. Heath, S. O'brien, Q. Zhang, Y. Liu, R. Curl, F. Tittel and R. Smalley, *J. Am. Chem. Soc.*, 1985, **107**, 7779–7780.
2 A. J. Stone and D. J. Wales, *Chem. Phys. Lett.*, 1986, **128**, 501–503.
3 D. L. Lichtenberger, L. L. Wright, N. E. Gruhn and M. E. Rempe, *Synth. Met.*, 1993, **59**, 353–367.
4 D. L. Lichtenberger, L. L. Wright, N. E. Gruhn and M. E. Rempe, *J. Organomet. Chem.*, 1994, **478**, 213–221.
5 V. Sokolov, *Russ. J. Coord. Chem.*, 2007, **33**, 711–724.
6 F. Liu and S. Yang, *Encyclopedia of Inorganic and Bioinorganic Chemistry*, 2014.
7 J. M. Hawkins, A. Meyer, T. A. Lewis, S. Loren and F. J. Hollander, *Science*, 1991, **252**, 312–313.
8 P. J. Fagan, J. C. Calabrese and B. Malone, *Science*, 1991, **252**, 1160–1162.
9 P. J. Fagan, J. C. Calabrese and B. Malone, *Acc. Chem. Res.*, 1992, **25**, 134–142.
10 A. L. Balch, V. J. Catalano, J. W. Lee, M. M. Olmstead and S. R. Parkin, *J. Am. Chem. Soc.*, 1991, **113**, 8953–8955.

This journal is © the Owner Societies 2021

Phys. Chem. Chem. Phys., 2021, **23**, 3646–3655 | **3653**

11 R. S. Koefod, M. F. Hudgens and J. R. Shapley, *J. Am. Chem. Soc.*, 1991, **113**, 8957–8958.

12 V. V. Bashilov, P. V. Petrovskii, V. I. Sokolov, S. Lindeman, I. A. Guzey and Y. T. Struchkov, *Organometallics*, 1993, **12**, 991–992.

13 B. Chase and P. J. Fagan, *J. Am. Chem. Soc.*, 1992, **114**, 2252–2256.

14 S. A. Lerke, B. Parkinson, D. H. Evans and P. J. Fagan, *J. Am. Chem. Soc.*, 1992, **114**, 7807–7813.

15 M. N. Bengough, D. M. Thompson, M. C. Baird and G. D. Enright, *Organometallics*, 1999, **18**, 2950–2952.

16 D. M. Thompson, M. Bengough and M. C. Baird, *Organometallics*, 2002, **21**, 4762–4770.

17 P. J. Fagan, J. C. Calabrese and B. Malone, *J. Am. Chem. Soc.*, 1991, **113**, 9408–9409.

18 A. V. Usatov, S. M. Peregudova, L. I. Denisovich, E. V. Vorontsov, L. E. Vinogradova and Y. N. Novikov, *J. Organomet. Chem.*, 2000, **599**, 87–96.

19 A. L. Balch, L. Hao and M. M. Olmstead, *Angew. Chem., Int. Ed. Engl.*, 1996, **35**, 188–190.

20 F. J. Brady, D. J. Cardina and M. Domin, *J. Organomet. Chem.*, 1995, **491**, 169–172.

21 H. Nagashima, Y. Kato, H. Yamaguchi, E. Kimura, T. Kawanishi, M. Kato, Y. Saito, M. Haga and K. Itoh, *Chem. Lett.*, 1994, 1207–1210.

22 H. Nagashima, A. Nakaoka, Y. Saito, M. Kato, T. Kawanishi and K. Itoh, *Chem. Commun.*, 1992, 377–379.

23 P. Fowler and A. Ceulemans, *J. Phys. Chem.*, 1995, **99**, 508–510.

24 A. L. Balch and M. M. Olmstead, *Chem. Rev.*, 1998, **98**, 2123–2166.

25 M. Sawamura, H. Iikura and E. Nakamura, *J. Am. Chem. Soc.*, 1996, **118**, 12850–12851.

26 M. Sawamura, H. Iikura, A. Hirai and E. Nakamura, *J. Am. Chem. Soc.*, 1998, **120**, 8285–8286.

27 M. Sawamura, Y. Kuninobu, M. Toganoh, Y. Matsuo, M. Yamanaka and E. Nakamura, *J. Am. Chem. Soc.*, 2002, **124**, 9354–9355.

28 Y. Matsuo and E. Nakamura, *Chem. Rev.*, 2008, **108**, 3016–3028.

29 M. Toganoh, Y. Matsuo and E. Nakamura, *J. Am. Chem. Soc.*, 2003, **125**, 13974–13975.

30 A. Chistyakov and L. Stankevich, *Russ. Chem. Bull.*, 1996, **45**, 2294–2301.

31 J. A. López and C. Mealli, *J. Organomet. Chem.*, 1994, **478**, 161–171.

32 A. Chistyakov, I. Stankevich and N. Gambaryan, *Russ. Chem. Bull.*, 1995, **44**, 828–831.

33 E. Nakamura, *Pure Appl. Chem.*, 2003, **75**, 427–434.

34 I. Stankevich and A. Chistyakov, *Russ. Chem. Bull.*, 2003, **52**, 1272–1279.

35 A. Chistyakov and I. Stankevich, *Russ. Chem. Bull.*, 2002, **51**, 230–239.

36 C. M. Alvarez, R. J. Angelici, A. Sygula, R. Sygula and P. W. Rabideau, *Organometallics*, 2003, **22**, 624–626.

37 S. Nagao, T. Kurikawa, K. Miyajima, A. Nakajima and K. Kaya, *J. Phys. Chem. A*, 1998, **102**, 4495–4500.

38 I. J. Mavunkal, Y. Chi, S.-M. Peng and G.-H. Lee, *Organometallics*, 1995, **14**, 4454–4456.

39 E. Jemmis and M. Manoharan, *Curr. Sci.*, 1999, **76**, 1122–1126.

40 E. D. Jemmis, M. Manoharan and P. K. Sharma, *Organometallics*, 2000, **19**, 1879–1887.

41 E. D. Jemmis, P. Parameswaran and A. Anoop, *Int. J. Quantum Chem.*, 2003, **95**, 810–815.

42 B. Molina, L. Pérez-Manríquez and R. Salcedo, *J. Mol. Model.*, 2017, **23**, 171.

43 M. D. Francis, O. V. Boltalina, J. F. Nixon and R. Taylor, *Fullerenes, Nanotubes, Carbon Nanostruct.*, 2003, **11**, 115–120.

44 J. Cioslowski, *J. Am. Chem. Soc.*, 1991, **113**, 4139–4141.

45 T. Pradeep, G. Kulkarni, K. Kannan, T. G. Row and C. Rao, *J. Am. Chem. Soc.*, 1992, **114**, 2272–2273.

46 E. Campbell, R. Tellgmann, N. Krawez and I. Hertel, *J. Phys. Chem. Solids*, 1997, **58**, 1763–1769.

47 F. Pichierri, V. Kumar and Y. Kawazoe, *Chem. Phys. Lett.*, 2005, **406**, 341–344.

48 C. Ramachandran and N. Sathyamurthy, *Chem. Phys. Lett.*, 2005, **410**, 348–351.

49 O. Shameema, C. Ramachandran and N. Sathyamurthy, *J. Phys. Chem. A*, 2006, **110**, 2–4.

50 T. A. Murphy, T. Pawlik, A. Weidinger, M. Höhne, R. Alcala and J.-M. Spaeth, *Phys. Rev. Lett.*, 1996, **77**, 1075.

51 C. Knapp, N. Weiden, H. Kass, K.-P. Dinse, B. Pietzak, M. Waiblinger and A. Weidinger, *Mol. Phys.*, 1998, **95**, 999–1004.

52 E. Dietel, A. Hirsch, B. Pietzak, M. Waiblinger, K. Lips, A. Weidinger, A. Gruss and K.-P. Dinse, *J. Am. Chem. Soc.*, 1999, **121**, 2432–2437.

53 A. A. Popov, S. Yang and L. Dunsch, *Chem. Rev.*, 2013, **113**, 5989–6113.

54 P. Ravinder and V. Subramanian, *J. Phys. Chem. A*, 2011, **115**, 11723–11733.

55 S. Aoyagi, E. Nishibori, H. Sawa, K. Sugimoto, M. Takata, Y. Miyata, R. Kitaura, H. Shinohara, H. Okada and T. Sakai, *Nat. Chem.*, 2010, **2**, 678–683.

56 O. V. d. Oliveira and A. d. S. Gonçalves, *Comput. Chem.*, 2014, **2**, 51.

57 Y. Garcia-Rodeja, M. Sola, F. M. Bickelhaupt and I. Fernandez, *Chem. – Eur. J.*, 2017, **23**, 11030.

58 T. D. Della and C. H. Suresh, *Phys. Chem. Chem. Phys.*, 2018, **20**, 24885–24893.

59 M. J. Frisch, G. W. Trucks, H. B. Schlegel, G. E. Scuseria, M. A. Robb, J. R. Cheeseman, G. Scalmani, V. Barone, G. A. Petersson, H. Nakatsuji, X. Li, M. Caricato, A. V. Marenich, J. Bloino, B. G. Janesko, R. Gomperts, B. Mennucci, H. P. Hratchian, J. V. Ortiz, A. F. Izmaylov, J. L. Sonnenberg, D. Williams-Young, F. Ding, F. Lipparini, F. Egidi, J. Goings, B. Peng, A. Petrone, T. Henderson, D. Ranasinghe, V. G. Zakrzewski, J. Gao, N. Rega, G. Zheng, W. Liang, M. Hada, M. Ehara, K. Toyota, R. Fukuda, J. Hasegawa, M. Ishida, T. Nakajima, Y. Honda, O. Kitao, H. Nakai, T. Vreven, K. Throssell,

3654 | *Phys. Chem. Chem. Phys.*, 2021, **23**, 3646–3655

This journal is © the Owner Societies 2021

J. A. Montgomery Jr, J. E. Peralta, F. Ogliaro, M. J. Bearpark, J. J. Heyd, E. N. Brothers, K. N. Kudin, V. N. Staroverov, T. A. Keith, R. Kobayashi, J. Normand, K. Raghavachari, A. P. Rendell, J. C. Burant, S. S. Iyengar, J. Tomasi, M. Cossi, J. M. Millam, M. Klene, C. Adamo, R. Cammi, J. W. Ochterski, R. L. Martin, K. Morokuma, O. Farkas, J. B. Foresman and D. J. Fox, *Gaussian 16 Rev. A.03*, Gaussian, Inc., Wallingford CT, 2016.

60 Y. Zhao and D. G. Truhlar, *J. Chem. Phys.*, 2006, **125**, 194101.

61 K. Remya and C. H. Suresh, *J. Comput. Chem.*, 2013, **34**, 1341–1353.

62 P. J. Fitzpatrick, Y. Le Page, J. Sedman and I. S. Butler, *Inorg. Chem.*, 1981, **20**, 2852–2861.

63 M. Kawano, Y. Kobayashi, T. Ozeki and M. Fujita, *J. Am. Chem. Soc.*, 2006, **128**, 6558–6559.

Check for updates

Guanidine as a strong CO_2 adsorbent: a DFT study on cooperative CO_2 adsorption†

Sebastian Anila[ab] and Cherumuttathu H. Suresh [iD] *[ab]

Among the various carbon capture and storage (CCS) technologies, the direct air capture (DAC) of CO_2 by engineered chemical reactions on suitable adsorbents has attained more attention in recent times. Guanidine (G) is one of such promising adsorbent molecules for CO_2 capture. Recently Lee *et al.* (*Phys. Chem. Chem. Phys.*, 2015, **17**, 10925–10933) reported an interaction energy (ΔE) of -5.5 kcal mol^{-1} for the G$\cdots CO_2$ complex at the CCSD(T)/CBS level, which was one of the best non-covalent interactions observed for CO_2 among several functional molecules. Here we show that the non-covalent G$\cdots CO_2$ complex can transform to a strongly interacting G–CO_2 covalent complex under the influence of multiple molecules of G and CO_2. The study, conducted at M06-2X/6-311++G** level density functional theory, shows $\Delta E = -5.7$ kcal mol^{-1} for G$\cdots CO_2$ with an N$\cdots$C distance of 2.688 Å while almost a five-fold increase in ΔE (-27.5 kcal mol^{-1}) is observed for the (G–CO_2)$_8$ cluster wherein the N–C distance is 1.444 Å. All the (G–CO_2)$_n$ clusters ($n = 2$–10) show a strong N–CO_2 covalent interaction with the N–C distance gradually decreasing from 1.479 Å for $n = 2$ to 1.444 Å for $n = 8 \cong 9$, 10. The N–CO_2 bonding gives (G$^+$)–(CO_2^-) zwitterion character for G–CO_2 and the charge-separated units preferred a cyclic arrangement in (G–CO_2)$_n$ clusters due to the support of three strong intermolecular O$\cdots$HN hydrogen bonds from every CO_2. The O$\cdots$HN interaction is also enhanced with an increase in the size of the cluster up to $n = 8$. The high ΔE is attributed to the large cooperativity associated with the N–CO_2 and O$\cdots$HN interactions. The quantum theory of atoms in molecules (QTAIM) analysis confirms the nature and strength of such interactions, and finds that the total interaction energy is directly related to the sum of the electron density at the bond critical points of N–CO_2 and O$\cdots$HN interactions. Further, molecular electrostatic potential analysis shows that the cyclic cluster is stabilized due to the delocalization of charges accumulated on the (G$^+$)–(CO_2^-) zwitterion *via* multiple O$\cdots$HN interactions. The cyclic (G–CO_2)$_n$ cluster formation is a highly exergonic process, which reveals the high CO_2 adsorption capability of guanidine.

Introduction

The balance of the planetary climate is facing a major challenge from the calamitous increase in global temperatures resulting from the increased emission of various anthropogenic greenhouse gases (GHG), most importantly CO_2.[1] To reduce the atmospheric CO_2 concentration and thereby to manage the long-term risks of persistent climate changes it has become highly important to remove CO_2 from the air faster than is achieved by nature.[2,3] Though a lot of research activities are going on in this area of carbon capture and storage (CCS),

we still need better sequestration methods, a long-term exploratory research effort for the development of air capture along with other direct methods for the active removal of CO_2 from the atmosphere.[4,5] One promising approach among the various negative emissions technologies (NETs), which aims at reducing the atmospheric CO_2 concentration, is direct air capture (DAC), a process that removes CO_2 from the air by engineered chemical reactions.[6–10] In 1999 Lackner *et al.* familiarized the concept of capturing CO_2 from the air for climate change mitigation.[11] This launched a discussion on whether DAC is an important and viable option for reducing greenhouse gas levels or not.[12–18] DAC is different from other NET methods, owing to its use of abiogenic means of removing CO_2 from the atmosphere.[19] Since the overall atmospheric concentration of CO_2 is very low, the absorbents should have a very strong binding affinity and good selectivity against other components in air like water. Another important challenge in DAC is the regeneration of the sorbent and the energy spent in these regeneration processes.

^{a} *Chemical Sciences and Technology Division, CSIR-National Institute for Interdisciplinary Science and Technology, Thiruvananthapuram, Kerala, 695 019, India. E-mail: sureshch@niist.res.in, sureshch@gmail.com; Tel: +91-471-2515472*
^{b} *Academy of Scientific and Innovative Research (AcSIR), Ghaziabad 201002, India*
† Electronic supplementary information (ESI) available: Optimized geometries, relevant tables, figures, *etc.* See DOI: 10.1039/d1cp00754h

Several experimental and theoretical studies have been carried out to understand the binding interaction of CO_2 with different molecules. Alkhabbaz et al. evaluated the CO_2 adsorption performance of aminosilica adsorbents prepared by the impregnation of guanidinylated poly(allylamine) (GPAA) into silica mesocellular foam supports. From CO_2 adsorption–desorption cycling experiments they found that the GPAA adsorbents have a better stability and regenerability at higher temperatures, making this class of materials suited for temperature swing cycles operating in a higher temperature regime than traditional aminosilica adsorbents based on poly(ethylenimine).[20] Wang et al. synthesized polybenzoxazine-based polymer spheres as a CO_2 adsorbent and reported that the nitrogen content of the carbon adsorbent is a booster for the CO_2 adsorption capacity at low pressures.[21] In this material the porous carbon spheres contain intrinsic nitrogen-containing groups. Sabet-Sarvestani et al. studied the role of four guanidine-based super bases 1,8-diazabicyclo[5.4.0]undec-7-ene (DBU), 1,5-diazabicyclo[4.3.0]non-5-ene (DBN), 1,1,3,3-tetramethylguanidine (TMG), and 1,5,7-triazabicyclo[4.4.0]dec-5-ene (MTBD) in the conversion of CO_2 and 2-aminobenzonitrile to quinazoline-2,4(1H,3H)-diones.[22] But the triazabicyclo derivative of guanidine-incorporated mesoporous silica nanoparticles (MCM) has shown a weak adsorption capacity for CO_2 compared with the other modified versions of MCM.[23] The aqueous solution of 2,6-pyridinebis(iminoguanidine), PyBIG, was found to be an efficient absorbent to be employed in the DAC process, owing to the low aqueous solubility of the carbonate salt, $(PyBIGH_2)(CO_3)(H_2O)_4$, even for the very low concentration of CO_2 in the air.[24,25] Mild heating at 120 °C is sufficient for regeneration of the PyBIG sorbent, which then can be reused in another DAC cycle. Thus, the overall process remains as an energy efficient DAC technology. Custelcean et al. studied the chemical bonding and intermolecular interactions in the highly insoluble carbonate salt of a 2,6-pyridine-bis(iminoguanidine), within the framework of the quantum theory of atoms in molecules (QTAIM) based on the experimental electron density derived from X-ray diffraction data obtained at 20 K.[26] They also patented guanidine compounds for CO_2 capture (US10583387B2).[27] Though first reported in 1898 by the German chemist Johannes Thiele,[28] iminoguanidines have attracted more attention in the past five years due to their high recognition abilities towards hydrophilic oxyanions through strong and complementary hydrogen bonding from the guanidinium groups.

Cooperativity originating from the long-range interactions between two identical or different sites has led various important implications for many systems, including ligand–receptor binding,[29] catalysis,[30–33] and CO_2 adsorption[34–37] through the tuning of these cooperative interactions. In 2001 Schmuck demonstrated the self-assembly of the 2-(guanidiniocarbonyl)-pyrrole-4-carboxylate zwitterion into oligomeric structures in DMSO due to ion pairing between the carboxylate function and the guanidinium group of neighboring monomers, resulting in one-dimensional assemblies.[38] Cooperative interactions enhance the CO_2 adsorption enthalpy with the CO_2-interaction energy of a functional group.[39] In 2017 Steinhardt et al. reported cooperative CO_2 absorption in a solution-phase system comprising bidentate guanidine and bidentate alcohol at ambient temperature.[40] Cooperative adsorption of gases by porous frameworks permits more efficient gas uptake and removal than the more usual non-cooperative (Langmuir-type) adsorption.[41] In the case of CO_2 capture by amines, the higher degrees of amination will not be necessarily favorable as excessive clustering of amine groups can interfere with CO_2 binding. This was clearly demonstrated by Vaidhyanathan et al. through combined experiment and simulation methods in which cooperative interactions between CO_2 molecules contribute significantly to binding energies, and sorbents with pores that bind higher aggregates of CO_2 will significantly enhance the heats of adsorption.[42] Recently Kim et al. reported a family of robust tetraamine-functionalized frameworks that retain cooperativity, leading to the potential for exceptional efficiency in capturing CO_2 under the extreme conditions relevant to natural-gas flue emissions.[43] Very recently Hosseini et al. investigated the ability of sphingosine kinase inhibitor (SphKI), which has multiple reaction centers including guanidine and oxadiazole groups to bind CO_2, using symmetry-adapted perturbation theory and a non-covalent interaction approach.[44] The strongest interaction energy between SphKI and CO_2 is -12.9 kcal mol^{-1}, in complex C1, indicating that guanidine in the polar head region plays an important role in CO_2 capture.

In 2015 Lee and co-workers reported a study on the interaction of CO_2 with various functional molecules using density functional theory (DFT) and wavefunction methods.[45] They suggested guanidine as one of the molecules having a strong interaction with CO_2, and the reported interaction energy -5.5 kcal mol^{-1} using the CCSD(T)/CBS method was better than that of many functional molecules. Though their study showed a high affinity for guanidine towards CO_2, the binding energy suggests only a weak non-covalent interaction, which may not be sufficient enough to explain the strong adsorption capability of guanidine as such an association process is always accompanied by entropy loss. A lowering of free energy would be expected for an association process when the binding energy for a two-body interaction is typically around -8 to -10 kcal mol^{-1}. Here a systematic study is proposed for analyzing both non-covalent and covalent interaction possibilities of guanidine (G) molecules with CO_2 molecules. The cooperativity involved in the CO_2 binding of the guanidine molecules is revealed in the study to suggest guanidine as a promising adsorbent for CO_2 capture. Most of the previously reported studies involve cooperativity in the adsorption of CO_2 molecules onto the material surface.[37,41,43,46–48] This study will focus on the molecular level analysis of the interaction between the CO_2 and G molecules and the cooperativity involved in the stabilization of their clusters.

Computational methods

All the geometry optimizations are carried out at the M06-2X/6-311++G** level of DFT using the Gaussian 16 suite of programs.[49] The M06-2X functional is regarded as one of the best methods for modelling intermolecular non-covalent interactions.[50] Vibrational frequency analysis has been carried out on all optimized geometries,

which confirms the energy minima nature of them with all real frequencies. The interaction energies of the guanidine–CO_2 complexes are calculated using the super-molecule approach. For any two interacting subsystems A and B, the stabilization energy or the energy of interaction (ΔE) of the super-molecule C is calculated using the equation

$$\Delta E = E_C - E_A - E_B \qquad (1)$$

where E_A, E_B, and E_C represent the zero-point energy (ZPE)-corrected energy of G, CO_2 and guanidine–CO_2 complex, respectively. Further, correction for the basis set superposition error (BSSE)[51–54] is made using the counterpoise (CP) approach of Boys and Bernardi.[55,56] Similarly, the free energy change and enthalpy change at standard temperature and pressure (STP) associated with the interaction are calculated using the super-molecule approach. Further, the entropy change involved in G$\cdots CO_2$ clustering is also calculated.

Bader's QTAIM analysis, based on the electron density (ρ) distribution, is carried out to gain a deeper insight into the covalent and non-covalent interactions present in the complexes as well as to understand the cooperativity of the interactions. The QTAIM plots contain bond paths, which are lines connecting the bonded nuclei through the distributed locally maximal electron density and the corresponding bond critical points.[57–59] The AIMAll package has been used to visualize the bond paths and to locate the bond critical points (bcps) in QTAIM analysis.[60] Atom–atom interactions are distinguished as covalent and non-covalent interactions based on the electron densities at the respective bcps (ρ_b) as well as from the sign of the corresponding Laplacian ($\nabla^2\rho$). The sum of electron density at the bcps ($\sum\rho_b$) and the sign of the Laplacian of electron density ($\nabla^2\rho$) are also analyzed for all the complexes.

Molecular electrostatic potential (MESP) analysis is carried out on all the complexes at the M06-2X/6-311++G** level of theory to understand the charge delocalization across the G and CO_2 units in the clusters.[61] MESP is a real physical property which is directly related to the electron density function $\rho(\mathbf{r})$.[62] MESP at any point $\mathbf{r}$ in space, $V(\mathbf{r})$, is defined by the equation

$$V(\mathbf{r}) = \sum_A^N \frac{Z_A}{|\mathbf{r} - \mathbf{R}_A|} - \int \frac{\rho(\mathbf{r}')\mathrm{d}^3 r'}{|\mathbf{r} - \mathbf{r}'|} \qquad (2)$$

where Z_A is the charge on the nucleus located at a distance $\mathbf{R}_A$, and $\rho(\mathbf{r}')$ is the electron density.[62,63]

Further, a benchmark set of calculations is done on a representative case at the B3LYP, B3LYP-D3, BP86-D3, M06-2X-D3 and wB97XD levels in conjunction with the basis set 6-311++G**. The D3 stands for Grimme's dispersion correction.[64]

Results and discussions

The interaction of the molecule G with molecules of CO_2 has been studied through the structure and energetics parameters. Fig. 1 gives the representative structures of the optimized geometries of G$(CO_2)_n$ clusters. The interaction energy ΔE of first molecule of CO_2 with an sp^2 hybridized (imine) N atom of G is -5.7 kcal mol^{-1} (Table 1). With the increase in the number of CO_2 molecules, total ΔE value increases. Additional CO_2 molecules are also found to be interacting with the imine N atom of G. The distance of interaction (d_{int}) of CO_2 with the imine N of G increases from 2.688 Å in G(CO_2) to an average value of 2.930 Å in G$(CO_2)_4$, which indicates a decrease in the strength of interaction of each CO_2 with the imine N. However, the $\Delta E_{/CO2}$ values given in Table 1 show that with the increasing number of molecules of CO_2, the value of $\Delta E_{/CO2}$ for G$(CO_2)_n$ systems is found to be comparable from $n = 3$. The phenomenon of maintaining a similar value of $\Delta E_{/CO2}$ could be due to additional stabilizations other than the N$\cdots CO_2$ interactions. To understand the additional stabilizations in the G$(CO_2)_n$ systems we carried out the QTAIM analysis.

The QTAIM plot of G(CO_2) shows the bcp for the imino(N)$\cdots CO_2$ interaction with the ρ_b value 0.0165 a.u. as well as the bcp for the NH$\cdots$OCO interaction with the ρ_b value 0.0121 a.u. In all other cases, the N$\cdots CO_2$ and NH$\cdots$OCO interactions are observed for at least one CO_2 molecule. Further, multiple N$\cdots CO_2$ interactions are identified in many cases through the location of bcps. In addition to N$\cdots CO_2$ and NH$\cdots$OCO interactions, all G$(CO_2)_n$ clusters with $n > 1$ showed (Fig. 2) bcps between the adsorbed CO_2 molecules, indicating the presence of secondary O$\cdots$C interactions. As n increases, multiple O$\cdots$C interactions occur in the G$(CO_2)_n$ clusters, leading to significant cooperative stabilization of the cluster. This kind of cooperative stabilizations has already been reported for the clustering of CO_2 around anions.[65]

Though the imine N$\cdots CO_2$ interactions become weaker with an increasing value of n, due to the additional stabilization from the O$\cdots$C interactions, $\Delta E_{/CO2}$ maintains a steady value around -4.4 kcal mol^{-1}, even up to $n = 10$. The OCO bond angle θ shows a small change of 3–5° from the free CO_2 molecule, indicating that the G$\cdots CO_2$ interaction does not create any significant structural deformation on CO_2. Also on the free energy scale, the
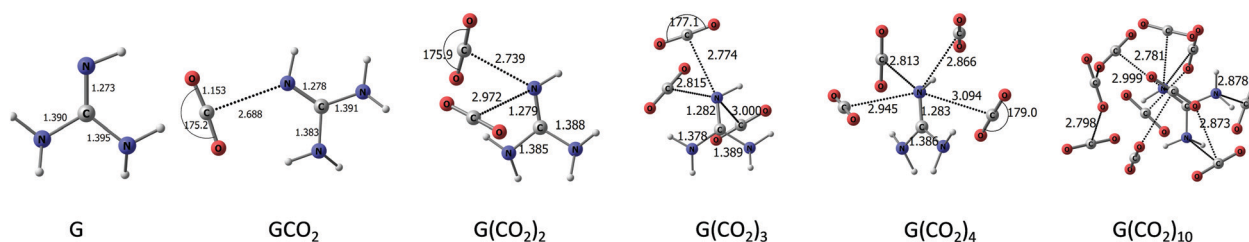

Fig. 1 Optimized geometries of G$(CO_2)_n$ complexes with their d_{int} (Å), and OCO angle θ (°) at the M06-2X/6-311++G** level.

Table 1 ZPE and BSSE corrected ΔE, ΔG, $\Delta E_{/CO2}$ and $\Delta G_{/CO2}$ (kcal mol^{-1}) of G(CO$_2$)$_n$ complexes at the M06-2X/6-311++G** level

n	ΔE (kcal mol^{-1})	$\Delta E_{/CO2}$ (kcal mol^{-1})	ΔG (kcal mol^{-1})	$\Delta G_{/CO2}$ (kcal mol^{-1})	ΔH (kcal mol^{-1})	$T\Delta S$ (kcal mol^{-1})
1	−5.7	−5.7	2.3	2.3	−5.5	−7.8
2	−10.3	−5.2	6.8	3.4	−9.9	−16.7
3	−14.1	−4.7	11.5	3.8	−13.3	−24.8
4	−18.4	−4.6	16.7	4.2	−17.4	−34.1
5	−21.6	−4.3	20.9	4.2	−20.2	−41.1
6	−26.6	−4.4	25.7	4.3	−25.2	−50.9
7	−31.9	−4.6	31.6	4.5	−30.3	−61.9
8	−35.2	−4.4	37.3	4.7	−33.3	−70.6
9	−38.9	−4.3	43.9	4.9	−36.9	−80.8
10	−43.6	−4.4	49.0	4.9	−41.5	−90.5

Fig. 3 Optimized geometries with respective ΔE values of (G)$_2$, (G)$_2$CO$_2$ and (G–CO$_2$)(G) complexes with their d_{int} (Å), θ (°) and ΔE and ΔG values (kcal mol^{-1}) at the M06-2X/6-311++G** level.

clustering of CO$_2$ around G is found to be an endergonic process (Table 1). This is due to the large decrease in entropy associated with the clustering. The energy data in Table 1 clearly suggest that spontaneous formation of the G(CO$_2$)$_n$ system is impossible under standard temperature and pressure (STP) conditions for any value of n. In order to further assess the affinity of CO$_2$ to bind with G, the G$\cdots$G interaction has to be addressed.

The guanidine dimer ((G)$_2$), shown in Fig. 3a, has two amino to imino NH$\cdots$H hydrogen bond interactions, resulting in a ΔE value of −12.2 kcal mol^{-1}. Such dimer formation is spontaneous as ΔG −2.7 kcal mol^{-1} indicates an exergonic process. This result also suggests that the G$\cdots$CO$_2$ interaction would be inadequate to break the G$\cdots$G interaction to make the G$\cdots$CO$_2$ complex. Hence the interaction of CO$_2$ with (G)$_2$ is considered. Two configurations are obtained for the (G)$_2\cdots$CO$_2$ complex: the first one, designated as (G)$_2$(CO$_2$), is depicted in Fig. 3b; and the second one, designated as (G–CO$_2$)(G) is given in Fig. 3c. Compared with (G)$_2$, the ΔE of (G)$_2$(CO$_2$) is enhanced by 1.2 kcal mol^{-1} whereas that of (G–CO$_2$)(G) is decreased by 2.1 kcal mol^{-1}. In both the cases, insertion of CO$_2$ occurs at the NH$\cdots$H hydrogen bond of (G)$_2$. In (G)$_2$(CO$_2$), the N$\cdots$C distance of 2.665 Å indicates a weak non-covalent bond whereas
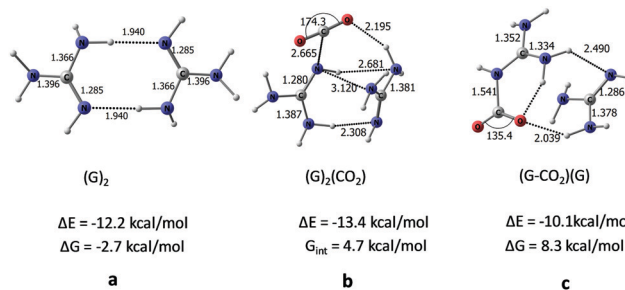
the N–C distance of 1.541 Å in (G–CO$_2$)(G) indicates the formation of a strong coordination bond. In addition, the formation of the N–C coordination bond changes the linear OCO to a bent OCO with an angle of 135.4°. Hereafter, the use of hyphen in the notation G–CO indicates the formation of a coordinate N–C bond. Both the complexations involve positive ΔG values and are less likely to occur at STP.

The G–CO$_2$ portion of (G–CO$_2$)(G) given in Fig. 3c can be regarded as the guanidinium carboxylate zwitterion (G$^+$)–(CO$_2^-$) and the unique aspect of this structure is that it cannot exist independently. Compared with the G$\cdots$CO$_2$ non-covalent interaction, the N–C bond formation in G–CO$_2$ leads to charge transfer from the imine N to the O centers of CO$_2$. The transformation of the G$\cdots$CO$_2$ interaction from non-covalent to a highly charge-separated (G$^+$)–(CO$_2^-$) interaction can happen only when the accumulated charges are utilized for developing further interactions. Fig. 4 depicts the + and − charge accumulation when (G)(CO$_2$) is changed to G–CO$_2$ in terms of the MESP plots on the isodensity surface for configurations optimized for various N–C distances. In the non-covalent G(CO$_2$) with a N$\cdots$C distance 2.688 Å, the imine N atom shows charge concentration (dark blue region on N) due to its lone pair. A clear shift of the electron cloud from G to CO$_2$ is evident when the distance of
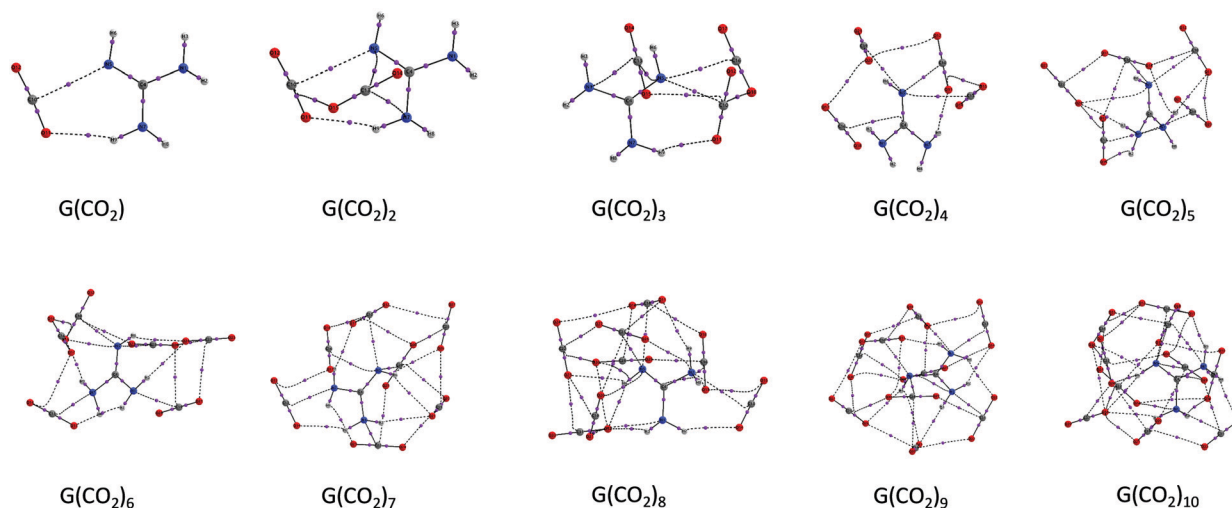

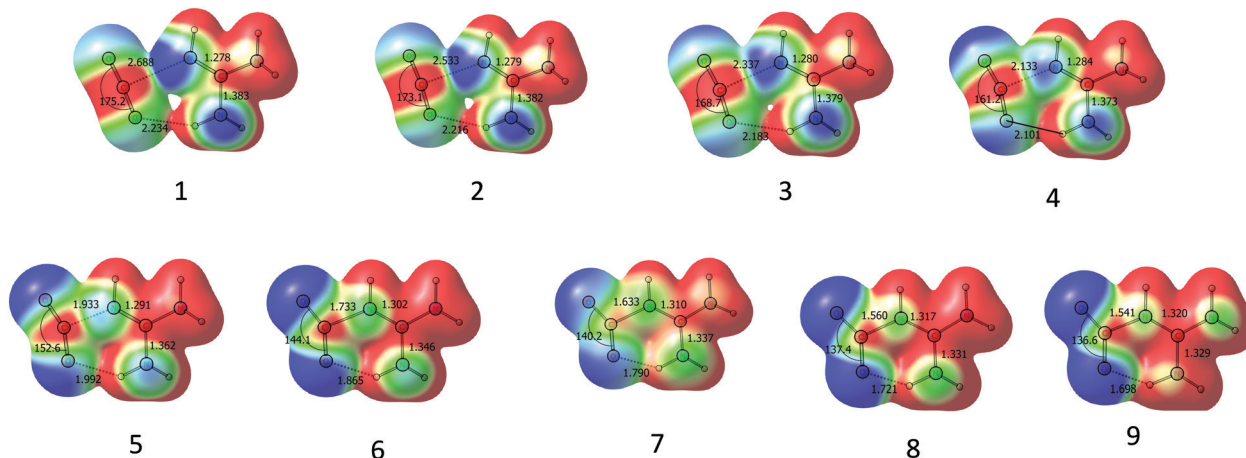**Fig. 2** QTAIM plots of G(CO$_2$)$_n$ complexes for n = 1–4 at the M06-2X/6-311++G** level.

Fig. 4 MESP topographic plots for the G–CO$_2$ unit with their d_{int} (Å) and θ (°) values at various N–C distances of interaction at the M06-2X/6-311++G** level at the isosurface value = 0.01 a.u.

interaction gradually changes to the covalent distance of 1.541 Å (the last configuration in Fig. 4). This zwitterion configuration $(G^+)-(CO_2^-)$ is clear from the MESP plot, which shows charge concentration on the O centers (dark blue) and charge depletion on the guanidinium portion (red region).

Although the $(G^+)-(CO_2^-)$ zwitterion structure does not exist, we consider the possibility of dimer formation of such a structure to derive additional stabilizing interactions. Surprisingly, the zwitterion dimer (Fig. 5a) is an energy minimum and corresponds to a total stabilization of −32.8 kcal mol^{-1} (the complexation energy for two G units with two CO$_2$ molecules). Also, the complexation leads to a lowering of the free energy by 1.00 kcal mol^{-1}. Compared with the zwitterion dimer, the non-covalent dimer $(G)_2(CO_2)_2$ (Fig. 5b) gives a complexation energy of −18.9 kcal mol^{-1} and the process is endergonic by 7.9 kcal mol^{-1}. The N–C bond length of the zwitterion dimer is 1.479 Å, which is 0.062 Å shorter than the G–CO$_2$(G) complex and indicates the improved interaction between G and CO$_2$ in the presence of the zwitterion compared with the simple G. The zwitterion species interact through better complementary electrostatic interactions than that involving neutral species. In the zwitterion dimer, strong interactions arise due to the large number of inter- and intra-molecular H-bonds, which cooperatively induce the binding of the activated G unit with the CO$_2$ molecule.

The complementary hydrogen bond interactions as seen in the zwitterion dimer can be extended to higher-order clusters.
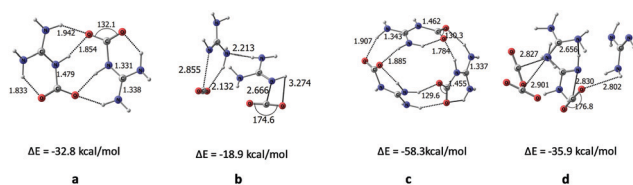
For instance, in the zwitterion trimer (Fig. 5c), the interaction energy is further enhanced to −58.3 kcal mol^{-1} with a lowering of the free energy by 3.1 kcal mol^{-1}. Here, the formation of the corresponding non-covalent trimer (Fig. 5d) can be regarded as unlikely due to the highly endergonic character (14.1 kcal mol^{-1}). The optimized geometries of the $(G-CO_2)_n$ clusters ($n = 4$–10) are given in Fig. 6 and the ΔE and ΔG values for all the clusters are listed in Table 2. A cyclic growth pattern emerges for these higher-order clusters.

The cyclic structure enables the participation of all the O centers for intermolecular hydrogen bond interaction with the NH bonds (O···HN interaction). In such structures, the positively charged guanidine portion is nicely poised for complementary interaction from the negatively charged carboxylate group leading to the formation of multiple hydrogen bonds and delocalization of the accumulated charges on each $(G^+)-(CO_2^-)$. For $n = 4$–7, the $(G-CO_2)_n$ shows a bowl-like shape. The bowl depth is at a maximum for $n = 4$ (2.890 Å) and it rapidly decreases to 2.508 Å for $n = 5$. For $n = 6$ and 7, the bowl depth further decreases to 1.947 Å and 1.013 Å, respectively, indicating the tendency towards planarization as n increases (ESI†). An almost planar structure is observed for $n = 8$, and this structure showed the highest interaction energy. Beyond $n = 8$, the structure tends to distort from planarity. Also, the N–C distance shows a decreasing trend as n goes from 4 to 8, indicating that the planarization enhances the stability of the complex. In addition, the bond angle of the O···HN interaction gradually increases from 145.2° for $n = 2$ to the highest value 178.5° for $n = 8$; thereafter, the O···HN angle decreases (Table S1, ESI†). It is clear that the highest strength for the hydrogen bond is provided by the geometrically preferred linear arrangement of the atoms of the O···HN interaction, which is achieved at the most planar configuration, $n = 8$.

Recently Bijina and Suresh used MESP analysis to derive the positive cooperativity in a large variety of intermolecular trimer complexes.[66] Always, the trimer showed a better bonding scenario than the dimer due positive cooperativity arising from the electron donor–acceptor nature of the interactions. Here in the $(G-CO_2)_n$ clusters, the G unit donates an N-lone pair of

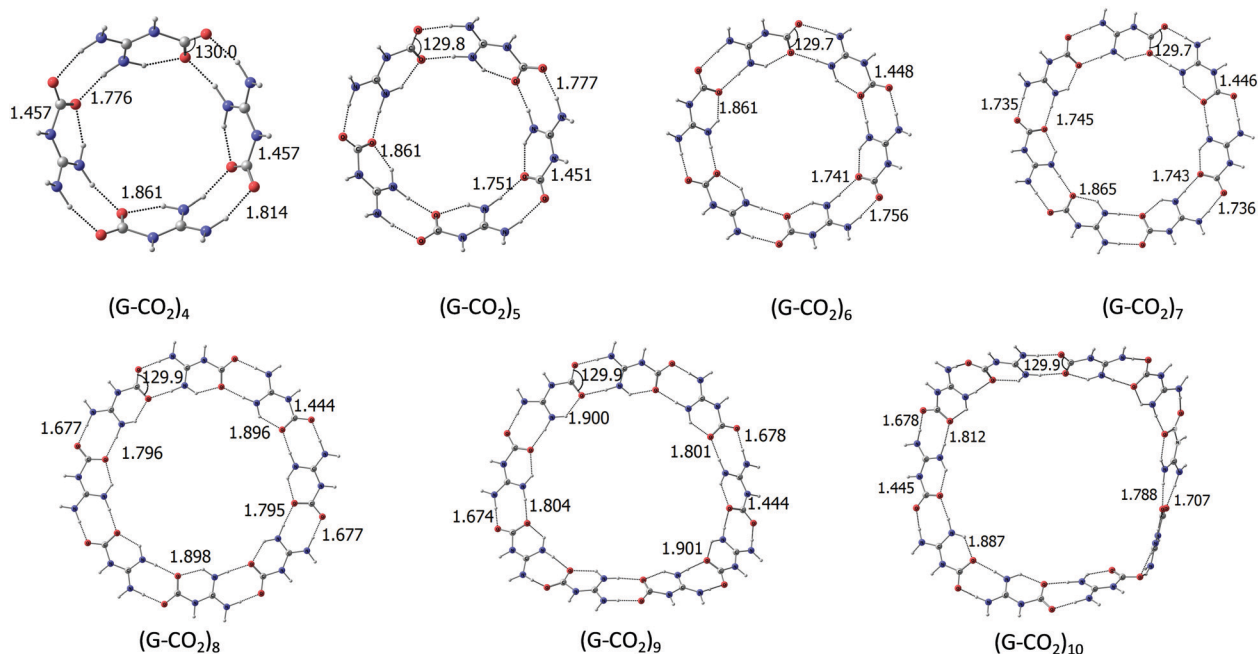**Fig. 5** Optimized geometries of the (G–CO$_2$) dimer and (G–CO$_2$) trimer complexes with their d_{int} (Å), θ (°) and their respective ZPE- and BSSE-corrected ΔE values in kcal mol^{-1} in three different possible orientations.

Fig. 6 Optimized geometries of $(G-CO_2)_n$ complexes at the M06-2X/6-311++G** level for $n = 4-10$.

Table 2 ZPE- and BSSE-corrected ΔE and ΔG (kcal mol^{-1}) of $(G-CO_2)_n$ complexes at the M06-2X/6-311++G** level

n	ΔE (kcal mol^{-1})	ΔG (kcal mol^{-1})
2	−32.8	−1.0
3	−58.3	−3.1
4	−93.4	−16.6
5	−126.6	−28.3
6	−158.8	−39.7
7	−191.5	−53.8
8	−219.9	−62.2
9	−244.4	−64.0
10	−265.0	−62.6

Fig. 7 Plot showing the enhancement in $\Delta E_{/CO2}$ (kcal mol^{-1}) and $\Delta G_{/CO2}$ (kcal mol^{-1}) with the increase in the number of (G−CO$_2$) units.

electrons to CO_2, and the resulting $(G^+)-(CO_2^-)$ zwitterion structures are assembled in a cyclic fashion due to complementary electrostatic interactions and positive cooperativity. The formation of $(G^+)-(CO_2^-)$ zwitterion structures is also observed in the NMR analysis of $(G-CO_2)_n$ clusters (Table S3, ESI†), as indicated by the presence of peaks corresponding to the carboxylate group (COO$^-$). Recently, Wang et al. observed the formation of zwitterionic guanidinium/carboxylate salts derived from amino acids through the bonding of carboxylate to the guanidine N–H bonds.[67] Also, the self-assembly formation of 2-(guanidiniocarbonyl)-pyrrole-4-carboxylate mediated via intermolecular ion pairing between the carboxylate of one molecule and the guanidinium group of another molecule was reported by Schmuck.[38] The linear growth pattern for $(G-CO_2)_n$ clusters is found to yield higher energy structures (ESI†).

Fig. 7 shows the variation of $\Delta E_{/CO2}$ and $\Delta G_{/CO2}$ with the number of $(G-CO_2)_n$ units. All cases show a negative $\Delta G_{/CO2}$, which increases as n increases and reaches the best at $n = 8$ (Table 2). Similarly, $\Delta E_{/CO2}$ shows the increasing stability of the complex as n increases. Larger clusters are thus associated with
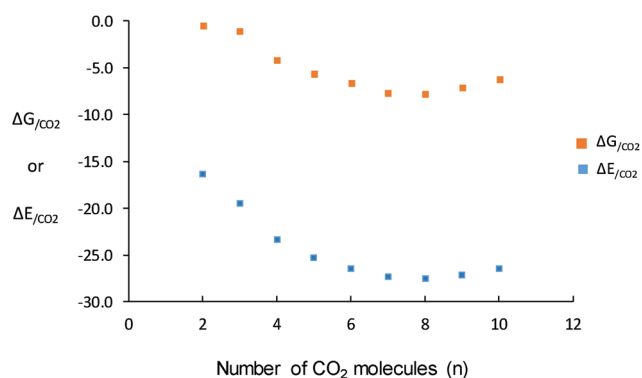
a higher degree of cooperativity in the CO_2 adsorption. The $(G-CO_2)_8$ cluster appears to be the most stable, and beyond $n = 8$ the stability of the complexes shows a decreasing trend.

QTAIM analysis

The QTAIM molecular plots of a representative set of $(G-CO_2)_n$ clusters ($n = 2, 4, 6,$ and 8) are given in Fig. 8 and the rest are given in the ESI.† The dotted lines indicate the bond paths for O···HN interactions and the purple spheres represent the bcps. According to the criterion of Koch and Popelier,[68,69] for a non-covalent interaction, ρ_b falls in the range of 0.002–0.040 a.u. and $\nabla^2\rho$ is positive, typically in the range of 0.024–0.139 a.u. The average values of ρ_b ($\rho_{b,avg}$) for the O···HN non-covalent interactions as well as for the N–C covalent interactions are given in Table 3. For $(G-CO_2)_n$ clusters, the Koch–Popelier criterion on ρ_b is valid for all the O···HN non-covalent
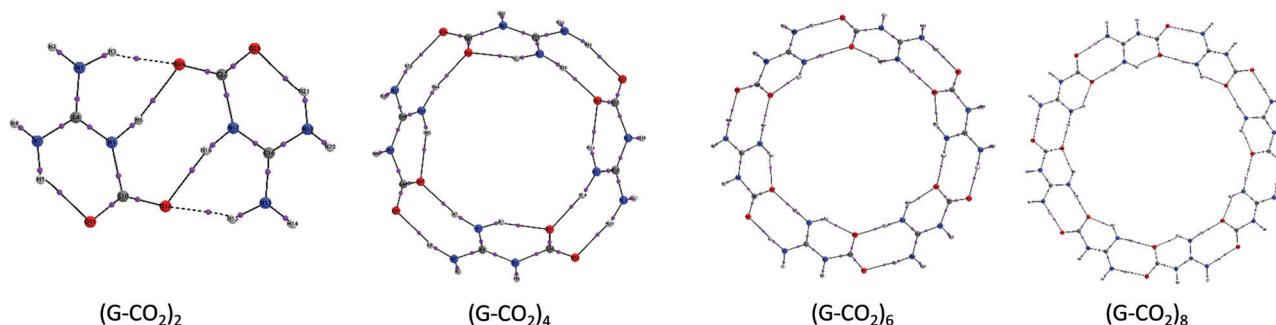
Fig. 8 QTAIM molecular plots of $(G-CO_2)_n$ clusters for n = 2, 4, 6, and 8 at the M06-2X/6-311++G** level .

Table 3 QTAIM parameters (in a.u.) of the non-covalent interactions and N–C covalent interactions in $(G-CO_2)_n$ clusters at the M06-2X/6-311++G** level

System	$\rho_{b,avg}$ of O···HN interaction	$\rho_{b,avg}$ of N–C interaction	$\sum \rho_b$
$G(CO_2)$	0.0143	0.0165	0.0452
$(G-CO_2)_2$	0.0307	0.2436	0.6711
$(G-CO_2)_3$	0.0273	0.2515	1.0003
$(G-CO_2)_4$	0.0344	0.2563	1.4378
$(G-CO_2)_5$	0.0362	0.2594	1.8406
$(G-CO_2)_6$	0.0372	0.2611	2.2373
$(G-CO_2)_7$	0.0378	0.2621	2.6279
$(G-CO_2)_8$	0.0302	0.2631	2.8300
$(G-CO_2)_9$	0.0375	0.2630	3.3782
$(G-CO_2)_{10}$	0.0363	0.2619	3.7071

interactions (Table 3) and the sign of $\nabla^2 \rho$ is positive whereas the N–C covalent bonds show large ρ_b and negative $\nabla^2 \rho$ values (ESI†). As the cluster size increases, the $\rho_{b,avg}$ of the N–C covalent interactions increases up to n = 8, while with a further increase in the cluster size it decreases. The value of ρ_b is often used as a measure of the strength of the interaction, while the sum of ρ_b ($\sum \rho_b$) for O···HN and N–C interactions can be indicative of the total stabilizing influence in the cluster.[65,70] The $\sum \rho_b$ values show a strong linear correlation with the total interaction energy ΔE (Fig. 9), indicating that reorganization of the electron density along the O···HN and N–C bonding regions is stabilizing the cluster.

MESP analysis

The MESP plots of $(G-CO_2)_n$ clusters ($n \geq 2$) are given in Fig. 10, and for every G–CO$_2$ covalent interaction, some amount of electron density gets transferred from G to the CO$_2$ whereas the additional O···H non-covalent interactions lead to further reorganization of the electron density. As observed from Fig. 4 the electron density was initially concentrated mostly on the N atom of the G molecule, but the N–C covalent interaction transfers the charge to the CO$_2$ unit. Accordingly, an increase in the negative potential on the O centers is observed, which is reflected as an enhancement in the minimum potential (V_m) at the O atoms. The electron-rich O centers show attractive interactions with the electron-deficient H–N bonds on another G–CO$_2$.
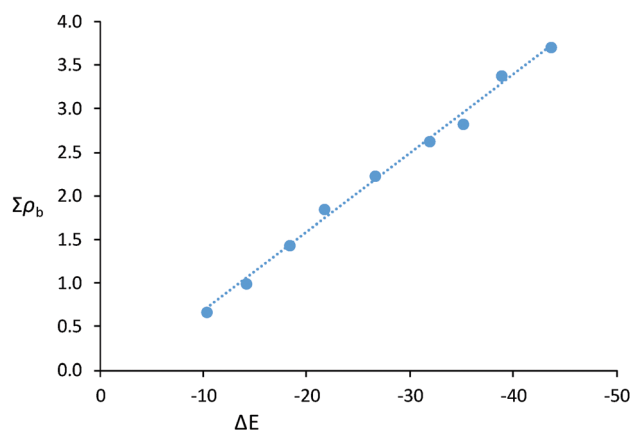

Fig. 9 Correlation between $\sum \rho_b$ in a.u. and ΔE in kcal mol^{-1} for $(G-CO_2)_n$ clusters.

The cyclic arrangement of the G–CO$_2$ in the cluster leads to the formation of maximum O···HN interactions. The O atoms at the outer edge of the cyclic structures interact with one H–N bond and show a more negative MESP minimum (V_m) than the O atoms at the inner edge (V_m') interacting with two H–N bonds (Table 4). Both the V_m and V_m' values are in linear correlation (Fig. 11) with the ΔE values, indicating that the total interaction energy is directly proportional to the ability of the system to undergo electron delocalization. It also suggests that the cooperativity from the neighbouring G–CO$_2$ units is very effective in dispersing the charge separation in the $(G^+)-(CO_2^-)$ zwitterion units.

Benchmark study on energetics and influence of dispersion effects

A benchmark study on $(G-CO_2)_n$ clusters is carried out using B3LYP and the dispersion-included methods, *viz.* B3LYP-D3, BP86-D3, M06-2X-D3 and wB97XD, in conjunction with basis set 6-311++G**. The ΔG data computed using these methods are compared with the M06-2X/6-311++G** data in Table 5. All except B3LYP give a similar trend for ΔG and ΔE (Table S11, ESI†), meaning that the dispersion effect is very important to derive the structure and energetics of $(G-CO_2)_n$ clusters. The intrinsic dispersion effects integrated within M06-2X give results similar to those obtained with other dispersion-correction-incorporated methods. A positive ΔG value observed for G–CO$_2$ in all the
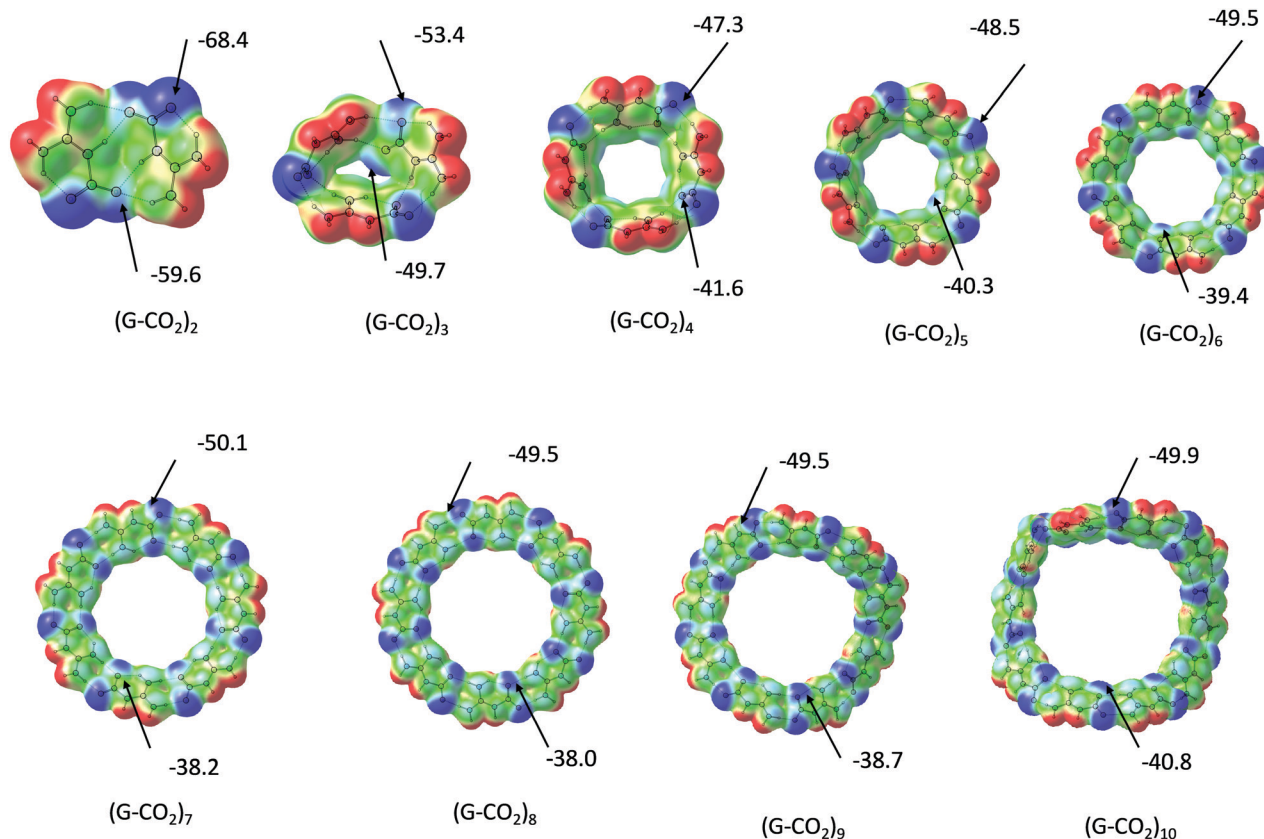
Fig. 10 MESP plotted on an isodensity surface of value 0.006 a.u. for $(G-CO_2)_n$ complexes. The V_m and V_m' values in kcal mol^{-1} at the M06-2X/6-311++G** level are also depicted. Color coding indicates the most electron-rich (blue) to the most electron-deficient (red) regions.

Table 4 V_m and V_m' values in kcal mol^{-1} of $(G-CO_2)_n$ clusters at the M06-2X/6-311++G** level

System	V_m	V_m'
$(G-CO_2)_2$	−136.8	−119.2
$(G-CO_2)_3$	−160.3	−149.0
$(G-CO_2)_4$	−189.3	−166.4
$(G-CO_2)_5$	−242.3	−201.5
$(G-CO_2)_6$	−297.1	−236.7
$(G-CO_2)_7$	−350.8	−267.2
$(G-CO_2)_8$	−396.0	−304.2
$(G-CO_2)_9$	−445.7	−348.1
$(G-CO_2)_{10}$	−498.9	−408.3

Table 5 BSSE- and ZPE-corrected ΔG (kcal mol^{-1}) for $(G-CO_2)_n$ complexes using different methods with dispersion correction in conjunction with the basis set 6-311++G**

System	B3LYP	B3LYP-D3	M06-2X	M06-2X-D3	BP86-D3	wB97XD
$G(CO_2)$	4.4	2.4	2.3	4.4	2.8	3.0
$(G-CO_2)_2$	11.8	2.7	−1.0	−1.6	−2.3	−0.3
$(G-CO_2)_3$	19.8	1.2	−3.1	−4.9	−6.7	−2.6
$(G-CO_2)_4$	10.9	−11.3	−16.6	−19.1	−20.9	−16.9
$(G-CO_2)_5$	5.4	−21.5	−28.3	−30.8	−33.1	−28.8
$(G-CO_2)_6$	0.6	−31.1	−39.7	−42.4	−44.9	−40.1
$(G-CO_2)_7$	−5.2	−42.3	−53.8	−56.1	−58.2	−52.8
$(G-CO_2)_8$	−9.9	−50.0	−62.2	−69.4	−66.6	−63.6
$(G-CO_2)_9$	−3.7	−50.2	−64.0	−67.7	−69.3	−64.0
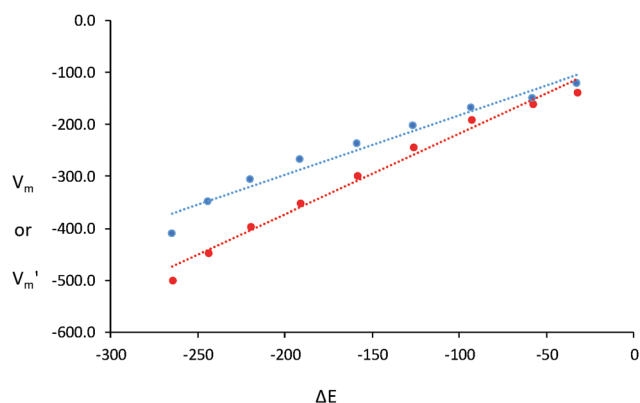
Fig. 11 Correlation between V_m and V_m' (kcal mol^{-1}) with ΔE (kcal mol^{-1}).

methods indicates that G alone cannot show a strong binding with CO_2, while the positive cooperativity generated from the $s(G^+)-(CO_2^-)$ zwitterionic units in the cluster strengthens the N–C interaction. The magnitude of ΔG values becomes more negative with increasing values of n, which can be easily understood from the $\Delta G_{/CO_2}$ values given in Table S13 of ESI.† The ΔG is the most negative for n = 8, indicating the higher probability of the formation of such closed-ring structures of CO_2 complexes of G.

Conclusions

The interactive behaviour of guanidine (G) with CO_2 molecules has been studied using the M06-2X/6-311++G** level of DFT. G

interacts with CO_2 molecules through non-covalent as well as covalent interactions. As reported by Lee *et al.*[45] we also observed non-covalent interaction between G and CO_2, with $\Delta E = -5.7$ kcal mol^{-1}. However, the application of G for CO_2 capture suggested better interaction possibilities, which was revealed through a systematic study on the $G(CO_2)_n$ and $(G-CO_2)_n$ clusters. For the purely non-covalent $G(CO_2)_n$ complexes, ΔE values improved with n and maintained a constant value of $\Delta E_{/CO2}$ beyond $n = 3$. But all these were associated with a positive ΔG value, which indicated the endergonic nature of the formation of $G(CO_2)_n$ complexes. However, in the analysis of $(G-CO_2)_n$ clusters, a pattern of cyclic cluster growth has been observed through the formation of the zwitterion $(G^+)-(CO_2^-)$, which involves strong N–C covalent interactions. The interaction between the zwitterion units also increased with n and the most stable cluster was observed for $n = 8$, with a $\Delta E_{/CO2}$ value of -27.5 kcal mol^{-1}. In addition to the N–C covalent interactions, the $O\cdots HN$ non-covalent interactions between $G–CO_2$ units contribute significantly to the stability of the large cyclic clusters, which is confirmed by the strong correlation between the interaction energy data and the electron density data of bond critical points in QTAIM analysis. MESP analysis also supported the N–C covalent bonding and the delocalization of charges of the zwitterion $(G^+)-(CO_2^-)$ through complementary $O\cdots HN$ hydrogen bonding interactions. Further, as the cluster size increases, the cooperative effect of $O\cdots HN$ and N–C interactions increases leading to a steady enhancement in ΔE. This study illustrates the remarkable influence of cooperativity in the stabilization of the large cyclic structure formations of $G–CO_2$ units with zwitterion character. The study on the influence of dispersion effects using different DFT methods showed that, for $n > 2$, the formation of clusters is exergonic and the most stable cluster is observed at $n = 8$. The exergonic character observed for the $(G–CO_2)_8$ cluster formation demands an experimental verification and we urge experimentalists to suggest a synthetic strategy for it. The high affinity of guanidine towards CO_2 cannot be justified by the weak $G\cdots CO_2$ non-covalent interaction whereas the cooperativity associated with the exergonic formation of zwitterionic $(G–CO_2)_n$ clusters suggests the high CO_2 adsorption capability of guanidine. Another advantage is that the desorption of CO_2 from the most stable $(G–CO_2)_n$ cluster is feasible by mild heating due the moderate value of the $G\cdots CO_2$ dissociation energy and the favorable entropy for the endergonic process. These theoretical results suggest G as a promising adsorbent for CO_2 capture.

Conflicts of interest

There are no conflicts to declare.

Acknowledgements

References

1 Intergovernmental Panel On Climate Change, *Climate Change 2014–Impacts, Adaptation and Vulnerability: Regional Aspects*, Cambridge University Press, 2014.

2 J. C. Stephens and D. W. Keith, *Clim. Change*, 2008, **90**, 217.

3 D. W. Keith, *Science*, 2009, **325**, 1654–1655.

4 D. W. Keith, M. Ha-Duong and J. K. Stolaroff, *Clim. Change*, 2006, **74**, 17–45.

5 P. Agreement, Paris agreement, 2015.

6 K. S. Lackner, S. Brennan, J. M. Matter, A.-H. A. Park, A. Wright and B. Van Der Zwaan, *Proc. Natl. Acad. Sci. U. S. A.*, 2012, **109**, 13156–13162.

7 E. S. Sanz-Perez, C. R. Murdock, S. A. Didas and C. W. Jones, *Chem. Rev.*, 2016, **116**, 11840–11876.

8 D. W. Keith, G. Holmes, D. S. Angelo and K. Heidel, *Joule*, 2018, **2**, 1573–1594.

9 S. Brandani, *Energy Environ.*, 2012, **23**, 319–328.

10 D. Sarewitz and R. Nelson, *Nature*, 2008, **456**, 871–872.

11 K. Lackner, H.-J. Ziock and P. Grimes, *Carbon dioxide extraction from air: is it an option?*, Los Alamos National Lab., NM (US), 1999.

12 F. S. Zeman and K. S. Lackner, *World Resour. Rev.*, 2004, **16**, 157–172.

13 K. S. Lackner and S. Brennan, *Clim. Change*, 2009, **96**, 357–378.

14 G. Chichilnisky and P. Eisenberger, *Nature*, 2009, **459**, 1053.

15 T. M. McDonald, W. R. Lee, J. A. Mason, B. M. Wiers, C. S. Hong and J. R. Long, *J. Am. Chem. Soc.*, 2012, **134**, 7056–7065.

16 Ocean Studies Board, National Academies of Sciences, Engineering and Medicine, *Negative emissions technologies and reliable sequestration: A research agenda*, National Academies Press, 2019.

17 Z. Hu, Y. Wang, B. B. Shah and D. Zhao, *Adv. Sustainable Syst.*, 2019, **3**, 1970002.

18 K. S. Lackner, *Science*, 2003, **300**, 1677–1678.

19 X. Shi, H. Xiao, H. Azarabadi, J. Song, X. Wu, X. Chen and K. S. Lackner, *Angew. Chem., Int. Ed.*, 2020, **59**, 6984–7006.

20 M. A. Alkhabbaz, R. Khunsupat and C. W. Jones, *Fuel*, 2014, **121**, 79–85.

21 S. Wang, W.-C. Li, L. Zhang, Z.-Y. Jin and A.-H. Lu, *J. Mater. Chem. A*, 2014, **2**, 4406–4412.

22 H. Sabet-Sarvestani, H. Eshghi and M. Izadyar, *Struct. Chem.*, 2017, **28**, 675–686.

23 T. C. dos Santos, S. Bourrelly, P. L. Llewellyn, J. W. d. M. Carneiro and C. M. Ronconi, *Phys. Chem. Chem. Phys.*, 2015, **17**, 11095–11102.

24 C. A. Seipp, N. J. Williams, M. K. Kidder and R. Custelcean, *Angew. Chem., Int. Ed.*, 2017, **56**, 1042–1045.

25 F. M. Brethomé, N. J. Williams, C. A. Seipp, M. K. Kidder and R. Custelcean, *Nat. Energy*, 2018, **3**, 553–559.

26 C. G. Gianopoulos, Z. Chua, V. V. Zhurov, C. A. Seipp, X. Wang, R. Custelcean and A. A. Pinkerton, *IUCrJ*, 2019, **6**, 56–65.

27 R. Custelcean, N. J. Williams and C. A. Seipp, *Google Patents*, 2020.

28 J. Thiele and E. Dralle, *Justus Liebieg's Ann. Chem.*, 1898, **302**, 275–299.

29 J.-M. Wurtz, W. Bourguet, J.-P. Renaud, V. Vivat, P. Chambon, D. Moras and H. Gronemeyer, *Nat. Struct. Biol.*, 1996, **3**, 87–94.

30 R. G. Konsler, J. Karl and E. N. Jacobsen, *J. Am. Chem. Soc.*, 1998, **120**, 10780–10781.

31 N. A. Brunelli, K. Venkatasubbaiah and C. W. Jones, *Chem. Mater.*, 2012, **24**, 2433–2442.

32 V. Lyaskovskyy and B. de Bruin, *ACS Catal.*, 2012, **2**, 270–279.

33 C. Song, Y. Chu, M. Wang, H. Shi, L. Zhao, X. Guo, W. Yang, J. Shen, N. Xue and L. Peng, *J. Catal.*, 2017, **349**, 163–174.

34 M. Caplow, *J. Am. Chem. Soc.*, 1968, **90**, 6795–6803.

35 P. Danckwerts, *Chem. Eng. Sci.*, 1979, **34**, 443–446.

36 T. L. Donaldson and Y. N. Nguyen, *Ind. Eng.*, 1980, **19**, 260–266.

37 I. Dovgaliuk, F. Nouar, C. Serre, Y. Filinchuk and D. Chernyshov, *Chem. – Eur. J.*, 2017, **23**, 17714–17720.

38 C. Schmuck, *Tetrahedron*, 2001, **57**, 3063–3067.

39 M. Saleh, H. M. Lee, K. C. Kemp and K. S. Kim, *ACS Appl. Mater. Interfaces*, 2014, **6**, 7325–7333.

40 R. Steinhardt, S. C. Hiew, H. Mohapatra, D. Nguyen, Z. Oh, R. Truong and A. Esser-Kahn, *ACS Cent. Sci.*, 2017, **3**, 1271–1275.

41 J. Kundu, J. F. Stilck, J.-H. Lee, J. B. Neaton, D. Prendergast and S. Whitelam, *Phys. Rev. Lett.*, 2018, **121**, 015701.

42 R. Vaidhyanathan, S. S. Iremonger, G. K. Shimizu, P. G. Boyd, S. Alavi and T. K. Woo, *Angew. Chem., Int. Ed.*, 2012, **124**, 1862–1865.

43 E. J. Kim, R. L. Siegelman, H. Z. Jiang, A. C. Forse, J.-H. Lee, J. D. Martell, P. J. Milner, J. M. Falkowski, J. B. Neaton and J. A. Reimer, *Science*, 2020, **369**, 392–396.

44 S. T. Hosseini, H. Raissi and M. Pakdel, *New J. Chem.*, 2020, **44**, 7771–7779.

45 H. M. Lee, I. S. Youn, M. Saleh, J. W. Lee and K. S. Kim, *Phys. Chem. Chem. Phys.*, 2015, **17**, 10925–10933.

46 J. D. Martell, P. J. Milner, R. L. Siegelman and J. R. Long, *Chem. Sci.*, 2020, **11**, 6457–6471.

47 V. Y. Mao, P. J. Milner, J. H. Lee, A. C. Forse, E. J. Kim, R. L. Siegelman, C. M. McGuirk, L. B. Porter-Zasada, J. B. Neaton and J. A. Reimer, *Angew. Chem., Int. Ed.*, 2020, **59**, 19468–19477.

48 R. L. Siegelman, T. M. McDonald, M. I. Gonzalez, J. D. Martell, P. J. Milner, J. A. Mason, A. H. Berger, A. S. Bhown and J. R. Long, *J. Am. Chem. Soc.*, 2017, **139**, 10526–10538.

49 M. J. Frisch, G. W. Trucks, H. B. Schlegel, G. E. Scuseria, M. A. Robb, J. R. Cheeseman, G. Scalmani, V. Barone, G. A. Petersson, H. Nakatsuji, X. Li, M. Caricato, A. V. Marenich, J. Bloino, B. G. Janesko, R. Gomperts, B. Mennucci, H. P. Hratchian, J. V. Ortiz, A. F. Izmaylov, J. L. Sonnenberg, D. Williams-Young, F. Ding, F. Lipparini, F. Egidi, J. Goings, B. Peng, A. Petrone, T. Henderson, D. Ranasinghe, V. G. Zakrzewski, J. Gao, N. Rega, G. Zheng, W. Liang, M. Hada, M. Ehara, K. Toyota, R. Fukuda, J. Hasegawa, M. Ishida, T. Nakajima, Y. Honda, O. Kitao, H. Nakai, T. Vreven, K. Throssell, J. A. Montgomery Jr., J. E. Peralta, F. Ogliaro, M. J. Bearpark, J. J. Heyd, E. N. Brothers, K. N. Kudin, V. N. Staroverov, T. A. Keith, R. Kobayashi, J. Normand, K. Raghavachari, A. P. Rendell, J. C. Burant, S. S. Iyengar, J. Tomasi, M. Cossi, J. M. Millam, M. Klene, C. Adamo, R. Cammi, J. W. Ochterski, R. L. Martin, K. Morokuma, O. Farkas, J. B. Foresman and D. J. Fox, *Gaussian 16 Rev. A.03*, Gaussian, Inc., Wallingford, CT, 2016.

50 Y. Zhao and D. G. Truhlar, *Theor. Chem. Acc.*, 2008, **120**, 215–241.

51 S. F. Boys and F. d. Bernardi, *Mol. Phys.*, 1970, **19**, 553–566.

52 P. Hobza and K. Müller-Dethlefs, *Non-covalent interactions: theory and experiment*, Royal Society of Chemistry, 2010.

53 Ł. Mentel and E. Baerends, *J. Chem. Theory Comput.*, 2013, **10**, 252–267.

54 C. D. Sherrill, T. Takatani and E. G. Hohenstein, *J. Phys. Chem. A*, 2009, **113**, 10146–10159.

55 C. D. Sherrill, *School of Chemistry and Biochemistry*, Georgia Institute of Technology, 2010.

56 A. Halkier, W. Klopper, T. Helgaker, P. Jo/rgensen and P. R. Taylor, *J. Chem. Phys.*, 1999, **111**, 9157–9167.

57 R. F. Bader, *Atoms in molecules: a quantum theory, International series of monographs on chemistry*, **22**, Oxford University Press, Oxford, 1990.

58 M. Jabłoński and M. Palusiak, *J. Phys. Chem. A*, 2010, **114**, 2240–2244.

59 H. J. Bohórquez, R. J. Boyd and C. F. Matta, *J. Phys. Chem. A*, 2011, **115**, 12991–12997.

60 T. Keith, *TK Gristmill Software: Overland Park, KS*, 2014.

61 N. Mohan and C. H. Suresh, *J. Phys. Chem. A*, 2014, **118**, 1697–1705.

62 P. Politzer and D. G. Truhlar, *Chemical applications of atomic and molecular electrostatic potentials: reactivity, structure, scattering, and energetics of organic, inorganic, and biological systems*, Springer Science & Business Media, 2013.

63 S. R. Gadre and R. N. Shirsat, *Electrostatics of atoms and molecules*, Universities Press, 2000.

64 N. Tasinato and S. Grimme, *Phys. Chem. Chem. Phys.*, 2015, **17**, 5659–5669.

65 S. Anila and C. H. Suresh, *Phys. Chem. Chem. Phys.*, 2019, **21**, 23143–23153.

66 P. V. Bijina and C. H. Suresh, *J. Phys. Chem. A*, 2020, **124**, 2231–2241.

67 W. Wang, J. Gu, X. Zou, W. Tong and H. Gong, *Tetrahedron Lett.*, 2015, **56**, 2684–2687.

68 U. Koch and P. L. Popelier, *J. Phys. Chem.*, 1995, **99**, 9747–9754.

69 P. Popelier, *J. Phys. Chem. A*, 1998, **102**, 1873–1878.

70 T. D. Della and C. H. Suresh, *Phys. Chem. Chem. Phys.*, 2017, **19**, 5830–5838.

PCCP

Check for updates

Imidazolium–fulleride ionic liquids – a DFT prediction†

Sebastian Anila[ab] and Cherumuttathu H. Suresh [iD] *[ab]

Ionic liquids (ILs) exhibit tunable physicochemical properties due to the flexibility of being able to select their cation–anion combination from a large pool of ions. The size of the ions controls the properties of the ILs in the range from ionic to molecular, and thus large ions play an important role in regulating the melting temperature and viscosity. Here, we show that the exohedral addition of anionic X^- moieties to C_{60} (X = H, F, OH, CN, NH_2, and NO_2) is a thermodynamically viable process for creating large X-fulleride anions $(C_{60}X)^-$. The addition of X^- to C_{60} is modelled by locating the transition state for the reaction between C_{60} and 1,3-dimethyl-2X-imidazole (IMX) at the M06L/6-311++G(d,p)//M06L/6-31G(d,p) level. The reaction yields the ion-pair complex $IM^+\cdots(C_{60}X)^-$ for X = H, F, OH, CN, NH_2, and NO_2 and the ordered pair of (activation free energy, reaction free energy) is found to be (14.5, 1.1), (6.1, 3.1), (16.7, 2.3), (14.7, −7.9), (27.9, 0.5) and (11.9, 12.4), respectively. The low barrier of the reactions suggests their feasibility. The reaction is slightly endergonic for X = H, F, OH, and NH_2, while X = CN shows a significant exergonic character. The X-fulleride formation is not observed when X = Cl and Br. The ion-pair interactions $(E_{ion-pair})$ observed for $IM^+\cdots(C_{60}X)^-$ range from −64.0 to −73.0 kcal mol^{-1}, which is substantially lower ($\sim$10%) than the typically reported values for imidazolium-based ionic liquids such as $[EMIm]^+[trz]^-$, $[EMIm]^+[dc]^-$, $[EMIm]^+[dtrz]^-$, and $[EMIm]^+[NH_2tz]^-$. The quantum theory of atoms in molecules (QTAIM) analysis showed that the C–X bonding in $(C_{60}X)^-$ is covalent, while that in $(IM^+\cdots X^-)\cdots C_{60}$ (for X = Cl and Br) is non-covalent. Furthermore, molecular electrostatic potential (MESP) analysis showed that the X-fulleride could behave as a large spherical anion due to the delocalization of the excess electron in the system over the entire carbon framework. The large anionic character of the X-fulleride is also revealed by the identification of several close lying local energy minima for the $IM^+\cdots(C_{60}X)^-$ ion-pair. The low $E_{ion-pair}$ value, the significant contribution of dispersion to the $E_{ion-pair}$ and the spherical nature of the anion predict low-melting point and highly viscous IL formation from X-fullerides and the imidazolium cation.

Introduction

Ionic liquids (ILs) are low-melting point salts, which, by definition, melt below 100 °C and are found to be useful as solvents in organic synthesis and extraction processes.[1,2] Theoretical methods to predict the properties of proposed cation–anion combinations before synthesis are useful in designing novel ILs to better meet the needs of particular applications by altering the combination of cations and anions. Bernard *et al.* have shown the variation of trends in the thermodynamic and transport properties of ionic liquids (ILs) with

their ion-pair-binding energy.[3] The high viscosity is one of the major limitations commonly encountered in the performance of ionic liquids when used as electrolytes in electrochemical devices.[4] Cyano-functionalized anions produce some of the most fluid and conductive ionic liquids with low melting temperatures and low viscosities.[5–7] A wide range of studies have been carried out on imidazolium-based ILs owing to their excellent properties of stability, their flexibility of molecular design, their ease of synthesis and adaptability to multiple functions.[8] The 1-ethyl-3-methylimidazolium cation ($[EMIm]^+$) has been well studied and tends to form low viscous liquids with a large number of anions.[9–11]

Tuning the ion-pair interactions in ILs has been one of the important strategies adopted in designing new ionic liquids. The size of the ions also exerts some control in regulating the properties of ILs ranging from ionic to molecular.[7] Lowering the melting point is directly related to lowering the viscosity of the ILs, which in turn is influenced by the electrostatic

[a] *Chemical Sciences and Technology Division, CSIR-National Institute for Interdisciplinary Science and Technology, Thiruvananthapuram, Kerala, 695 019, India. E-mail: sureshch@niist.res.in, sureshch@gmail.com; Tel: +91-471-2515472*
[b] *Academy of Scientific and Innovative Research (AcSIR), Ghaziabad 201002, India*
† Electronic supplementary information (ESI) available: Optimized geometries, relevant tables, figures, *etc.* See DOI: 10.1039/d1cp03455c

interaction forces between the ions in the salts.[12] Since these interactions are mostly electrostatic in nature, the strength of the interaction decreases with an increase in the local minimum distance and this can be easily achieved by increasing the size of the ions. Thus, from this particular aspect, large ions are of great interest. Although it is quite difficult to lower the viscosity of the ILs, large ions are certainly effective in lowering the melting temperature and viscosity.[13]

Compared with other all carbon allotropes, the discovery of C_{60} fullerene has transformed the chemistry of carbon.[14–22] Maciel et al. have studied the solvation of C_{60} in ionic liquids via molecular dynamics simulations, and the spatial distributions revealed different patterns for the solvation of the C_{60}.[23] Later, García et al. analysed the solvation of C_{60} fullerene by 24 different ionic liquids belonging to the imidazolium, piperazinium, and cholinium families using classic molecular dynamics simulations and density functional theory (DFT) methods.[24,25] They extended their theoretical investigations to study the interaction of other carbon nanostructures with ionic liquids.[26,27] In 2015, Campisciano et al. synthesized and characterized a series of fullerene–ionic liquid hybrids in which the fullerene–malonate derivatives were synthesized and substituted with a number of IL moieties to form new fullerene–ionic liquid hybrids.[28] They also applied this new fullerene derivative conjugate for the immobilization of palladium nanoparticles through ion exchange followed by reduction with sodium borohydride. Chaban et al. carried out theoretical investigations into the concept of solvating fullerenes using room-temperature ionic liquids (RTILs), which opened a new direction to obtaining well-dispersed fullerene-containing systems by comparing a range of common molecular solvents and novel ionic solvents to the RTIL 1-butyl-3-methylimidazolium tetrafluoroborate ([BMIm]$^+$[BF$_4$]$^-$).[29] In another study, they observed that the imidazolium ionic liquid helps to disperse fullerenes in water.[30] Both theoretical[31–35] and experimental[36–39] studies on endohedral[32,40–43] as well as exohedral[14,44,45] modification of the fullerene cage have been performed to generate the new materials of interest. According to the DFT and Born–Oppenheimer molecular dynamics (BOMD) calculations of Ravinder and Subramanian, the stability of the endohedral fullerenes depends on the size of both the anion and the fullerene cage.[46] The BOMD simulations of Chaban et al. suggested novel C_{60}–RTIL systems on the basis of the systematically positive effective electrostatic charge that is developed on the C_{60} fullerene via the electronic polarization of C_{60} fullerene by imidazolium-based RTILs.[47] They also studied the possibility of using fullerene-based systems for medicinal applications and CO_2 capture.[48,49] In addition, Salehzadeh et al. showed that the interaction energy value ranges from -62.5 to -79.2 kcal mol^{-1} for the encapsulation of halides within fullerenes at the MP2/6-311++G** level.[50] As an extension to the study on the influence of encapsulation of the anion inside the C_{60} fullerene cage on its exohedral reactivity, García-Rodeja et al. studied the Diels–Alder reaction between 1,3-cyclohexadiene and M@C_{60} (M = Li$^+$, Na$^+$, K$^+$, Be^{2+}, Mg^{2+}, Al^{3+}, and Cl$^-$).[51] They reported a significant enhancement in

the Diels–Alder reactivity for systems having an endohedral cation, whereas a decrease in the reactivity is observed when an anion is encapsulated in the C_{60} cage. They also studied the Bingel–Hirsch (BH) addition of ethyl bromomalonate over a series of ion-encapsulated M@C_{60} (M = Li$^+$, Na$^+$, K$^+$, Mg^{2+}, Ca^{2+}, and Cl$^-$) and found that K$^+$@C_{60} was the one that leads to the fastest BH reaction, whereas Cl$^-$@C_{60} led to the slowest reaction.[52]

All of the previous studies have been either on the confinement of the encapsulated species inside the cage or on the binding interactions of the fullerene cage with the functional moieties. Although Campisciano et al. reported the fullerene derivative-incorporated IL, the use of fullerene systems either in the cationic or in the anionic form has not yet been reported for the development of ILs. In a recent study using DFT methods, Suresh et al. showed that anion-encapsulated endohedral fullerenes behave as closed-shell anions and are represented as (X@C_{60})$^-$.[53] Apart from the endohedral modifications on fullerenes, the exohedral changes also have an influence on the chemical reactivity and the properties of the C_{60} cage. Very recently, we have shown that endohedral and exohedral chloro-fullerides act as strong η^5 ligands to cationic transition metal fragments.[54] This study, carried out at the M06L/6-311++G(d,p)//M06L/6-31G(d,p) level of DFT, explained the delocalisation of the negative charge across the fullerene cage, resulting in the bulky anionic nature and strong coordination ability of chloro-fulleride. The present study investigates the idea that a large-sized anion, characterized by the spherical distribution of the negative charge, can be effectively utilized for designing new ion-pair combinations to develop novel ILs. Here, the interaction of the X-fullerides (($C_{60}X$)$^-$) with the imidazolium cation (IM$^+$) has been studied for X = H, F, Cl, Br, OH, CN, NH$_2$, and NO$_2$, and the feasibility of the formation of these anion$\cdots$cation complexes is also evaluated by modelling the transition state for the reaction between 1,3-dimethyl-2X-imidazole (IMX) and C_{60}.

Computational methods

All calculations were carried out at the M06L/6-311++G(d,p)//M06L/6-31G(d,p) level of DFT[55–58] using the Gaussian 16 suite of programs.[59] Vibrational frequency analysis was carried out to confirm the optimized geometries as true energy minima. A previous benchmark study has reported that the M06L method is a robust method for calculating the geometry and interaction energy of non-covalent dimers.[60] Furthermore, recent studies have benchmarked some of the dispersion-corrected methods[61,62] for anionic fullerene systems and have found that M06L is a reliable method.[53] The energy of the reaction between 1,3-dimethyl-2X-imidazole (IMX) and C_{60} (E_{rea}) is calculated as

$$E_{rea} = E_2 - E_1, \quad (1)$$

where E_1 and E_2 are the zero-point energy (ZPE)-corrected energies of the reactant complex ($C_{60}\cdots$IMX) and the product (IM$^+$)$\cdots$($C_{60}X$)$^-$ ion-pair complex, respectively. The free energy

(G_{rea}) associated with the reaction is also calculated in a similar fashion.

The ion-pair-binding energy ($E_{ion\text{-}pair}$) is calculated as

$$E_{ion\text{-}pair} = E_2 - (E_3 + E_4), \tag{2}$$

where E_3 and E_4 are the ZPE-corrected energies of $(C_{60}X)^-$ and IM^+, respectively. In the case of Cl^- and Br^-, the $IM^+\cdots X^-$ ion-pair is found to interact non-covalently with C_{60} to form the $(IM^+\cdots X^-)\cdots C_{60}$ complex. Here, the non-covalent interaction energy (E_{noncov}) of C_{60} with $IM^+\cdots X^-$ is calculated as

$$E_{noncov} = E_7 - (E_5 + E_6), \tag{3}$$

where E_5, E_6 and E_7 are the ZPE-corrected energies of C_{60}, $IM^+\cdots X^-$ and $(IM^+\cdots X^-)\cdots C_{60}$, respectively.

Molecular electrostatic potential (MESP) analysis was carried out to analyse the intermolecular interactions and charge delocalization in the complexes.[63–65] MESP topology features have been widely used to quantitatively scrutinize the chemical reactivity and related concepts such as covalent and non-covalent bonding, nucleophilic and electrophilic reactivity, the substituent effect, etc.[66–71] For any molecular system, the MESP at a point **r** in space, $V(\mathbf{r})$, is defined by eqn (4), where Z_A represents the charge on the nucleus located at a distance $\mathbf{R}_A$, $\rho(\mathbf{r})$ is the electron density and $\mathbf{r}'$ is a dummy integration variable.

$$V(\mathbf{r}) = \sum_A^N \frac{Z_A}{|\mathbf{r} - \mathbf{R}_A|} - \int \frac{\rho(\mathbf{r}')d\mathbf{r}'}{|\mathbf{r} - \mathbf{r}'|} \tag{4}$$

Bader's quantum theory of atoms in molecules (QTAIM) analysis, based on the electron density ($\rho(\mathbf{r})$) distribution, was carried out using the AIMAll package.[72–74] The QTAIM plots contain bond paths through the locally maximal electron density and the corresponding $(3, -1)$ bond critical points (bcps) between interacting atoms.[75–78] Atom–atom interactions can be characterised as covalent or non-covalent, based on the electron densities at the respective BCPs (ρ_b) and from the sign of the corresponding Laplacian ($\nabla^2\rho$).

Results and discussion

The imidazolium cation is one of the most frequently encountered cationic species in ionic liquids. Here, we look at the possibility of the reaction between neutral 1,3-dimethyl-2X-imidazole (IMX) and C_{60} (Scheme 1) for X = H, F, Cl, Br, OH, CN, NH_2, and NO_2. Two possible outcomes of this reaction are shown in Scheme 1, *viz.* the formation of the ion-pair $IM^+\cdots(C_{60}X)^-$ or the formation of the $(IM^+\cdots X^-)\cdots C_{60}$ complex.

Among the different anions in this study, H^-, F^-, CN^-, OH^-, NH_2^- and NO_2^- are observed to follow reaction pathway (i), while the anions Cl^- and Br^- follow the reaction pathway (ii). The X-fullerides $(C_{60}X)^-$ formed in pathway (i) show the C–X covalent bonding interaction and suggest that the anionic charge is delocalized over the whole carbon framework. Thus, $(C_{60}X)^-$ can be considered as a large anion and it interacts with IM^+ for electrostatic stabilization to form the ion-pair $IM^+\cdots(C_{60}X)^-$. In $(IM^+\cdots X^-)\cdots C_{60}$, C_{60} interacts non-covalently with the ion-pair $IM^+\cdots X^-$.

The optimized geometries of the reactant complex, the transition state and the product of a representative case (X = OH) for pathway (i) are shown in Fig. 1. Here, the binding energy for the van der Waals complex $IM(OH)\cdots C_{60}$ is 7.7 kcal mol^{-1} and it passes through the transition state $ts1_{OH}$ to yield the ion-pair complex $IM^+\cdots(C_{60}OH)^-$. The structure of $ts1_{OH}$ shows the C–OH bond breaking of IMX at 2.12 Å and the initiation of C–OH bond formation on fullerene at 2.01 Å. The E_{rea} value for $IM^+\cdots(C_{60}OH)^-$ formation is 0.2 kcal mol^{-1}, is slightly endothermic, and requires an activation energy (E_{act}) of 15.4 kcal mol^{-1}, which is surmountable at room temperature.

Fig. 2 shows the energy profile for the reaction between C_{60} and IM(CN), which is slightly different from that of C_{60} and IM(OH) as it takes place in two steps. Here, the C–CN distance
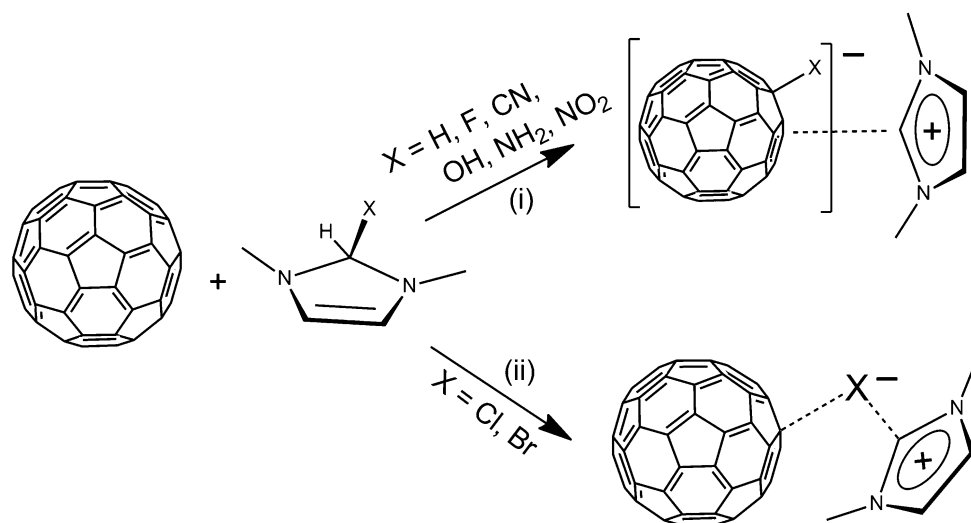
Scheme 1 Two possible outcomes of the reaction between IMX and C_{60}.
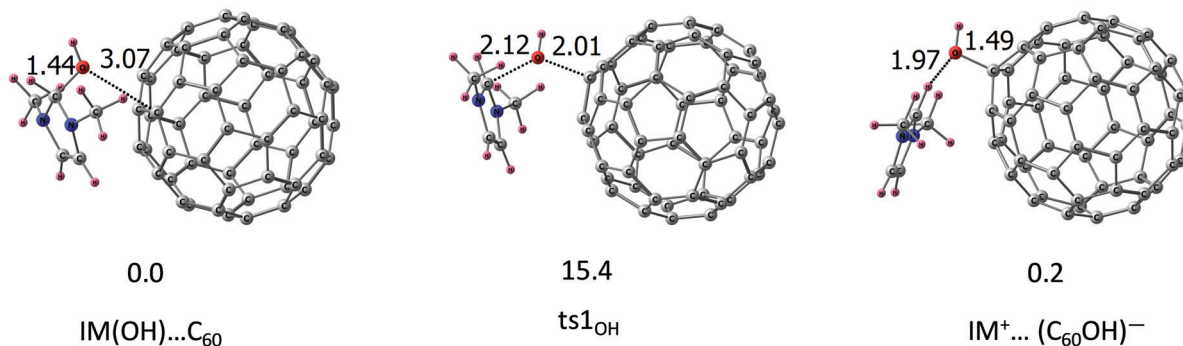
Fig. 1 Optimized geometries of the reactant, the transition state and the product for the reaction between IM(OH) and C_{60} at the M06L/6-31G(d,p) level with their local minimum distances in Å. Relative ZPE-corrected energies in kcal mol^{-1} at the M06L/6-311++G(d,p)//M06L/6-31G(d,p) level are also depicted.
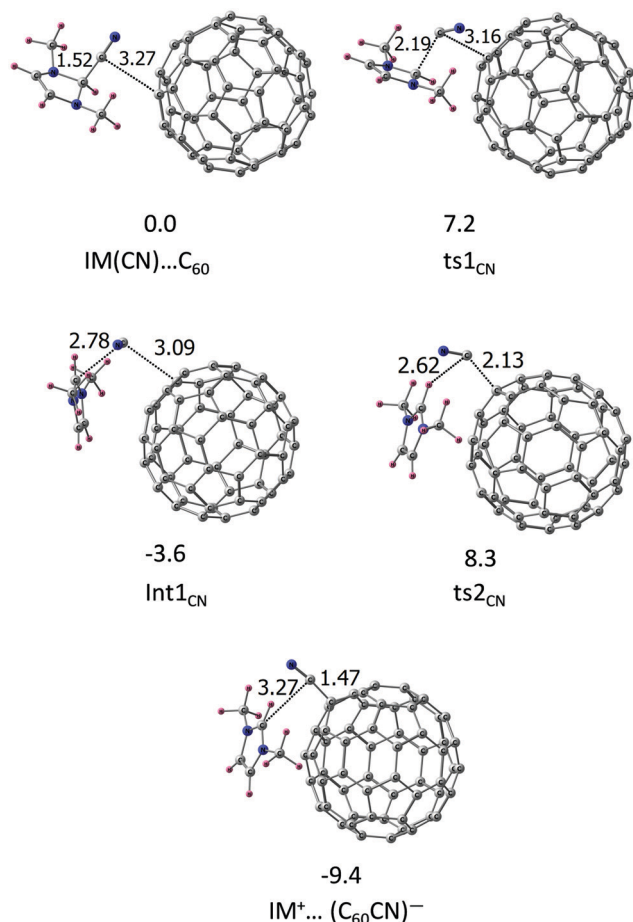

Fig. 2 Optimized geometries of the reactant, the transition states and the product for the reaction between IM(CN) and C_{60} at the M06L/6-31G(d,p) level with their local minimum distances in Å. Relative ZPE-corrected energies in kcal mol^{-1} at the M06L/6-311++G(d,p)//M06L/6-31G(d,p) level are also depicted.

of 3.16 Å in $ts1_{CN}$ suggests that a fully cleaved CN^- from IMX will be reacting on C_{60} through the formation of an intermediate $Int1_{CN}$. In $Int1_{CN}$, the $C_{60}\cdots CN$ and $IM\cdots CN$ distances are 3.09 and 2.78 Å, respectively. In the second step, C_{60}–CN bond formation occurs by passing through the transition state $ts2_{CN}$,

wherein the C–CN distance is 2.13 Å. The $ts1_{CN}$ transition state suggests an E_{act} value of 7.2 kcal mol^{-1} for the formation of $Int1_{CN}$ at -3.6 kcal mol^{-1}, while $ts2_{CN}$ requires an E_{act} value of 11.9 kcal mol^{-1} to yield the product. The intermediate $Int1_{CN}$ can be represented as $(IM^+\cdots CN^-)\cdots C_{60}$. The product $IM^+\cdots(C_{60}CN)^-$ formation is exothermic by 9.4 kcal mol^{-1}. The energetic parameters including the free energy parameters are given in Table 1.

The optimized structures of the $IM^+\cdots(C_{60}X)^-$ ion-pairs for X = H, F, NH_2, and NO_2 are shown in Fig. 3, along with the local minimum distances. The first four structures show covalent bond formation between C_{60} and X, which is evident from the C–H, C–F, C–NH_2 and C–NO_2 distances of 1.11, 1.55, 1.51, and 1.68 Å, respectively, whereas the nearest distance from X to IM^+ indicates either a weak non-covalent interaction (for X = H) or a hydrogen-bond interaction, as observed in the previous cases of X = OH or CN. All these ion-pairs have an $E_{ion-pair}$ value ranging from -64.0 to -73.0 kcal mol^{-1} (Table 1).

For Cl^- and Br^-, the IMX compound itself exists as an ion-pair $IM^+\cdots X^-$. The $IM^+\cdots X^-$ ion-pair interacts weakly with C_{60} to form the non-covalent $(IM^+\cdots X^-)\cdots C_{60}$ complexes (Fig. 3). This is reflected in the large local minimum distance between C_{60} and $IM^+\cdots X^-$, *viz.* 3.31 Å and 3.39 Å for X = Cl and Br, respectively. The E_{noncov} values observed for C_{60} with $IM^+\cdots Cl^-$ and $IM^+\cdots Br^-$ are -9.3 and -9.9 kcal mol^{-1}, respectively. It should also be noted that in $(IM^+\cdots X^-)\cdots C_{60}$, the interaction energy values between IM^+ and $(X^-\cdots C_{60})$ for X = Cl and Br are -82.4 and -80.2 kcal mol^{-1}, respectively. The QTAIM analysis shows the negative $\nabla^2\rho_b$ values and the ρ_b value in the range of

Table 1 ZPE-corrected $E_{ion-pair}$, $G_{ion-pair}$, E_{rea}, G_{rea}, E_{act} and G_{act} values (kcal mol^{-1}) of the $IM^+(C_{60}X)^-$ systems at the M06L/6-311++G(d,p)//M06L/6-31G(d,p) level

System	$E_{ion-pair}$	$G_{ion-pair}$	E_{rea}	G_{rea}	E_{act}	G_{act}
$IM^+\cdots(C_{60}H)^-$	-64.0	-52.1	-0.03	1.1	11.8	14.5
$IM^+\cdots(C_{60}F)^-$	-71.8	-59.1	0.3	3.1	4.7	6.1
$IM^+\cdots(C_{60}OH)^-$	-72.0	-58.9	0.2	2.3	15.4	16.7
$IM^+\cdots(C_{60}CN)^-$	-69.6	-57.1	-9.4	-7.9	11.9	14.7
$IM^+\cdots(C_{60}NH_2)^-$	-73.0	-61.3	-0.6	0.5	24.7	27.9
$IM^+\cdots(C_{60}NO_2)^-$	-71.0	-57.7	8.8	12.4	7.0	11.9

Fig. 3 Optimized geometries of the $IM^{+}\cdots(C_{60}X)^{-}$ ion-pairs for X = H, F, NH_2, NO_2, Cl, and Br at the M06L/6-31G(d,p) level with their local minimum distances in Å.

0.1636–0.2592 a.u. for the C–X interaction in $(C_{60}X)^{-}$ for X = H, F, CN, OH, NH_2 and NO_2, indicating the covalent character of the C–X bonding interaction. The positive $\nabla^2\rho$ values and ρ_b values of 0.0093 a.u. and 0.0092 a.u., respectively, for X = Cl and Br suggest the weak non-covalent nature of the C$\cdots$X

interaction in $(IM^{+}\cdots X^{-})\cdots C_{60}$ complexes. The QTAIM plots of the complexes and their QTAIM data are shown in the ESI† (Fig. S4 and Table S7).

MESP features

Fig. 4 represents the MESP mapped on an isodensity surface of 0.01 a.u. for C_{60}, $C_{60}^{\bullet-}$, and the X-fullerides. The dark blue pattern observed for the MESP analysis of $C_{60}^{\bullet-}$ and X-fullerides indicates a very similar electron-rich nature of the carbon framework, while the pale green surface observed for C_{60} indicates a relatively high electron deficiency. Furthermore, a quantification of the MESP feature is available from the most negative MESP value (V_m) on the fullerene cage (V_{m1}) and from the most negative MESP value on the X group (V_{m2}). The V_{m1} value of the $(C_{60}X)^{-}$ species (X = H, F, CN, OH, NH_2 and NO_2) lies in the range of −65.8 to −72.2 kcal mol^{-1} and those of $Cl^{-}\cdots C_{60}$ and $Br^{-}\cdots C_{60}$ are −50.8 and −51.6 kcal mol^{-1}, respectively (Table 2). The magnitude of the V_{m1} value of $(C_{60}X)^{-}$ is higher than that of $C_{60}^{\bullet-}$, which suggests that the carbon cage of the X-fullerides will behave as an electron-rich anionic cage. On the basis of the magnitude of V_{m1}, the anionic nature of the X-fullerides can be assessed[79] as $(C_{60}H)^{-}$ > $(C_{60}NH_2)^{-}$ > $(C_{60}OH)^{-}$ > $(C_{60}CN)^{-}$ > $(C_{60}F)^{-}$ > $(C_{60}NO_2)^{-}$. The strength of the C–X bond of the fulleride is found to be proportional to the anionic character of the fulleride (Fig. S2, ESI†).

The V_{m2} value indicates the nature of the negative MESP around the lone-pair-bearing X group in $(C_{60}X)^{-}$ as X = H is devoid of such a minimum. If X^{-} alone is analyzed for the V_m data (Table S3, ESI†), one may notice that the observed values, viz. −188.4, −240.3, −186.0, −241.5, −237.6, and −186.4, for X = H, F, CN, OH, NH_2 and NO_2, respectively, are much more
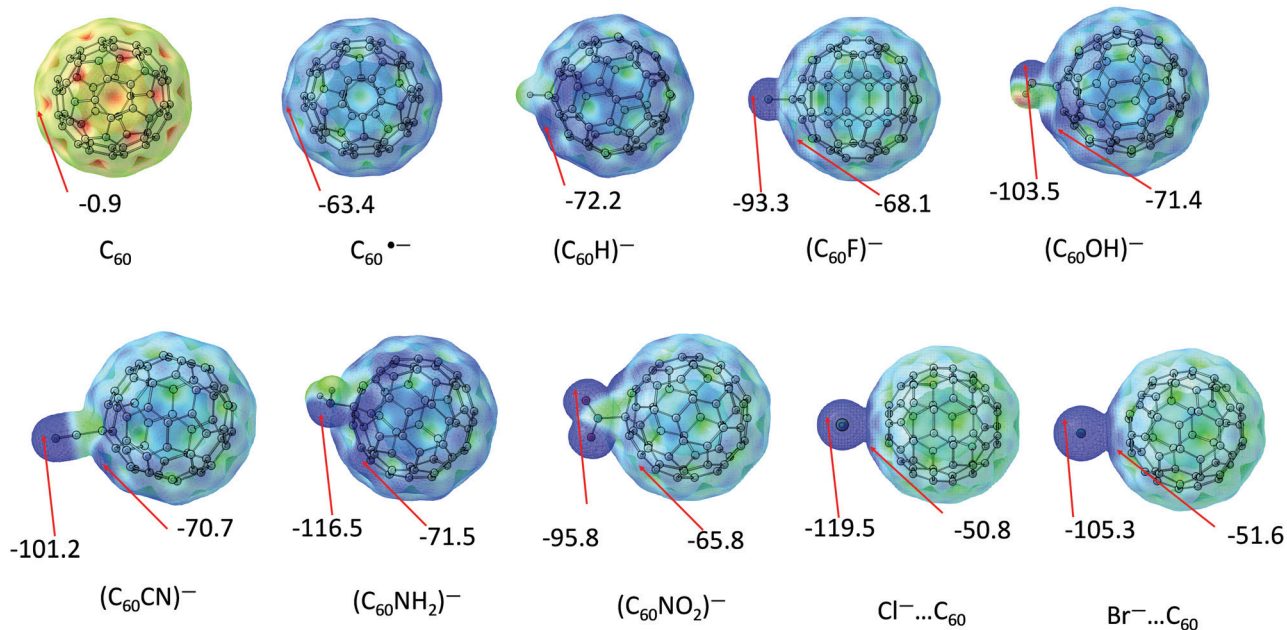

Fig. 4 MESP topographic plots for exohedral fullerides at the M06L/6-311++G(d,p)//M06L/6-31G(d,p) level with the V_{m1} value (kcal mol^{-1}) on the right-hand side and the V_{m2} value (kcal mol^{-1}) on the left-hand side at an isosurface value of 0.01 a.u.

Table 2 Most negative MESP values (in kcal mol^{-1}) for exohedral fullerides at the M06L/6-311++G(d,p)//M06L/6-31G(d,p) level

System	V_{m1}	V_{m2}
$(C_{60}H)^-$	−72.2	—
$(C_{60}F)^-$	−68.1	−93.3
$(C_{60}OH)^-$	−71.4	−103.5
$(C_{60}CN)^-$	−70.7	−101.2
$(C_{60}NH_2)^-$	−71.5	−116.5
$(C_{60}NO_2)^-$	−65.8	−95.8
$Cl^- \cdots C_{60}$	−50.8	−119.5
$Br^- \cdots C_{60}$	−51.6	−105.3

negative ($\sim$54%) than the V_{m2} value observed for the corresponding $(C_{60}X)^-$, while a deviation of, on average, 31% is observed in the V_m data for X = Cl and Br. This feature supports that the excess electron in the system is delocalized over the entire carbon cage of the X-fulleride and it will behave as a large spherical anion. A negative-valued MESP isosurface engulfing the whole carbon cage is located in each X-fulleride (Fig. S3, ESI†), which also illustrates the anionic character of the carbon cage.[63,80]

Energy minimum structures of the $IM^+\cdots(C_{60}X)^-$ ion-pair

The $IM^+\cdots(C_{60}X)^-$ ion-pair systems (X = H, F, CN, OH, NH$_2$ and NO$_2$) show multiple energy minima, wherein the location of the cation is nearly randomized. This indicates that the anionic character is distributed all over the carbon framework of the fulleride and the cation can approach the anion from any direction for a substantial stabilization. A representative case of the $IM^+\cdots(C_{60}OH)^-$ ion-pair is shown in Fig. 5. Among these structures, IM^+ located close to the 'OH' region of $(C_{60}OH)^-$ is found to be the most stable (structure i), with an ion-pair energy value of −72.0 kcal mol^{-1}. However, the least stable structure is the one showing the farthest distance between the OH region and the cation (structure v), with an ion-pair energy value of −59.0 kcal mol^{-1}. The energy difference between the two extreme structures is 13.0 kcal mol^{-1}.
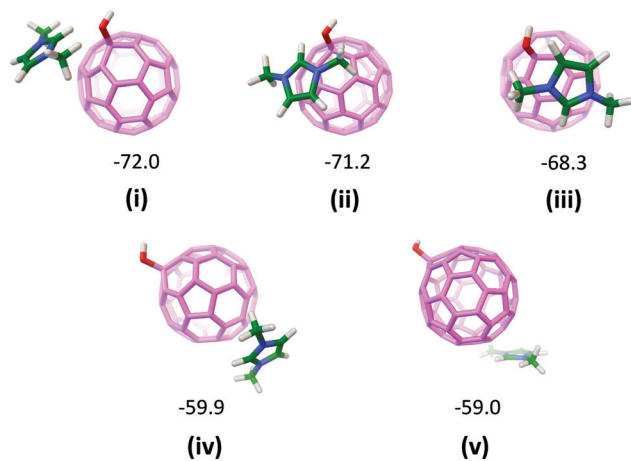

Fig. 5 Geometry of the $IM^+\cdots(C_{60}OH)^-$ ion-pair optimized at the M06L/6-31G(d,p) level with IM^+ at various positions around the fullerene cage. ZPE-corrected ion-pair-binding energies in kcal mol^{-1} are also depicted.

Fig. 6 Geometries of the $IM^+\cdots(C_{60}H)^-$ ion-pair optimized at the M06L/6-31G(d,p) level with IM^+ at various positions around the fullerene cage. ZPE-corrected ion-pair binding energies in kcal mol^{-1} are also depicted.
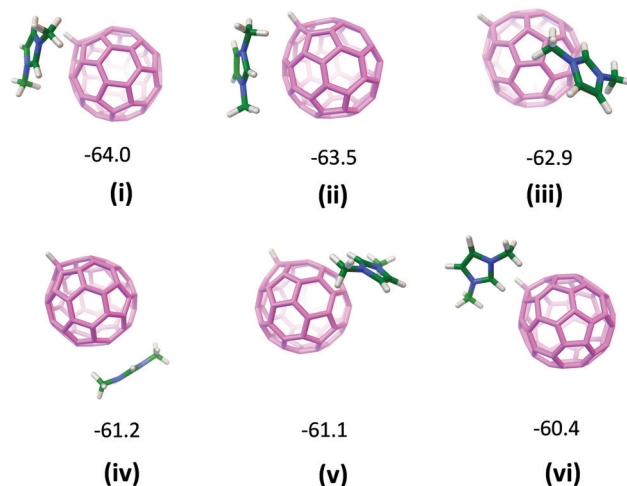
Another representative example of the $IM^+\cdots(C_{60}H)^-$ ion-pair shows six local minima, wherein IM^+ is located at various positions around the fullerene cage. Here, the interaction is also observed to be the best when IM^+ is facing the cage from the direction of H (structure (i) in Fig. 6), which is 3.6 kcal mol^{-1} superior in ion-pair binding than the least stable structure (vi). The positioning of the cation on the fullerene cage is very random and these energetically close lying multiple minima indicate the smooth delocalization of the anionic charge. However, these minima suggest that the movement of the cation from one minimum position to another is nearly barrierless and the whole potential energy surface will behave like a slippery surface. The presence of different minima has been identified in other $IM^+\cdots(C_{60}X)^-$ ion-pair systems as well (Table S4, ESI†). This slippery nature of the ion-pair interactions makes the $IM^+\cdots(C_{60}X)^-$ complexes a suitable candidate for developing ILs for lubricant applications. The viscous nature of the ILs, owing to the large spherical nature of the anion, also supports the ability of the ILs to act as lubricants.

Benchmark study

To analyze the influence of dispersion effects on the ion-pair interactions, we also carried out a benchmark study on the $IM^+\cdots(C_{60}X)^-$ complexes, using dispersion-included methods, *viz.* wB97XD, BP86-D3, M06-2X, and B3LYP-D3, in conjunction with the 6-311++G** basis set. The $E_{ion-pair}$ data computed using these methods are compared with the M06L/6-311++G** data in Table 3. All these dispersion methods show a similar trend in the $E_{ion-pair}$ values. The intrinsic dispersion effects integrated within M06L give results similar to those methods with the dispersion correction, with a slight deviation of 0–4 kcal mol^{-1}. Furthermore, the influence of dispersion effects is brought out from the $E_{ion-pair}$ values calculated at the B3LYP/6-311++G** level, a method without any dispersion correction. At this level, the $E_{ion-pair}$ value ranges from −53.9 to −62.4 kcal mol^{-1}, which is $\sim$15–20% kcal mol^{-1} lower than that observed for the

Table 3 $E_{\text{ion-pair}}$ values (kcal mol^{-1}) for the IM$^+\cdots$(C$_{60}$X)$^-$ complexes using different methods in conjunction with the 6-311++G** basis set

System	wb97XD	BP86-D3	M06-2X	M06L	B3LYP-D3	B3LYP
IM$^+\cdots$(C$_{60}$H)$^-$	−68.3	−68.6	−65.7	−64.5	−66.0	−53.9
IM$^+\cdots$(C$_{60}$F)$^-$	−75.7	−76.1	−72.8	−72.8	−73.9	−61.7
IM$^+\cdots$(C$_{60}$OH)$^-$	−76.1	−76.2	−74.2	−73.3	−73.9	−61.6
IM$^+\cdots$(C$_{60}$CN)$^-$	−74.3	−73.9	−71.9	−70.5	−71.5	−58.3
IM$^+\cdots$(C$_{60}$NH$_2$)$^-$	−78.3	−77.5	−75.6	−73.9	−75.0	−62.4
IM$^+\cdots$(C$_{60}$NO$_2$)$^-$	−75.3	−75.3	−73.8	−71.8	−73.1	−59.1

dispersion-included methods. The high dispersion effect also supports the charge delocalization involved in the interaction between the X-fullerides and IM$^+$. ILs based on conjugated rings or bulkier anions with multiple non-covalent interaction sites are also expected to have a significant contribution from dispersion forces to their $E_{\text{ion-pair}}$ values that clearly influence their thermodynamic and transport properties.[81] The theoretical studies by Bernard *et al.* have illustrated that the ratio of the total ion-pair-binding energy and its dispersion energy component correlates well with the melting point of the IL.[3] The $E_{\text{ion-pair}}$ values for the IM$^+\cdots$(C$_{60}$X)$^-$ complexes are significantly lower in magnitude than those observed for the ion-pairs of imidazolium-based ILs reported in the literature, *viz.*, −80.6, −87.3, −96.3, and −96.9 kcal mol^{-1} for [EMIm]$^+$[trz]$^-$, [EMIm]$^+$[dc]$^-$, [EMIm]$^+$[dtrz]$^-$, and [EMIm]$^+$[NH$_2$tz]$^-$, respectively.[82] The lower $E_{\text{ion-pair}}$ values observed for IM$^+\cdots$(C$_{60}$X)$^-$ and the significant dispersion contribution to the interaction suggest that these ion-pairs are expected to result in the formation of one of the lowest melting-point categories of ILs.[3,81]

Conclusions

DFT analysis of the reaction between C$_{60}$ and IMX, studied at the M06L/6-311++G(d,p)//M06L/6-31G(d,p) level showed the facile formation of the IM$^+\cdots$(C$_{60}$X)$^-$ ion-pair for X = H, F, OH, CN, NH$_2$, and NO$_2$. The reaction showed an exothermic character for X = H, CN, and NH$_2$, while X = F, OH, and NO$_2$ showed an endothermic character. Moreover, among all the reactions studied, a high exergonic nature was observed for X = CN. The energetics of the reaction strongly support the possibility of the development of X-fulleride-based IM$^+\cdots$(C$_{60}$X)$^-$ ion-pair systems. These systems were characterized by significantly lower $E_{\text{ion-pair}}$ values compared with those of the ion-pairs of known ionic liquids.[82] For X = Cl and Br, fulleride formation was not observed as the system remained in the non-covalent state (IM$^+\cdots$X$^-$)$\cdots$C$_{60}$. The benchmark study using different DFT methods, *viz.* wB97XD, BP86-D3, M06-2X, B3LYP-D3, and B3LYP, showed that the results derived using the M06L method are reliable. MESP analysis of all the (C$_{60}$X)$^-$ complexes showed that the excess electron in the system is no longer concentrated on X but is distributed almost evenly over the whole carbon cage. This analysis also supports that the anionic character on X is transferred to the whole fullerene cage, and the X-fulleride system (C$_{60}$X)$^-$ will behave as a large anion. Unlike the (C$_{60}^{\bullet-}$) anion, the closed-shell system (C$_{60}$X)$^-$

is expected to be stable for the development of novel ILs. Furthermore, the anionic nature of the carbon cage is found to be increasing with an increase in the strength of the C–X covalent bonding interaction. This bonding assures that the π-space of the unsaturated 59 carbon atoms is defined by sixty electrons.

The identification of many local minimum structures within a narrow energy range for the IM$^+\cdots$(C$_{60}$X)$^-$ ion-pair indicates a slippery potential energy surface for the system, which also supports that these large spherical anions are useful for the development of highly viscous ILs.[8,83] As per the study by Bernard *et al.*, the low magnitude of the $E_{\text{ion-pair}}$ and its high dispersion contribution propose the formation of low-melting-point ILs for imidazolium-based X-fulleride IM$^+\cdots$(C$_{60}$X)$^-$ systems. We predict that these ILs will show properties that are suitable for designing novel lubricants, halogen-free green ILs and low-melting-temperature materials for space applications.[84–88]

Abbreviations

[EMIm]$^+$ 1-Ethyl-3-methylimidazolium cation
[BMIm]$^+$ 1-Butyl-3-methylimidazolium cation
[dc]$^-$ Dicyanamide
[trz]$^-$ 1,2,4-Triazolate
[dtrz]$^-$ 3,5-Dinitro-1,2,4-triazolate
[NH$_2$tz]$^-$ 5-Aminotetrazolate

Conflicts of interest

There are no conflicts to declare.

Acknowledgements

References

1 P. Wasserscheid and T. Welton, *Ionic liquids in synthesis*, John Wiley & Sons, 2008.
2 K. N. Marsh, J. A. Boxall and R. Lichtenthaler, *Fluid Ph. Equilibria*, 2004, **219**, 93–98.
3 U. L. Bernard, E. I. Izgorodina and D. R. MacFarlane, *J. Phys. Chem. C*, 2010, **114**, 20472–20478.
4 G. Pandey and S. Hashmi, *Bull. Mater. Sci.*, 2013, **36**, 729–733.
5 K. B. Dhungana, L. F. Faria, B. Wu, M. Liang, M. C. Ribeiro, C. J. Margulis and E. W. Castner Jr, *J. Chem. Phys.*, 2016, **145**, 024503.
6 D. Weingarth, I. Czekaj, Z. Fei, A. Foelske-Schmitz, P. J. Dyson, A. Wokaun and R. Koetz, *J. Electrochem. Soc.*, 2012, **159**, H611.

7 M. Marszalek, Z. Fei, D.-R. Zhu, R. Scopelliti, P. J. Dyson, S. M. Zakeeruddin and M. Grätzel, *Inorg. Chem.*, 2011, **50**, 11561–11567.

8 F. Zhou, Y. Liang and W. Liu, *Chem. Soc. Rev.*, 2009, **38**, 2590–2599.

9 M. Galiński, A. Lewandowski and I. Stępniak, *Electrochim. Acta*, 2006, **51**, 5567–5580.

10 I. Kuusik, M. Berholts, J. Kruusma, V. Kisand, A. Tõnisoo, E. Lust and E. Nõmmiste, *RSC Adv.*, 2018, **8**, 30298–30304.

11 I. Kuusik, M. Berholts, J. Kruusma, A. Tõnisoo, E. Lust, E. Nõmmiste and V. Kisand, *RSC Adv.*, 2019, **9**, 33140–33146.

12 J. Garche, C. Dyer, P. Moseley, Z. Ogumi, D. Rand and B. Scrosati, *Encyclopedia of electrochemical power sources*, 2009, vol. 1, pp. 154–155.

13 H. Spohr and G. Patey, *J. Chem. Phys.*, 2008, **129**, 064517.

14 N. Martín, *Chem. Commun.*, 2006, 2093–2104.

15 P. D. Boyd and C. A. Reed, *Acc. Chem. Res.*, 2005, **38**, 235–242.

16 E. Nakamura and H. Isobe, *Acc. Chem. Res.*, 2003, **36**, 807–815.

17 Y. Rubin, S. Khan, D. I. Freedberg and C. Yeretzian, *J. Am. Chem. Soc.*, 1993, **115**, 344–345.

18 R. Taylor and D. R. Walton, *Nature*, 1993, **363**, 685–693.

19 Y. Zhang, D. Wang and W. Wang, *Comput. Theor. Chem.*, 2018, **1128**, 56–59.

20 J. López-Andarias, A. Bauzá, N. Sakai, A. Frontera and S. Matile, *Angew. Chem.*, 2018, **130**, 11049–11053.

21 J. López-Andarias, A. Frontera and S. Matile, *J. Am. Chem. Soc.*, 2017, **139**, 13296–13299.

22 C. Sikorska, *Phys. Chem. Chem. Phys.*, 2016, **18**, 18739–18749.

23 C. Maciel and E. E. Fileti, *Chem. Phys. Lett.*, 2013, **568**, 75–79.

24 G. García, M. Atilhan and S. Aparicio, *J. Phys. Chem. B*, 2014, **118**, 11330–11340.

25 G. García, M. Atilhan and S. Aparicio, *J. Phys. Chem. B*, 2015, **119**, 12224–12237.

26 C. Herrera, R. Alcalde, G. Garcia, M. Atilhan and S. Aparicio, *J. Phys. Chem. C*, 2015, **119**, 27080–27094.

27 G. García, M. Atilhan and S. Aparicio, *J. Phys. Chem. B*, 2015, **119**, 10616–10629.

28 V. Campisciano, V. La Parola, L. F. Liotta, F. Giacalone and M. Gruttadauria, *Chem. – Eur. J.*, 2015, **21**, 3327–3334.

29 V. V. Chaban, C. Maciel and E. E. Fileti, *J. Solution Chem.*, 2014, **43**, 1019–1031.

30 E. E. Fileti and V. V. Chaban, *J. Phys. Chem. Lett.*, 2014, **5**, 1795–1800.

31 S. Osuna, M. Swart and M. Solà, *Phys. Chem. Chem. Phys.*, 2011, **13**, 3585–3603.

32 Y. Wang, D. Tománek and R. S. Ruoff, *Chem. Phys. Lett.*, 1993, **208**, 79–85.

33 J. Cioslowski and K. Raghavachari, *J. Chem. Phys.*, 1993, **98**, 8734–8741.

34 A. A. Popov and L. Dunsch, *Chem. – Eur. J.*, 2009, **15**, 9707–9729.

35 E. D. Jemmis, G. Subramanian, G. N. Sastry, G. Mehta, R. N. Shirsat and S. R. Gadre, *J. Chem. Soc., Perkin Trans. 2*, 1996, 2343–2346.

36 L. Dunsch and S. Yang, *Phys. Chem. Chem. Phys.*, 2007, **9**, 3067–3081.

37 A. Krachmalnicoff, R. Bounds, S. Mamone, S. Alom, M. Concistrè, B. Meier, K. Kouřil, M. E. Light, M. R. Johnson and S. Rols, *Nat. Chem.*, 2016, **8**, 953–957.

38 K. Kurotobi and Y. Murata, *Science*, 2011, **333**, 613–616.

39 E. C. Escudero-Adán, A. Bauzá, L. P. Hernández-Eguía, F. Würthner, P. Ballester and A. Frontera, *CrystEngComm*, 2017, **19**, 4911–4919.

40 X. Wu and X. Lu, *J. Am. Chem. Soc.*, 2007, **129**, 2171–2177.

41 R. E. Estrada-Salas and A. A. Valladares, *THEOCHEM*, 2008, **869**, 1–5.

42 K. Komatsu, M. Murata and Y. Murata, *Science*, 2005, **307**, 238–240.

43 J. Cioslowski and A. Nanayakkara, *J. Chem. Phys.*, 1992, **96**, 8354–8362.

44 A. L. Balch and M. M. Olmstead, *Chem. Rev.*, 1998, **98**, 2123–2166.

45 K. Lee, H. Song and J. T. Park, *Acc. Chem. Res.*, 2003, **36**, 78–86.

46 P. Ravinder and V. Subramanian, *J. Phys. Chem. A*, 2011, **115**, 11723–11733.

47 V. V. Chaban and E. E. Fileti, *Phys. Chem. Chem. Phys.*, 2015, **17**, 15739–15745.

48 N. A. Andreeva and V. V. Chaban, *J. Chem. Thermodyn.*, 2018, **116**, 1–6.

49 V. V. Chaban, E. E. Fileti and T. Malaspina, *Comput. Theor. Chem.*, 2016, **1083**, 7–11.

50 S. Salehzadeh, F. Yaghoobi and M. Bayat, *Comput. Theor. Chem.*, 2014, **1034**, 73–79.

51 Y. Garcia-Rodeja, M. Sola, F. M. Bickelhaupt and I. Fernandez, *Chem. – Eur. J.*, 2017, **23**, 11030.

52 P. Besalú Sala, J. M. Luis Luis and M. Solà i Puig, *Chem. – Eur. J.*, 2020, **26**, 14481–14487.

53 T. D. Della and C. H. Suresh, *Phys. Chem. Chem. Phys.*, 2018, **20**, 24885–24893.

54 S. Anila and C. H. Suresh, *Phys. Chem. Chem. Phys.*, 2021, **23**, 3646–3655.

55 Y. Zhao and D. G. Truhlar, *J. Chem. Phys.*, 2006, **125**, 194101.

56 Y. Zhao and D. G. Truhlar, *Acc. Chem. Res.*, 2008, **41**, 157–167.

57 S. Zahn, D. R. MacFarlane and E. I. Izgorodina, *Phys. Chem. Chem. Phys.*, 2013, **15**, 13664–13675.

58 D. H. Wu and D. G. Truhlar, *J. Chem. Theory Comput.*, 2021, **17**, 3967–3973.

59 M. J. Frisch, G. W. Trucks, H. B. Schlegel, G. E. Scuseria, M. A. Robb, J. R. Cheeseman, G. Scalmani, V. Barone, G. A. Petersson, H. Nakatsuji, X. Li, M. Caricato, A. V. Marenich, J. Bloino, B. G. Janesko, R. Gomperts, B. Mennucci, H. P. Hratchian, J. V. Ortiz, A. F. Izmaylov, J. L. Sonnenberg, D. Williams-Young, F. Ding, F. Lipparini, F. Egidi, J. Goings, B. Peng, A. Petrone, T. Henderson, D. Ranasinghe, V. G. Zakrzewski, J. Gao, N. Rega, G. Zheng, W. Liang, M. Hada, M. Ehara, K. Toyota, R. Fukuda, J. Hasegawa, M. Ishida, T. Nakajima, Y. Honda, O. Kitao, H. Nakai, T. Vreven, K. Throssell,

J. A. Montgomery Jr., J. E. Peralta, F. Ogliaro, M. J. Bearpark, J. J. Heyd, E. N. Brothers, K. N. Kudin, V. N. Staroverov, T. A. Keith, R. Kobayashi, J. Normand, K. Raghavachari, A. P. Rendell, J. C. Burant, S. S. Iyengar, J. Tomasi, M. Cossi, J. M. Millam, M. Klene, C. Adamo, R. Cammi, J. W. Ochterski, R. L. Martin, K. Morokuma, O. Farkas, J. B. Foresman and D. J. Fox, *Gaussian 16 Rev. A.03*, Gaussian, Inc., Wallingford CT, 2016.

60 K. Remya and C. H. Suresh, *J. Comput. Chem.*, 2013, **34**, 1341–1353.

61 S. Grimme, *J. Comput. Chem.*, 2006, **27**, 1787–1799.

62 S. Grimme, J. Antony, S. Ehrlich and H. Krieg, *J. Chem. Phys.*, 2010, **132**, 154104.

63 S. R. Gadre and R. N. Shirsat, *Electrostatics of atoms and molecules*, Universities Press, 2000.

64 P. Politzer and D. G. Truhlar, *Chemical applications of atomic and molecular electrostatic potentials: reactivity, structure, scattering, and energetics of organic, inorganic, and biological systems*, Springer Science & Business Media, 2013.

65 J. S. Murray and K. Sen, *Molecular electrostatic potentials: concepts and applications*, Elsevier, 1996.

66 S. R. Gadre and R. K. Pathak, *Nonexistence of local maxima in molecular electrostatic potential maps*, 1990.

67 S. R. Gadre and P. K. Bhadane, *Resonance*, 1999, **4**, 8–19.

68 J. S. Murray and P. Politzer, *Wiley Interdiscip. Rev.: Comput. Mol. Sci.*, 2017, **7**, 1326.

69 P. Politzer, P. R. Laurence and K. Jayasuriya, *Environ. Health Perspect.*, 1985, **61**, 191–202.

70 E. Espinosa, C. Lecomte, N. Ghermani, J. Devemy, M. Rohmer, M. Bénard and E. Molins, *J. Am. Chem. Soc.*, 1996, **118**, 2501–2502.

71 S. R. Gadre, C. H. Suresh and N. Mohan, *Molecules*, 2021, **26**, 3289.

72 T. Keith, *TK Gristmill Software*, Overland Park, KS, 2014.

73 R. Parthasarathi, V. Subramanian and N. Sathyamurthy, *J. Phys. Chem. A*, 2006, **110**, 3349–3351.

74 S. J. Grabowski, *J. Phys. Chem. A*, 2001, **105**, 10739–10746.

75 R. F. Bader, *Atoms in molecules: a quantum theory, International series of monographs on chemistry*, Oxford University Press, Oxford, 1990, vol. 22.

76 M. Jabłoński and M. Palusiak, *J. Phys. Chem. A*, 2010, **114**, 2240–2244.

77 Á. M. Pendás and C. Gatti, in *3 Quantum theory of atoms in molecules and the AIMAll software*, ed. G. Simon, De Gruyter, 2021, pp. 43–74.

78 G. Saleh, D. Ceresoli, G. Macetti and C. Gatti, *Computational Materials Discovery*, 2018, pp. 117–175.

79 S. Anila and C. H. Suresh, *Phys. Chem. Chem. Phys.*, 2021, **23**, 13662–13671.

80 S. Anila and C. H. Suresh, *Phys. Chem. Chem. Phys.*, 2019, **21**, 23143–23153.

81 E. I. Izgorodina, D. Golze, R. Maganti, V. Armel, M. Taige, T. J. Schubert and D. R. MacFarlane, *Phys. Chem. Chem. Phys.*, 2014, **16**, 7209–7221.

82 E. Thomas, K. P. Vijayalakshmi and B. K. George, *RSC Adv.*, 2015, **5**, 71896–71902.

83 S. Seki, T. Kobayashi, Y. Kobayashi, K. Takei, H. Miyashiro, K. Hayamizu, S. Tsuzuki, T. Mitsugi and Y. Umebayashi, *J. Mol. Liq.*, 2010, **152**, 9–13.

84 M. Cai, Q. Yu, W. Liu and F. Zhou, *Chem. Soc. Rev.*, 2020, **49**, 7753–7818.

85 C. Ye, W. Liu, Y. Chen and L. Yu, *Chem. Commun.*, 2001, 2244–2245.

86 G. Mordukhovich, J. Qu, J. Y. Howe, S. Bair, B. Yu, H. Luo, D. J. Smolenski, P. J. Blau, B. G. Bunting and S. Dai, *Wear*, 2013, **301**, 740–746.

87 Y. Xia, Z. Wang and Y. Song, *Ind. Lubr. Tribol.*, 2014, **66**, 443–451.

88 N. Dörr, A. Merstallinger, R. Holzbauer, V. Pejaković, J. Brenner, L. Pisarova, J. Stelzl and M. Frauscher, *Tribol. Lett.*, 2019, **67**, 1–18.

RESEARCH ARTICLE

Journal of COMPUTATIONAL CHEMISTRY   **WILEY**

Fulleride-metal η^5 sandwich and multi-decker sandwich complexes: A DFT prediction

Sebastian Anila[1,2] | Cherumuttathu H. Suresh[1,2] [iD]

[1]Chemical Sciences and Technology Division, CSIR − National Institute for Interdisciplinary Science and Technology, Thiruvananthapuram, Kerala, India

[2]Academy of Scientific and Innovative Research (AcSIR), Ghaziabad, India

Correspondence
Cherumuttathu H. Suresh, Chemical Sciences and Technology Division, CSIR − National Institute for Interdisciplinary Science and Technology, Thiruvananthapuram, Kerala 695 019, India.
Email: sureshch@niist.res.in and sureshch@gmail.com

Abstract

The $(C_{60}CN)^-$ formed by the reaction of CN^- with fullerene shows high electron rich character, very similar to $C_{60}^{\cdot-}$, and it behaves as a large anion. Similar to Cp^-, the bulky anion, $(C_{60}CN)^-$, acts as a strong η^5 ligand towards transition metal centers. Previous studies on η^5 coordination of fullerene cage are reported for pseudo fullerenes whereas the present study deals with sandwich complexes of $(C_{60}CN)^-$ with Fe(II), Ru(II), Cr(II), Mo(II), and Ni(II) and multi-decker sandwich complexes of CN–fullerides with Fe(II). The structural parameters of these complexes and the corresponding Cp^- complexes showed very close resemblance. Analysis of the metal-to-carbon bonding molecular orbitals showed that sandwich complex $[Fe(η^5\text{-}(C_{60}CN)^-)_2]$ exhibit bonding features very similar to that of ferrocene. Also, a 6-fold decrease in the band gap energy is observed for $[Fe(η^5\text{-}(C_{60}CN)^-)_2]$ compared to ferrocene. The energy of dissociation (ΔE) of the ligand $(C_{60}CN)^-$ from $[Fe(η^5\text{-}(C_{60}CN)^-)_2]$ is slightly lower than the ΔE of a Cp* ligand from a ferrocene derivative wherein each cyclopentadienyl unit is substituted with four tertiary butyl groups. The $(C_{60}CN)^-$ ligand behaved as one of the bulkiest ligands in the chemistry of sandwich complexes. Further, the coordinating ability of the dianion, $(C_{60}(CN)_2)^{2-}$ is evaluated which showed strong coordination ability simultaneously with two metal centers leading to the formation of multi-decker sandwich and pearl-necklace type polymeric structures.

KEYWORDS
anionic fullerides, DFT calculations, multi-decker sandwich complexes, polymeric sandwich complexes, sandwich complexes, η^5 coordination

1 | INTRODUCTION

Independent researches by Pauson and Kealy and by Miller and co-workers led to the accidental discovery of the biscyclopentadienyl complex of iron, $[Fe(C_5H_5)_2]$, called ferrocene,[1,2] which established the concept of pπ–dπ complexes.[3] The electronic structure of ferrocene was solved independently by Fischer[4] and Woodward and Wilkinson[5,6] as a 6d-electron Fe(II) atom sandwiched between a pair of 6π-electron aromatic pentagonal carbon arrays (cyclopentadienyl anion = Cp^-).[7] The X-ray crystallography by Eiland and Pepinski confirmed the sandwich-type configuration of ferrocene.[8] Later Dunitz

and Orgel explained the high stability of ferrocene with molecular orbital theory.[9] This discovery of ferrocene opened up a completely new gateway to the organometallic chemistry of sandwich complexes, commonly known as metallocenes.[10–12] The applications of metallocenes are based on their behavior as reducing agents, antioxidants, and as excellent organic carriers of iron in high concentration and are also used as a catalyst for various organic reactions.[13]

The tuning of the properties of sandwich complexes is achieved through modifying the Cp^- ligand by different alkyl substitution resulting to the synthesis of various bulky sandwich complexes.[14–16] Further, the five membered ring of a fullerene cage has been

considered as a replacement for Cp⁻ ligand for developing new set of sandwich complexes. Ravinder and Subramanian reported a DFT study on the structure and stability of fullerene based endohedral sandwich complexes.[17] Previous theoretical studies predicted the formation of Cp-type π-complexes of fullerene derivatives, for example, the fullerene analogue of ferrocene, bis(η^5-fullerenyl-R$_5$)Fe.[18–22] Here "R" substituted five α-carbon centers around the five-membered ring were saturated which created pure Cp⁻ character and such modified fullerene derivatives are known as "pseudo fullerenes."[23] Nakamura group gave an experimental validation for the existence of ferrocene-type singlet ground state configurations of η^5-pseudo fullerene complexes of Fe(II), Ru(II).[24–29] They also synthesized group 6 metal complexes of the η^5-pentamethyl[60]fullerene.[30] Muhammad et al.[31] theoretically studied the diradical character and nonlinear optical properties of buckyferrocenes by suitably modifying the pseudo fullerene fragments.

All the studies on sandwich complexes developed with fullerene derivatives have utilized a five-membered ring surrounded with saturated carbon centers for η^5 coordination whereas a ferrocene analogue of fullerene C$_{60}$ is not yet reported. Although C$_{60}$ is capable of forming compounds in various coordination forms such as η^2, η^3, η^4, η^5, and η^6, most of the experimental studies were focused on the η^2 mode of coordination towards the metal. Owing to the conjugated π-electron cloud, a simple η^5 coordination from five-membered ring or η^6 coordination from six-membered ring appeared difficult which can be attributed to the electron deficient character of the fullerene cage. The unique properties of fullerene such as low reduction potentials and strong electron acceptor nature make it a potential source of new materials or chemotherapeutic agents.[32–37] This has instigated several theoretical[38–44] and experimental[45–47] studies on endohedral[39,48–50] as well as exohedral[51–54] modifications on the fullerene cage to generate the new materials of interest.[55–58]

Shortly after the bulk synthesis of C$_{60}$, different kinds of fullerene polymers have been synthesized, including the so-called "pearl necklace", or main-chain, structures, in which the fullerene molecules are joined together with short bridging groups, and the "charm bracelet", or side-chain, polymers, where the fullerenes dangle from the backbone of existing polymers.[59–61] Organometallic C$_{60}$ polymers was an area of significant interest and in 1992 Nagashima and co-workers synthesized the first example of such a polymer with pearl-necklace structure.[62,63] Recently, Leng et al.[64] have reported spontaneously self-assembled -C$_{60}$-Ru-C$_{60}$- polymeric chains as spherical particles. Their DFT calculations showed that the metal Ru exhibited the η^2 to η^6 modes of coordination with the C$_{60}$ and the stable configuration was observed to possess the η^2 mode of coordination and a stabilization of 86 kcal/mol was observed for C$_{60}$-Ru-C$_{60}$. Organometallic C$_{60}$ polymers may have potential applications in catalysis,[63] electrochemistry,[65] and other areas.[66] The extended sandwich structures (triple-deckers, tetra-deckers, etc.) containing d-transition metals are well established and literature also gives reports on the multi-decker sandwich complexes of f-elements with sterically demanding ligands.[67–69] However, such multi-decker sandwich complexes containing fulleride ligands are not reported yet.

Recently, in a study using the M06L/6-311++G(d,p)//M06L/6-31G(d,p) level of DFT, we have shown that both endohedral and exohedral chloro-fullerides act as an η^5 ligand similar to Cp⁻ with cationic transition metal fragments.[70] This study also revealed that in comparison to the simple C$_{60}$, the chloro-fullerides act as bulky anionic ligands in η^5 or η^6 mode of coordination. The binding energy observed for the complexes of chloro-fullerides (110–160 kcal/mol) was twice than that of the complexes formed by C$_{60}$ (50–90 kcal/mol). The encapsulation of an anion in the fullerene cage is very difficult to accomplish while the exohedral modification of fullerene cage has been found to be a possible way to obtain the anionic fullerene derivatives. Very recently, DFT studies predicted the exothermic formation of anionic exohedral fullerides (X-fullerides, X = H, F, OH, CN, NH$_2$, and NO$_2$) from C$_{60}$ and an X-substituted imidazolium (IMX) compound.[71] The X-fullerides showed the delocalised distribution of the extra electron on the fullerene cage. As a result, compared to fullerene, the C$_{60}$ cage of fulleride showed high electron rich character very similar to C$_{60}$ anion. Further, the proposed mechanism of formation IM$^+$(C$_{60}$X)$^-$ ion-pairs from C$_{60}$ and 1,3-dimethyl-2X-imidazole (IMX) supported the formation of low melting imidazolium-fulleride ionic liquids. Among the different reactions, the formation of IM$^+$(C$_{60}$CN)$^-$ was the most exergonic. Considering the electron rich character of the X-fullerides, here we explore the η^5 coordination tendency of them towards the formation of sandwich complexes. The (C$_{60}$CN)$^-$ is selected as the η^5 ligand for different transition metals viz. Fe, Ru, Cr, Mo, and Ni. Further, (C$_{60}$(CN)$_2$)$^{2-}$ dianion species is considered for developing extended structures of fulleride-sandwich complexes.

2 | COMPUTATIONAL METHODS

All calculations have been carried out at the M06L/6-311++G(d,p)//M06L/6-31G(d,p) level of density functional theory[72–74] using the Gaussian16 suite of programs.[75] M06L functional has been suggested as the best method in overall performance for organometallic, and noncovalent interactions.[72] Previous extensive benchmark study by Remya and Suresh showed that M06L method is a robust method for calculating the structure and energetics of even very weakly interacting complexes with accuracy close to CCSD.[76] Recently our group has benchmarked the accuracy of the method for Grimme's dispersion correction[77,78] in calculating the interaction energy of anionic fullerene systems.[79] The vibrational frequency analysis has been done to confirm the optimized geometries as the true energy minima. The energy required to dissociate one of the ligands from the sandwich complex (ΔE) is calculated using the supermolecule approach.

$$\Delta E = E_3 - (E_1 + E_2) \qquad (1)$$

where, E_1, E_2, and E_3 stand for the zero-point energy (ZPE)-corrected energy of the organometallic fragment, (C$_{60}$CN)$^-$ and sandwich complex, respectively. Here the ZPE-correction obtained from M06L/6-31G(d,p) level is added to the single point energy calculated

at M06L/6-311++G(d,p) level. The free energy change (ΔG) associated with the reaction is also calculated in a similar fashion.

$$\Delta G = G_3 - (G_1 + G_2) \quad (2)$$

where, G_1, G_2, and G_3 stand for corrected free energy of the organometallic fragment, $(C_{60}CN)^-$ and sandwich complex, respectively.

Molecular electrostatic potential (MESP) analysis has been widely used to quantitatively asses the electron rich/deficient features, charge transfer character, nucleophilic and electrophilic reactivity, substituent effect, and so forth of molecules.[80–84] Anionic systems show high negative MESP values and they always exhibit a directional negative valued minimum along any arbitrary direction.[85,86] MESP topology analysis is performed on ligands and complexes to locate their most negative-valued point, a (3, +3) critical point, also known as V_{min}.[84]

Bader's quantum theory of atoms in molecules (QTAIM) analysis, based on the electron density (ρ) distribution is carried out by locating (3, −1) bond critical points (BCPs) between interacting atoms using AIMAll package.[87–89] Atom–atom interactions could be characterized as covalent or noncovalent, based on the electron densities at the respective BCPs (ρ_b) as well as from the sign of the corresponding Laplacian ($\nabla^2\rho$). Further, natural bond orbitals (NBO) analysis, as implemented in Gaussian 16 is used for understanding the charge transfer from ligand to metal center.[90,91] NBO attempts to connect the numerical content of wave function with concepts of bonding theory.[92]

3 | RESULTS AND DISCUSSIONS

Figure 1 shows the optimized geometries of the sandwich complexes of Fe(II) viz. $[Fe(\eta^5-Cp)_2]$, $[Fe(\eta^5-C_5(t-Bu_3)_2]$, $[Fe(\eta^5-(C_{60}CN)^-)(\eta^5-Cp)]$ and $[Fe(\eta^5-(C_{60}CN)^-)_2]$ which are labeled as 1, 2, 3, and 4, respectively with the shortest Fe–C distance (d_1) and longest Fe–C distance (d_2) with each ligand in Å. The stable conformation of the ferrocene molecule has the Cp^- rings in the eclipsed configuration[93] with the average Fe–C bond length of 2.01 Å and a distance of 1.60 Å is observed between the Fe atom and center of the Cp^- ring (d_3) which are in agreement with the experimental values.[94,95] In the $[Fe(\eta^5-C_5(t-Bu)_3)_2]$ complex, three H atoms on each Cp^- ring is substituted with bulky tertiary butyl (t-Bu) groups. This bulky ferrocene derivative has d_3 1.65 Å which is comparable with the experimental observation.[96] This increase in the Fe–C bond length and Fe–Cp^- distance (d_3) is due to steric influence from the bulky substituents on the Cp ring. The replacement of one of the Cp^- with $(C_{60}CN)^-$ gives the hybrid complex 3, with d_3 1.59 Å towards Cp^- ligand, is very similar to that of the ferrocene molecule while d_3 1.65 Å towards the fulleride indicates that this ligand is bulkier than the $C_5(t-Bu)_3$ ligand. As observed in the case of the ferrocene, the pentagonal ring of the $(C_{60}CN)^-$ unit is in eclipsed conformation with the Cp^- ligand. Replacement of both the Cp^- rings with two $(C_{60}CN)^-$ units gives the complex 4, with d_3 1.66 Å. These results confirm that the sandwich complexes of $(C_{60}CN)^-$ with Fe(II) is analogues to ferrocene.

The energy required to dissociate one of the Cp^- ligands (ΔE) from complex 1 is −237.9 kcal/mol whereas the same observed for the $C_5(t-Bu)_3$ ligand is −192.8 kcal/mol (Figure 1). The ΔE for the $(C_{60}CN)^-$ ligand in the complexes 3 and 4 is −151.8 and −145.8 kcal/mol, respectively. The lower range of ΔE for the fulleride complexes can be attributed to the bulky nature of the fulleride ligand; in fact, the data support it as one of the bulkiest ligands in organometallic chemistry. Hence we also studied the ferrocene derivative of tetra substituted Cp^- ligand, 5, $[Fe(\eta^5-C_5(t-Bu)_4)_2]$. A penta-substitution on the Cp^- ring with t-Bu appears was not possible due to spatial congestions from several methyl groups. Though the structural parameters of complex 5 is not available in the literature, the DFT study has shown that the d_3 is 1.69 Å and the ΔE −159.7 kcal/mol is very close to that of the complexes 3 and 4.

We also studied the η^6 coordination of the $(C_{60}CN)^-$ ligand in the complex 3 and 4 (Figure S3 and Table S5). The slightly inferior ΔE values −137.1 and −130.0 kcal/mol, respectively for the complex 3 and 4 in η^6 coordination clearly illustrates the preference for the η^5 coordination in sandwich complexes.

3.1 | MESP analysis

The electron rich sites characterized by (3, +3) critical points are often referred as MESP minimum, V_{min} (Table S3). Figure 2 gives the MESP plots and V_{min} values of the ligands Cp^-, $(C_5(t-Bu)_3)^-$, $(C_{60}CN)^-$, and

$Fe(\eta^5-C_5H_5)_2$
$\Delta E = -237.9$ kcal/mol

1

$Fe(\eta^5-C_5(t-Bu)_3)_2$
$\Delta E = -192.8$ kcal/mol

2

$Fe(\eta^5-C_5H_5)(\eta^5-C_{60}CN^-)$
$\Delta E = -151.8$ kcal/mol

3

$Fe(\eta^5-C_{60}CN^-))_2$
$\Delta E = -145.8$ kcal/mol

4

$Fe(\eta^5-C_5(t-Bu)_4)_2$
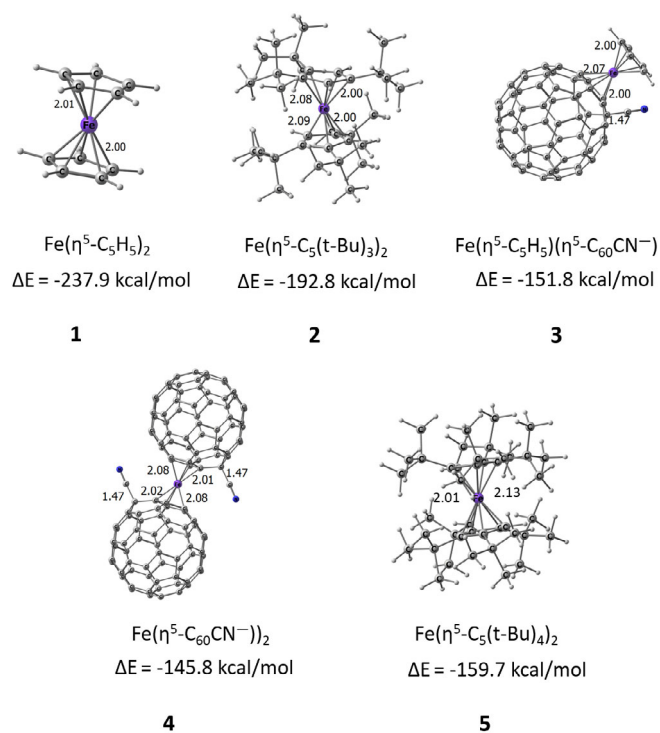$\Delta E = -159.7$ kcal/mol

5

FIGURE 1 Optimized geometries of the sandwich complexes with their bond lengths in Å unit at M06L/6-31G(d,p) level. The ligand dissociation energy ΔE of these complexes, at M06L/6-311++G (d,p)//M06L/6-31G(d,p) level, is also depicted in kcal/mol
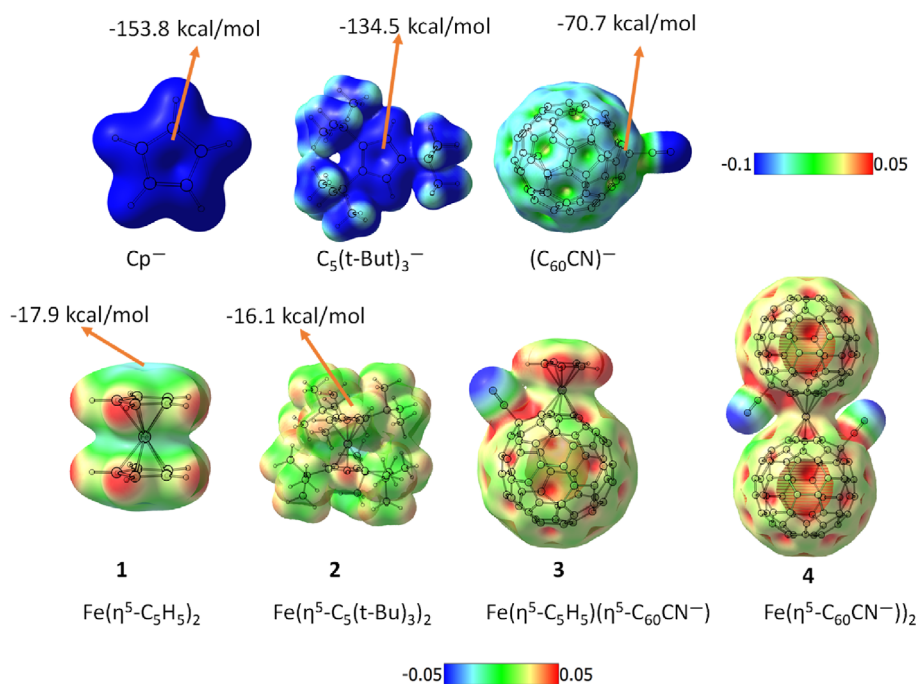
FIGURE 2 MESP of ligands and complexes plotted on isodensity surface 0.005 au, at M06L/6-311++G(d,p)//M06L/6-31G(d,p) level DFT. MESP value at a (3, +3) critical point, V_{min} is also depicted. MESP, molecular electrostatic potential

their sandwich complexes viz. **1**, **2**, **3**, and **4**. Both Cp^- ligand and $(C_5(t\text{-}Bu)_3)^-$ show high negative V_{min} (intense blue region) over the five-membered ring whereas $(C_{60}CN)^-$ shows lower magnitude for V_{min} which can be attributed to the delocalization of the extra electron over the 59 sp^2 hybridized carbon centers. The electron delocalization feature is also displayed using the minimum value of MESP that engulfs the whole anion (Figure S6).[85] Up on coordination with the metal center, a drastic reduction in the magnitude of negative MESP occurs for both Cp^- and $(C_5(t\text{-}Bu)_3)^-$ in the corresponding metallocenes while $(C_{60}CN)^-$ show only positive potential (except for the lone pair region of CN unit). The observed change in MESP can be attributed to the strong electron donating η^5-coordination of the ligands with the metal center which leads to charge transfer from the ligand to the metal. The five-membered ring adjacent to the CN substitution is identified as the most strongly coordinating η^5-region due to the appearance of the highest negative MESP features over there.

The NBO natural charge observed for Fe(II) center is −0.52, −0.42, −0.40, −0.29 and −0.28 for **1**, **2**, **3**, **4**, and **5**, respectively (Table S4). This data suggests that the charge transfer is maximum in ferrocene while both fulleride-sandwich complex **4** and the highly substituted ferrocene derivative **5** show similar but diminished charge transfer features which can be attributed to the high steric effect in both the cases.

3.2 | Molecular orbital analysis

A few important bonding molecular orbitals (MOs) of the sandwich compounds, ferrocene and **4,** are given in Figure 3. The MO diagram shows the significant "d"-orbital nature of the typical doubly degenerate HOMO (HOMO$_a$ and HOMO$_b$) for ferrocene. The HOMO-2 orbital also shows high "d" orbital character with

minimum interactions from the Cp^- ligands. Significant overlap between Cp^- orbitals is seen in the degenerate HOMO-3$_a$ and HOMO-3$_b$ and they represent the pπ-pπ interactions in ferrocene. The degenerate HOMO-5$_a$ and HOMO-5$_b$ represent the dπ–pπ interactions between metal and ligand orbitals.

In comparison with ferrocene, a similar case of bonding scenario is observed in complex **4** as well, but the energy levels show significant variations which can be attributed to the bulky nature and lower symmetry of the $(C_{60}CN)^-$ than Cp^- ligand. The HOMO of **4** has high metal "d" orbital character and it resembles to the HOMO-2 of ferrocene. This MO is more stabilized in **4** than ferrocene. The HOMO-2 and HOMO-6 of **4** are similar to the degenerate HOMO$_a$ and HOMO$_b$ of ferrocene and are more stabilized in **4**. The orbitals HOMO-7, HOMO-8, HOMO-9, and HOMO-10 are analogous to HOMO-3$_a$, HOMO-3$_b$, HOMO-5$_a$, and H-5$_b$ of ferrocene, respectively. Though the bonding features appear to be similar in these four MOs, they are slightly destabilized in comparison with that of ferrocene. The LUMO of ferrocene is at 0.95 eV which makes the HOMO–LUMO band gap at 3.54 eV. In complex **4**, LUMO appears at −4.71 eV which indicates high stabilization, resulting to a very low band gap 0.55 eV. The lower band gap exhibited by fulleride sandwich complex than ferrocene can be attributed the weaker interactions between the ligands arising from their steric effects.[22] Compared to ferrocene, **2** and **5** also show lower band gap, 3.09 and 2.54 eV, respectively.

3.3 | QTAIM analysis

The nature of coordination of fulleride with metal is confirmed from the QTAIM BCP analysis (Figure S1). The BCPs of the Fe–C bonding interactions show positive Laplacian of electron density ($\nabla^2\rho$) values
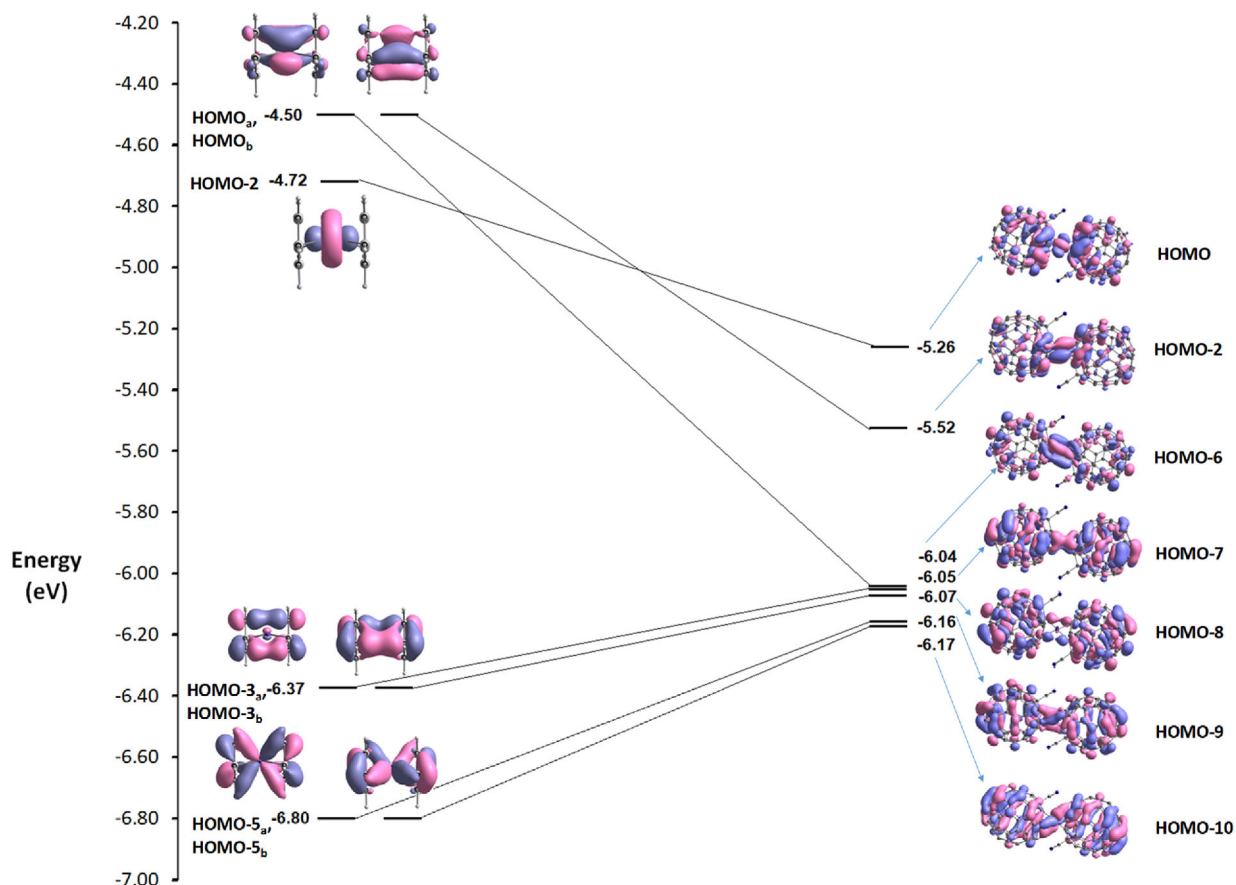
FIGURE 3 Molecular orbital correlation diagram for ferrocene (left, isosurface = 0.04 au) and complex **4** (isosurface = 0.015 au), at M06L/6-311++G(d,p)//M06L/6-31G(d,p) level DFT

while negative values are observed for total electron energy density (H) (Table S2). Thus these interactions can be considered as closed shell interactions with partial covalent nature.[97]

Previous studies analyzed the bonding in ferrocene and different derivatives of it for understanding the contributions of electrostatic.

and covalent interactions.[93,98,99] Frenking et al. showed that the Fe–C bonding interactions in ferrocene is from 53% to 58% electrostatic attraction and the rest is from covalent interactions. The $\nabla^2\rho$ plots in Figure 4 and also those given in Figure S2 show that the Fe–C bonding interactions in both ferrocene and fulleride-sandwich complexes are very similar. The red to blue variation in $\nabla^2\rho$ plot indicates the noncovalent to covalent changes in the bonding interactions. As observed from the ρ and $\nabla^2\rho$ values, the strength of the Fe–C bonding interactions in complex **4** is slightly weaker than that of **1** (Figure 4 and Figure S2), which is reflected in the more intense red region in the $\nabla^2\rho$ plot of **1** than **4**. Also the H values show the most negative character in the complex **1**, and it decreases in the order **1**, **2**, **3**, **5**, and **4**. Hence, compared to ferrocene a reduced degree of covalent character is expected in the case of fulleride-sandwich complex **4**, which can be attributed to the high steric effects from the fulleride ligand.
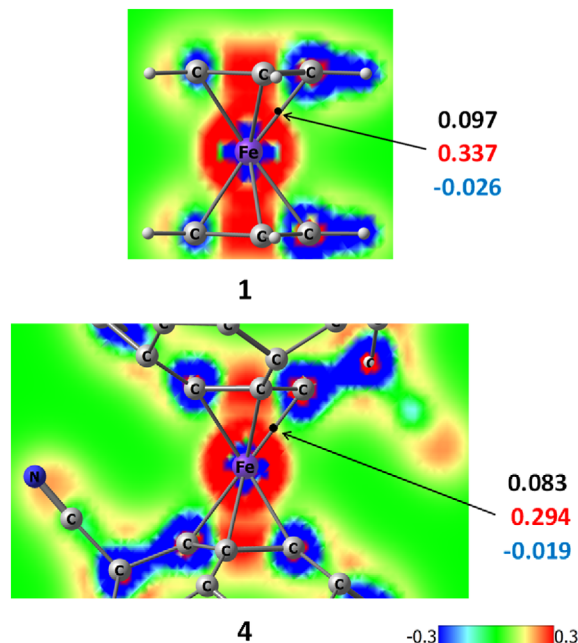

FIGURE 4 $\nabla^2\rho$ values plotted on a plane passing through one of the Fe–C bond for complexes **1** and **4**. The BCP for the Fe–C bonding is indicated with ρ (black), $\nabla^2\rho$ (red) and H (blue) values in au. BCP, bond critical point
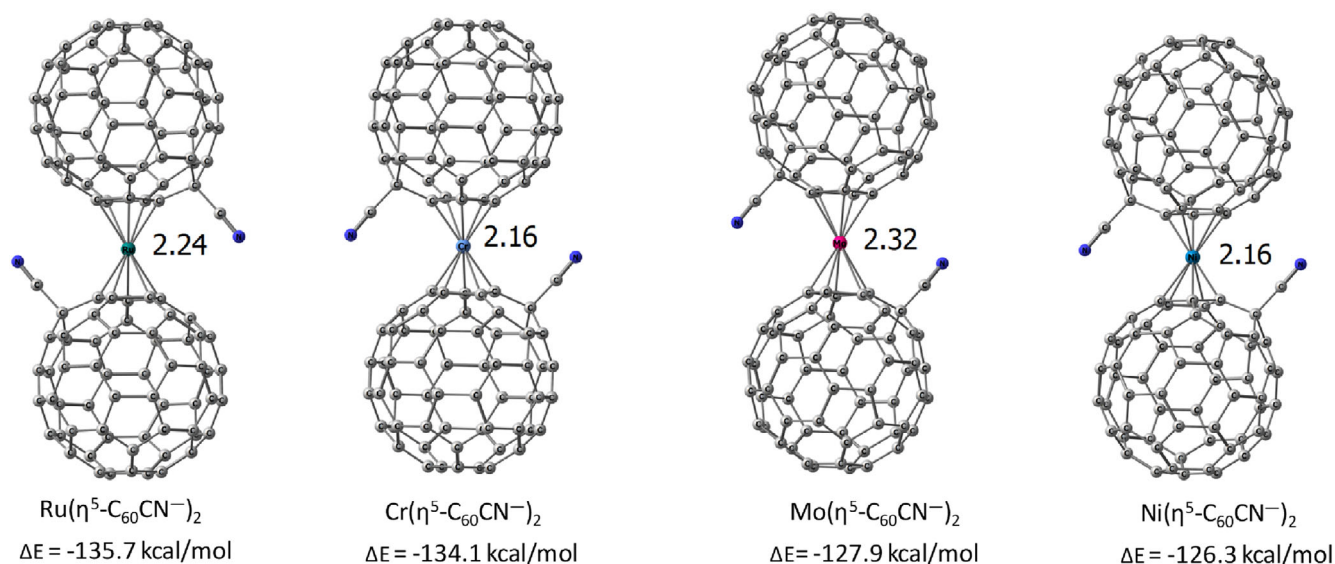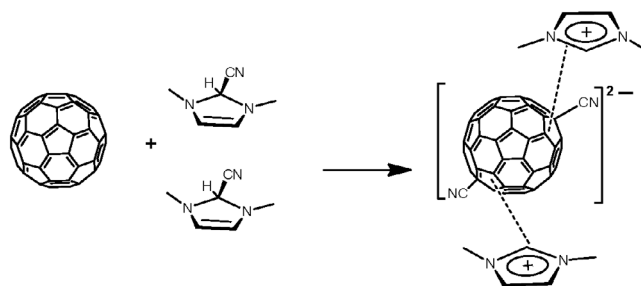
FIGURE 5 Optimized geometries of the sandwich complexes of Ru(II), Cr(II), Mo(II), and Ni(II) with the shortest metal—C bond length in Å unit at M06L/6-31G(d,p) level. The ΔE values at M06L/6-311++G(d,p)//M06L/6-31G(d,p) level are also depicted in kcal/mol

SCHEME 1 Reaction of C_{60} with IMCN to give dianionic fulleride

3.4 | Sandwich complexes of other metals

Similar to ferrocene, Ru(II) also gives the stable 18 electron sandwich complex Ru(η^5-($C_{60}CN$)$^-$)$_2$ (Figure 5) with an average Ru–C bond length 2.24 Å which is higher than the corresponding value 2.19 Å in ruthenocene (Figure S4 and Table S6).[100] For Cr(II) and Mo(II), the sandwich complexes exhibit 16-electron configuration with average metal-carbon distance 2.16 and 2.32 Å, respectively which agree well with the corresponding experimental values of their Cp$^-$ complex.[101,102] Experimental studies show that Cp$^-$ complexes of Mo(II) often undergoes either further coordination with additional two ligands (Cl$^-$ or H$^-$) or dimerizes to a stable 18-electron configuration. Here the bulky fulleride ligands may prevent the metal centers from further coordination to yield the 16-electron complex. In the case of Ni(II), the [Ni(η^5-($C_{60}CN$)$^-$)$_2$] complex has 20-electron configuration with average Ni–C distance 2.16 Å which is in good agreement with the corresponding Cp$^-$ complex.[103]

The energy required to dissociate of one ($C_{60}CN$)$^-$ ligand from the sandwich complex (ΔE) is calculated for each case (Figure 5 and

Table S1).The ΔE of [Ru(η^5-($C_{60}CN$)$^-$)$_2$] is found to be -135.7 kcal/mol which is 10 kcal/mol lower than that of Fe-complex **4**. The decrease in the magnitude of ΔE can be attributed to the slightly inferior Ru–C interactions owing to the larger size of the Ru atom. Similarly, the ΔE value of Cr(II) complex is higher in magnitude than that of Mo(II) by about 6 kcal/mol. The 20-electron fulleride-sandwich complex, [Ni(η^5-($C_{60}CN$)$^-$)$_2$] has ΔE -126.3 kcal/mol, which indicates that Ni–C interactions are slightly weaker than those in 16- and 18-electron complexes. Similar to the Fe(II) complexes, these complexes also prefer the η^5 coordination mode over the η^6. For instance Cr(η^5-($C_{60}CN$)$^-$)$_2$ is more stable than the corresponding η^6 complex by 11.1 kcal/mol (Figure S5).

3.5 | Multi-decker sandwich complexes

The exohedral addition of two CN$^-$ to the fullerene cage can create a dianion ((C_{60}(CN)$_2$)$^{2-}$). The energetics of the reaction of two molecules of 1,3-dimethyl-2,3-dihydro-2-cyano-imidazole (IMCN) and C_{60}
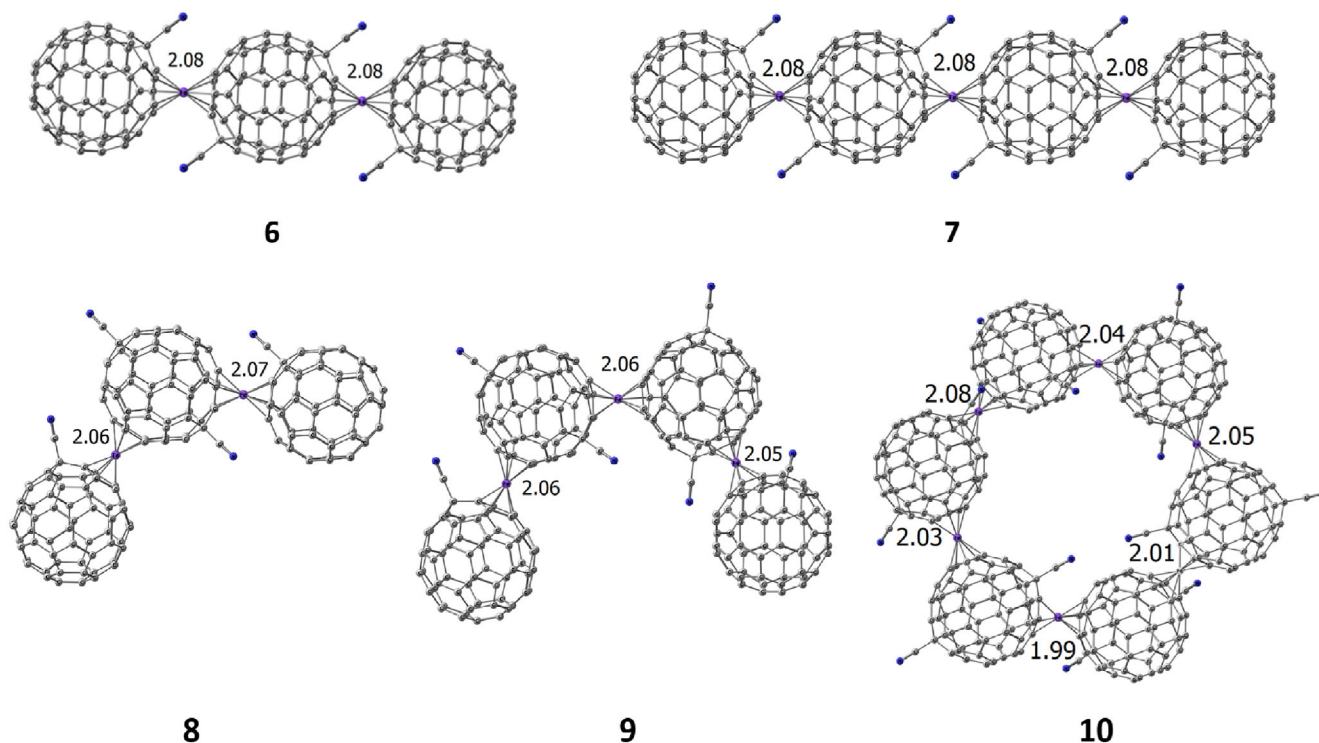
FIGURE 6 Optimized geometry of sandwich fulleride polymer complexes of Fe(II) at M06L/6-31G(d,p) level

TABLE 1 The dissociation pattern in each sandwich complex, the total energy of dissociation (ΔE_{total}), the dissociation energy per Fe(II) ($\Delta E_{/Fe(II)}$) and the free energy change (ΔG_{total})

Complex	Dissociation	ΔE_{total}	$\Delta E_{/Fe(II)}$	ΔG_{total}
1	$Fe^{2+} + 2Cp^-$	−735.4	−735.4	−224.9
2	$Fe^{2+} + 2(C_5(t\text{-}Bu)_3)^-$	−711.5	−711.5	−176.8
3	$Fe^{2+} + Cp^- + (C_{60}CN)^-$	−649.3	−649.3	−138.4
4	$Fe^{2+} + 2(C_{60}CN)^-$	−556.7	−556.7	−132.2
5	$Fe^{2+} + 2(C_5(t\text{-}Bu)_4)^-$	−683.3	−683.3	−140.1
6	$2Fe^{2+} + 2(C_{60}CN)^- + (C_{60}(CN)_2)^{2-}$	−1174.9	−587.5	−174.9
7	$3Fe^{2+} + 2(C_{60}CN)^- + 2(C_{60}(CN)_2)^{2-}$	−1792.9	−597.6	−189.7
8	$2Fe^{2+} + 2(C_{60}CN)^- + (C_{60}(CN)_2)^{2-}$	−1161.5	−580.8	−168.8
9	$3Fe^{2+} + 2(C_{60}CN)^- + 2(C_{60}(CN)_2)^{2-}$	−1768.6	−589.5	−182.0
10	$6Fe^{2+} + 6(C_{60}(CN)_2)^{2-}$	−3635.5	−605.9	−594.0

Note: Value in kcal/mol at M06L/6-311++G(d,p)//M06L/6-31G(d,p) level DFT.

(Scheme 1) suggests that formation of the imidazolium complex of the dianionic fulleride $(C_{60}(CN)_2)^{2-}$ is exothermic by 23.3 kcal/mol and the corresponding free energy change (ΔG) is 0.7 kcal/mol. The dianionic character of $(C_{60}(CN)_2)^{2-}$ suggests the utilization of two pentagonal units for making η^5 coordination with metal centers. Moreover, large number of such fullerides may assemble in presence of cationic metal centers to form polymeric metallocenes. Recent report by Leng et al. on the formation of nanoclusters of C_{60} in presence of Ru and their DFT modeling of one-dimensional -C_{60}-Ru-C_{60}- and other bulk structures suggested favorable η^2 type interactions between metal center and C_{60}. Here we modeled five polymeric structures, viz. **6**, **7**, **8**, **9**, and **10** (Figure 6) wherein multiple

Fe(II) centers exist in ferrocene-type sandwich configuration with Cp units of fulleride cage. The **6** and **8** are made by two $(C_{60}CN)^-$ and one $(C_{60}(CN)_2)^{2-}$, **7** and **9** are made by two $(C_{60}CN)^-$ and two $(C_{60}(CN)_2)^{2-}$ while **10**, a cyclic sandwich polymeric structure is made with six $(C_{60}(CN)_2)^{2-}$ units.

Further, the strength of the η^5 coordination in the multi-decker sandwich/polymeric complexes is analyzed by dissociating them into Fe(II) and the corresponding fullerides. The dissociation scheme of each complex is given in Table 1. In each case, the total energy of dissociation (ΔE_{total}), the free energy change (ΔG_{total}) and the dissociation energy per Fe(II) ($\Delta E_{/Fe(II)}$) are calculated (Table 1). Ferrocene has the highest magnitude for $\Delta E_{/Fe(II)}$, −735.4 kcal/mol. The tertiary

butyl (t-Bu) substituted derivatives **2** and **5** have lower magnitude of $\Delta E_{/Fe(II)}$ than ferrocene and the value further decreases in complex **4**. The linear pearl-necklace type polymer **6** and **7** have $\Delta E_{/Fe(II)}$ -587.5 and -597.6 kcal/mol, which are better than the sandwich complex $[Fe(\eta^5\text{-}(C_{60}CN)^-)_2]$, **4**. Compared to the multi-decker linear sandwich complexes **6** and **7**, their corresponding angular isomers **8** and **9** show slightly lower $\Delta E_{/Fe(II)}$. Further, $\Delta E_{/Fe(II)}$ shows better values when moving from normal sandwich to triple-decker to tetra-decker systems. The complex **10** is a cyclic hexamer structure, similar to a closed pearl-necklace polymer, composed of six Fe(II) and six units of $(C_{60}(CN)_2)^{2-}$. The complete fragmentation of the polymer to constituent units gives $\Delta E_{/Fe(II)}$ -303.0 kcal/mol indicating that dianionic fulleride has higher coordination ability than the anionic fullerides. On the free energy scale, all the reactions given in Table 1 appear exergonic in nature. Despite the decreased entropy factor, the hexamer **10** formation from dianionic fullerides appears highly feasible in terms of both ΔE and ΔG terms. Also the trend in $\Delta E_{/Fe(II)}$ shows that the energetics is better for the formation of the higher order structures **7** and **9** than **6** and **8**, respectively.

4 | CONCLUSIONS

Similar to ferrocene, the η^5 coordinated sandwich complexes have been observed for the metals Fe(II), Ru(II), Cr(II), Mo(II), and Ni(II) with the $(C_{60}CN)^-$ ligand. The structural parameters of these fulleride sandwich complexes are comparable to those of the corresponding Cp^- sandwich complexes. The η^5 coordination mode of $(C_{60}CN)^-$ is preferred over η^6 coordination. The MESP analysis showed the delocalized anionic nature of the ligand $(C_{60}CN)^-$. Further, upon coordination with the metal center, a drastic decrease in the negative character of the MESP is observed in the complex which indicated strong η^5 mode of coordination of the ligand. The MO analysis has shown that the η^5 Fe–C bonding features of $[Fe(\eta^5\text{-}(C_{60}CN)^-)_2]$ is very similar to that of ferrocene. The similarity in the metal–ligand bonding as well as the covalent-noncovalent nature of the Fe–C bonding interactions is further confirmed from the QTAIM analysis.

The coordination ability of dianionic fulleride, $(C_{60}(CN)_2)^{2-}$ with metal centers is better than the anionic fullerides. Also $(C_{60}(CN)_2)^{2-}$ can simultaneously utilize two of its five-membered rings to develop η^5 coordination with metal centers which lead to the formation of multi-decker sandwich complexes and pearl-necklace type polymers. The growth patterns of the complexes in both linear and bent directions as well as formation of cyclic structures are found to be energetically feasible. The analysis of $\Delta E_{/Fe(II)}$ values of each multi-decker system has shown that the energetics is favorable for the formation of polymeric structures. The highest magnitude of $\Delta E_{/Fe(II)}$ is observed for the closed pearl-necklace structure composed of dianionic fulleride and Fe(II) centers. These results clearly suggest that CN–fullerides are very bulky and versatile η^5 ligands which can be utilized for the development of hitherto unknown multi-decker sandwich and pearl-necklace type polymeric structures.

ORCID

Cherumuttathu H. Suresh https://orcid.org/0000-0001-7237-6638

REFERENCES

[1] T. Kealy, P. Pauson, *Nature* **1951**, *168*, 1039.
[2] S. Miller, J. Tebboth, J. Tremaine, *J. Chem. Soc., Perkin Trans.* **1952**, *2*. https://pubs.rsc.org/en/content/articlelanding/1952/jr/jr9520000 632/unauth
[3] E. Nakamura, *Pure Appl. Chem.* **2003**, *75*, 427.
[4] E. O. Fischer, W. Pfab, *Z. Naturforsch. B* **1952**, *7*, 377.
[5] G. Wilkinson, M. Rosenblum, M. Whiting, R. Woodward, *J. Am. Chem. Soc.* **1952**, *74*, 2125.
[6] R. Woodward, M. Rosenblum, M. Whiting, *J. Am. Chem. Soc.* **1952**, *74*, 3458.
[7] H. Werner, *Angew. Chem., Int. Ed.* **2012**, *51*, 6052.
[8] P. F. Eiland, R. Pepinsky, *J. Am. Chem. Soc.* **1952**, *74*, 4971.
[9] J. Dunitz, L. Orgel, *Nature* **1953**, *171*, 121.
[10] G. Wilkinson, *J. Am. Chem. Soc.* **1952**, *74*, 6146.
[11] G. Wilkinson, P. Pauson, F. Cotton, *J. Am. Chem. Soc.* **1954**, *76*, 1970.
[12] G. Wilkinson, J. Birmingham, *J. Am. Chem. Soc.* **1954**, *76*, 4281.
[13] M. Rausch, M. Vogel, H. Rosenberg, *J. Chem. Educ.* **1957**, *34*, 268.
[14] M. Roemer, D. Heinrich, Y. K. Kang, Y. K. Chung, D. Lentz, *Organometallics* **2012**, *31*, 1500.
[15] B. Kashyap, P. Phukan, *RSC Adv.* **2013**, *3*, 15327.
[16] A. Paul, R. Borrelli, H. Bouyanfif, S. Gottis, F. Sauvage, *ACS Omega* **2019**, *4*, 14780.
[17] P. Ravinder, V. Subramanian, *Comput. Theor. Chem.* **2012**, *998*, 106.
[18] J. A. López, C. Mealli, *J. Organomet. Chem.* **1994**, *478*, 161.
[19] A. Chistyakov, I. Stankevich, N. Gambaryan, *Russ. Chem. Bull.* **1995**, *44*, 828.
[20] A. Chistyakov, L. Stankevich, *Russ. Chem. Bull.* **1996**, *45*, 2294.
[21] E. D. Jemmis, M. Manoharan, *Curr. Sci.* **1999**, *76*, 1122.
[22] H. S. Kang, *J. Comput. Chem.* **2007**, *28*, 594.
[23] V. Sokolov, *Russ. J. Coord. Chem.* **2007**, *33*, 711.
[24] M. Sawamura, H. Iikura, E. Nakamura, *J. Am. Chem. Soc.* **1996**, *118*, 12850.
[25] M. Sawamura, H. Iikura, A. Hirai, E. Nakamura, *J. Am. Chem. Soc.* **1998**, *120*, 8285.
[26] M. Sawamura, Y. Kuninobu, M. Toganoh, Y. Matsuo, M. Yamanaka, E. Nakamura, *J. Am. Chem. Soc.* **2002**, *124*, 9354.
[27] M. Toganoh, Y. Matsuo, E. Nakamura, *J. Am. Chem. Soc.* **2003**, *125*, 13974.
[28] Y. Matsuo, Y. Kuninobu, S. Ito, E. Nakamura, *Chem. Lett.* **2004**, *33*, 68.
[29] Y. Matsuo, E. Nakamura, *Chem. Rev.* **2008**, *108*, 3016.
[30] Y. Matsuo, A. Iwashita, E. Nakamura, *Organometallics* **2008**, *27*, 4611.

[31] S. Muhammad, S. Ito, M. Nakano, R. Kishi, K. Yoneda, Y. Kitagawa, M. Shkir, A. Irfan, A. R. Chaudhry, S. AlFaify, A. Kalam, A. G. Al-Sehemi, *Phys. Chem. Chem. Phys.* **2015**, *17*, 5805.

[32] P. J. Fagan, P. J. Krusic, D. H. Evans, S. A. Lerke, E. Johnston, *J. Am. Chem. Soc.* **1992**, *114*, 9697.

[33] F. Wudl, *Acc. Chem. Res.* **1992**, *25*, 157.

[34] R. Taylor, D. R. Walton, *Nature* **1993**, *363*, 685.

[35] E. Nakamura, H. Isobe, *Acc. Chem. Res.* **2003**, *36*, 807.

[36] T. Hasobe, H. Imahori, P. V. Kamat, S. Fukuzumi, *J. Am. Chem. Soc.* **2003**, *125*, 14962.

[37] P. D. Boyd, C. A. Reed, *Acc. Chem. Res.* **2005**, *38*, 235.

[38] J. Cioslowski, K. Raghavachari, *J. Chem. Phys.* **1993**, *98*, 8734.

[39] Y. Wang, D. Tománek, R. S. Ruoff, *Chem. Phys. Lett.* **1993**, *208*, 79.

[40] A. A. Popov, L. Dunsch, *Chem. – Eur. J.* **2009**, *15*, 9707.

[41] S. Osuna, M. Swart, M. Sola, *Phys. Chem. Chem. Phys.* **2011**, *13*, 3585.

[42] Y. Zhang, D. Wang, W. Wang, *Comput. Theor. Chem.* **2018**, *1128*, 56.

[43] M. Alipour, K. Kargar, *J. Comput. Chem.* **2020**, *41*, 1912.

[44] B. S. Tan, R. F. Peng, H. B. Li, B. Jin, S. J. Chu, X. P. Long, *J. Comput. Chem.* **2010**, *31*, 2233.

[45] L. Dunsch, S. Yang, *Phys. Chem. Chem. Phys.* **2007**, *9*, 3067.

[46] K. Kurotobi, Y. Murata, *Science* **2011**, *333*, 613.

[47] A. Krachmalnicoff, R. Bounds, S. Mamone, S. Alom, M. Concistrè, B. Meier, K. Kouřil, M. E. Light, M. R. Johnson, S. Rols, *Nat. Chem.* **2016**, *8*, 953.

[48] K. Komatsu, M. Murata, Y. Murata, *Science* **2005**, *307*, 238.

[49] X. Wu, X. Lu, *J. Am. Chem. Soc.* **2007**, *129*, 2171.

[50] R. E. Estrada-Salas, A. A. Valladares, *J. Mol. Struct. THEOCHEM* **2008**, *869*, 1.

[51] A. L. Balch, M. M. Olmstead, *Chem. Rev.* **1998**, *98*, 2123.

[52] K. Lee, H. Song, J. T. Park, *Acc. Chem. Res.* **2003**, *36*, 78.

[53] J. López-Andarias, A. Bauzá, N. Sakai, A. Frontera, S. Matile, *Am. Ethnol.* **2018**, *130*, 11049.

[54] J. López-Andarias, A. Frontera, S. Matile, *J. Am. Chem. Soc.* **2017**, *139*, 13296.

[55] K. Fujiwara, Y. Murata, T. S. Wan, K. Komatsu, *Tetrahedron* **1998**, *54*, 2049.

[56] P. Sofou, Y. Elemes, E. Panou-Pomonis, A. Stavrakoudis, V. Tsikaris, C. Sakarellos, M. Sakarellos-Daitsiotis, M. Maggini, F. Formaggio, C. Toniolo, *Tetrahedron* **2004**, *60*, 2823.

[57] A. Hirsch, *Phys. Status Solidi B* **2006**, *243*, 3209.

[58] J. Yang, K. Wang, J. Driver, J. Yang, A. R. Barron, *Org. Biomol. Chem.* **2007**, *5*, 260.

[59] F. Giacalone, N. Martin, *Chem. Rev.* **2006**, *106*, 5136.

[60] P. Ravi, S. Dai, C. Wang, K. C. Tam, *J. Nanosci. Nanotechnol.* **2007**, *7*, 1176.

[61] E. Grądzka, M. Wysocka-Żołopa, K. Winkler, *Adv. Energy Mater.* **2020**, *10*, 2001443.

[62] H. Nagashima, A. Nakaoka, Y. Saito, M. Kato, T. Kawanishi, K. Itoh, *J. Chem. Soc., Chem. Commun.* **1992**, 377.

[63] H. Nagashima, A. Nakaoka, S. Tajima, Y. Saito, K. Itoh, *Chem. Lett.* **1992**, *21*, 1361.

[64] F. Leng, I. Gerber, P. Lecante, W. Bacsa, J. Miller, J. Gallagher, S. Moldovan, M. Girleanu, M. Axet, P. Serp, *RSC Adv.* **2016**, *6*, 69135.

[65] E. Brancewicz, E. Grądzka, K. Winkler, *J. Solid State Electrochem.* **2013**, *17*, 1233.

[66] P. J. Harris, *C* **2020**, *6*, 71.

[67] T. Kurikawa, Y. Negishi, F. Hayakawa, S. Nagao, K. Miyajima, A. Nakajima, K. Kaya, *J. Am. Chem. Soc.* **1998**, *120*, 11766.

[68] F. T. Edelmann, *New J. Chem.* **2011**, *35*, 517.

[69] T. N. Gribanova, R. M. Minyaev, V. I. Minkin, *Phys. Chem. Chem. Phys.* **2012**, *14*, 14803.

[70] S. Anila, C. H. Suresh, *Phys. Chem. Chem. Phys.* **2021**, *23*, 3646.

[71] S. Anila, C. H. Suresh, *Phys. Chem. Chem. Phys.* **2021**, *23*, 20086.

[72] Y. Zhao, D. G. Truhlar, *J. Chem. Phys.* **2006**, *125*, 194101.

[73] Y. Zhao, D. G. Truhlar, *Acc. Chem. Res.* **2008**, *41*, 157.

[74] S. Zahn, D. R. MacFarlane, E. I. Izgorodina, *Phys. Chem. Chem. Phys.* **2013**, *15*, 13664.

[75] M. J. Frisch, G. W. Trucks, H. B. Schlegel, G. E. Scuseria, M. A. Robb, J. R. Cheeseman, G. Scalmani, V. Barone, G. A. Petersson, H. Nakatsuji, X. Li, M. Caricato, A. V. Marenich, J. Bloino, B. G. Janesko, R. Gomperts, B. Mennucci, H. P. Hratchian, J. V. Ortiz, A. F. Izmaylov, J. L. Sonnenberg, D. Williams-Young, F. Ding, F. Lipparini, F. Egidi, J. Goings, B. Peng, A. Petrone, T. Henderson, D. Ranasinghe, V. G. Zakrzewski, J. Gao, N. Rega, G. Zheng, W. Liang, M. Hada, M. Ehara, K. Toyota, R. Fukuda, J. Hasegawa, M. Ishida, T. Nakajima, Y. Honda, O. Kitao, H. Nakai, T. Vreven, K. Throssell, J. A. Montgomery Jr., J. E. Peralta, F. Ogliaro, M. J. Bearpark, J. J. Heyd, E. N. Brothers, K. N. Kudin, V. N. Staroverov, T. A. Keith, R. Kobayashi, J. Normand, K. Raghavachari, A. P. Rendell, J. C. Burant, S. S. Iyengar, J. Tomasi, M. Cossi, J. M. Millam, M. Klene, C. Adamo, R. Cammi, J. W. Ochterski, R. L. Martin, K. Morokuma, O. Farkas, J. B. Foresman, D. J. Fox, *Gaussian 16 Rev. A.03*, Gaussian, Inc, Wallingford CT **2016**.

[76] K. Remya, C. H. Suresh, *J. Comput. Chem.* **2013**, *34*, 1341.

[77] S. Grimme, *J. Comput. Chem.* **2006**, *27*, 1787.

[78] S. Grimme, J. Antony, S. Ehrlich, H. Krieg, *J. Chem. Phys.* **2010**, *132*, 154104.

[79] T. D. Della, C. H. Suresh, *Phys. Chem. Chem. Phys.* **2018**, *20*, 24885.

[80] J. S. Murray, K. Sen, *Molecular Electrostatic Potentials: Concepts and Applications*. Elsevier, Amsterdam, Netherlands **1996**.

[81] S. R. Gadre, R. N. Shirsat, *Electrostatics of Atoms and Molecules*. Universities Press, Hyderabad, India **2000**.

[82] P. Politzer, D. G. Truhlar, *Chemical Applications of Atomic and Molecular Electrostatic Potentials: Reactivity, Structure, Scattering, and Energetics of Organic, Inorganic, and Biological Systems*. Springer Science & Business Media, Springer-Verlag US **2013**.

[83] J. S. Murray, P. Politzer, *Wiley Interdiscip. Rev. Comput. Mol. Sci.* **2017**, *7*, 1326.

[84] S. R. Gadre, C. H. Suresh, N. Mohan, *Molecules* **2021**, *26*, 3289.

[85] R. K. Pathak, S. R. Gadre, *J. Chem. Phys.* **1990**, *93*, 1770.

[86] S. R. Gadre, I. H. Shrivastava, *J. Chem. Phys.* **1991**, *94*, 4384.

[87] Á. M. Pendás, C. Gatti, in *3 Quantum Theory of Atoms in Molecules and the AIMAll Software* (Ed: G. Simon and U. Bern), De Gruyter, Switzerland **2021**, p. 43.

[88] G. Saleh, D. Ceresoli, G. Macetti, C. Gatti, in *Computational Materials Discovery* (Eds: A. R. Oganov, G. S. Alexander, G. Kvashnin), The Royal Society of Chemistry, London **2019**, p. 117.

[89] T. Keith, *TK Gristmill Software*, Overland Park, KS **2014**.

[90] A. E. Reed, L. A. Curtiss, F. Weinhold, *Chem. Rev.* **1988**, *88*, 899.

[91] E. Glendening, A. Reed, J. Carpenter, F. Weinhold, NBO Version 3.1 **1998**.

[92] F. Weinhold, C. R. Landis, *Valency and Bonding: A Natural Bond Orbital Donor-acceptor Perspective*, Cambridge University Press, Cambridge, United Kingdom **2005**.

[93] V. M. Rayón, G. Frenking, *Organometallics* **2003**, *22*, 3304.

[94] A. Haaland, J. Nilsson, *Acta Chem. Scand.* **1968**, *22*, 2653.

[95] A. Haaland, *Acc. Chem. Res.* **1979**, *12*, 415.

[96] C. A. P. Goodwin, M. J. Giansiracusa, S. M. Greer, H. M. Nicholas, P. Evans, M. Vonci, S. Hill, N. F. Chilton, D. P. Mills, *Nat. Chem.* **2021**, *13*, 243.

[97] G. Golding Sheeba, D. Usha, M. Amalanathan, M. Sony Michael Mary, H. Marshan Robert, *Spectrosc. Lett.* **2021**, *54*, 419.

[98] J. Frunzke, M. Lein, G. Frenking, *Organometallics* **2002**, *21*, 3351.

[99] V. Y. Lee, R. Kato, A. Sekiguchi, A. Krapp, G. Frenking, *J. Am. Chem. Soc.* **2007**, *129*, 10340.

[100] M. Nakada, T. Kuwabara, S. Furukawa, M. Hada, M. Minoura, M. Saito, *Chem. Sci.* **2017**, *8*, 3092.

[101] K. R. Flower, P. B. Hitchcock, *J. Organomet. Chem.* **1996**, *507*, 275.

[102] K. Prout, T. S. Cameron, R. A. Forder, S. R. Critchley, B. Denton, G. V. Rees, *Acta Crystallogr. B* **1974**, *30*, 2290.

[103] P. Seiler, J. D. Dunitz, *Acta Crystallogr. B* **1980**, *36*, 2255.

SUPPORTING INFORMATION

Additional supporting information may be found in the online version of the article at the publisher's website.

Article

Demarcating Noncovalent and Covalent Bond Territories: Imine-CO$_2$ Complexes and Cooperative CO$_2$ Capture

Published as part of The Journal of Physical Chemistry virtual special issue "Vincenzo Barone Festschrift".

Sebastian Anila, Cherumuttathu H. Suresh,* and Henry F. Schaefer, III*

Cite This: https://doi.org/10.1021/acs.jpca.2c03221

Read Online

ACCESS | Metrics & More | Article Recommendations | SI Supporting Information

ABSTRACT: Chemical bond territory is rich with covalently bonded molecules wherein a strong bond is formed by equal or unequal sharing of a quantum of electrons. The noncovalent version of the bonding scenarios expands the chemical bonding territory to a weak domain wherein the interplay of electrostatic and π-effects, dipole–dipole, dipole–induced dipole, and induced dipole–induced dipole interactions, and hydrophobic effects occur. Here we study both the covalent and noncovalent interactive behavior of cyclic and acyclic imine-based functional molecules (XN) with CO$_2$. All parent XN systems preferred the formation of noncovalent (**nc**) complex XN···CO$_2$, while more saturated such systems (XN′) produced both **nc** and covalent (**c**) complexes XN′$^+$−(CO$_2$)$^−$. In all such cases, crossover from an **nc** to **c** complex is clearly demarcated with the identification of a transition state (**ts**). The complexes XN′···CO$_2$ and XN′$^+$−(CO$_2$)$^−$ are bond stretch isomers, and they define the

weak and strong bonding territories, respectively, while the **ts** appears as the demarcation point of the two territories. Cluster formation of XN with CO$_2$ reinforces the interaction between them, and all become covalent clusters of general formula (XN$^+$−(CO$_2$)$^−$)$_n$. The positive cooperativity associated with the NH···OC hydrogen bond formation between any two XN′$^+$−(CO$_2$)$^−$ units strengthened the N−C coordinate covalent bond and led to massive stabilization of the cluster. For instance, the stabilizing interaction between the XN unit with CO$_2$ is increased from 2−7 kcal/mol range in a monomer complex to 14−31 kcal/mol range for the octamer cluster (XN′$^+$−(CO$_2$)$^−$)$_8$. The cooperativity effect compensates for the large reduction in the entropy of cluster formation. Several imine systems showed the exergonic formation of the cluster and are predicted as potential candidates for CO$_2$ capture and conversion.
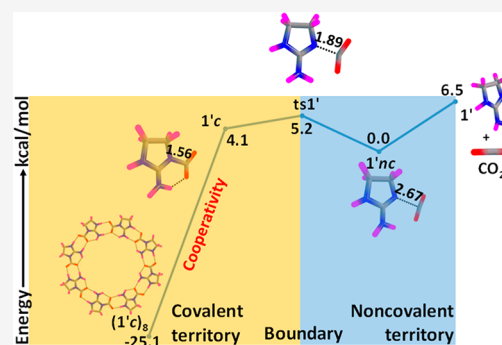
INTRODUCTION

The chemical bond is regarded as one of the fundamental territories of chemistry, populated by a large variety of covalent (nonpolar), ionic (polar), and metallic bonds.[1] Advanced quantum mechanical studies have led to electron density (ρ)-based descriptions of bonding between pairs of atoms, while new bonding features unearthed from such studies provided accurate interpretations of structure and reactivity of molecules and materials. According to IUPAC, a covalent bond refers to the region of relatively high electron density between nuclei, which arises at least partly from sharing of electrons and gives rise to an attractive force and characteristic internuclear distance.[2] A more sophisticated view suggests that covalent bonding involves synergism between several interactions, including the intricate interplay of interatomic and intra-atomic interactions. Electrostatic attraction, exchange (Pauli) repulsion, and further factors contribute to the intricate combination that yields a chemical bond.[3] A covalent bonding interaction in the purest form is proposed in the case of homonuclear diatomic species, while a degree of polarization in the bond may develop when heteroatoms are involved, which

gives some ionic bond characteristics. The covalent bond energy typically ranges from 40 to 100 kcal/mol for the single bonds involving main block elements such as B, C, N, O, etc. The energy decomposition analysis (EDA)[1,4] and natural bond orbital (NBO)[5,6] analysis are powerful theoretical tools for the study of bonding situations. The EDA studies by Frenking et al. have contributed immensely to the understanding and explaining of the chemical bond in terms of quasiclassical electrostatic interactions, Pauli repulsion, and attractive orbital interactions.[7−15]

Although the covalent bond is intimately connected with equal or unequal sharing of a quantum of electrons, the noncovalent version of the bonding scenarios arises often in molecular assemblies.[16] Such interactions refer to almost any interaction weaker than a covalent bond, typically less than 15 kcal/mol. The chemical bonding landscape expands greatly with the advent of noncovalent interactions such as electro-
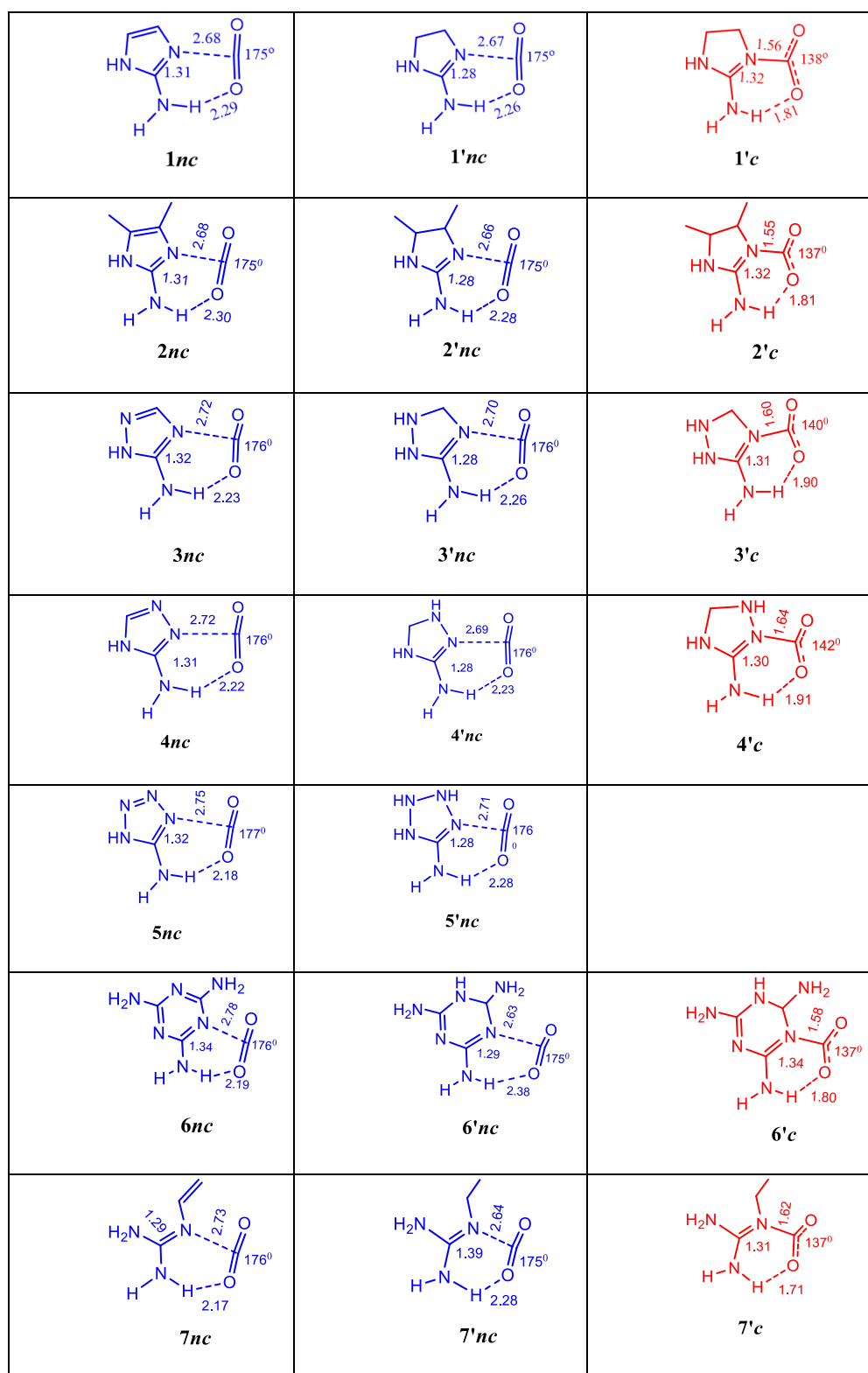
A

Figure 1. Geometry parameters of optimized $(XN)(CO_2)$ complexes in the **nc** (blue) and **c** (red) bond regimes. Distances in angstroms and angles in degrees.

static (ionic, hydrogen, and halogen bonds), π-effects ($\pi-\pi$ interactions and cation-π and anion-π interactions), van der Waals forces (dipole−dipole interactions, dipole−induced dipole interactions, and induced dipole−induced dipole interactions), and hydrophobic effects.[17] One of the most thoroughly studied noncovalent interactions is the hydrogen

bond.[18−21] As per the IUPAC definition, the form of association between an electronegative atom and a hydrogen atom attached to a second, relatively electronegative atom is considered as the hydrogen bond.[2,22] Though the concept of bond energy seems to be one means of making the distinction between covalent and noncovalent bonds, unfortunately, things

B

are not always very straightforward. There are a number of different interactions with bond energies in the standard noncovalent range, but through a systematic strengthening of the interactions, for instance, via appropriate modifications of substituents, they can advance into the energy range normally reserved for covalent bonds. Jemmis et al. explained the possible formation of a relatively "strong bond" without much covalent bonding character via the example of the halogen bond that shortens and strengthens the bridge bond of [1.1.1]propellane and the open form of [2.2.2]propellane.[23] Very recently Dereka et al. illustrated the crossover of the hydrogen bonding into covalent bonding interaction in terms of the H···F/H−F interactions in bifluoride anion [F−H−F]$^-$.[24] Also recently Scheiner et al. observed that slight modifications in the electronic environment of the substrate can lead to strengthening of the tetrel bonding interactions.[25] Though these studies suggest the possibility of crossover of interacting molecular systems from noncovalent to covalent bonding territory, a clear demarcation of the bonding territories is yet to be established.

Bader's quantum theory of atoms in molecules (QTAIM) topology analysis of electron density (ρ) has been effectively used for the interpretation of both the covalent and noncovalent bonding interactions.[26−29] In the Bader analysis, atom−atom interactions are distinguished as covalent and noncovalent based on the minimum value of ρ on bond paths (bond critical point (bcp)) as well as from the sign of the corresponding Laplacian ($\nabla^2\rho$). According to Koch and Popelier,[30,31] for a noncovalent interaction, ρ at the bcp (ρ_b) falls in the range of 0.002−0.040 au, and $\nabla^2\rho_b$ is positive, typically in the range of 0.024−0.139 au. Although negative $\nabla^2\rho_b$ values generally indicate covalent interactions, there are exceptions to this, such as the charge-shift bonds proposed by Shaik et al.[32,33]

A recent DFT M06-2X/6-311++G** study on the interactive behavior of CO_2 with guanidine (G) has shown that noncovalently interacting G···CO_2 can transform to a strongly interacting G-CO_2 covalent complex under the influence of multiple G and CO_2 units.[34] The fivefold increase in binding energy observed in the (G-CO_2)$_8$ cluster was attributed to large cooperativity associated with the (G$^+$)-(CO_2^-) zwitterion nature of G-CO_2. The reinforcement of the interaction observed for the guanidine-carbon dioxide system from weak noncovalent to strong covalent nature has inspired us to perform the present research. Here we examine the noncovalent-covalent transformation behavior as a general phenomenon in the chemical bond territory and also locate the crossover point for such transformations. The boundary crossing occurs with a slight variation in the electronic structure through the promotion of positive cooperativity in the interactions.

COMPUTATIONAL METHODS

The M06-2X/6-311++G**, a robust density functional theory (DFT) method for modeling intermolecular noncovalent interactions, as implemented in the Gaussian 16 suite of programs, is used for locating all minimum energy (XN)(CO_2) structures and transition state (**ts**) geometries (XN corresponds to an N-heterocyclic or N-rich acyclic molecule containing at least one imine functionality).[34−36] The zero-point energy (ZPE)-corrected binding energy (E_b) between XN and CO_2 is calculated using the supermolecule approach given in eq 1

$$E_b = E_{(XN)(CO2)} - E_{XN} - E_{CO2} + E_{bsse} \qquad (1)$$

where E_{bsse} corresponds to the basis set superposition error[37−40] as per the counterpoise (CP) approach of Boys and Bernardi.[41,42] Similarly the free energy change (ΔG) and enthalpy change (ΔH) at standard temperature and pressure (STP) associated with the complex formation are also computed using supermolecule approach. The deformation energy (E_{def}) for the XN−CO_2 interaction is calculated as

$$E_{def} = E_{def-XN} + E_{def-CO2}$$
$$= (E_{XN} - E_{XN*}) + (E_{CO2} - E_{CO2*}) \qquad (2)$$

where E_{XN*} and E_{CO2*} are the energies of the deformed XN-unit and deformed CO_2 in the complex, respectively.

Further, QTAIM, molecular electrostatic potential (MESP) and nuclear magnetic resonance (NMR) analyses were performed for all (XN)(CO_2) complexes with the M06-2X/6-311++G** method.[26−29,43,44] The ρ and $\nabla^2\rho$ features provided in the QTAIM anlysis are useful for the characterization of the intermolecular bonded regions through the identification of bond paths and bcps, while MESP is useful to interpret the electron reorganization due to the bond formation. The MESP at any point **r** in space, $V(\mathbf{r})$, is intimately connected with the $\rho(\mathbf{r})$ distribution via eq 3

$$V(\mathbf{r}) = \sum_A^N \frac{Z_A}{|\mathbf{r} - \mathbf{R}_A|} - \int \frac{\rho(\mathbf{r}')\mathrm{d}^3\mathbf{r}'}{|\mathbf{r} - \mathbf{r}'|} \qquad (3)$$

where Z_A is the charge on the nucleus A, which is located at the position $\mathbf{R}_A$, and N is the total number of nuclei in the molecule.[45,46] The Gauge-Independent Atomic Orbital (GIAO) method is used to derive NMR data.[47,48]

RESULTS AND DISCUSSION

For the (XN)(CO_2) complexes studied here, the imino XN systems are designated as **1−7** and **1′−7′**. The **1−7** molecules contain a CC or NN or CN double bond adjacent to the imino nitrogen, whereas **1′−7′** are made by changing such a double bond to a single bond (Figure 1. See also Table S1 for IUPAC names of the imines). This change in structure assures us that, in terms of its electron-rich character, the lone pair bearing an imino nitrogen in the "nonprimed" structures is slightly different from that in the "primed" structures. Since the imino N-lone pair is used as the two-electron donor to CO_2, an assessment of the electronic feature of this center is made from the MESP minimum (V_{min}) corresponding to this lone pair (Figure S1). Compared to XN, the more saturated systems (XN′) showed a higher negative character for the V_{min}, indicating that XN′ has better interaction ability than XN with CO_2 (Table 1).

Table 1. V_{min} Values (in kcal/mol) for All N-Heterocyclic and N-Rich Acyclic Molecules

notation	V_{min}
1 & 1′	−67.5 & −71.1
2 & 2′	−70.5 & −71.5
3 & 3′	−58.7 & −63.4
4 & 4′	−66.7 & −66.9
5 & 5′	−55.8 & −57.9
6 & 6′	−54.8 & −68.6
7 & 7′	−63.5 & −69.3

Two classifications are made for the optimized $(XN)(CO_2)$ complexes (Figure 1), specifically, (i) noncovalent (nc) XN···CO_2 complexes wherein the imino N to CO_2 interaction occurs at a distance from 2.63 to 2.78 Å, which is far greater than a covalent bond distance, and (ii) covalent (c) XN−CO_2 complexes, which are characterized by an imino N-CO_2 coordinate covalent bond with N−C distance in the range of 1.55−1.65 Å. Hereafter, the nc or c notation is used along with the number notation to specify the nature of the complex. The O···H distance in the range from 2.17 to 2.30 Å observed for nc complexes suggests very weak interactions, whereas the similar interaction seen in the c complexes is expected to be stronger due to shorter O···H distances in the range of 1.70−1.91 Å (Figure 1). Except 5′, all other primed structures show the formation of both nc and c complexes, while the nonprimed structures show only the formation of nc complexes. This suggests that electron-rich XN′ have the ability to force a covalent bond formation with the CO_2.

The E_b data given in Table 2 suggest that nc complexes of primed structures lie lower in energy than the c complexes. A

Table 2. Energy Parameters (kcal/mol) for $(XN)(CO_2)$ Complexes

notation	E_b	ΔG	E_{def-XN}	$E_{def-CO2}$
1nc	−5.6	2.5	0.1	0.4
1′nc, 1′c	−6.0, −2.4	1.9, 7.8	0.1, 6.6	0.5, 39.6
2nc	−6.0	2.3	0.1	0.4
2′nc, 2′c	−6.3, −3.7	1.9, 6.8	0.1, 6.7	0.5, 40.9
3nc	−5.4	2.7	0.1	0.3
3′nc, 3′c	−5.6, 2.4	2.2, 12.2	0.1, 5.2	0.4, 34.9
4nc	−5.3	2.7	0.1	0.4
4′nc, 4′c	−5.4, 2.4	2.4, 12.4	0.1, 5.0	0.3, 31.6
5nc	−5.1	3.0	0.1	0.3
5′nc	−5.1	2.8	0.1	0.3
6nc	−6.4, −2.0	1.7	0.1, 8.1	0.3, 41.0
6′nc, 6′c	−6.9	1.5, 8.6	0.1	0.5
7nc	−5.9, −1.1	2.4	0.2, 6.9	0.4, 39.5
7′nc, 7′c	−5.2	3.2, 9.2	0.1	0.5

net destabilization of 2.4 kcal/mol is found for both 3′c and 4′c, while the rest show stabilization with respect to infinitely separate XN or XN′ and CO_2. On the free energy scale, due to loss of entropy, the complex formation appears endergonic for all, by 1.5−12.4 kcal/mol. Although a strong N−C bond is formed in the c complexes, it does not guarantee high stabilization for the complex. The reason for this can be attributed to the large deformation induced on CO_2; ~38−46° deviation for the OCO bond angle and significant elongation of the CO bond distance. Since $E_{def-CO2}$ for the c complexes is high, in the range from 36.7 to 49.5 kcal/mol (Table 2), the N−C bond energy has to be higher or close to $E_{def-CO2}$ to attain net stabilization. The intramolecular NH···OCO interaction also contributes to the stabilization of the c complexes. In the case of nc complexes, E_{def} is at most 0.6 kcal/mol and suggests that E_b is almost fully accounted by the N···C noncovalent interaction. E_{def-XN} is negligible for nc complexes, while this quantity for c complexes is ~14% of the total deformation energy E_{def}.

For the primed structures, the noncovalent and covalent regions of bond formation can be demarcated by identifying a ts for their interconversion. The transition states ts1′−ts7′ are located for 1′nc−7′nc conversion to 1′c−7′c. The energy

profile in Figure 2 depicts the conversion of 2′nc to 2′c via ts2′, and the results for the other systems are given in
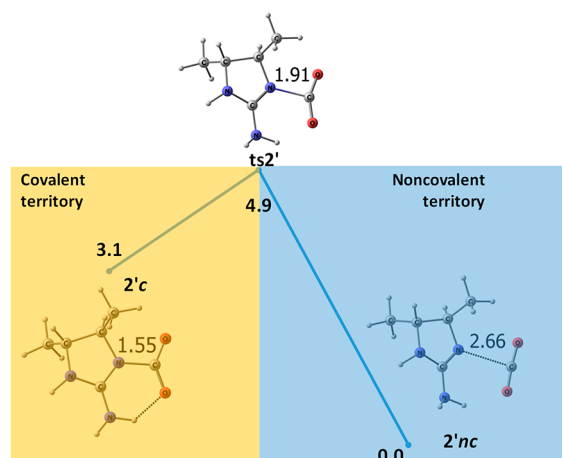

Figure 2. XN−CO_2, XN···CO_2, and the ts for their interconversion. Bond lengths in angstroms and ZPE-corrected relative energy in kilocalories per mole.

Supporting Information (Figure 3 & Table S2). The ts2′ appears as a demarcation point between the noncovalent and covalent realms of bond formation, which takes place at the N···C distance of 1.91 Å. Below this distance, covalent character develops between the N and C atoms.

The QTAIM analysis using the molecular graph in Figure 4, $\nabla^2\rho$ plots (Figure 5), and QTAIM data (Tables S3 & S4) can clearly demarcate the bonding territories of $(XN)(CO_2)$ complexes. The molecular graph is characterized by bond paths for N−C/N···C and NH···OCO interactions. The covalent N−C bond is established from the high value of electron density at the bond critical point (ρ_b) and high negative values of $\nabla^2\rho_b$, whereas noncovalent complexes show very small ρ_b and small positive $\nabla^2\rho_b$ values (Figure 4). The $\nabla^2\rho$ plots for 2′nc, ts2′, and 2′c (Figure 5) give positive, positive, and negative values, respectively, at the N−C/N···C bonding region. Hence, as per QTAIM criteria, the transition state lies in the noncovalent territory, very close to the border with the covalent territory. The values of local kinetic (G_b), potential (V_b), and total electron (H_b) energy densities at the bond critical points are given in Tables S3 for the N−C/N···C interaction and Table S4 for the NH···OCO interaction. In the c complexes, $|V_b| > 2G_b$ and negative H_b values confirm the covalent nature of N−C interactions, while NH···OCO and N···C interactions (in nc complexes) show $|V_b| < G_b$ and positive H_b, which confirm their noncovalent nature.[49,50]

The QTAIM molecular graphs given in Figure 4 and Figure S2 as well as the identification of ts1′−ts7′ for the interconversion of 1′nc−7′nc to 1′c−7′c suggest that nc and the corresponding c complexes differ only in the length of bonds. They can be regarded as bond stretch isomers (BSIs) as per the criteria proposed by Hoffmann et al.[51,52] An unambiguous experimental validation of the existence of a genuine BSI in chemistry[53−58] is yet to be furnished,[59] while the present results give a beautiful illustration of this concept and also ascertain that BSI connects two contrasting bonding territories.

The MESP plots given in Figure 6 and Figure S3 are useful to distinguish the nc and c covalent formations in $(XN)(CO_2)$ complexes. For example, the 2nc and 2′nc complexes show the
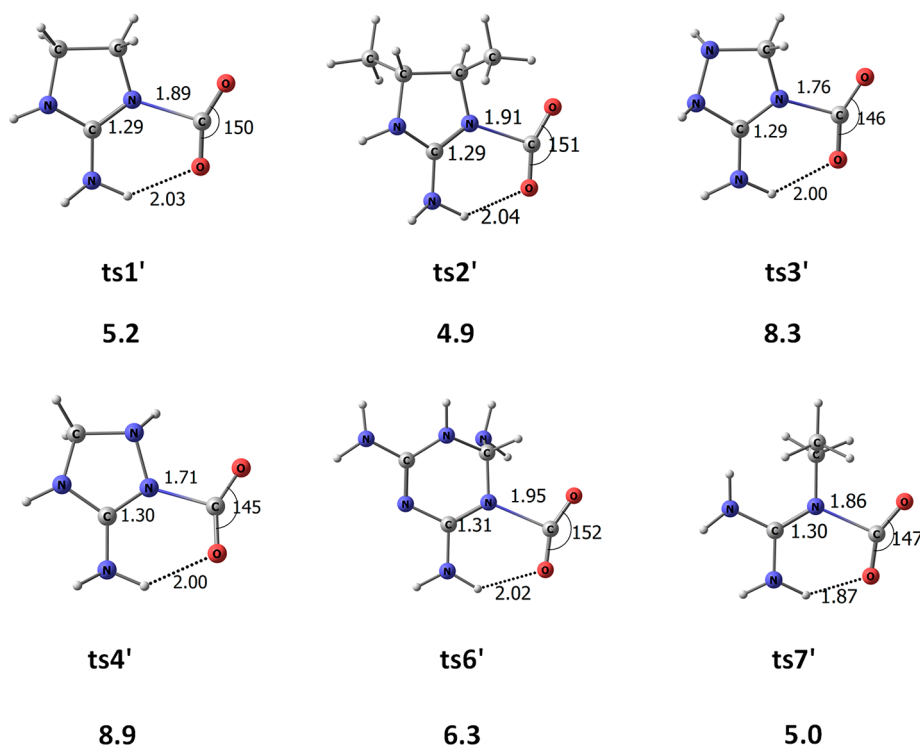
Figure 3. Optimized geometries and ZPE-corrected relative energy (kcal/mol) for the transition states with respect to $(XN)(CO_2)$ **nc** complexes. Bond distance in angstroms and angles in degrees.
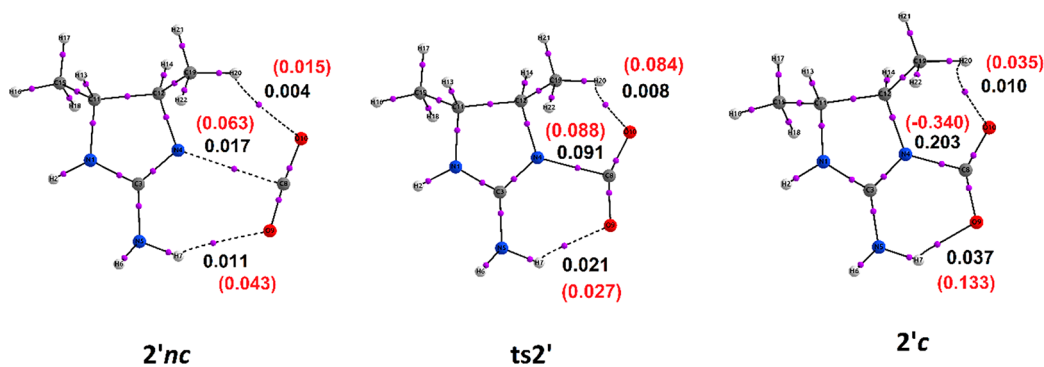

Figure 4. QTAIM molecular graph of **2′nc**, **ts2′**, and **2′c**. Values in black and red colors are ρ_b and $\nabla^2\rho_b$ in atomic unit.
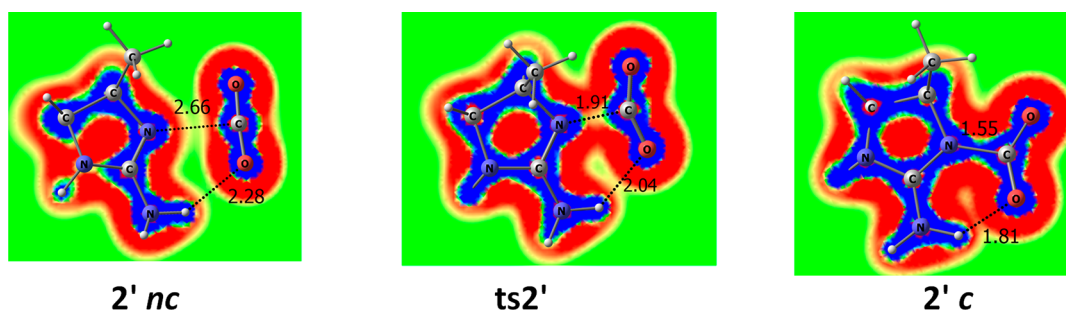

Figure 5. Laplacian of the electron density plotted on a plane that passes through the N-CO$_2$ bonded region. Red and blue colors indicate positive and negative regions, respectively.

characteristic electron-deficient C center of CO_2 in the MESP plot as a red strip around the C center. In contrast, the coordinate covalent N−C bond formed in **2′c** leads to an accumulation of large negative MESP around the O centers of CO_2 (blue region around O centers) as well as large positive

MESP over the imine molecule (red regions). The MESP analysis suggests that the characteristic electronic features of both imine and CO_2 are nearly unaffected by the **nc** bond formation, whereas the chemical nature of both the molecules drastically changes in the **c** complex due to the development of
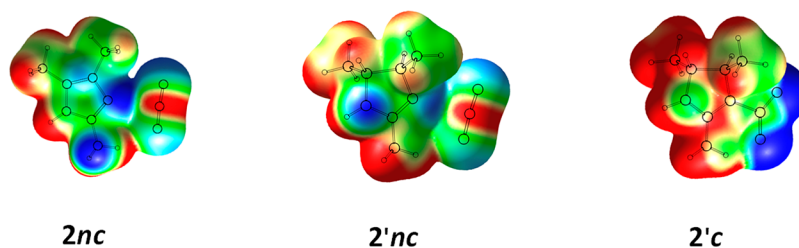
Figure 6. MESP textured on to 0.005 au electron density isosurface in (the color code ▮▮▮▮▮ from blue to red is from −0.05 to 0.05 au).
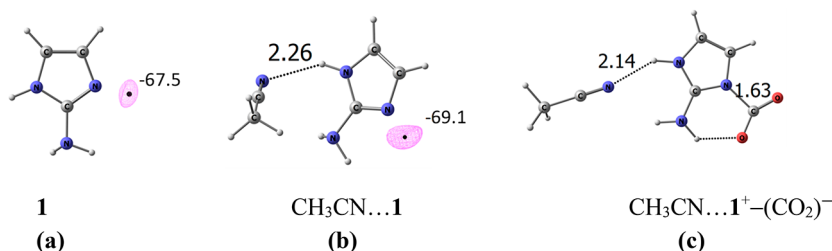

Figure 7. MESP minimum (kcal/mol) of (a) imine **1**, (b) hydrogen-bonded **1** with CH_3CN, and (c) covalent complex of **1** with CO_2 in the presence of CH_3CN. The distances are in angstroms.
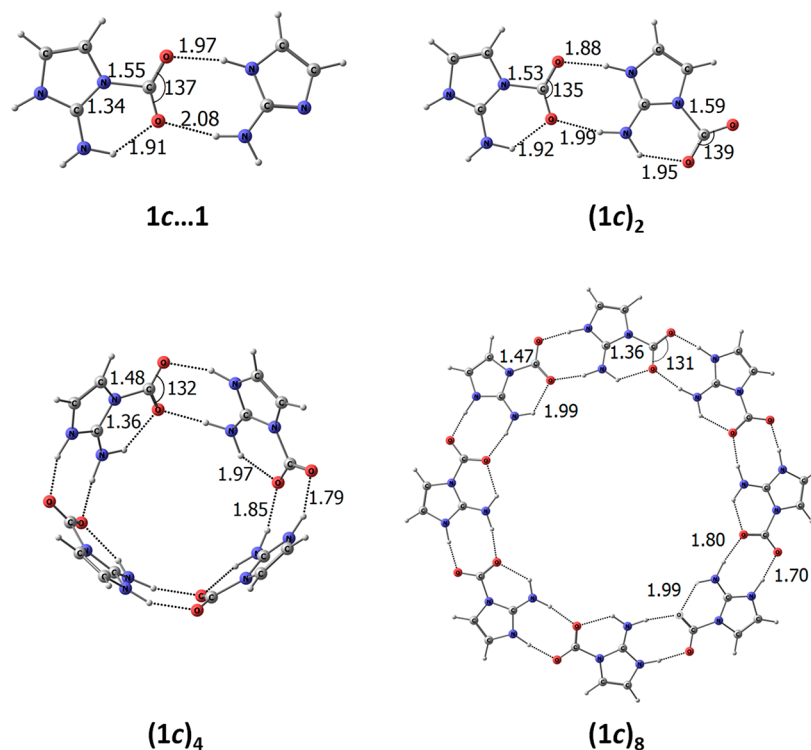

Figure 8. Molecular complexes and clusters of **1** with CO_2. Distances in angstroms and angles in degrees.

$XN^+−(CO_2)^−$ zwitterion character. Further, the NMR chemical shift values of the C on $(XN)(CO_2)$ complexes confirm the transformation of CO_2 into $(CO_2)^−$ in the **c** complexes (Table S5).

The higher electron-rich character of XN′ over XN (as per the V_{min} data given in Table 1) is previously invoked to explain the ability of the XN′ to yield a **c** complex with CO_2. The data in Figure 7 show that XN can also yield a **c** complex if it comes under the influence of a hydrogen bond with a solvent molecule such as acetonitrile. For instance, the hydrogen bond in $CH_3CN···1$ slightly enhances the negative character of V_{min} at the lone-pair region of imine N-center. Such a small

variation in the electronic feature of **1** promotes the formation of a covalent bond between **1** and CO_2. In other words, $CH_3CN···1^+−(CO_2)^−$ exists as a minimum on the potential energy surface, while $1^+−(CO_2)^−$ does not. The formation of $CH_3CN···1^+−(CO_2)^−$ explains a hitherto unknown phenomenon in chemical bonding theory—formation of a covalent bond due to the influence of a noncovalent bond. Formation of the complex **1c...1** (Figure 8) can also be regarded as an example for this scenario because **1c** does not exist if **1** is removed from **1c...1**.

Further, the binding energy per CO_2 ($E_{b/CO2}$) for the energy minimum **1nc**, −5.6 kcal/mol, is enhanced to −7.7 kcal/mol

for **1c**...**1**, which can be attributed to the NH⋯OC hydrogen bond interactions between **1c** and **1**. Similarly, the higher-order clusters $(1c)_2$, $(1c)_4$, and $(1c)_8$ (Figure 8) show a steady improvement in binding energy per CO_2 ($E_{b/CO2}$) due to the NH⋯OC interactions between adjacent **1c** pairs (Table 3).

Table 3. Energy Parameters (kcal/mol) for Molecular Complexes and Clusters of 1H-Imidazol-2-amine with CO_2

notation	E_b	ΔG	$E_{b/CO2}$	$\Delta G_{/CO2}$
1nc	−5.6	2.5	−5.6	2.5
1c...1	−7.7	12.3	−7.7	12.3
$(1c)_2$	−11.0	19.9	−5.5	9.9
$(1c)_4$	−77.4	1.7	−19.4	0.4
$(1c)_8$	−189.2	−25.8	−23.7	−3.2

The most stable $(1c)_8$ has $E_{b/CO2}$ of −23.7 kcal/mol, and most importantly, this cluster formation is exergonic by −3.2 kcal/mol as per the free energy change per CO_2 ($\Delta G_{/CO2}$). As the cluster size increases, a decreasing trend in both N−C bond distance and OCO angle is observed, which indicates the increasing covalent character of the N−C bond in higher-order clusters. The NH⋯OC interaction leads to the delocalization of the accumulated negative charge on the deformed CO_2 unit, which in turn improves the donating power of the imine lone pair (Figure S4) to yield only the covalent complex. These observations are valid for complexes of all other nonprimed and primed $(XN)(CO_2)$ systems, except **6** and **6′**. In all such octamer clusters, the $XN^+−(CO_2)^−$ units adopt nearly a planar arrangement (Figure S5). Unlike other systems, **6** and **6′** cannot operate through double NH⋯OC interactions to support higher-order clusters. The cooperativity effect is very high for the octamer cluster, and this can be verified from the tremendous increase in the magnitude of $E_{b/CO2}$ data (Table 4, Table S6) compared to that of the monomer $(XN)(CO_2)$ complexes.

Table 4. Energy Parameters (kcal/mol) for $(XN^+−(CO_2)^−)_8$ Clusters

notation	E_b	ΔG	$E_{b/CO2}$	$\Delta G_{/CO2}$
$(1c)_8$	−189.2	−25.8	−23.7	−3.2
$(1′c)_8$	−243.5	−80.0	−30.4	−10.0
$(2c)_8$	−191.4	−29.9	−23.9	−3.7
$(2′c)_8$	−247.0	−82.2	−30.9	−10.3
$(3c)_8$	−136.9	26.6	−17.1	3.3
$(3′c)_8$	−168.6	−6.4	−21.1	−0.8
$(4c)_8$	−188.7	−22.1	−23.6	−2.8
$(4′c)_8$	−191.4	−27.5	−23.9	−3.4
$(5c)_8$	−116.7	47.8	−14.6	6.0
$(5′c)_8$	−165.2	−1.5	−20.7	−0.2
$(7c)_8$	−170.3	−3.3	−21.3	−0.4
$(7′c)_8$	−219.1	−53.9	−27.4	−6.7

The interaction of CO_2 with guanidine and related compounds in the process of CO_2 capture and conversion has been investigated during the past two decades. The compounds 1,5,7-triazabicyclo [4.4.0]dec-5-ene (TBD), 7-methyl-1,5,7-triazabicyclo[4.4.0]dec-5-ene (MTBD), tetramethylguanidine (TMG), and 1,8-diazabicyclo[5.4.0]undec-7-ene (DBU) are a few of the important guanidine derivatives widely studied for CO_2 capture.[60−62] Hence we also studied the interaction of the experimentally proven imine systems like

TBD, DBU, and their derivatives with a CO_2 molecule (Figure S10). TBD (**8′**) and its unsaturated version (**8**) have given the **nc** complex as the minimum-energy structure and the **c** complex as a higher-energy isomer (Table S9). In the case of DBU derivatives, **9′** and its unsaturated version **9** have given only **nc** complexes with CO_2, while **10** & **10′** have given both **nc** and **c** complexes. Similar to **6** and **6′**, a planar arrangement of the zwitterion units to support higher-order clusters is difficult for these imine systems due to the possibility of only one NH⋯OC interaction between adjacent units. These results suggest that, in comparison to the molecular systems based on TBD or DBU, the molecular design patterns similar to the imines **1−7** and **1′−7′** are more efficient for CO_2 adsorption.

The formation of the octamer complex with only non-covalent interactions is also analyzed for the imine molecule **1**. One of the possible configurations of the octamer cluster is optimized by selecting a starting structure containing several N⋯CO_2 noncovalent interactions. This structure after 417 optimization cycles (Figures S6 & S7) converged to a configuration $(1nc)_8$ with several imine⋯imine noncovalent interactions (Figure 9) instead of N⋯CO_2 interactions. This shows that the imine−imine NH⋯N hydrogen bond is stronger than imine⋯CO_2 and CO_2...CO_2 noncovalent interactions. The E_b data for the formation of imine cluster $(1)_8$ (−120.6 kcal/mol) and that of $(CO_2)_8$ cluster[63] (−25.5 kcal/mol) support this point. Also the E_b value of −170.4 kcal/mol observed for $(1nc)_8$ indicates that its formation from $(1)_8$ and $(CO_2)_8$ is exothermic by 24.3 kcal/mol (Figure 8). The E_b of $(1c)_8$ is 49.1 kcal/mol higher in magnitude than $(1nc)_8$ suggesting that the additional stabilization of the former is due to 16 NH⋯OC intermolecular interactions (between **1c**) and eight NH⋯OC intramolecular interactions (Figure 9). The transformation of NH⋯OC intermolecular interactions to N⋯HOC interactions via the proton transfer from N to O is also modeled for $(1c)_4$. This reaction will generate the cluster of the carboxylic acid derivative of the N-heterocycle (Figure S9). Such a cluster is 23.1 kcal/mol less stable than $(1c)_4$. However, in the case of octamer, all attempts to optimize the acid cluster have converged to the zwitterionic cluster $(1c)_8$. These results suggest that the captured CO_2 by **1** is preserved in the cluster with anionic character and that the system resists the conversion of the CO_2 to the acid.

The $(1c)_8$ cluster, a zwitterionic $(XN^+−(CO_2)^−)_8$ system composed of several inter- and intramolecular NH⋯OC interactions, is expected to show large positive cooperativity. Although $(1c)_8$ is composed of zwitterion units $XN^+−(CO_2)^−$ (**1c***—the geometry of **1c** in the cluster), the stable form of the monomer is the **nc** complex **1nc**. The sum of the difference between the energy of **1nc** and the energy of each unit of $XN^+−(CO_2)^−$ in $(1c)_8$ can be considered as the deformation energy ($E_{def-oct}$) associated with the octamer formation. The $E_{def-oct}$ 118.0 kcal/mol suggests that changing the structure from **1nc** to **1c*** requires 14.75 kcal/mol energy per monomer. The NH⋯OC intramolecular interaction in **1c*** is also accounted here. The conversion of eight **1nc** to $(1c)_8$ is exothermic by −165.6 kcal/mol meaning that the total stabilizing interaction (E_S) in the cluster due to the eight deformed species **1c*** is −283.6 kcal/mol (Figure S8). The pairwise interaction energy (E_p) between each pair of **1c*** in the octamer is also calculated (Tables S7 & S8), which showed stabilizing interaction for every pair. The adjacent pairs showed the highest stabilization of −25.9 kcal/mol due to two NH⋯OC interactions, while the rest of the pairs showed E_p in the
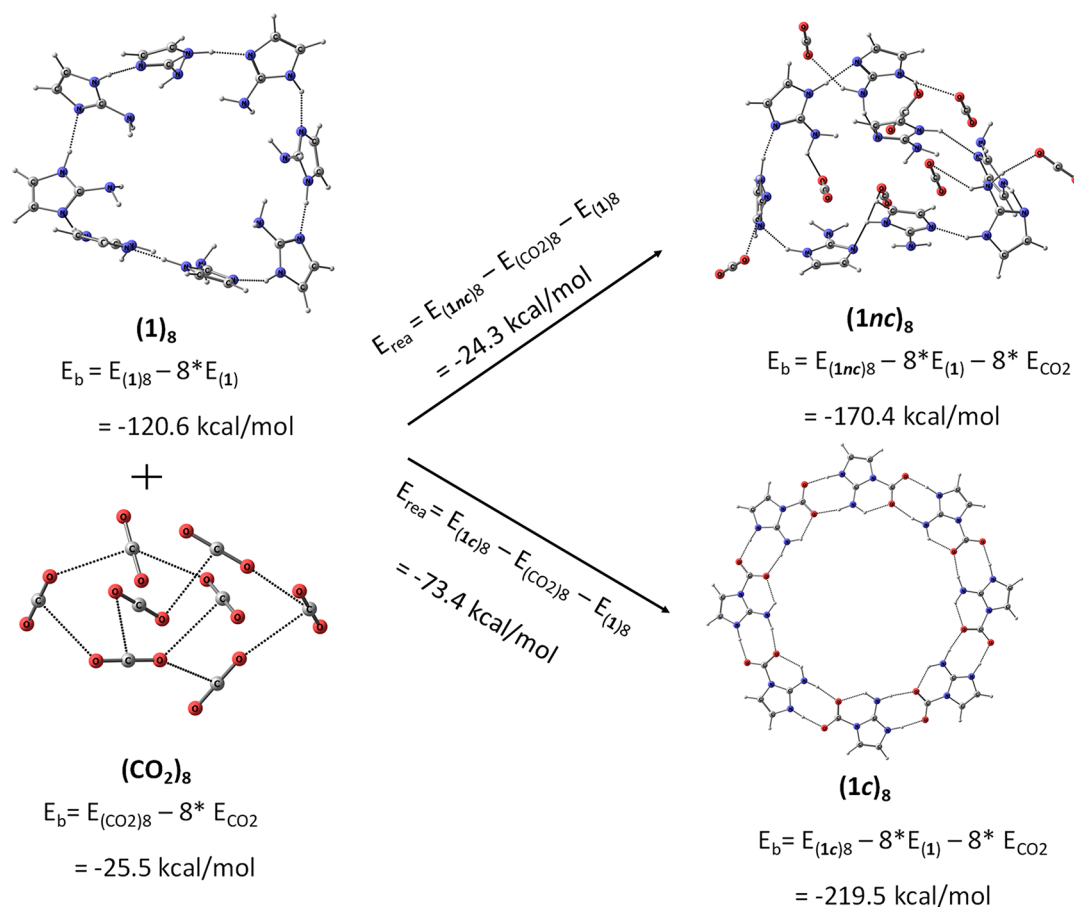
Figure 9. Octamer clusters of imine **1**, CO_2, and imine-CO_2 systems. The binding energy (E_b) and the energy of formation (E_{rea}) are given (in kcal/mol).

range from -0.5 to -2.2 kcal/mol. The total pairwise interaction energy $\sum E_p$ is found to be -232.3 kcal/mol, which is 51.2 kcal/mol less in magnitude compared to E_S, which can be attributed as the positive cooperativity effect (18%) due to the octamer assembly. Thus it is clear that, in addition to the pairwise interaction energy or the hydrogen bonding energy, a substantial degree of cooperativity effect is involved in the stabilization of the octamer complex.

The negative entropy factor associated with the cluster formation (assembly of 16 molecular units) is easily overcome by the thermodynamic stabilization due to high positive cooperativity in many cases, and the process becomes exergonic in nature for the octamer complexes except **3c** and **5c**. Among the different octamer clusters studied, **1′**, **2′**, and **7′** show the best E_{b/CO_2}, and they are proposed as promising systems for cooperative CO_2 capture and conversion.

CONCLUSIONS

This research has shown that the interaction of imine systems XN with CO_2 results in the formation of XN···CO_2 complexes in the noncovalent territory. With a slight improvement in the electronic density of the imine lone pair, the more saturated XN′ systems showed N−C bonding interactions in the covalent territory to yield zwitterionic $XN^+-(CO_2)^-$ complexes. This zwitterionic complex is identified as the bond stretch isomer of XN···CO_2. The bond stretch isomerism occurs through a **ts**, which is proposed as the boundary crossing point for the noncovalent and covalent bond

territories. The zwitterionic $(XN^+-(CO_2)^-)_n$ cluster formation is observed for all types of XN imines, wherein both intra- and intermolecular NH···OC noncovalent interactions provided additional stabilization to the cluster. These cooperative interactions enhance the N−C coordinate covalent bond, and the cluster is devoid of any N···C noncovalent interactions. Transforming eight XN···CO_2 systems to one covalent octamer cluster $(XN^+-(CO_2)^-)_8$ led to a fivefold increase in the binding energy, which is attributed to the large cooperativity effect associated with N−C covalent and NH···OC non-covalent interactions, whereas the corresponding noncovalent cluster $(XN\cdots CO_2)_8$ showed significantly lower binding energy than the covalent cluster. The pairwise interaction energy for each monomer pair in the covalent cluster is stabilizing in nature, while the total stabilization of the cluster exceeded the total pairwise interaction energy by 18% (51.2 kcal/mol), which is nearly the same as the energy difference between the noncovalent and covalent octamer clusters. This result proves that the covalent cluster formation is truly driven by positive cooperativity. Moreover, many XN systems showed an exergonic nature for the cluster formation up to octamer. The favorable energetics and the carboxylate character developed for CO_2 in the zwitterionic clusters suggest that many XN systems are highly promising molecules for CO_2 capture.

Though the noncovalent to covalent boundary crossing problem is addressed only for the imines and CO_2 combinations, one may visualize that many such noncovalent to covalent bonding territory crossovers may have happened

during the origin of life when small molecules were reacted to give larger ones. A noteworthy example is the formation of $CH_3CN\cdots\mathbf{1}^+-(CO_2)^-$ complex, which explains a hitherto unknown phenomenon in chemical bonding theory—formation of a covalent bond due to the influence of a noncovalent bond. The previous studies on the transformation of the weak hydrogen or tetrel bonds into strong covalent bonds also support this crossover trend in chemical bonding. The transition state (**ts**) structures identified in this study stand as the demarcating point for such a crossover from weak noncovalent to strong covalent bonding territory.

■ ASSOCIATED CONTENT

Ⓢ Supporting Information

The Supporting Information is available free of charge at https://pubs.acs.org/doi/10.1021/acs.jpca.2c03221.

> IUPAC names of imines, optimized geometries, QTAIM data, NMR data, MESP data, energy data, and Cartesian coordinates of optimized geometries (PDF)

■ AUTHOR INFORMATION

Corresponding Authors

Cherumuttathu H. Suresh − *Chemical Sciences and Technology Division, CSIR− National Institute for Interdisciplinary Science and Technology, Thiruvananthapuram 695 019 Kerala, India; Academy of Scientific & Innovative Research (AcSIR), Ghaziabad 201 002, India;* ⓞ orcid.org/0000-0001-7237-6638; Email: sureshch@gmail.com

Henry F. Schaefer, III − *Center for Computational Quantum Chemistry, University of Georgia, Athens 30602 Georgia, United States;* ⓞ orcid.org/0000-0003-0252-2083; Email: ccq@uga.edu

Author

Sebastian Anila − *Chemical Sciences and Technology Division, CSIR− National Institute for Interdisciplinary Science and Technology, Thiruvananthapuram 695 019 Kerala, India; Academy of Scientific & Innovative Research (AcSIR), Ghaziabad 201 002, India*

Complete contact information is available at:
https://pubs.acs.org/10.1021/acs.jpca.2c03221

Notes

The authors declare no competing financial interest.

■ ACKNOWLEDGMENTS

■ REFERENCES

(1) Frenking, G.; Shaik, S. *The chemical bond: fundamental aspects of chemical bonding;* John Wiley & Sons: Germany, 2014.

(2) McNaught, A. D.; Wilkinson, A. *Compendium of chemical terminology;* Blackwell Science: Oxford, UK, 1997.

(3) Zhao, L. L.; Pan, S.; Holzmann, N.; Schwerdtfeger, P.; Frenking, G. Chemical Bonding and Bonding Models of Main-Group Compounds. *Chem. Rev.* **2019**, *119*, 8781−8845.

(4) Zhao, L. L.; von Hopffgarten, M.; Andrada, D. M.; Frenking, G. Energy decomposition analysis. *Wiley Interdiscip. Rev.-Comput. Mol. Sci.* **2018**, *8*, 37.

(5) Landis, C. R.; Hughes, R. P.; Weinhold, F. Bonding Analysis of $TM(cAAC)_2$ (TM = Cu, Ag, and Au) and the Importance of Reference State. *Organometallics* **2015**, *34*, 3442−3449.

(6) Weinhold, F.; Landis, C. R.; Glendening, E. D. What is NBO analysis and how is it useful? *Int. Rev. Phys. Chem.* **2016**, *35*, 399−440.

(7) Esterhuysen, C.; Frenking, G. The nature of the chemical bond revisited. An energy partitioning analysis of diatomic molecules E_2 (E = N-Bi, F-I), CO and BF. *Theor. Chem. Acc.* **2004**, *111*, 381−389.

(8) Lein, M.; Frenking, G. *Theory and applications of computational chemistry: the first 40 years;* Elsevier, Amsterdam, 2005; p 291.

(9) Kovacs, A.; Esterhuysen, C.; Frenking, G. The nature of the chemical bond revisited: An energy-partitioning analysis of nonpolar bonds. *Chem.-Eur. J.* **2005**, *11*, 1813−1825.

(10) Esterhuysen, C.; Frenking, G. The nature of the chemical bond revisited. An energy partitioning analysis of diatomic molecules E_2 (E = N-Bi, F-I), CO and BF. *Theor. Chem. Acc.* **2005**, *113*, 294−294.

(11) Krapp, A.; Bickelhaupt, F. M.; Frenking, G. Orbital overlap and chemical bonding. *Chem.-Eur. J.* **2006**, *12*, 9196−9216.

(12) Frenking, G.; Krapp, A. Unicorns in the world of chemical bonding models. *J. Comput. Chem.* **2007**, *28*, 15−24.

(13) Zhao, L. L.; Hermann, M.; Schwarz, W. H. E.; Frenking, G. The Lewis electron-pair bonding model: modern energy decomposition analysis. *Nat. Rev. Chem.* **2019**, *3*, 48−63.

(14) Pan, S.; Frenking, G. A Critical Look at Linus Pauling's Influence on the Understanding of Chemical Bonding. *Molecules* **2021**, *26*, 14.

(15) Zhao, L.; Zhi, M.; Frenking, G. The strength of a chemical bond. *Int. J. Quantum Chem.* **2021**, e26773.

(16) Shaik, S. The Lewis legacy: The chemical bond - A territory and heartland of chemistry. *J. Comput. Chem.* **2007**, *28*, 51−61.

(17) Scheiner, S. Understanding noncovalent bonds and their controlling forces. *J. Chem. Phys.* **2020**, *153*, 140901.

(18) Scheiner, S. *Hydrogen bonding: a theoretical perspective;* Oxford University Press: New York, 1997.

(19) Gilli, G.; Gilli, P. *The nature of the hydrogen bond: outline of a comprehensive hydrogen bond theory;* Oxford University Press: Oxford, England, 2009.

(20) Bodesheim, D.; Kieslich, G.; Johnson, M.; Butler, K. T. Understanding the Balance of Entropy and Enthalpy in Hydrogen-Halide Noncovalent Bonding. *J. Phys. Chem. Lett.* **2020**, *11*, 3495−3500.

(21) Hunt, P. A. Quantum Chemical Modeling of Hydrogen Bonding in Ionic Liquids. *Top. Curr. Chem.* **2017**, *375*, 22.

(22) Berg, J. M.; Tymoczko, J. L.; Stryer, L. *Biochemistry;* New York: Freeman and Company: New York, 2002.

(23) Joy, J.; Akhil, E.; Jemmis, E. D. Halogen bond shortens and strengthens the bridge bond of [1.1. 1] propellane and the open form of [2.2. 2] propellane. *Phys. Chem. Chem. Phys.* **2018**, *20*, 25792−25798.

(24) Dereka, B.; Yu, Q.; Lewis, N. H.; Carpenter, W. B.; Bowman, J. M.; Tokmakoff, A. Crossover from hydrogen to chemical bonding. *Science* **2021**, *371*, 160−164.

(25) Liu, N.; Xie, X.; Li, Q.; Scheiner, S. Enhancement of the Tetrel Bond by the Effects of Substituents, Cooperativity, and Electric Field: Transition from Noncovalent to Covalent Bond. *ChemPhysChem* **2021**, *22*, 2305−2312.

(26) Bader, R. F. *Atoms in molecules: a quantum theory;* International series of monographs on chemistry; Oxford University Press: Oxford, England, 1990; Vol. 22.

(27) Popelier, P. L. A.; Aicken, F.; O'Brien, S. *Atoms in molecules;* Prentice Hall: Manchester, England, 2000.

(28) Jabłoński, M.; Palusiak, M. Basis set and method dependence in atoms in molecules calculations. *J. Phys. Chem. A* **2010**, *114*, 2240−2244.

(29) Bohórquez, H. J.; Boyd, R. J.; Matta, C. F. Molecular model with quantum mechanical bonding information. *J. Phys. Chem. A* **2011**, *115*, 12991−12997.

(30) Koch, U.; Popelier, P. L. Characterization of CHO hydrogen bonds on the basis of the charge density. *J. Phys. Chem.* **1995**, *99*, 9747−9754.

(31) Popelier, P. Characterization of a dihydrogen bond on the basis of the electron density. *J. Phys. Chem. A* **1998**, *102*, 1873−1878.

(32) Shaik, S.; Danovich, D.; Wu, W.; Hiberty, P. C. Charge-shift bonding and its manifestations in chemistry. *Nat. Chem.* **2009**, *1*, 443.

(33) Bohórquez, H. J.; Boyd, R. J.; Matta, C. F. Molecular model with quantum mechanical bonding information. *J. Phys. Chem. A* **2011**, *115*, 12991−12997.

(34) Anila, S.; Suresh, C. H. Guanidine as a strong CO2 adsorbent: a DFT study on cooperative CO2 adsorption. *Phys. Chem. Chem. Phys.* **2021**, *23*, 13662−13671.

(35) Zhao, Y.; Truhlar, D. G. The M06 suite of density functionals for main group thermochemistry, thermochemical kinetics, non-covalent interactions, excited states, and transition elements: two new functionals and systematic testing of four M06-class functionals and 12 other functionals. *Theor. Chem. Acc.* **2008**, *120*, 215−241.

(36) Frisch, M. J.; Trucks, G. W.; Schlegel, H. B.; Scuseria, G. E.; Robb, M. A.; Cheeseman, J. R.; Scalmani, G.; Barone, V.; Petersson, G. A.; Nakatsuji, H.; et al. *Gaussian 16,* rev. A.03; Gaussian, Inc.: Wallingford, CT, 2016.

(37) Boys, S. F.; Bernardi, F. d. The calculation of small molecular interactions by the differences of separate total energies. Some procedures with reduced errors. *Mol. Phys.* **1970**, *19*, 553−566.

(38) Sherrill, C. D.; Takatani, T.; Hohenstein, E. G. An assessment of theoretical methods for nonbonded interactions: Comparison to complete basis set limit coupled-cluster potential energy curves for the benzene dimer, the methane dimer, benzene− methane, and benzene− H₂S. *J. Phys. Chem. A* **2009**, *113*, 10146−10159.

(39) Hobza, P.; Müller-Dethlefs, K. *Non-covalent interactions: theory and experiment*; Royal Society of Chemistry: Cambridge, England, 2010.

(40) Mentel, Ł.; Baerends, E. Can the counterpoise correction for basis set superposition effect be justified? *J. Chem. Theory Comput.* **2014**, *10*, 252−267.

(41) Halkier, A.; Klopper, W.; Helgaker, T.; Jorgensen, P.; Taylor, P. R. Basis set convergence of the interaction energy of hydrogen-bonded complexes. *J. Chem. Phys.* **1999**, *111*, 9157−9167.

(42) Sherrill, C. D. *Counterpoise correction and basis set superposition error*; School of Chemistry and Biochemistry, Georgia Institute of Technology, 2010.

(43) Mohan, N.; Suresh, C. H. A molecular electrostatic potential analysis of hydrogen, halogen, and dihydrogen bonds. *J. Phys. Chem. A* **2014**, *118*, 1697−1705.

(44) Keith, T. *AIMAll (ver. 14.04. 17)*; TK Gristmill Software: Overland Park, KS, 2014.

(45) Gadre, S. R.; Shirsat, R. N. *Electrostatics of atoms and molecules*; Universities Press: Hyderabad, India, 2000.

(46) Politzer, P.; Truhlar, D. G. *Chemical applications of atomic and molecular electrostatic potentials: reactivity, structure, scattering, and energetics of organic, inorganic, and biological systems*; Springer Science & Business Media: New York, 2013.

(47) Ditchfield, R. Self-consistent perturbation theory of diamagnetism: I. A gauge-invariant LCAO method for NMR chemical shifts. *Mol. Phys.* **1974**, *27*, 789−807.

(48) Casabianca, L. B. Calculating nuclear magnetic resonance chemical shifts in solvated systems. *Magn. Reson. Chem.* **2020**, *58*, 611−624.

(49) Gibbs, G. V.; Cox, D.; Crawford, T. D.; Rosso, K. M.; Ross, N.; Downs, R. Classification of metal-oxide bonded interactions based on local potential-and kinetic-energy densities. *J. Chem. Phys.* **2006**, *124*, 084704.

(50) Kumar, P. S. V.; Raghavendra, V.; Subramanian, V. Bader's theory of atoms in molecules (AIM) and its applications to chemical bonding. *J. Chem. Sci.* **2016**, *128*, 1527−1536.

(51) Stohrer, W. D.; Hoffmann, R. Electronic structure and reactivity of strained tricyclic hydrocarbons. *J. Am. Chem. Soc.* **1972**, *94*, 779−786.

(52) Stohrer, W. D.; Hoffmann, R. Bond-stretch isomerism and polytopal rearrangements in $(CH)_5^+$, $(CH)^{5-}$, and $(CH)_4CO$. *J. Am. Chem. Soc.* **1972**, *94*, 1661−1668.

(53) Jean, Y.; Lledos, A.; Burdett, J. K.; Hoffmann, R. Bond-stretch isomerism in transition-metal complexes. *J. Am. Chem. Soc.* **1988**, *110*, 4506−4516.

(54) Parkin, G. Bond-stretch isomerism in transition metal complexes: a reevaluation of crystallographic data. *Chem. Rev.* **1993**, *93*, 887−911.

(55) Rohmer, M.-M.; Strich, A.; Bénard, M.; Malrieu, J.-P. Metal−Metal Bond Length Variability in $Co_3(dipyridylamide)_4Cl_2$: Bond-Stretch Isomerism, Crystal Field Effects, or Spin Transition Process? A DFT Study. *J. Am. Chem. Soc.* **2001**, *123*, 9126−9134.

(56) Clérac, R.; Cotton, F. A.; Daniels, L. M.; Dunbar, K. R.; Murillo, C. A.; Wang, X. Tuning the Metal−Metal Bonds in the Linear Tricobalt Compound $Co_3(dpa)_4Cl_2$: Bond-Stretch and Spin-State Isomers. *Inorg. Chem.* **2001**, *40*, 1256−1264.

(57) Comba, P.; Kerscher, M.; Merz, M.; Müller, V.; Pritzkow, H.; Remenyi, R.; Schiek, W.; Xiong, Y. Structural Variation in Transition-Metal Bispidine Compounds. *Chem.-Eur. J.* **2002**, *8*, 5750−5760.

(58) Labinger, J. A. Bond-stretch isomerism: a case study of a quiet controversy. *C. R. Chim.* **2002**, *5*, 235−244.

(59) Di Nicola, F. P.; Lanzi, M.; Marchetti, F.; Pampaloni, G.; Zacchini, S. Is bond stretch isomerism in mononuclear transition metal complexes a real issue? The misleading case of the MoCl5/tetrahydropyran reaction system. *Dalton Trans.* **2015**, *44*, 12653−12659.

(60) Pereira, F. S.; deAzevedo, E. R.; da Silva, E. F.; Bonagamba, T. J.; da Silva Agostini, D. L.; Magalhaes, A.; Job, A. E.; Perez Gonzalez, E. R. Study of the carbon dioxide chemical fixation-activation by guanidines. *Tetrahedron* **2008**, *64*, 10097−10106.

(61) Heldebrant, D. J.; Jessop, P. G.; Thomas, C. A.; Eckert, C. A.; Liotta, C. L. The reaction of 1, 8-diazabicyclo [5.4. 0] undec-7-ene (DBU) with carbon dioxide. *J. Org. Chem.* **2005**, *70*, 5335−5338.

(62) Rether, C.; Sicking, W.; Boese, R.; Schmuck, C. Self-association of an indole based guanidinium-carboxylate-zwitterion: formation of stable dimers in solution and the solid state. *Beilstein J. Org. Chem.* **2010**, *6*, 3.

(63) Yeole, S. D.; Sahu, N.; Gadre, S. R. Structures, energetics and vibrational spectra of CO_2 clusters through molecular tailoring and cluster building algorithm. *Phys. Chem. Chem. Phys.* **2012**, *14*, 7718−7723.